



HAL
open science

Crustal deformation at Ambrym (Vanuatu) imaged with satellite geodesy: constraints on magma storage, migration, and outgassing

Tara Shreve

► To cite this version:

Tara Shreve. Crustal deformation at Ambrym (Vanuatu) imaged with satellite geodesy: constraints on magma storage, migration, and outgassing. *Volcanology*. Institut de Physique du Globe de Paris; Université de Paris, 2020. English. NNT: . tel-03171509

HAL Id: tel-03171509

<https://theses.hal.science/tel-03171509>

Submitted on 19 Mar 2021

HAL is a multi-disciplinary open access archive for the deposit and dissemination of scientific research documents, whether they are published or not. The documents may come from teaching and research institutions in France or abroad, or from public or private research centers.

L'archive ouverte pluridisciplinaire **HAL**, est destinée au dépôt et à la diffusion de documents scientifiques de niveau recherche, publiés ou non, émanant des établissements d'enseignement et de recherche français ou étrangers, des laboratoires publics ou privés.

UNIVERSITÉ DE PARIS



Thèse préparée à l'Institut de Physique du Globe de Paris
École doctorale STEP'UP - ED560
Équipe de Tectonique et Mécanique de la Lithosphère

Crustal deformation at Ambrym (Vanuatu) imaged with satellite geodesy: constraints on magma storage, migration, and outgassing

par
Tara Shreve

présentée et soutenue publiquement le 8 décembre 2020

Thèse de doctorat des Sciences de la Terre et de l'Environnement
Spécialité: Géophysique
dirigée par Raphaël Grandin & Jean-Christophe Komorowski

Juliet Biggs	Professor (University of Bristol)	Rapportrice
Clive Oppenheimer	Professor (University of Cambridge)	Rapporteur
Michael Poland	Scientist-in-Charge (Yellowstone Volcano Observatory, USGS)	Examinateur
Anne Le Friant	Directrice de recherche (CNRS - Université de Paris, IPGP)	Présidente du jury
Aline Peltier	Physicienne (Université de Paris, IPGP)	Invitée
Raphaël Grandin	Maître de Conférences (Université de Paris, IPGP)	Directeur de thèse
Jean-Christophe Komorowski	Physicien (Université de Paris, IPGP)	Co-directeur de thèse

Acknowledgments

“The stars may be large, but they cannot think or love; and these are qualities which impress me far more than size does.”

Frank Ramsey

More than anything, my PhD journey has taught me to value my support system. I am grateful to those who have provided me with their unwavering support over the years.

My advisors made this PhD possible, from the beginning to the end. I'd like to acknowledge Jean-Christophe Komorowski for sharing his enthusiasm and vivacity for volcanology, as well as the importance and difficulty of risk communication. I value our conversations, regardless of whether they took place in the classroom, the field, or over a glass of Ti' Punch. To Raphaël Grandin: you encouraged me since day one, and I cannot thank you enough. Not only did you take me on as your first PhD student as a primary advisor, you also took on a project that was in no way guaranteed. Neither of us knew what we might find, and we most certainly did not anticipate the events that transpired, which became the PhD's backbone. Although the PhD subject was, in some sense, a risk, it made the journey that much more fascinating. I am so thankful I had your curiosity, creativity, rigor, and humanity as a guide. Simply, thank you for sharing your time and knowledge— which you provided selflessly.

Within IPGP's community, the members of the Laboratoire de Tectonique et Mécanique de la Lithosphère provided me with many opportunities to learn beyond my PhD topic. This occurred during coffee break conversations, lab seminars, and field trips. The PhD students, postdocs, and engineers in the lab made daily life enjoyable. I looked forward to seeing you everyday— Benjamin Lauer, Chloé Seibert, Matthieu Ribot, Christelle Guilbaud, Jesus Muñoz, Roxane Tissandier, Tania Habel, Solène Antoine, Gino de Gelder, Arthur Delorme, Armel Menant, Liqing Jiao, Yacine Benjelloun. I always say that, once I leave Paris, I will miss France's food and wine the most. That's not completely true— above all, I will miss spending time with you. Laurent Pinon, thank you for facilitating the administrative duties needed to undertake field work and conferences. Your work is greatly appreciated, and it was always a pleasure to see you around the lab. I'd also like to acknowledge Jean-Bernard De Chabalier for his camaraderie and patience during my first GPS campaign in Guadeloupe. Thank you Francisco Delgado for sharing your knowledge and interest in volcano geodesy with me over the past 2 years of my PhD. I am so happy with the collaboration we have

developed, including your (often difficult) questions, which allowed me to grow as a scientist. In the Laboratoire Systèmes Volcaniques, I'm grateful for conversations with Marina Rosas-Carbajal, Giulia Del Manzo, and Mathilde Henri. Thank you to Patrick Allard; our discussion at the start of my PhD about your "beloved" volcano Ambrym amplified my fascination with this volcanic system.

Outside of IPGP, I had the grand pleasure of collaborating with Delphine Smittarello, Valérie Cayol, and Virginie Pinel. Over the course of my PhD, Delphine, you greatly motivated me with your openness, as well as your drive. Thank you to all of those who contributed their time and efforts to analyze the 2018 Ambrym eruption: Marie Boichu, Bernard Peltier, Yves Moussallam, Valérie Ballu, Frédérique Leclerc, Martin Vallée, Nicolas Henriot, Pierre Lebellegard, as well the Vanuatu Metereology and Geohazards Department.

I'd also like to acknowledge my jury, composed of Dr. Juliet Biggs, Dr. Clive Oppenheimer, Dr. Michael Poland, Dr. Anne Le Friant, and Dr. Aline Peltier. You brought this PhD to a close in a profound way. Our conversations, driven by your thoughtful questions, provided the opportunity to reflect on almost 4 years of work, and to place my work in a broader context. The defense also allowed me to assess weaknesses I would like to address in the future, a necessary exercise at any step of one's career. Thank you also to the members of my comité de thèse, who provided much appreciated advice and insights: Antoine Lucas, Raphaël Pik, and Aline Peltier.

All of this being said, my PhD journey did not stop in the laboratory. I am grateful for those with whom I spent hours at Arkose or on the Fountainebleau boulders—Delphine Tardif, Benjamin Wheeler, Erica Lieberman, Meredith Sopher. Our time together developed into cherished friendships that I hold close to my heart. I hope we have many more adventures to come. Thanks to Delphine Tardif, Marie Troyano, and Tatiana Savranskaia for an incredible road trip. Your inquisitiveness led me to rediscover my own country. Thank you Ariel Matalon for being a steadfast support in this past year and for letting me into your world. Camila Bramorski, without a doubt your curiosity led me to view the world with more wonder than ever before. I think the world of the time we spent together. To my friends abroad—Alex Greenwald, Gwen Tom, Kat Marjanovic, Denis Sgouros, Michi Wenner—although far apart, somehow it never felt too far. Love you all so much. To Rick Wunderman, thank you for introducing me to this fascinating field and for your enthusiastic encouragement. This journey began because of you.

Finally, I need to acknowledge my family, who provided me with more blessings than I can count. Aaron, you never fail to make me laugh, and I love knowing I have you on my side in all I do. Dad, thank you for your sense of humor and discernment. I realize each day how you have shaped me into the person I am. Rock on 🖤. Mom, you've been my anchor.

I treasure our talks deeply, and appreciate our ability to discuss differing point of views, especially during a time when division can be so destructive. You have all my love, always.

Crustal deformation at Ambrym (Vanuatu) imaged with satellite geodesy: constraints on magma storage, migration, and outgassing

by
Tara Shreve

Abstract

Basaltic caldera-rift systems provide unique opportunities to study a range of volcanic processes, including lateral magma transport, caldera collapse, and magma replenishment. Some of the largest basaltic calderas in the world, however, are located in dangerous or difficult-to-access regions. In such regions, remote sensing measurements of ground deformation, degassing, and thermal anomalies offer alternative means to assess volcanic activity.

Ambrym, an exceptionally active, basaltic volcanic island in Vanuatu has undergone numerous episodes of ground deformation over the past 20 years. Since 2015, two eruptions have occurred within its 12 km wide caldera. The first event, a moderate-sized eruption in February 2015, occurred after more than 15 years of persistent degassing and lava lake activity, punctuated by intervals of quiescence. It activated a portion of the caldera-ring fault and drained a reservoir located ~ 4.1 km depth. The most recent event, which occurred in December 2018, was significantly larger. This event drained the main craters' lava lakes and intruded >0.4 km³ of magma into the SE rift zone. The dike travelled more than 20 km away from the main craters, and had an opening of >4 m at depth. Magma drainage from a central storage region caused widespread caldera subsidence and ring-fault activation, and resulted in the eruption of basaltic pumice offshore.

These two events confirm that Ambrym's caldera ring-faults are active structures. Ring-fault reactivation may contribute to continued deepening of Ambrym's large caldera, whose formation mechanism is contested. Some authors [Robin et al., 1993] propose that caldera ring-faults were formed by an initial Plinian eruption and subsequent phreatomagmatic eruptions. Ring-fault activation detected with Interferometric Synthetic Aperture Radar (InSAR) allows us to hypothesize that hundreds of moderate- to large sized dike intrusions may contribute to further deepening of the caldera by draining magma from one of Ambrym's numerous magma lenses.

Separate from these main eruptive events, we document two inter-eruptive episodes of fast subsidence measured with InSAR (2004 – 2007 and 2015 – 2017, ~ 10 cm year⁻¹). Neither of these time periods are associated with recorded eruptions. Inter-eruptive subsidence is challenging to interpret without additional constraints. Using the understanding gleaned

from the 2015 and 2018 eruptions, we investigate possible physical mechanisms explaining these deformation signals. We conclude that the 2004 – 2007 episode is most likely due to a dike intrusion, accompanied by depressurization of the shallow sill hydraulically connected to the lava lakes. This interpretation is drawn from the joint analysis of ground deformation, SO₂ gas emissions, and thermal anomalies. We then hypothesize that the 2015 – 2017 subsidence episode may be due to degassing-induced depressurization of a large (>10 km³) magmatic reservoir, using a theoretical model developed by [Girona et al. \[2014\]](#) to couple degassing and reservoir depressurization.

To investigate the role played by replenishment of the system, two periods of uplift have been identified. Variations in thermal anomalies and SO₂ degassing complement displacement measurements, allowing for more robust interpretations of the volcanic deformation episodes. At Ambrym, uplift during replenishment may be limited to time periods when the system is closed, such as after lava lake drainage in 2019 – 2020 and perhaps in 2007 – 2010, following the previously unreported diking event in 2005.

Remote sensing data has allowed us to analyse the activity of Ambrym volcano over the past two decades. By comparing Ambrym’s unrest with that of other calderas (Kīlauea, Bárðarbunga, Sierra Negra, etc.), the results obtained in this dissertation can further our understanding of basaltic caldera-rift systems and their underlying magmatic plumbing systems.

Key words: Remote sensing; volcanism; caldera; dike intrusion; lava lake; degassing

Déformation crustale à Ambrym (Vanuatu) imagée par la géodésie spatiale : contraintes sur le stockage, la migration de magma et le dégazage

par
Tara Shreve

Résumé

Les systèmes volcaniques rift-caldera basaltiques fournissent les conditions propices à l'étude de plusieurs processus volcaniques, comme le transport de magma, les effondrements de caldera et le remplissage magmatique. Certaines des plus grandes calderas dans le monde, cependant, sont situées dans des régions isolées dont l'accès peut être dangereux ou logistiquement complexe. La télédétection des déformations du sol, du dégazage et des anomalies thermiques, offre une alternative pour y suivre l'activité volcanique.

Ambrym, une île volcanique du Vanuatu isolée mais très active, a subi de nombreux épisodes de déformation du sol au cours des 20 dernières années. Depuis 2015, deux éruptions ont eu lieu à l'intérieur de sa caldera de 12 km de diamètre. La première éruption a eu lieu après 15 ans de dégazage passif et d'activité des lacs de lave. L'éruption la plus récente, en décembre 2018, a vidangé les lacs de lave des cratères sommitaux, provoquant l'intrusion d'un volume $>0.4 \text{ km}^3$ dans la zone de rift sud-est. Le dike engendré a parcouru une distance de plus de 20 km, et s'est ouvert de plus de 4 mètres en profondeur. La vidange du magma a produit une subsidence de la caldera à grande échelle, associée à une activation des failles bordant la caldera, et a alimenté une éruption sous-marine de ponces basaltiques. Une éruption plus modeste a eu lieu en février 2015, activant également une portion de la caldera, et extrayant du magma depuis une chambre située à une profondeur de $\sim 4.1 \text{ km}$.

Ces deux événements confirment que les failles bordières de la caldera d'Ambrym sont des structures actives. L'activité de ces failles contribue à la topographie de la caldera d'Ambrym, dont le mécanisme de formation est discuté (éruption Plinienne initiale à 2ka, suivie d'éruptions phréatomagmatiques). La détection d'une activation des failles de caldera par la géodésie spatiale nous permet de formuler l'hypothèse que des centaines d'intrusions de tailles modérées à grandes peuvent contribuer à un approfondissement de la caldera, en drainant le magma stocké temporairement sous la caldera d'Ambrym.

Outre ces deux événements éruptifs majeurs, nous mettons en évidence deux épisodes (2004 – 2007, 2015 – 2017) de subsidence rapide ($\sim 10 \text{ cm an}^{-1}$), mesurés par InSAR. Aucune de ces deux périodes n'est associée à une éruption répertoriée. A partir des informations

glanées au cours des éruptions de 2015 et 2018 (e.g., la profondeur des zones de stockage, le volume des intrusions, la relation entre l'activité éruptive et les lacs de lave), nous explorons les mécanismes physiques pouvant expliquer cette subsidence inter-éruptive. L'épisode de 2004 – 2007 est probablement associé à une intrusion de dike (en l'absence d'éruption), engendrant la dépressurisation d'un sill superficiel, hydrauliquement connecté aux lacs de lave. A partir d'un modèle théorique proposé par [Girona et al. \[2014\]](#), en couplant le dégazage passif (mesuré par spectroscopie satellitaire) et la dépressurisation du réservoir magmatique (déduite de la géodésie spatiale), nous proposons que l'épisode de 2015 – 2017 ait pour origine la dépressurisation d'un réservoir magmatique de grande taille ($>10 \text{ km}^3$). Par contraste, de courtes périodes de soulèvement pourraient être limité aux périodes de temps pendant lesquelles le système est fermé, par exemple en 2019 – 2020 après l'épisode de vidange des lacs de lave en 2018, et potentiellement en 2007 – 2010 à la suite d'un événement d'intrusion non répertorié en 2005.

En comparant les phases de regain d'activité d'Ambrym avec celles observées dans les autres systèmes rift-caldera basaltiques (Kīlauea, Bárðarbunga, Sierra Negra, etc.), les résultats obtenus dans cette dissertation permettent de mieux comprendre l'activité des lacs de lave, le développement de la caldera, les processus de déformation induits par le dégazage, le remplissage magmatique, et la géométrie et le fonctionnement des systèmes rift-caldera basaltiques.

Mots clés: Télédétection; volcanisme; caldera; intrusion de magma; lac de lave; dégazage



Contents

Acknowledgements	i
Abstract	iv
Résumé	vi
Table of Contents	viii
Roadmap	xiii
1 Regional introduction	1
1.1 Tectonic setting of the New Hebrides arc	1
1.1.1 Subduction/collision of D’Entrecasteaux Ridge (DER) and West Torres Massif (WTM)	1
1.1.2 Growth of the back-arc thrust belt (BATB)	4
1.1.3 Stress perturbation due to DER collision	6
1.2 Volcanism in the New Hebrides arc	10
1.2.1 MORB geochemical signatures	11
1.2.2 Tectonic influence on volcanism in the New Hebrides arc	13
1.3 Current understanding of Ambrym volcano	13
1.3.1 Volcanological characteristics	14
1.3.2 Historical eruptions	16
1.3.3 Passive degassing	18
1.3.4 Magma composition and storage conditions	18
1.3.5 Caldera formation	19
1.4 Focus questions	21
1.4.1 Question 1: How is Ambrym’s magmatic plumbing system organized?	22
1.4.2 Question 2: How did Ambrym’s caldera form and develop?	22
1.4.3 Question 3: What are the dynamics of Ambrym’s magmatic system?	22

2	Methods	25
2.1	Spaceborne SAR geodesy	25
2.1.1	Measuring small ground displacements: differential InSAR	27
2.1.2	Measuring large ground displacements: additional SAR methods	38
2.1.3	Current SAR satellite missions	40
2.1.4	Earth science applications	43
2.2	Geodetic inverse modelling	45
2.2.1	Defining the inverse problem	46
2.2.2	Choosing the appropriate analytical model	50
2.3	Complementary remote sensing methods	63
3	Magmatic architecture and dynamics of a basaltic caldera rift-zone system in a compressive tectonic setting	67
3.1	Scientific context	68
3.1.1	Rift zone dike intrusions	68
3.1.2	Driving stress of a lateral dike intrusion	71
3.1.3	Factors influencing the driving stress	71
3.1.4	What can we learn about the mechanisms driving a rift zone intrusion?	75
3.1.5	Magma transport in volcanic systems: additional considerations	75
3.2	Paper 1: “ <i>From prodigious volcanic degassing to caldera subsidence and quiescence at Ambrym (Vanuatu): the influence of regional tectonics</i> ”	76
4	Mechanical models of caldera ring-fault reactivation at a broad and shallow basaltic magmatic system	115
4.1	Scientific context	115
4.1.1	Caldera collapse	115
4.1.2	Caldera ring-fault activation	118
4.1.3	What can we learn about the threshold for caldera ring-fault reactivation?	122
4.2	Paper 2: “ <i>What triggers caldera ring-fault subsidence at Ambrym volcano? Insights from the 2015 dike intrusion and eruption</i> ”	123
5	Discussion	183
5.1	Organization of Ambrym’s magmatic plumbing system	183
5.1.1	Magma storage inferred from geodesy: evidence for a vertically extensive plumbing system	183

5.1.2	A candidate physical mechanism driving inter-eruptive subsidence: passive degassing	190
5.1.3	A broader view of the magmatic system provided by petrology	212
5.1.4	Synthesis of results from geodesy and petrology	216
5.2	Ambrym’s caldera: formation and long-term development	218
5.2.1	Ambrym’s disputed 2 ka Plinian eruption	218
5.2.2	Successive stages of caldera development at Ambrym	222
5.2.3	Episodic subsidence at other volcanic systems	224
5.2.4	Caldera fault reactivation: silicic vs. basaltic systems	226
5.3	Revisiting 20 years of volcanic activity using multisensor observations: Evidence for an unreported dike intrusion in 2005	230
5.3.1	2004 – 2009 deformation episode	231
5.3.2	Evidence for system repressurization	234
6	Conclusion and perspectives	239
6.1	Focus questions	239
6.1.1	Question 1: Ambrym’s vertically and laterally extensive magma plumbing system	239
6.1.2	Question 2: Episodic caldera subsidence and ring-fault reactivation at Ambrym	240
6.1.3	Question 3: Decadal fluctuations in Ambrym’s volcanic activity	240
6.2	Open questions	241
6.3	Next steps	242
6.4	Take home message	243
A	Classic Slip Inversion software: Analytical volcano source models	245
B	Lava dome growth at Ibu volcano from 2000 – 2018 (Molucca Islands, Indonesia)	263
B.1	Ibu volcano	263
B.2	Digital Elevation Models of dome growth	263
C	Paper 3: The 2018 unrest phase at La Soufrière of Guadeloupe (French West Indies) andesitic volcano: Scrutiny of a failed but prodromal phreatic eruption	269

D Degassing-induced depressurization model: Constant expansion and symbols	299
Bibliography	302

Roadmap

“If you [are] on a road for whatever reason, then that’s the road you should take.”

Graham Gladwell

The road leading to the conception of this dissertation was not direct. The original objective of this PhD project was to *"monitor remote equatorial and tropical volcanoes using multi-sensor spaceborne imagery and in situ geophysical data"*. I planned to apply interferometry synthetic aperture radar (InSAR) geodesy to several volcanically active regions—Vanuatu, the Molucca Islands (Indonesia) and Guadeloupe. These regions had yet to be studied in detail using InSAR geodesy, at least in part due to the inherent difficulty of InSAR measurements in tropical regions caused by heavy vegetation.

In December 2018, a year after diving into this project, one of the volcanoes of interest—Ambrym—erupted. This was the largest unrest episode the volcano had experienced in nearly a century, and the subject of the PhD quickly reoriented itself to focus on this exceptional event. This event, which may have been the culmination of more than 15 years of volcanic unrest, opened our eyes to the complexity— and intriguing nature — of Ambrym’s magmatic system.

Accordingly, this dissertation begins with a chapter introducing the region of interest (the New Hebrides arc). A regional focus is maintained to provide the reader with an adequate background of the tectonic and volcanological setting of Ambrym Island. Three focus questions are presented that will direct the discussion of the dissertation. A methods chapter follows, summarizing the state of the art of InSAR and geodetic modelling, focusing on the methods used throughout this dissertation. There is also a brief description of other volcano monitoring remote sensing methods that can be qualitatively integrated with geodesy. The next two chapters are studies on two separate eruptions at Ambrym (2018 and 2015), followed by a discussion chapter. Here, the results from the two previous chapters are combined to present an updated understanding of Ambrym’s magmatic system, caldera development, and system dynamics. The final chapter— the conclusions and perspectives— reflects on the focus questions presented in the introduction.

Before deciding to refocus this dissertation, I had the opportunity and pleasure to work on two additional volcanoes— Ibu (Indonesia) and La Soufrière (Guadeloupe). A brief summary of the results tracking Ibu’s growing lava dome are presented in Appendix B. I also had the opportunity to take part in a GNSS campaign at La Soufrière in Spring 2018, during which we

felt the island’s largest volcano-tectonic (VT) earthquake in more than 40 years. The “failed phreatic eruption” that occurred in April 2018 sparked a study led by Roberto Moretti, presented in Appendix C. Additional field work was cancelled due to the unprecedented events of 2020, confining billions worldwide. Nonetheless, this experience in Guadeloupe, coupled with the near real-time analysis of Ambrym’s 2018 unrest episode, reaffirmed my decision to apply geodetic techniques to answer the complex and challenging questions posed by volcanic systems.

Chapter 1

Regional introduction

The goal of this dissertation is to better understand the storage and movement of magma beneath Ambrym volcano, a basaltic volcanic island located in the New Hebrides (NH) arc (Vanuatu). To provide context for Ambrym’s volcanic activity, we will briefly describe the tectonics of the arc region. The tectonic structures of the central NH subduction zone reflect the complex stress regime which influence magma ascent through the crust, as well as magma migration and eruption at the surface.

1.1 Tectonic setting of the New Hebrides arc

1.1.1 Subduction/collision of D’Entrecasteaux Ridge (DER) and West Torres Massif (WTM)

The NH arc is a 1500 km-long arc where the Indo-Australian plate subducts beneath the North Fiji Basin [Isacks et al., 1981, Collot et al., 1985, Louat et al., 1988, Lagabrielle et al., 2003] (See Figure 1-1). In the Late Miocene, a subduction polarity reversal caused the extinction of the north-east vergent Vitiaz Trench (See Figure 1-2) [Chase, 1971, Kroenke, 1971, Falvey, 1971, Auzende et al., 1988, 1995]. This reversal resulted in the opening of the North Fiji back-arc basin, which rifted the active NH arc away from the extinct Vitiaz arc. According to Greene and Collot [1994], around 2 – 3 Ma, another extinct Eocene-Oligocene volcanic arc, the D’Entrecasteaux Ridge (DER), began colliding with the NH arc (See Figure 1-2). Other studies propose that subduction/collision of the DER, which can be divided further into the northern D’Entrecasteaux Ridge and the southern D’Entrecasteaux seamount chain, began soon after the subduction polarity reversal, in the Late Miocene [Greene et al., 1988, Meffre and Crawford, 2001]. Subsequently, as subduction proceeded to “consume” the Indo-Australian plate, at around 0.7 Ma, a plateau called the West Torres Massif (WTM) also entered the trench and began subducting/colliding with the NH arc to the north of the DER (See Figure 1-1)[Meffre and Crawford, 2001].

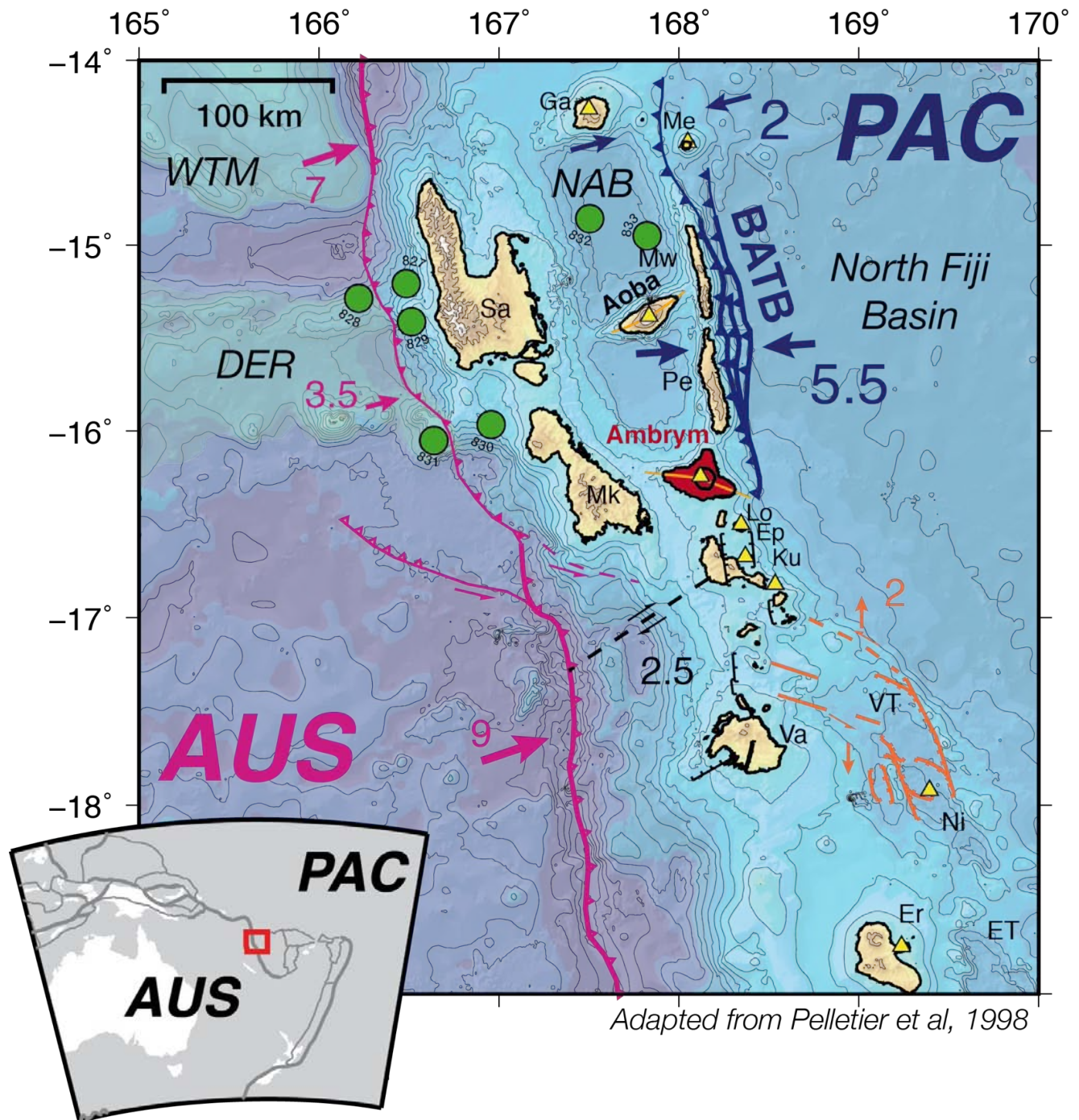


Figure 1-1: **Tectonic framework of the central NH arc.** The D'Entrecasteaux Ridge (DER) and West Torres Massif (WTM), located on the Indo-Australian (AUS) plate, are colliding with the New Hebrides (NH) arc (pink). Convergence rates are shown in pink. These structures are subducting beneath the North Fiji basin, located on the Pacific (PAC) plate. The collision results in shortening accommodated by growth of the back-arc thrust belt (BATB). Arrows and numbers indicate relative velocities (in cm year^{-1} from Bergeot et al. [2009]) across the BATB (blue) and Vate trough (VT, orange). Yellow triangles are active volcanoes, orange lines indicate volcanic rift zones, and green circles show the drilling sites of Briquieu et al. [1994]. NAB: North Aoba Basin; Va: Vate; Ku: Kuwae; Ep: Epi; Lo: Lopevi; Mk: Malekula; Sa: Santo; Pe: Pentecost; Mw: Maewo; Ga: Gaua; Me: Mere Lava; Ni: Nifonea; Er: Erromango; ET: Erromango Trough. Adapted from Pelletier et al. [1998].

The collision of both the DER and WTM in the central portion of the NH arc results in strong interplate coupling and compression along the width of the arc [Taylor et al., 1995, Bergeot et al., 2009, Taylor et al., 2005, Collot et al., 1985], and gives rise to the central arc’s distinct characteristics. The NH subduction zone slab dips steeply ($60\text{-}70^\circ$) towards the east. However, the subduction interface has a shallower dip in the central portion of the arc near the DER collision, as determined using earthquake locations and focal mechanisms from local and global catalogues (See Figure 1-3) [Baillard et al., 2015, Foix et al., 2019]. This change in dip is hypothesized to be due to the buoyant DER resisting subduction into a denser asthenosphere [Baillard et al., 2015]. The convergence rate is also significantly slowed in the central portion of the arc (35 mm year^{-1} versus 90 mm year^{-1} to the south, Figure 1-1 [Calmant et al., 2003, Pelletier et al., 1998, Bergeot et al., 2009]). Meffre and Crawford [2001] propose that the convergence rate began to decrease no earlier than 1 Ma; if it began earlier, the arc would be notably offset. Therefore, the slowed convergence may be due to the onset of collision of the West Torres Massif. In the region where the DER collides with the NH arc, the trench is uplifted and a backthrust has developed. As a result, the backstop is tilted, resulting in an uplift of the forearc and subsidence of the arc volcanoes [Taylor et al., 1980, Collot et al., 1985]. This tilting can be evidenced by the topography of Santo and Malekula Islands (See Figure 1-1). Collision-induced compression also causes uplift of the arc-backarc transition [Calmant et al., 2003]. The uplifted regions, together with the arc volcanoes, form three parallel island chains [Mitchell and Warden, 1971, Carney and MacFarlane, 1982] (See Figure 1-1).

Both coseismic and nonseismic tectonic uplift have been measured using emerged coral heads. Similar to trees, corals have annual growth bands, which record when a portion of the coral head emerges from the water and dies [Scoffin et al., 1978, Stoddart and Scoffin, 1979]. A coherence exists between the regional topography, the regions uplifted during the Late Quaternary (measured from coral reef terraces off the west coast of Santo, with maximum rates of $0.6 - 0.7\text{ cm year}^{-1}$ [Taylor et al., 1980]) and those with coral heads emerged since 1946 [Taylor et al., 1987]. By comparing uplift rates over various lengths of time, Taylor et al. [1987] found that the forearc is segmented into four blocks (See Figure 1-3). Each block has a different response to the DER collision, possibly indicating differences in plate coupling based on the locations of the topographic highs of the D’Entrecasteaux Ridge [Taylor et al., 1987]. Similar along-strike segmentation has been proposed to reflect differences in the phases of material underplating in a context of cyclic uplift-then-subsidence in Chile [Menant et al., 2020].

The DER collision results in permanent (inelastic) deformation and shortening (uplift and eastward motion) of the central arc. However, on short time scales (tens to hundreds of years), this deformation can be difficult to discriminate from surface deformation due to mainly elastic, interseismic strain accumulation on the main thrust zone of the subduction interface [Davies and House, 1979]. According to the back-slip model of Savage [1983], nearly all of this elastic strain is released during coseismic events, resulting in no net deformation. Using this model, Taylor et al. [2005] concluded that permanent deformation is instead due to shortening induced by the motion of seamounts during coseismic events, because the plate is “permanently” locked at depths of $< 15\text{ km}$ (See Figure 1-4). In fact, seismic hazard may be dominated by intermediate-to-deep earthquakes (See Figure 1-5). Lack of megathrust earthquakes in historical data (largest shallow earthquake was M7.9 in 1903 [Centre, 2020])

may suggest moderate potential for release of elastic strain. Instrumental seismicity since 1970 may also be interpreted as being compatible with $M_{max} < 8.0$ [Suckale and Grünthal, 2009]. On even shorter timescales, such as over the past 15 years, GPS measurements of interseismic deformation south of the DER can also be explained by locking of the shallow (< 15 km depth) portion of the subduction interface. However, the inelastic component of interseismic deformation (i.e., from GPS measurements facing the DER) induced by the ridge collision and back-arc thrusting has yet to be fully modelled [Bergeot et al., 2009].

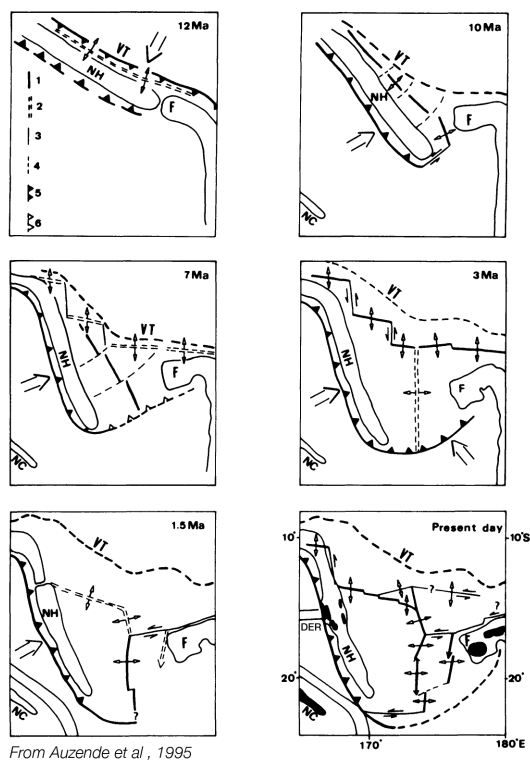


Figure 1-2: **Geodynamic evolution of NH arc.** The geodynamic evolution of the North Fiji Basin and New Hebrides arc over the past 12 million years. Thick solid lines (1) are active ridge axes, double dashed lines (2) are incipient ridge axes, thin solid lines (3) are transform faults, dashed lines (4) are flowlines, black triangles (5) are active subduction zones, and white triangles (6) are incipient subduction zones. F: Fiji Platform; NC: New Caledonia; NH: New Hebrides arc; VA: Vitiiaz trench; DER: D'Entrecasteaux Ridge. From Auzende et al. [1995].

1.1.2 Growth of the back-arc thrust belt (BATB)

While the forearc is being tilted and uplifted by the collision, the eastward motion of the central segment (compared to the rest of the arc) is accommodated along the back-arc thrust belt (BATB) [Collot et al., 1985, Louat and Pelletier, 1989, Pelletier et al., 1994, Taylor et al., 1995, Pelletier et al., 1998, Lagabrielle et al., 2003]. The BATB is composed of three thrust faults to the east of Pentecost and Maewo, which merge to a single thrust to the east of

Ambrym (See Figure 1-1). Either lower amounts of shortening or a reduced sedimentary supply may explain the transition from a series of thrusts to a single thrust in the south [Lagabrielle et al., 2003]. Since the onset of the DER collision, the BATB is thought to have undergone ~ 50 km shortening (See Figure 1-6c) [Lagabrielle et al., 2003]. Back-arc shortening is proposed to occur at a rate of 5.5 cm year^{-1} , such that more convergence is accommodated at the BATB than at the trench (See Figure 1-1) [Pelletier et al., 1998, Calmant et al., 2003, Bergeot et al., 2009]. Crustal thickening beneath Maewo, Pentecost, and possibly Ambrym, may be due to progressive stacking of slices of the oceanic crust in this back-arc region (See Figure 1-6c) [Lagabrielle et al., 2003]. There is also thrusting east of the Pentecost and Maewo islands, and the eastward propagating thrust wedge incorporates oceanic lithosphere from the North Fiji basin.

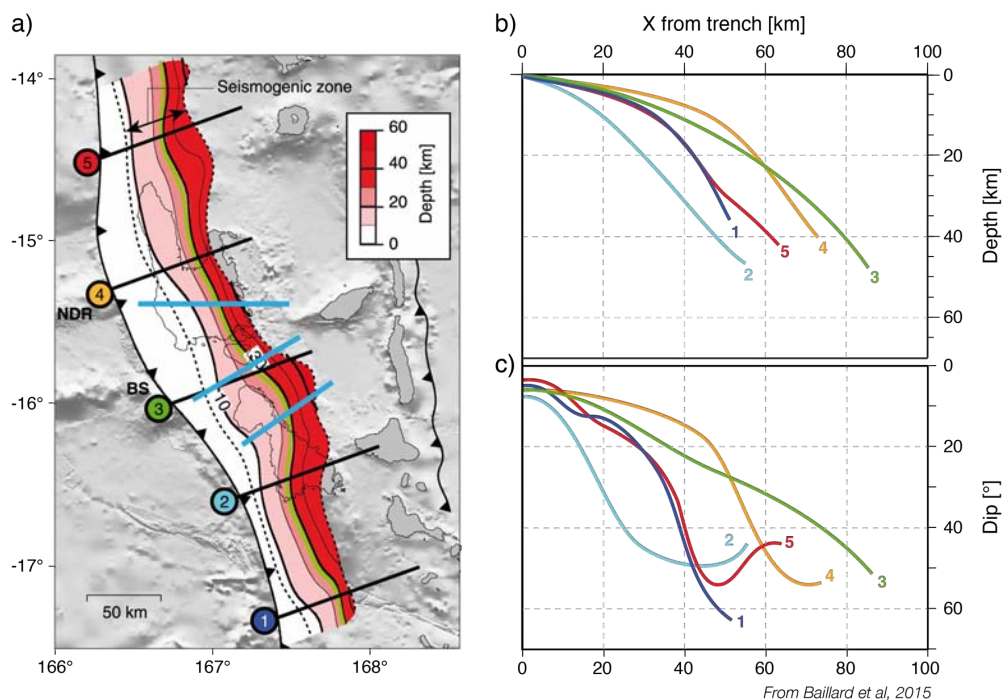


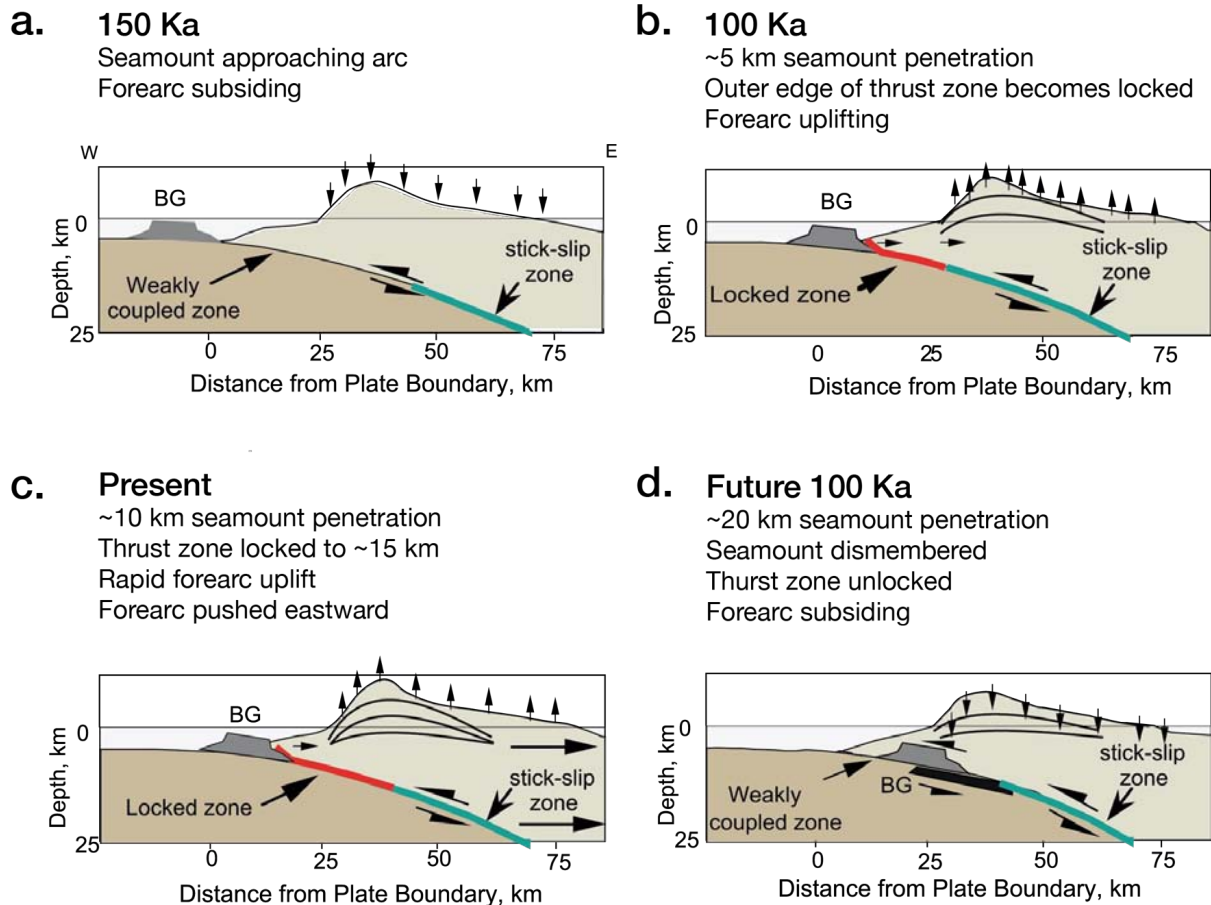
Figure 1-3: **Subduction interface geometry.** **a.** The subduction interface of the central portion of the NH subduction zone in map view, manually determined by Baillard et al. [2015] from earthquake locations. The color indicates the interface depth, the dotted lines indicate the updip and downdip extents of the seismogenic zone, and the green contour is the intersection with the fore-arc Moho. The blue lines are the divisions between the forearc block segments determined by Taylor et al. [1980, 1987]. NDR: North D'Entrecasteaux ridge; BS: Bougainville seamount. **b.** Cross-section of the subduction interface depth. The profile is indicated by the corresponding colored number in **a.** **c.** Cross-section of the subduction interface dip along the subduction front. From Baillard et al. [2015].

On 26 November 1999, a large thrust earthquake (M_w 7.5) took place in the BATB [Pelletier et al., 2000b, Régnier et al., 2003]. The ruptured fault is located at the southern end of the BATB, and the epicenter was only 10 km northeast of Ambrym [Lagabrielle et al., 2003] (See Figure 1-6a,b). The fault scarp is located only 13 km from the eastern tip of Ambrym, and is visible in the bathymetry (See 1-6a,b)[Pelletier et al., 2000a, Lagabrielle et al., 2003]. If one considers the offshore extension of Ambrym’s rift zone, then the fault scarp may be less than 5 km from this volcanic structure (See 1-6b).

Using mapping and dating of raised coral and reefs on Ambrym’s SE coast, Lagabrielle et al. [2003] estimated that progressive, accumulating uplift along the back-arc thrust belt has been occurring at a rate of $3.5 - 4 \text{ mm yr}^{-1}$ over the past 8000 years. This uplift rate was calculated assuming coseismic and interseismic uplift of only tectonic or seismogenic origin. However, we will show in Chapter 3 that volcanic deformation from a single rift zone dike intrusion can result in more than 2 m of permanent uplift of Ambrym’s SE coast. We emphasize that future studies measuring long-term tectonic displacement using uplift markers on Ambrym’s coasts should consider the contribution of volcanic deformation. Nonetheless, there is an indisputable line of evidence for tectonic uplift occurring in the backarc [Lagabrielle et al., 2003, Taylor et al., 1987].

1.1.3 Stress perturbation due to DER collision

Three arc volcanoes (Ambrym, Ambae, and Gaua) are aligned N-S to the west of the BATB. Both Ambrym and Ambae have well-defined rift zones, oriented $N105^\circ\text{S}$ and $N55^\circ\text{S}$, respectively. Some authors have posited the existence of faults cutting the volcano edifices in the direction of the rift zones [Mallick, 1973, Greene and Collot, 1994], although the extension of these faults into the forearc (Malekula and Espiritu Santo Islands) is disputed [Meffre and Crawford, 2001]. Regardless of whether the existence of these faults is confirmed, the orientation of the rift zones may indicate the direction of regional stress [Nakamura, 1977]. Collot et al. [1985] determined the stress distribution in this region from the rift zone orientations, among other geological structures, as well as from seismicity. The minimum compressive stress (σ_3) is vertical and the maximum compressive stress (σ_1) is horizontal (nearly E-W) in the central section of the NH arc, consistent with compression parallel to the direction of the colliding DER.



Adapted from Taylor et al, 2005

Figure 1-4: **D'Entrecasteaux ridge subduction/collision.** Evolution over time of the DER collision in the central portion of the NH arc. BG is the Bougainville Guyot of the Southern D'Entrecasteaux seamount chain. The arrows show the uplift of the forearc as the seamount approaches and collides with the arc. Once the feature has been fully subducted (how this occurs is still debated), rapid subsidence occurs on timescales similar to uplift. Adapted from Taylor et al. [2005].

By plotting the earthquake focal mechanisms from the GCMT catalogue since 1976, we note a vertical σ_3 and horizontal (approx. E-W) σ_1 in both the forearc and backarc of the central NH arc (See Figure 1-7) (Raphaël Grandin, personal communication). At about the latitude of Ambrym, σ_3 rotates from vertical to horizontal, oriented NE-SW. To the SE of Ambrym island, σ_1 remains horizontal but rotates slightly to the NW-SE. Ambrym is thus located at the southern edge of the segment experiencing a compressive stress regime, as has been shown by both the BATB fault scarp, as well as historical seismicity (See Figure 1-7).

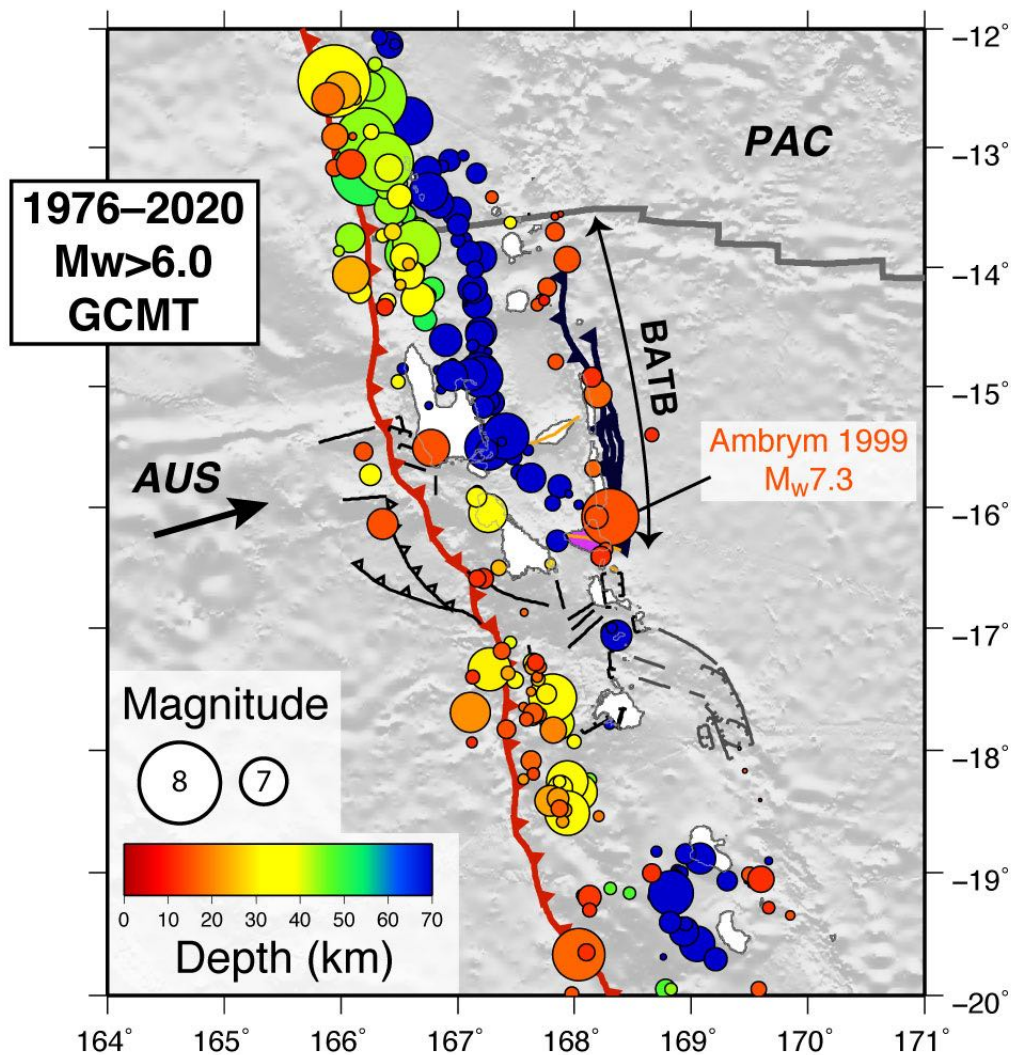


Figure 1-5: **Historical earthquakes.** Earthquakes with $M_w > 6.0$ from 1976 to 2020 in the NH arc, from the GCMT catalogue. Color indicates depth, and size of the circle indicates the magnitude. Note the absence of shallow earthquakes in the central NH arc and the seismically active back-arc thrust belt. The M_w 7.3 1999 BATB earthquake near Ambrym is labeled. From R. Grandin, personal communication.

Farther to the south, a transtensional tectonic regime dominates, also thought to be a result of the DER collision [Collot et al., 1985]. The transition between the shortening segment and this transtensional segment is characterized by a right-lateral transverse shear zone from west of Vate Island to the west of Epi Island (See Figure 1-1). Magma-deficient back-arc rifting occurs in the Coriolis Troughs (which includes the Vate, Eromango, and Futuna Troughs, whose ages of initiation are still debated, but may be ~ 5 Ma [Maillet et al., 1995, Crawford et al., 1995]) as the New Hebrides arc rotates clockwise [Anderson et al., 2016]. Stress heterogeneities induced by the colliding DER caused segmentation of the arc, and may have contributed to the strong focusing of basaltic eruptions in the Vate

Trough, to the SE of Vate Island (See Figure 1-1) [Anderson et al., 2016]. This magmatic activity resulted in the formation of Nifonea volcano, a large shield volcano with a 5×8 km summit caldera.

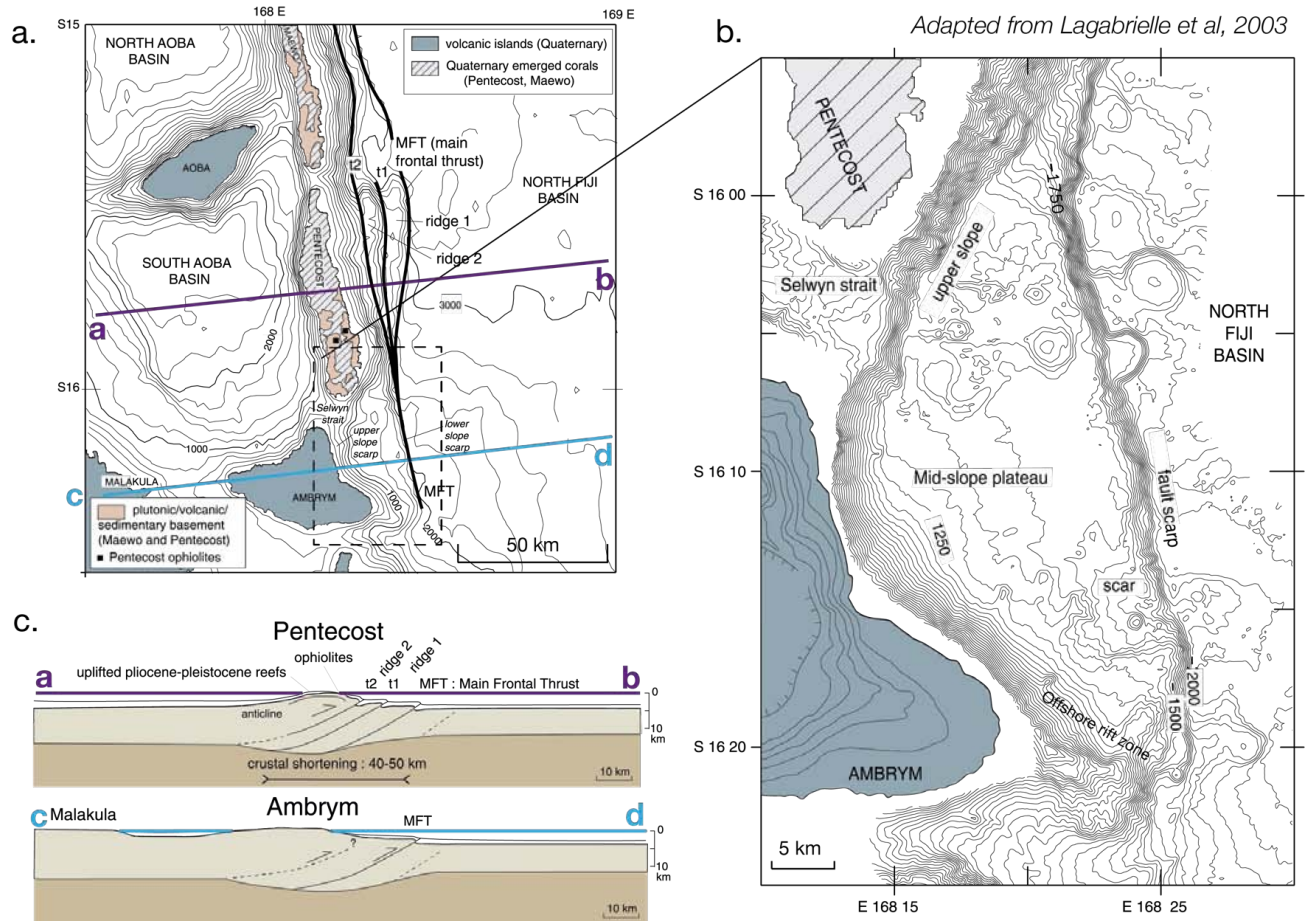


Figure 1-6: **Structure of the back-arc thrust belt.** **a.** A bathymetric map based on Pelletier et al. [1998] with contour intervals at 200 m. Mapping of emerged reef limestones based on Mallick and Neef [1974]. **b.** Zoom of a March 2000 bathymetric map obtained from the ALAUF1 cruise of R/V *L'Atalante* [Pelletier et al., 2000a]. The contour intervals are 50 m. **c.** Crustal sections at the profiles a – b and c – d in **a.** Inferred from geophysical and bathymetry data. Collot et al. [1985] estimated 1 km of Quaternary sediments, a Moho depth of 12 km in the Aoba basin, and the crustal root beneath Pentecost and Ambrym to be 18 – 20 km. Figure from Lagabrielle et al. [2003]

The unique tectonic setting of the NH arc gave rise to a variety of basaltic and andesitic volcanism starting from 6 Ma, initially in the south on the islands of Erromango, Tanna and Anatom [Mitchell and Warden, 1971]. This includes, but is not limited to, rift zone volcanism and lava lake activity. Studies of magma composition provide clues to link magma genesis with the peculiarities of the tectonic setting.

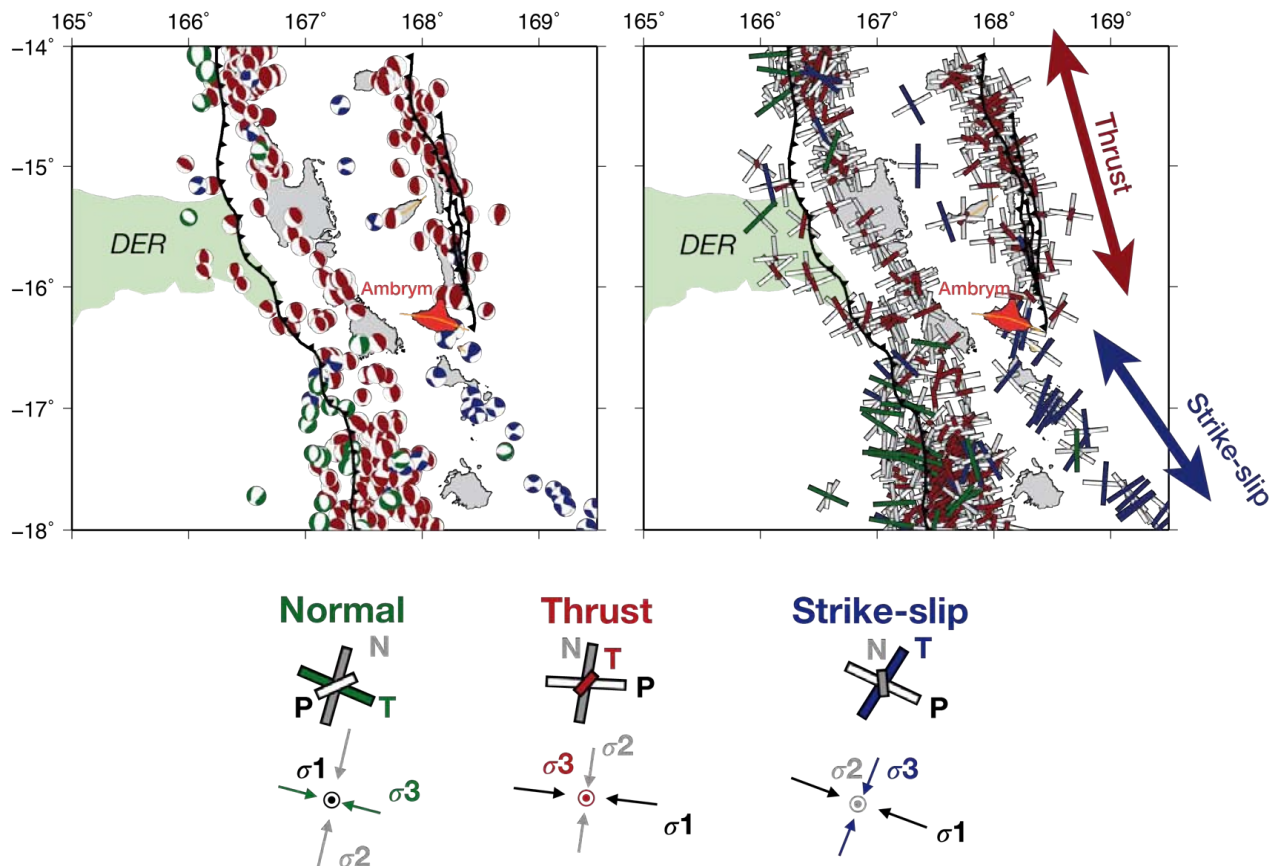


Figure 1-7: **40 years of focal mechanisms in the NH arc.** The map on the left shows GCMT focal mechanisms from 1 January 1976 to 1 April 2019 of earthquakes at depths less than 200 km. The map on the right shows orientation of the pressure and tension axes of the corresponding focal mechanisms. We observe that σ_3 rotates from vertical in the central portion of the New Hebrides subduction zone, which is undergoing compression due to the DER collision, to NE-SW in the vicinity of the back-arc basins to the south. Ambrym lies on the transition between these compressional and transtensional stress regimes, as denoted by the red and blue lines.

1.2 Volcanism in the New Hebrides arc

In the NH arc, 14 volcanoes have been active in the Holocene, 9 of which have erupted in the past 150 years [Global Volcanism Program, 2020]. The arc-scale tectonics of the New Hebrides has been studied in detail [e.g., Collot et al., 1985, Taylor et al., 1980, 1987, Louat and Pelletier, 1989, Pelletier et al., 1994, 1998], and several studies have been undertaken to investigate the relationship between tectonics and volcanism in this region. These studies mainly address the varying magma composition along the arc [Briqueu et al., 1994, Crawford et al., 1995, Monzier et al., 1997, Peate et al., 1997, Turner et al., 1999, Beaumais, 2013].

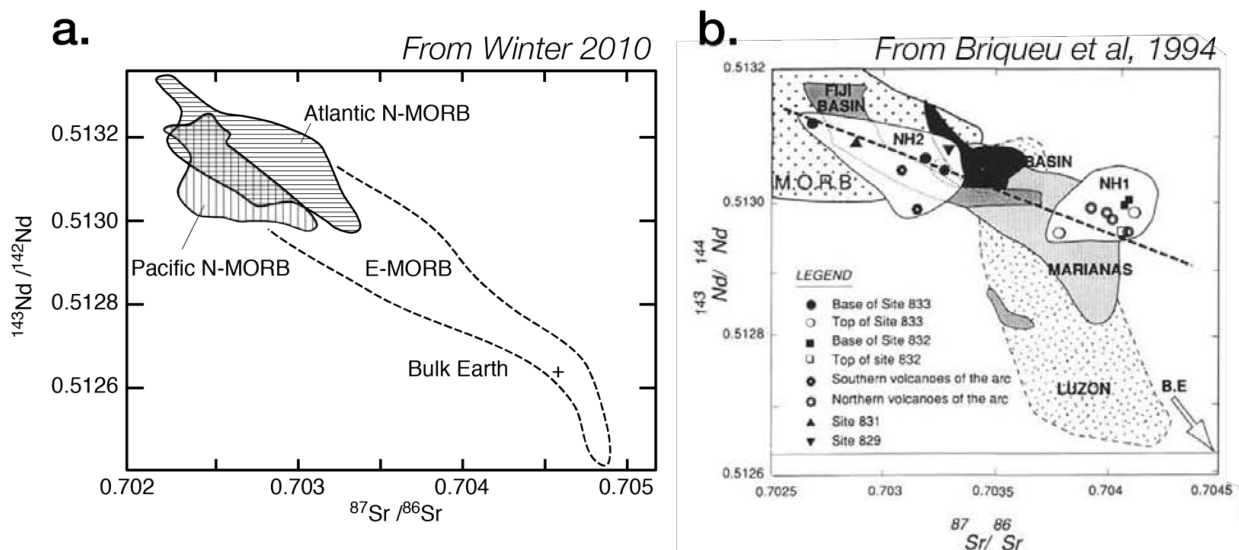
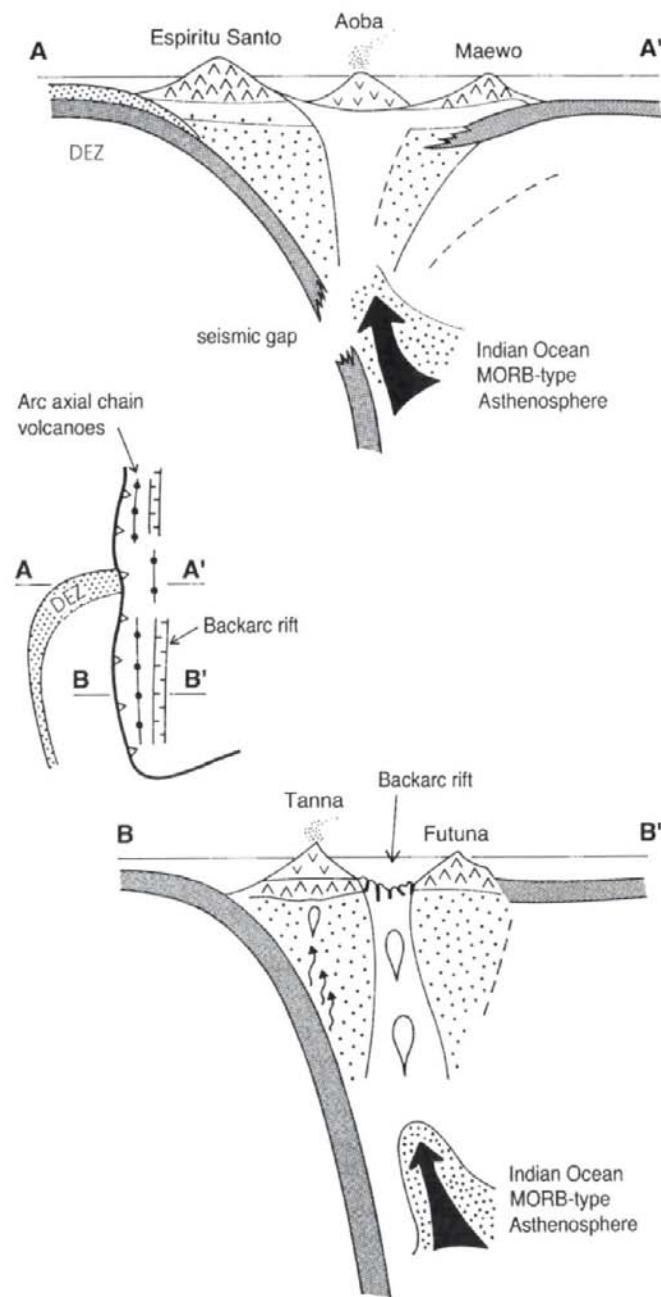


Figure 1-8: **MORB trace element isotopic ratios.** **a.** Isotopic ratios of trace elements Sr and Nd for Pacific/Atlantic MORB and Indian MORB. From Winter [2010]. **b.** The same isotopic ratios for various intra-oceanic arcs, including the New Hebrides arc. The domains NH1 and NH2 include samples from drilling sites 829, 831, 832, and 833 (See Figure 1-1). Samples from drilling site 833 that are within the NH2 domain represent pre-DER collision volcanics. BE represents bulk earth isotopic ratios. From Briquet et al. [1994].

1.2.1 MORB geochemical signatures

We will first make a slight digression to review how varying magma composition at the arc-scale relates to differing magma genesis sources. The compositions of basalts erupted at intra-oceanic settings provide a window into magma genesis, in particular because they are not contaminated by the continental crust, which is enriched in trace elements. Therefore, the elemental composition of island arc basalts may reflect the mantle source [Pearce, 1983].

Ocean-ridge magmatism comprises $\sim 75\%$ of Earth's volcanism [Crisp, 1984]. Mid-ocean ridge basalts (MORBs) are found at these oceanic spreading centers, generally due to passive mantle ascent and partial melting. The chemical reservoir from which MORBs are extracted (the upper mantle) is generally depleted in incompatible trace elements with respect to the bulk Earth [Turcotte and Schubert, 2014]. However, MORB compositions differ depending on where they are erupted. In order to differentiate between levels of depletion in incompatible elements, the radiogenic isotopic ratios of trace elements are measured. For example, depleted ratios of $^{87}\text{Sr}/^{86}\text{Sr}$, $^{143}\text{Nd}/^{144}\text{Nd}$, $^{176}\text{Hf}/^{177}\text{Hf}$ indicate, over geological timescales, low Rb/Sr, Nd/Sm, and Hf/Lu ratios [Workman and Hart, 2005].



From Crawford et al, 1995

Figure 1-9: **Asthenosphere ascent in the NH arc.** Schematic illustration explaining E-MORB asthenosphere ascent in the central portion of the NH arc. The A-A' section (top) and B-B' section (bottom) cut the central and southern segments of the arc, respectively. From Crawford et al. [1995].

Although the isotopic signatures of MORBs are fairly constant, variations in depletion of incompatible trace elements allow for differentiating MORB sources into Pacific and Atlantic N-MORB (depleted, “normal” source), as well as Indian E-MORB (relatively “en-

riched” source) (See Figure 1-8a) [Winter, 2010]. The absolute level of incompatible major elements–K, for example– can also help distinguish between N-MORB and E-MORB sources. N-MORBs tend to have lower potassium contents, while E-MORBs have high potassium contents, for a given amount of differentiation [Winter, 2010].

1.2.2 Tectonic influence on volcanism in the New Hebrides arc

Both N-MORB and E-MORB sources have been determined for magmas erupted in the New Hebrides arc (which can be divided into the northern, southern, and central segments) [Briqueu et al., 1994, Crawford et al., 1995, Turner et al., 1999]. Lavas erupted from arc volcanoes in the northern and southern segments have N-MORB isotopic signatures, while lavas erupted in the arc volcanoes in the central segment (from Gaua to Vate islands) have E-MORB isotopic signatures (See Figure 1-8b)[Crawford et al., 1995]. Samples from an Ocean Drilling Program in the North Aoba basin (See Figure 1-1, green circles) provide evidence that older volcanics in the central segment (>2-3 Ma, around the time of onset of DER collision), had isotopic compositions similar to N-MORB (See Figure 1-8b) [Briqueu et al., 1994]. The E-MORB isotopic signatures can only be explained by a long-term (> 500 Myr) enrichment process, and the Pb and Sr isotopic signatures are not consistent with sediments or volcanics sampled from the subducting plate [Briqueu et al., 1994, Crawford et al., 1995]. Therefore, Crawford et al. [1995], Peate et al. [1997] hypothesize that, due to collision with the DER, magma genesis in the arc’s central segment has shifted downward, and 50 km eastward, intersecting with a passively upwelling asthenosphere with E-MORB signatures (See Figure 1-9). Upwelling is thought to be due to extension of backarc troughs in the northern and southern segments [Crawford et al., 1995]. Volcanism in the central segment may also be related to the detachment of the lithospheric slab, as determined by a seismic gap from 50 – 150 km depth beneath Malakula and Vate islands [Louat et al., 1988, Picard et al., 1995] (See Figure 1-9).

However, some studies propose that the varying isotopic signatures along the arc are not related to the DER collision, since lavas with E-MORB affinities are found in regions currently thought to be unaffected by the DER collision (Gaua) [Monzier et al., 1997]. Monzier et al. [1997] proposes an alternative hypothesis based on a combination of geochemical and seismic data. They state that a strip of E-MORB asthenosphere exists beneath the North Fiji Basin, extending upward and westward beneath Gaua and Aoba islands [Monzier et al., 1997]. Further studies of isotopic signatures of lavas in older parts of the arc and backarc are needed to differentiate between these hypotheses.

1.3 Current understanding of Ambrym volcano

The geochemical studies on the scale of the arc, summarized above, provide hints regarding the genesis of New Hebrides magmas. In this dissertation, we will focus on an exceptionally active volcano on the southern boundary of the central segment of the NH arc– Ambrym. Using satellite geodesy (mainly from SAR satellites), we will investigate magmatic processes at Ambrym such as magma storage in the crust and lateral migration away from the central volcanic system. These processes, although occurring at shallow levels within the lithosphere,

are also affected by the region's tectonic evolution. Although this dissertation probes magmatic processes through the lens of geodesy, these results, in combination with geochemical and petrological studies, will help establish a better view of the volcanism in the central NH arc— from the mantle to surface.

1.3.1 Volcanological characteristics

We have summarized the tectonics and magma geochemistry in the NH arc, and will now concentrate on Ambrym in particular. Ambrym is a basaltic volcanic island measuring 35×50 km, whose summit rises 1800 m above the seafloor (1270 m a.s.l.) [New Hebrides Geological Survey, 1976, Chase and Seekins, 1988] (See Figure 1-10). An older volcanic edifice is located in the northern sector of the island, and is made of three cones aligned N10°S—Tuvio, Vetlam and Dalahum [Picard et al., 1995]. This edifice is constructed primarily of pyroclastic deposits and basaltic lava flows. Neither the age of onset nor extinction of this volcanism is known.

Volcanism then shifted ~ 10 km to the south, where the morphology of the island changes. Two rift zones radiate N105°S from the center of a 12-km wide caldera for more than 20 km, both towards the SE and the NW (See Figure 1-10). Two main craters, Marum and Benbow, are situated near the western border of the caldera. Semi-permanent lava lakes are hosted within the vents of Benbow (unnamed vents) and Marum (Mbewesu and Niri Mbwelesu). These lava lakes are the sources of persistent, passive degassing [Allard et al., 2015, Carn et al., 2017]. An intra-caldera eruption in 1988 – 1989 was fed by a vent south of Marum, Niri Mbwelesu Taten (also called Maben Mbwelesu by locals) [Allard et al., 2015]. In addition to hosting lava lakes, these vents also produce Strombolian eruptions.

Tuff rings and vents exist in other portions of the caldera (i.e., Lewolembwi crater, See Figure 1-11b), indicating that intra-caldera activity also manifests itself by fissure-fed lava flows away from the main craters [Picard et al., 1995]. In addition, magma laterally migrates away from the caldera, along the rift zone, and can erupt on or offshore, tens of kilometers downrift (volcanic rift zones will be introduced in more detail in Chapter 3). Tuff rings and maars along the coast reflect the potential hazards of these rift zone eruptions— they may result in explosive phreatomagmatic eruptions when lava interacts with ocean water, demonstrated by the eruption of 1913 [Marshall, 1915, Frater, 1917, Németh and Cronin, 2011].

1.3.2 Historical eruptions

The most devastating historical eruption at Ambrym occurred along the NW rift zone in 1913. The eruption began with explosions in the caldera craters, and fissures migrated down-rift, opening up every few kilometers towards the west coast [Frater, 1917]. The progression of the fissure opening along the rift zone indicates the westward lateral propagation of a dike intrusion. Within twelve hours, the intrusion had reached the west coast, and a fissure had opened near the Presbyterian Mission Station hospital (See Figure 1-11b) [Frater, 1917]. Explosions of steam and pyroclasts (with varying degrees of phreatomagmatic and magmatic fragmentation) lasted for 4 days and destroyed the hospital [Marshall, 1915, Németh and Cronin, 2011]. A second vent opened ~ 1.6 km off Ambrym's western coast, creating a tuff ring and extending the island's coastline. Explosions continued for four more days [Marshall, 1915]. Subsequent rift zone eruptions were recorded at Ambrym in 1915 (east coast) and 1929 (west coast). During the course of this PhD (in December 2018), a dike intrusion migrated towards the east coast, feeding a submarine eruption (See Chapter 3).

In addition to rift zone eruptions, historical volcanic activity over the past two centuries (1774 – 1991) has been compiled by Eissen et al. [1991] (See Figure 1-11a). Intra-caldera eruptions, forming new fissure vents, have occurred most recently in 1986, 1988-1989, 2015, and 2018. Lava flows originating within the caldera have breached the caldera wall and travelled down Ambrym's flanks, sometimes reaching the ocean (e.g., in 1863, 1914, and 1942). Intense degassing at Ambrym was first recorded by Captain James Cook in 1774 [Beagle-hole, 1961]. Activity in the main vents (including the presence of lava lakes, Strombolian eruptions, ash fallout, and degassing) was recorded more or less continuously in the 1960's through the 1990's. It is quite possible that lava lakes were present in the main craters during earlier time periods, but were not recorded due to observation gaps. Following the November 1999 BATB earthquake, there were no observations of the lava lakes, and their disappearance was eventually confirmed in January 2000 [Global Volcanism Program, 2000]. Lava lake activity resumed, at the latest, in August 2000 [Global Volcanism Program, 2001]. Other reports of lava lake activity are described by Global Volcanism Program [2020], and will be discussed further, in relationship to Ambrym's magmatic system, in Chapter 5.

1.3.3 Passive degassing

During periods of persistent lava lake activity, Ambrym passively degasses on such an extreme scale that it was the strongest volcanic source of passively emitted SO_2 from 2005 – 2015 (7 kt day^{-1} , according to satellite SO_2 observations) [Carn et al., 2017, Fioletov et al., 2016]. SO_2 and BrO column densities of Ambrym’s plume were measured with Differential Optical Absorption Spectroscopy (DOAS) using an airborne UV spectrometer in January 2005, March and July 2005, and August 2007 [Bani et al., 2009]. The total SO_2 flux was $15 - 24 \text{ kt day}^{-1}$ in January 2005, with more gas emitted by Marum than Benbow [Bani et al., 2009]. For reference, SO_2 flux at other lava-lake hosting volcanoes are 3.3 kt day^{-1} at Nyiragongo (DRC), 0.1 kt day^{-1} at Erta ’Ale (Ethiopia), 0.06 kt day^{-1} at Erebus (Antarctica) [Sawyer et al., 2008, Oppenheimer et al., 2004, Sweeney et al., 2008]. A similarly high flux was detected at Ambrym using airborne measurements in March 2005 ($\sim 32 \text{ kt day}^{-1}$), and a lower flux was detected in July 2005 ($\sim 2 \text{ kt day}^{-1}$) and August 2007 ($\sim 4 \text{ kt day}^{-1}$) [Bani et al., 2009]. Other DOAS measurements from another field campaign in October 2007 and October 2008 measured an average SO_2 flux of 7.8 kt day^{-1} [Allard et al., 2015]. Although these values are consistent with the estimates of Carn et al. [2017], degassing flux can vary greatly over the span of just a few months (as reported by Bani et al. [2009]), and mean passive degassing fluxes are most insightful when compared to other long-term (years-long) physical processes.

1.3.4 Magma composition and storage conditions

The tectonic evolution of the NH arc may have affected the ascent of mantle material, resulting in the distinct compositional signatures of lava erupted in the central segment. The compressive stress regime imposed by the DER and WTM collision also impacts the location of magma ascent towards the surface and transport of magma at shallower levels (i.e., formation and persistence of rift zone volcanic activity at Ambrym), although this relationship has yet to be explored in depth.

The most primitive lavas (highest MgO content) at Ambrym are those in the older volcanic edifice to the north, which also have medium-K trends [Picard et al., 1995]. Farther south, pre- and post-caldera samples follow medium- to high-K trends (similar to other volcanoes in the central NH arc). These erupted lavas are either tholeiitic to calc-alkaline basalts, or are more evolved (rhyodactic compositions) (See Figure 1-12a). Basalts are enriched in light rare earth elements (LREE) such as Rb, Ba, K, Sr, and P, which may indicate a magmatic source with E-MORB affinities [Picard et al., 1995]. The evolved products are mainly related to a postulated Plinian eruption that may have caused the onset of caldera formation 2 ka (see Section 1.3.5). In addition, more evolved products (up to 60 wt% SiO_2) with high-K affinities have also been erupted from vents in the eastern portion of the caldera (e.g., 1986 lava flow) [Robin et al., 1993, Picard et al., 1995]. Picard et al. [1995] concluded that partial melting of the mantle beneath Ambrym is thought to occur at depths of 60 – 45 km for the northern volcanics and more recent products with medium-K affinities, and 45 – 30 km for more recent basalts. However, this upward migration of the mantle source contradicts the conclusion of Crawford et al. [1995], who hypothesized that the DER collision led to an eastward and downward shift of the mantle magma source. This contradiction

warrants a more detailed comparison of these studies.

The organization of Ambrym’s crustal magma storage system has been investigated in various studies [Legrand et al., 2005, Allard et al., 2015, Firth et al., 2016, Sheehan, 2016, Hamling et al., 2019, Hamling and Kilgour, 2020]. At deep levels, mineral-melt thermobarometry of erupted products from both intra-caldera and extra-caldera eruptions have shown that magma stalls at depths ranging from 4 – 30 km b.s.l [Firth et al., 2016, Sheehan, 2016]. Firth et al. [2016] found no mixing in the primitive rift-zone eruptive products, and thus proposed that rift zone eruptions are sourced from a deeper reservoir (> 6 km) than the magma feeding the lava lakes. They also propose that during rift zone eruptions, ascending magma bypasses the shallower reservoir. This hypothesis will be revisited in Section 5.1.3.2.

At shallow levels, magma may be stored at depths of $\sim 2.7 - 2.9$ km b.s.l, as estimated by the locations of Very Long Period Tremors [Legrand et al., 2005]. Legrand et al. [2005] proposed the existence of two laterally separated sources– one source in the eastern portion of the caldera and one in the western portion. This depth is consistent with melt inclusion entrapment pressures found by Allard et al. [2015], corresponding to depths ranging from 2.6 km – 8.3 km b.s.l. Multiple sources at depths of < 5 km have also been modelled using InSAR geodesy, using ground displacement measurements from the 2015 and 2018 eruptions [Hamling et al., 2019, Hamling and Kilgour, 2020, Shreve et al., 2019, 2021].

1.3.5 Caldera formation

While Ambrym has many striking features, its large caldera– one of the largest basaltic calderas on Earth [Pike, 1978, Wood, 1984]– may be the most controversial.

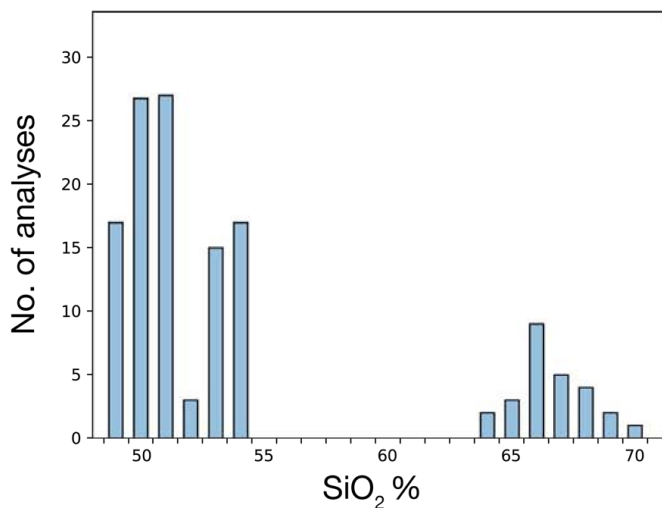
The age of the caldera was estimated by McCall et al. [1969] to be 2 ka, based on radiocarbon dating of charcoal associated with pre-caldera deposits in two locations. The first location was on the NE caldera rim, and the second was on the NW caldera flank [McCall et al., 1969]. Due to these limited dating measurements, further field campaigns to confirm the timing of pre-caldera activity would be of interest. In addition to the age of onset, McCall et al. [1969] also estimated a minimum caldera subsidence of 600 m, assuming a conical shape of the pre-collapse edifice, whose height was determined based on the current edifice’s slope.

The formation mechanism of Ambrym’s caldera is a topic of debate in the literature. On one hand, McCall et al. [1969] hypothesize that caldera formation was gradual, with the caldera subsiding when magma drains from a central reservoir by lateral rift zone intrusions [McCall et al., 1969, Cronin and Németh, 2005, Németh and Cronin, 2008, 2009, Sigmundsson, 2019]. This mechanism of formation will be discussed in more detail in Chapter 4. On the other hand, Robin et al. [1993] propose that caldera formation began with a Plinian eruption, which deposited dacitic ignimbrites around the island.

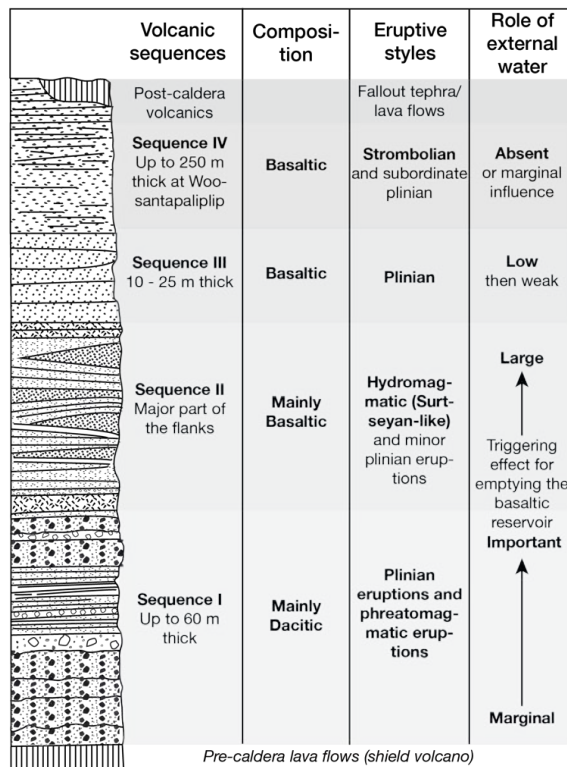
1.3.5.1 Evidence for Ambrym’s Plinian eruption

Robin et al. [1993] reported four primary pyroclastic deposits (which together comprise the Ambrym Pyroclastic Series (APS)) on the flanks of the volcano and up to the caldera rim (See Figure 1-12b). The APS includes a 60 m thick sequence of pyroclastic flow deposits which overlay pre-caldera basaltic lava flows, located on the north coast. A fallout ash layer in the

a.



b.



Adapted from Robin et al, 1993

Figure 1-12: **Ambrym Pyroclastic Series.** a. A bimodal distribution of SO₂ content from 137 samples of vitric clasts from the Ambrym Pyroclastic Series. From Robin et al. [1993]. b. Ambrym Pyroclastic Series section from Robin et al. [1993].

middle of this sequence indicates that there may have been two major pyroclastic flows, with evidence of interaction with water during the sequence. The next sequence, hypothesized to be between 50 – 200 m thick, is comprised of ash, quenched glass fragments and accretionary lapilli, indicating magma-water interaction. The third sequence is mainly ash flow deposits and is a total of 10 – 25 m thick. The final sequence is composed of basaltic Strombolian deposits with a thicknesses of up to 200 m, thought to originate from the Woosantapaliplip vent (near Tower Peak, See Figure 1-10). A 20 – 25 m thick basaltic-andesite lava flow extends from within the northern portion of the caldera, where it was intersected by the collapse, to the coast [Robin et al., 1993]. The total duration of these eruptive sequences is not constrained, but they may have occurred over months or years.

Robin et al. [1993] concludes that the sequence deposits are most likely not reworked because the vesiculated clasts and shards are fragile, the beds are sorted, and accretionary lapilli are preserved. Other works have challenged this statement. Cronin and Németh [2005], Németh and Cronin [2008], Németh et al. [2009] argue that the APS is made of altered mafic deposits, with no evidence for dacites. The deposits are either from phreatomagmatic eruptions or from caldera sediments that had been deposited in the valleys on the volcano’s flank by lahars and rivers [Németh et al., 2009]. Further details of this fieldwork, however, are unpublished.

Given the aforementioned studies, we cannot discount the possibility of an initial Plinian eruption initiating caldera collapse. In summary, the sequence of caldera formation at Ambrym, according to Robin et al. [1993] is as follows:

1. “Earlier caldera collapse” due to a Plinian phase, with the possibility of a pre-existing caldera at the top of the original shield volcano edifice,
2. “Construction of the tuff cone as collapse enlarges,” and
3. “Eruptive vents on the ring fracture.”

1.4 Focus questions

Ambrym’s activity has been recorded over the past century, and the depth of magma genesis and storage have been investigated through geochemical and petrological studies. However, many questions regarding the activity of this volcano remain. Episodes of unrest have been reported at Ambrym in the past, but the physical mechanisms driving these events remain enigmatic. During the course of this PhD, a rift zone intrusion occurred, briefly opening a window through which the mechanisms driving lateral magma transport and magma storage could be further investigated. This window just as rapidly closed when Ambrym’s lava lakes drained in December 2018, cutting off the magma storage system from the surface for 2 years (at the time of writing they had yet to return). Using the information gleaned from this noteworthy volcanic event, past volcanic activity could be investigated in further detail. This dissertation culminates with a conceptual understanding of the magmatic system that controls Ambrym’s eruptions, replenishment, and quiescence, and how these periods of activity can be discriminated using data from spaceborne satellites.

Within this dissertation, we aim, through the lens of satellite volcano geodesy, to answer the following questions:

1.4.1 Question 1: How is Ambrym’s magmatic plumbing system organized?

While past studies investigated deeper (e.g., > 6 km depth) levels of Ambrym’s magma storage system, the organization of the shallower levels— for example, the reservoir(s) feeding dike intrusions— is not yet fully understood. We will discuss 7 episodes of deformation observed at Ambrym over the past 20 years, whose deformation source models are located at shallower levels in the system (< 6 km depth). The deformation source models, and possible physical mechanisms driving deformation, are discussed throughout Chapters 3, 4, and 5.1. Two of these episodes include intra-caldera dike intrusions and eruptions, and the physical processes driving the other 5 may include magma reservoir drainage, degassing, and magma replenishment. One significant motivation to better understand Ambrym’s shallower magmatic system is that changes to this system may produce deformation before volcanic eruptions (i.e., precursors). In addition, studying Ambrym’s magmatic system can help us determine whether the vigorous magmatic activity is a consequence of deep (magma genesis and ascent from the asthenosphere) or shallow (middle- to- upper crust) magmatic processes, or some combination of the two.

1.4.2 Question 2: How did Ambrym’s caldera form and develop?

The mechanism that formed and developed Ambrym’s signature 12 km wide caldera is still debated. Although we were not able to go into the field to address the existing hypotheses, using satellite geodesy (in particular, InSAR), we will discuss how Ambrym’s current magmatic system can provide clues to determine whether the caldera formation mechanism is explosive or gradual, or a combination of both. For example, caldera ring-fault reactivation was identified with InSAR multiple times in the past two decades. This indicates that the caldera ring-faults are active structures that cause contemporary caldera subsidence (as discussed in Chapters 3, 4, and 5.2). We will refine the hypotheses posited by past studies [McCall et al., 1969, Robin et al., 1993, Cronin and Németh, 2005] using these geodetic observations. Also, we will discuss how the depths, sizes, and geometries of Ambrym’s present-day magma reservoir(s) may have been influenced by the formation of Ambrym’s caldera. By understanding how Ambrym’s caldera formed and developed, we can have a better idea of whether this volcano’s present-day magmatic system could produce a similar caldera-forming eruption in the future.

1.4.3 Question 3: What are the dynamics of Ambrym’s magmatic system?

Past studies have not been able to provide many constraints on the timescales of activity of Ambrym— for example, rates of replenishment, eruption recurrence times, or dynamics of magma transport. In Chapter 5.3, by jointly analyzing two decades of ground deformation, gas emissions, and lava lake activity (through thermal anomaly detection), we will discuss first-order interpretations of changes to Ambrym’s shallow magmatic system over time. We propose physical processes that may explain changes to the observed datasets. Physical processes within this open system due to volatile exsolution and degassing, for example,

may produce seemingly contradictory observations at the surface. Identifying the physical mechanisms controlling Ambrym's activity will help discern precursors of volcanic unrest.

Chapter 2

Methods

“Volcanology is in the midst of a revolution, and geodesy is helping to lead the way.”

Daniel Dzurisin

Since the early 1900’s, it was understood that geodetic techniques could measure volcanic deformation, providing a vision, albeit blurry, of subsurface magmatic activity. This vision has sharpened over the past few decades, largely due to the launch of numerous Earth Observation (EO) satellites. In particular, Synthetic Aperture Radar (SAR) satellites can measure, from space, centimetric ground displacements over hundreds of square kilometers. By enhancing and broadening ground displacement measurements thanks to satellites, geodesists are able to conduct detailed studies of volcanic deformation in remote regions of the world. The magmatic systems of remote volcanoes can be deciphered through analytical and numerical models which relate ground deformation to the stress and strain induced by pressure changes in the lithosphere. This wealth of new observations push these models to their limits.

2.1 Spaceborne SAR geodesy

In 1993, [Massonnet et al. \[1993\]](#) measured coseismic ground displacements of the 1992 Landers earthquake. These measurements were obtained from radar satellite observations, employing a technique called Interferometric Synthetic Aperture Radar (InSAR). Just a few years later, in 1995, (hypothesized) volcanic deformation was observed at Etna volcano (Italy) using InSAR [[Massonnet et al., 1995](#)]. Although a portion of this deformation was later concluded to be an atmospheric artifact (See Section 2.1.1.3) [[Beauducel et al., 2000](#)], these measurements sparked the interest of the volcanology community. The potential of measuring ground deformation from space was apparent, but so was the necessity to correctly distinguish signal from noise before including this technique in volcano monitoring and decision-making.

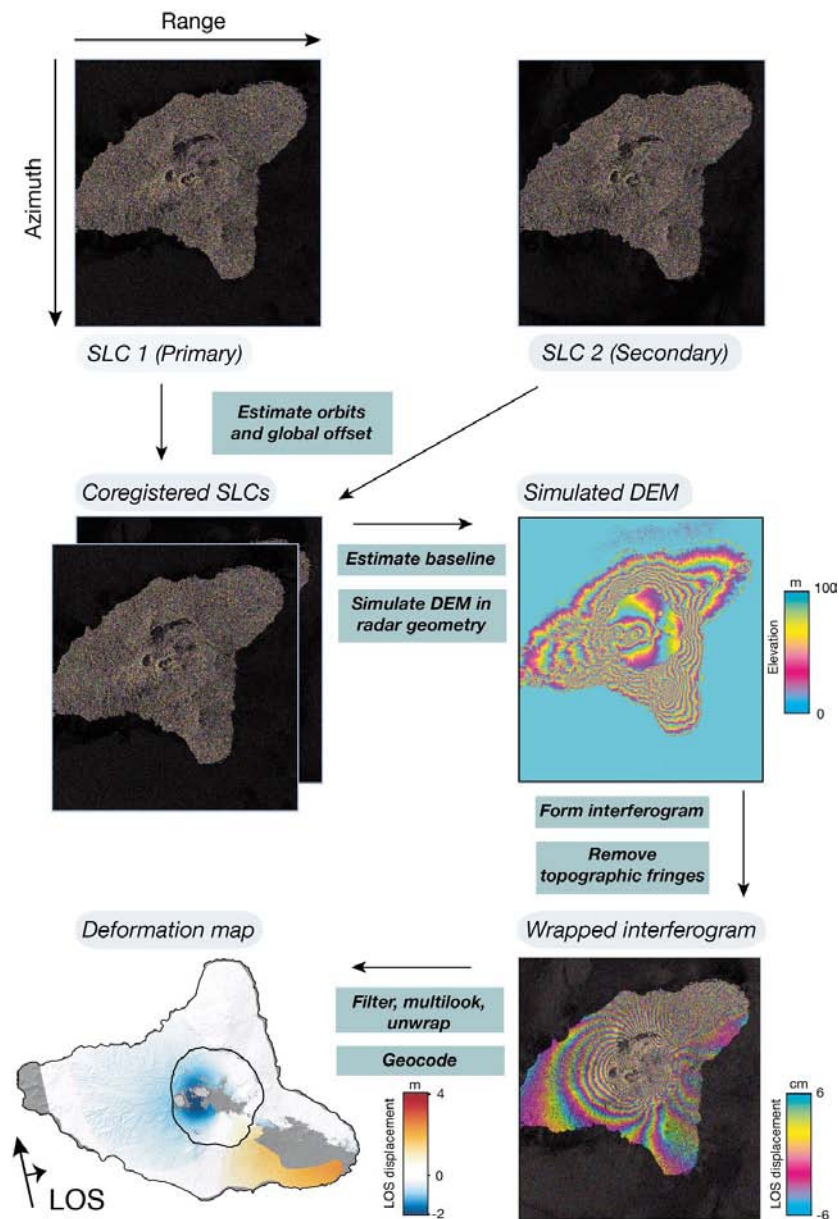


Figure 2-1: **Interferogram formation workflow.** A typical workflow to form an interferogram from two SAR Single Look Complex (SLC) images. The workflow begins when two SLCs are coregistered using high-precision orbits and cross-correlation. An interferogram is formed, and the topographic fringes are removed using a digital elevation model (DEM). Finally, the wrapped interferogram is filtered, multilooked, unwrapped, and geocoded to obtain the final deformation map in geographical coordinates.

These landmark InSAR measurements ushered in a new era of space-borne earth observation. Since the early 1990's, the number of SAR satellites in orbit has increased more than tenfold. Time between SAR image acquisitions is as little as one day using the satellite constellation COSMO-SkyMed from the Italian Space Agency, and, with the European Space Agency's Sentinel-1 twin satellites, systematic image acquisition occurs worldwide every 6

days. Future missions, such as the joint National Aeronautics and Space Administration and Indian Space Research Organisation satellite NISAR, promise that the era of Earth Observation by SAR data is only just beginning.

2.1.1 Measuring small ground displacements: differential InSAR

The technique of differential InSAR has been exhaustively explained by a number of sources [e.g., [Rosen et al., 2000](#), [Simons and Rosen, 2007, 2015](#), [Massonnet and Souyris, 2008](#)], as well as implemented in software packages, both research [e.g., [Rosen et al., 2004](#), [Rosen et al., 2012](#), [Doin et al., 2011](#), [Sandwell et al., 2011](#), [Kampes and Usai, 1999](#)] and commercial [e.g., [Werner et al., 2000](#)]. Here we will briefly summarize the fundamentals of a standard InSAR processing workflow, which includes acquiring and forming a SAR image from radar echoes, coregistering two SAR images, the formation of the interferogram, and any post-processing steps such as multilooking, filtering, and unwrapping (see [Figure 2-1](#)). We will also review the various contributions to the interferometric phase.

2.1.1.1 Acquiring and forming a SAR image

The following summary of Real and Synthetic Aperture Radar has been summarized from [Massonnet and Souyris \[2008\]](#) and [Cumming and Wong \[2005\]](#), and more advanced developments of the following concepts can be found within.

Radar systems release pulses of electromagnetic radiation in the microwave spectrum, which bounce off scatterers at the Earth’s surface (see [Figure 2-2](#)). These echoes are received by the sensor and ordered in a 2D coordinate system as an image. The two dimensions are called range (across-track, perpendicular to flight path) and azimuth (along-track, parallel to flight path).

Scattering can be either due to surface or volume effects. Both effects are influenced by the surface or volume’s dielectric properties, in particular the water content. In addition, the former results from the roughness of the surface on the scale of the radar wavelength (centimeters). The radar response due to surface effects increases when either the surface roughness or water content increases. Volume effects, on the other hand, result from the fact that scatterers’ density and distribution depend on the media. One may imagine a forest canopy– the scatterers include rocks, trunks, and leaves. Electromagnetic radiation interacts with this cloud of scatterers at different vertical extents, where each scatterer class (rock, trunk, leaf, etc.) has its own properties, such as its structure and dielectric constant.

The amplitude of the radar return depends on two main factors. On one hand, many scatterers may exist within a single resolution element, and their scattered radiation adds coherently to produce the final radar echo of that element. Radar images display a “speckle” effect because constructive or destructive interference between scatterers’ contributions results in large variations in amplitude and phase between resolution neighbors. Although speckle is due to the surface’s physical properties, it is unpredictable and therefore considered multiplicative noise. However, speckle can be reduced by averaging neighboring pixels, otherwise known as multilooking.

On the other hand, a single scatterer may dominate the energy received from a given resolution element, or pixel. As a result, speckle noise does not affect the pixel amplitude.

The phase and amplitude of such a pixel remains stable over many acquisitions. These pixels are called permanent scatterers (PSs), and the PS time series approach exploits their stable properties to extract reliable ground displacement measurements over time [Ferretti et al., 2001]. Typically, PSs are associated with targets with a large radar cross-section, a characteristic of many man-made structures. Hence, PSs are densely distributed in urban areas, and they are rare in natural terrain.

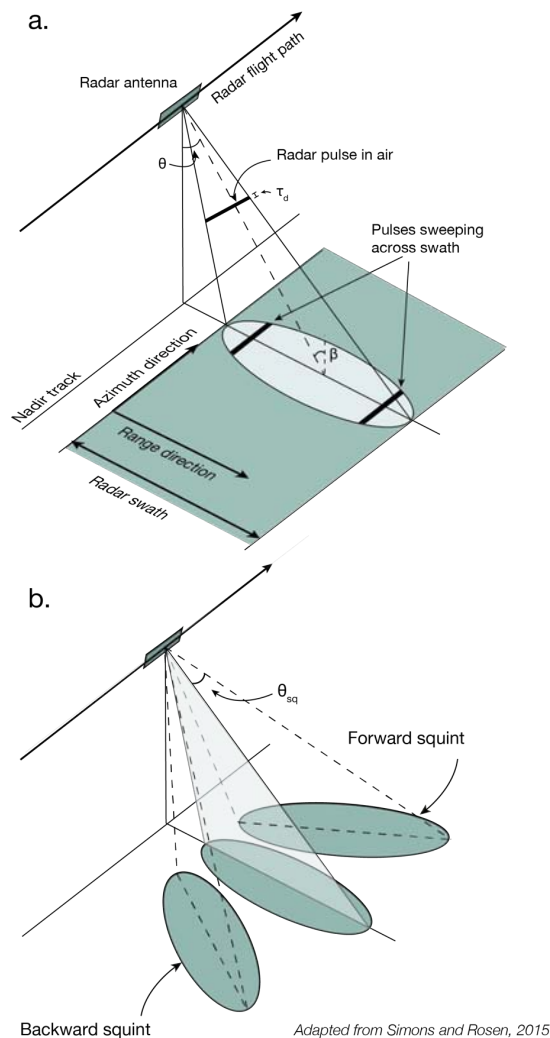


Figure 2-2: **Radar acquisition geometry.** **a.** The geometry of a radar acquisition, indicating the azimuth (radar flight path) and range directions, as well as the swath extent. The pulse duration is τ_d . The average look angle, θ , and the average incidence angle, β , are both measured at the middle of the swath. **b.** A representation of the squint angle θ_{sq} , which can be directed either forward or backward. Figures adapted from Simons and Rosen [2015].

The emitted radar pulse has a center frequency and wavelength within the microwave portion of the electromagnetic spectrum. The most common wavelength bands are X-, C-, and L-band, which are centered at respective wavelengths of $\lambda \approx 3.1$ cm, 5.7 cm, and 24

cm. Wavelength determines several properties of the radar pulse. It affects the penetration depth, or how far into a medium the wave will propagate before its amplitude attenuates by more than $\frac{1}{\sqrt{e}}$ [Massonnet and Souyris, 2008]. For a given dielectric constant and dispersive media, longer wavelengths penetrate deeper. Furthermore, shorter wavelengths scatter off smaller features, such as leaves or branches, whose orientation, and scattering properties, vary between two acquisitions [Zebker and Villasenor, 1992]. Consequently, in vegetated regions, shorter wavelengths have lower coherence (Section 2.1.1.4).

A two-dimensional image can be formed by measuring a target’s distance on the Earth from the sensor (slant range or “fast time”), and its position along the sensor flight path (azimuth or “slow time”). The ability to resolve two different targets on the ground in the range direction (ground range resolution) depends on the sensor incidence angle, β , and the duration of the emitted pulse, τ_d (see Figure 2-2a). The latter may either be the true pulse length, or obtained by frequency modulation (chirping) and matched filtering. The radar sensor looks to the side, as opposed to vertical, to ensure an unambiguous distance between the sensor and the targets. In Real Aperture Radar, the ability to resolve two different targets separated by a distance x along azimuth (azimuth resolution) scales inversely with the length of the radar antenna, L . In other words, the azimuth resolution is directly related to the beam aperture, α_b , such that α_b is proportional to $\frac{\lambda}{L}$. Targets can be resolved when $\frac{\lambda}{L} < \frac{x}{R}$, where R is the slant range distance. Considering a satellite-based SAR sensor with $R \approx 1000$ km, the antenna length would need to be unrealistically long (5 km!) to obtain a fine azimuth resolution of tens of meters, assuming $\lambda \approx 5$ cm.

In Synthetic Aperture Radar, the azimuth resolution is improved by imaging ground targets with multiple pulses. The frequency of the received pulses will be “Doppler frequency shifted”, due to the motion of the target relative to the sensor. The antenna’s aperture is synthetically lengthened over the distance of the sensor path during which the target is illuminated. This is the origin of the name *Synthetic Aperture Radar*. For any target, the received pulses will drift over a range of frequencies, defining the target’s Doppler frequency history. If the sensor’s point of closest approach matches with the middle of the illuminated zone, then the targets will (in the time domain) be placed at their zero-Doppler time, and (in the frequency domain) have a zero Doppler centroid. In practice, however, the antenna squints either forwards or backwards (see Figure 2-2b), resulting in a shifted, or non-zero, Doppler centroid, which can be estimated from the received data.

The total change in the frequency of a target while it is illuminated is known as its Doppler bandwidth. The azimuth resolving power scales with the Doppler bandwidth, and high resolution can be obtained from this frequency modulated signal using pulse compression techniques called *matched filtering*. The azimuth resolution can be found to be approximately $\rho_a \approx \frac{L}{2}$, if the squint angle of the satellite (see Figure 2-2b) is close to zero. Hence, with $L = 10$ m, we obtain $\rho_a \simeq$ a few meters.

Just as the signal is frequency modulated in azimuth, range resolution can also be improved by frequency modulation, or a chirped signal. Shorter pulses can distinguish targets from one another, resulting in a finer resolution. However, for a given transmission power, a short pulse has a low signal-to-noise ratio (SNR). A more energetic pulse will have a higher SNR, but the pulse’s energy is limited by the antenna’s peak transmitted power. A chirped signal has a longer duration, and thus a higher SNR, and fine resolution can still be obtained using matched filtering.

The above discussion defines range and azimuth resolution, however, characteristics of the signal sampling ultimately determine the pixel size on the ground. The range pixel size on the ground, p_g , depends on the range sampling frequency, f_r , through the relationship $p_g = \frac{c}{2f_r \sin(\theta)}$, where θ is the sensor look angle (Figure 2-2a) and c is the speed of light in a vacuum. If the sampling frequency f_r is not high enough (larger than the chirp bandwidth), the radar echo will be aliased. On the other hand, the azimuth pixel size (p_a) is determined by the pulse repetition frequency, or PRF , such that $p_a = \frac{v}{PRF}$, where v is the velocity of the sensor platform. The PRF is calibrated to ensure the azimuth signal is correctly sampled. To avoid aliasing, the PRF must be larger than the azimuth signal bandwidth, according to the Nyquist sampling rate [Cumming and Wong, 2005].

After compression of the raw electromagnetic echos in range and azimuth, the image format obtained is called “Single Look Complex”, or SLC. Today, most available SAR images can be downloaded from space agencies directly in SLC format. Every pixel in the two-dimensional SLC is comprised of a complex number, $(x, y) = Ae^{-i\phi}$. The amplitude A indicates the amount of radiation received by the sensor, and provides information regarding a combination of various surface properties— including roughness, topographic slope, and dielectric properties, as mentioned previously. The phase ϕ , which is cyclic from $[-\pi, \pi]$, relates directly to the distance traveled from the sensor to Earth, and back.

Synthetic Aperture Radar sensors can be mounted on various moving vehicles, including airplanes, satellites, unmanned aerial vehicles (i.e., drones), or cars. Throughout this dissertation, we will focus on satellite-based SAR sensors. Although aircraft-mounted SAR sensors exist for Earth science applications (e.g., UAVSAR [Lundgren et al., 2011], GLISTIN-A [Lundgren et al., 2019]), their use is currently limited within the volcano geodesy community.

2.1.1.2 Coregistering SAR images

To calculate an interferogram, two SAR images must be acquired at different times, from the same sensor and the same orbital path. Before the phase difference can be calculated, corresponding pixels in the SAR images must image the same targets on the ground. Any satellite orbital separation between acquisitions results in a distortion between SAR images. The difference in position between the satellite on the two acquisitions is called the baseline, B (see Figure 2-3). The perpendicular baseline, B_{\perp} , can be calculated by $B_{\perp} = B \cos(\theta - \alpha)$ (where α is the angle of the baseline relative to a horizontal plane, Fig. 2-3). The component of the baseline parallel to the primary image’s LOS is $B_{\parallel} = B \sin(\theta - \alpha)$.

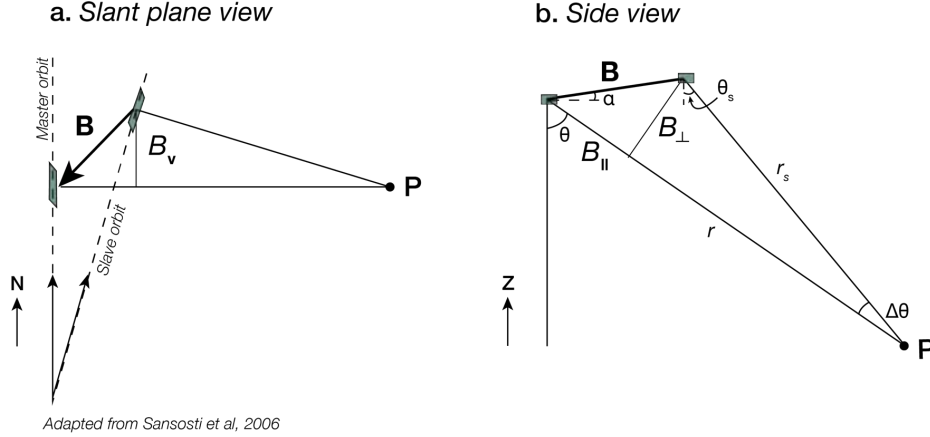


Figure 2-3: **Orbital baseline.** **a.** A slant plane view of the satellite orbits (dotted lines) during the primary and secondary acquisitions. The baseline between the two satellite positions while imaging the ground point \mathbf{P} is indicated by \mathbf{B} . The along-track component of the baseline is B_v . We assume the satellite orbits are rectilinear and coplanar. The reference geometry orbit's inclination is shown to be purely north-south. Most SAR satellites have an inclination that is slightly skewed from true north. Adapted from Sansosti et al. [2006]. **b.** The side view of the satellite during the primary and secondary acquisitions. The perpendicular baseline is B_{\perp} , the parallel baseline is B_{\parallel} , the look angle and range of the primary image are θ and r , respectively, and the look angle and range of the secondary image are θ_s and r_s , respectively. The angle the baseline makes with a horizontal plane is denoted by α . The difference between θ and θ_s is $\Delta\theta$. We again assume the satellite orbits are rectilinear and coplanar. Adapted from Sansosti et al. [2006].

Coregistration is the process of resampling one image to another so that corresponding pixels in each image view the same target. This is typically done by first modelling the satellite's orbital parameters during each acquisition, in order to resolve a target's theoretical range and azimuth shift between the two SAR images. These theoretical shifts assume no topography. In reality, this “flat Earth” assumption induces azimuth shift errors, Δj_{err} . Assuming that the satellites are at the same height during each pass, that the azimuth pixel spacing, Δ_{az} , does not change between passes, and a small α , Δj_{err} can be expressed by

$$\Delta j_{err} \approx \frac{B_v}{R_0 \sin(\theta)} \cot(\theta) \left(\frac{\delta h}{\Delta_{az}} \right), \quad (2.1)$$

where R_0 is the slant range during the first pass and δh is the topography error such that $\delta h = |\delta \mathbf{P}| \sin(\theta)$ ($\delta \mathbf{P}$ is the error of a point on the ground) [Sansosti et al., 2006]. Similarly, the range shift error would be

$$\Delta i_{err} \approx \frac{B_{\perp}}{R_0 \sin(\theta)} \left(\frac{\delta h}{\Delta_{range}} \right), \quad (2.2)$$

where we assumed that the range pixel spacing, Δ_{range} , does not change, as well as that $R_0 \gg \mathbf{B}$. Using a previously acquired digital elevation model (DEM), δh is known, and

these additional shifts can be corrected. Finally, cross-correlation can be used to adjust the image geometries to account for a global offset, related to the acquisition start times [Sansosti et al., 2006, Doin et al., 2011]. These steps ensure the two SAR images are coregistered with sub-pixel accuracy, increasing interferometric phase coherence.

2.1.1.3 Calculating an interferogram

Once the two SAR acquisitions have been coregistered, each corresponding pixel should image the same target. The complex product of the first image and the complex conjugate of the second image results in the interferogram

$$I_{int} = I_1 \cdot \bar{I}_2 = A_1 A_2 e^{i(\phi_2 - \phi_1)}. \quad (2.3)$$

The interferometric phase, $\Delta\phi = \phi_2 - \phi_1$, is the sum of the following contributions

$$\Delta\phi = \Delta\phi_{orb} + \Delta\phi_{topo} + \Delta\phi_{def} + \Delta\phi_{iono} + \Delta\phi_{atmo} + \Delta\phi_{noise} \quad (2.4)$$

For InSAR, the term we wish to isolate is $\Delta\phi_{def}$, or the ground displacement in the radar's line of sight (LOS) between the two acquisitions. All other contributions that mask this signal should ideally be removed.

The first term, $\Delta\phi_{orb}$, is a contribution originating from the orbital differences of the SAR sensor between the two acquisitions, which manifests itself as a ramp across the image in the range direction. The orbits of modern SAR satellites are known with high-precision, and the orbital phase ramp can be calculated and removed. Residual orbital ramps sometimes linger in interferograms and can be removed empirically by fitting a bilinear polynomial ramp in the post-processing [Simons and Rosen, 2007].

The next phase contribution, $\Delta\phi_{topo}$, is due to the presence of topography. The phase contribution due to topography [Simons and Rosen, 2007] is

$$\Delta\phi_{topo} = \frac{-4\pi B_{\perp} \delta h}{\lambda R_0 \sin(\theta)}. \quad (2.5)$$

If the topography is known *a priori* with a DEM, this phase contribution can be calculated and removed. The DEM is projected into the radar viewing geometry, and the range distance, as well as the perpendicular baseline of the satellites during the two acquisitions, is calculated at each pixel. Increasingly high-resolution global DEMs are available to simulate and remove the $\Delta\phi_{topo}$ contribution. These include global DEMs acquired by the Shuttle Radar Topography Mission (SRTM) [Farr et al., 2007] and TanDEM-X [Wessel, 2016], with pixel postings of 30 and 12 m, respectively.

The ionosphere may also induce phase shifts, resulting in the contribution $\Delta\phi_{iono}$. Charged particles in the ionosphere affect its refractive index and subsequently result in a phase advance of the propagating signal [Meyer, 2011]. Because the total electron content (TEC) in the ionosphere varies with time and space, these phase shifts can induce interferometric phase errors or even cause unpredictable curving of ray trajectories, resulting in a coherence decrease [Meyer, 2011, Gomba et al., 2016]. The phase advance is dispersive, scaling

inversely with the frequency, f , and can be expressed as

$$\Delta\phi_{iono}(f) = \frac{4\pi K}{cf} TEC, \quad (2.6)$$

where $K = 40.28 \text{ m}^3\text{s}^{-2}$ [Belcher, 2008]. Ionospheric effects are thus more prominent for low-frequency, or long-wavelength, signals (e.g., L-band, $\lambda \approx 24 \text{ cm}$). Leveraging the dispersive property of ionospheric phase advances, a “diverse-wavelength” system would be able to empirically estimate and remove the ionospheric contribution [Simons and Rosen, 2007]. This technology will be implemented in the future NISAR mission. Some InSAR software packages, such as InSAR Scientific Computing Environment (ISCE) [Rosen et al., 2012], now include modules to remove ionospheric signal using both the Faraday rotation method and the range split-spectrum method [Rosen et al., 2011, Liang et al., 2019].

The final phase contribution that can be mitigated is $\Delta\phi_{atmo}$, or the tropospheric phase delay. The atmosphere has an inhomogeneous index of refraction which is higher than that of free space, slowing down the propagating signal [Zebker et al., 1997]. Tropospheric phase delays are due to spatial and temporal atmospheric variations in pressure, temperature, and water vapor content [Zebker et al., 1997]. Atmospheric contributions may result from the fact that pressure, temperature, and water content vary with time and with altitude, resulting in interferometric phase delays which correlate with a region’s topography. This “stratified” atmospheric contribution can be removed empirically, by fitting a polynomial to the elevation versus phase delay [Beauducel et al., 2000, Remy et al., 2003, Doin et al., 2009].

Alternatively, atmospheric water content can be modeled with global weather models, such as the High Resolution European Centre for Medium-Range Weather Forecasts (HRES-ECMWF) numerical weather model [Yu et al., 2018], the ERA40 reanalysis [Doin et al., 2009], or the ERA-Interim global meteorological model [Jolivet et al., 2011]. These meteorological models use data assimilation methods to retrospectively reconstruct atmospheric parameters, such as temperature or water vapor content, multiple times per day for various altitudes or pressure levels [Dee et al., 2011]. The spatial resolution varies from 75 km for ERA-Interim to less than 15 km for HRES-ECMWF. Yu et al. [2018] integrated water vapor content measurements from GPS, acquired every 5 minutes, into the HRES-ECMWF global meteorological model, to develop the Generic Atmospheric Correction Online Service (GACOS), which provide users with atmospheric correction maps for interferograms. Tropospheric phase delays, whose spatiotemporal variations can be more than 10 cm [Zebker et al., 1997], are especially prominent in tropical regions [Ebmeier et al., 2013], or in areas with significant topographic relief [Beauducel et al., 2000]. However, the necessity of mitigating these phase delays depends on the relative magnitude of $\Delta\phi_{def}$. For large dike intrusions or earthquakes, for example, the magnitude of ground displacement can be orders of magnitude larger than that of the atmospheric noise.

The tropospheric phase delay also includes contributions from turbulent atmospheric effects, which are random in time and heterogeneous in space. They result from changes in tropospheric conditions, due to phenomena such as wind vortices or other dynamic processes, which change the atmosphere’s index of refraction [Hanssen, 2001]. Turbulent contributions affect both flat and mountainous regions. They cannot be theoretically modelled or empirically removed due to insufficient information on the state of the atmosphere. Nonetheless,

because they are temporally uncorrelated, “stacking” (or averaging) multiple interferograms reduce their effect and produce an average velocity map [Simons and Rosen, 2007]. Turbulent atmospheric contributions are also spatially correlated, and can be taken into consideration by estimating the error covariance in a non-deforming region of the interferogram (See Section 2.2.1.3.2) [Sudhaus and Jónsson, 2009].

After the removal of the above four phase contributions, we are left with $\Delta\phi_{def}$ and $\Delta\phi_{noise}$. The former is the signal of interest, and the latter is inherent system noise in conjunction with any other unmodelled effects (moisture, DEM errors, etc.) that cannot be systematically removed. Once $\Delta\phi_{def}$ has been unwrapped from a domain of $[-\pi, \pi]$ to $[-\infty, \infty]$ (See Section 2.1.1.4.2), the displacement in meters can be calculated by

$$\Delta u_{def} = \frac{-\lambda\Delta\phi_{def}}{4\pi}. \quad (2.7)$$

Up to this point, the SLCs and interferograms have all been processed in radar geometry (i.e., slant range and azimuth). In order to produce an exploitable deformation map, radar coordinates must be transformed into geographical coordinates through a process called geocoding. Each pixel in the image is assigned a location on the surface of Earth using the DEM which has been simulated into the radar geometry. This method is assuming that no significant topographic change has occurred.

2.1.1.4 Post-processing

InSAR is especially useful due to both its sub-centimetric precision and all-weather, day-and-night capabilities. However, it is not without limitations. These include phase shifts due to atmospheric and ionospheric effects (See 2.1.1.3), as well as decorrelation.

Decorrelation occurs when surface properties change between two SAR acquisitions. For example, leaves may act as scatterers, but the position and orientation of leaves change rapidly, causing random scattering properties in two images. Surface changes are more likely to occur when two acquisitions have a long temporal baseline. Decorrelation may also occur when the perpendicular baseline between the satellite passes is greater than a few hundred meters. When the viewing geometry changes, the phases of off-center scatterers of each resolution element will change as well in a non-systematic way (random effect) [Simons and Rosen, 2007].

The similarity between two SAR acquisitions, I_1 and I_2 , can be quantified by the coherence, calculated as

$$\gamma = \frac{\sum_{i=1}^N I_{1,i} \cdot \bar{I}_{2,i}}{\sqrt{\sum_{i=1}^N |I_{1,i}|^2 \sum_{i=1}^N |I_{2,i}|^2}}, \quad (2.8)$$

where N is the number of pixels used to calculate the coherence, and $|I_{1,i}|$ is the modulus, or amplitude, of image I_1 for pixel i [Simons and Rosen, 2007]. In order to improve the SNR in densely vegetated regions, such as at tropical volcanic islands, we use the following workflow for filtering and unwrapping. Both algorithms take into account the coherence, in order to extract robust information from coherent regions.

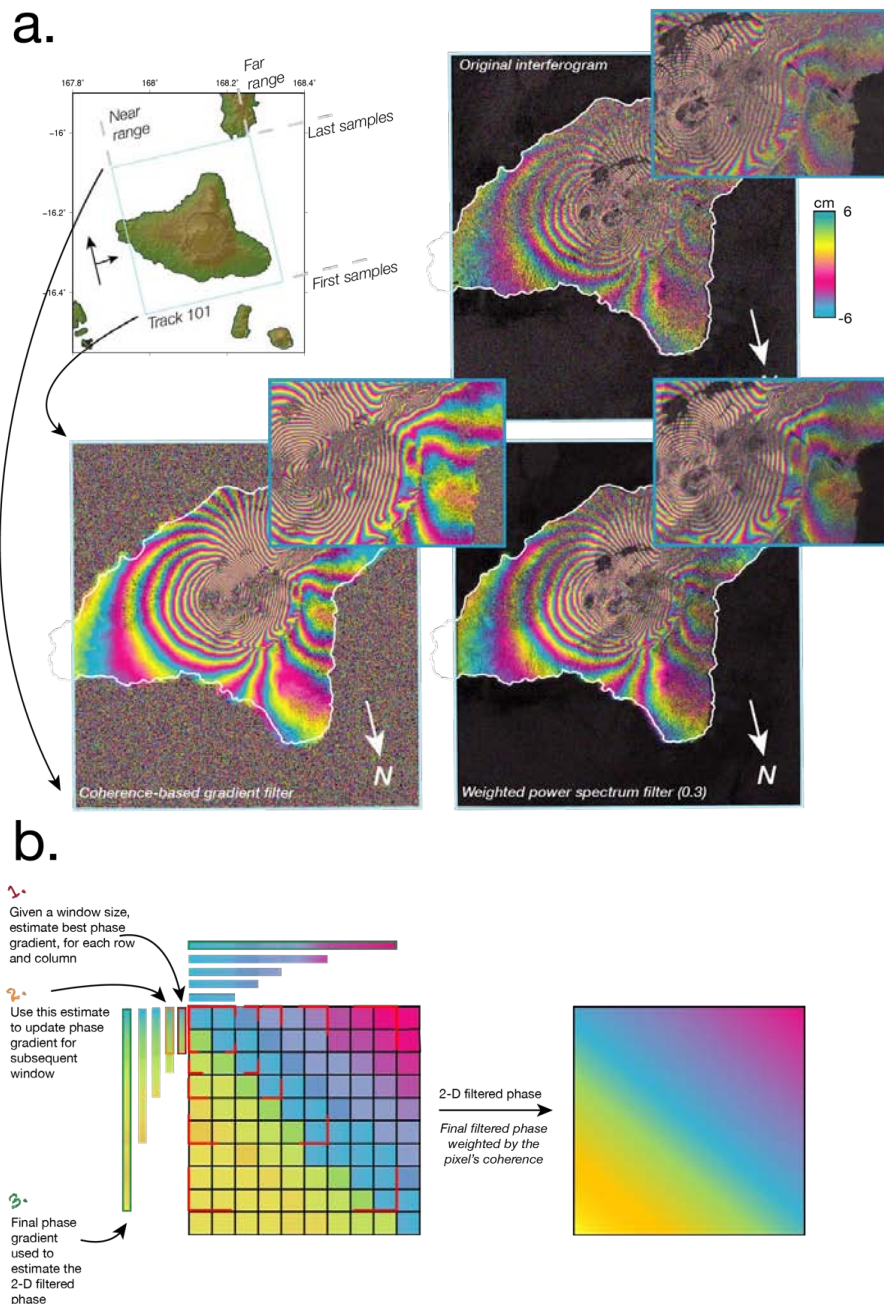


Figure 2-4: **Coherence-based gradient filtering.** **a.** The top left hand corner of the figure shows the ALOS-2 swath footprint, indicating the near and far range, as well as the first and last acquired samples, of the ascending orbit. The top right hand corner of the figure shows the unfiltered, wrapped interferogram. The bottom right hand corner shows the wrapped interferogram filtered using the weighted power spectrum approach with a strength of 0.3, and the bottom left hand corner shows the wrapped interferogram filtered using the coherence-based gradient approach. **b.** A visualization of the steps used to filter the wrapped interferogram using the coherence-based gradient approach. Each colored box represents a single phase value. The corners of the various window sizes (5 of the 8 are shown here) are indicated with red lines. The phase gradient for each row and column is iteratively estimated for each window size. The iterative procedure is visualized here for a single column and row.

2.1.1.4.1 Coherence-based gradient filtering

A weighted power spectrum filter is initially applied with a low-to-medium strength (~ 0.3 on a filter strength scale from 0 to 1) [Goldstein and Werner, 1998]. A second coherence-based filter further improves the SNR. This filter was already implemented in the NSBAS software package by Marie Pierre Doin and Romain Jolivet [Doin et al., 2011]. It combines square sliding windows of eight difference sizes (widths, w_i , of 2, 3, 4, 6, 9, 12, 15, and 20). The user provides both the complex interferogram, I , and the coherence, γ , for each pixel, (i, j) . They also provide an amplitude threshold, a_{thresh} .

Within a given window, each pixel’s phase is filtered with a bilinear plane that best fits the window’s phase gradient along range and azimuth. If the pixel’s coherence is greater than a_{thresh} , the filtered phase is weighted by the pixel’s coherence γ_{ij} . Otherwise, the filtered phase is set to 0.

For each window size, the gradient is iteratively updated if the filtered phase is above an empirical threshold. This ensures an increasingly accurate phase gradient approximation for each window size. Taking into consideration the phase gradient, as well as a pixel’s coherence, enables this filter to perform well when there is a high fringe gradient, as well as when the coherence varies substantially over the scene.

An interferogram filtered using this approach, compared to the weighted power spectrum filter, is shown in Figure 2-4. Although there may be artifacts in the phase, the coherence, which itself was incorporated in the phase filtering, can be used to mask out these unreliable values. Alternatively, these artifacts may be included during the unwrapping stage, after which they can be masked out by the unwrapping iteration number (See 2.1.1.4.2).

2.1.1.4.2 Coherence-based unwrapping

After filtering, the phase is still “wrapped”, where $\phi_{wrapped} \in [-\pi, \pi]$. Typically, analytical and numerical models of ground displacement produce outputs such that $\phi_{model} \in [-\infty, \infty]$. To facilitate data and model comparison, $2k\pi$ should be added to $\phi_{i,j}$, where $k \in \mathbb{Z}$. However, the direction in which the algorithm unwraps is non-unique, resulting in a non-unique value of k . Various unwrapping techniques have been created to compute a continuous, smooth $\phi_{unwrapped}$, without erroneous jumps of 2π between pixels.

Two main families of unwrapping algorithms exist— branch-cut [Goldstein et al., 1988] and statistical cost network flow [Chen and Zebker, 2001] techniques. The former introduces “branches” between pixels that have residues with opposite signs. Residues occur when the sum of a closed path of pixel phases is nonzero. The algorithm will not unwrap across these branches. The latter maximizes the unwrapped solution’s conditional probability using the wrapped phase, image amplitude, and coherence [Chen and Zebker, 2001].

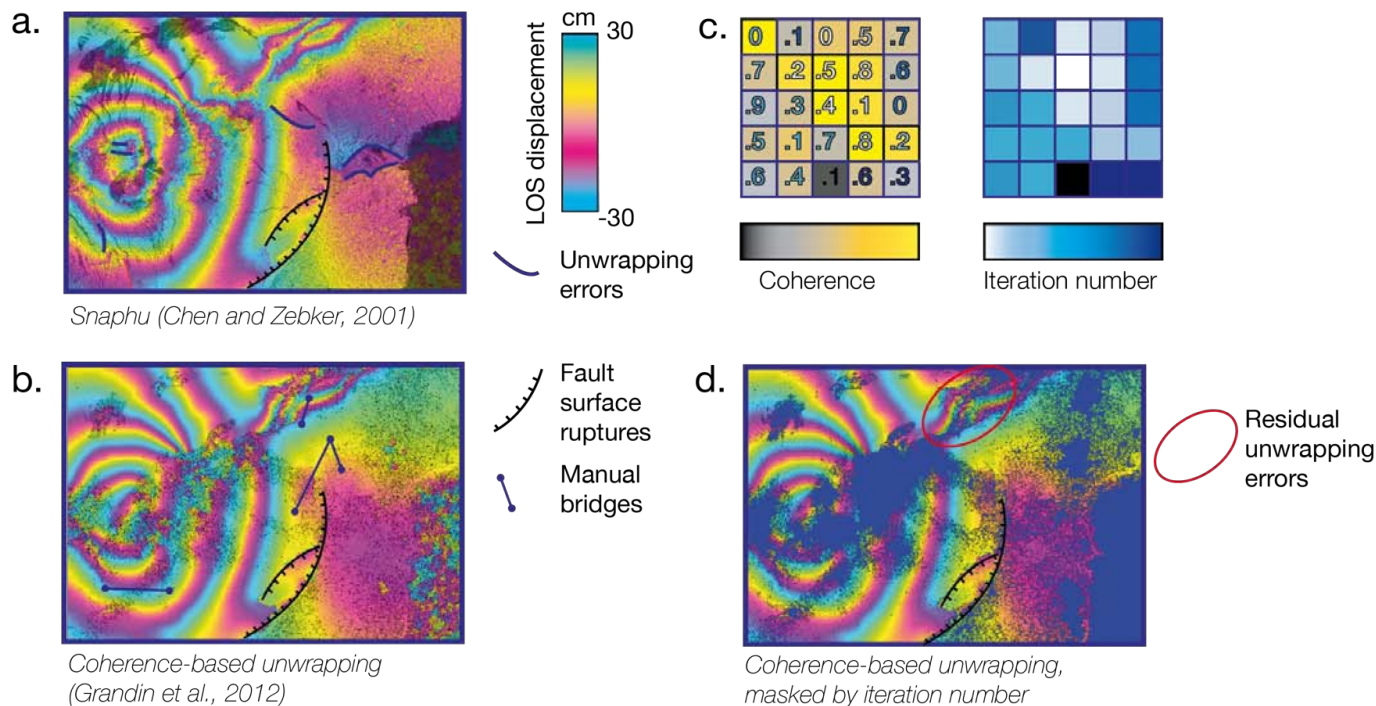


Figure 2-5: **Coherence-based unwrapping.** **a.** Unwrapping performed by the *snapu* algorithm of Chen and Zebker [2001]. Heavy dark blue lines indicate unwrapping errors. Fault surface ruptures due to caldera ring-faulting are also indicated with toothed lines. **b.** Unwrapping performed by the coherence-based unwrapping algorithm of NSBAS [Doin et al., 2011] described by Grandin et al. [2012]. User-defined bridges which connect fringes by integer multiples of 2π are indicated with dark blue, circle-capped lines. **c.** A visualization of the unwrapping algorithm and how the iteration number is determined. In the first column, each square’s color represents the coherence, with yellow being a high coherence, and black being a low coherence. The numbers in each square represent the wrapped phase, and each number’s color represent its iteration count. In the second column, the iterations begin with the seed pixel, in this case the pixel in the center, which has the highest coherence. Each square’s color represents its iteration number, with white being the first iteration, and dark blue being a later iteration. The black square is not unwrapped, as its coherence is below the minimum coherence threshold. See the text for more details of this coherence-based iterative unwrapping. **d.** The final unwrapped interferogram, after masking pixels above a certain iteration count threshold. Although this masking ensures that the majority of noisy pixels are discarded, some residual unwrapping errors remain, as noted by the red oval. These errors can be masked out by hand.

In this dissertation, we mainly utilise a variant of the branch-cut unwrapping algorithm that considers the coherence of a pixel (i, j) to determine the unwrapping path. The user inputs a minimum coherence threshold γ_{min} , a seed pixel where the unwrapping begins, (i_0, j_0) , as well as a list of connected points that should be unwrapped manually (the integer multiples of 2π must also be provided). This unwrapping method was implemented in NSBAS by Marie Pierre Doin [Doin et al., 2011], and described by Grandin et al. [2012] (see

Figure 2-5).

This unwrapping algorithm starts at point (i_0, j_0) with a phase of $\phi_{i_0, j_0, unw} = \phi_{i_0, j_0}$ and an iteration number, $n = 0$. The user also provides a minimum coherence threshold, γ_{min} . If a pixel, for example $(i_0 + 1, j_0)$, in the direct vicinity of (i_0, j_0) has not been unwrapped, and its coherence is above the current coherence threshold, γ_{thresh} , then we calculate the unwrapped phase such that

$$\phi_{i_0+1, j_0, unw} = \phi_{i_0, j_0, unw} - \arg(I_{i_0, j_0} \cdot \bar{I}_{i_0+1, j_0}), \quad (2.9)$$

where $I_{i, j} = A_{i, j} e^{i\phi_{i, j}}$.

This procedure is repeated for all four pixels surrounding (i_0, j_0) . If no surrounding pixels can be unwrapped during this step, a user-defined bridge may be applied. A bridge between two points, (i_1, j_1) and (i_2, j_2) , performs the same operation as Equation 2.9, but adds the appropriate k integer multiples of 2π , such that

$$\phi_{i_2, j_2, unw} = \phi_{i_1, j_1} - \arg(I_{i_1, j_1} \cdot \bar{I}_{i_2, j_2}) - 2k\pi. \quad (2.10)$$

The algorithm performs a set number of iterations, in this case 150000. If no pixels surrounding the current pixel can be unwrapped because their coherence is below the current γ_{thresh} , then γ_{thresh} is decreased by 0.018. Once $\gamma_{thresh} \leq \gamma_{min}$, no further pixels are unwrapped. If 6 pixels are consecutively unwrapped without lowering γ_{thresh} , then γ_{thresh} will be increased by 0.018, to direct the unwrapping path along the pixels with the highest coherence.

The final products obtained from this unwrapping method are the final unwrapped phase, which is added to the interferogram filtered with the weighted power spectrum. Other products include each pixel's iteration number and γ_{thresh} when it was unwrapped. The iteration number map can be used to mask the final unwrapped interferogram (see Figure 2-5d), where a lower iteration number is a proxy for a more reliable unwrapped phase. Because this algorithm unwraps along a path of the most coherent pixels, as well as includes the option to include user-defined bridges, it performs well when interferometric coherence varies significantly across the scene.

2.1.2 Measuring large ground displacements: additional SAR methods

To complement InSAR, other techniques to measure ground displacements include pixel offset tracking and multiple aperture interferometry. Both of these techniques are able to measure ground deformation in the azimuth direction, or the direction of the satellite flight path. Due to the near-polar orbits of SAR satellites, this component is mostly sensitive to N-S displacement.

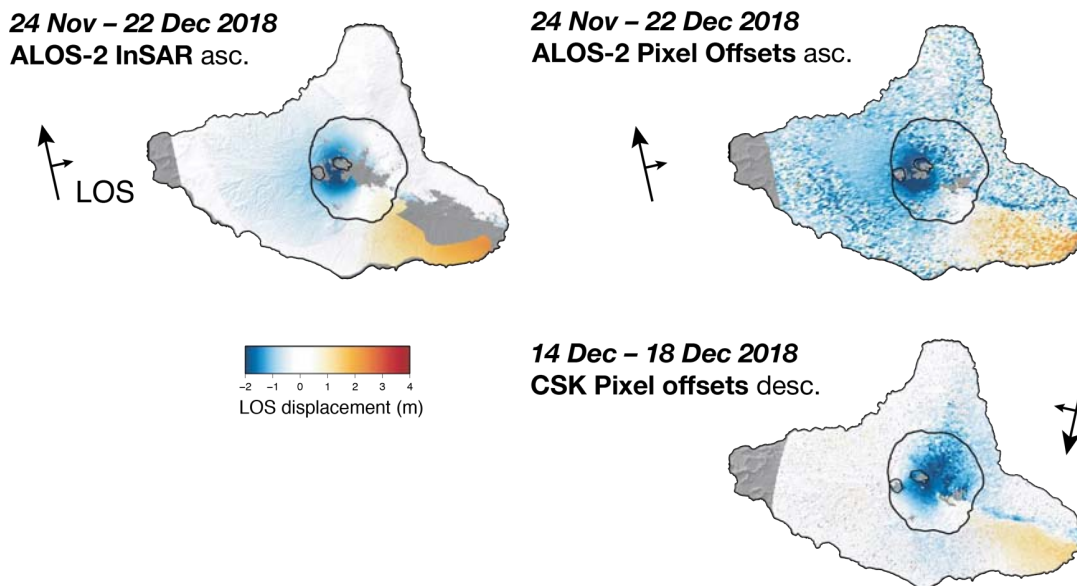


Figure 2-6: **InSAR vs. SAR pixel offsets.** The left hand column shows the unwrapped LOS displacement field spanning the 2018 Ambrym dike intrusion, as measured by ALOS-2 using InSAR. The right hand column shows the amplitude pixel offsets measured by both ALOS-2 (top row) and COSMO-SkyMed (bottom row). Pixel offsets are able to resolve displacement close to the dike trace, where InSAR is decorrelated. In addition, COSMO-SkyMed pixel offsets have a higher SNR than ALOS-2 pixel offsets, most likely due to the smaller pixel size (~ 2 m vs. ~ 4 m).

2.1.2.1 Amplitude pixel offset tracking

Large ground displacements may result in decorrelated InSAR measurements. In addition to measuring azimuth ground displacements, amplitude pixel offset tracking (incoherent cross-correlation) also maintains a coherent signal regardless of the magnitude of ground displacement (see Figure 2-6). Pixel offset tracking is not restricted by the magnitude of ground displacement because the algorithm relies on tracking amplitude features by finding the cross-correlation peak between the amplitudes of an $N \times M$ pixel window in two SAR images [Michel et al., 1999]. Therefore, large ground displacements can be measured as long as the extent of the correlation search window is large enough to include the target in both images. Typical applications of this technique include large earthquakes [Lauer et al., 2020] or glacier flow [Michel and Rignot, 1999]. Pixel offset tracking, however, is less accurate than InSAR because the measurement sensitivity (10-15 cm for SAR satellites, or $\sim 10 - 15\%$ of the pixel size) depends on pixel size [Simons and Rosen, 2007].

2.1.2.2 Multiple aperture interferometry

Another method used to measure azimuth displacement is to split an interferogram into one forward- and one backward- looking interferogram, as first proposed by Bechor and Zebker

[2006]. This can be done by processing only a portion of the antenna beamwidth, with a squinted beam angle and a reduced beam azimuth aperture, for both the forward- and backward-looking cases (see Figure 2-7). This processing results in two separate apertures, hence the name *multiple aperture* interferometry. The difference between the forward- and backward-looking interferograms is proportional to the azimuth displacement. Any phase contributions from topography, non-azimuthal deformation, or atmosphere are the same in both interferograms, due to their independence from the squint angle. These contributions cancel out in the final multiple aperture interferogram, leaving only the azimuth displacement. The accuracy of MAI is lower than LOS InSAR, due to the reduced angular aperture. The accuracy is instead comparable to that of amplitude pixel offsets, although the phase is used instead.

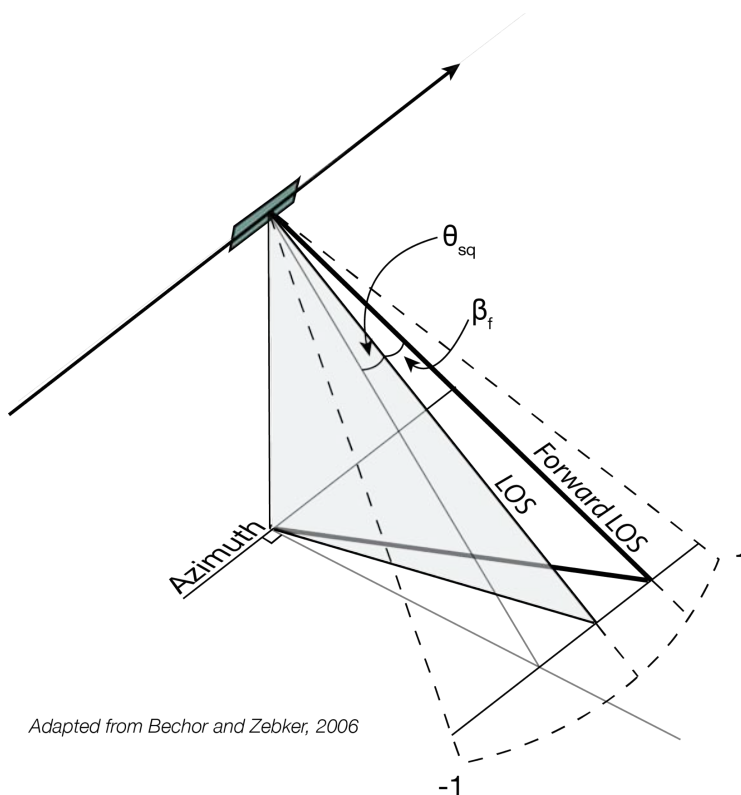


Figure 2-7: **Multiple aperture interferometry.** In multiple aperture interferometry (MAI), forward- and backward-looking interferograms are processed. This figure shows the mid-beam line of sight (LOS), which is squinted by θ_{sq} , as well as the forward-looking LOS, squinted further by β_f . The backward-looking LOS is squinted $-\beta_f$. The full beam width is shown by the dotted line labelled -1 to 1. Adapted from [Bechor and Zebker \[2006\]](#).

2.1.3 Current SAR satellite missions

Data availability and SAR system characteristics, such as wavelength, acquisition mode, and repeat time, dictate which techniques are most useful on a case-by-case basis. There are currently 8 main SAR missions with constellations in orbit, operated by national or

international (e.g., ESA) space agencies. Half of these have X-band wavelengths– TerraSAR-X/TanDEM-X, PAZ, KOMPSAT-5, and COSMO-SkyMed. There are two current missions for C-band wavelengths– RADARSAT-2 and Sentinel-1, and two for L-band– ALOS-2 and SAOCOM. See Figure 2-8 for a summary of current and past SAR missions.

These SAR satellites are able to acquire images in a variety of modes, resulting in data products with varying image footprints and spatial resolutions (see Figure 2-9). The fundamental SAR acquisition mode is Stripmap, where the antenna’s look and squint direction are fixed. Stripmap pixel size of satellite-borne SAR sensors range from $\sim 5 - 10$ m, and an image footprint (ground swath dimensions) between 50 and 100 km wide. In SAR systems, a compromise must be made between swath width and azimuth resolution. A larger swath width results in a longer pulse echo, which can only be fully resolved if the *PRF* is decreased. A lower *PRF* results in a coarser azimuth pixel spacing [Grandin, 2019]. In other words, a wide swath cannot have a fine azimuth resolution.

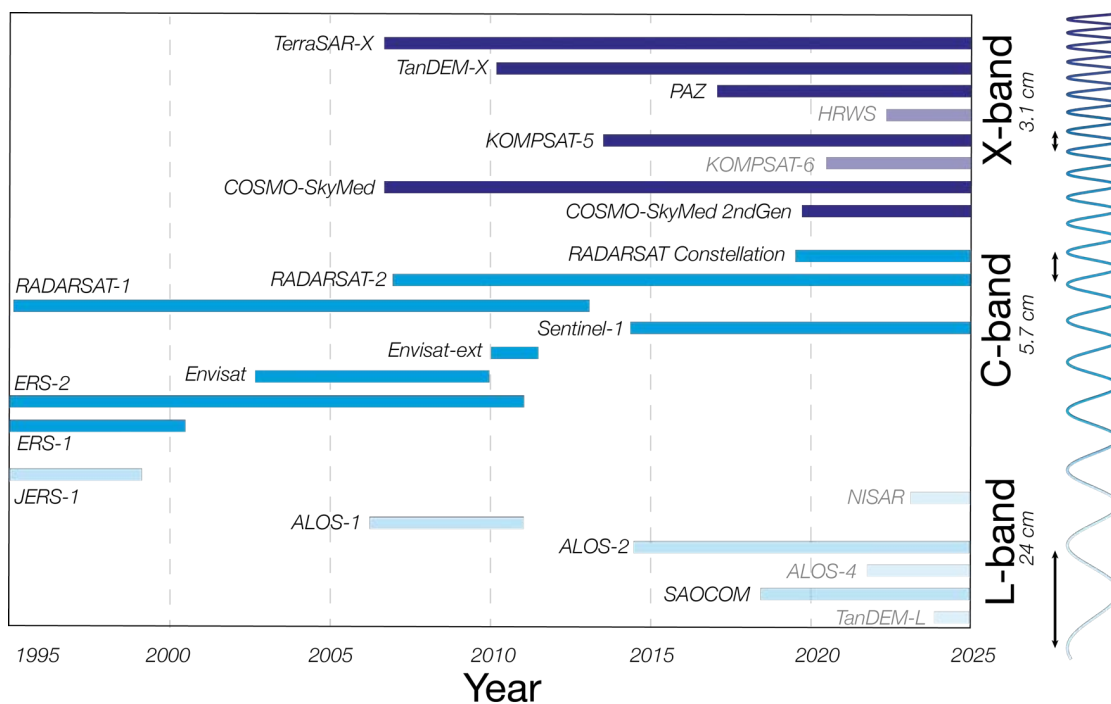


Figure 2-8: **Civilian SAR missions.** Past and current SAR missions, and their corresponding radar wavelength. Missions that have yet to be launched at the time of writing are shown in lighter colors.

High-resolution products ($< 1 - 2$ m pixel spacing) can be generated using special acquisition modes, such as Staring Spotlight. Staring Spotlight mode increases azimuth resolution by following the same spot on the Earth for an extended period. This increases a target’s illumination time and consequently its Doppler bandwidth [Massonnet and Souyris, 2008]. In Earth science applications, high resolution SAR is particularly useful for observing amplitude changes or pixel tracking. However, the high resolution is obtained at the cost of non-continuous observations when the antenna is following a point on the ground. Hence,

images have a limited length in azimuth. The PRF is also increased, which reduces the swath width.

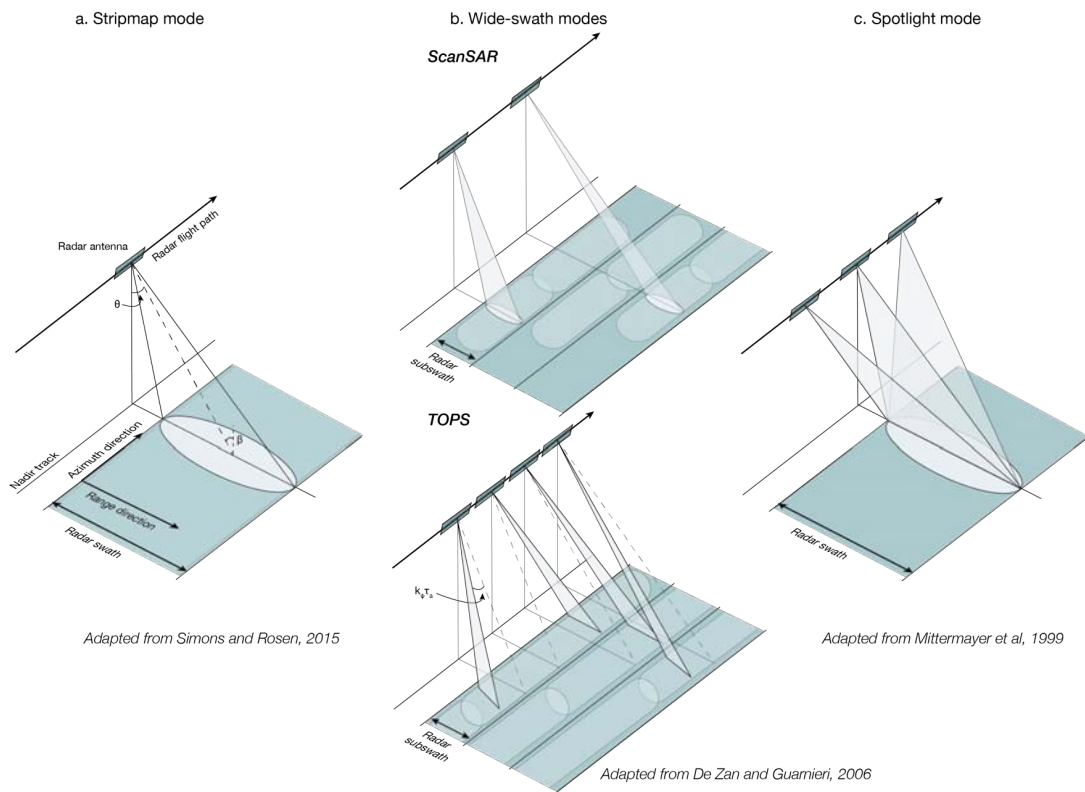


Figure 2-9: **SAR acquisition modes.** **a.** The fundamental Stripmap mode, where θ is the look angle and β is the incidence angle, both measured at the center of the swath. Adapted from [Simons and Rosen \[2015\]](#). **b.** The Wide Swath modes *ScanSAR* and *Terrain Observation by Progressive Scans (TOPS)*, each with three radar subswaths. In *ScanSAR*, the satellite’s squint angle is fixed. In *TOPS*, the beam angle in azimuth changes during the satellite flight path according to $\psi_{dc} = k_{\psi}\tau_a$, where τ_a is the azimuth time and k_{ψ} is the antenna rotation rate. Adapted from [De Zan and Guarnieri \[2006\]](#). **c.** The Spotlight mode, which increases the illumination time of a particular target by pointing the antenna in that direction for an extended period of time. This figure specifically displays the Staring Spotlight mode. Adapted from [Mittermayer et al. \[1999\]](#).

An opposite strategy consists of using Wide Swath acquisition modes, such as *ScanSAR* and *Terrain Observation by Progressive Scans (TOPS)*, resulting in large (up to 500 km wide) ground swaths. This allows for InSAR studies over large geographic areas, especially useful for regional tectonic studies. This also allows for a frequent revisit time, which is useful for studying volcanic systems. The original Wide Swath mode was *ScanSAR*, where pulse bursts consecutively image multiple subswaths (see Figure 2-9). However, a target’s Doppler bandwidth is reduced according to the number of swaths, decreasing azimuth resolution [[Massonnet and Souyris, 2008](#)]. *ScanSAR* is also susceptible to an effect called scalloping,

where the gain of the antenna radiation pattern seen by a target varies along azimuth, creating periodic fluctuations in the amplitude, if uncorrected. Azimuth-varying ambiguities also occur when echos received of a target are imaged by both the antenna pattern's main and side lobes. TOPS, on the other hand, is an acquisition mode [De Zan and Guarnieri, 2006] that was created to improve effects from scalloping and azimuth-varying ambiguities. In addition to sending bursts to image subswaths, the antenna beam also rotates progressively forward in the azimuth direction, which results in a longer burst where each target is seen by the same antenna pattern. TOPS is currently implemented in the European Space Agency's Sentinel-1, which systematically acquires SAR images of the globe every 6 – 12 days.

2.1.4 Earth science applications

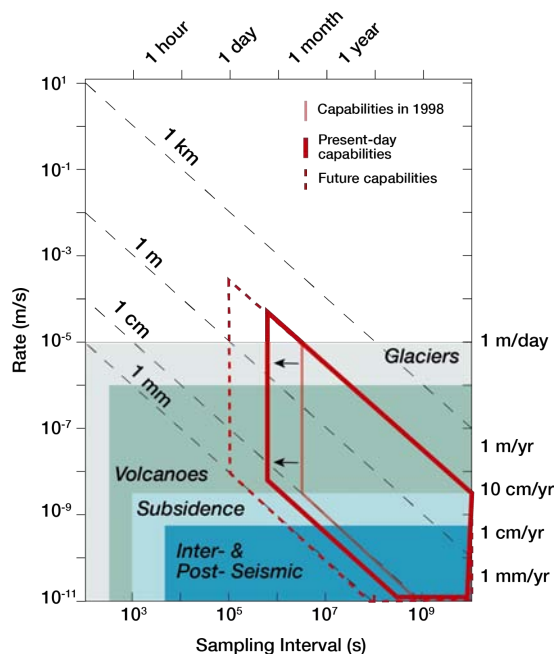
InSAR can obtain spatially dense ground displacement measurements regardless of weather or time of day, making it a powerful tool in Earth sciences. Study areas in Earth science may range from a tens of meters to hundreds of kilometers— from the growing Merapi lava dome to the creeping San Andreas fault. Processes within the Earth's crust also occur on all timescales, from seconds to millennia. Now that the SAR archive extends back 30 years, these processes can be studied on decadal timescales. In addition, commercial nanosatellite SAR missions (e.g. ICEYE, Cappella Space), may allow for geodetic observations of deformation processes occurring on hourly timescales. Phenomena that can be studied using ground displacement measurements include, but are not limited to, aquifer compaction, glacier flow, earthquakes, and volcanic unrest (see Figure 2-10).

Anthropogenic deformation may occur during ground water extraction, resulting in subsidence. In regions where ground water extraction supports agricultural or urban activities, such as Mexico and California, InSAR measures subsidence on both large and local spatial scales [Chaussard et al., 2014]. InSAR measurements are also sensitive to aquifer response due to modulating water extraction rates or seasonal meteorological conditions [Schmidt and Bürgmann, 2003, Murray and Lohman, 2018]. The spatially dense and extensive measurements of InSAR are necessary to map the widespread effect of ground water extraction across entire regions.

InSAR applied to glacier flow is of particular interest in the context of the changing climate. Ice sheets move at high velocities of up to 1 m day^{-1} , and accurate velocity measurements help constrain dynamic models [Bindschadler, 1998]. InSAR is able to map ice motion of large glaciers (in Greenland [Joughin et al., 2004], for example). There is even potential for InSAR to map ice flow velocity for the entirety of Antarctica [Mouginot et al., 2012]. Accurate velocity measurements help ensure accurate estimates of the mass balance of ice sheets [Mouginot et al., 2012].

The tectonics community has also taken full advantage of the capabilities of InSAR to measure deformation over different spatial and temporal scales. InSAR is used to study all aspects of the earthquake cycle— including coseismic ground displacement, postseismic deformation, and interseismic fault creep [Massonnet and Feigl, 1998]. As mentioned previously, the first coseismic interferogram measured ground displacement produced by the 1992 Landers earthquake [Massonnet et al., 1993]. Recent coseismic InSAR measurements, such as during the 2016 Kaikōura earthquake, have resulted in the realization that fault ruptures and segmentation are much more complex than previously thought [Hamling et al., 2017].

Multitemporal InSAR time series allow for measurements of aseismic fault creep with sub-centimetric accuracy across entire fault segments, such as the San Andreas [Jolivet et al., 2015] or the North Anatolian [Rousset et al., 2016] faults.



Adapted from Massonnet and Feigl, 1998

Figure 2-10: **Ground displacement via geological processes.** The rate and duration of ground displacement for various geological phenomena. The region within the solid red line shows the displacement that can be measured by present-day InSAR, with a revisit time of 6 days and a sub-centimetric accuracy. The light red line indicates the capabilities of InSAR in 1998, according to Massonnet and Feigl [1998]. The dotted red line shows the best-case scenario for future SAR satellite capabilities (daily acquisitions, millimetric accuracy). The top right of the figure is restricted due to phase decorrelation resulting from large deformation gradients. Adapted from Massonnet and Feigl [1998].

The above applications are by no means exhaustive. We end this section with a focus on the application of InSAR to volcanic unrest, which drives the bulk of the results found in this dissertation. As SAR acquisitions become increasingly temporally dense, InSAR can be used to study and model the various volcanic processes driving crustal deformation. Volcanic deformation may be due to a variety of processes which occur at depths ranging from the surface (e.g., lava flow compaction and cooling) to the mid-to-low crust (e.g., magmatic injection). In the late 1990's, just as InSAR was beginning to gain attention in the tectonics community, only 44 volcanoes were known to be deforming [Dvorak and Dzurisin, 1997]. In 2016, this number jumped to more than 220 [Biggs and Pritchard, 2017]. This surge is due to the increasing prevalence of volcano monitoring using InSAR to complement ground-based techniques such as Global Navigation Satellite System (GNSS) [Dzurisin, 2007, Pinel et al., 2014]. Interferograms are now produced routinely by volcano observatories worldwide, and

are used in conjunction with other datasets to drive decision-making during eruptions (such as during the 2018 Kīlauea rift zone eruption and caldera collapse [Neal et al., 2018]).

As SAR observational strategies improve and expand, the quantity of observed volcanoes will increase, as will geodesists’ ability to disentangle signals from the various volcanic processes that induce ground deformation. Analytical and numerical models of pressurized deformation sources embedded within the Earth’s crust may fit observations at the surface to the first order. However, they are far from representing a transcrustal magmatic system consisting of melt and crystal-rich mush (See Section 5.1.1.3). While SAR data availability is increasing exponentially, we must not forget that to translate these observations into a furthered physics-based understanding of volcanic systems, we must continue to develop our qualitative, and quantitative, understanding of the interacting constituents of a magmatic system.

2.2 Geodetic inverse modelling

Volcanic crustal deformation is the surface manifestation of physical processes occurring kilometers beneath the Earth’s surface. The injection or migration of magma, as well as phase changes (e.g., volatile exsolution or crystallization), result in pressure changes in the magmatic or hydrothermal system. The lithosphere will deform in response to the given pressure change (imposed stress), and the resulting surface displacement depends on the crustal properties and the shape of the cavity. Magma can also open fractures in the brittle crust and migrate into these fractures, forming magmatic intrusions. If the crust is assumed to be homogeneous and elastic (which is reasonable for time scales on the order of seconds to months), its deformation can be calculated analytically for sources with various shapes and sizes (e.g., spheres, ellipsoids, rectangular dislocations) using the theory of linear elasticity [Mogi, 1958, Okada, 1985, McTigue, 1987, e.g.,].

These analytical formulations were developed when surface deformation was measured using sparse GNSS, tiltmeters, or trilateration lines measurements (such datasets typically only included tens of data points) [Segall and Harris, 1987, Harris and Segall, 1987]. InSAR measurements, however, produce dense (nearly continuous) 2-D maps of ground displacements, making it easier to identify discrepancies between models and data. For example, complexities that are ignored in the aforementioned analytical formulations include complex geometries of the deformation sources or interactions between multiple sources.

In this dissertation, we attempt to explain complex spatial patterns of co-eruptive surface deformation at Ambrym by several sources with non-planar geometries (i.e., curved dikes and caldera ring-faults). We employ various inversion techniques, both linear and nonlinear, as well as analytical and numerical methods, depending on the data availability and the complexity of the source(s). We will begin this section by defining and setting up a general “inverse problem”. Then, we will discuss the mathematical formulations and numerical methods which can be used to relate deformation source parameters to measured surface displacements.

2.2.1 Defining the inverse problem

Inverse problem theory can be used to estimate the source parameters necessary to explain geodetically measured surface displacements. Solving an inverse problem consists of finding m (the model parameters) from

$$d = g(m), \quad (2.11)$$

where d is the observations and g is an operator which relates the physical model to the observation [Tarantola, 2005]. Equation 2.11 defines the *forward problem*. The forward problem can be used, for example, to calculate InSAR surface displacements d given the appropriate operator g determined by linear elasticity, as well as the location and geometry of the deformation source, described by m . The approach used to solve for m in Equation 2.11 depends on whether the inverse problem is linear or nonlinear.

2.2.1.1 Linear inverse theory

If the operator g is linear, then Equation 2.11 can be rewritten as the following

$$\mathbf{d} = \mathbf{G}\mathbf{m}, \quad (2.12)$$

where \mathbf{d} is the data vector, \mathbf{m} is the model parameter vector, and \mathbf{G} is a matrix defining the mathematical relationship between the model parameters and the data. When modelling surface deformation with InSAR, we often have more InSAR observations than model parameters, resulting in an *overdetermined* system of equations. In other words, our linear system of equations, expressed by Equation 2.12, has more equations than unknowns, and hence has no single solution that satisfies all of the observations. To solve an overdetermined linear system of equations, the least squares criterion can be applied [Tarantola, 2005]. Under the assumption that the priors are Gaussian, we minimize the L2 norm between the predicted observables \mathbf{d}_{pred} and the measured observables \mathbf{d}_{obs} , which can be expressed as the misfit function:

$$S(m) = \frac{1}{2} \left[(\mathbf{d}_{pred} - \mathbf{d}_{obs})^T \mathbf{C}_d^{-1} (\mathbf{d}_{pred} - \mathbf{d}_{obs}) + (\mathbf{m} - \mathbf{m}_0)^T \mathbf{C}_m^{-1} (\mathbf{m} - \mathbf{m}_0) \right], \quad (2.13)$$

where \mathbf{C}_d is the data covariance matrix (See Section 2.2.1.3.2), \mathbf{C}_m is the model covariance matrix (See Section 2.2.2.5.1), and \mathbf{m}_0 represents the *a priori* model parameters. The solution that minimizes $S(m)$ can be computed by

$$\mathbf{m}_{est} = \mathbf{m}_0 + \mathbf{C}_m \mathbf{G}^T (\mathbf{G} \mathbf{C}_m \mathbf{G}^T + \mathbf{C}_d)^{-1} (\mathbf{d}_{obs} - \mathbf{G} \mathbf{m}_0). \quad (2.14)$$

In a broader sense, since the posterior uncertainties to the solution of a linear inverse problem are Gaussian, we can consider \mathbf{m}_{est} to be the center, or mean, of the posterior probability density function σ_M [Tarantola, 2005]. Minimizing $S(m)$ is the same as maximizing σ_M (or finding the maximum posterior likelihood).

2.2.1.2 Nonlinear inverse theory

In many cases, the operator g is nonlinear, or g is linear but the priors are non-Gaussian. In both cases, the posterior probability density function will not be Gaussian. To solve a weakly nonlinear inverse problem, it is possible to linearize the operator around some determined prior model \mathbf{m}_0 (See Figure 2-11c). Solving this linearized problem becomes the same as solving the linear problem [Tarantola, 2005].

When the problem cannot be linearized, but is quasilinear near \mathbf{m} (e.g. Figure 2-11d), iterative “steepest descent algorithms” can be used to estimate \mathbf{m} . One such approach is the Quasi-Newton method [Tarantola, 2005], which is implemented in this dissertation using the code of Briole et al. [1987]. Each model parameter is given an *a priori* value, around which the algorithm can explore according to the provided “step” value. A larger step value results in the algorithm searching farther away from the *a priori* value, exploring a larger parameter space, but increasing the chance that the final \mathbf{m} estimated will represent a local, not global, minima.

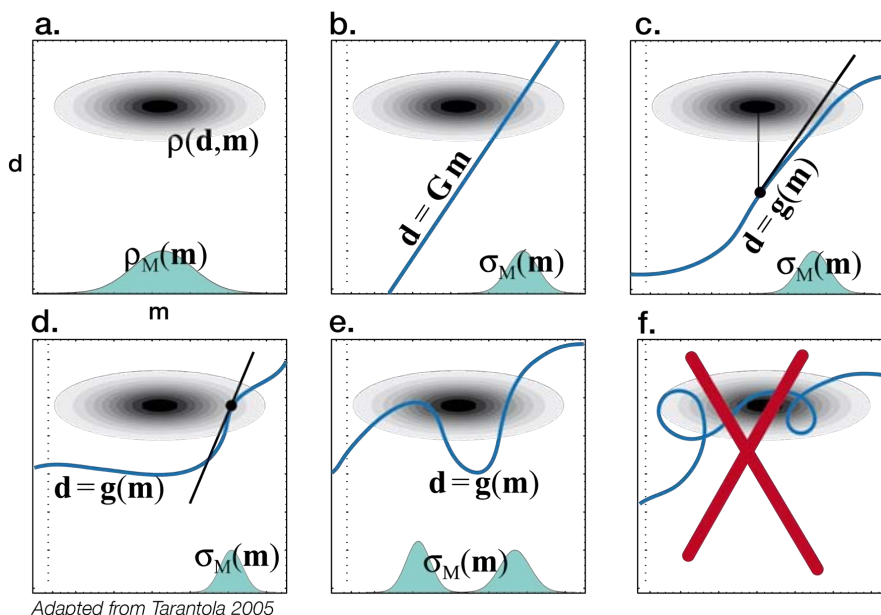


Figure 2-11: **Nonlinearity in forward problems.** Plots showing a variety of levels of nonlinearity that can be encountered in the forward problem. **a.** The probability density $\rho(\mathbf{d}, \mathbf{m})$ and marginal $\rho_M(\mathbf{m})$ which represent the *a priori* information on \mathbf{d} and \mathbf{m} . **b.** The case when the forward problem is linear, and the posterior probability density $\sigma_M(\mathbf{m})$ is Gaussian. **c.** The forward problem is weakly nonlinear, and can be linearized around \mathbf{m}_0 . **d.** The forward problem can be linearized around the maximum likelihood point, which can be estimated by iterative methods. **e.** The forward problem cannot be linearized, and other techniques, such as Monte Carlo approaches, are necessary. **f.** The nonlinearities of the forward problem are so strong that more sophisticated techniques are necessary. Adapted from Tarantola [2005].

When inverse problems become highly nonlinear (many local maxima in the posterior

probability density), Monte Carlo methods have to be implemented (See Figure 2-11e). Monte Carlo methods are extensive explorations of the model parameter space. They are optimized to sample a multi-dimensional probability density function in a (pseudo)random, yet efficient, manner [Tarantola, 2005]. The optimization algorithms are called sampling methods (e.g., Gibbs Sampler, Metropolis Algorithm). The goal of the optimization is to densely sample areas of significant probability, which are small compared to the entire multi-dimensional parameter space [Tarantola, 2005]. By performing random walks with probabilistic rules that reject or accept the direction of the next step, these algorithms efficiently sample the distributions of interest [Tarantola, 2005]. The specific Monte Carlo method that has been utilised in this dissertation– the neighborhood algorithm [Sambridge, 1999a,b]– will be discussed further in Chapter 4.

2.2.1.3 Data preparation

As discussed previously, two of the main inputs of the inverse problem are the observation vector \mathbf{d} (in geodetic modelling, chosen via data downsampling) and the uncertainty of this data (incorporated via the data covariance matrix).

2.2.1.3.1 Data downsampling

InSAR displacement maps may include millions of data points. Appropriately downsampling the data, or choosing a subset of the data points, renders the inverse problem computationally feasible, while ensuring a representative data subset. The downsampled data should retain the spatial structure of displacement field (even in areas where the displacement gradient is high) and the full range of displacement values. To achieve this, data should be sampled finely in areas of high displacement or high displacement gradient (i.e., the near-field), and coarsely sampled in regions with low displacement (i.e., the far-field). Even measurements in the far-field, where there is no displacement, are necessary to determine the spatial extent of the deformation signal. In addition, the projection of 3-D surface displacements into a radar’s line-of-sight (LOS) may result in null LOS displacement in the near-field, information that must be included to estimate the correct model parameters [Grandin, 2009, Smittarello et al., 2019].

Given these requirements, we can explore various downsampling schemes to establish the most suited for our problem. The first is uniform downsampling, which averages neighboring pixels to obtain a regular grid with fewer data points than the original dataset (See Figure 2-12a). However, this method oversamples the far-field, which includes redundant information that would not improve model parameter estimates.

Another downsampling method is based on distance, with increasing increments farther away from the source (See Figure 2-12b). In other words, the data points are sampled finely, yet uniformly, near the deformation source, and more coarsely farther away. Other methods (“quadtree”) include subdividing quadrants of data until the variance (or displacement gradient) within each quadrant is below an (often arbitrarily-chosen) threshold [Jónsson et al., 2002]. However, this technique may undersample regions that have low LOS deformation in the near field, due to the projection of the displacement vector into the LOS, as mentioned above. Additional methods consider the generalized inverse problem itself– so-called

“resolution-based” downsampling. Data points are chosen if the diagonal of the model resolution matrix ($\mathbf{G}\mathbf{G}^{-g}, \mathbf{G}^{-g} = (\mathbf{G}\mathbf{G}^T)^{-1}\mathbf{G}^T$) is greater than a chosen threshold [Lohman and Simons, 2005]. The data values themselves do not influence the downsampling, which may be useful when the data is noisy. However, there must be *a priori* knowledge on the deformation source, which may be complicated when the data is incoherent, or the displacement field is complex. In practice, since the model resolution depends strongly on distance, a “resolution-based” downsampling will be similar to the distance-based approach.

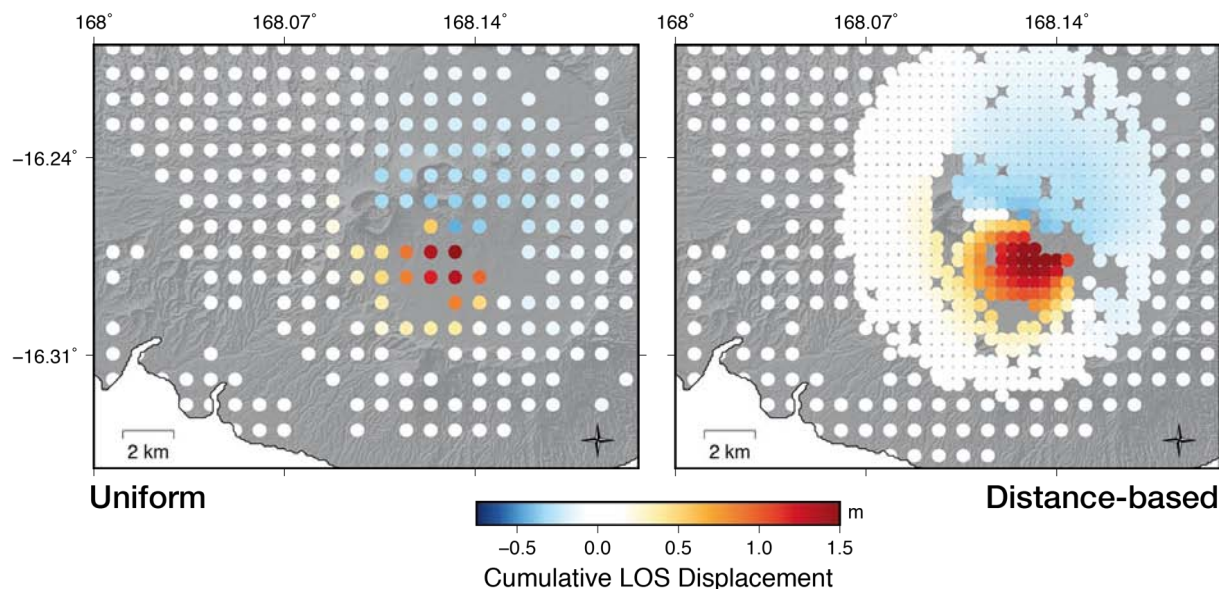


Figure 2-12: **Downsampling methods.** Example of uniform (lefthand map) and distance-based (righthand map) downsampling with data from an eruption in 2015 at Ambrym.

2.2.1.3.2 Data covariance matrix

As mentioned in Section 2.1.1.3, atmospheric and ionospheric phase delays in the data cannot be fully removed from an interferogram. Nonetheless, the structure of this “noise” can be incorporated in the inversion with the data covariance matrix C_d , which weights the data according to the strength and distance of spatially correlated noise sources. Throughout this dissertation, we account for spatially correlated noise using a data covariance matrix populated with an empirically calculated semivariogram [Chilés and Delfiner, 1999]. A semivariogram is computed by taking the squared difference of a random subset of data points in non-deforming areas. Phase changes in these regions are thought to be only affected by noise, and noise structure is assumed to be similar in non-deforming and deforming areas [Lohman and Simons, 2005, Sudhaus and Jónsson, 2009]. This value is then plotted against the distance between the two points [Lohman and Simons, 2005, Fukushima et al., 2005, Sudhaus and Jónsson, 2009] (See Figure 2-13). The semivariogram is fit by an exponential decay of the form $(C - \sigma_d^2 \cdot \exp^{-\frac{\|k_1, k_2\|}{a}})$, where $\|k_1, k_2\|$ is the Euclidean distance between two subsampled pixels $k_1 = (x_1, y_1)$ and $k_2 = (x_2, y_2)$, σ_d is the variance, a is the correlation distance, and C is the horizontal asymptote.

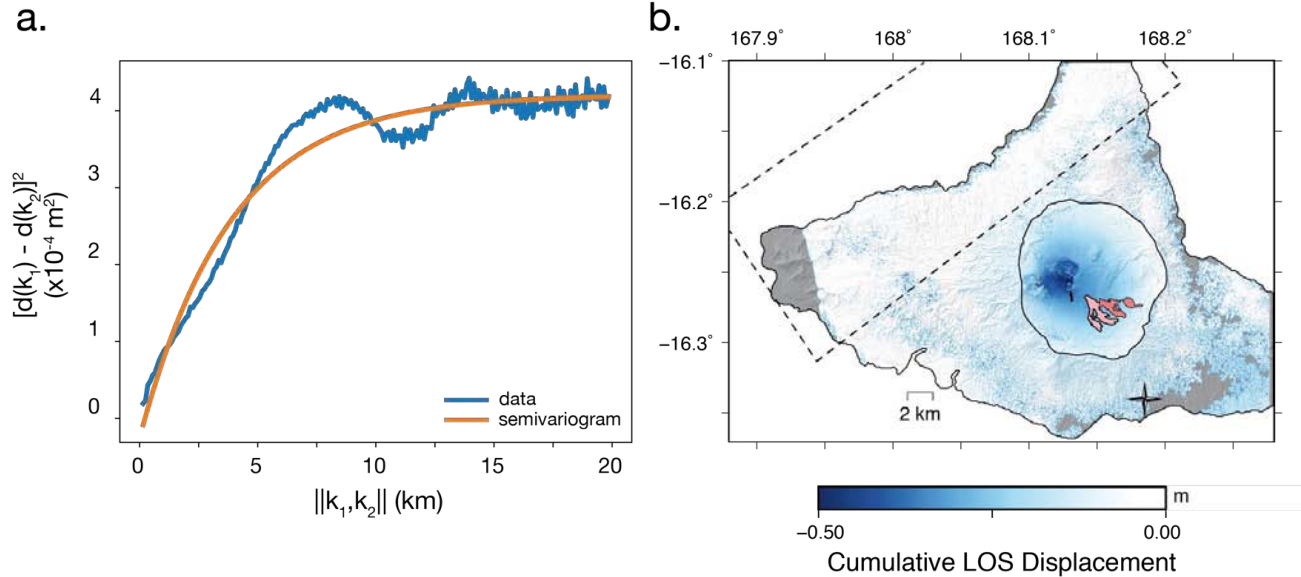


Figure 2-13: **InSAR semivariogram.** **a.** Semivariogram calculated from random data points k_1 and k_2 selected from a non-deforming section of the interferogram in **b.** The Euclidean distance between k_1 and k_2 is $\|k_1, k_2\|$. **b.** An interferogram showing post-intrusion subsidence spanning 22 December 2019 – 16 February 2020. The semivariogram is calculated from data points randomly selected from within the dotted box.

Estimating an empirical semivariogram means that no assumptions have to be made *a priori* about the error origin (atmosphere, ionosphere, but also post-processing steps like filtering) [Lohman and Simons, 2005]. The data covariance matrix can then be populated for each pair of pixels in the interferogram through the following

$$C_d(k_1, k_2) = \sigma_d^2 \cdot \exp\left(-\frac{\|k_1, k_2\|}{a}\right). \quad (2.15)$$

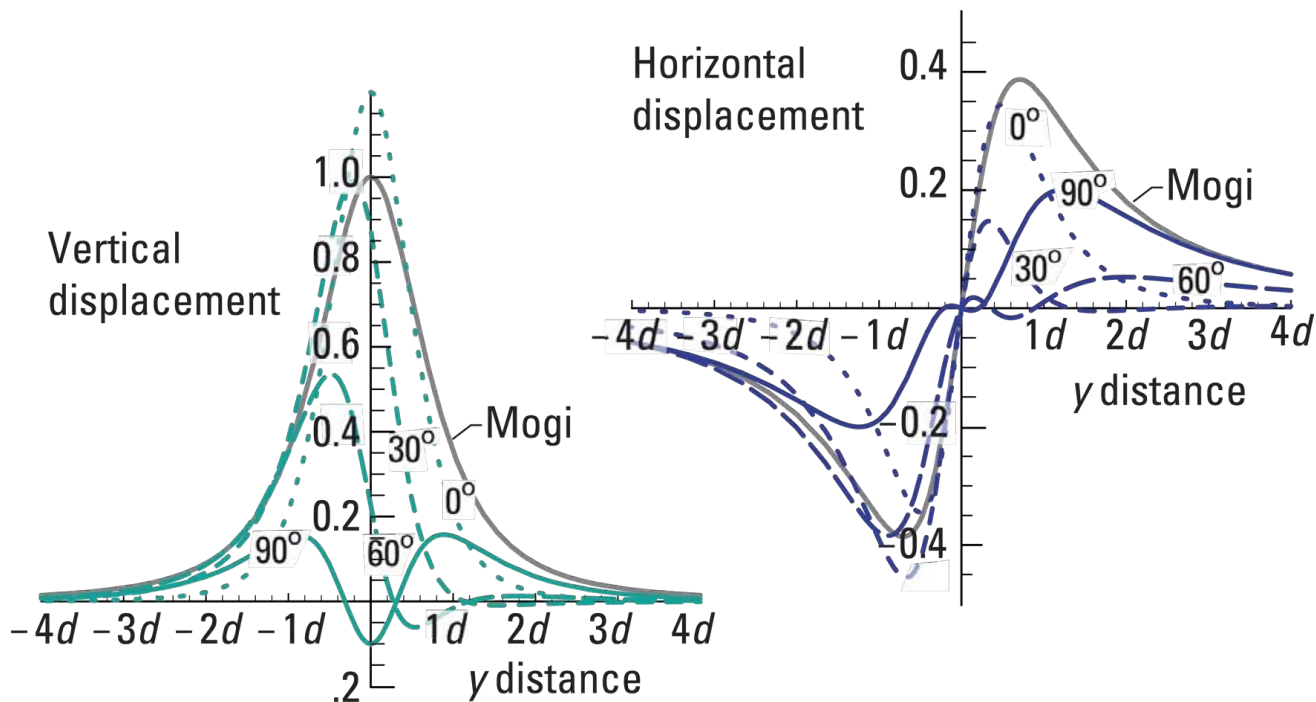
[Fukushima et al., 2005]. This function makes C_d positive-definite, hence always invertible [Armstrong and Jabin, 1981].

Once the data and data covariance matrix have been prepared, they define the \mathbf{d} vector and \mathbf{C}_d matrix. In order to set up the system of linear equations in Equation 2.12, we must still choose the appropriate matrix \mathbf{G} .

2.2.2 Choosing the appropriate analytical model

By choosing \mathbf{G} , we are defining the appropriate mathematical operator that relates the model parameters to the surface observations. As mentioned previously, analytical formulations [Mogi, 1958, Okada, 1985, McTigue, 1987] have been derived to model volcanic deformation sources. Mode I fractures represent opening (or closing) dikes or sills, while ellipsoids or spheres represent magmatic reservoirs undergoing pressure changes. The type of analytical solution used needs to be chosen *a priori*, based on the spatial pattern of surface deformation and a conceptual understanding of the particular volcanic system. If the source geometry

(shape, location, size, orientation) is also fixed *a priori*, we can use the linear least squares criterion to estimate volume or pressure changes. However, these analytical solutions have nonlinear relationships between source depth and surface displacements. Therefore, nonlinear inversion techniques must be implemented to solve for the source geometries.



Adapted from Lisowski 2006

Figure 2-14: **Ground displacements due to dike inflation.** The vertical and horizontal displacements along a perpendicular cross-section at the center of an inflating point tension crack, for various dike dips (0° , 30° , 60° , 90°). The displacements are normalized to the displacements of a Mogi source with an equivalent moment (indicated by the gray line). Adapted from Lisowski [2006].

2.2.2.1 Common analytical volcanic sources

Two of the most widely used deformation sources used to model volcanic deformation are the Mogi (spherical pressurized cavity, represents a reservoir) and Okada (rectangular dislocation, represents a dike or sill) models. The simplest (i.e., requires the least amount of parameters) volcanic deformation source is the Mogi model, or a spherical source embedded in an homogeneous elastic half-space [Mogi, 1958].

The surface displacements (which are axisymmetric around the source's center) at a point (u, v, w) can be calculated according to the relationship

$$\begin{pmatrix} u \\ v \\ w \end{pmatrix} = \alpha^3 \Delta P \frac{(1-\nu)}{G} \begin{pmatrix} \frac{x}{R^3} \\ \frac{y}{R^3} \\ \frac{d}{R^3} \end{pmatrix}, \quad (2.16)$$

such that $(x, y, -d)$ is the cavity location, α is the radius, G is the elastic modulus, ν is

Poisson's ratio, and $R = \sqrt{x^2 + y^2 + d^2}$ or the radial distance from the source to the surface (See Figure 2-15a). Surface displacements for a Mogi source depend only on its location, the cavity radius α , the pressure change ΔP of the source, as well as properties of the host rock. The depth $-d$ must be much greater than the radius α for the point source approximation to be valid.

Difficulties arise when attempting to estimate ΔP in Equation 2.16. The cavity size and ΔP are coupled, such that a large cavity with a small pressure change may produce the same surface displacements as a small cavity with a large pressure change. In addition, the elastic modulus of the host rock tends to be poorly constrained, resulting in uncertainties on ΔP that may reach an order of magnitude [Lisowski, 2006]. On the other hand, the source volume change ΔV can be robustly estimated given the surface displacement measurements. ΔV is proportional to the surface volume change $\Delta V_s = 2(1-\nu)\Delta V = 1.5\Delta V$ when $\nu = 0.25$ [Delaney and McTigue, 1994]. The factor of 1.5 comes from the presence of the free surface, which induces dilatation above the cavity [Lisowski, 2006]. To bypass the aforementioned difficulties, ΔP can be related to ΔV of a point source by the relationship $\Delta V \simeq \frac{\Delta P}{G}\pi\alpha^3$ [McTigue, 1987]. Equation 2.16 is therefore often expressed as a function of $\frac{\Delta V}{\pi}$ instead of $\frac{\alpha^3\Delta P}{G}$.

A second commonly used model, developed by Okada [1985], is a rectangular tensile dislocation with uniform opening embedded in a homogeneous elastic half-space. Its geometrical parameters are shown in Figure 2-15b. The full analytical expressions can be found in Okada [1985]. A shearing Okada rectangular dislocation is commonly used to describe earthquake deformation (i.e., slip on a fault). Tensile dislocations can also approximate, in the far-field, a fluid-filled elliptical crack, as described by Pollard and Holzhausen [1979] in 2-D [Davis, 1983]. Vertical displacements are symmetric when the plane has a dip of 0° and 90° (analogously, horizontal displacements are antisymmetric when the plane has a dip of 0° and 90°) (See Figure 2-14). Subsidence is observed directly above an opening vertically-dipping tensile dislocation due to the dislocation's finite length. Outside of this region of extension, the surrounding host rock is under compression. This compression results in the following relationship between the surface volume change and dike volume change

$$\Delta V_s = \frac{3}{4}\Delta V, \quad (2.17)$$

if $\nu = 0.25$ [Lisowski, 2006].

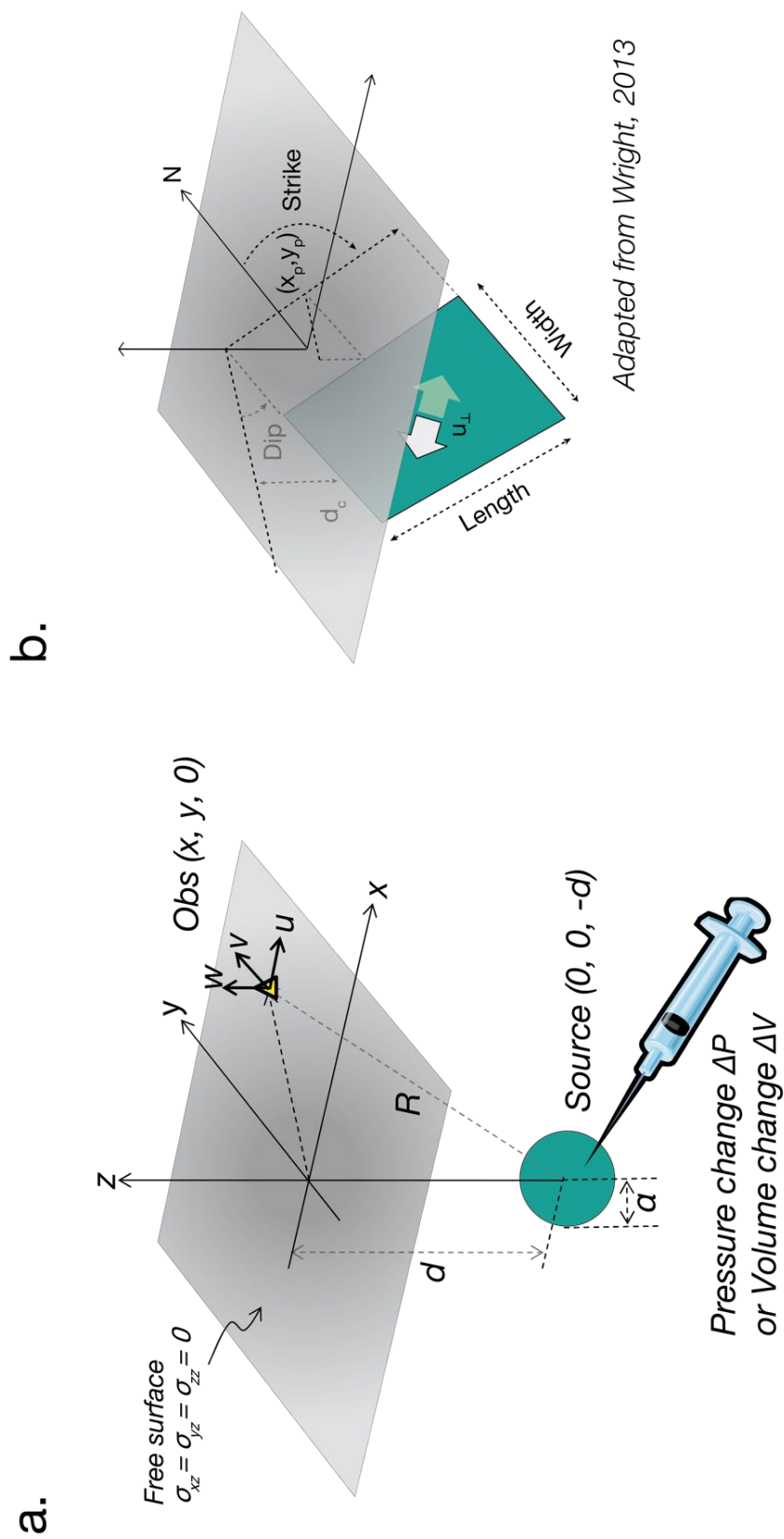


Figure 2-15: Mogi and Okada geometries. The geometrical parameters necessary to define a **a.** pressurized Mogi source or an **b.** opening rectangular dislocation. Adapted from Wright [2013].

Other analytical solutions that represent volcanic cavities allow for finite and/or non-spherical sources, whose surface displacement depends on the axis ratios. These include the model of [McTigue \[1987\]](#), who derived the approximate analytical solution for surface displacements due to a pressurized finite spherical source, and of [Davis \[1986\]](#), who found the point source approximation of an ellipsoid. There are also analytical solutions for prolate spheroids and horizontally-dipping cracks [[Yang et al., 1988](#), [Fialko et al., 2001](#)]. While these models are useful, they also have limitations. For example, the analytical solution for the prolate spheroid of [Yang et al. \[1988\]](#) is only valid as long as the source's depth remains greater than the upper surface's radius of curvature. This inaccuracy arises due to the addition of image solutions to obtain the analytical formulation in a half-space, modifying the pressure boundary conditions on the spheroid's surface [[Yang et al., 1988](#)].

A comparison of surface displacements produced by different cavity geometries can be found in [Figure 2-16](#). Horizontal displacements vary depending on the cavity geometry, with prolate ellipsoids ("pill-shaped" stock in [Figure 2-16](#)) producing the most horizontal motion. However, if the source depth is scaled accordingly, the vertical displacements between different cavities are similar. InSAR measurements are more sensitive to vertical than horizontal displacements. As a result, a single interferogram may not adequately capture the horizontal displacements, making discrimination between the various cavity geometries difficult. A combination of multiple acquisition geometries with azimuth displacements can produce a 3-D displacement map, which may help to resolve a cavity's geometry (integrating 3-D GPS measurements would also be invaluable, if such measurements are available).

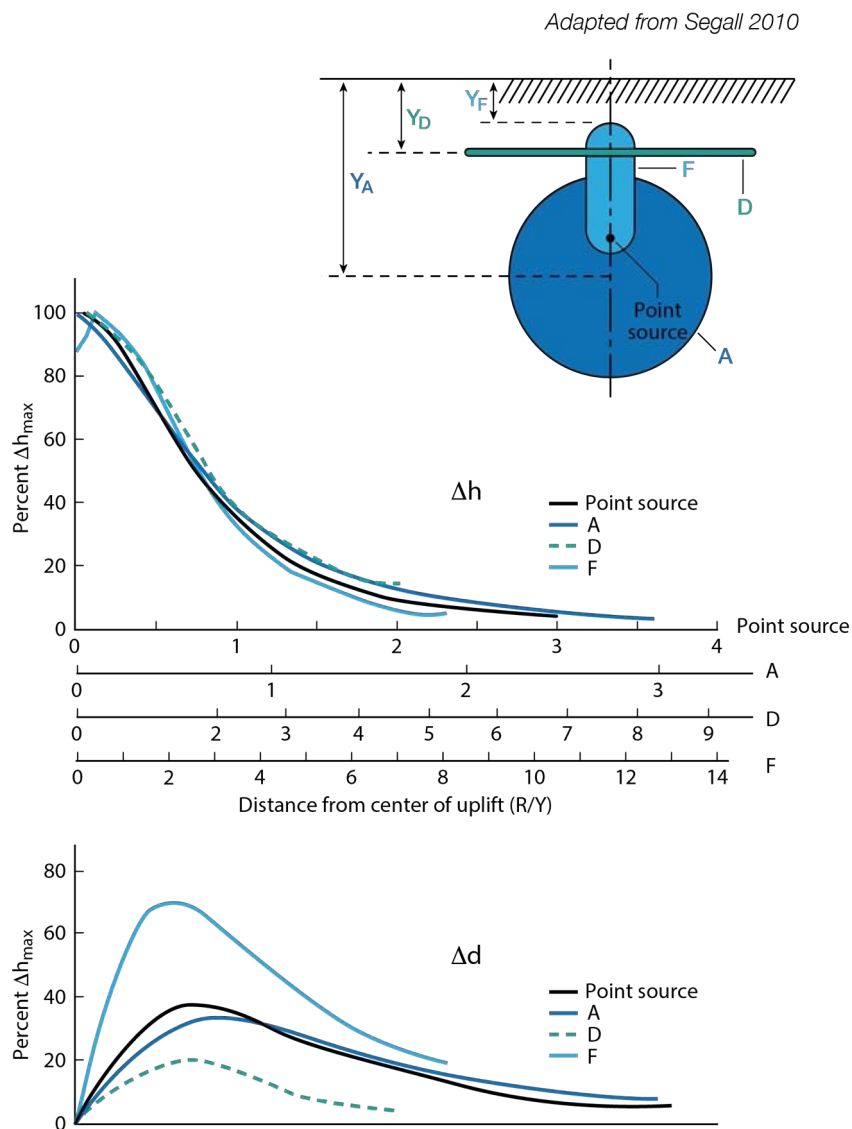


Figure 2-16: **Ground displacements of inflating cavities.** Profiles of vertical and horizontal surface displacements for a sphere (A), a circular sill (D), a “pill-shaped” stock (F), and a point source computed with the finite element method, normalized to the maximum vertical displacement. Note the horizontal scale (radial distance) is normalized according to the source depth. Adapted from Segall [2010], Dieterich and Decker [1975].

2.2.2.2 Compound Dislocation Model

As shown in Figure 2-16, the type of volcanic source chosen to explain InSAR observations affects the estimated model parameters (depth, pressure/volume change). With this in mind, a universal analytical model, which could represent both fractures and all cavity geometries, would alleviate the need to accurately choose a single type of model *a priori*. Such a universal model can be mathematically described by three orthogonal rectangular dislocations (Compound Dislocation Model, CDM developed by Nikkhoo et al. [2017]). A

CDM's geometry can be fully explained by 10 parameters— three location parameters (x , y , z), three rotational parameters ($\omega_X, \omega_Y, \omega_Z$), three shape parameters (semi-axis lengths a, b, c), and the uniform opening of each dislocation (u) (See Figure 2-17). The surface deformation induced by each of these 3 individual rectangular dislocations is calculated from an improved version of Okada's equations, to account for the fact that the upper edge of the dislocations is not necessarily parallel to the surface [Nikkhoo et al., 2017].

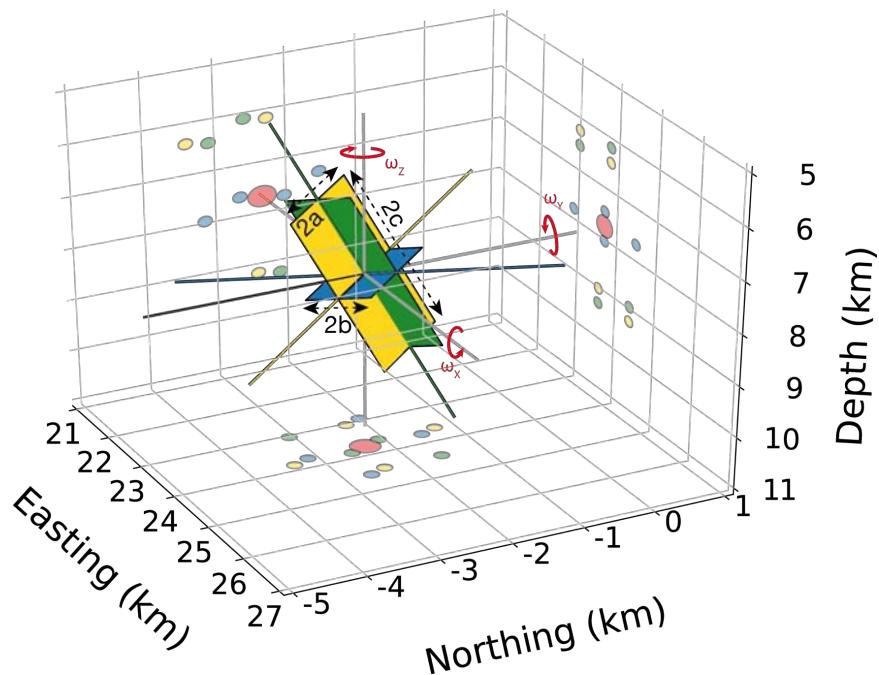


Figure 2-17: **CDM geometry.** The Compound Dislocation Model (CDM), composed of three orthogonal rectangular tensile dislocations, and three rotational degrees of freedom ($\omega_X, \omega_Y, \omega_Z$). Adapted from Nikkhoo et al. [2017].

2.2.2.3 Moment tensors equivalencies

In order to quantitatively demonstrate the equivalence of the CDM to the analytical models mentioned above, their respective moment tensors can be compared. Moment tensors are widely used in seismology because they can provide information regarding source strengths and fault orientations and can be determined from long-wavelength teleseismic data [Aki and Richards, 2002]. The moment tensor's eigenvalues determine the principal axes of the source [Jost and Herrmann, 1989]. Seismic sources (shear dislocations) can be described with purely double-couple moment tensors that have a zero trace (sum of the eigenvalues) [Jost and Herrmann, 1989]. If the trace is non-zero, then the moment tensor contains an isotropic component, which provides information of the source's volume change.

In volcano geodesy, moment tensors can also be convenient to quantitatively compare deformation from sources with various geometries [Amoruso and Crescentini, 2009, Nikkhoo et al., 2017]. All point ellipsoidal cavities can be represented as a combination of orthogonal dipoles with varying strengths, and thus have corresponding moment tensors. The CDM is composed of three orthogonal tensile cracks, each of which produces far-field deformation

that can be represented using a moment tensor of three orthogonal dipoles (i.e., force pairs that have equal magnitudes but opposite signs). The specific moment tensor representation for a single tensile crack in the XY plane is

$$M = M_A \begin{bmatrix} \lambda & 0 & 0 \\ 0 & \lambda & 0 \\ 0 & 0 & (\lambda + 2\mu) \end{bmatrix},$$

where M_A is the dislocation potency ($M_A = 4bc(u)$), while λ and μ are the Lamé coefficients, which define the elastic properties of the medium ($\lambda = \mu$ if $\nu = 0.25$). It follows that the moment tensor representation of the CDM is thus

$$M^{CDM} = 4ab(u) \begin{bmatrix} (\lambda + 2\mu) & 0 & 0 \\ 0 & \lambda & 0 \\ 0 & 0 & \lambda \end{bmatrix} + 4ac(u) \begin{bmatrix} \lambda & 0 & 0 \\ 0 & (\lambda + 2\mu) & 0 \\ 0 & 0 & \lambda \end{bmatrix} + 4bc(u) \begin{bmatrix} \lambda & 0 & 0 \\ 0 & \lambda & 0 \\ 0 & 0 & (\lambda + 2\mu) \end{bmatrix}.$$

The total potency, ΔV_p , of the CDM, for example, can thus be calculated from its moment tensor, such that

$$\Delta V_p = \frac{M_{kk}^{CDM}}{3K}, \quad (2.18)$$

where M_{kk}^{CDM} is the trace of M^{CDM} , and $K = \lambda + \frac{2}{3}\mu$ [Nikkhoo et al., 2017]. To compare the potency and volume change of a point ellipsoid to its corresponding CDM, the following relationship can be used

$$\Delta V_p = \Delta V + \frac{pV}{K}, \quad (2.19)$$

where p is the uniform pressure in the cavity, V is the cavity volume, and ΔV is the actual volume change [Nikkhoo et al., 2017].

The far-field surface displacements of the CDM can be compared directly to previously analytical formulations of spheroids or ellipsoids based on the relationship between their moment tensors, as shown in Figure 2-18. The CDM spans a wider range of moment tensors than the analytical solutions (which include spheres, spheroids, and ellipsoids). In other words, not all combinations of three mutually orthogonal opening dislocations can be associated with an inflating ellipsoidal cavity. We note that the full range of universal moment tensors include those that have one axis expanding while another is contracting. For example, the compensated linear vector dipole (CLVD) component of a moment tensor has two orthogonal dipoles with the same magnitude and polarity. The third dipole has the opposite polarity and is twice as large, so that the total volume change is zero [Julian et al., 1998, Shuler et al., 2013]. These types of sources are not addressed by Nikkhoo et al. [2017] in their description of the CDM.

While the CDM is useful when the type of cavity cannot be determined *a priori*, one should consider the fact that the axis ratios cannot always be well resolved, as discussed in Amoruso and Crescentini [2009]. As discussed above, the strain of the host rock due to a pressurizing ellipsoid (or CDM) can be described, in the far field, by an appropriate moment tensor. If the source's axes are aligned with the coordinate axes, the eigenvalues of the moment tensor are proportional to the source volume multiplied by the pressure change

[Amoruso and Crescentini, 2009]. However, small variations in eigenvalues ratios can result in large differences in the semi-axis ratios (See Figure 2-19). This means that, while the volume change can be well constrained from an inversion of far-field deformation, the axis ratios cannot always be easily inverted— for example, if the $\frac{c}{b}$ ratio is small (< 0.4) (i.e., cavities with very different shapes can produce similar surface displacements, see Figure 2-16) [Amoruso and Crescentini, 2009]. While the CDM is useful for first-order interpretations of source shapes, it is still important to consider additional available geophysical or geological information that constrain the volcanic reservoir’s shape when modelling the magmatic plumbing system.

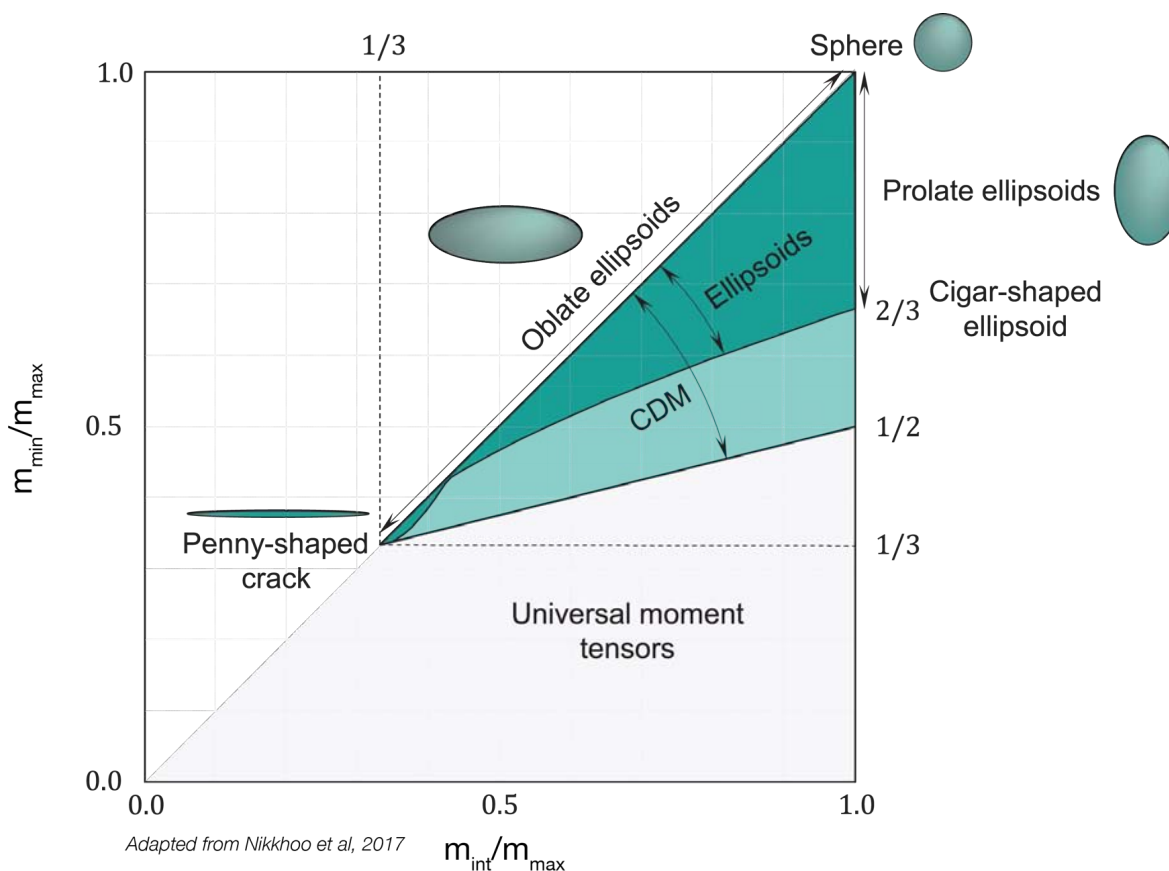


Figure 2-18: **Ellipsoid and CDM moment tensor spectrum.** Moment tensor spectrum in a medium with $\mu = \lambda$ as a function of the moment tensor eigenvalue ($m_{max} \geq m_{int} \geq m_{min}$) ratios. The point ellipsoid moment tensors are a subset of the CDM moment tensors. Adapted from Nikkhoo et al. [2017].

The analytical formulations for various volcanic deformation sources, including the CDM, Mogi and Yang, have, over the course of this PhD, been implemented in the Classic Slip Inversion software [Jolivet et al., 2015]. This implementation has expanded the software to allow for deformation modelling of volcanic activity. A manual for this version of the software is included in Appendix A, and the updated software will soon be available on github.

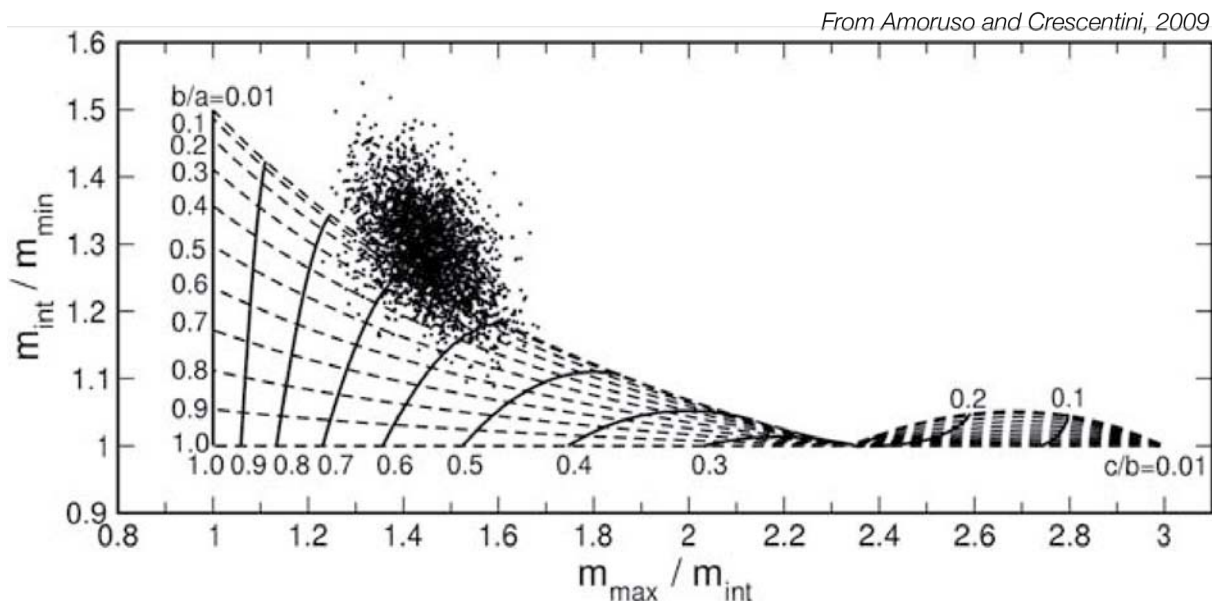


Figure 2-19: **Moment tensor spectrum vs. Ellipsoid semi-axis ratios.** The semi-axis (a, b, c) ratios of an ellipsoid as a function of the moment tensor eigenvalue ratios. The dots are random eigenvalues from Gaussian distributions describing a 1970 deformation episode at Kīlauea. The medium is a Poisson solid, such that $\mu = \lambda$. From [Amoruso and Crescentini \[2009\]](#).

2.2.2.4 System compressibility

The analytical models summarized above are often used to estimate magma volume changes within a volcanic system. Volcanic eruptions must be fed by a source at depth, which depressurizes as magma is withdrawn. However, not all eruptions are accompanied by subsidence [[Rivalta and Segall, 2008](#)]. One explanation could be that the reservoir is located deep within the crust, and no geodetically measurable deformation is produced when the reservoir drains. In other cases, there is a volume change imbalance between the source and the eruption due to the compressibility of the system (the volume of erupted material may be an order of magnitude greater than that of the source even though mass balance is satisfied [[Rivalta and Segall, 2008](#)]). The compressibility of the system is comprised of the chamber compressibility, defined as $\beta_c = \frac{1}{V} \frac{dV}{dP}$ where V is the cavity volume and P is the internal pressure, and magma compressibility, defined as $\beta_m = \frac{1}{\rho_m} \frac{d\rho_m}{dP}$ where ρ_m is the magma density [[Rivalta and Segall, 2008](#)]. The chamber compressibility changes with chamber geometry—sills, for example, are more compliant than spherical sources [[Rivalta and Segall, 2008](#), [Anderson and Segall, 2011](#)]. The volume change ratio between the erupted volume (ΔV_s) and the source (ΔV_c), $\frac{\Delta V_s}{\Delta V_c} = r_v = 1 + \frac{\beta_m}{\beta_c}$, is only equal to 1 if the magma is incompressible, $\beta_m \rightarrow 0$, or the host medium is compliant, $\beta_c \gg \beta_m$. This is not likely the case in reality, and it is therefore important to consider the influence of magma compressibility when estimating volume changes with geodetic models.

2.2.2.5 Other modelling schemes

While the analytical solutions discussed above are able to model volcanic deformation to the first order, sometimes deformation sources— especially dikes and faults— have complex geometries that cannot be represented by uniform opening on a single plane. There are two general ways to address this issue:

1. “Distributed opening” models. Adjacent rectangular dislocations with uniform opening (or closing) represent a source with varying opening (or closing) along strike and dip. In this dissertation, the geometry of the adjacent elements is determined *a priori*.
2. Numerical methods, such as Boundary or Finite Elements. In this dissertation, the Boundary Element method is applied in conjunction with a Monte Carlo inversion scheme to estimate complex source geometries.

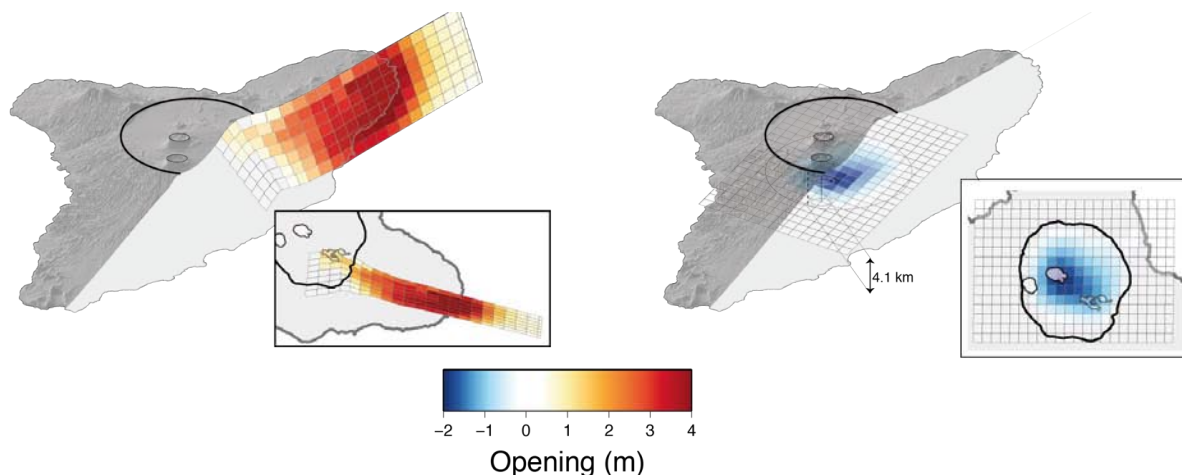


Figure 2-20: **Distributed opening models.** Distributed opening along a dike and a sill from the 2018 – 2019 Ambrym unrest episode (See Chapter 3).

2.2.2.5.1 Distributed opening models

Distributed opening models take advantage of the analytical solutions for rectangular dislocations discussed previously. In reality, however, dike/sill opening (or closing) may vary along strike or dip, and a uniform rectangle dislocation can only roughly approximate this complex opening distribution. An alternative method is to create a more complex source opening (or closing) distribution by placing rectangular dislocations (elements) side-by-side, and imposing a certain amount of opening or closing on each dislocation (See Figure 2-20). In reality, the pressure within a hydraulic crack is constant (disregarding vertical lithostatic gradients), and thus the opening is not expected to change drastically over short distances. To create a smooth opening distribution, a constraint on spatial smoothing can be introduced using two approaches— Tikhonov regularization [e.g., Segall and Harris, 1986] or, as used in this dissertation, with a model covariance matrix. Introducing a model covariance matrix controls the strength and distance of correlation between the opening of nearby elements [Radiguet et al., 2011]. We fix the location, orientation, size of the elements, and the

smoothing constraint, and solve for the distributed opening using the least squares criterion. The model covariance matrix C_m , discussed in Section 2.2.1.1, is constructed such that

$$C_m(i, j) = \sigma_m \left(\frac{\lambda_0}{\lambda} \right)^2 e^{-\frac{\|i, j\|}{\lambda}}, \quad (2.20)$$

where $\|i, j\|$ is the Euclidean distance between elements i and j , λ is the correlation length, σ_m is the *a priori* model parameter standard deviations, and λ_0 is a scaling factor [Radiguet et al., 2011]. After fixing σ_m and λ_0 , we empirically estimate λ through an “L-curve” analysis [Jónsson et al., 2002]. As shown in Figure 2-21, the knee of this curve represents a compromise between a smooth model and a model with a low misfit.

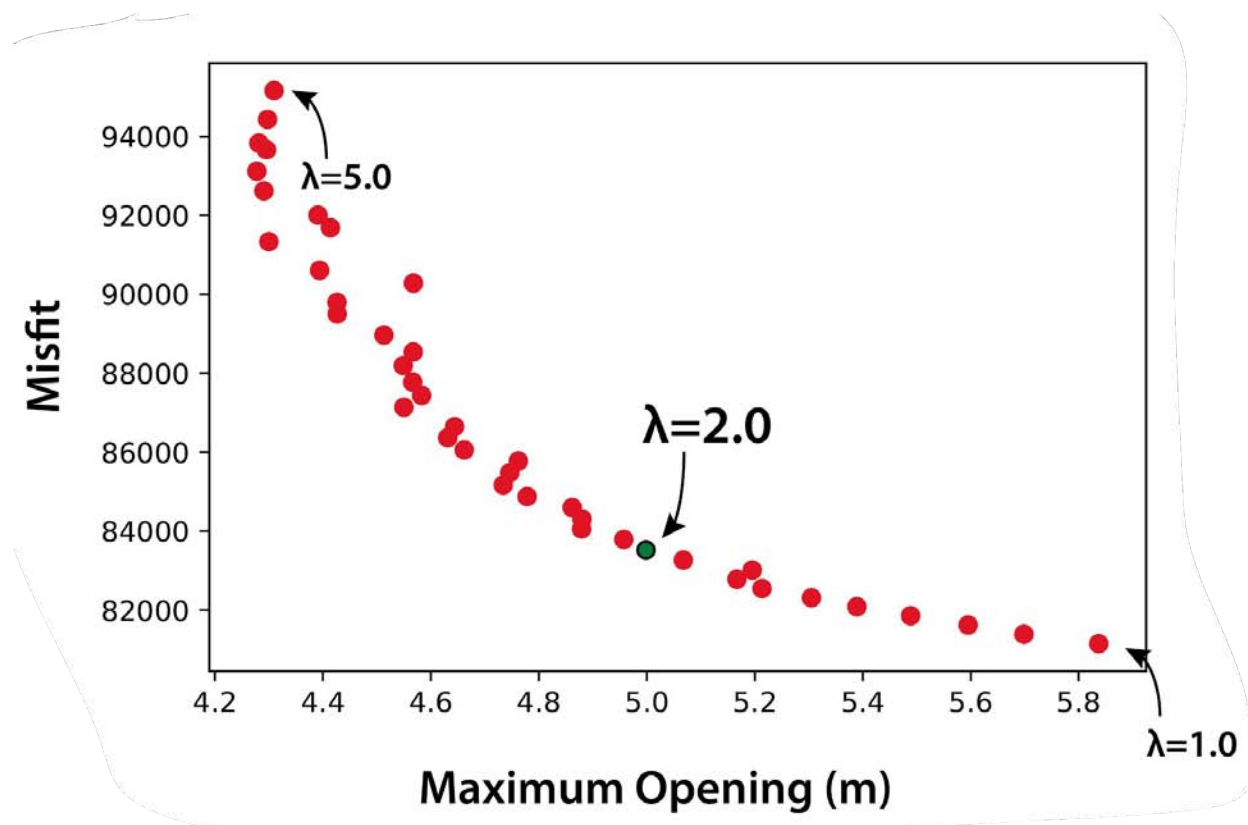


Figure 2-21: **L-curve**. An example of an L-curve plot, used to find the appropriate λ , which balances model smoothness (the smaller the maximum opening, the smoother the model) and the misfit (the rougher the model, the better the model will fit the data).

One of the weaknesses of distributed opening models is the arbitrary nature of the smoothing constraints, as well as the tradeoff between the number of parameters (number of elements) and the model fit to the data. For example, if our model has many small elements and a rough opening distribution, we would be able to explain complex surface displacements. However, the resulting opening distribution may be physically unrealistic. A more realistic modelling technique is based on a constant pressure across a single fracture, and using analytical solutions for linear elasticity to calculate the normal and parallel tractions

(opening and shear) based on the orientation of the element. The opening distribution of the source would therefore be determined uniquely for a given source geometry and imposed pressure, with no required smoothing [Fukushima et al., 2005]. This approach is possible using Boundary Element numerical methods.

2.2.2.5.2 Boundary Element method

Using a numerical method called the Boundary Element method (BEM) allows for more realistic source geometries and boundary conditions [Crouch, 1976]. In particular, instead of imposing uniform or distributed opening on a plane, pressure is imposed on a fracture with an arbitrary geometry. The volume change of a cavity can also be computed, regardless of the axes ratio.

Throughout this dissertation, we run initial geodetic nonlinear inversions based on analytical models to gain an understanding of what type of source is active (See Sections 3, 4, 5.1.1, and 5.3.1). Then, we model complex source geometries using the 3D Mixed Boundary Element (BE) method numerical approach developed by Cayol and Cornet [1997, 1998]. 3-D BE methods are used to uniquely solve partial differential equations explaining the physics of region R given constraints on the, often complex, boundary conditions. A 3-D boundary is divided into N elements with simple geometries (e.g., triangles) for which an analytical solution to the partial differential equations exists. If the partial differential equations are linear, the imposed boundary conditions are obtained by summing the appropriate strengths of each analytical solution of the N boundary elements. In the case of deformation modelling, the 3-D boundaries may represent pressurized dikes or cavities, shearing faults, and traction-free topography. A mesh of triangular elements with adjoining sides can effectively represent any source geometry, as well as the free surface (i.e., the topography). The solution is the displacement across the fractures or at the free surface, or at the boundary of the cavity.

More formally, the 3D Mixed Boundary Element (BE) method numerical approach of Cayol and Cornet [1997, 1998] combines two BE methods– the displacement discontinuity method and the direct method. The former is numerically stable for fractures, while the latter is more exact and computationally efficient for massive boundaries (such as topographies and pressurized cavities).

In the displacement discontinuity approach, a fracture boundary is first discretized into N elements. We can then solve the system of equations $\mathbf{AB} = \mathbf{P}$. In this system, \mathbf{P} is the vector of $3N$ imposed traction conditions and \mathbf{A} is the matrix of influence coefficients relating a unit displacement across element j to the stress on the centroid of element i according to linear elasticity. The unknown, \mathbf{B} , is the vector of $3N$ amplitudes of displacements D_j across an element ($D_j = u_j^+ - u_j^-$, $j = (x, y, z)$, where u_j^+ and u_j^- are the displacement on the positive and negative sides of j). By solving the system of $3N$ linear equations with $3N$ unknowns, we can find the unique solution \mathbf{B} (i.e., the distribution of slip or opening that satisfies the imposed stress \mathbf{P} , given \mathbf{A}). Once the displacements D_j across the planar element are known, stresses and displacements anywhere else in the finite elastic body can be calculated [Crouch and Starfield, 1983, Crouch, 1976].

The direct method, according to its name, solves directly for the unknown displacements and stresses on the boundary [Lachat and Watson, 1976]. The reciprocal theorem of Sokol-

nikoff [1956] considers reciprocity of work between the unknown boundary conditions of the current problem and the boundary conditions of a problem with a known analytical solution (i.e., a point load in an infinite body). Similar to above, a system of equations $\mathbf{H}\mathbf{U} = \mathbf{F}$ can be solved for \mathbf{U} , the vector of $3N$ unknown displacements on the boundary Γ of a finite elastic body Ω [Cayol and Cornet, 1997]. The matrix \mathbf{H} is composed of the influence coefficients, computed by evaluating the boundary integral of stresses and displacements produced on element j due to a unit load on element i in an infinite medium. The known vector \mathbf{F} has a size $3N$, including the prescribed boundary tractions. When these two approaches are implemented together, as in Cayol and Cornet [1997, 1998], the 3-D Mixed BE method can compute surface displacements due to a variety of volcanic sources. These sources encompass geometries equivalent to the analytical formulations mentioned above, but also allow for more complex geometries, while making it possible to model the mutual influence between the reservoirs and cracks, as well as topographic effects.

Non-negativity constraint

The BEM solution takes into consideration the stress interaction between multiple sources. The analytical solutions of Section 2.2.2.1 do not consider these interactions. Stress interactions are particularly relevant in volcanic environments, when there may be multiple sources—dikes, faults, and reservoirs—activated over a short period of time (i.e., a single eruption), and all of which contribute to the deformation source [Pascal et al., 2013]. In some cases, however, the stress interaction between nearby sources may induce geologically unrealistic behavior of the structure, such as fracture interpenetration (i.e., closing on a fault). In order to prevent interpenetration, a non-negativity constraint must be imposed on the system of linear equations that solves for the displacement across the fracture, hence making the inverse problem nonlinear (See Section 2.2.1.2). Cayol et al. [2014] uses the method of Lagrangian multipliers to impose these non-negativity constraints.

To implement this method, the system of equations for the Mixed BE of Cayol and Cornet [1997, 1998] can be expressed as $\mathbf{A}\mathbf{X} = \mathbf{R}$, where \mathbf{A} is the influence coefficient matrix for displacements of N_L reservoir elements and displacement discontinuities of N_F fracture elements [Cayol et al., 2014]. The unknown vector \mathbf{X} is composed of both the displacements and displacement discontinuities, and \mathbf{R} is the vector of imposed boundary tractions [Cayol et al., 2014].

The aforementioned expression can be rewritten as the symmetric system $\mathbf{A}^T\mathbf{A}\mathbf{X} = \mathbf{A}^T\mathbf{R}$. This system's solution is found by the minimization of

$$J(\mathbf{X}) = \frac{1}{2}\mathbf{X}^T\mathbf{A}^T\mathbf{A}\mathbf{X} - \mathbf{R}^T\mathbf{A}\mathbf{X} \quad (2.21)$$

under the constraints $\mathbf{N}\mathbf{X} \leq 0$, where the matrix \mathbf{N} has N_F rows and $N = N_F + N_L$ columns. Equation 2.21 is minimized with the augmented Lagrangian method [Fortin and Glowinski, 1983], as described in Cayol et al. [2014].

2.3 Complementary remote sensing methods

SAR geodesy and geodetic modelling allows for studying remote volcanic activity, and is the primary focus of this dissertation. Geodetic modelling provides estimates on the location,

depth and organization of the subsurface volcanic system, as well as the volume of magma moving through this system. Nonetheless, such studies face limitations— for example, the temporal resolution (between 6 – 12 days for systematic acquisitions) limits studying a magmatic system’s dynamics. We will briefly discuss three additional methods that can be used to study remote volcanoes. These methods will be incorporated at some point throughout this dissertation to help interpret geodetic models. These methods include recording gas emissions, thermal anomalies, and seismicity.

Gas spectroscopy can be ground-based, airborne, or spaceborne. Of particular interest are satellite spectrometers, which can measure gas emissions from even the most remote volcanoes. Satellite spectrometers can measure the quantity of SO_2 emitted from a volcano using either ultraviolet (UV) or infrared (IR) sensors. UV sensors in operation include the Ozone Monitoring Instrument (OMI), the Ozone Mapping and Profiler Suite (OMPS), and the TROPospheric Ozone Monitoring Instrument (TROPOMI). These instruments are sensitive to SO_2 emitted down to the lower troposphere (< 2 km). This is in contrast with IR sensors, which are mainly sensitive to gas emissions in the higher troposphere or stratosphere (> 7 km). OMI provides daily global coverage with a $13 \text{ km} \times 24 \text{ km}$ resolution, and successfully tracked the mass of volcanic SO_2 emissions over the past decade [Carn et al., 2017]. The feasibility of OMPS to continue these SO_2 measurements for volcanic sources has been verified during moderate-sized eruptions [Carn et al., 2015]. In addition, TROPOMI— launched by the European Space Agency in 2017— has a significantly improved spatial resolution of $5.5 \text{ km} \times 3.5 \text{ km}$ [Theys et al., 2017]. IR sensors, such as the Infrared Atmospheric Sounding Interferometer (IASI), can also provide estimates for SO_2 mass, as well as SO_2 column heights [Clarisse et al., 2014, Clerbaux et al., 2009].

Satellite-based thermal anomaly detection can also be used to track volcanic eruptive activity. Algorithms to detect thermal emissions have been developed using data from the satellite-mounted MODerate Resolution Imaging Spectroradiometer sensor (MODIS) aboard NASA’s Aqua and Terra satellites. This sensor operates in the middle and longwave infrared wavelengths, and has a repeat time of twice per day, making it especially useful to detect changes in thermal emissions during eruptions [Wright et al., 2004]. Two detection algorithms using MODIS images are MODVOLC and Middle InfraRed Observation of Volcanic Activity (MIROVA), developed specifically to report thermal anomalies at volcanoes worldwide [Wright et al., 2004, 2015, Coppola et al., 2016b]. In addition, moderate- to high-resolution optical satellites such as LANDSAT [Oppenheimer and Francis, 1997, Harris et al., 1998, Gray et al., 2019] and Sentinel-2 are also being utilized to detect thermal anomalies through algorithms such as HOTSPOT [Murphy et al., 2016]. Sensors onboard of meteorological geostationary satellites, such as SEVIRI (onboard Meteosat Second Generation) or AHI (onboard Himawari-8) allow for detecting thermal emissions and SO_2 emissions nearly continuously (< 20 min intervals), albeit at reduced spatial resolution and high detection thresholds [Prata and Kerkmann, 2007, Bonaccorso et al., 2011, Shreve et al., 2019].

Seismicity is also of particular interest for understanding the physical and dynamic processes occurring within volcanic systems. Seismicity is not considered “remote sensing” like the methods mentioned previously. However, teleseismic data can be used to study remote regions which may not have well established regional seismic networks. For example, analysis of global teleseismic data provided the first indications of volcanic activity near Mayotte [Cesca et al., 2020]). Long-period seismicity, for example, relates directly to fluid migration

and pressure changes within a magmatic system [Chouet, 1996]. Earthquakes with large non-double-couple components (i.e., vertical compensated linear vector dipoles) may also occur during volcanic unrest episodes, possibly due to physical mechanisms such as caldera ring-faulting [Shuler et al., 2013].

Chapter 3

Magmatic architecture and dynamics of a basaltic caldera rift-zone system in a compressive tectonic setting

This chapter is based on a multidisciplinary study published as “From prodigious volcanic degassing to caldera subsidence and quiescence at Ambrym (Vanuatu): the influence of regional tectonics”, *Scientific Report*, 9, 18868 in 2019. The collaboration included researchers from Institut de Physique du Globe de Paris, Université de Paris (Raphaël Grandin, Francisco Delgado, Martin Vallée), Laboratoire d’Optique Atmosphérique, Université de Lille (Marie Boichu, Nicolas Henriot), Vanuatu Meteorology and Geohazards Department (Esline Garaebiti, Sandrine Cevuard, Dan Tari), Laboratoire Magmas et Volcans, Université Clermont Auvergne (Yves Moussallam), Laboratoire Littoral Environnement et Sociétés, Université de La Rochelle (Valérie Ballu), Géoazur, Université Nice Sophia Antipolis (Frédérique Leclerc), and Géoazur, Institut de recherche pour le développement, Nouméa (Pierre Lebellegard, Bernard Pelletier).

This study synthesizes various multidisciplinary datasets to conclude that Ambrym’s 2018 unrest episode included a voluminous rift zone intrusion, magma withdrawal from various levels in the storage system, and a prolonged submarine eruption. The first author processed the geodetic data, as well as performed and interpreted the geodetic modelling. The coauthors contributed ultraviolet, infrared and optical satellite, seismic, petrological, GPS, coastal uplift, and bathymetric datasets. The geodetic models were essential for the main conclusion and discussion of this paper, and comprise the bulk of the quantitative results throughout this study. In addition to the geodetic modelling, the first author also wrote the article’s initial draft. Subsequent drafts were also reworked by the first author, with contributions from R. Grandin, M. Boichu, and B. Pelletier. R. Grandin also coordinated the collaboration, including the visualization of the datasets. The results found in this article were covered in an article by *National Geographic* in 2020 (<https://www.nationalgeographic.com/science/2020/01/lava-lakes-drained-catastrophically-scientists-caught-action/>). The chapter begins with an introduction to diking events in various tectonic settings, followed by a summary of the factors that influence lateral dike propagation. We then proceed with the published article and Supplementary Information.

3.1 Scientific context

3.1.1 Rift zone dike intrusions

The largest contemporary diking event on Earth occurred from September to October 2005 in the Manda Hararo-Dabbahu rift of the central portion of the Afar triple junction (Ethiopia). It was the first of 14 diking events, which constituted a larger rifting episode lasting from 2005 – 2010 [Wright et al., 2006]. Approximately $1 - 2 \text{ km}^3$ of magma intruded into the crust during the initial diking event [Grandin et al., 2009]. A similar rifting episode occurred at Krafla in Iceland from 1975 – 1984, but the cumulative intruded magma volume from the 21 dikes was only half of the Manda Hararo-Dabbahu event [Tryggvason, 1984, Wright et al., 2012]. Both in Afar and Iceland, magma injection accommodates extensional tectonic stress at these divergent plate boundaries [Buck et al., 2006], yet the size of individual events is limited by magma availability at the time of diking [Qin and Buck, 2008].

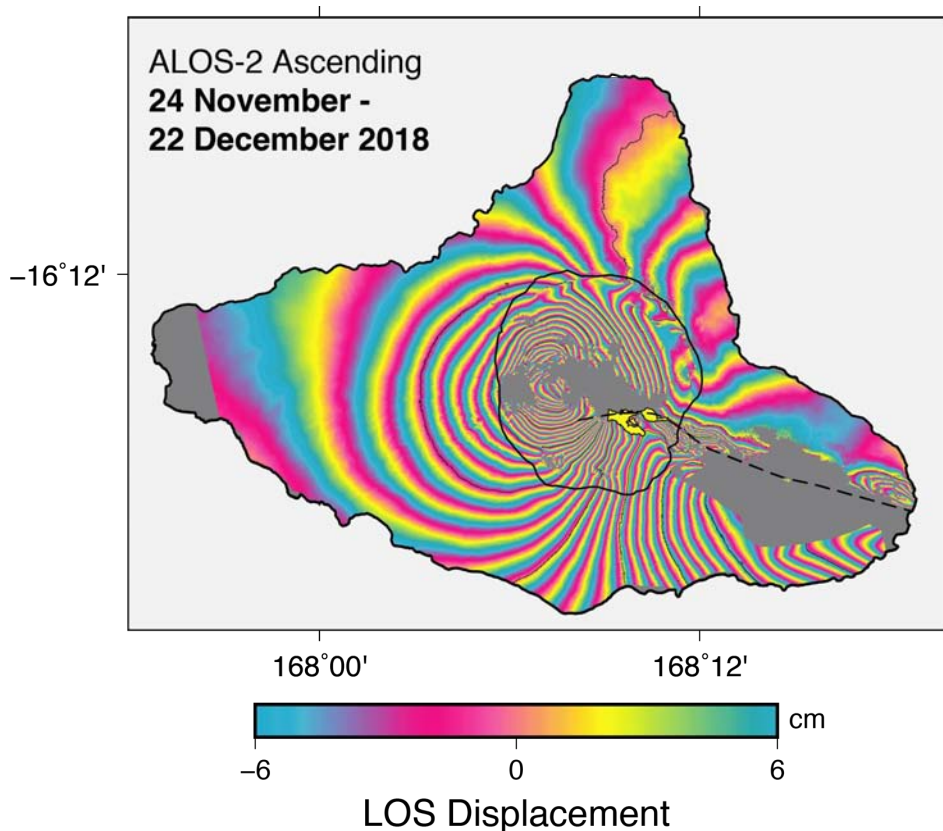


Figure 3-1: **Interferogram spanning Ambrym’s 2018 rift zone intrusion.** An ALOS-2 (L-band) interferogram spanning 24 November to 22 December 2018, during which $> 0.4 \text{ km}^3$ intruded into Ambrym’s SE rift zone, resulting in more than 2 meters of coastal uplift and caldera subsidence. The caldera rim is outlined in black, the dike trace is depicted by a dotted line, and the intra-caldera lava flow is yellow.

However, rift zones are not found only at divergent plate boundaries. Table 3.1 lists

examples of notable diking events that took place in rift zones in the past 50 years, including their geodynamic context, duration, and size. As noted in the table, rift zones are found in all tectonic settings [Walker, 1999].

In some cases, these volcanic rift zones are mechanically coupled with a caldera, providing evidence for a central magma body, and forming a caldera-rift system. Caldera-rift volcanic systems form when magma migrates laterally in a preferred orientation, draining the central magmatic storage area [Sigmundsson, 2019]. At the surface, the preferred intrusion orientation builds out a rift zone, or a corridor of fractures and fissures that can extend anywhere from a few to tens of kilometers away from the central reservoir. As the reservoir drains, its depressurization may cause the rock above the roof to sag, or, in extreme cases, collapse under its own weight, causing the formation of surrounding caldera ring-faults (See Chapter 4).

Rift zone intrusions can travel laterally tens of kilometers away from an active volcanic center, and are therefore significant hazards for distal populations. Hazards associated with these events tend to take the form of lava flows, as opposed to explosive eruptions (unless magma and water/ice interaction occurs) [Németh and Cronin, 2009, 2011]. For example, in 1977, a dike intrusion travelled more than 6 km along Piton de la Fournaise’s (La Réunion) NE rift zone, feeding a lava flow that destroyed 21 houses and a church [Global Volcanism Program, 1977, Kieffer et al., 1977]. This event resulted in the creation of the Volcanological Observatory of Piton de La Fournaise. At Nyiragongo (Democratic Republic of Congo), a dike intrusion travelled 16 km away from the volcano’s main crater along the Southern Rift zone in 2002, destroying the homes of 120,000 people and claiming 70 – 100 victims [Komorowski et al., 2002/2003].

Forecasting the timing and location of these events remains a challenge. The duration and magnitude of the 2018 Kīlauea rift zone eruption, which damaged more than 700 structures, were not well constrained at the eruption onset [Neal et al., 2018, Poland and Anderson, 2020]. Table 3.1 emphasizes how widely the duration and size of diking events vary between volcanic systems.

In order to improve forecasting of caldera-rift zone unrest episodes, a few overarching questions should be kept in mind:

1. When is magma transported laterally as opposed to vertically?
2. How far will magma travel laterally from a volcanic center, and how is this propagation influenced by changes within the magma reservoir?
3. Where and how is magma stored within the crust, and is there a continuous magma supply available?

The objective of the study presented in this chapter is to better understand the interplay between tectonics and magmatism at Ambrym volcano, which hosts two well-defined rift zones and a broad caldera. Using observations of a rift zone intrusion and widespread caldera subsidence that occurred in December 2018 (see Figure 3-1), we develop a conceptual model for the persistence of Ambrym’s rift zones and the development of its caldera.

Table 3.1: **Major rift zone diking events.** A summary of major diking events associated with rift zones over the past 50 years. Expanded from Table 1 in Gudmundsson et al. [2016]. Red cells with question marks indicate that the data was not available. Data for Bárðarbunga from Sigmondsson et al. [2014], Gudmundsson et al. [2016], for Fernandina from Stix and Kobayashi [2008], Simkin and Howard [1970], Filson et al. [1973], for Krafla from Neal et al. [2018], Lundgren et al. [2019], for Miyakejima from Stix and Kobayashi [2008], Geshi et al. [2002], Shuler et al. [2013], Kaneko et al. [2005], Amma-Miyasaka et al. [2005], Nishimura et al. [2001], for Nyiragongo from Komorowski et al. [2002/2003], Tedesco et al. [2007], Shuler and Ekström [2009], Wauthier et al. [2012], for Pion de la Fournaise from Staudacher et al. [2009], Michon et al. [2011, 2007], Fontaine et al. [2014], Di Mauro et al. [2014], Fontaine et al. [2019], for Krafla from Björnsson et al. [1977], Tryggvason [1984], for Manda Hararo from Grandin et al. [2009], Ayale et al. [2007], Wright et al. [2006]

	Geodynamic context	Lava comp.	Year	Duration (days)	Intrusion length (km)	Intruded volume (km ³) [⊖]	Erupted volume (km ³) [⊕]	Largest earthquake (M _w) [⊕]	Summ. seismic energy release (×10 ¹⁵ J) [⊕]
Bárðarbunga	Oceanic divergent boundary/hotspot	Basalt	2014 - 2015	180 [†]	48	0.5	1.4	5.8	2.5
Fernandina	Hotspot	Basalt	1989	12 [‡]	≥ 10.5	N/A	0.2	5.2	2
Kilauea	Hotspot	Basalt	2018	94 [‡]	20	0.08	0.448 [*]	6.9	1.40 [†]
Miyakejima	Intraoceanic convergent boundary	Basalt	2000	40 [†]	35	1.2	0.01 [†]	5.6	2.2
Nyiragongo	Continental divergent boundary	Basalt	2002	0.5-2 [†]	10	0.21	0.01875 [*]	5.3	N/A
Pion de la Fournaise	Hotspot	Basalt	2007	7 [†]	7	0.02	0.13	5.2	0.3
Krafla	Oceanic divergent boundary/hotspot	Basalt	1975	57 [†]	> 60	0.1 - 0.2 (minimum)	0.003	6.3	N/A
Manda Hararo [‡]	Continental divergent boundary/hotspot	Initial alkali eruption, then basalt	2005	20 [†]	65	1.5 - 2	No basaltic eruption	6.3	1.7

[†] Duration of caldera collapse
[‡] Duration of eruption
[⊕] Duration based on seismicity
[⊖] Duration based on radiocarbon
^{*} Dome-rock equivalent
[‡] Dome-rock equivalent, assuming 25% vesicularity
[⊕] Only includes the first diking event of the rifting episode
[⊖] Converted by multiplying cumulative M₀ by a factor of 5×10^{-6} , based on energy-moment relationship from Kanamori et al. [1998]
[†] Based on geodetic inversions or seismicity locations, except for Fernandina (distance between caldera and eruptive vent) and Nyiragongo (distance of fracture network from main crater)
[⊕] Maximum earthquake magnitude associated with caldera formation or other propagation (determined from surface waves (M_s) for Fernandina, from duration magnitude (M_d) for very-long-period (VLP) events at Miyakejima and Bárðarbunga, and from M_w for highly non-double-couple earthquakes at Nyiragongo)
[†] Energy release from the 6.3 M_w earthquake related to slip on the basal detachment fault

3.1.2 Driving stress of a lateral dike intrusion

A conceptual understanding of a particular volcanic system— including its geological and tectonic context— is necessary to address the three questions listed above. Magma often rises vertically through the crust, either arresting at depth or erupting at the surface. Buoyancy drives a dike’s vertical ascent, resulting from density differences between the magma (ρ_m) and the solid host rock (ρ_r) [Weertman, 1971]. A dike can also travel laterally for more than ten kilometers, such as along a rift zone. Whether a dike travels laterally or vertically depends fundamentally on the relationship between the magma pressure in the dike (P_m) and the remote stress normal to the dike opening (σ_3 , using the convention that positive σ_3 indicates compressive stress) (see Figure 3-2) [Rubin and Pollard, 1987]. The difference between these two values defines the driving stress, P_d , such that

$$P_d = P_m - \sigma_3. \quad (3.1)$$

The driving stress must be sufficiently high to allow crack propagation (i.e., overcome the fracture toughness, κ_c , of the host rock at the dike tip) [Broek and Rice, 1975]. The gradient of driving stress defines the direction of preferential propagation of the dike. Lateral migration can occur due to either a high P_m or a low σ_3 , as long as the horizontal gradient of driving stress is greater than that of buoyancy [Rubin and Pollard, 1987]. On long time scales (thousands of years) and larger spatial scales (the entire rift zone), questions such as— *Why did the rift zone develop? What are the stresses that drive its persistence? How does it accommodate spreading due to hundreds or thousands of dike intrusions?*— can be addressed using the dependance of P_d on P_m and σ_3 in Equation 3.1.

3.1.3 Factors influencing the driving stress

3.1.3.1 Exogenous stress, σ_3

Various ideas have been proposed to explain the exogeneous stresses that control the lateral distance travelled by dikes, as well as their direction. On one hand, either the overlying rock burden, thickness of the elastic-brittle lithosphere, any crustal layering, or a combination of these factors, is thought to control the lateral distance dikes travel. On the other hand, either regional tectonic stresses or local gravitational stresses are thought to control the orientation of dikes, and ultimately the orientation of the rift zone.

Lister and Kerr [1991] proposed that magma travels laterally at a depth where the crustal density becomes lower than that of the ascending magma (“level of neutral buoyancy”). The ability of dikes to travel long distances laterally then results at least in part from topography-induced horizontal gradients in stress, if considering little horizontal variation in tectonic stress [Fialko and Rubin, 1999].

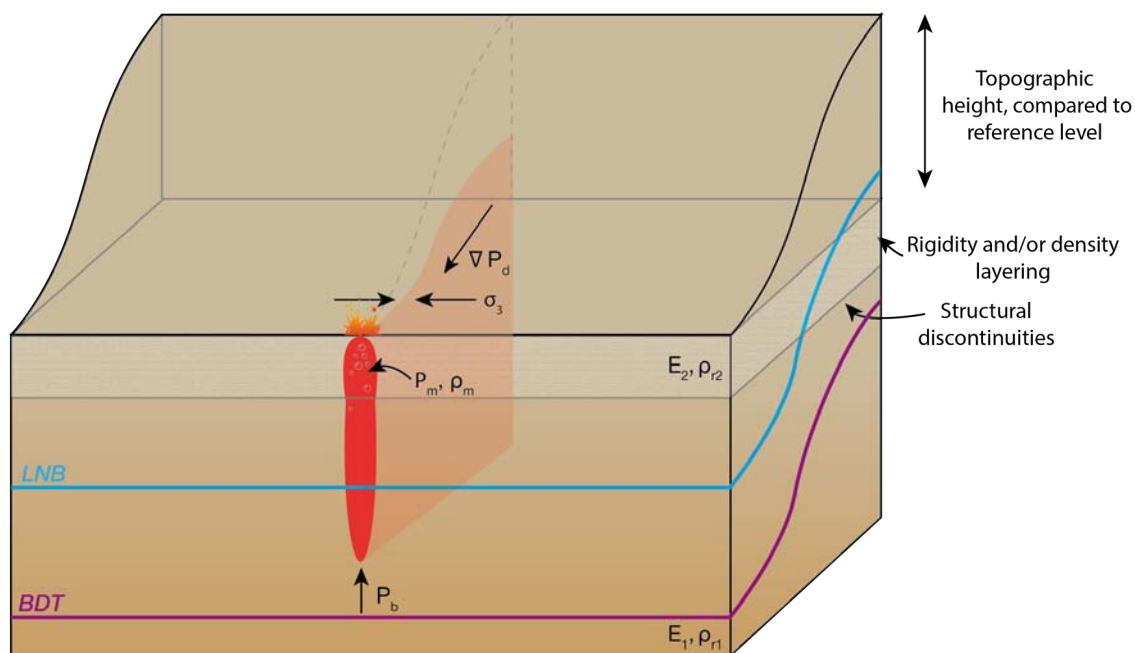


Figure 3-2: **Factors influencing dike propagation.** The distance travelled by the dike is determined by the balance between the stress normal to the dike opening σ_3 and the magma pressure P_m , according to Equation 3.1: $P_d = P_m - \sigma_3$. If the horizontal gradient in driving pressure, ∇P_d , is above a certain “breakout pressure”, and greater than buoyancy P_b , the dike will leave the reservoir and migrate laterally [Buck et al., 2006]. Structural discontinuities, rigidity and density layering in the host rock, and the topography, can all influence the dike’s shape and path. This illustration shows a dike propagating in a host rock with a Young’s modulus E_1 and density ρ_{r1} . The topography decreases ahead of the dike’s path. There is a layer in the host rock with a lower rigidity, denoted by a Young’s modulus E_2 , where the dike width increases. The Level of Neutral Buoyancy, LNB , and the brittle ductile transition BDT , may control at what depth and how far the dike will laterally propagate. The tip of the dike may be filled with exsolved gases or cooling magma [Fialko and Rubin, 1999]. The dike itself may be vesiculated due to bubble growth, resulting in a lower magma pressure at the top of the dike [Rubin and Pollard, 1987]. The dike path in this illustration is approximate— the top of the dike may be anywhere within the transparent red path, and if the dike will feed an eruption when it intersects the surface.

Yet, deviatoric stresses due to tectonic plate motion play a significant role in directing dike opening and propagation distance. Mode I crack planes orient perpendicular to the local σ_3 direction, and aggregate rift zone orientations are parallel to the direction of maximum horizontal compressive stress, σ_1 [Nakamura, 1977]. Rift zone orientations then reflect the regional distribution of stresses resulting from the tectonic setting. In extensional tectonic contexts, such as mid-ocean ridges, or in Afar and Iceland, Grandin et al. [2012] proposes that lateral dikes are emplaced near the brittle-ductile transition (BDT). The crust near the locus of magmatic upwelling is thermally weakened, therefore the farther away from these supply zones, the thicker the elastic-brittle lithosphere (in other words, the deeper the BDT). This thickening of the elastic-brittle lithosphere layer may control the distance travelled by

dikes, which is not always correlated with topography (as observed during the 2005 – 2010 rifting episode in Afar) [Grandin et al., 2012].

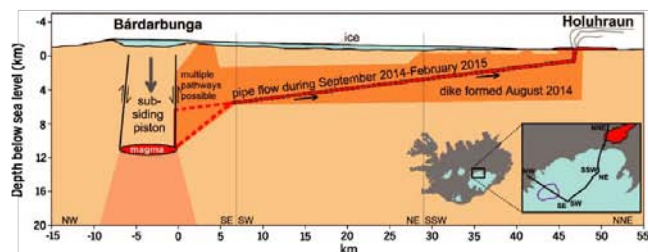
In addition, the orientation of rift zones may also be influenced by local stress effects due to gravitational forces. This may be due to the edifice topography, resulting in gravitational spreading of the volcanic edifice [Borgia, 1994]. At some volcanic islands, these gravitational stresses result in persistent flank instability [Poland et al., 2017]. Once initiated, sliding of an unstable flank results in extensional stress within the volcanic edifice, which accommodates dike opening during hundreds or thousands of repetitive events, and plays a dominant role in controlling lateral propagation direction (e.g., south flank of Kīlauea) [Fiske and Jackson, 1972, Dieterich, 1988, Münn et al., 2006]. There may be a feedback between rift zone intrusions and flank instability. Stress transferred by dike intrusions bring basal décollement faults closer to failure. Fault slip can then lead to further extension (unclamping) perpendicular to the rift zone, restarting the repeated process of flank sliding and rift zone intrusion (e.g., east and south flanks of Etna) [Acocella et al., 2003, Walter et al., 2005a,b, Lundgren et al., 2003].

Finally, differing properties of the host rock may also influence dike propagation direction and distance. Such inhomogeneities include crustal rigidity differences (changes in elastic properties and thus changes in σ_3), density differences, and discontinuities (faults, joints, bedding interfaces, etc.) [Pollard, 1973, Rubin and Pollard, 1987, Gudmundsson and Loetveit, 2005, Urbani et al., 2018].

3.1.3.2 Magma pressure, P_m

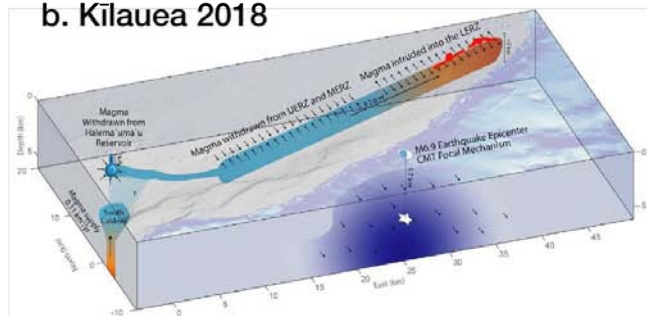
As discussed above, σ_3 determines a rift zone's orientation, and to some extent the distance that the dike will travel. The magnitude of P_m may vary based on the magma reservoir pressure or increased vesicularity from bubble growth at the top of the dike. To trap dikes within a rift zone and cause them to migrate laterally without erupting at the surface, P_d must be greater in the downrift edge of the dike than the top and bottom. Rubin and Pollard [1987] showed, however, that P_m will never achieve this stress distribution. Therefore, only variations in σ_3 , not P_m , can explain why dikes propagate laterally over long distances [Rubin and Pollard, 1987].

a. Bárðarbunga 2014 - 2015



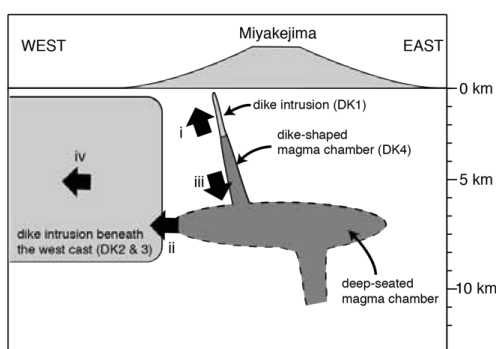
From Gudmundsson et al, 2016

b. Kīlauea 2018



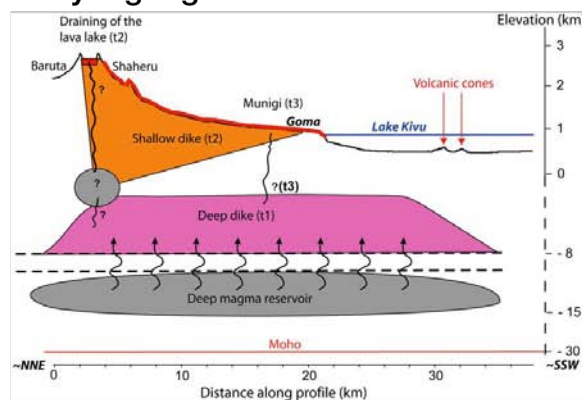
From Nealet et al, 2018

c. Miyakejima 2000



From Ueda et al, 2005

d. Nyiragongo 2002



From Wauthier et al, 2012

Figure 3-3: **Examples of rift zone diking events.** **a.** The schematic cross-section of the 2014 – 2015 Bárðarbunga dike intrusion and caldera collapse. Gravity-driven piston subsidence into the reservoir is hypothesized to have prolonged the eruption. From Gudmundsson et al. [2016]. **b.** Schematic magma plumbing system of Neal et al. [2018] summarizing the deformation sources acting during the 2018 Kīlauea rift zone intrusion and caldera collapse. The red colors indicate inflation, while the light blue colors indicate contraction. Flank motion is indicated by the arrows on the dark blue patch. **c.** Schematic illustration of the Miyakejima dike intrusion, caldera collapse, and submarine eruption. The unrest episode included 4 separate dikes (DK1 – DK4), whose order of emplacement is represented by the roman numerals, i – iv. From Ueda et al. [2005]. **d.** The schematic magma plumbing system which fed the 2002 Nyiragongo rift zone intrusion and eruptions. The different phases of the unrest episode are denoted by t1 – t3. From Wauthier et al. [2012].

Nevertheless, variations in P_m control whether or not the dike has a sufficient gradient in P_d to continue to open and propagate [Rubin and Pollard, 1987, Rubin, 1990]. Knowledge of the location and size of the magma reservoir feeding the dike intrusion would help determine whether or not a magmatic system is able to initiate or sustain a far-travelling diking event. This can be related to whether a continuous magma supply exists, which may result in

shorter recurrence times between diking events [Rubin, 1990]. Alternatively, if the magma supply is limited, as is hypothesized at magma-starved oceanic spreading centers (e.g., certain segments of the Mid Atlantic Ridge, the SW Indian Ridge), a dike's P_m during the course of an intrusion may decrease to a point that the driving stress is no longer sufficient for dike propagation while the crust remains under tension [Qin and Buck, 2008, Buck et al., 2006]. In this case, once the magma chamber pressure has been sufficiently recovered— by an influx of new magma, or other pressurization source (i.e., exsolution of volatiles)— diking events can restart.

3.1.4 What can we learn about the mechanisms driving a rift zone intrusion?

The magnitude of σ_3 and P_m , as well as the magma availability, determine the direction, distance, frequency, and volume of dike intrusions and eruptions in rift zone settings. Decoupling these three factors for a specific volcano helps us answer the aforementioned questions of— *Why did the rift zone develop? What are the stresses that drives its persistence? How does it accommodate spreading due to hundreds or thousands of dike intrusions?*. Once we know conceptually what drives a rift zone's persistence (topography, tectonic stress, depth of BDT, etc.), we can direct quantitative modelling efforts to reflect these understandings (using the correct assumptions). These models may provide insights that can be used to answer the three overarching questions posed earlier in this section.

For example, the understanding that dikes accommodate spreading at the divergent plate boundary in Iceland led to the quantitative models of Buck et al. [2006], which explain the alternating direction, length of, and distance travelled by individual diking events during the Krafla 1975 – 1984 rifting episode. The study of Heimisson et al. [2015] hindcasted trajectories of the 2014 and 1996 dikes originating from Bárðarbunga in Iceland using a model that minimizes potential energy, and found that the 1996 dike direction was mainly influenced by tectonic stresses, while the 2014 dike direction was directed by gravitational stresses from varying topography. Dieterich [1988] aimed to answer the above questions directly for the case of Hawaiian rift zones, focusing on the feedback between a sliding fault at the edifice-seafloor interface, and rift zone spreading due to dike intrusions. The fact that slip on this fault accommodates large amounts of spreading along the rift zone has led to studies demonstrating the relationship between seismicity rates and crustal stress changes [Dieterich et al., 2000, Amelung et al., 2007].

3.1.5 Magma transport in volcanic systems: additional considerations

The aforementioned stress balance between σ_3 and P_m allows for conceptually investigating factors that influence the distance travelled by dikes and the orientation of rift zones. Even if datasets are sparse in time or space, Equation 3.1 is an appropriate starting point to understand the stresses driving magma propagation at volcanoes that may not be extensively monitored. However, additional factors also influence dike propagation. Although we did not develop these factors in our study at Ambrym, they should be mentioned for completeness.

The first of these considerations is the fracture criteria necessary for the crack to propagate. In brittle host rock, fracturing at the dike tip (called the “process zone”) is complex, due to inelastic deformation resulting from the large stress concentration in this zone. The effects of inelasticity are not well constrained, and the fracture toughness, as defined previously, is instead used [Rubin, 1995].

The next consideration involves the fluid mechanical and thermodynamical aspects of dike propagation. Lateral dikes may arrest due to the cooling of magma within a rigid-walled channel, as explored by Fialko and Rubin [1998]. It is possible to estimate numerically the “thermal entry” length, or the distance the dike travels before losing all its heat to its surroundings [Fialko and Rubin, 1998]. However, these estimates merely provide upper bounds on distance travelled, due to lack of constraints on input parameters, such as the channel thickness and dynamic viscosity.

Up until this point, we have not considered the dynamics of lateral dike propagation. As discussed by Segall et al. [2001], a mechanically coupled propagating dike and decompressing magma chamber can reasonably explain dike volume histories during the course of magma injection, as modelled using continuous GPS data. Solving these coupled nonlinear equations can ultimately provide constraints on whether a dike will erupt or arrest at depth. Similarly, analytical solutions to a simplified formulation of the problem were derived by Rivalta [2010] after including magma and chamber compressibilities. Unfortunately, datasets required to constrain such studies are rare, because they require high SNR, spatiotemporally dense measurements from continuous GPS, tiltmeters, and/or seismometers. This approach is also an oversimplification, as the magmatic system is certainly more complex than a dike coupled to a single magma chamber.

Finally, dike propagation distance and volume may be modulated by pressurization of the magma chamber during caldera collapse. In these extreme cases, the host rock above the reservoir may collapse in a piston-like manner [Gudmundsson et al., 2016, Patrick et al., 2019b, Neal et al., 2018]. Once a channel for lateral magma propagation opens, withdrawal of magma from the reservoir can be prolonged by the intrusion of the overlying host rock into the reservoir, repressurizing the system [Gudmundsson et al., 2016]. As mentioned previously, the rift zone eruption and caldera collapse at Kilauea in 2018 is a prime example of an eruption whose duration and magnitude were not well constrained at the onset of the eruption. Surges in the eruptive rate, and the duration of the eruption itself, were likely influenced by incremental piston collapses [Patrick et al., 2019b, Neal et al., 2018, Anderson et al., 2019]. This final consideration is relevant to our study, because Ambrym’s submarine eruption in 2018 – 2019 may have been prolonged due to a collapse of the reservoir roof at depth.

3.2 Paper 1: “*From prodigious volcanic degassing to caldera subsidence and quiescence at Ambrym (Vanuatu): the influence of regional tectonics*”

In this article, we combine multidisciplinary dataset from 8 different earth observations satellites, ranging from radar to UV/infrared to optical imagery, to document a rift zone

intrusion that we conclude is strongly influenced by the regional tectonic stress field. Not only is a rift zone eruption at Ambrym studied geodetically for the first time, but the temporal sampling of the geodetic observations allows us to distinguish between multiple stages of the dike intrusion, and how the location of the initial intra-caldera dike intrusion triggered the lateral migration towards the island's coast. In addition, inverse modelling images a central reservoir with multiple storage levels, activated at different stages during the eruption. At Ambrym, there is a competition between the vigorous influx of magmatic activity in the central portion of the broad caldera (resulting in persistent magmatic activity at the surface in the form of lava lakes), and the tectonic stresses imposed by the Back Arc Thrust Belt (BATB) (which can lead to complete silencing the volcano's surface activity). The volcano-tectonic relationship thus dictates fluctuations in Ambrym's activity on both long (edifice formation) and short (decadal cycles of lava lake persistence) time scales.

OPEN From prodigious volcanic degassing to caldera subsidence and quiescence at Ambrym (Vanuatu): the influence of regional tectonics

Tara Shreve^{1*}, Raphaël Grandin^{1*}, Marie Boichu^{2,3}, Esline Garaebiti⁴, Yves Moussallam^{5,6}, Valérie Ballu⁷, Francisco Delgado¹, Frédérique Leclerc⁸, Martin Vallée¹, Nicolas Henriot², Sandrine Cevuard⁴, Dan Tari⁴, Pierre Lebellegard⁹ & Bernard Pelletier⁹

Eruptive activity shapes volcanic edifices. The formation of broad caldera depressions is often associated with major collapse events, emplacing conspicuous pyroclastic deposits. However, caldera subsidence may also proceed silently by magma withdrawal at depth, more difficult to detect. Ambrym, a basaltic volcanic island, hosts a 12-km wide caldera and several intensely-degassing lava lakes confined to intra-caldera cones. Using satellite remote sensing of deformation, gas emissions and thermal anomalies, combined with seismicity and ground observations, we show that in December 2018 an intra-caldera eruption at Ambrym preceded normal faulting with >2 m of associated uplift along the eastern rift zone and 2.5 m of caldera-wide subsidence. Deformation was caused by lateral migration of >0.4 cubic kilometers of magma into the rift zone, extinguishing the lava lakes, and feeding a submarine eruption in the rift edge. Recurring rifting episodes, favored by stress induced by the D'Entrecasteaux Ridge collision against the New Hebrides arc, lead to progressive subsidence of Ambrym's caldera and concurrent draining of the lava lakes. Although counterintuitive, convergent margin systems can induce rift zone volcanism and subsequent caldera subsidence.

Broad caldera formation (>10 km in diameter) is often attributed to ignimbrite-forming, explosive eruptions¹. For mafic to intermediate systems, however, caldera-forming processes may also be linked to the lateral propagation of dikes that arrest at depth^{2–5}. Consequently, geological traces of associated magma discharge are often missing. Understanding caldera-forming processes thus relies heavily on contemporaneous observations, such as in 1968 at Fernandina and 2000 at Miyakejima^{6,7}. Ambrym, a remarkably active volcanic island in the Vanuatu archipelago, hosts a 12-km wide caldera, making it one of the largest basaltic shield calderas on Earth^{8,9}. Ambrym's caldera has been previously interpreted as resulting from the collapse of a giant tuff cone resulting from a sequence of explosive phreatomagmatic eruptions¹⁰. Onset of caldera subsidence is dated around 2000 BP, based on two ¹⁴C dates of charcoal embedded in debris flows on the caldera rim and flank¹¹. However, geological evidence for emplacement of voluminous ignimbrites coinciding with this dating is controversial^{12–14}, raising questions about the process of caldera formation.

Ambrym, in addition to its broad caldera, also hosts two well-defined straight rift zones oriented at N105°S, radiating bilaterally^{10,11,15–17} (Fig. 1). Ambrym's caldera is the site of intense eruptive activity, with frequent strombolian eruptions originating from at least two permanent lava lakes within or on the flanks of the cones of Marum and Benbow as well as occasional intra-caldera lava flows, most recently in 1986, 1988 and 2015^{12,18,19}. Continuous

¹Université de Paris, Institut de physique du globe de Paris, CNRS, F-75005, Paris, France. ²Univ. Lille, UMR 8518 - LOA - Laboratoire d'Optique Atmosphérique, F-59000, Lille, France. ³CNRS, UMR 8518, F-59000, Lille, France. ⁴Vanuatu Meteorology and Geohazards Department (VMGD), Port Vila, Vanuatu. ⁵Laboratoire Magmas et Volcans (LMV), Université Clermont Auvergne, Clermont-Ferrand, 63170, France. ⁶Lamont-Doherty Earth Observatory, Columbia University, New York, USA. ⁷Laboratoire Littoral Environnement et Sociétés (LIENSs), Université de La Rochelle, La Rochelle, 17000, France. ⁸Géoazur, Univ. Nice Sophia Antipolis (Univ. Côte d'Azur, CNRS, IRD, Observatoire de la Côte d'Azur), Géoazur UMR 7329, 250 rue Albert Einstein, Sophia Antipolis, 06560, Valbonne, France. ⁹Géoazur, Institut de recherche pour le développement, Nouméa, 98800, New Caledonia. *email: shreve@ipgp.fr; grandin@ipgp.fr

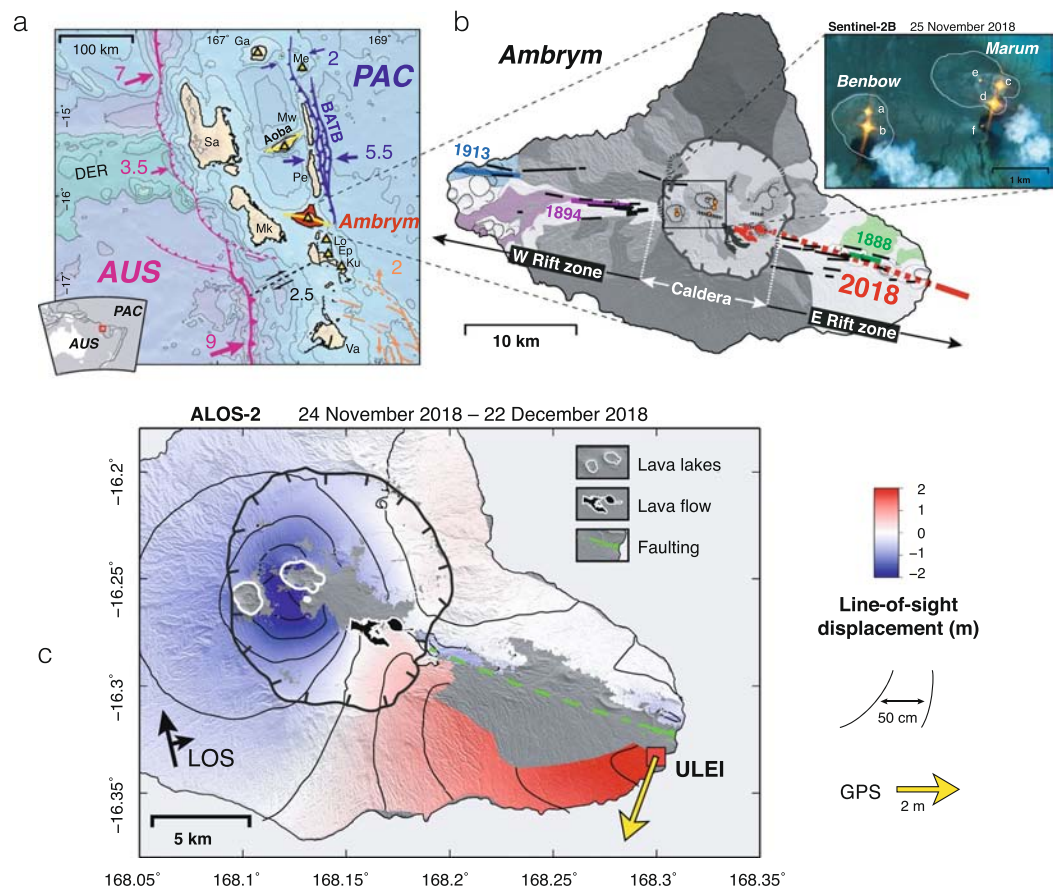


Figure 1. Tectonic and volcanic context of Ambrym. (a) Tectonic framework of the Central Vanuatu arc (modified after⁷¹). Collision of the D'Entrecasteaux Ridge (DER), carried by the Australian plate (AUS) leads to (1) along-strike variations of the convergence rate (pink arrows) of AUS w.r.t Pacific plate (PAC) across the New Hebrides subduction (pink) and (2) deformation of the Vanuatu arc on the border of the Pacific plate, accommodated by the back-arc thrust belt (BATB), giving rise to an uplifted bivergent thrust wedge. Arrows indicate local relative velocities across the BATB (blue) and Vate trough (orange). Velocities in cm/yr are from⁷². Yellow triangles are active volcanoes. Yellow lines indicate rift zones. Va: Vate; Ku: Kuwae; Ep: Epi; Lo: Lopevi; Mk: Malekula; Sa: Santo; Pe: Pentecost; Mw: Maewo; Ga: Gaua; Me: Mere Lava. (b) Simplified geological map of Ambrym (after¹¹ and¹⁸). Younger volcanic formations are indicated by light shading. Locations of historical fissure vents along the rift zones are shown by thick colored lines. Approximate locations of the 2018 intra-caldera eruption and extra-caldera intrusion are indicated in red. Inset is a false-color Sentinel-2 image acquired on 25 November 2018 (R: band 12; G: band 11; B: band 08), showing six thermal anomalies associated with lava lakes and open vents. (c) Unwrapped ascending ALOS-2 interferogram spanning between 24 November 2018 and 22 December 2018. Blue (respectively red) indicates motion away from the satellite (respectively toward the satellite). Maps were generated with GMT version 5.4.3 (<http://gmt.soest.hawaii.edu>) and edited in Adobe Illustrator version 16.0.4 (<https://www.adobe.com/products/illustrator.html>).

open-vent passive degassing from the lava lakes, first reported by Captain James Cook in 1774²⁰, ranks Ambrym first in worldwide volcanic sulfur dioxide (SO₂) emissions over the past decade^{21–24}.

Between 1820 and 1937, 10 extra-caldera rift eruptions were reported at Ambrym¹⁸. Notably, in 1913, a phreatomagmatic eruption on the island's west coast completely destroyed a large hospital²⁵. Based on geochemical evidence, these eruptions are believed to be fed from a central reservoir situated beneath the caldera, and magma transported to the coast by lateral dikes²⁶. However, the response of the caldera ring faults during these past lateral eruptions is undetermined, due to a lack of direct observations. Hence, whether the broad caldera of Ambrym should be interpreted as a relict structure, or should be considered an active fault system, remains an open question. More broadly, the relationship between the evolution of Ambrym's caldera, the rift zone's persistence, and the complex tectonic setting of the New Hebrides is yet to be explored.

Results

Precursory intra-caldera eruption. On 14 December 2018, a volcano-seismic crisis begins at Ambrym when 8 $M < 3$ seismic events are detected inside the caldera between 13h00 and 20h00 UTC (Fig. 2b). Between 23h20 and 23h40 UTC, Himawari-8 geostationary satellite observations of thermal anomalies and SO₂ emissions indicate the onset of an intra-caldera eruption (Fig. 2c,d, Supplementary Figs. S1, S2). Field observations (Fig. 2e)

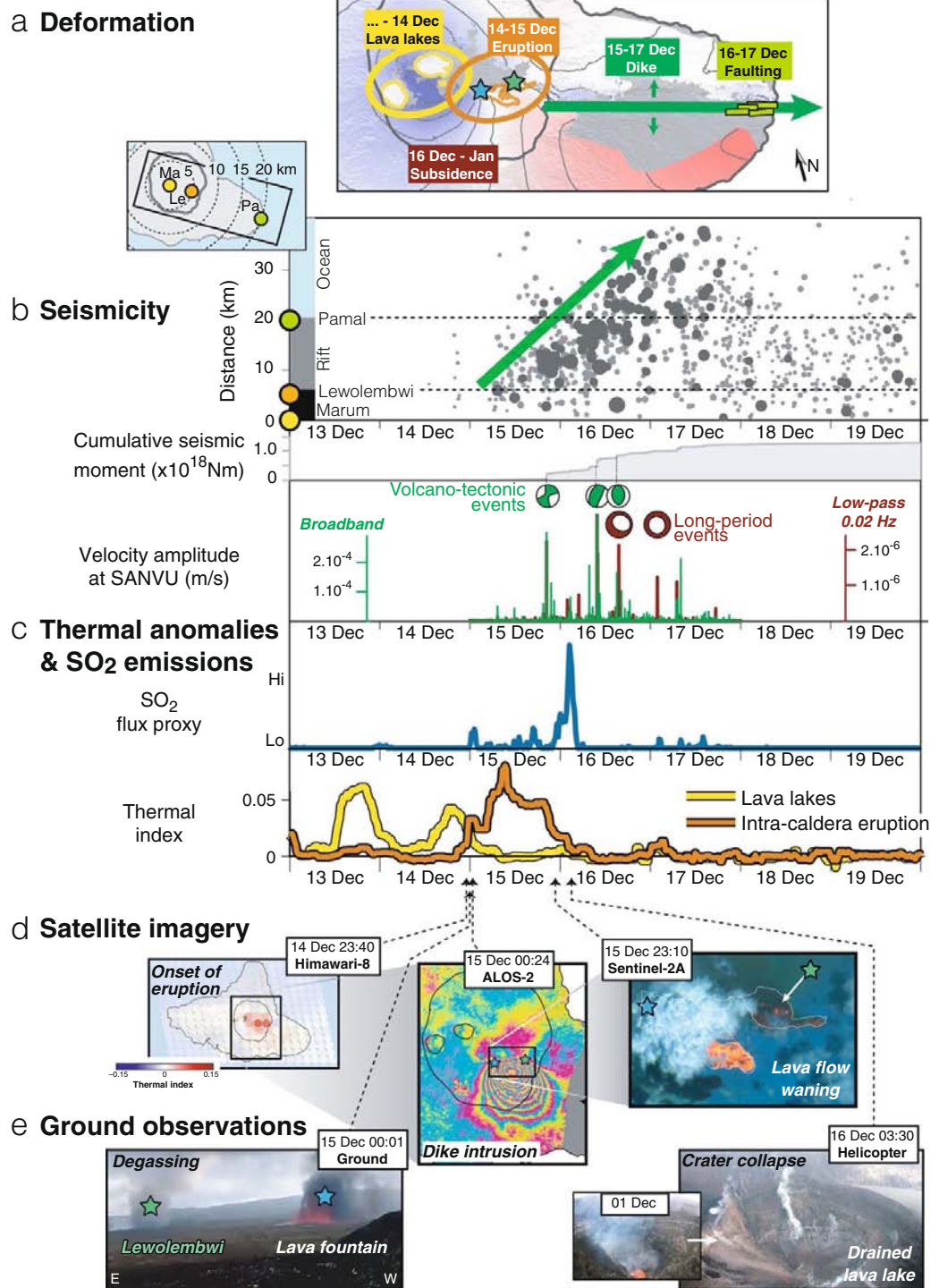


Figure 2. Temporal evolution of eruptive activity during the December 2018 event. (a) ALOS-2 interferogram of Fig. 1c (JAXA). (b) Upper panel: seismicity versus time, as a function of planimetric distance with respect to Marum lava lake. Symbol size increases with earthquake magnitude (dark grey: $M > 3.5$; light grey: $M < 3.5$). Green arrow highlights migration of seismicity along the east rift zone. Middle panel: cumulative seismic moment release. Focal mechanisms are from USGS (green) and GCMT (maroon). Lower panel: Absolute value of broadband (green) and low-passed (maroon) seismogram at SANVU Geoscope station (epicentral distance ~ 150 km)³¹. Spikes in the low-passed seismogram indicate detection of long period (LP) events. These events are not included in the cumulative seismic moment curve, which only includes volcano-tectonic (VT) events reported by VMGD. See Supplementary Fig. S14 for details and station location. (c) SO_2 flux proxy and thermal index of the lava lakes (yellow) and intra-caldera eruption (orange) derived from Himawari-8. (d) Satellite images acquired during the course of the eruption. Left: Himawari-8 (multispectral, geostationary)

(Japan Meteorological Agency). Center: ALOS-2 (ScanSAR) (JAXA). Right: Sentinel-2 (optical). (e) Ground observations. Left: gas emissions at Lewolembwi (green star) and lava fountaining associated with vent opening on the SE flank of Marum (blue star). Image courtesy of and copyright to John Tasso, Vanuatu Island Experience. Right: Comparison of lava lake crater at Benbow before and in the final hours of the eruption. Maps generated with GMT and edited in Adobe Illustrator.

reveal that the eruption initiated along a N110° pre-existing fracture at 590 meters a.s.l. at Lewolembwi tuff ring (Supplementary Fig. S3), and was characterized by scoria deposits associated with lava fountaining. Petrological analysis of scoria indicates an erupted magma of basaltic-trachy-andesitic composition (Supplementary Table S4). Once the eruption begins, thermal anomalies associated with the lava lakes progressively disappear within 12 hours, suggesting a drop in lava lake level (Fig. 2c, Supplementary Fig. S1). A helicopter flight (on 16 December 03h30 UTC) confirms both drainage of all the lava lakes and the partial collapse of Benbow and Marum (Fig. 2e). A lava flow, accompanied by lava fountaining and producing SO₂ and ash-rich emissions, is also emitted for ~24 hours from a second vent trending nearly N–S at 730 meters a.s.l. on the SE flank of Marum (Fig. 2c,e, Supplementary Fig. S3).

During this phase, surface deformation is measured with interferometric synthetic aperture radar (InSAR) thanks to the serendipitous acquisition of an image by the ALOS-2 satellite at 00h24 UTC on 15 December, about an hour after the eruption's onset²⁷ (Fig. 2d, Supplementary Table S1). The deformation field spanning 3 November to 15 December measures ~1.2 m of motion towards the satellite, consistent with an intra-caldera dike dipping 40°S and a maximum opening of ~2 m, yielding a total volume of intruded magma of ~34 × 10⁶ m³ (Supplementary Fig. S4). Until then, InSAR measures neither subsidence related to magma reservoir deflation, nor extra-caldera displacement, particularly no motion along the rift zones.

While Sentinel-2 satellite optical images indicate that lava flows reach their full extent on 15 December 23h10 (Fig. 2d), the eruption ends on 16 December around 07h00 UTC with a disappearance of thermal anomalies and an abrupt decrease of SO₂/ash emissions (Fig. 2c). Spaceborne imaging of SO₂ by Sentinel-5P TROPOMI sensor constrains the total mass of released SO₂ during the eruption to at least ~50–60 kt (Supplementary Fig. S10), corresponding to a volume of degassed magma of ~13 × 10⁶ m³ (calculated assuming <5% crystal content and 0.075 wt% of sulphur in the melt²³). First-order agreement with the volume of erupted material derived from mapping of the flow of ~10 × 10⁶ m³ (constrained by multiplying the spatial extent of ~1.95 × 10⁶ m² for the lava flow, Supplementary Fig. S3, and an estimated average lava flow thickness of ~5 m extrapolated from 3D mapping of the previous 2015 intra-caldera lava flow, Supplementary Fig. S11) suggests that the magma remaining trapped in the dike did not contribute significantly to the observed degassing.

Triggering of extra-caldera dike injection. Following a M_w 5.6 strike-slip earthquake on 15 December at 20h21, a sharp increase in the seismic moment release is detected, marking the beginning of magma propagation into the SE rift zone (Fig. 2b). A few hours before the intra-caldera eruption's end, the lateral propagation of a voluminous dike is evidenced by a migration of seismicity from the caldera toward the eastern tip of the island, reaching 30 km from the eastern caldera rim by 17 December 12h00 UTC. Sub-pixel correlation of a Sentinel-2 optical image acquired on 15 December 23h10 UTC indicates that at that time the dike tip is leaving the caldera but did not reach farther than halfway to the east coast (Supplementary Fig. S15). On 16–17 December, local inhabitants report progressive fracturing at the coastal village of Pamal (13 km from the caldera border) (Fig. 3a,b). Joint inversion of SAR data (Supplementary Table S1) reveals ~3 m of opening along a >30 km long dike, extending from within the caldera to beyond the eastern coast²⁷ (Figs. 2a and 4b). These SAR geodetic observations indicate the emplacement of a dike with a total volume of intruded magma between 419 and 532 × 10⁶ m³ (depending on the maximum depth and how far offshore the model extends, Supplementary Figs. S5, S6). Surface deformation across the trace of the dike is asymmetric, with more deformation to the south (Fig. 3a), indicating that the dike dips ~70° to the south. Due to this asymmetry, coastal uplift in excess of 2 meters occurred along the southeastern coast of the island, as later confirmed during a field campaign in early February and by a single GPS measurement at Ulei (Fig. 3a,c).

Submarine eruption and caldera subsidence. The extremely narrow breadth of the faulted corridor observed above the dike at the surface, as small as 400 m along the east coast (Fig. 3b), indicates that the dike almost reached the surface. However, magma does not erupt from on-shore fractures and only minor gas emissions are detected from space until 17 December 14h00 UTC (Fig. 2c). The end of dike propagation, marked by an abrupt decrease of seismic moment release, takes place around 17 December 16h00 UTC (Fig. 2b). InSAR-derived models predict that maximum opening at the surface occurs offshore (Fig. 4b, Supplementary Fig. S6), suggesting a submarine eruption. This is confirmed on 18–19 December, when basaltic pumice is collected on the beach near Pamal and Ulei (Fig. 3c,d), indicating that lava erupted underwater. Although the depth and exact location of the underwater fissure are uncertain, the nature of erupted material (basaltic pumice) indicates a shallow (<100 m b.s.l.) and high-rate underwater magma supply able to sustain a protective gas-rich envelope which allows pumice to cool before contact with sea water, preventing it from sinking²⁸. This transport method differs from, for example, floating eruption products collected during basaltic eruptions in the Azores, when gas trapped in hollow cavities caused buoyant basaltic balloons to float to the ocean surface²⁹. An alignment of volcanic cones visible in the bathymetry is consistent with an offshore prolongation of the rift zone, suggesting that similar submarine eruptions took place in the past (Fig. 3a).

In addition to the dike intrusion, we also measure >2 m of subsidence at Ambrym's summit craters, consistent with deflation of a nearly symmetrical pressurized source, roughly centered on Marum at ~4.5 km

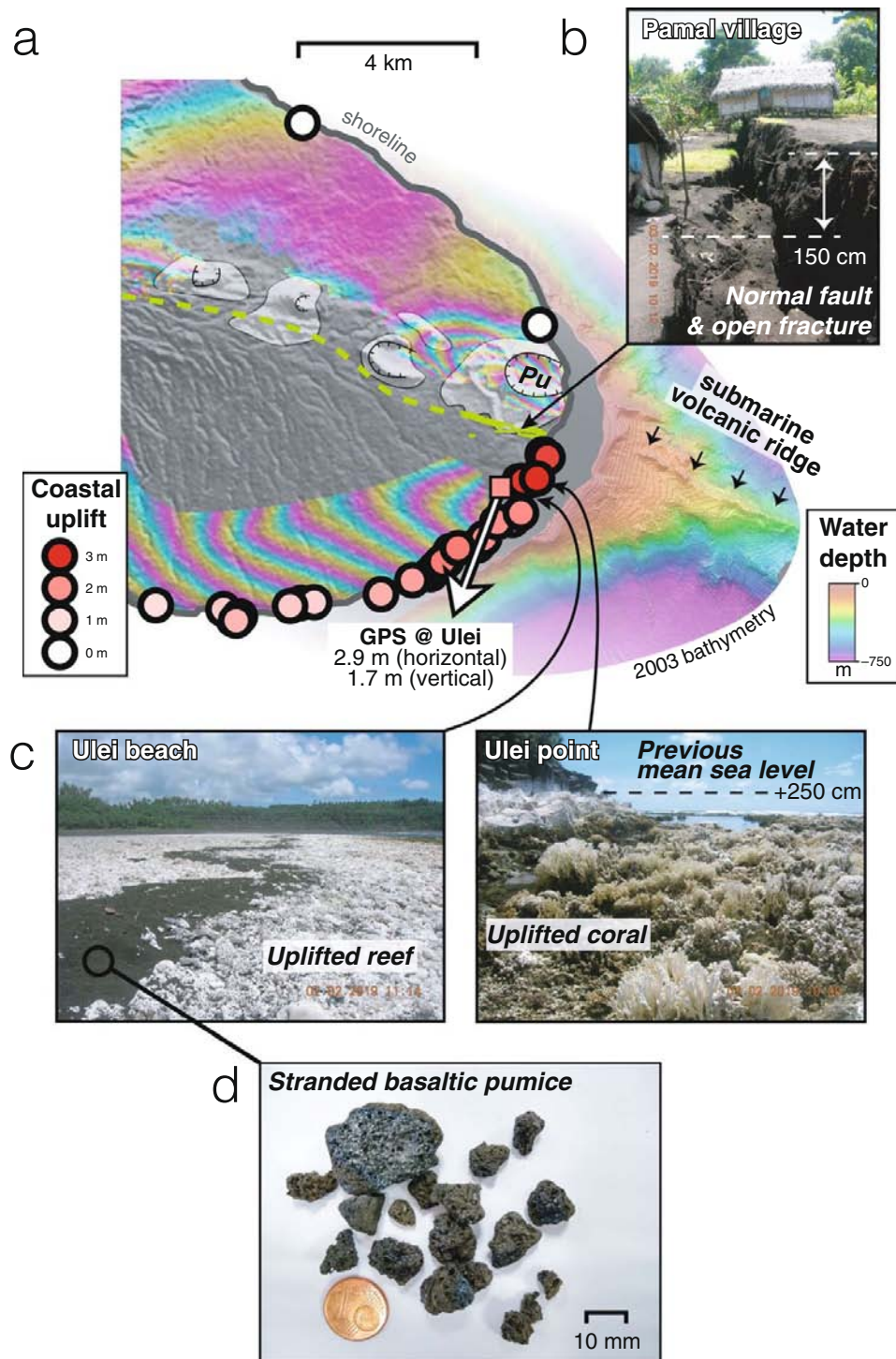


Figure 3. Faulting, coastal uplift and submarine eruption at the east coast of Ambrym. **(a)** Circles: coastal uplift derived from field mapping of dead coral and red algae. Green segments: fractures mapped in the field. Dashed green line: trace of the dike derived from SAR data. White arrow: motion of GPS Ulei site. Small black arrows indicate the location of a submarine volcanic ridge visible in high-resolution bathymetry acquired in 2003 (see Supplementary Methods). Pu: Pulvenu cone. Background is the wrapped ALOS-2 interferogram of Fig. 1c, where each fringe represents 12.1 cm of motion toward or away from the satellite. DEM ©DLR 2017. Maps generated with GMT and edited in Adobe Illustrator. **(b)** Normal faulting and fracturing at Pamal village. **(c)** Evidence for coastal uplift from dead coral. Black deposits consist of pumice stranded along the coast at Ulei. **(d)** Detail of a pumice sample.

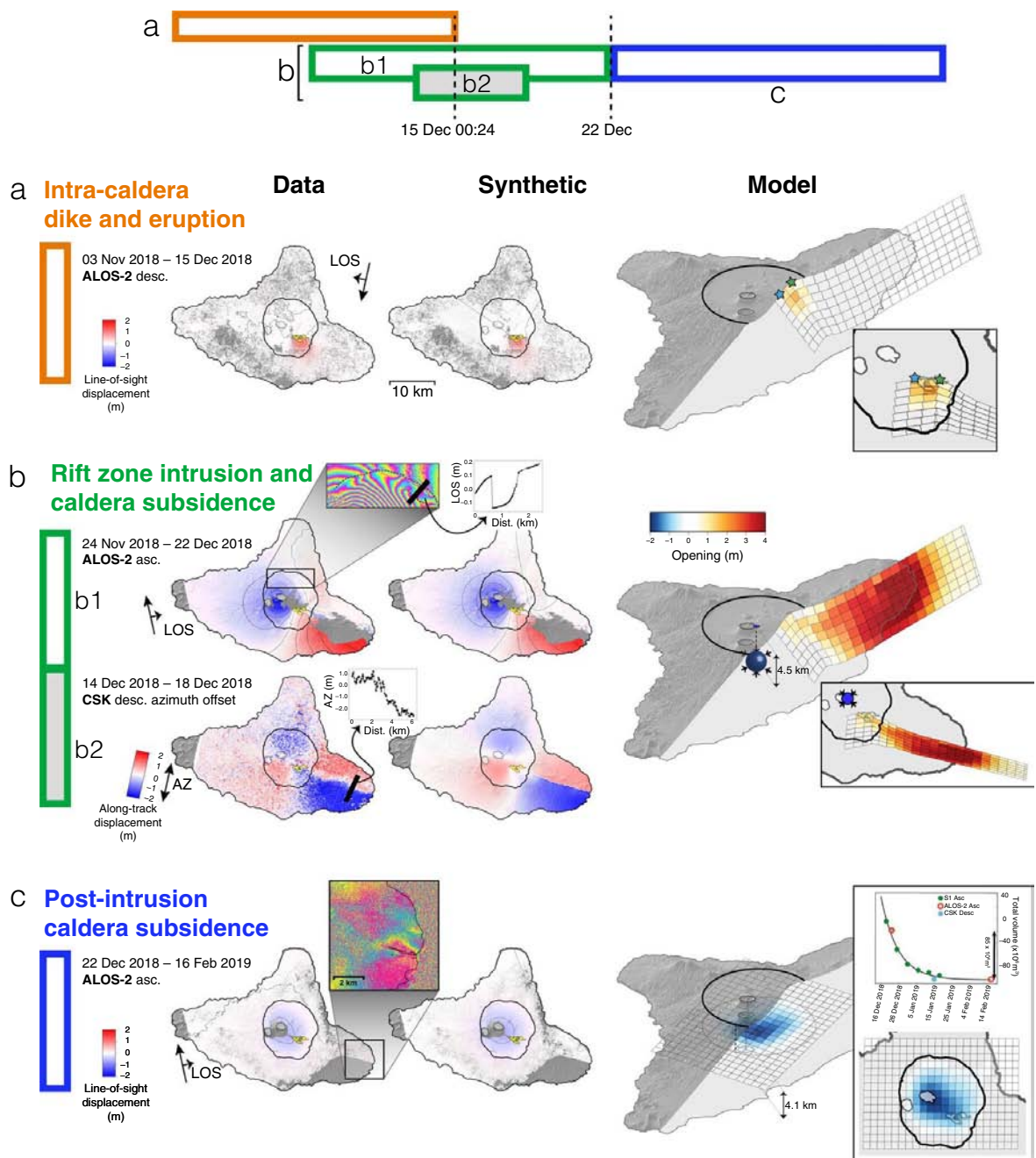


Figure 4. Deformation during and after the December 2018 event from InSAR. Left: data. Middle: synthetic. Right: model. (a) ALOS-2 interferogram covering the small-volume dike intrusion emplaced on 14 December (last image acquired on 15 December, 00h24). Dike inflation is indicated by red colors. Contraction or deflation is indicated by blue colors. (b) ALOS-2 interferogram (top) and COSMO-SkyMed azimuth offsets (bottom) covering the 15–18 December time interval. First inset shows local fringe discontinuities across the northern caldera rim, evidence of normal faulting. Second inset shows a profile of horizontal displacement across the dike. (c) ALOS-2 interferogram covering the post-intrusion caldera subsidence (first image acquired on 22 December). Inset to the left shows detail of deformation along the east coast. Inset to the right shows temporal evolution of post-intrusion subsidence derived from Sentinel-1, ALOS-2 and CSK (See Supplementary Fig. S7). Maps were generated with GMT version 5.4.3 (<http://gmt.soest.hawaii.edu>) and edited in Adobe Illustrator version 16.0.4 (<https://www.adobe.com/products/illustrator.html>).

depth, with a volume change ranging between 195 and $231 \times 10^6 \text{ m}^3$ (depending on the depth and amount of post-eruptive deformation included in the data, Supplementary Fig. S7, Table S3) (Fig. 4c). The 2:1 volume ratio between the dike and deflating Mogi source is in fact consistent with mass conservation assuming standard

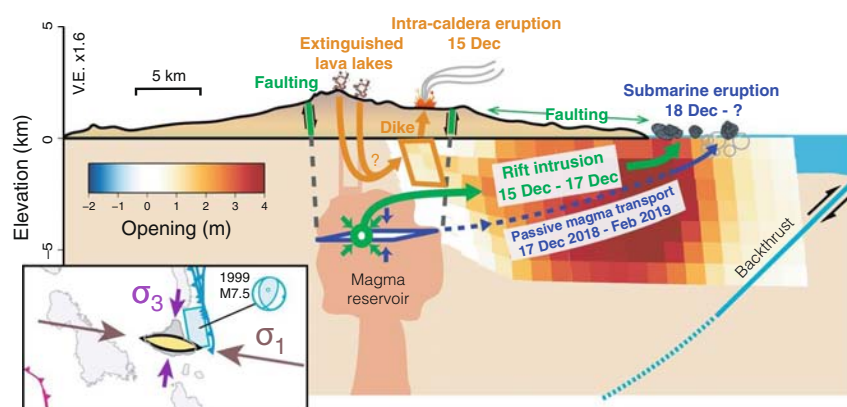


Figure 5. Conceptual model of the December 2018 event. Magma injection into the rift zone occurred in two stages. First, on 14 December, a small-volume dike was emplaced in the eastern part of the caldera. The dike breached the surface and fed an eruption lasting ~24 hours. Deflation of Ambrym's magma plumbing system as a result of the intra-caldera eruption induced a drop of pressure in the magma column, leading to lava lake drainage. On 15–16–17 December, a large-volume dike injection took place along the east rift zone, likely fed through the conduit opened by the previous intra-caldera dike. During its propagation and inflation, the voluminous dike intrusion induced intense faulting and fissuring above its upper edge, especially at the coastal village of Pamal, suggesting a shallow depth of emplacement. However, the dike did not produce any onshore eruption nor any substantial degassing. From 18 December, pumice washed up on the eastern shore of Ambrym indicating a submarine eruption. Continued subsidence of Ambrym caldera during the weeks following this eruption, as well as continuation of localized faulting at Pamal (Fig. 3c), suggest a prolongation of the submarine eruption without substantial additional inflation of the main dike, compatible with passive magma transport from Ambrym's central reservoir toward the submarine eruption site. The inset is a zoom on Ambrym's tectonic setting, emphasizing that Ambrym's rift zone orientation is sub-parallel to the regional maximum compressive stress, allowing us to interpret Ambrym as a large tension fracture. The activated plane and focal mechanism of the 1999 thrust earthquake are noted on the sketch in light blue.

magma compressibility and host-rock shear modulus³⁰. Furthermore, SAR data indicate that caldera subsidence occurred between 15 December 00h24 and 18 December 06h10, hence was coeval to the extra-caldera dike intrusion (Fig. 4b2). There are several locations to the north of the caldera where the ascending ALOS-2 fringe pattern is discontinuous, indicating ~0.4 m slip along the caldera faults (Fig. 4b1, Supplementary Fig. S8). Two M_w ~5.6 earthquakes with vertical compensated-linear-vector-dipole (CLVD) focal mechanisms are recorded in the migration's final 24 hours, on 16 December 15h34 UTC and 17 December 01h49 (Fig. 2b). These events are characterized by a long period (LP) content and long duration (exceeding 10 s of seconds) (Fig. 2b, Supplementary Fig. S14). At least 4 additional LP signals are recorded at station SANVU (~150 km away) on 16–17 December³¹. These LP events with CLVD mechanisms are consistent with caldera ring faulting or pressure drop within a reservoir³².

In the weeks following the dike emplacement, caldera-wide subsidence, reaching ~80 cm at Marum crater and decaying exponentially with a half-life of about 6 days, is measured using ALOS-2 and Sentinel-1 InSAR (Fig. 4c, Supplementary Fig. S7). Exponentially decaying subsidence is consistent with elastic response to magma outflow driven by pressure difference between the central reservoir and the eruption site³³. Modeling of this subsidence indicates a horizontal sill at ~4.1 km depth deflating with a total volume change of $\sim 85 \times 10^6 \text{ m}^3$ (Fig. 4c). This sill-shaped post-intrusion deflation contrasts with the Mogi-shaped co-intrusion deflation, suggesting that the central reservoir consists of several storage levels³⁴. Low-magnitude seismicity during this phase is shallow (<6 km depth) and located within the caldera, possibly related to continued caldera faulting visible in post-eruptive interferograms (Supplementary Figs. S12, S13).

Although no additional large-scale deformation is observed along the east rift zone after 22 December, a localized <12 cm discontinuity is measured across the fractures mapped along the SE coast (Fig. 4c), suggesting a continuation of the distal submarine eruption, driving the progressive drainage of the central magma reservoir, similar to the 2014 Bárarbunga or the 2018 Kilauea eruptions^{35,36}. Field surveys confirm that the submarine eruption may have continued past the 27 December, as more pumice was observed on 3 February 2019 than on 27 December 2018. At the time of writing (August 2019), there has been no satellite detection of sulphur dioxide above background levels since late January 2019, contrasting starkly with the intense persistent degassing measured over the past decade²⁴.

Discussion

The December 2018 Ambrym diking event sheds light on the stress state that prevails at the scale of Ambrym island, while providing insight into the magma storage conditions beneath Ambrym's caldera (Fig. 5). Joint analysis of remote sensing and seismicity demonstrates that the condition initiating the rift intrusion in December 2018 was the creation of an open fracture at Lewolembwi, connecting the caldera's localized magma supply to the rift zone. Once such a connection is made, a blade-like fluid-filled crack (dike) is able to travel tens of kilometers

away from its source, neither erupting at the surface, nor degassing significantly to the atmosphere. To sustain lateral magma propagation, pressure in the dike (P_m) must be greater than the host rock's minimum principal stress normal to the dike plane (σ_3 , positive), a difference defined as the driving stress (P_d) ($P_d = P_m - \sigma_3$)^{37–39}. Furthermore, to travel horizontally for long distances, there must be a strong horizontal gradient of driving stress in the direction of magma propagation⁴⁰. Magmatic systems in an extensionally-loaded host rock (low σ_3) do not necessarily require high magma overpressures to drive large diking events (high P_d)⁴¹. When comparing diking events at Icelandic and Hawaiian volcanoes, dike widths tend to be thicker in Iceland (higher P_d in Iceland), but dikes reach the surface more often in Hawaii (higher P_m in Hawaii). The >3 m dike thickness at Ambrym brings us to the conclusion that P_d is high without having a large P_m ⁴¹. A similar conclusion was drawn after the dike intrusions and lava lake drainage of the 2002 Nyiragongo flank eruption^{42,43}. In spite of enhanced thermal activity and increased lava lake vigor (Supplementary Figs. S16, S17), an absence of uplift in the months to years prior to the 2018 Ambrym crisis is evidenced (Supplementary Fig. S9), consistent with this inferred lack of overpressure⁴⁴. The fact that the central magma reservoir was able to store a large volume of magma (0.4 km³) and sustain dike propagation over large distances without prior overpressurization is consistent with vigorous supply of a relatively volatile-poor magma²³.

The thick 2018 dike—similar in width to dikes at plate boundaries in Iceland or Afar⁴⁵—and energetic earthquake migration indicate that lithospheric stresses primed for magma injection drove lateral magma propagation. Assuming a minimum volume of intruded magma in the 2018 eruption (400×10^6 m³), we calculate a minimum expansion rate along Ambrym's rift of ~2 cm/yr (assumptions: last event = 81 years ago; SE rift length = 25 km; height = 10 km). Gravitationally-induced extension can be plausibly discarded as a mechanism generating these stresses, due to the lack of curvature of Ambrym's rift zone⁴⁶ and to the fact that the 2018 rift zone intrusion led to uplift of the entire south-eastern part of the island, hence working against gravity. On the other hand, tectonic stresses induced by the proximity of regional faults involved in the convergence between the Pacific and Australian plates may provide the stress conditions driving rift development at Ambrym. Ambrym is facing the collision-subduction of the D'Entrecasteaux Ridge (DER) and, farther to the north, of the West Torres Massif (WTM) (Fig. 1a). The DER and WTM perturb the Vanuatu arc, resulting in the late Quaternary uplift of the western Santo-Malekula islands^{47,48} and the growth of a back-arc thrust belt (BATB), uplifting the eastern islands of Pentecost-Maewo (Fig. 1a)^{49–51}. Ambrym's east coast is located at the southern tip of the BATB, which was last activated in the thrusting 1999 M_w 7.5 earthquake^{52,53}. We note that the focal mechanisms during the 2018 diking event have P-axis orientations consistent with this regional compression (Fig. 2b). This triggered seismicity does not appear consistent with stress change caused by the dike inflation (increased compressive stress oriented perpendicular to the dike, i.e. N20°) but rather reflects the regional stress state (σ_3 oriented N110°), revealing the dominant overprint of this background compressive stress⁵⁴. In this context, Ambrym may be envisioned as a giant tension fracture oriented sub-parallel to the local maximum compression axis σ_1 (inset of Fig. 5). The importance of the regional stress field's maximum compression axis was also emphasised after the 2000 lateral dike intrusion at Miyakejima, likewise situated in a convergent margin setting⁵⁵.

The 2018 diking event illustrates how tectonically-induced stresses drive magma transport into Ambrym's well-defined rift zone, efficiently siphoning magma away from the caldera in a relatively silent manner for an observer at the surface. Similar to past events in hot-spot basaltic volcanoes of the Galapagos, especially in 1968 at Fernandina^{56,57}, caldera subsidence was associated with non-explosive activity, thereby leaving little geological trace at the surface. Rather, the elevated rate of Ambrym's volcanic activity witnessed in the past decades contrasts with the near-complete muting of degassing and thermal activities at the surface during and since the December 2018 extra-caldera dike intrusion (Supplementary Fig. S17). Modulation of volcanic activity at Ambrym's lava lakes over historical times¹⁸ may therefore be reinterpreted as resulting from recurrent pumping of magma into the rift zone, leading to episodic subsidence of the caldera floor. Open-vent degassing in the years prior to the 2018 eruption may have allowed for an increasing availability of non-overpressurized magma, with lava lakes acting as piezometers of a magma plumbing system that is well-connected to the surface. This offers a glimpse into a system where magma ascent, lateral magma transport, and caldera formation are controlled by regional compressive tectonics.

Methods

Himawari processing. Himawari-8 is a meteorological satellite operated by the Japan Meteorological Agency, providing multispectral observations from a geostationary orbit at 140.7°E. The Advanced Himawari Imager (AHI) covers 16 channels spanning visible to thermal infrared, and acquires images every 20 minutes. Images have a resolution of ~2.3 km at the location of Ambrym.

Following⁵⁸, a raw thermal index is calculated by computing the normalized difference between top-of-atmosphere brightness temperatures from infrared channels centered on 10.41 microns and 3.9 microns:

$$TI^{raw} = \frac{BT_{3.9\mu m} - BT_{10.4\mu m}}{BT_{3.9\mu m} + BT_{10.4\mu m}} \quad (1)$$

In order to mitigate the impact of clouds and diurnal variations in brightness temperature, a background thermal index is estimated by extracting the raw thermal index for a reference pixel situated at the border of the caldera, that is not affected by the thermal anomaly of lava and ash emissions while sharing similar ground properties as the intra-caldera pixels. This background thermal index is subtracted from the raw thermal index, yielding a corrected thermal index.

The thermal index time series of Fig. 2c is then estimated by calculating the thermal index averaged in two regions corresponding to the lava lakes and lava flows. Supplementary Fig. S1 shows the same time series of Fig. 2c on a longer time window.

The SO₂ flux proxy is estimated in two steps. First, following⁵⁹, a SO₂ column amount proxy is calculated for each pixel by differencing top-of-atmosphere brightness temperatures from infrared channels centered on 10.41 microns and 8.5 microns:

$$CA_{SO_2} \propto BT_{10.4\mu m} - BT_{8.5\mu m} \quad (2)$$

Then, the time series of SO₂ flux proxy Q_{SO_2} in Fig. 2c is calculated by summing, for each acquisition, the value of CA_{SO_2} for all pixels with a CA_{SO_2} greater than 4 K within a $\sim 50 \times 35$ km box centered on Ambrym (dashed polygon in Supplementary Fig. S2b). The threshold is intended to distinguish the signal associated with the presence of volcanic SO₂ from background oscillations. Supplementary Fig. S2a shows the SO₂ flux proxy of Fig. 3c on a longer time window, plotted both on a linear scale and a logarithmic scale.

InSAR processing. The SAR images used in this study are listed in Supplementary Table S1. Processing of SAR data from the SLC level to wrapped, unfiltered interferograms is performed using the Interferometric SAR scientific computing environment (ISCE)⁶⁰ for ALOS-2 StripMap (SM3) and Cosmo-SkyMed (CSK) StripMap data and Generic Mapping Tool's software GMTSAR⁶¹ for ALOS-2 wide-swath (WD1) data, with additional post-processing using the NSBAS⁶². Topographic fringes are removed using DLR's TanDEM-X 12 meter Global (TDX) DEM (an average of DEMs acquired between 14 January 2011 and 22 November 2014)⁶³. Interferograms are filtered with a weighted power spectrum filter⁶⁴, followed by a cascading high-pass filter, especially useful in the areas with a high-gradient fringe rate and on the vegetated flanks⁶⁵. An iterative, coherence-based unwrapping method is then used⁶⁵, which we will call MPD, and is a module in NSBAS (see Supplementary Methods). The final unwrapped interferograms are then geocoded.

CSK interferograms have low coherence across the island, due to vegetation, atmospheric effects, and a high rate of deformation. Therefore, CSK descending pixel offsets, which complement the ascending ALOS-2 measurements, were exploited to measure deformation during the rift zone intrusion and the post-intrusion caldera subsidence. After unwrapping and geocoding, swaths F1 and F2 are merged for ALOS-2 WD1 interferograms. We also merge along-track frames for ALOS-2 SM3 interferograms, to ensure that the far-field signal (Pentecost island to the north and Lopevi, Paama, and Namuka islands to the south) is included in the inversion.

Geodetic modeling. *Inversion procedure.* We then perform the same inversion procedure for each of the three datasets, respectively corresponding to the (a) intra-caldera dike, (b) rift zone intrusion and caldera subsidence, and (c) post-intrusion caldera subsidence (Fig. 4). To focus on the first-order geometry of the pressure sources, we mask localized, near-field signals that may bias the model misfits (i.e. masking localized deformation within 2 km of the dike trace, deformation close to the craters that may be due to conduit pressurization, or subsidence due to lava flow cooling and compaction).

After downsampling the data using a distance-based averaging, we then run a non-linear inversion to find the first order geometry of the pressure sources⁶⁶ (See Supplementary Table S2). The forward model includes dislocations⁶⁷ and Mogi sources⁶⁸. We find that the intra-caldera phase (a) is best explained by a single inflating dike, whereas the rift zone intrusion and caldera subsidence in phase (b) require an inflating dike and a deflating Mogi. We find that post-intrusion caldera subsidence in phase (c) cannot be explained by the same deflating Mogi as in phase (b), whereas a laterally extensive sill-like deflating source better reproduces the deformation measured in post-eruptive interferograms.

Following this non-linear inversion, the geometry of the pressurized sources is held fixed, and we then performed a constrained least squares inversion to investigate separately the distributed opening of the intra-caldera dike, extra-caldera rift intrusion (modeling the residual deformation field after removing the synthetic deformation from the deflating Mogi), and the closing of the post-intrusion sill^{45,69} (see Supplementary Methods).

During the rift zone intrusion, there was significant deformation offshore, limiting the model's resolution. Therefore, we perturb the geometry of the dike used to model the rift zone intrusion by extending the depth, as well as the length offshore, by several kilometers. We derive four end-member models to determine a reasonable range of volumes, taking into account uncertainties imposed by the lack of model resolution (Supplementary Fig. S6). Final volumes range from 419 to 532×10^6 m³, with an "average" model chosen with a reasonable misfit, which extends 6 km offshore and 6 km along depth.

Once the distributed opening along the rift-zone dike is determined, we perform a final iteration to ensure that the initial removal of the Mogi model's synthetic deformation does not propagate significant model errors into the distributed opening inversion. We subtract the synthetic deformation field derived from the "average" model from the original datasets, and rerun the nonlinear inversion to solve for the Mogi depth and volume change. The volume and depth do not change significantly (<6% and <3%, respectively).

Temporal evolution of post-intrusion subsidence. In addition to an ALOS-2 interferogram and CSK pixel offsets measuring deformation after the rift zone intrusion (Fig. 4c), ascending Track 81 Sentinel-1 images were also acquired every 6 days, starting from 19 December 2018. The magnitude of deformation measured in the 6-day pairs decreases with time, allowing us to investigate the temporal evolution of the subsidence. The full extent of the deformation signal is not captured in some of the interferograms because coherence is limited to within the unvegetated part of the caldera. Conversely, ALOS-2 interferograms exhibit a better coherence, which allows for

mapping the deformation outside the caldera. However, the temporal resolution of ALOS-2 data is insufficient to capture the temporal evolution of this transient post-intrusion subsidence signal.

In order to combine the high temporal resolution of Sentinel-1 and the high coherence of ALOS-2, we design a specific strategy by (a) first estimating the parameters (shape, depth) of the deflating source from the deformation pattern visible in ALOS-2 data and (b) solving for the temporal evolution of the deflation source by fitting the deformation signal projected in the line of sight (LOS) against the deformation measured in Sentinel-1 data.

To exploit the high coherence of the ALOS-2 interferogram, we use the same inversion procedure as mentioned above to invert for closing on a horizontal sill, fixed to a depth of 4.1 km, with patches 1 km × 1 km (Supplementary Fig. S4). The depth was derived from an initial non-linear inversion of a closing Okada plane. We then project the synthetic deformation field into the ascending Sentinel-1 LOS, and scale the model to fit the 15 interferograms spanning 19 December 2018 to 18 January 2019. The scaling is determined such that:

$$\gamma_k = \frac{\bar{u}_k}{\bar{u}_{model}}, \quad (3)$$

where k is the interferogram index, \bar{u}_k and \bar{u}_{model} are the average velocities of the data and model, respectively (i.e. the displacement divided by the time span). Here, γ_k is the scalar for interferogram k representing the rate of deformation in the time interval spanned by the interferogram. See Supplementary Methods for more details.

We then multiply each scalar by the total magma volume loss in the initial inversion ($-85 \times 10^6 \text{ m}^3$), and perform a least squares inversion to find volume loss for each acquisition (Fig. 4c)⁷⁰. An exponential is fit to the volume loss vs. time,

$$F(t) = A \cdot \exp\left(\frac{-t}{B}\right) - C, \quad (4)$$

such that $A = 0.144 \text{ m}^3$, $B = 9.55 \text{ days}$, $C = 0.1 \text{ m}^3$, and t is the time in days since 16 December 2018, which corresponds with the inferred time of onset of caldera subsidence based on seismicity. The half-life of the exponential decay is thus $\sim 6.6 \text{ days}$.

Removing post-intrusion subsidence. The datasets spanning the rift zone intrusion and main caldera subsidence also span the beginning of the post-intrusion subsidence. We scale the post-intrusion synthetic deformation field, using the exponential described above, to remove post-intrusion deformation from the co-intrusion ALOS-2 and CSK data. However, after rerunning the non-linear inversion on these corrected interferograms, the RMS was not improved—24.03 (without removal) vs. 24.74 (with removal). This may be because the source geometry does not remain constant throughout the entire post-intrusion subsidence phase (especially in the days immediately after the intrusive event, 18–22 December, which are not covered by the initial post-intrusion ALOS-2/CSK inversion). We therefore decide to proceed without removing the post-intrusion deformation.

Received: 28 June 2019; Accepted: 17 October 2019;

Published online: 11 December 2019

References

- Druitt, T. H. & Sparks, R. S. J. On the formation of calderas during ignimbrite eruptions. *Nature* **310**, 679–681, <https://doi.org/10.1038/310679a0> (1984).
- Walker, G. P. L. Basaltic-volcano systems. *Geol. Soc. London, Special Publ.* **76**, 3–38, <https://doi.org/10.1144/GSL.SP.1993.076.01.01> (1993).
- Gudmundsson, A. Formation and development of normal-fault calderas and the initiation of large explosive eruptions. *Bull. Volcanol.* **60**, 160–170 (1998).
- Acocella, V. Understanding caldera structure and development: An overview of analogue models compared to natural calderas. *Earth-Science Rev.* **85**, 125–160 (2007).
- Michon, L., Massin, F., Famin, V., Ferrazzini, V. & Roult, G. Basaltic calderas: Collapse dynamics, edifice deformation, and variations of magma withdrawal. *J. Geophys. Res. Solid Earth* **116**, 1–18, <https://doi.org/10.1029/2010JB007636> (2011).
- Simkin, T. & Howard, K. A. Caldera collapse in the Galápagos Islands, 1968. *Science* **169**, 429–437, <https://doi.org/10.1126/science.169.3944.429> (1970).
- Geshi, N., Shimano, T., Chiba, T. & Nakada, S. Caldera collapse during the 2000 eruption of Miyakejima Volcano, Japan. *Bull. Volcanol.* **64**, 55–68, <https://doi.org/10.1007/s00445-001-0184-z> (2002).
- Pike, R. J. Volcanoes on the inner planets: Some preliminary comparisons of gross topography. *Proc. Lunar Planet Sci. Conf.* **9**, 3239–3273 (1978).
- Wood, C. A. Calderas: a planetary perspective. *J. Geophys. Res.* **89**, 8391–8406, <https://doi.org/10.1029/JB089iB10p08391> (1984).
- Robin, C., Eissen, J. P. & Monzier, M. Giant tuff cone and 12-km-wide associated caldera at Ambrym Volcano (Vanuatu, New Hebrides Arc). *J. Volcanol. Geotherm. Res.* **55**, 225–238, [https://doi.org/10.1016/0377-0273\(93\)90039-T](https://doi.org/10.1016/0377-0273(93)90039-T) (1993).
- Mccall, G. J. H., Lemaitre, R. W., Malahoff, A., Robinson, G. P. & Stephenson, P. J. The Geology and Geophysics of the Ambrym Caldera, New Hebrides. In *Symposium Volcanoes and their Roots*, 681–696 (Oxford, England, 1969).
- Németh, K. & Cronin, S. J. Volcanic craters, pit craters and high-level magma-feeding systems of a mafic island-arc volcano: Ambrym, Vanuatu, South Pacific. *Geol. Soc. London, Special Publ.* **302**, 87–102, <https://doi.org/10.1144/SP302.6> (2008).
- Németh, K., Cronin, S. J., Stewart, R. B. & Charley, D. Intra- and extra-caldera volcanoclastic facies and geomorphic characteristics of a frequently active mafic island-arc volcano, Ambrym Island, Vanuatu. *Sedimentary Geol.* **220**, 174–188, <https://doi.org/10.1016/j.sedgeo.2009.04.019> (2009).
- Cronin, S. J. & Németh, K. Where are the giant tuff cone and ignimbrites of Ambrym? A more conventional story of mafic volcanism at Ambrym Volcano, Vanuatu. In *Geological Society of New Zealand 50th Annual Conference*, 21–22 (Geological Society of New Zealand, Kaikoura, New Zealand, 2005).
- Stephenson, P. *et al.* Geology of Pentecost and Ambrym, 1:100,000. *New Hebrides Geological Survey Sheet* **6**. (1976).

16. MacFarlane, A., Carney, J. N., Crawford, A. J. & Greene, H. Vanuatu - A review of the onshore geology. In H.G., G. & F.L., W. (eds.) *Geology and offshore resources of Pacific island arcs - Vanuatu region, Circum-Pacific, no. 8 in Earth Science Series*, 45–91 (Circum-Pacific Council for Energy and Mineral Resources, 1988).
17. Picard, C., Monzier, M., Eissen, J.-P. & Robin, C. Concomitant evolution of tectonic environment and magma geochemistry, Ambrym volcano (Vanuatu, New Hebrides arc). *Geol. Soc. London, Special Publ.* **81**, 135–154 (1994).
18. Eissen, J. P., Blot, C. & Louat, R. Chronology of the historic volcanic activity of the New Hebrides island arc from 1595 to 1991. *Tech. Rep., ORSTOM, Nouméa* (1991).
19. Coppola, D., Laiolo, M. & Cigolini, C. Fifteen years of thermal activity at Vanuatu's volcanoes (2000–2015) revealed by MIROVA. *J. Volcanol. Geotherm. Res.* **322**, 6–19, <https://doi.org/10.1016/j.jvolgeores.2015.11.005> (2016).
20. Gregory, J. The Ambrym eruptions of 1913–1914. *Geol. Mag.* **1917**, 496–503 (1917).
21. Bani, P. *et al.* Surge in sulphur and halogen degassing from Ambrym volcano, Vanuatu. *Bull. Volcanol.* **71**, 1159–1168, <https://doi.org/10.1007/s00445-009-0293-7> (2009).
22. Bani, P. *et al.* First estimate of volcanic SO₂ budget for Vanuatu island arc. *J. Volcanol. Geotherm. Res.* **211–212**, 36–46 (2012).
23. Allard, P. *et al.* Prodigious emission rates and magma degassing budget of major, trace and radioactive volatile species from Ambrym basaltic volcano, Vanuatu island Arc. *J. Volcanol. Geotherm. Res.* **304**, 378–402, <https://doi.org/10.1016/j.jvolgeores.2015.08.022> (2015).
24. Carn, S. A., Fioletov, V. E., McLinden, C. A., Li, C. & Krotkov, N. A. A decade of global volcanic SO₂ emissions measured from space. *Sci. Reports* **7**, 1–12, <https://doi.org/10.1038/srep44095> (2017).
25. Németh, K. & Cronin, S. J. Drivers of explosivity and elevated hazard in basaltic fissure eruptions: The 1913 eruption of Ambrym Volcano, Vanuatu (SW-Pacific). *J. Volcanol. Geotherm. Res.* **201**, 194–209, <https://doi.org/10.1016/j.jvolgeores.2010.12.007> (2011).
26. Firth, C., Handley, H., Turner, S., Cronin, S. & Smith, I. Variable conditions of magma storage and differentiation with links to eruption style at Ambrym volcano, Vanuatu. *J. Petrol.* **57**, 1049–1072, <https://doi.org/10.1093/petrology/egw029> (2016).
27. Hamling, I. J., Cevuard, S. & Garaebiti, E. Large scale drainage of a complex magmatic system: Observations from the 2018 eruption of Ambrym volcano, Vanuatu. *Geophys. Res. Lett.* (2019).
28. Newton, A. *Ocean-transported pumice in the North Atlantic*. Ph.D. thesis, University of Edinburgh (2000).
29. Kueppers, U., Nichols, A. R., Zanon, V., Potuzak, M. & Pacheco, J. M. Lava balloons-peculiar products of basaltic submarine eruptions. *Bull. Volcanol.* **74**, 1379–1393, <https://doi.org/10.1007/s00445-012-0597-x> (2012).
30. Rivalta, E. & Segall, P. Magma compressibility and the missing source for some dike intrusions. *Geophys. Res. Lett.* **35**, 0–4, <https://doi.org/10.1029/2007GL032521> (2008).
31. Institut de Physique du Globe de Paris and Ecole et Observatoire des Sciences de la Terre de Strasbourg (EOST), GEOSCOPE - French Global Network of broadband seismic stations, 10.18715/GEOSCOPE.G (1982).
32. Shuler, A., Ekström, G. & Nettles, M. Physical mechanisms for vertical-CLVD earthquakes at active volcanoes. *J. Geophys. Res. Solid Earth* **118**, 1569–1586, <https://doi.org/10.1002/jgrb.50131> (2013).
33. Dvorak, J. J. & Okamura, A. T. A hydraulic model to explain variations in summit tilt rate at Kilauea and Mauna Loa volcanoes. *US Geol. Surv. Prof. Pap* **1350**, 1281–1296 (1987).
34. Baker, S. & Amelung, F. Top-down inflation and deflation at the summit of Kilauea Volcano, Hawai'i observed with InSAR. *J. Geophys. Res.* **117**, 1–14, <https://doi.org/10.1029/2011JB009123> (2012).
35. Neal, C. A. *et al.* The 2018 rift eruption and summit collapse of Kilauea Volcano. *Science* **7046**, 1–14, <https://doi.org/10.1126/science.aav7046> (2018).
36. Gudmundsson, M. T. *et al.* Gradual caldera collapse at Bárðarbunga volcano, Iceland, regulated by lateral magma outflow. *Science* **353**, aaf8988 (2016).
37. Buck, W. R., Einarsson, P. & Brandsdóttir, B. Tectonic stress and magma chamber size as controls on dike propagation: Constraints from the 1975–1984 Krafla rifting episode. *J. Geophys. Res. Solid Earth* **111**, 1–15, <https://doi.org/10.1029/2005JB003879> (2006).
38. Pollard, D. D., Delaney, P. T., Duffield, W. A., Endo, E. T. & Okamura, A. T. Surface deformation in volcanic rift zones. *Tectonophysics* **94**, 541–584, <https://doi.org/10.1016/B978-0-444-42198-2.50036-5> (1983).
39. Rubin, A. M. & Pollard, D. D. Origin of blade-like dikes in volcanic rift zones. In Decker, R., Wright, T. & Stauffer, P. (eds.) *Volcanism in Hawaii* Professional Paper, 1449–1470, 1350 edn (U.S. Geol. Surv., 1987).
40. Grandin, R. *et al.* Thickness control of lateral dyke intrusion at mid-ocean ridges. *Earth Planet. Sci. Lett.* **319–320**, 83–95, <https://doi.org/10.1016/j.epsl.2011.12.011> (2012).
41. Rubin, A. M. A comparison of rift-zone tectonics in Iceland and Hawaii. *Bull. Volcanol.* **52**, 302–319 (1990).
42. Komorowski, J.-C. *et al.* The January 2002 flank eruption of Nyiragongo volcano (DRC): chronology, evidence for a tectonic rift trigger, and impact of lava flows on the city of Goma. *Acta Vulcanologica* **14/15**, 27–62 (2004).
43. Wauthier, C., Cayol, V., Kervyn, F. & d'Oreye, N. Magma sources involved in the 2002 Nyiragongo eruption, as inferred from an InSAR analysis. *J. Geophys. Res. Solid Earth* **117** (2012).
44. Cervelli, P. *et al.* The 12 September 1999 Upper East Rift Zone dike intrusion at Kilauea Volcano, Hawaii. *J. Geophys. Res. Solid Earth* **107**, 1–13, <https://doi.org/10.1029/2001jb000602> (2002).
45. Grandin, R. *et al.* September 2005 Manda hararo-dabbahu rifting event, Afar (Ethiopia): Constraints provided by geodetic data. *J. Geophys. Res. Solid Earth* **114**, <https://doi.org/10.1029/2008JB005843> (2009).
46. Nakamura, K. Volcanoes as possible indicators of tectonic stress orientation - principle and proposal. *J. Volcanol. Geotherm. Res.* **2**, 1–16, <https://doi.org/10.1007/BF02199968> (1977).
47. Taylor, F. W., Isacks, B. L., Jouannic, C., Bloom, A. L. & Dubois, J. Coseismic and Quaternary vertical tectonic movements, Santo and Malekula Islands, New Hebrides Island Arc. *J. Geophys. Res.* **85**, 5367–5381, <https://doi.org/10.1029/JB085iB10p05367> (1980).
48. Collot, J., Daniel, J. & Burne, R. Recent tectonics associated with the subduction/collision of the d'Entrecasteaux zone in the central new hebrides. *Tectonophysics* **112**, 325–356, [https://doi.org/10.1016/0040-1951\(85\)90185-4](https://doi.org/10.1016/0040-1951(85)90185-4) (1985).
49. Louat, R. & Pelletier, B. Seismotectonics and present-day relative plate motions in the Tonga-Lau and Kermadec-Havre region. *Tectonophysics* **165**, 237–250, [https://doi.org/10.1016/0040-1951\(89\)90049-8](https://doi.org/10.1016/0040-1951(89)90049-8) (1989).
50. Pelletier, B., Meschede, M., Chabernaud, T., Roperch, P. & Zhao, X. Tectonics of the Central New Hebrides Arc, North Aoba Basin. *Proceedings of the Ocean Drilling Program, 134 Scientific Results* **134**, 431–444, <https://doi.org/10.2973/odp.proc.sr.134.023.1994> (1994).
51. Taylor, F. W. *et al.* Geodetic measurements of convergence at the New Hebrides island arc indicate arc fragmentation caused by an impinging aseismic ridge. *Geology* **23**, 1011–1014, <https://doi.org/10.1130/0091-7613> (1995).
52. Lagabriele, Y., Pelletier, B., Cabioch, G., Regnier, M. & Calmant, S. Coseismic and long-term vertical displacement due to back arc shortening, central Vanuatu: Offshore and onshore data following the Mw 7.5, 26 November 1999 Ambrym earthquake. *J. Geophys. Res.* **108**, 2519, <https://doi.org/10.1029/2002JB002083> (2003).
53. Regnier, M., Calmant, S., Pelletier, B., Lagabriele, Y. & Cabioch, G. The M_w 7.5 1999 Ambrym earthquake, Vanuatu: A back arc intraplate thrust event. *Tectonics* **22**, 1–11, <https://doi.org/10.1029/2002TC001422> (2003).
54. Roman, D. C. & Heron, P. Effect of regional tectonic setting on local fault response to episodes of volcanic activity. *Geophys. Res. Lett.* **34**, 1–5, <https://doi.org/10.1029/2007GL030222> (2007).
55. Ueda, H. *et al.* Magma intrusion and discharge process at the initial stage of the 2000 activity of Miyakejima, Central Japan, inferred from tilt and GPS data. *Geophys. J. Int.* **161**, 891–906, <https://doi.org/10.1111/j.1365-246X.2005.02602.x> (2005).
56. Bagnardi, M. & Amelung, F. Space-geodetic evidence for multiple magma reservoirs and subvolcanic lateral intrusions at Fernandina Volcano, Galápagos Islands. *J. Geophys. Res. B: Solid Earth* **117**, 1–19, <https://doi.org/10.1029/2012JB009465> (2012).

57. Munro, D. C. & Rowland, S. K. Caldera morphology in the western Galápagos and implications for volcano eruptive behavior and mechanisms of caldera formation. *J. Volcanol. Geotherm. Res.* **72**, 85–100. [https://doi.org/10.1016/0377-0273\(95\)00076-3](https://doi.org/10.1016/0377-0273(95)00076-3) (1996).
58. Wright, R., Flynn, L., Garbeil, H., Harris, A. & Pilger, E. Automated volcanic eruption detection using MODIS. *Remote. sensing environment* **82**, 135–155 (2002).
59. Prata, A. & Kerkmann, J. Simultaneous retrieval of volcanic ash and SO₂ using MSG-SEVIRI measurements. *Geophys. Res. Lett.* **34** (2007).
60. Rosen, P. A., Gurrrola, E., Sacco, G. F. & Zebker, H. The InSAR scientific computing environment. In *EUSAR 2012; 9th European Conference on Synthetic Aperture Radar*, 730–733 (2012).
61. Sandwell, D., Mellors, R., Tong, X., Wei, M. & Wessel, P. Open radar interferometry software for mapping surface deformation. *Eos, Transactions Am. Geophys. Union* **92**, 234–234 (2011).
62. Doin, M.-P. *et al.* Presentation of the small baseline NSBAS processing chain on a case example: the Etna deformation monitoring from 2003 to 2010 using Envisat data. In *Proceedings of the ESA'Fringe 2011 Workshop, Frascati, Italy*, (19–23 September 2011), 19–23 (2011).
63. Wessel, B. TanDEM-X Ground Segment - DEM Products Specification Document. Tech. Rep. 3.1, EOC, DLR, Oberpfaffenhofen, Germany, <https://doi.org/10.1002/hyp.3360050103> (2016).
64. Rosen, P. A., Hensley, S., Peltzer, G. & Simons, M. Updated Repeat Orbit Interferometry Package Released. *Eos* **85**, 47 (2004).
65. Grandin, R. Long-term growth of the Himalaya inferred from interseismic InSAR measurement. *Geology* **40**(12), 1059–1062 (2012).
66. Tarantola, A. & Valette, B. Generalized nonlinear inverse problems solved using the least squares criterion. *Rev. Geophys.* **20**, 219–232 (1982).
67. Okada, Y. Surface Deformation Due to Shear and Tensile Faults in a Half-Space. *Bull. Seismol. Soc. Am.* **75**, 1135–1154. [https://doi.org/10.1016/0148-9062\(86\)90674-1](https://doi.org/10.1016/0148-9062(86)90674-1) (1985).
68. Mogi, K. Relations between the eruptions of various volcanoes and the deformations of the ground surfaces around them. *Bull. Earthquake Res. Inst.* **36**, 99–134 (1958).
69. Jolivet, R., Simons, M., Agram, P. S., Duputel, Z. & Shen, Z. K. Aseismic slip and seismogenic coupling along the central San Andreas Fault. *Geophysical Research Letters* **42**(2), 297–306 (2015).
70. Berardino, P., Fornaro, G., Lanari, R. & Sansosti, E. A new algorithm for surface deformation monitoring based on small baseline differential SAR interferograms. *IEEE Transactions on Geosci. Remote. Sens.* **40**, 2375–2383. <https://doi.org/10.1109/TGRS.2002.803792> (2002).
71. Pelletier, B., Calmant, S. & Pillet, R. Current tectonics of the Tonga-New Hebrides region. *Earth Planet. Sci. Lett.* **164**, 263–276. [https://doi.org/10.1016/S0012-821X\(04\)00049-4](https://doi.org/10.1016/S0012-821X(04)00049-4) (1998).
72. Bergeot, N. *et al.* Horizontal and vertical interseismic velocity fields in the Vanuatu subduction zone from GPS measurements: Evidence for a central Vanuatu locked zone. *J. Geophys. Res. Solid Earth* **114** (2009).

Acknowledgements

Photo in Fig. 2e courtesy of John Tasso, Vanuatu Island Experience, <http://vanuatuilandexperience.com/guides/>. Nial Peters is thanked for sharing photos taken in the field. We thank Noel Naki and the Department of Lands and Survey of Vanuatu for their help during fieldwork. We thank Valérie Cayol, Virginie Pinel, Delphine Smittarello, Eleonora Rivalta and Matt Pritchard for fruitful discussions. We thank Romain Jolivet for sharing the CSI software, available on github (<https://github.com/jolivetr/csi>). Several calculations used the S-CAPAD cluster of IPGP. We are grateful to the providers of data for this study. We thank the European Space Agency for rapid tasking of Sentinel-1 satellite in response to the event. Project carried out using CSK® Products, ©ASI (Italian Space Agency), delivered under an ASI license to use under project No. 702. We also thank the Japanese Space Agency (JAXA 6th Research Agreement No. 3245) for providing access to radar imagery used in this study. We thank Planet for their cubesat data via Planet's Education and Research Program. We thank the AERIS/ICARE Data and Services Center for providing access to the Himawari-8 data used in this study. M.B. and N.H. acknowledge support from the French National Research Agency (ANR) for funding the VOLCPLUME project (ANR-15-CE04-0003-01). Y.M. acknowledges support from the National Geographic grant number CP-122R-17 (Trail by Fire II—Closing the Ring project) and from IRD. We thank the CNES for the funding of geodesy work in Vanuatu through the TOSCA program “GEOV”. We thank Université Nice Sophia Antipolis for funding the bathymetry processing through the CSI program “ARCHI-BATH”. This project has also received funding from the European Union's Horizon 2020 research and innovation programme under the Marie Skłodowska-Curie grant agreement No 665850. This is IPGP contribution number 4081. We thank both Karoly Nemeth and a second anonymous reviewer for their helpful comments.

Author contributions

T.S. processed the InSAR data, produced the geodetic models and contributed to writing. R.G. supervised the geodetic analysis and coordinated writing of the manuscript. M.B. supervised the thermal and gas data processing and contributed to writing. E.G. supervised the seismic analysis. Y.M. contributed field observations and collected and analyzed petrological data. V.B. processed the GPS data. F.L. processed the bathymetric data. M.V. processed the Geoscope seismic analysis. F.D. contributed to the InSAR data processing. N.H. contributed to the Himawari-8 data processing. D.T. contributed to fieldwork. S.C. and P.L. contributed to seismic analysis. B.P. conducted fieldwork, analyzed coastal uplift and contributed to writing.

Competing interests

The authors declare no competing interests.

Additional information

Supplementary information is available for this paper at <https://doi.org/10.1038/s41598-019-55141-7>.

Correspondence and requests for materials should be addressed to T.S. or R.G.

Reprints and permissions information is available at www.nature.com/reprints.

Publisher's note Springer Nature remains neutral with regard to jurisdictional claims in published maps and institutional affiliations.



Open Access This article is licensed under a Creative Commons Attribution 4.0 International License, which permits use, sharing, adaptation, distribution and reproduction in any medium or format, as long as you give appropriate credit to the original author(s) and the source, provide a link to the Creative Commons license, and indicate if changes were made. The images or other third party material in this article are included in the article's Creative Commons license, unless indicated otherwise in a credit line to the material. If material is not included in the article's Creative Commons license and your intended use is not permitted by statutory regulation or exceeds the permitted use, you will need to obtain permission directly from the copyright holder. To view a copy of this license, visit <http://creativecommons.org/licenses/by/4.0/>.

© The Author(s) 2019

1 **From prodigious volcanic degassing to caldera**
2 **subsidence and quiescence at Ambrym (Vanuatu):**
3 **the influence of regional tectonics- Supplementary**
4 **Information**

5 **Tara Shreve^{a,*}, Raphaël Grandin^{a,*}, Marie Boichu^{b,c}, Esline Garaebiti^d, Yves**
6 **Moussallam^{e,f}, Valérie Ballu^g, Francisco Delgado^a, Frédérique Leclerc^h, Martin Vallée^a,**
7 **Nicolas Henriot^b, Sandrine Cevuard^d, Dan Tari^d, Pierre Lebellegardⁱ, and Bernard**
8 **Pelletierⁱ**

9 ^aUniversité de Paris, Institut de physique du globe de Paris, CNRS, F-75005 Paris, France

10 ^bUniv. Lille, UMR 8518 - LOA - Laboratoire d'Optique Atmosphérique, F-59000 Lille, France

11 ^cCNRS, UMR 8518, F-59000 Lille, France

12 ^dVanuatu Meteorology and Geohazards Department (VMGD), Port Vila, Vanuatu

13 ^eLaboratoire Magmas et Volcans (LMV), Université Clermont Auvergne, 63170, France

14 ^fLamont-Doherty Earth Observatory, Columbia University, New York, USA

15 ^gLaboratoire Littoral Environnement et Sociétés (LIENSs), Université de La Rochelle, 17000, France

16 ^hGéoazur, Univ. Nice Sophia Antipolis (Univ. Côte d'Azur, CNRS, IRD, Observatoire de la Côte d'Azur), Géoazur

17 UMR 7329, 250 rue Albert Einstein, Sophia Antipolis 06560 Valbonne, France.

18 ⁱGéoazur, Institut de recherche pour le développement, Nouméa, 98800, Nouvelle-Calédonie

19 *shreve@ipgp.fr; grandin@ipgp.fr

Supplementary Methods

InSAR processing

MPD uses the interferogram's coherence, calculated in the previous filtering step, to optimize the unwrapping path. It begins unwrapping the phase at a seed pixel that is above a coherence threshold. MPD will slightly decrease the coherence threshold at each iteration, and will continue the phase unwrapping with nearby pixels that have a coherence above this new threshold. Pixels with coherence beneath a minimum threshold will not be unwrapped. Bridges defined manually are used to connect fringes that are determined to be continuous, but which pass through incoherent regions. Unwrapping errors that could not be corrected with bridges are shifted manually by adding integer multiples of 2π . Each pixel in the unwrapped interferogram has an iteration number, which represents a proxy for coherence and phase reliability. This value is used to mask the interferograms after the unwrapping is completed.

Geodetic Modeling

Inversion procedure

The Classic Slip Inversion (CSI) software is used to setup the forward problem¹. Before performing the least squares inversion, the synthetic deformation from the Mogi source is removed from interferograms spanning the rift zone intrusion and caldera subsidence, and the synthetic deformation from the non-linear inversion is used to shift the phase values of the spatially disconnected islands by an appropriate integer multiple of 2π .

Datasets are downsampled by a distance-based averaging, with a denser spacing in the region of high gradients in the deformation field, and coarser spacing in regions with less deformation (i.e. in the far-field)¹. We define a starting and minimum block size ($S_{block,start}$ and $S_{block,min}$), a characteristic distance D_{char} , and an exponent α (≥ 1), such that the block is divided into four smaller blocks if the following condition is met:

$$D_{block} - D_{char} < S_{block}^{\alpha}, \quad (1)$$

where D_{block} is the current distance from the source and S_{block} is the current block size. After downsampling, the size of the decimated data vector is between 200 and 1000 points per image.

The data covariance matrix for each interferogram is created by calculating the covariogram from 5000 random samples in a region where no deformation is measured, after removing a phase ramp. The covariogram, γ_h , is calculated from data binned every 0.5 km for InSAR measurements and every 0.2 km for pixel offsets, and is fit by an exponential of the form $\gamma_h = \gamma_0 - (\sigma_d^2) \cdot \exp(-\frac{x}{\lambda_d})$, where x is the distance between two points. This allows for empirically estimating the values of γ_0 , σ_d and λ_d . The covariance matrix, $C_d(i, j)$, is populated according to:

$$C_d(i, j) = \sigma_d^2 \exp(-\frac{D}{\lambda_d}), \quad (2)$$

where D is the distance between the elements in the matrix.

We assume the same dike geometry for both the intra-caldera dike and the extra-caldera rift intrusion, because the ALOS-2 ascending and CSK descending datasets span the emplacement of both the intra-caldera and extra-caldera dikes. Within the caldera, the westernmost portion of the dike has a dip of 40° , and becomes progressively more vertical to the east, with a final dip of 70° along the rift zone intrusion (See Fig. 4). The patches are 1.7 km wide along-dip and 1.17 km long along-strike.

The model covariance matrix controls the roughness of the model, and is defined as²:

$$C_m(i, j) = \frac{\sigma_m \lambda_0^2}{\lambda_m} \exp(-\frac{\|i, j\|_2}{\lambda_m}), \quad (3)$$

where i and j are two distinct patches, σ_m is the correlation amplitude, λ_0 is a normalizing distance, λ_m is the correlation length, and $\|i, j\|_2$ is the distance between patches i and j . We fix λ_0 to 4 km, and in order to find optimal values for the correlation length λ_m and amplitude σ_m , we plot an L-curve of maximum slip vs. misfit for various values of λ_m and σ_m (Fig. S5). The constrained least squares inversion utilizes a Sequential Least Squares Programming algorithm from the python package SciPy to invert for opening on each of the patches. We constrain the opening along the dike to the positive, and we do not allow for slip. A planar ramp is also fit and removed from the data.

59 **Temporal evolution of post-intrusion subsidence**

60 We determine \bar{u}_k and \bar{u}_{model} by finding the average velocities within a 30x30 pixel box in the southern portion of the caldera
61 (168.144324/168.168324/-16.284603/-16.260603). After exploring several different locations inside and outside the caldera,
62 the scalar calculated in this location explains the most data variance. Several Sentinel-1 interferograms and their residuals
63 ($u_{res} = u_k - (u_{model} * \gamma_k)$) are shown in Fig. S7. All final scalars are shown in Tab. S3.

64 **GPS data**

65 The GPS displacement vector in ULEI is obtained by comparison of a series of measurements conducted before (15–16 July
66 2018) and after (04–09 February 2019) the volcanic event. The ground marker is sealed in a concrete basement and has been
67 installed in 1999 following the 26 November 1999 M_w 7.5 Ambrym earthquake. This point belongs to the Vanuatu geodetic
68 network and is remeasured periodically as part of a long-term post-seismic deformation study. Data have been collected using a
69 dual frequency Topcon GB1000 receiver and a Topcon PG_A1 with ground-plane antenna installed on a mast of known height
70 above the ground marker. We calculated daily positions in the ITRF2014 reference frame with a IPPP strategy (Precise Point
71 Positioning with Integer ambiguity fixing) using the processing software GINS developed at CNES/GRGS³, with GRG orbits
72 and clocks products and IGS igs14.atx file for antenna calibration. Wet tropospheric delays are estimated every two hours based
73 on VMF1 global mapping functions⁴ and GPT2 empirical slant delay model GPT2⁵.

74 **Bathymetric data**

75 Bathymetric data were acquired from 8–22 December 2003 during the Terralis cruise (PI: B. Pelletier) on board R/V Alis (IRD),
76 using the multibeam echo sounder (MBES) SIMRAD EM1002 (Kongsberg). This MBES is designed to acquire high-resolution
77 data of coastal areas down to a depth of 1000 m, operating with a frequency of 93 kHz. Acoustic signal duration is shorter than
78 2 ms, inducing a vertical accuracy of the seafloor measurements ≤ 8 cm. The MBES consists of 111 beams ($2^\circ \times 2^\circ$ beamwidth)
79 that are distributed over an angular coverage of 150° across track, as to acquire seafloor measurements equidistant transversally
80 (every 6 or 20 m for a seafloor at 100 of 300 mbsl respectively). Data were acquired at a vessel speed < 8 knots inducing an
81 along-track inter-ping distance of a few meters at 100 m water-depth and ~ 9 m at 1000 m water-depth. The GPS system was
82 however able to provide position with an absolute horizontal accuracy of only 10–15 m.

83 Bathymetric data were processed using the CARAIBES and SONARSCOPE softwares (©IFREMER). The processing
84 consisted mainly in the correction of the navigation when artefacts were present, and in the automatic and manual filtering of
85 the bathymetric data. These data were merged into a Digital Elevation Model gridded at 25 m/pixel in a WGS84 geographic
86 reference system. They are represented in Figure 3a.

Himawari-8 – Thermal index

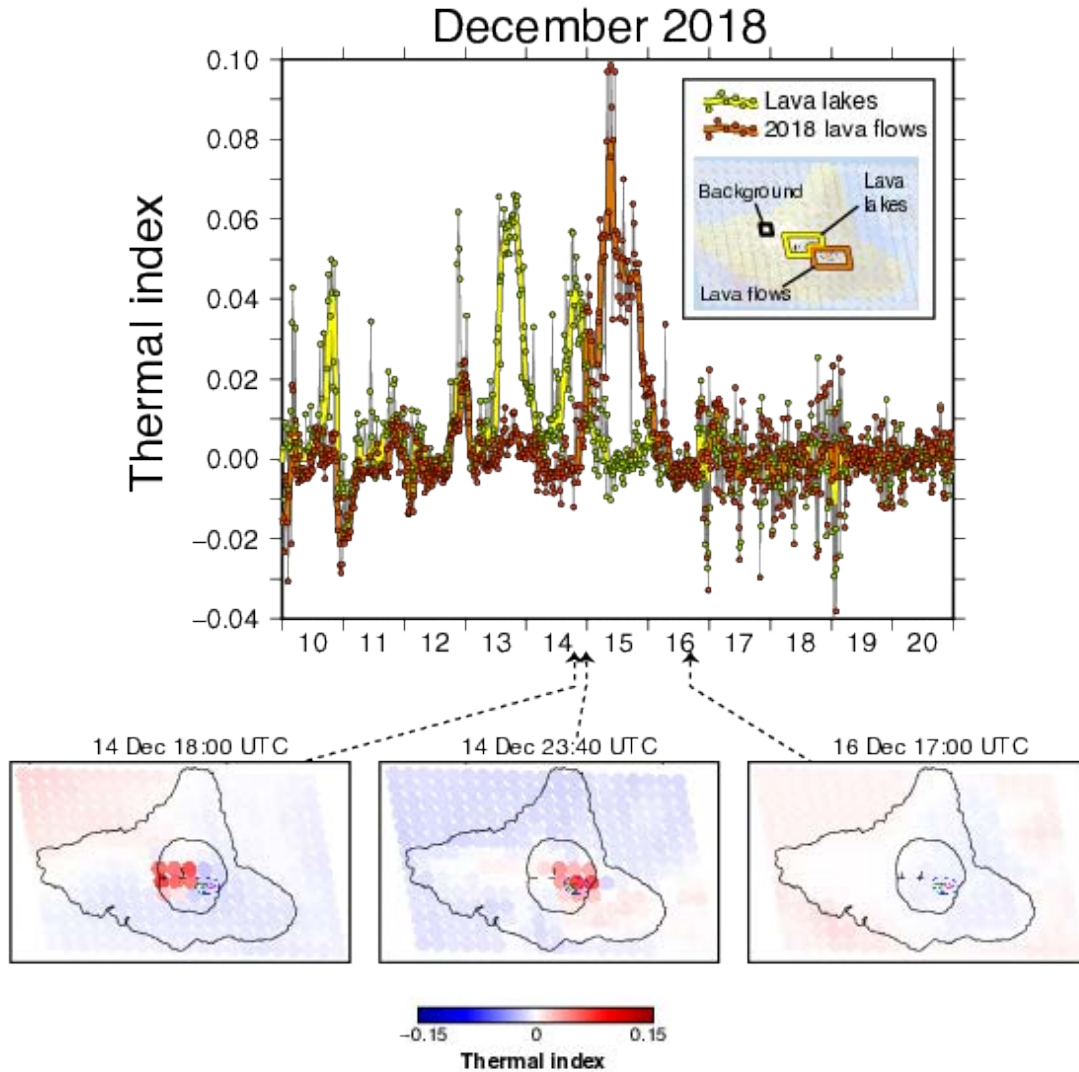
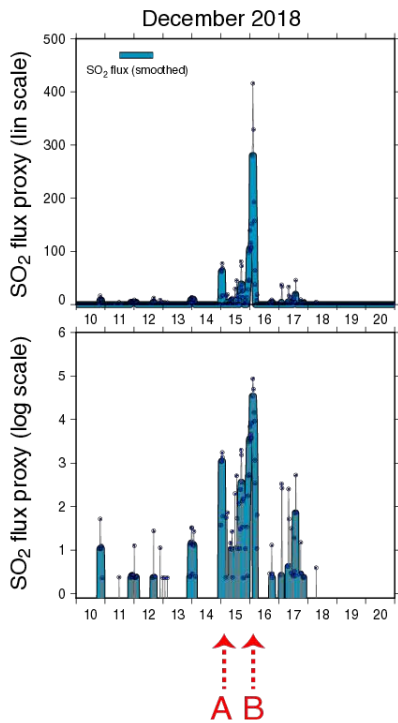


Figure S1. Time series of thermal index at Ambrym from geostationary Himawari-8 imagery. Upper panel: time series of the normalized thermal index⁶ retrieved for Himawari-8 pixels corresponding to the lava lakes (yellow) and the 2018 intra-caldera lava flows (orange). Map in the inset shows the pixels used for the definition of these two locations. Color circles represent the thermal index with respect to a reference background pixel (shown in black in inset) derived from individual images acquired every 20 minutes. Thick color lines represent the smoothed time series after applying a median filter over 10 points (i.e. filter width: 200 minutes). Lower panel: maps of normalized thermal index at three different times corresponding to (a) lava lake activity prior to the 2018 eruption, (b) onset of the eruption and (c) lack of thermal anomaly after the end of the eruption. Himawari-8 imagery provided by AERIS/ICARE Data and Service Center and Japan Meteorological Agency. Maps were generated with GMT version 5.4.3 (<http://gmt.soest.hawaii.edu>) and edited in Adobe Illustrator version 16.0.4 (<https://www.adobe.com/products/illustrator.html>).

a Himawari-8 – SO₂ flux



b

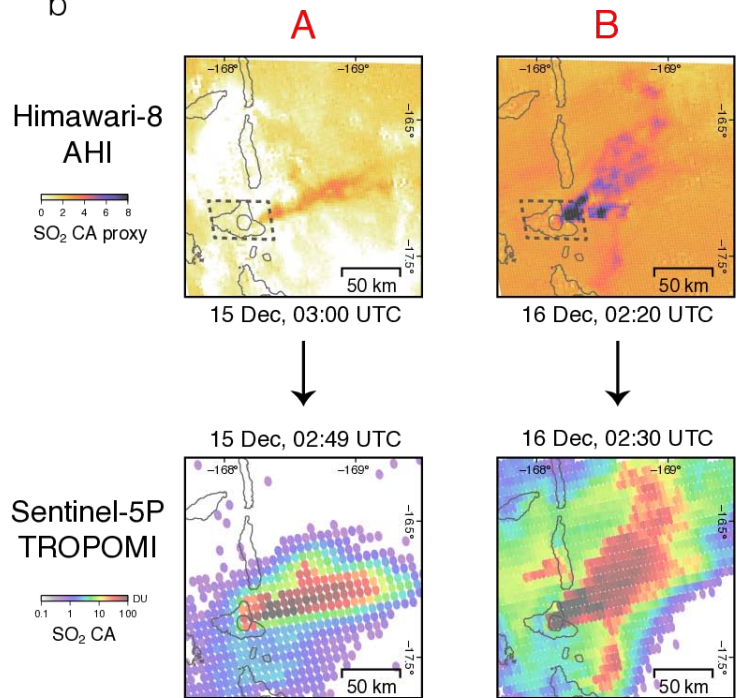


Figure S2. **a.** Upper panel: time series of SO₂ flux proxy at Ambrym from geostationary Himawari-8 imagery. Blue dots show the SO₂ flux proxy calculated from each acquisition, at 20 minutes interval. Thick blue curve is the filtered time series. Y-axis scaling is linear. Lower panel: same as upper panel, with a logarithmic scaling on the Y-axis. **b.** Comparison of SO₂ maps derived from Himawari-8 (this study) and Sentinel-5P TROPOMI acquired at approximately the same time. A: 15 December 2018, 03h00 UTC (Himawari-8), 02h49 (TROPOMI). B: 16 December, 02h20 UTC (Himawari-8), 02h30 (TROPOMI). Grey dashed box shows the area used for calculating the SO₂ flux proxy. Himawari-8 imagery provided by AERIS/ICARE Data and Service Center and Japan Meteorological Agency.

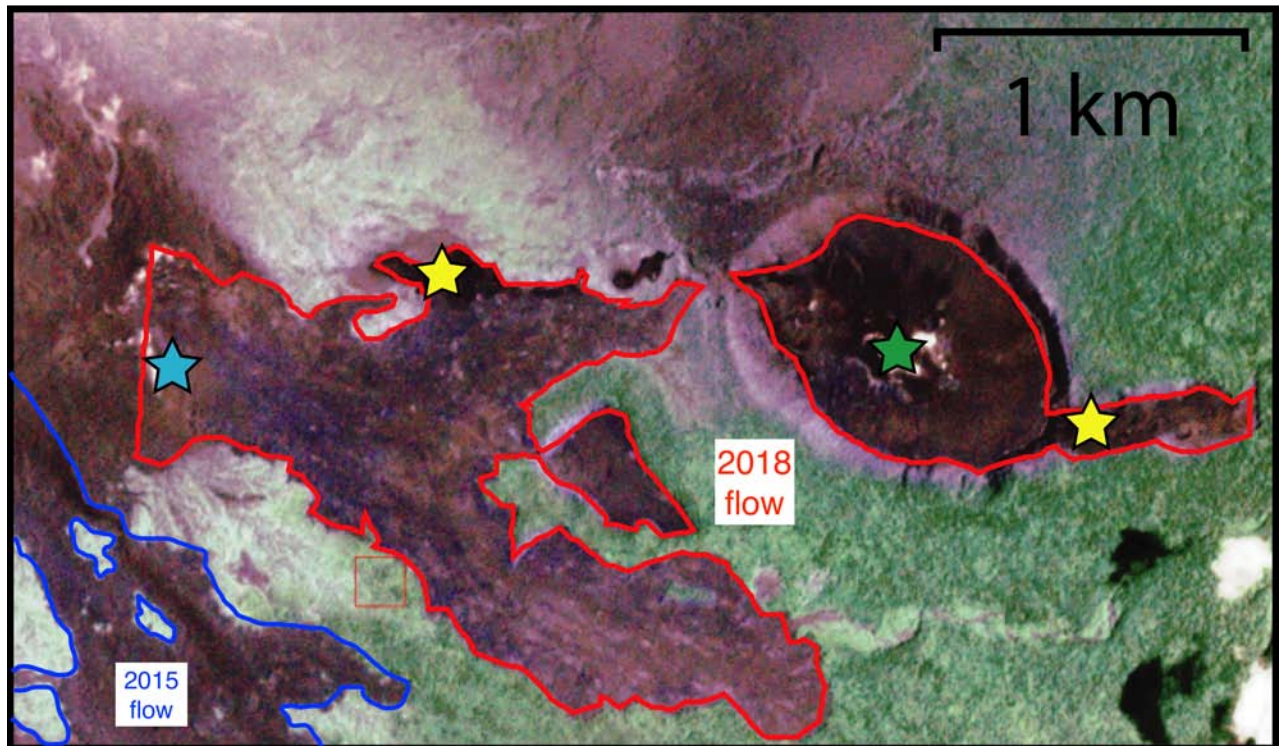


Figure S3. Planet Labs optical image, acquired on January 31, 2019. The full extent of the intra-caldera lava flow is outlined in red. The blue and green stars correspond, respectively, to the sources of lava fountaining and degassing visible in Fig. 2e in the text. Yellow stars mark the location of thermal anomalies noticed in the Sentinel-2 image acquired at 23h10 on 15 December (Fig. 2d), possibly indicating the secondary vents. Optical imagery obtained from Planet Labs (<https://api.planet.com>)⁷. Map created with ENVI Classic version 5.5.1 (<https://www.harris.com/solution/envi>).

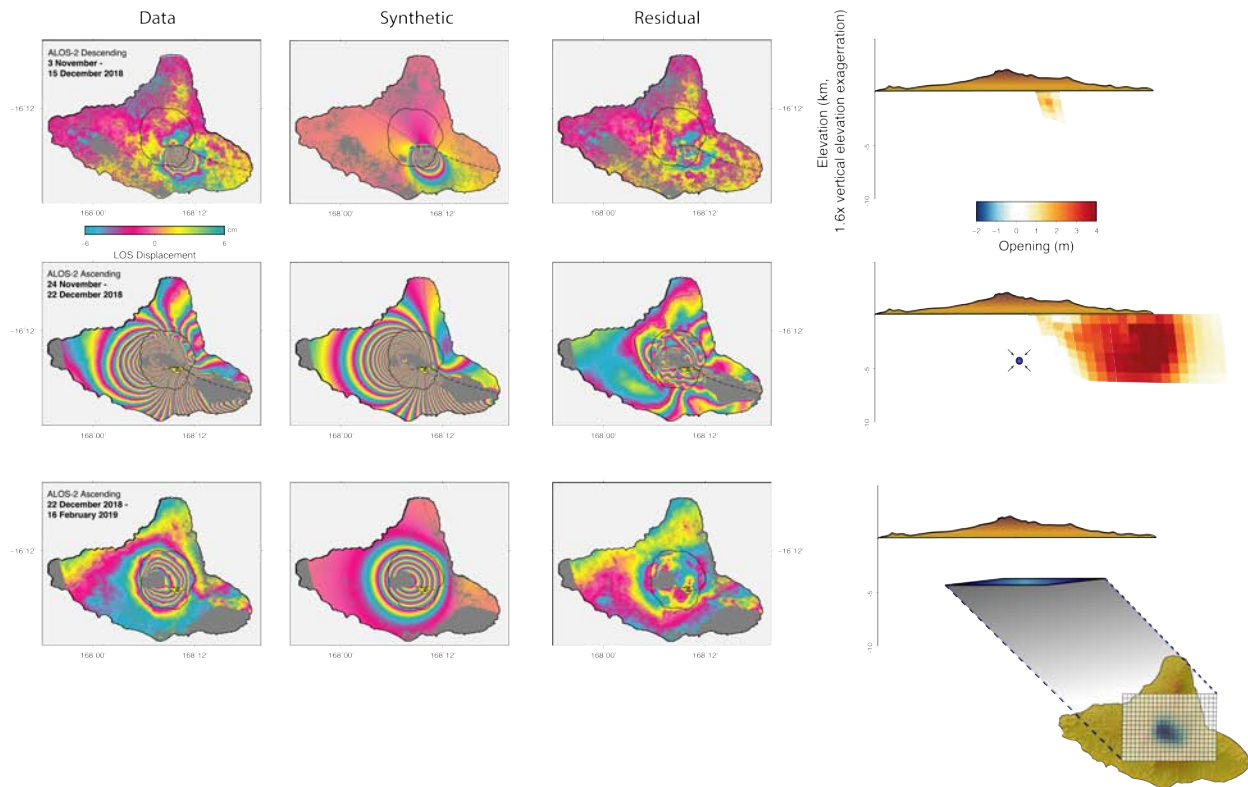


Figure S4. Wrapped data, model, and residuals. The first three columns correspond, respectively, to the data, model, and residual of interferograms displayed in Fig. 4 in the text, wrapped such that one fringe = 12.12 cm (ALOS-2 fringe rate). For all three rows, the model is derived from a distributed opening constrained least square's inversion, as outlined in the supplementary text. The opening distribution is shown in the fourth column. First row: data, model, and residual for a single interferogram used to invert for opening of the initial, intra-caldera dike intrusion feeding the effusive eruptions. We fix the dike geometry (See Fig. 4 in text) to be the same for both this inversion and the rift zone intrusion. Second row: data, model, and residual for the most coherent of the four datasets used to invert for the rift zone intrusion and caldera subsidence (see Table S1). Remaining residuals may be related to oversimplified geometry of the decompressing source (Mogi, fixed at a depth of 4.5 km), as well as the fact that the near field (<2 km) signal along the dike was masked, and therefore not fit by the inversion. Third row: data, model, and residual for one of three datasets (see Table S1) used to invert for exponentially decaying subsidence lasting more than 2 months after the rift zone intrusion. The horizontal sill is fixed at a depth of 4.1 km.

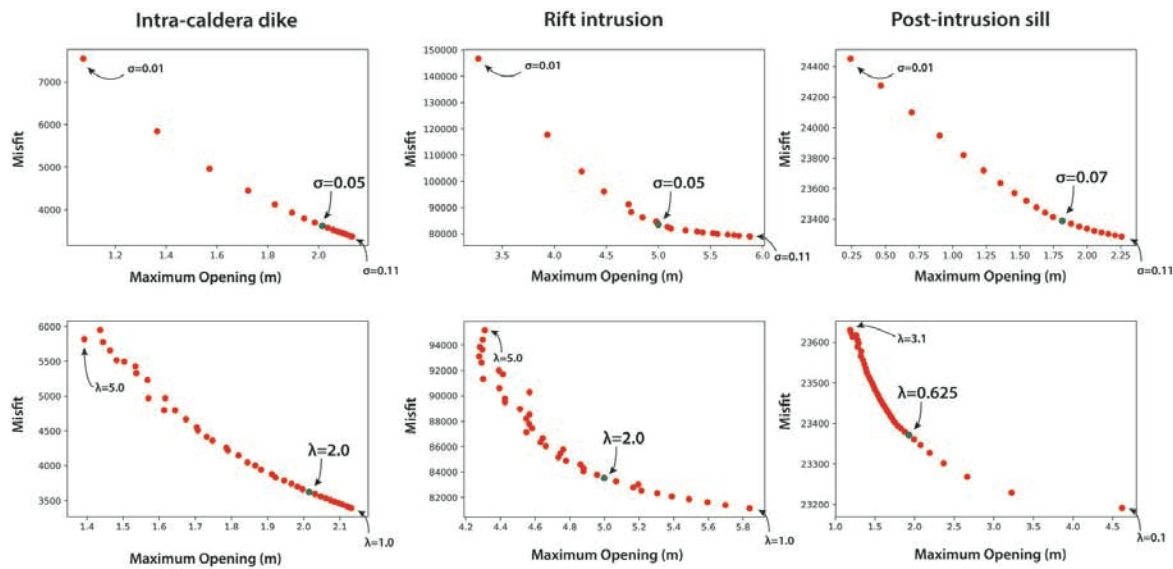


Figure S5. L-curve analysis for model smoothing parameters. To find the optimal amplitude of correlation (σ) and correlation distance (λ) for the model smoothing parameters, we iterate through a range of σ and λ values, and plot the model misfit vs. maximum opening. The maximum opening acts as a proxy for the model roughness, with a larger opening corresponding to a rougher model (smaller λ or larger σ). We initially run the iteration of σ with a fixed value of λ (2 for the dike intrusions, 0.8 for the sill), and then subsequently iterate for λ given the optimal values for σ . To remain consistent between the intra-caldera dike and rift zone intrusion, we choose the same σ and λ for both of these inversions.

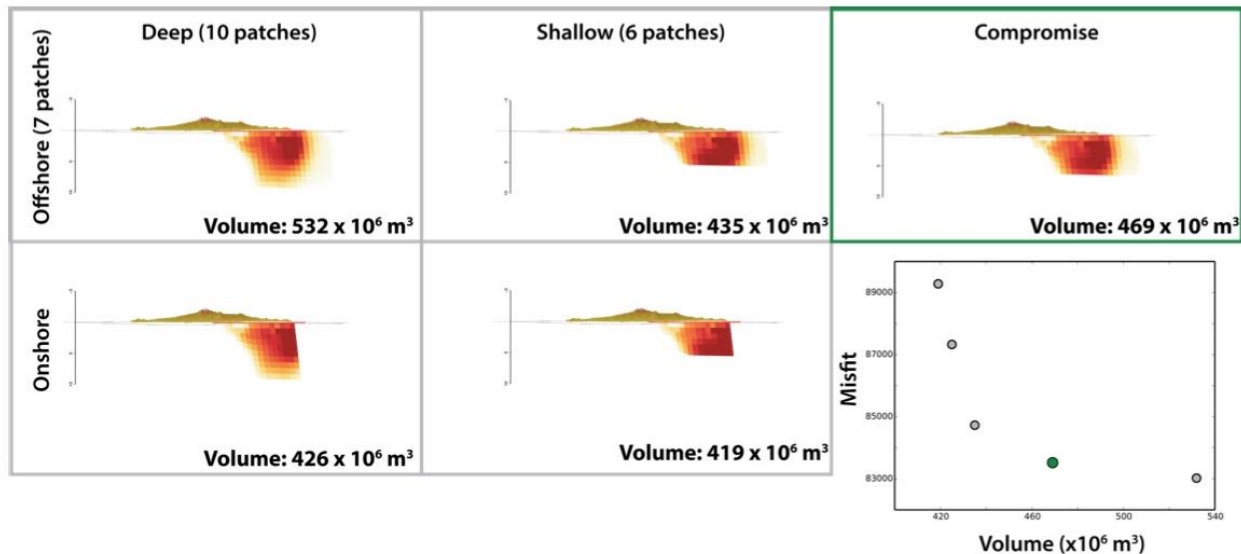


Figure S6. End-member distributed opening models. Four end-member models, resulting from the constrained least square's inversion of distribution opening, showing the uncertainty of volume estimates, ranging from 419 to 532 x 10⁶ m³. Total volume depends on the final model depth and extent offshore. Based on the misfit of these end-members, a compromise is found with the dike extending offshore ~6 km and to a depth of ~6 km.

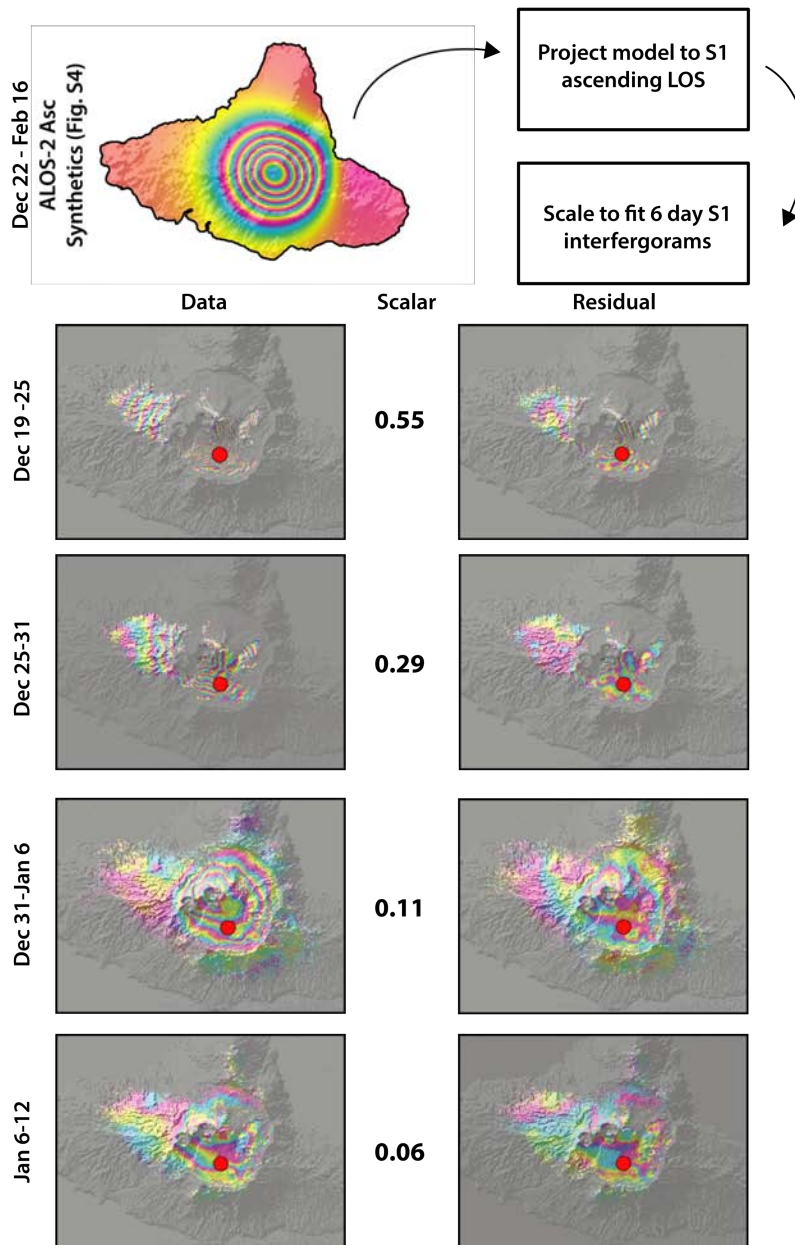


Figure S7. Temporal evolution of post-intrusion subsidence from Sentinel-1 interferograms. Synthetic deformation of a sill model, derived from the inversion of CSK pixel offsets and an ALOS-2 interferogram (22 Dec 2018 – 16 Feb 2019) that is coherent across the entire island, is scaled to fit the displacement field in Sentinel-1 6-day interferometric pairs, in order to investigate the temporal evolution of post-intrusion caldera subsidence. The lack of coherence in the S1 interferograms precluded a standard time series inversion. Instead, a scaling constant is determined for all 15 interferograms spanning 19 Dec – 18 Jan 2019 (assuming the source geometry has not changed), and the sill model volume ($85 \times 10^6 \text{ m}^3$) is scaled accordingly for each interferogram. Refer to the supplementary text for more detail.

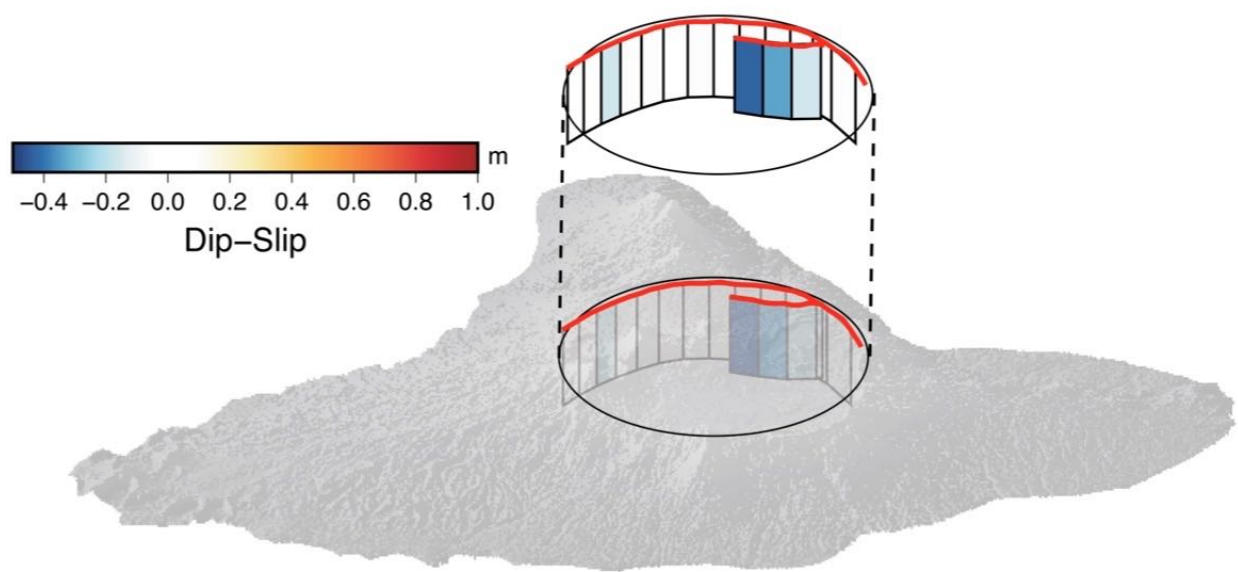


Figure S8. Caldera ring faulting. We model the dip-slip component of caldera ring faulting using the distributed opening constrained least squares inversion described in the supplementary text. The strike of these faults was obtained by mapping fringe discontinuities in the 24 Nov – 22 Dec 2018 ALOS-2 ascending interferogram. Vertical fault patches extend to 2 km depth and have a length of 1.04 km along-strike for the outer caldera fault, and 1.17 km along-strike for the inner caldera fault. The model finds a maximum dip-slip (normal faulting) of -0.4 m along the inner caldera fault in the NE portion of the caldera.

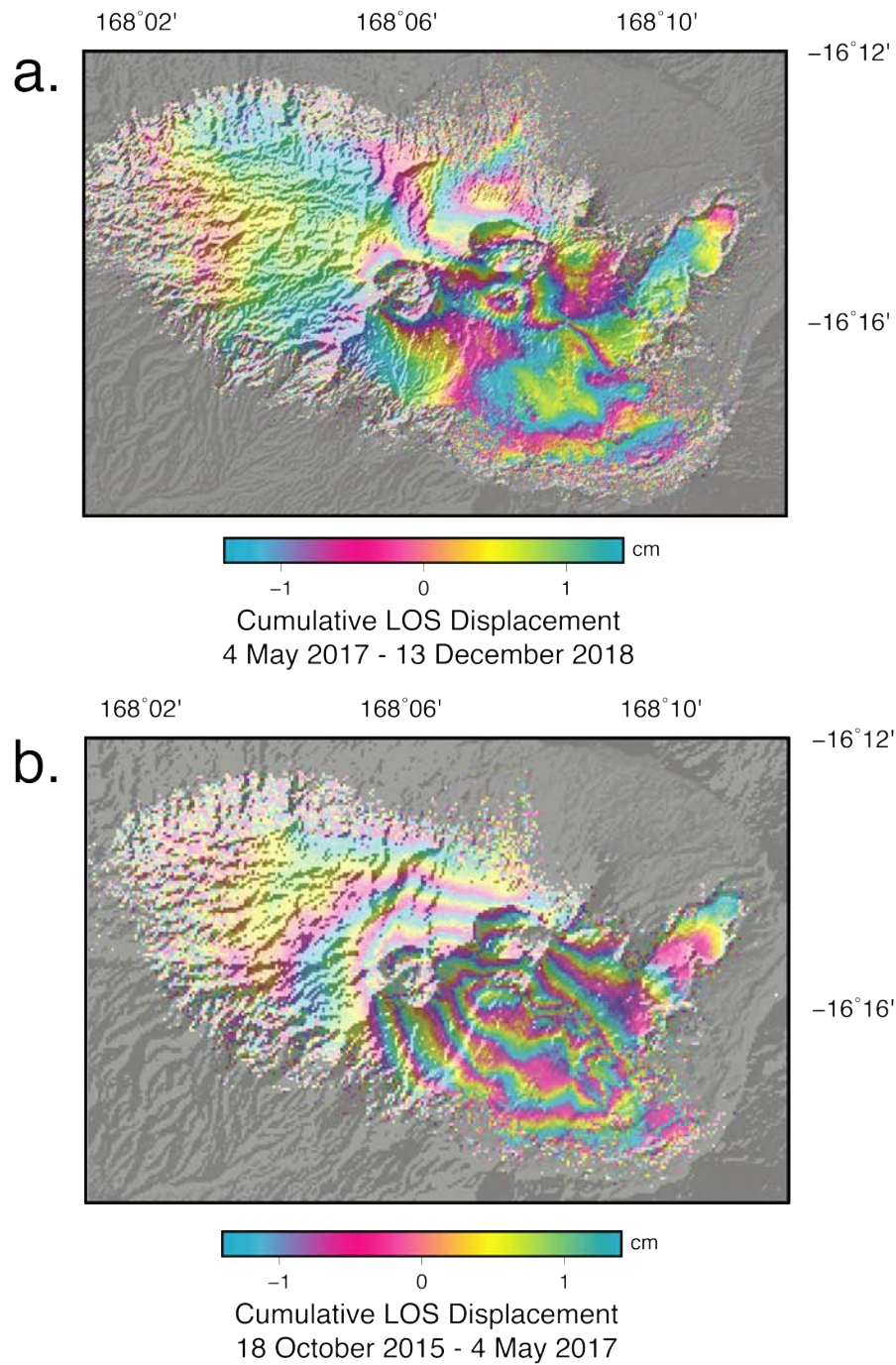


Figure S9. Absence of pre-eruptive uplift. Top panel: A temporal series analysis, calculated using Sentinel-1 interferograms and NSBAS (Doin, et al. 2011), measures very little (if any) pre-eruptive deformation (at most 3 cm uplift centered to the south of Marum). Bottom panel: In the years prior to the 2018 event, subsidence within the caldera dominated during the time period 2015–2017, following the 2015 February eruption, at a rate of approximately -1 cm/month, elongated in the direction of the rift zone.

Sentinel-5P Tropomi – SO₂ concentration @ 7 km a.s.l.

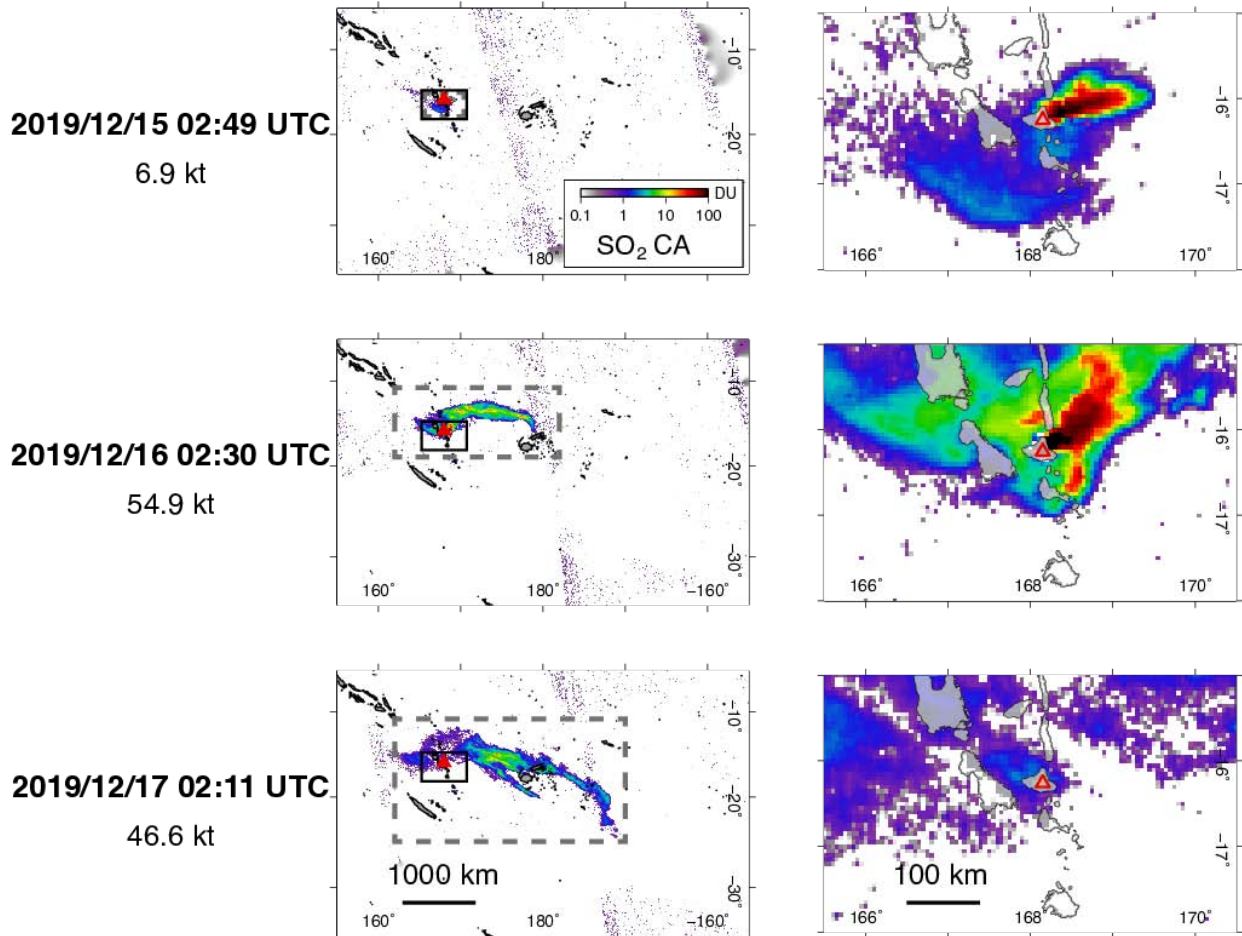


Figure S10. SO₂ emissions from Sentinel-5P TROPOMI Daily SO₂ total vertical column density from Sentinel-5P TROPOMI, processed at Level 2. Left: broad-scale view over SW Pacific. Right: detailed view over Ambrym. SO₂ column amount (CA) is estimated assuming a SO₂ plume at 7 km altitude w.r.t. the sea level. Plume altitude is approximately constrained by HYSPLIT simulations of plume dispersal. DU: Dobson Unit. Total burden of SO₂ is estimated by computing a surface integral in the area outlined by the grey dashed rectangles.

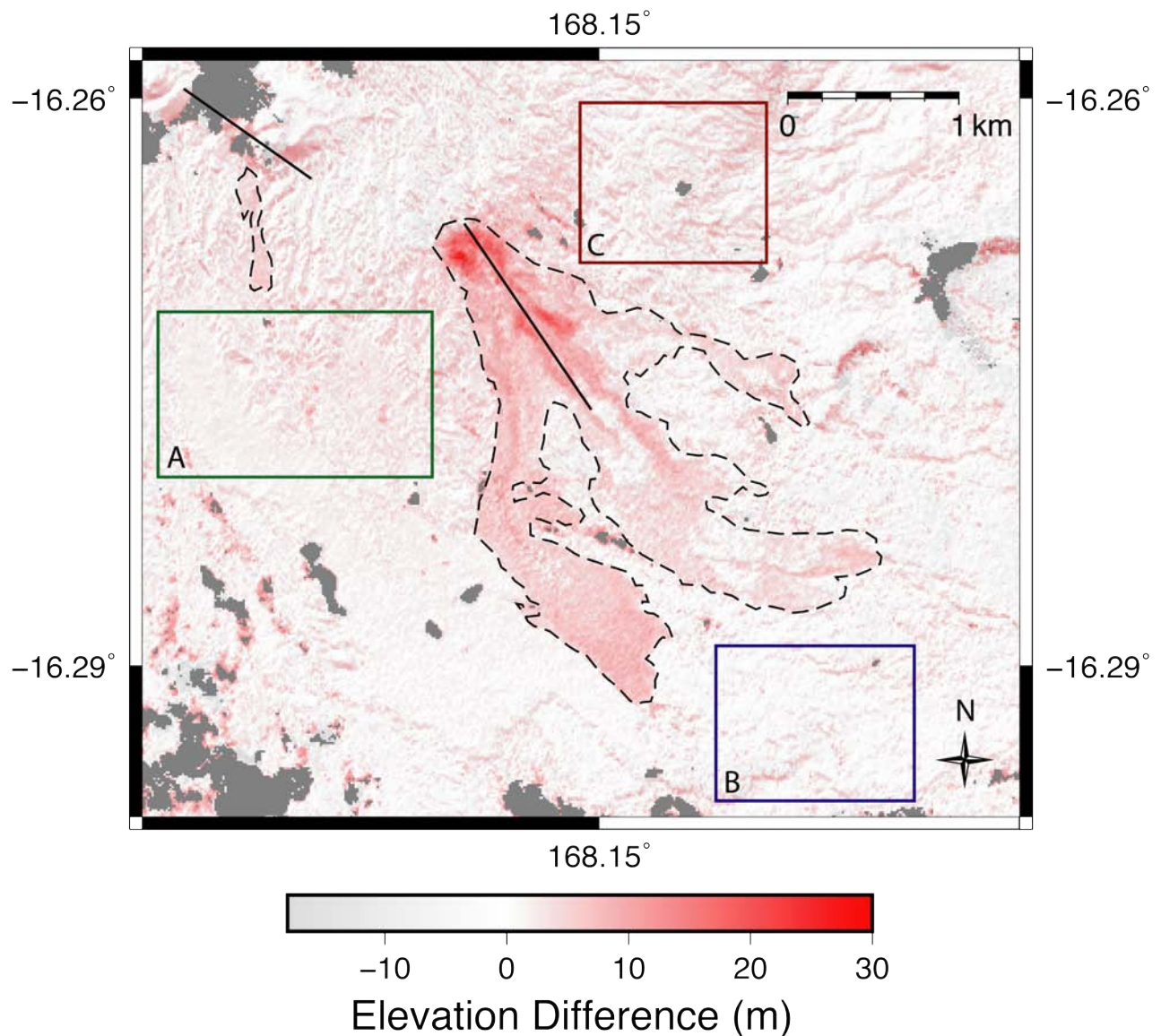


Figure S11. Difference between DEM's pre- and post- February 2015. A DEM difference that measures the extent of the lava flows from the February 2015 eruption⁸. The post-eruption DEM is calculated using Micmac software (<https://micmac.ensg.eu>)⁹ derived from Pleiades optical images. By measuring the lava flow thickness from historical eruptions, we can estimate the volume of lava emitted during the 2018 eruption. The total volume from the 2015 lava flow is calculated to be $12.41 \times 10^6 \text{ m}^3$, with an average lava flow thickness of $\sim 5.17 \text{ m}$. In control areas A, B, and C, where no lava was emplaced, the mean elevation of the DEM difference is 1.11 m, -0.341 m , and 0.239 m , with standard deviations of 1.4 m, 1.64 m, and 1.87 m, respectively. Pre-eruption DEM ©DLR 2017, post-eruption DEM ©CNES 2018, Distribution AIRBUS DS. Map was generated with GMT version 5.4.3 (<http://gmt.soest.hawaii.edu>) and edited in Adobe Illustrator version 16.0.4 (<https://www.adobe.com/products/illustrator.html>)

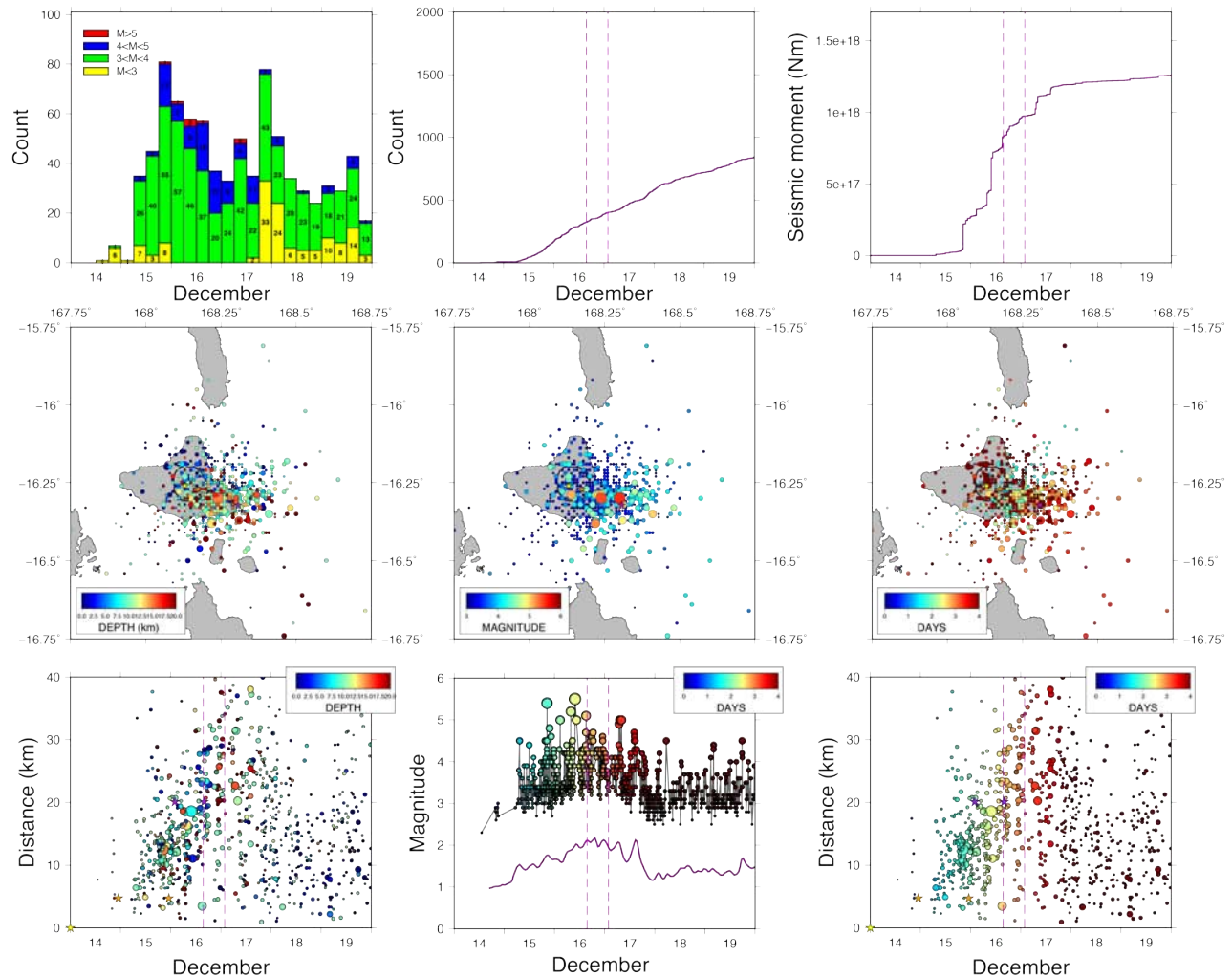


Figure S12. Seismicity during eruption. Details of seismicity reported by Vanuatu Meteorology and Geohazard Department (VMGD). Time span covered by these plots is from 14 December 2018 00:00 UTC to 19 December 2018 23:59 UTC. Only earthquakes with $M > 2$ and depth < 60 km are shown. Top left: earthquake count by magnitude. Bin size is 3 hours. Top center: cumulative earthquake count. Dashed pink lines correspond to occurrence of two earthquakes with a P-vertical CLVD mechanism, associated with caldera collapse (Fig. 2b). Top right: cumulative seismic moment release. Middle left: seismicity map with earthquakes colored by depth. Middle center: seismicity map with earthquakes colored by magnitude. Middle right: seismicity map with earthquakes colored by elapsed time from a reference time of 14 December 2018 00:00 UTC. Bottom left: evolution of seismicity as a function of distance from Marum, with earthquakes colored by depth. Bottom center: evolution of seismicity as a function of magnitude, with earthquakes colored by date. Bottom right: evolution of seismicity as a function of distance from Marum, with earthquakes colored by date.

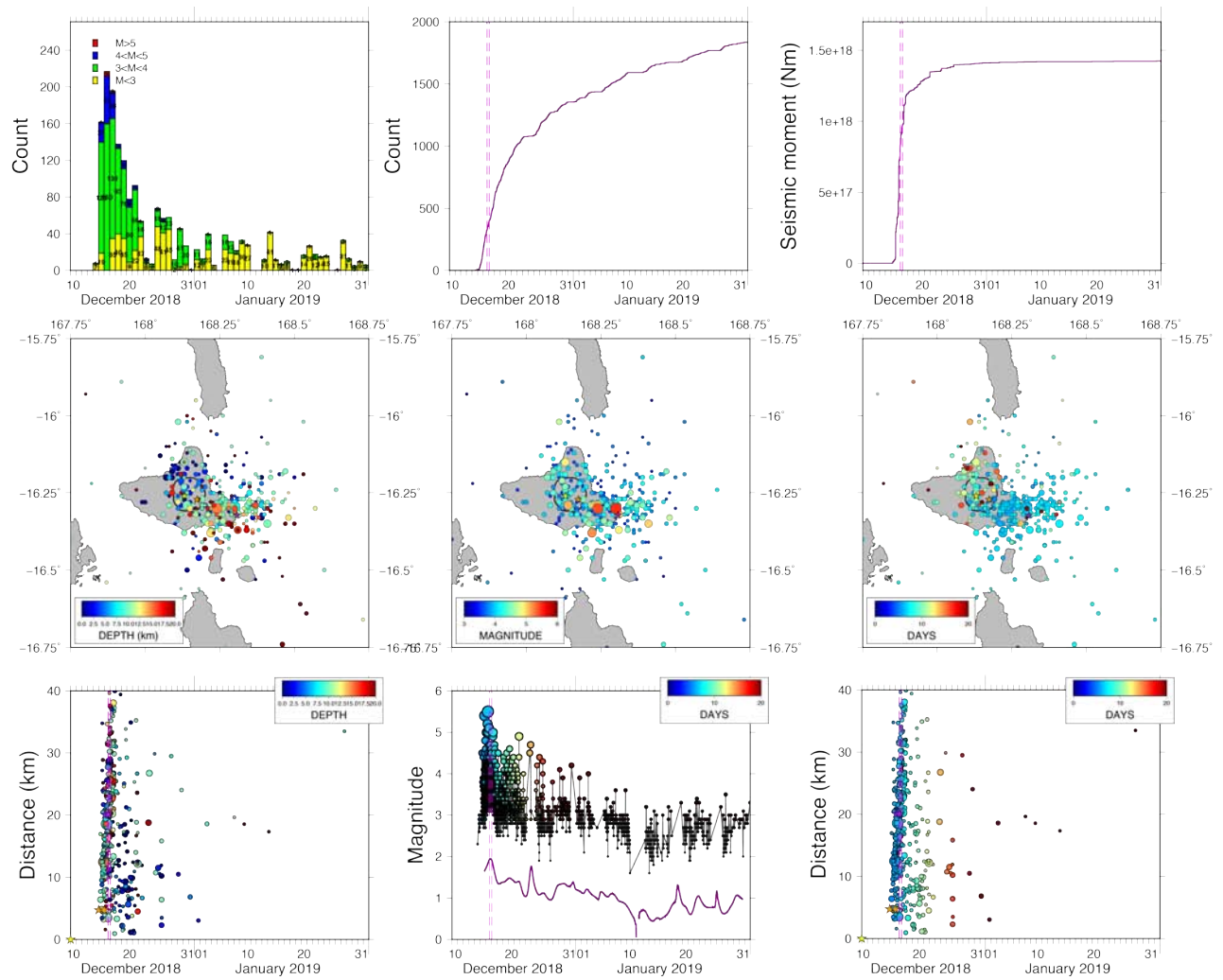


Figure S13. Seismicity during eruption and after event. Same as Fig. S12, but for the time interval from 10 December 2018 00:00 UTC to 31 January 2019 23:59 UTC, for earthquakes with $M > 3.5$.

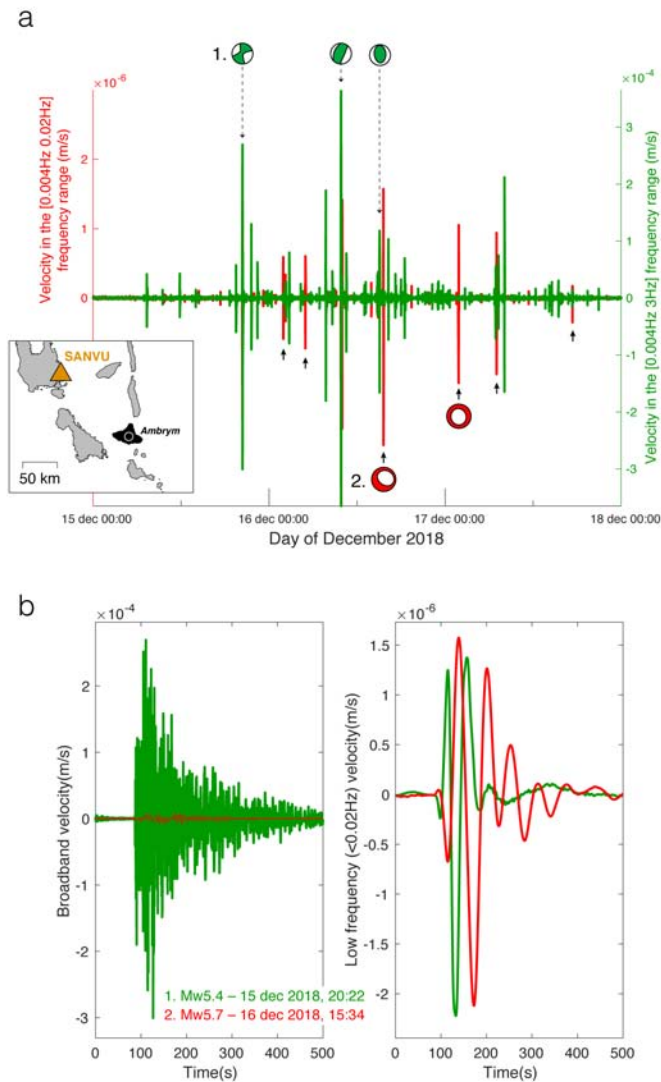


Figure S14. Broadband and low frequency seismograms. **a** Comparison between broadband (green) and low frequency (red) velocity seismograms at Geoscope station SANVU¹⁰. The raw record has first been corrected for instrument response and high-pass filtered at 0.004 Hz (250 seconds). The broadband and low frequency seismograms have then been obtained after a lowpass filter at 3Hz and 0.02Hz (0.3 seconds and 50 seconds), respectively. Green and red focal mechanisms of the largest events are from USGS and Global CMT, respectively, as in Fig. 2. Note the different vertical scales for the broadband and filtered seismograms. Peaks in the broadband (green) seismograms indicate events with a high frequency content (volcano-tectonic events, VT) associated with the Ambrym seismic crisis. Black arrows indicate events with a ratio of low-frequency-to-high-frequency exceeding significantly the average inferred from VT (red spikes), indicating a low frequency content (long-period events, LP). Station location is shown in inset. **b** Same as a., but keeping an identical vertical scale. Here, two events with contrasting low-frequency-to-high-frequency ratios are compared. The first event (1) is the main VT event of 15 December 2018 (Mw5.4, 15 December 2018, 20:22). The second event (2) is the first LP event of 16 December 2018 with a P-vertical CLVD mechanism reported by Global CMT (Mw5.7 16 December 2018, 15:34). The LP event produces a much smaller signature in the broadband seismogram (left). In contrast, after low-pass filtering, both events show a similar amplitude (right). In addition, the clear differential signal duration between both events is a direct evidence of a long source process (at least several tens of seconds) for the Mw5.7 LP event.

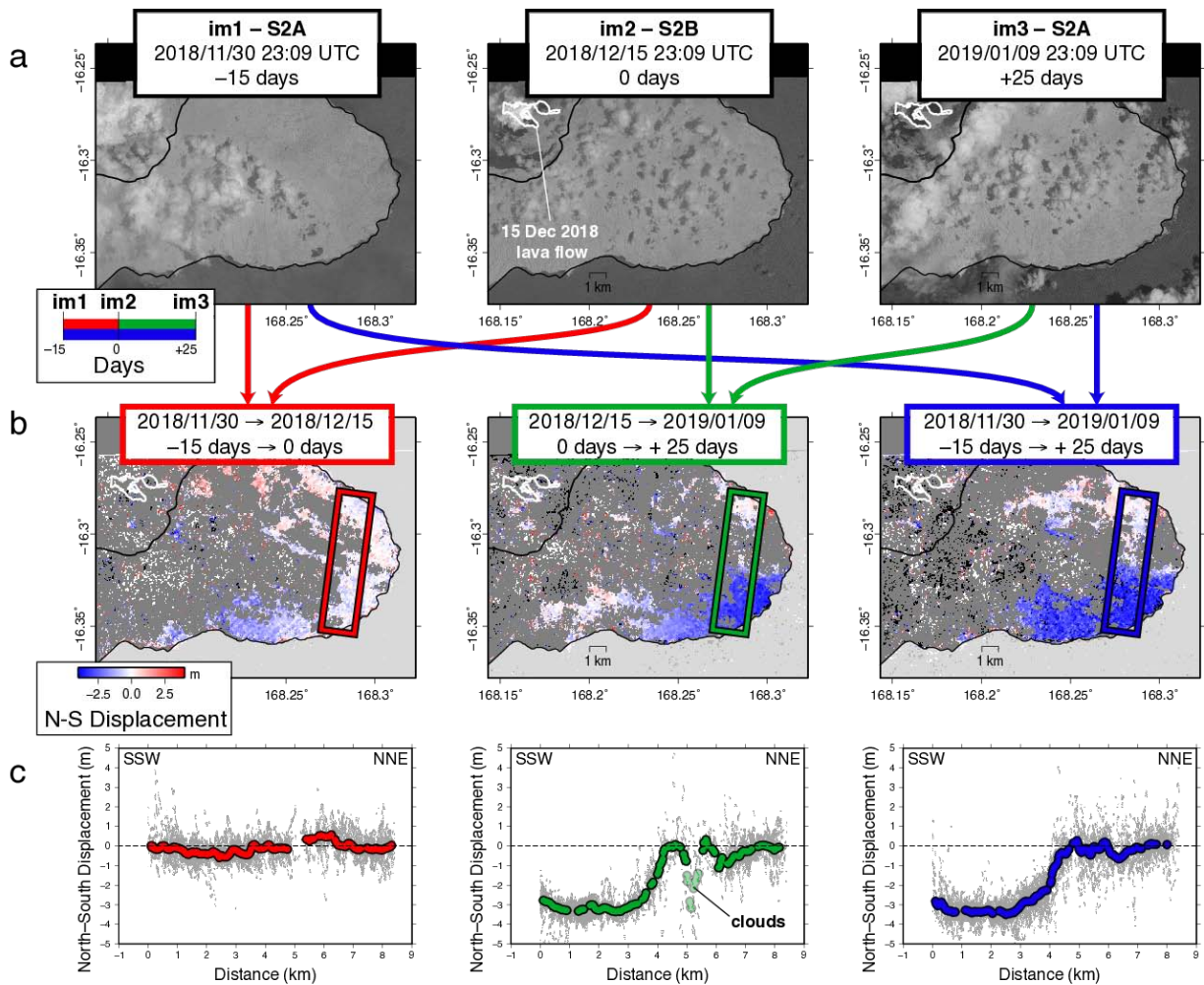


Figure S15. Sentinel-2 optical image correlation. Sub-pixel correlation of Sentinel-2 optical images covering the eastern rift zone of Ambrym with mild cloud cover. Images are acquired on (a) 30 November 2018, (b) 15 December 2018, 23:09 UTC, and (c) 9 January 2019. Upper row shows a preview of images for band 8 (near-infrared, 767–908 μm) which is characterized by a high reflectivity in vegetated area. Image resolution is 10 meters. Central row is the result of pair-wise sub-pixel correlation, processed with MicMac software⁹ (<https://micmac.ensg.eu>). Lower row shows swath profiles in the boxes indicated by the rectangles in the central row. Grey points show raw results in a box spanning ± 1 km from a reference profile. The location of the box is shown in b. The colored curves are computed by applying a 0.2 km-wide median filter to the raw data. Negative (blue): motion toward the south. Positive (red): motion toward the north.

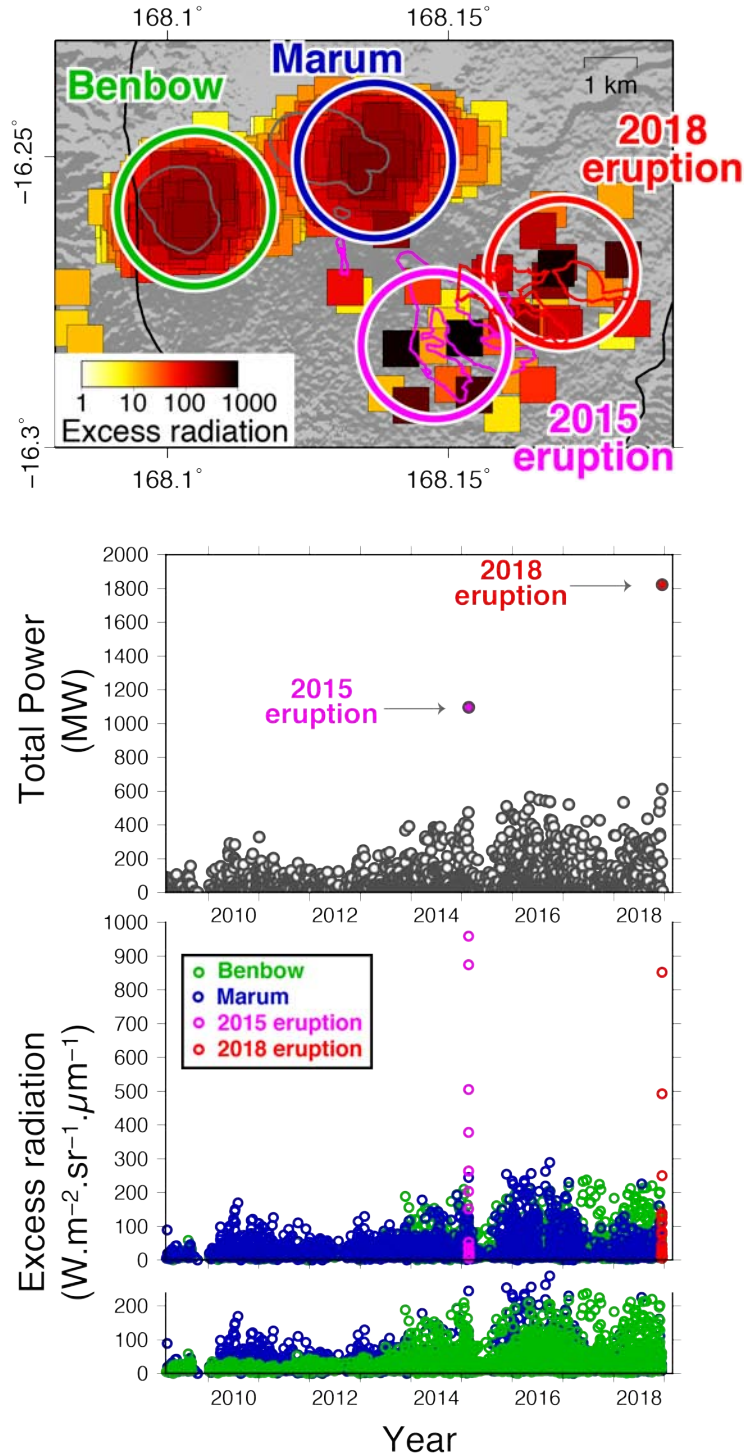


Figure S16. 10-year MODIS thermal activity. Time-series of excess thermal radiation and total radiated power from 2009 to 2019, derived from MODIS (Wright et al., 2016). Upper panel shows the spatial distribution of thermal anomalies. Middle graph shows the total power over the whole Ambrym caldera as a function of time. Lower graph shows excess radiation as a function of time, colored according to the location of the radiation (green: Benbow; blue: Marum; pink: 2015 eruption; red: 2018 eruption). Circles in the upper panel indicate the spatial regions corresponding to each of the 4 locations. Processed data is from the MODVOLC service (<http://modis.higp.hawaii.edu/algorithm.html>)⁶.

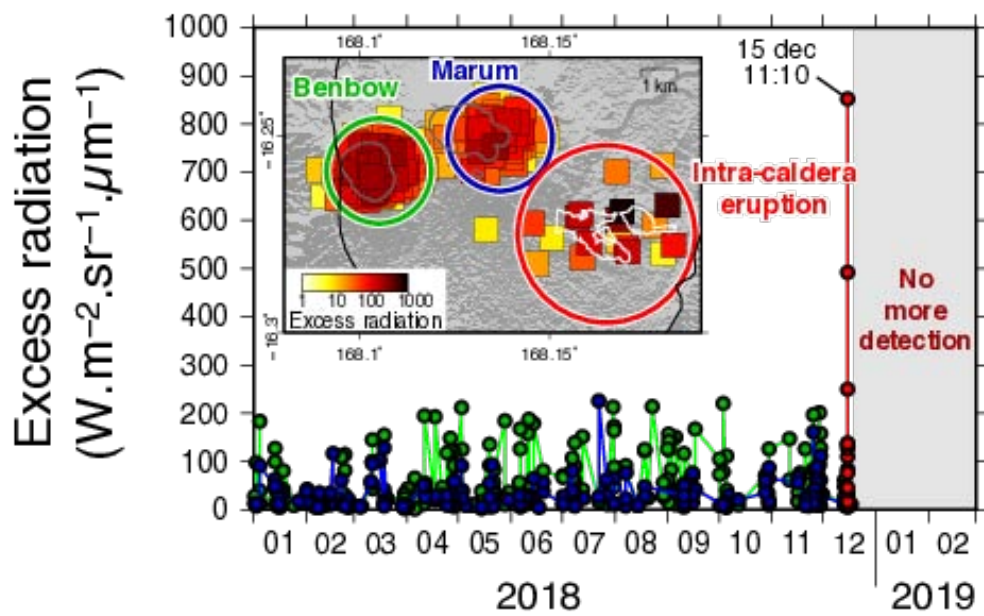


Figure S17. 1-year MODIS thermal activity. Same as Fig. S16a for the period between 1 January 2018 and 28 February 2019. Note that no anomaly was detected after the last detection of 17 December 2018 14:05 UTC.

Table S1. SAR data used in inversions

Inversion	Master date (UTC)	Slave date (UTC)	Sensor	Mode	Geometry/Track	Data type
Intra-caldera dike	2018/11/03 00:24	2018/12/15 00:24	ALOS-2	Wideswath (WD1)	Descending T203	InSAR
Rift zone intrusion and caldera subsidence	2018/11/24 13:14	2018/12/22 13:14	ALOS-2	Stripmap (SM3)	Ascending T101	InSAR
	2018/12/15 00:24	2019/01/26 00:24	ALOS-2	Wideswath (WD1)	Descending T203	InSAR
	2018/12/14 06:10	2018/12/18 06:10	CSK	Stripmap (H4-04)	Descending	Azimuth/range pixel offsets
Post-intrusion caldera subsidence	2018/12/22 13:14	2019/02/16 13:14	ALOS-2	Stripmap (SM3)	Ascending T101	InSAR
	2018/12/18 06:10	2019/01/15 06:10	CSK	Stripmap (H4-04)	Descending	Azimuth/range pixel offsets

Table S2. First-order geometries derived from non-linear inversion.

Inversion	Source type	Center position (lat/lon)	Strike	Dip	Depth (km)	Length (km)	Width (km)	Opening (m) / Volume (km ³)
Intra-caldera dike	Okada	168.165°E -16.267°N	88°	38°	0.4	3.25	3.46	1.96/0.022
Rift zone intrusion and caldera subsidence	Okada	168.165°E -16.267°N	109°	72°	0.0 [†]	27.36	6.94	4.0/0.76
	Mogi	168.136°E -16.253°N	N/A	N/A	4.5	N/A	N/A	N/A/-0.231
Post-intrusion caldera subsidence	Okada	168.146°E -16.255°N	-41°	0.0 [†]	4.1	7.74	6.14	-1.30/0.062

[†] : fixed.

Table S3. Sentinel-1 acquisition dates and scalars.

Master date	Slave date	Scalar
2018/12/19	2018/12/25	0.55
2018/12/19	2018/12/31	0.87
2018/12/19	2019/01/06	1.03
2018/12/19	2019/01/12	1.04
2018/12/19	2019/01/18	1.09
2018/12/25	2018/12/31	0.29
2018/12/25	2019/01/06	0.41
2018/12/25	2019/01/12	0.47
2018/12/25	2019/01/18	0.52
2018/12/31	2019/01/06	0.11
2018/12/31	2019/01/12	0.17
2018/12/31	2019/01/18	0.23
2019/01/06	2019/01/12	0.06
2019/01/06	2019/01/18	0.12
2019/01/12	2019/01/18	0.06
2018/12/22	2019/01/15	1.00 [‡]
2018/12/22	2019/02/16	1.00 [‡]

[‡] : reference (fixed).

Table S4. Average major element composition for lava erupted during the intra-caldera eruption at Lewolembwi. Given the very low crystal content (< 5%) of the rock samples and the close correspondence between melt inclusions and embayment and matrix glasses composition, these analyses can also be considered representative of the bulk rock composition.

Sample type	SiO ₂	TiO ₂	Al ₂ O ₃	FeO	MnO	MgO	CaO	Na ₂ O	K ₂ O	P ₂ O ₅	Total
Melt inclusions (N=9)	53.30	1.17	16.09	10.80	0.20	3.50	8.77	3.23	2.48	0.45	100.00
Embayments and matrix glasses (N=6)	53.24	1.08	16.32	10.90	0.23	3.62	8.60	3.16	2.43	0.42	100.00

References

1. Grandin, R. *et al.* September 2005 Manda hararo-dabbahu rifting event, Afar (Ethiopia): Constraints provided by geodetic data. *J. Geophys. Res. Solid Earth* **114**, DOI: [10.1029/2008JB005843](https://doi.org/10.1029/2008JB005843) (2009).
2. Radiguet, M. *et al.* Spatial and temporal evolution of a long term slow slip event: The 2006 Guerrero Slow Slip Event. *Geophys. J. Int.* **184**, 816–828, DOI: [10.1111/j.1365-246X.2010.04866.x](https://doi.org/10.1111/j.1365-246X.2010.04866.x) (2011).
3. Marty, J. *et al.* Gins: the cnes/grgs gnss scientific software. In *3rd International Colloquium Scientific and Fundamental Aspects of the Galileo Programme, ESA Proceedings WPP326*, vol. 31, 8–10 (2011).
4. Böhm, J., Niell, A., Tregoning, P. & Schuh, H. Global mapping function (gmf): A new empirical mapping function based on numerical weather model data. *Geophys. Res. Lett.* **33** (2006).
5. Lagler, K., Schindelegger, M., Böhm, J., Krásná, H. & Nilsson, T. Gpt2: Empirical slant delay model for radio space geodetic techniques. *Geophys. research letters* **40**, 1069–1073 (2013).
6. Wright, R., Flynn, L., Garbeil, H., Harris, A. & Pilger, E. Automated volcanic eruption detection using MODIS. *Remote sensing environment* **82**, 135–155 (2002).
7. Planet Team. Planet Application Program Interface: In *Space for Life on Earth* (2017). San Fransisco, CA. <https://api.planet.com>.
8. Coppola, D., Laiolo, M. & Cigolini, C. Fifteen years of thermal activity at Vanuatu’s volcanoes (2000 - 2015) revealed by MIROVA. *J. Volcanol. Geotherm. Res.* **322**, 6–19, DOI: [10.1016/j.jvolgeores.2015.11.005](https://doi.org/10.1016/j.jvolgeores.2015.11.005) (2016).
9. Rosu, A. M., Pierrot-Deseilligny, M., Delorme, A., Binet, R. & Klinger, Y. Measurement of ground displacement from optical satellite image correlation using the free open-source software MicMac. *ISPRS J. Photogramm. Remote. Sens.* **100**, 48–59, DOI: [10.1016/j.isprsjprs.2014.03.002](https://doi.org/10.1016/j.isprsjprs.2014.03.002) (2015).
10. Institut de Physique du Globe de Paris and Ecole et Observatoire des Sciences de la Terre de Strasbourg (EOST). GEOSCOPE - French Global Network of broadband seismic stations, DOI: [10.18715/GEOSCOPE.G](https://doi.org/10.18715/GEOSCOPE.G) (1982).

Chapter 4

Mechanical models of caldera ring-fault reactivation at a broad and shallow basaltic magmatic system

This chapter is based on the study submitted as “What triggers caldera ring-fault subsidence at Ambrym volcano? Insights from the 2015 dike intrusion and eruption” to *Journal of Geophysical Research: Solid Earth*. In this study, the first author processed the primary geodetic datasets, performed and interpreted the geodetic numerical modelling, and wrote the initial draft. R. Grandin contributed to interpretations of the geodetic data and models, D. Smittarello and V. Cayol helped adapt the numerical model for use in this study, V. Pinel contributed to the interpretation of the geodetic models, M. Boichu contributed the IASI SO₂ data analysis, and Y. Morishita processed the ScanSAR-to-stripmap interferogram. All authors commented on the final draft.

In this chapter, we will first provide a summary of the factors affecting caldera ring-fault formation and reactivation. The former occurs during caldera collapse. Ring-fault reactivation can occur either during a subsequent collapse event, or during episodes of moderate subsidence or uplift. Finally, we will present the submitted article and Supplementary Information, which discuss an episode of caldera ring-fault reactivation at Ambrym volcano.

4.1 Scientific context

4.1.1 Caldera collapse

Before discussing caldera ring-fault reactivation, it is important to understand the mechanisms of caldera formation. Calderas are created during an initial collapse that forms the caldera ring-faults. Caldera collapse styles have been divided into five main endmembers—piston, piecemeal, trap-door, downsag, and funnel (See Figure 4-1a) [Lipman, 1997, Cole et al., 2005, Acocella, 2007]. Acocella [2007] developed an additional classification of the caldera’s stage of development based on the amount of caldera subsidence (See Figure 4-1b). However, this characterization may be difficult to apply when the collapse structure observed at the surface results from repeated collapse events.

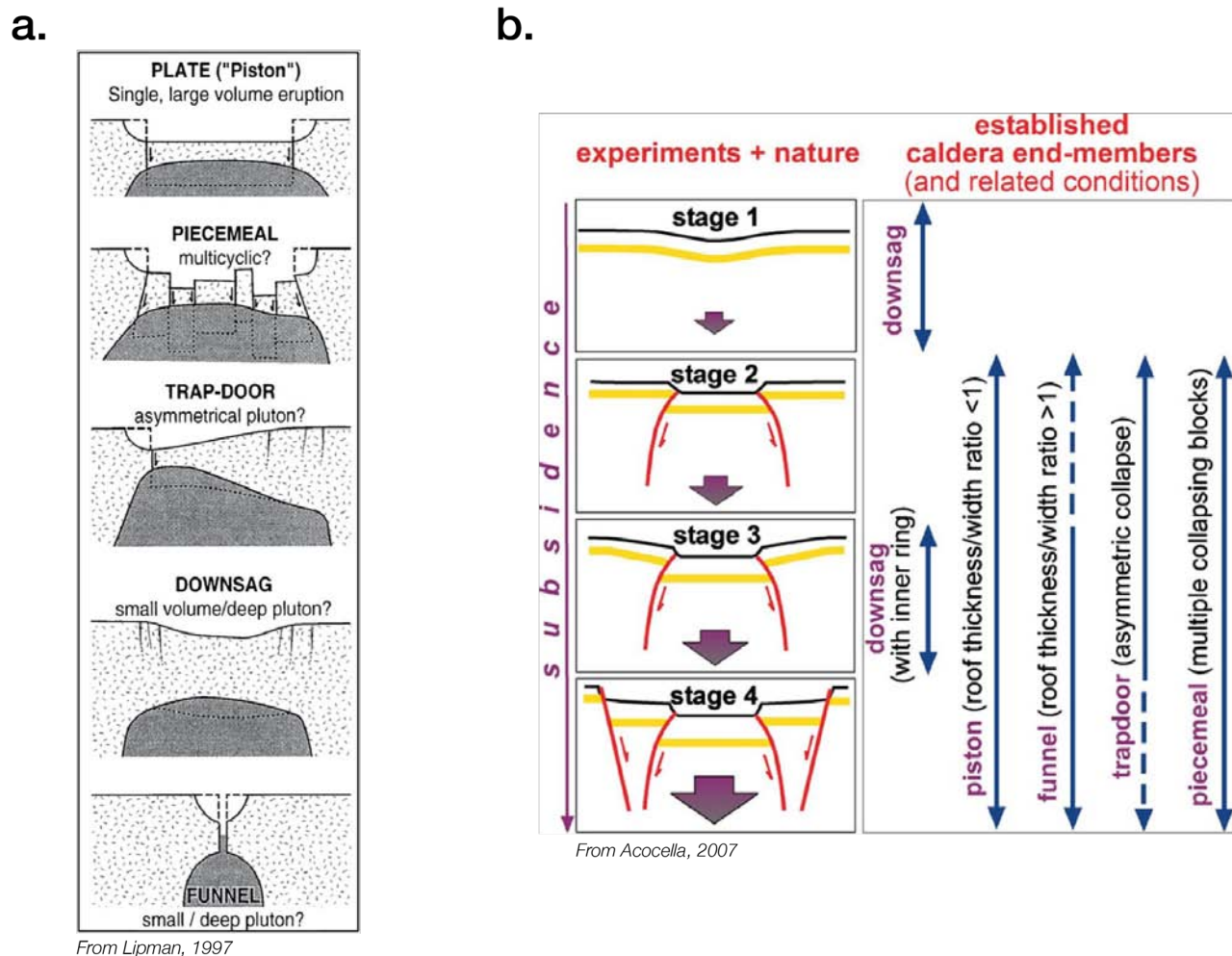


Figure 4-1: **Caldera collapse styles and stages.** **a.** The five end-member caldera collapse styles, as defined by Lipman [1997]. **b.** The evolution of caldera development with increasing subsidence, compared to the collapse styles of Lipman [1997]. From Acocella [2007].

Two types of volcanic activity can cause caldera collapse— either explosive eruptions or the lateral injection of magma into rift zones (possibly leading to effusive eruptions) [Acocella, 2007, Sigmundsson, 2019]. In both cases, a large volume of material is withdrawn from the magma storage system, which induces an underpressure in the central reservoir, resulting in collapse of the caldera roof under its own weight. Once the collapse has initiated along the caldera ring-faults, the weight of the subsiding caldera roof may continue to push the magma out of the reservoir, such as during the 2014 – 2015 Bárðarbunga caldera collapse [Marti and Gudmundsson, 2000, Sigmundsson, 2019].

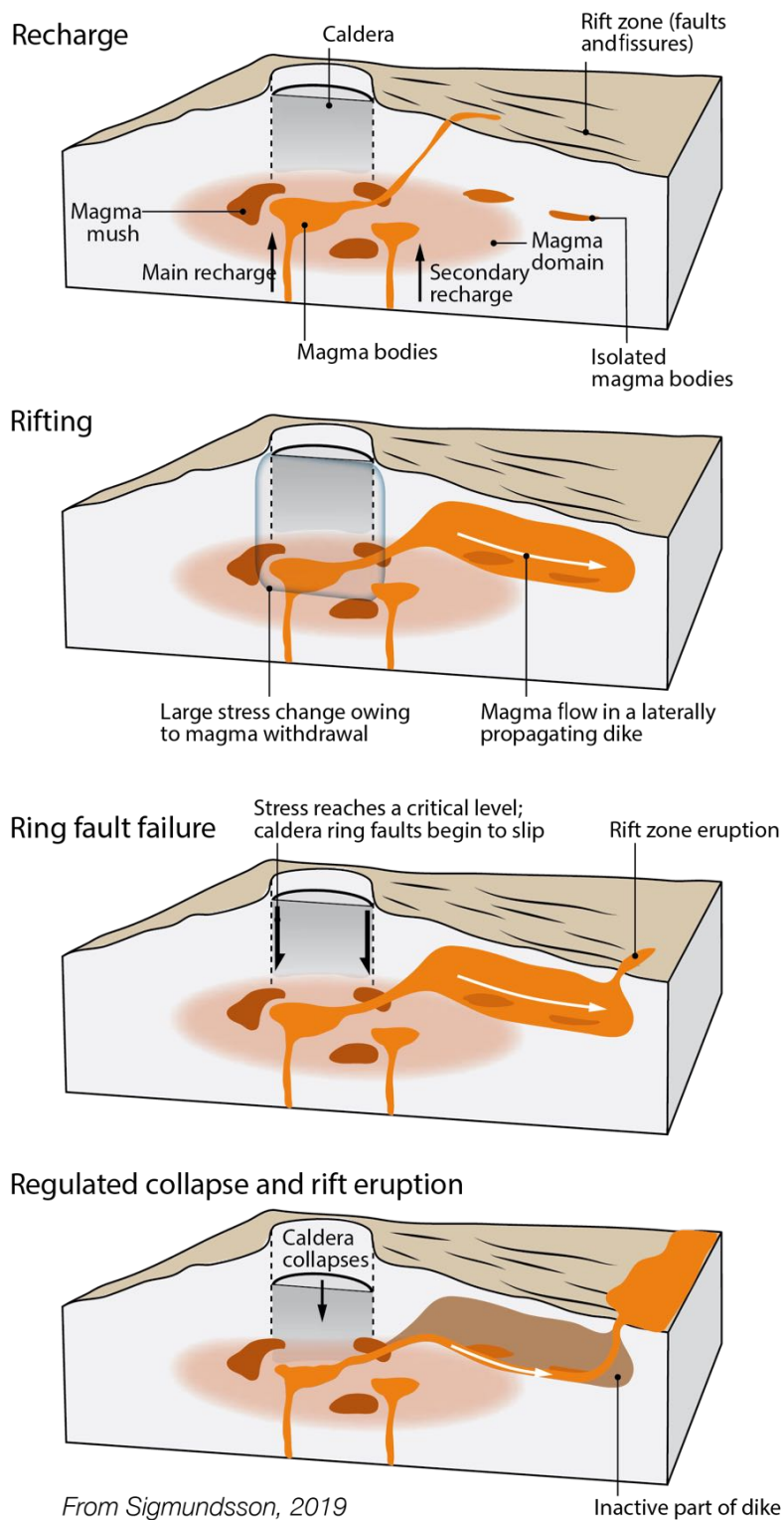


Figure 4-2: **Caldera collapse at a caldera-rift system.** A schematic illustration of the steps leading up to, and following, a caldera collapse caused by propagation of magma into a rift zone. From Sigmundsson [2019].

Plinian or ultra-Plinian eruptions are common triggers for caldera collapse at silicic magmatic systems. Such eruptions may expel hundreds to thousands of cubic kilometers of erupted material in a single event, and it is this rapid removal of material that induces caldera collapse. Evidence of such caldera-forming eruptions has been recorded at the largest calderas in the world, such as at Yellowstone (40×65 km), Toba (100×30 km), and Long Valley (29×15 km) [Christiansen, 1984, Chesner and Rose, 1991, Carle, 1988]. In Chapters 1.3.5 and 5.2, we discuss the possibility of a Plinian eruption occurring at Ambrym volcano 2000 ka. This eruption may have produced tens of cubic kilometers of pyroclastic material, and initiated the formation of the caldera's ring-faults. However, as discussed in Chapter 3, we also observe caldera ring-fault reactivation during lateral rift zone intrusions. This leads us to the next possible driver of caldera collapse.

In the past 20 years, five caldera collapse events at basaltic caldera-rift systems (Fernandina, Miyakejima, Piton de la Fournaise, Bárðarbunga, and Kīlauea) have led to an increased understanding of the role of lateral magma injections in caldera formation [Sigmundsson et al., 2020]. During these events, magma drains from the central reservoir and travels kilometers into the rift zone (as discussed in Chapter 3). Although lava may erupt at the surface, there are cases when large dike intrusions may not be associated with significant subaerial eruptions, because magma is either erupted underwater or arrested at depth (e.g., Manda Hararo-Dabbahu, Miyakejima, Fernandina, etc.). Once enough magma has drained the reservoir, it becomes significantly underpressurized, and the caldera roof collapses.

The lateral propagation of magma may continue for days to weeks, resulting in periodic collapses as magma is gradually removed from the central reservoir [Sigmundsson, 2019, Anderson et al., 2019, Segall et al., 2019]. Each individual collapse can repressurize the reservoir, causing it to sustain the weight of the caldera roof. Once enough magma has been removed due to the ongoing lateral magma migration, another collapse occurs [Kumagai et al., 2001, Anderson et al., 2019, Segall et al., 2019]. Many of the large dike intrusions mentioned in Table 3.1 resulted in caldera collapses, emphasizing the mechanical coupling between these two phenomena.

4.1.2 Caldera ring-fault activation

Regardless of the formation mechanism, the collapse of a caldera roof occurs along caldera-ring faults, which can be either inward or outward dipping. After these caldera ring-faults have formed, they can be reactivated during subsequent collapse events which may deepen the caldera floor by hundreds of meters. Repetitive caldera collapse events occur at both silicic and mafic systems, with shorter time intervals at mafic systems (tens [Delaney and McTigue, 1994, Anderson et al., 2019] to thousands [Tsukui and Suzuki, 1998] of years).

4.1.2.1 Fault geometry and collapse style

Conceptual models of caldera formation are based primarily on results from analogue modelling [Marti et al., 1994, Roche et al., 2000, Acocella et al., 2000, Geyer and Martí, 2010]. Analogue models of caldera collapse are performed by embedding a magma analogue (air, water, or silicone) in a brittle crust analogue (sand, flour, or clay) and causing it to subside [Acocella, 2007]. Regardless of the analogue crust's strength or the magma analogue's viscos-

ity, nearly all models produced outward dipping reverse faults, propagating from the top of the chamber towards the surface. At early stages of fault propagation, and thus early stages of collapse, diffuse deformation around the fault tip results in crustal downsag (See Figure 4-4), until eventually the deformation is fully localized at the fault scarp [Acocella, 2007]. If enough slip occurs on the reverse faults, inward dipping normal faults also propagate upwards, surrounding the reverse faults [Acocella, 2007] (See Figure 4-4).

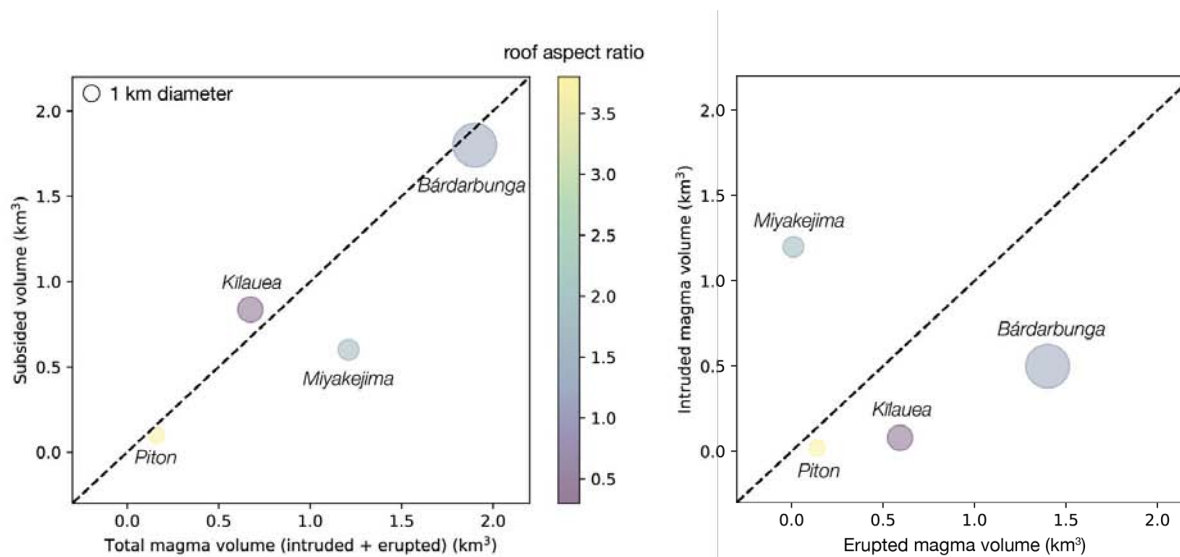


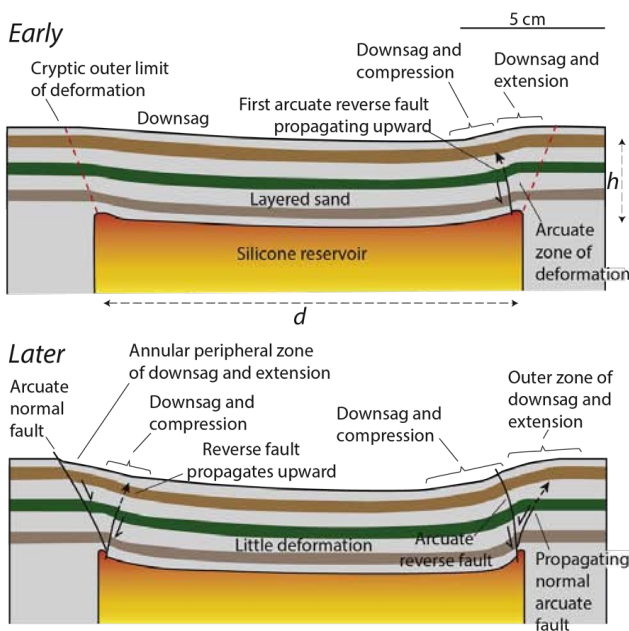
Figure 4-3: **Caldera collapse comparisons.** The left-hand plot shows the total caldera subsided volume versus the total magma volume intruded and erupted at various caldera collapses observed in the past two decades. The size of the circle is the caldera diameter, and the color is the roof aspect ratio. The righthand plot uses the same dataset, but displays the intruded magma volume versus the erupted magma volume. Data from Gudmundsson et al. [2016], Neal et al. [2018], Anderson et al. [2019], Geshi et al. [2002], Fontaine et al. [2014].

The analogue modelling of Roche et al. [2000] also revealed that the structural development of the caldera depends on the roof aspect ratio, which is defined as $R_a = \frac{h}{d}$, where h is the depth of the magmatic reservoir and d is the caldera diameter. On one hand, calderas that overlay shallow and broad magmatic reservoirs have low roof aspect ratios ($R_a \ll 1$), and tend to host a single set of reverse faults surrounded by a single set of normal faults (See Figure 4-1). This fault geometry favors an initial flexural downsag, followed by coherent or asymmetrical subsidence [Roche et al., 2000]. On the other hand, deeper and smaller magmatic systems result in calderas with high aspect ratios. Higher aspect ratios tend to form multiple outward dipping reverse faults. This often results in piecemeal collapse, since faults intersect at depth before reaching the surface [Roche et al., 2000].

Concentric reverse and normal ring-faults have been observed in nature. For example, seismicity was concentrated on subvertical normal faults during the caldera collapse of Bárðarbunga [Ágústsdóttir et al., 2019], as well on outward dipping reverse faults during the eruptions of Pinatubo and Mt. St. Helens (although no fault activation was observed at

the surface) [Scandon and Malone, 1985, Mori et al., 1996]. Both outward dipping reverse faults and inward dipping normal faults were also observed during the early stages of the Miyakejima caldera collapse [Geshi et al., 2002].

a. Roof aspect ratio, $h/d \ll 1$



Adapted from Branney et al, 2015

b. Roof aspect ratio, $h/d = 1$

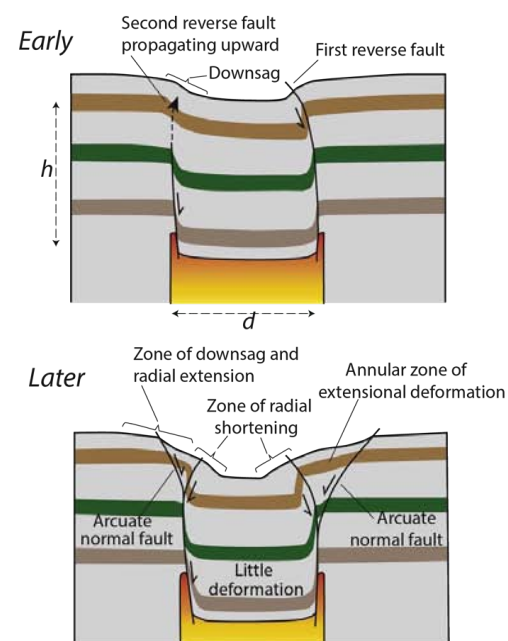


Figure 4-4: **Analogue modelling of caldera collapse.** Caldera ring-fault structural development inferred from analogue models at the beginning of collapse (top row) and later in the collapse (bottom row). Results based on roof aspect ratios **a.** $R_a \ll 1$ and **b.** $R_a = 1$. Figure adapted from Branney and Acocella [2015], Roche et al. [2000].

4.1.2.2 Fault activation thresholds

The roof aspect ratio plays a role not only in determining the collapse style, but also the timing of fault activation. Geyer et al. [2006] performed analogue modelling where water is gradually emptied from a balloon buried in sand. They recorded the volume fraction, f , of water removed from the balloon at the onset of fault formation. They categorize fault formation into two separate families– the formation of fractures at the surface, and the appearance of reverse faults at the surface (See Figure 4-5). As shown in Figure 4-5, a lower roof aspect ratio R_a results in a lower f threshold.

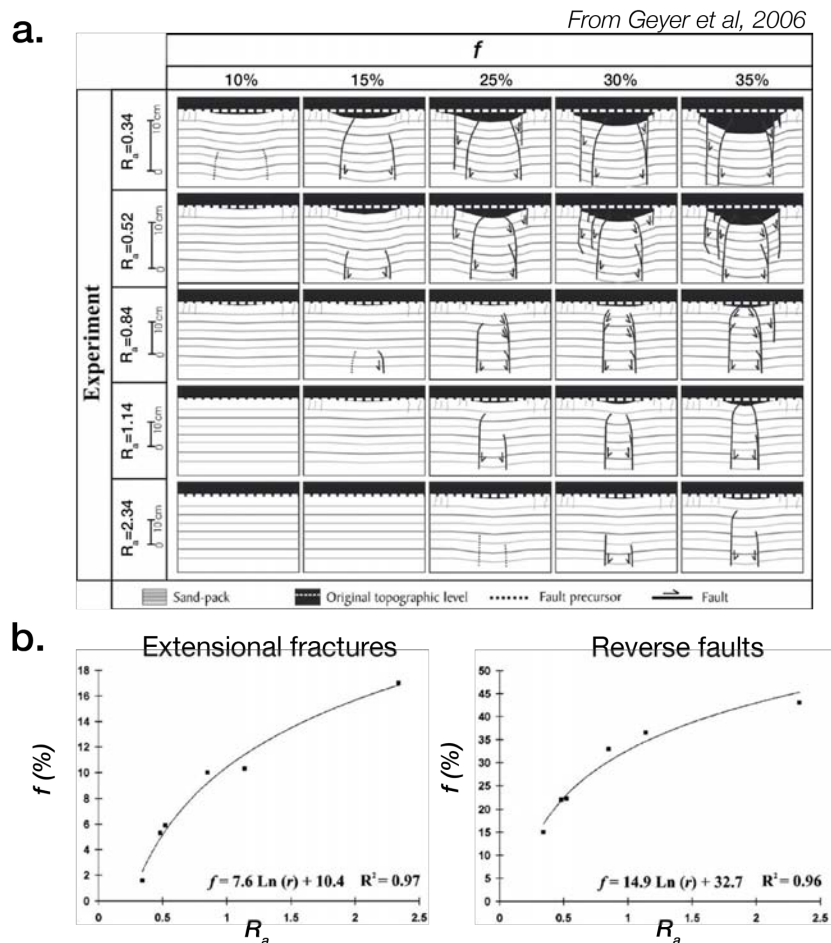


Figure 4-5: **Caldera ring-fault formation thresholds.** **a.** The progression of fracture and fault formation as a function of volume fraction removed from the reservoir, f , and roof aspect ratio R_a . **b.** The empirical relationship between the roof aspect R_a and the volume fraction f for surface fracturing initiating (lefthand figure) or for the arrival of the reverse faults at the surface (righthand figure). Adapted from Geyer et al. [2006].

Analytical models have also been used to investigate the timing of caldera collapse onset. Geshi et al. [2014] derived an analytical expression to estimate the critical volume fraction, f_{crit} , needed to exceed the maximum static friction on a vertical cylindrical ring-fault with a Mohr Coulomb behavior [Geshi et al., 2014]. They obtain a lower bound on f_{crit} as follows

$$f_{crit} = \frac{\rho g h^2}{r \kappa} \tan \phi, \quad (4.1)$$

where ρ is the host rock density, h is the depth of the magma chamber, r is the radius of the subsiding block, κ is the magma bulk modulus, and ϕ is the host rock's angle of internal friction. Similar to the findings from Roche et al. [2000], Geyer et al. [2006], f_{crit} is lower for smaller R_a (See Figure 4-6). This is related to the fact that, provided a fixed caldera radius, shallower reservoirs have a smaller fault surface area, and hence a lower value of maximum static friction.

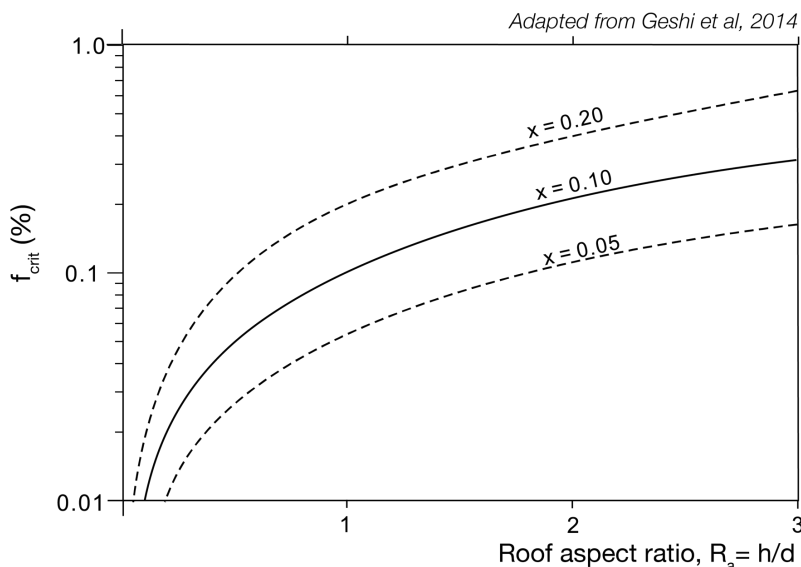


Figure 4-6: **Critical volume fraction for caldera collapse.** The analytical relationship between the roof aspect ratio R_a and the volume fraction of magma extracted from the reservoir at the onset of caldera collapse f_{crit} (See Equation 4.1). The magma bulk modulus κ plays a role in Equation 4.1, and is a function of the bubble fraction in the magma. Here f_{crit} is calculated using bubble fractions $x = 0.2, 0.1,$ and 0.05 . Adapted from Geshi et al. [2014].

4.1.3 What can we learn about the threshold for caldera ring-fault reactivation?

Both analogue and analytical studies emphasize that the lower the roof aspect ratio R_a , the lower the f threshold for caldera ring-fault activation. Up until this point, we have addressed the mechanisms and conditions under which caldera ring-faults *form*, but not specifically their *reactivation*. Because caldera ring-faults are pre-existing weaknesses, the reactivation threshold f is likely lower than that necessary to form the faults, due to a lower frictional resistance, but quantification of this threshold is lacking [Sibson, 1985]. If this threshold could be calculated, and the typical eruption volume and recurrence time are known, it may be possible to calculate the amount of long-term subsidence due to ring-fault reactivation (taking into account the amount of uplift due to magma replenishment). This value could be compared to the total caldera subsidence, in order to calculate the amount of initial ring-fault subsidence during the caldera formation. Unfortunately, aside from a few geophysical studies regarding seismicity or ground deformation [Scandon and Malone, 1985, Mori et al., 1996, Cesca et al., 2020, Liu et al., 2019, and references within], caldera ring-fault reactivation has been rarely been observed in nature.

4.2 Paper 2: “*What triggers caldera ring-fault subsidence at Ambrym volcano? Insights from the 2015 dike intrusion and eruption*”

In the presented study, we analyse an episode of caldera ring-fault reactivation at Ambrym caldera during a moderate-sized eruption (VEI 2/3). A different portion of the ring-fault was also reactivated during the much larger rift zone intrusion in 2018, as discussed in Chapter 3. The rich InSAR dataset available during the 2015 event allows us to investigate the conditions necessary to reactivate caldera ring-faults, a phenomenon that is rarely observed by geophysical methods. Through geodetic modelling of both an inflating dike, a draining magma reservoir, and a slipping ring-fault, this study infers an upper-bound of the volume fraction f necessary to reactivate pre-existing caldera ring-faults (taking into account magma compressibility), an upper-bound of the pressure change ΔP , and a lower bound for the volume of the tapped reservoir. In accordance with the ideas introduced above, our study discusses the influence of Ambrym’s roof aspect ratio on the caldera fault reactivation threshold, as well as its influence on the long-term development of Ambrym’s caldera.

What triggers caldera ring-fault subsidence at Ambrym volcano? Insights from the 2015 dike intrusion and eruption

T. Shreve¹, R. Grandin¹, D. Smittarello^{2*}, V. Cayol³, V. Pinel², M. Boichu⁴,
Y. Morishita⁵

¹Université de Paris, Institut de physique du globe de Paris, CNRS, F-75005, Paris, France

²University Grenoble Alpes, University Savoie Mont Blanc, CNRS, IRD, IFSTTAR, ISTERre, Grenoble,
France

³Université Clermont Auvergne, CNRS, IRD, OPGC, Laboratoire Magmas et Volcans, F-6300,
Clermont-Ferrand, France

⁴Université Lille, UMR 8518 – LOA – Laboratoire d’Optique Atmosphérique, F-59000, Lille, France

⁵Geospatial Information Authority of Japan, Ibaraki, Japan

Key Points:

- Ground displacement at Ambrym in February 2015 was caused by a dike intrusion, decompressing reservoir, and normal slip on a ring-fault
- At most 1.9 - 5.8% of the magma in the reservoir was extracted, which suffices to activate the caldera ring-fault
- Subsidence along Ambrym’s caldera ring-fault can occur during moderate-sized eruptions, contributing to caldera development

*Currently at the European Center for Geodynamics and Seismology, 19 rue Josy Welter, L-7256 Walferdange, Gd Duchy of Luxembourg

Corresponding author: Tara Shreve, shreve@ipgp.fr

Abstract

Surface deformation accompanying dike intrusions is dominated by uplift and horizontal motion directly related to the intrusions and may include subsidence due to associated magma reservoir deflation. When reservoir deflation is large enough, it can form, or activate pre-existing, caldera ring-faults, sometimes resulting in full-scale caldera collapse. Ring-fault activation, however, is rarely observed during moderate-sized eruptions. On February 21st, 2015 at Ambrym volcano (Vanuatu), a basaltic dike intrusion produced more than 1 meter of co-eruptive uplift, as measured by InSAR, SAR correlation, and Multiple Aperture Interferometry (MAI). Here we show that up to 30 cm of subsidence occurred on a normal caldera ring-fault during this moderate-sized event, which intruded a volume of $\sim 30 \times 10^6 \text{ m}^3$ and erupted $\sim 12 \times 10^6 \text{ m}^3$ of lava. We explore the stress change imposed by the opening dike and the decompressing reservoir on a passive, frictionless fracture (fault). Normal fault slip, at the surface and at depth, is promoted when stress is transferred from a decompressing reservoir beneath one of Ambrym’s main craters. After estimating magma compressibility, we provide an upper-bound on the critical fraction ($f = 1.9 - 5.8\%$) of material extracted from the reservoir needed to trigger fault slip. We infer that broad basaltic calderas may form in part by hundreds of subsidence episodes no greater than a few meters, due to magma extraction from the reservoir during moderate-sized dike intrusions.

Plain Language Summary

Many volcanoes feature large depressions, called calderas. Calderas form when enough magma leaves a deep reservoir, and the solid rock lid above this reservoir can no longer support its own weight. Caldera faults, or cracks surrounding the reservoir which extend kilometers from the reservoir to Earth’s surface, form as the lid collapses. Ground sinking at wide calderas along caldera faults has been attributed to large, explosive eruptions. Ambrym volcano (Vanuatu) has a 12-km wide caldera, and researchers propose it formed during an explosive eruption 2000 years ago. However, in 2018, Ambrym’s caldera sunk along caldera faults during a non-explosive eruption, questioning the aforementioned conclusion. Furthermore, in February 2015, an eruption 10 times smaller than in 2018 also caused the ground to sink along caldera faults. Utilizing ground motion data obtained from satellite radar systems to model magma reservoir outflow and fault displacement, we conclude that, in 2015, the ground sank along caldera faults because a small amount of magma was removed from the reservoir. We therefore propose that Ambrym’s wide caldera may have formed as a result of many frequently occurring medium-sized eruptions. This challenges the thought that wide calderas mainly form as a result of large eruptions.

1 Introduction

Although all calderas host collapse structures, instrumentally recorded caldera ring-fault activation is rare. A handful of extreme cases of caldera ring-fault activation—catastrophic caldera collapse—have been observed historically (Neal et al., 2018; Gudmunds-

son et al., 2016; Peltier et al., 2009; Geshi et al., 2002). The majority of these spectacular events were characterized by noncoherent, or piecemeal, collapse, where upwards propagating faults break up the collapsing piston (Ágústsdóttir et al., 2019; Neal et al., 2018; Peltier et al., 2009). On the other hand, volcanoes that host shallow and broad magmatic chambers tend to collapse in a coherent fashion, and the central portion of the collapsing piston stays intact (Roche et al., 2000). Walker (1984) hypothesized that silicic calderas may form incrementally by downsagging, which can be accompanied by caldera ring-faulting. The fraction of material removed from a magma reservoir needed to activate caldera ring-faults does not depend strongly on eruptive style. Incremental caldera ring-fault activation may also occur during frequent eruptions at broad, shallow basaltic calderas. Notably, at Sierra Negra, which hosts the largest caldera in the Galápagos (9 km maximum diameter), there is no evidence of catastrophic caldera collapse, despite voluminous historical eruptions (Reynolds et al., 1995; Munro & Rowland, 1996).

Confirming that incremental subsidence is an important driver of caldera development at broad, shallow basaltic systems is challenging. Any significant subsidence would only accumulate over timescales of hundreds of years. Little geological trace would be left at the surface, especially if lateral intrusions, which may arrest at depth, were the dominant mechanism of magma withdrawal from a central magmatic plumbing system. Nonetheless, accurately reconstructing the historical timeline of caldera formation is important, as it plays a role in determining which volcanoes are candidates to produce VEI 7 eruptions in the future (Newhall et al., 2018). Increased space-geodetic monitoring of volcanoes worldwide improve the chances of measuring caldera subsidence and ring-fault activation during moderate-sized eruptions (VEI<3)(Pinel et al., 2014).

Caldera ring-faults are activated due to an underpressure within a reservoir as material is extracted from the central magmatic plumbing system. At basaltic caldera-rift systems, this extraction occurs primarily through lateral dike intrusions (Sigmundsson, 2019). However, in some cases of dike propagation, regardless of whether or not ring-faults have been activated, surface displacements associated with a decompressing reservoir are not observed geodetically. This can either be due to a masking of the subsidence signal by the large displacements related to the dike intrusion (Grandin et al., 2009), or other factors such as host rock or magma compressibility (Rivalta & Segall, 2008). Accounting for mechanical source interactions allows additional constraints to help identify a decompressing source.

In February 2015, a dike intrusion fed an eruption at Ambrym volcano and produced more than 1 meter of asymmetrical uplift to the SW of the fissure, as measured by synthetic aperture radar (SAR) data. To understand the process of dike intrusions leading to caldera subsidence and ring-fault activation, we combine Boundary Element Method calculations with a neighborhood inversion algorithm to determine the deformation sources contributing to the surface displacement. We then calculate the static stress change on the fault to investigate the possible contribution of the dike opening and reservoir depletion on caldera ring-fault activation, as well as determine bounds on the pressure and volume change of the magma reservoir needed to trigger caldera ring-faulting.

1.1 Volcanological and Tectonic Setting

Ambrym volcano is a basaltic volcanic island located in the central portion of the New Hebrides subduction zone in Vanuatu. The island hosts two rift zones oriented N105°S, which radiate bilaterally from the island's central 12-km wide caldera (McCall, G.J.H. and Lemaitre, R.W. and Malahoff, A. and Robinson, G.P. and Stephenson, P.J., 1969). The caldera has been previously interpreted as resulting from the collapse of a giant tuff cone during a sequence of explosive phreatomagmatic eruptions (Robin et al., 1993). This view was later challenged by Cronin and Németh (2005). In December 2018, the first geodetically monitored rift zone intrusion occurred, with $>0.4 \text{ km}^3$ of magma travelling more than 20 km into the SE rift zone, resulting in a submarine eruption that emitted basaltic pumice onto the nearby shoreline (Shreve et al., 2019). Coeval with the 2018 rift zone intrusion, the caldera floor subsided by more than 2 meters. The caldera ring-faults also activated, most notably in the northern half of the caldera. The decompressing deformation source was modelled to be between 1 - 5 km beneath the summit, depending on how many sources were included (Hamling et al., 2019; Shreve et al., 2019).

This event confirms that the caldera-ring faults are part of an active fault system, not solely relict structures resulting from a major collapse 2000 years ago (Robin et al., 1993). Due to these observations of meter-scale caldera subsidence, in conjunction with historical documentation of reoccurring rift zone intrusions, recent studies (Hamling et al., 2019; Shreve et al., 2019) have invoked the hypothesis that Ambrym's caldera developed as a result of hundreds of similar rift zone intrusions, building out the elongation of the island, while simultaneously causing the gradual, incremental subsidence of the caldera floor. The rift zone intrusion in 2018 provided an example of caldera ring-fault activation at Ambrym, but did not provide minimum constraints on the thresholds necessary to activate these faults. More frequently-occurring moderate-sized eruptions, such as a fissure eruption that occurred in 2015, provide additional constraints.

1.2 Gas and thermal remote sensing during the February 2015 eruption

Ambrym's volcanic activity over the past decades includes lava lakes and Strombolian explosions within the nested pit craters located in the two main volcanic cones, Marum and Benbow, near the western caldera rim (see Figure 1)(Németh & Cronin, 2008). In addition to lava lake activity, occasional intra-caldera fissure eruptions have occurred, most notably in 1986 and 1988–89 (Eissen et al., 1991). The former took place in the eastern portion of the caldera, and erupted lava with a slightly elevated SiO_2 content (60 wt% SiO_2), compared to eruptive products from the main cones (~ 50.5 wt% SiO_2) (Fig. 1c). This suggests various degrees of melt differentiation within the magmatic system (Robin et al., 1993; Eissen et al., 1991).

In February 2015, another fissure eruption occurred, with a main fissure located ~ 3 km SE of Marum (Fig. 1d) (Coppola, Laiolo, & Cigolini, 2016; Hamling & Kilgour, 2020). This event was preceded by a 6.4 M_w earthquake on 19 February 2015 at 13:18 UTC with a hypocenter 30 km southeast of Ambrym's craters and a depth of ~ 5 km (Fig. 1a, 16.50°S, 168.28°E, according to the location from the Oceania Regional Seismic NET-

work (ORSNET), event ID *ird2015dmnz*). The earthquake had a reverse focal mechanism and moment tensor solution that included only 61% double couple component (Fig. 1a). According to thermal anomalies detected by the Middle Infrared Observation of Volcanic Activity (MIROVA) system (Coppola, Laiolo, Cigolini, Delle Donne, & Ripepe, 2016), the eruption lasted for ~ 44 hours, initiating sometime between 20 February 14:30 UTC and 21 February 2:40 UTC, and ending, at the latest, on 22 February 11:10 UTC (Coppola, Laiolo, & Cigolini, 2016) (see Supporting Information Text S1 for confirmation of this onset time using Hybrid Single-Particle Lagrangian Integrated Trajectory model (HYSPPLIT) (Stein et al., 2015; Crawford et al., 2016) and the Infrared Atmospheric Sounding Interferometer (IASI) (Clarisse et al., 2014)). Coppola, Laiolo, and Cigolini (2016) estimates the maximum effusion rate was $64 (\pm 32) \text{ m}^3\text{s}^{-1}$, emitting a total of $4.8 (\pm 2.4) \times 10^6 \text{ m}^3$ of lava from the main fissure oriented $\sim \text{N}135^\circ\text{S}$, travelling ~ 3 km.

To directly constrain the lava flow volume, we calculate a digital elevation model (DEM) using MicMac software (Rupnik et al., 2018) and post-eruption Pléiades optical satellite images with no cloud cover over the lava flow. We estimate an improved lava flow volume of $\sim 12.4 (\pm 0.08) \times 10^6 \text{ m}^3$ (see Supporting Information Text S2 and Table S1), with an average flow thickness of ~ 5 m (Fig. S1). Uncertainties were calculated using the methods of Bagnardi et al. (2016) and Favalli et al. (2010). We also note that in addition to the main fissure to the SE of Marum, a secondary fissure opened closer to Marum, ~ 200 m south of Niri Mbwelesu Taten (see Figure 1d), oriented $\text{N}133^\circ\text{S}$, which fed a 900 m-long lava flow.

We use the Ozone Mapping and Profiler Suite (OMPS) products to conservatively estimate ~ 40 kt of sulfur dioxide (SO_2) emitted during the eruption (see Text S3 and Figure 1e). Calibration was done for SO_2 column density estimates of plumes with a center of mass altitude (CMA) between 5 to 10 km (Li et al., 2017). An SO_2 mass estimate of ~ 40 kt is consistent with degassing of a lava volume corresponding to the $\sim 12.4 \times 10^6 \text{ m}^3$ lava flow (see Supporting Information Text S3). After 25 February, SO_2 degassing returned to passive background levels (~ 7 kt/day, according to Carn et al. (2017)). These estimates of erupted lava volumes and emitted gas will be compared with volume changes at depth, as constrained by geodesy. This comparison will provide constraints on the balance between the erupted and intruded masses, and the overall size of the magma reservoirs at depth.

2 Geodetic Data

In this study, we exploit multiple synthetic aperture radar (SAR) datasets to measure the co-eruptive ground displacement (Table S2). A joint analysis of differential InSAR and Multiple Aperture Interferometry from ALOS-2, and pixel offset tracking from CosmoSky-Med (CSK) allows to decompose the 3D co-eruptive displacement field.

2.1 Differential InSAR

The Japan Aerospace Exploration Agency’s L-band SAR satellite ALOS-2 acquired images before and after the eruption, in both ascending (stripmap) and descending orbit geometries (stripmap and ScanSAR). With a wavelength of 24 cm, interferograms produced using data acquired from L-band SAR satellites maintain coherence in vegetated regions, such as tropical volcanic islands. We process interferograms from ascending stripmap mode (SM3) images spanning 24 January to 21 March 2015 with the Interferometric SAR scientific computing environment (ISCE) (Rosen et al., 2012). Filtering and unwrapping are performed with NSBAS modules (Doin et al., 2011; Rosen et al., 2004; Grandin et al., 2012). Supporting Information Text S4 describes in detail the processing steps.

Before the eruption, the ALOS-2 descending archive consists of only ScanSAR (interferometric wide-swath mode, WD1) acquisitions. Coherent ScanSAR-to-ScanSAR interferograms can only be calculated with images acquired after 8 February 2015, due to inadequate (less than 50%) burst synchronization on the ground for acquisitions before this date (Lindsey et al., 2015; Natsuaki et al., 2016). This was due to an issue with ALOS-2’s navigation system, which was fixed on 8 February 2015 (Lindsey et al., 2015). As a result, standard ScanSAR-to-ScanSAR processing is replaced by ScanSAR-to-stripmap processing for descending images spanning 17 January 2015 to 14 March 2015 (Ortiz et al., 2007; Natsuaki et al., 2016; Kobayashi et al., 2015). This is implemented with the GSISAR software developed by the Geospatial Information Authority of Japan (Kobayashi et al., 2015; Tobita, 2003). A 30-m mesh Advanced Spaceborne Thermal Emission and Reflection Radiometer (ASTER) Global Digital Elevation Model (GDEM) was used to remove the topographic fringes (Tachikawa et al., 2011). The post-interferogram formation steps (multilooking, filtering, unwrapping and geocoding) are performed with NSBAS modules, as described in the Supporting Information Text S4. The descending interferogram is multilooked 1 time in range and 8 times in azimuth.

2.2 Multiple aperture interferometry

In addition to differential InSAR, which measures satellite LOS displacements, we also process a multiple aperture interferogram (MAI) (Bechor & Zebker, 2006; Liang & Fielding, 2017), in order to derive the along-track, or azimuth, displacement using ascending SM3 images spanning 24 January to 4 April 2015. Azimuth common-band filtering with a normalized squint of 0.66 generates sub-aperture single-look-complex (SLC) pairs which are used to calculate forward and backward looking interferograms with a multilook factor of 8 and 16 in range and azimuth, respectively. The difference between these interferograms provides the along-track displacement, albeit with a lower accuracy than differential InSAR. The postprocessing steps include filtering (Goldstein & Werner, 1998), unwrapping, and geocoding with a pixel spacing of ~ 85 m x 70 m.

2.3 Pixel offset tracking

Sub-pixel offset tracking measures surface displacement by finding the cross-correlation peak of two SAR image amplitudes (Michel et al., 1999). Pixel offsets are less accurate than InSAR (Michel et al., 1999), yet complementary as they measure both LOS and azimuth displacement, as well as provide measurements in areas where phase is not coherent or surface displacements are large.

We obtained CSK descending acquisitions spanning 13 to 25 February 2015. Pixel offsets in both range and azimuth are calculated using ISCE. Pixel offsets from the ALOS-2 ascending pair spanning 24 January to 21 March are also calculated. All of our pixel offset calculations are run using ISCE with a window size of 64, a skip width of 32, and a search width of 20. Images are then geocoded, and post-processing includes scaling by pixel size (3.6 m/pixel for ALOS-2 azimuth, 1.1 m/pixel for CSK range and 2.1 m/pixel for CSK azimuth), referencing to the median of a 15×15 pixel box to the northwest of the caldera (near 168.05°E, 16.24°S), clipping unreasonable displacement values, filtering, masking based on SNR, and masking densely vegetated areas outside the caldera (Table S3).

2.4 3D decomposition

Following the method of T. J. Wright et al. (2004), we invert for the 3D co-eruptive displacement field using the InSAR LOS measurements, pixel offsets and MAI measurements. This results in the inversion of an overdetermined system of equations, and we can solve for the horizontal (N-S and E-W) and vertical components of deformation. Given the measured displacement and the satellites' LOS vectors, we perform a least squares inversion and decompose the 3D displacement field (see Figure 2). Each dataset was weighted equally in the inversion, which assumes similar accuracy for all measurements. InSAR has a higher accuracy than the other datasets, but the equal weighting ensures that contributions from the pixel offsets and MAI, such as displacement along the satellite azimuth, are not under-prioritized in the 3D decomposition (Grandin et al., 2018).

2.5 Co-eruptive displacement field description

The ascending and descending interferograms measure, respectively, up to 1.5 and 1 meters of line-of-sight (LOS) shortening (movement towards the satellite). This discrepancy indicates that horizontal displacements contribute to the LOS measurements. The cross-sections in Figure 2 display the ratio of vertical to horizontal motion. In addition to horizontal motion, we emphasize three notable characteristics of the co-eruptive 3D displacement field:

1. There exists a N-S asymmetry and discontinuity across the eruptive fissures in all components (see Figure 2, Profile A-A'). The maximum LOS shortening is located just to the south of the main fissure, and this signal is most likely associated with the dike intrusion feeding the eruption. The ratio of subsidence to the north of the fissures compared to uplift to the south implies a dike dipping towards the SW.

2. There is also an E-W asymmetry in the western portion of the caldera, across a region that follows the caldera rim, and is incoherent and discontinuous in the interferograms (see Figure 2, Profile B-B'). This asymmetry is observed in all components. The ratio of horizontal to vertical displacement indicates that this signal may be attributed to normal slip on a portion of the caldera ring-fault. As measured by CSK pixel offsets, this displacement occurred before 6:00 UTC on 21 February, during the onset of the eruption (Fig. S3).
3. The 3D displacement field also estimates >20 cm of subsidence in the coherent region to the NW of the dike, beneath Marum crater (see *3D Decomposition*, Figure 2). The ascending interferogram shows ~ 24 cm (2 fringes) of LOS lengthening in the northern portion of the caldera, following the northeastern caldera rim. However, this vegetated portion of the caldera is incoherent in the descending interferogram, limiting the ability to exploit two independent measurements to confirm whether these fringes are attributed to ground displacement or atmospheric effects. This signal, confined to within the caldera, is reminiscent of deformation which occurred in the month following the 2018 rift zone intrusion. The 2018-2019 deformation was modelled by a shallow (4-5 km depth) decompressing sill (Shreve et al., 2019).

3 Inversion of Deformation Sources

The displacement field's complexity hints at contributions from multiple sources. Geodetic modelling of volcanic deformation often capitalizes on computationally efficient analytical solutions to describe displacement due to pressure sources (Mogi, 1958), as well as shear or tensile dislocations (Okada, 1985). When multiple sources are involved, the displacement fields produced by each of these sources in an elastic, homogeneous medium are added linearly. Any mechanical interaction, or stress transfer, between the sources is implicitly neglected.

Given the hypothesis that multiple sources are at play during this eruption, and the geological complexity of caldera systems (pre-existing weaknesses and faults due to caldera collapse (Acocella, 2007)), we choose to proceed with a numerical method, the Mixed Boundary Element Method (BEM) (Cayol & Cornet, 1997, 1998). This method calculates the surface displacement due to pressure changes within massive boundaries or within fractures with complex geometries (curvature, dip, etc.), as well as calculates the mechanical interaction between all modelled sources, which influence the final surface displacements. By combining the Mixed BEM forward models with a non-linear inversion, we are able to estimate the sources' geometries, while simultaneously inverting for a uniform stress change on the structures (i.e. pressure or shear stress changes).

3.1 Data subsampling and covariance matrix

To compare modelled and measured surface displacements, measurements must first be subsampled to include a reasonable number of datapoints in the inversion, while still retaining enough information to robustly estimate the relevant model parameters. We

include and subsample both the ascending and descending InSAR measurements in the inversion. SAR pixel offsets are not included due to their low signal-to-noise ratio, however, we project modelled surface displacements into the LOS for all available datasets a posteriori (Fig. S4). The data is subsampled using an adaptive quadtree decomposition algorithm (Walstead, 1999; Jónsson et al., 2002), as described in the Supporting Information Text S5, Table S4 and Figure S5.

Displacement values at subsampled points may be spatially correlated due to phase contributions from atmospheric, ionospheric, or other noise sources (Sudhaus & Jónsson, 2009). To account for this spatially-correlated noise in the interferometric phase, the correlation distance and data variance are used to populate a data covariance matrix, according to $C_d(k_1, k_2) = \sigma_d^2 \cdot \exp(-\frac{\|k_1, k_2\|}{a})$, where σ_d^2 is the variance, a is the correlation length, and $\|k_1, k_2\|$ is the Euclidian distance between two subsampled pixels $k_1 = (x_1, y_1)$, and $k_2 = (x_2, y_2)$ (Tarantola, 1987). The data covariance matrix thus weights the data in the inversion, taking into account the correlated noise between two pixels that may be spatially correlated over wavelengths of up to $5a$ (Smittarello et al., 2019). According to Fukushima et al. (2005), reasonable values for $\sigma_d^2 = 3 \times 10^{-4} \text{ m}^2$ and $a = 330 \text{ m}$. Similarly to these authors, we found that varying these values did not result in significant changes to the inversion results (Fig. S6).

3.2 Mixed Boundary Element Method

As previously mentioned, we estimate the geometry and stress change of multiple pressure sources with a 3D Mixed BEM numerical approach (Cayol & Cornet, 1997, 1998). In the Mixed BEM forward calculation, boundary conditions are the traction-free topography and uniform pressure changes on either surfaces (tensile cracks or shear fractures) or massive boundaries (reservoirs or the ground surface). Triangular elements are used to discretize all boundaries. The surface topography is derived from a 12 m resolution TanDEM-X DEM (Fig. S7a) (Wessel, 2016). Stress changes can either be imposed on the meshed triangular elements of the fractures or massive boundaries, or result from stress transfer from nearby sources, or both.

The Mixed BEM combines the displacement discontinuity and direct displacement methods (Lachat & Watson, 1976; Sokolnikoff, 1956; Crouch, 1976). A description of these methods can be found in the Supporting Information Text S6. Nine parameters control the fracture geometry (Fig. S8) (Fukushima et al., 2010). The fractures are connected to the topography mesh by user-defined echelons at the surface. While the location of the echelon has a degree of uncertainty, we use high-resolution optical satellite imagery from the Pléiades constellation to map the fissures that opened during the eruption (see Figure 1d). For the caldera ring-fault, the surface trace is determined using the SAR pixel offsets, in conjunction with identifying the incoherent regions in the InSAR measurements.

Displacements and stresses are discretized and interpolated on the boundaries. Thus, the more refined the mesh, the more precise the solutions. There is a tradeoff between accuracy and computational efficiency of the forward model, controlled by the number of meshed elements used to represent the topography (see Figure S7b for a plot of model

run duration versus accuracy). In order to have a reasonable accuracy versus precision balance, the mesh is finer close to the echelons, where displacement is largest, and coarser in the far-field, where little-to-no displacement is measured (Fig. S7a). A Young’s modulus of 5 GPa and a Poisson’s ratio of 0.25 are chosen, consistent with in-situ measurements and depth of the inverted structures (Cayol & Cornet, 1998) and confirmed by laboratory measurements (Heap et al., 2019).

3.3 Non-linear inversion: Neighborhood algorithm

The stress change and geometry of the fractures or reservoirs are inverted using a neighborhood algorithm (Sambridge, 1999b; Fukushima et al., 2005). An initial exploration of the parameter space picks NS_1 random combinations of the inverted parameters (Sambridge, 1998; Tridon et al., 2016). According to Tridon et al. (2016), NS_1 is determined based on an exponential function which corresponds to the number of natural neighbors (Sambridge, 1998), which is a function of the number of inverted parameters, k , such that $NS_1 = 9.775 \cdot e^{0.457 \cdot k}$. Each subsequent iteration picks NS_2 combinations of parameters, searching within the multi-dimensional Voronoi cells (nearest neighbor regions) with the lowest misfit in the previous iteration. Assuming the algorithm converges, a large NS_2 results in a more explorative search, while a small NS_2 results in a more exploitative search. Typically, NS_2 is taken to be 48, because it was found to be a reasonable compromise by Fukushima et al. (2005).

The misfit is defined as $\chi^2(m) = (u_o - u_m)^T C_d^{-1} (u_o - u_m)$, where u_o is the data, u_m is the modelled displacements, and C_d is the data covariance matrix, as defined in Section 3.1. This iterative procedure continues until a threshold criterion, σ_{NLST} , based on the standard deviation of the misfit values from the last $NLST$ forward calculations (we set $NLST = NS_2$) is reached. Alternatively, the search can be terminated based on a pre-defined total number of iterations NIT . We terminate Inversion 3 after 1500 iterations. Even though the standard deviation threshold has not been reached, the estimated parameters are well-constrained (Fig. 4a). To calculate posterior probability density functions (PPD’s), marginal PPD’s, mean model parameters, and model uncertainties, we follow the bayesian inference framework (Tarantola, 1987) described in Sambridge (1999a) and implemented by Fukushima et al. (2005) (Supporting Information Text S7).

The inversion procedure inverts for a phase constant, but does not invert for ramp parameters in the InSAR data that may be due to residual orbital errors (Zebker et al., 1994). However, this does not effect the final geometry of the source, although it does slightly bias the estimated volume change. Figure S9 shows the results of an inversion with a deramped ascending interferogram (the only dataset with a far-field large enough to estimate the orbital ramp), to demonstrate the source geometry’s insensitivity to this parameter.

3.4 Final inversions

Using the inversion scheme outlined in Section 3.3, we run three inversions of increasing complexity to test the necessity of adding multiple deformation sources. The

number of non-linearly inverted free parameters and number of forward models for each inversion are listed in Table 1. In order to justify increasing complexity (i.e. adding a new source), we can calculate the Akaike Information Criterion for each inversion, defined as $AIC = 2k + \chi^2 + \log |C_d| + N \times \log(2\pi)$, where k is the number of inverted parameters, χ^2 is the misfit, $|C_d|$ is the determinant of the data covariance matrix, and N is the number of data points (Akaike, 1974). The most likely models correspond to the lowest AIC. In each inversion, we use the same subsampled datasets and data covariance matrix from Section 3.1. Therefore, to compare the AIC of inversions, we can simply compare $AIC = 2k + \chi^2$. Changing the values of σ^2 and λ for the C_d creation will change the value of χ^2 and the relative influence of the number of parameters in the final AIC value, but does not change the dike geometry or volume significantly (Fig. S6). In our case, when increasing the number of parameters, the decrease of the misfit largely counterbalances this increase, resulting in the AIC being equivalent to the misfit.

3.4.1 *Dike (Inversion 1)*

According to (1) in Section 2.5, the N-S asymmetry across the eruptive fissure implies a dike dipping towards the SW. The first inversion inverts non-linearly for the 9 dike geometry parameters and for the pressure change. The echelons are fixed at the surface, using mapping of eruptive fissures from optical satellite imagery, as described previously. To avoid inverting for pressure as a linear parameter, the modelled surface displacements are scaled by a constant to find the pressure change that best fits the data. The best-fit model, as well as data, synthetics and residuals, are shown in Figure 3. The mean model, with 95% uncertainty intervals, are listed in the Supporting Information for all inversions (Table S5). The best-fit model dike is submitted to a scaled pressure change of $\Delta P = 2.9$ MPa and the total scaled volume change is $\Delta V = 3.0 \times 10^7$ m³. When the ramp is removed from the ascending interferogram, $\Delta P = 2.2$ MPa and $\Delta V = 2.7 \times 10^7$ m³ (Fig. S9).

3.4.2 *Dike and fault (Inversion 2)*

The residuals from Inversion 1 reflect more than 20 cm of unexplained displacement in the western portion of the caldera, corresponding to the signal discussed in (2) in Section 2.5. The second inversion includes both a dike, as well as a frictionless fault, whose top edge is predefined and intersects the topography mesh. We invert for 3 additional parameters— the dip, bottom edge depth, and uniform shear stress change (normal fault motion) on the fault plane. To reduce the number of non-linearly inverted parameters, and ensure computational feasibility, we do not invert the angle of the bottom edge of the fault, the twist, shear, or any curvature (see Fukushima et al. (2010) for a description of these parameters). We justify this simplification because analogue and numerical models have found caldera ring-faults to be straight at depth (Beauducel et al., 2004; Gudmundsson et al., 2016; Liu et al., 2019). We only include the portion of the fault that we hypothesize was activated in 2015.

Because the fault and dike orientations are perpendicular, pressurization of the dike results in closing (fracture wall interpenetration) on some sections of the fault plane (Fig. S10). We impose a nonnegativity constraint to avoid fracture wall interpenetration and thus ensuring a geologically realistic model. This nonnegativity constraint is enforced in the Mixed BEM through Lagrange multipliers, as described in Cayol et al. (2014) (from hereon we call this constraint “preventing interpenetration”). Inversions have also been run without imposing this nonnegativity constraint, and the comparison between the resulting misfits and inversion durations is shown in Figure 3b. We remark that the misfit improves when the nonnegativity constraint is imposed.

The best-fit model, along with the dike opening and fault shear distributions, is shown in Figure S11. The dike’s scaled pressure change is 2.4 MPa, the dike’s total scaled volume change is $\Delta V = 2.6 \times 10^7 \text{ m}^3$, the fault’s shear stress change is -0.26 MPa, and the fault’s average slip is 0.5 m.

3.4.3 *Dike, fault and reservoir (Inversion 3)*

The misfit is significantly improved in Inversion 2 compared to Inversion 1 (Table 1 and Figure 3b). However, there remain long-wavelength residuals postulated to result from reservoir decompression, with a similar spatial footprint to the caldera floor subsidence measured after the Ambrym 2018 rift zone intrusion (see (3) in Section 2.5). Therefore, a final inversion includes a reservoir approximating a thin (semi-minor axis of 2.5 m), horizontal, oblate spheroid structure, whose location (beneath Marum crater, at 168.12°E , 16.25°S) and depth (4.1 km b.s.l) are fixed according to the post-intrusion deflation source estimated in Shreve et al. (2019). Again, we invert for normal and shear stress changes on the dike and fault as non-linear parameters. We approximate the reservoir as a thin oblate spheroid as opposed to a horizontal fracture because the nonnegativity constraint restricts closing on all fractures in the inversion. Instead of closing of a horizontal fracture, we impose an internal negative pressure change within a massive boundary. The reservoir volume V and change in pressure ΔP are inversely proportional (Amoruso & Crescentini, 2009), resulting in the high ΔP obtained by the inversion given the thin reservoir. After running Mixed BEM computations for spheroids with various thicknesses, we find that the difference in both the surface displacement and the source volume change are negligible as long as the spheroid remains “thin” (with a ratio of semi-minor c to semi-major axis $a = b$, $\frac{c}{a} < 0.05$).

We invert for the same parameters as Inversion 2, as well as the reservoir radius (assuming it is axisymmetric) and internal pressure change. The best-fit model of Inversion 3 is shown in Figure 3, the marginal PPD’s are shown in Figure 4a, and the slip and opening distribution of the sources is shown in Figure 4b. Pressure change (scaled) of the best-fit model dike is 2.9 MPa, the total scaled volume change of the dike is $\Delta V = 2.9 \times 10^7 \text{ m}^3$, the total scaled volume change of the reservoir is $\Delta V = -1.3 \times 10^7 \text{ m}^3$, and the average closing on the reservoir is -1.5 m. The fault’s shear stress change is -0.13 MPa and the average slip on the fault is 0.6 m. Fault slip reaches one meter at depth, close to the reservoir.

Deformation sources	Number of free parameters inverted non-linearly	Number of total forward models (NS1/NS2/NIT)	Misfit (prevent interpenetration)	Convergence criteria
Dike	10	1440/48/478	20669	Standard Deviation (0.5)
Dike and fault	13	9600/48/1304	17224	Standard Deviation (0.5)
Dike, fault, and reservoir	15	9600/48/1500	14146	Maximum Iterations (1500)

[h]

Table 1. The number of free parameters, number of total forward models, misfit, and convergence criterion for each of the inversion runs.

3.4.4 *Inversion comparisons*

We note that the final dike geometries diverge primarily at depth (Fig. 3), due at least in part to the lack of sensitivity of the surface displacement to pressure changes from deep sources (Du et al., 1992). The misfit (and AIC), however, improves when adding additional sources, emphasizing that the surface displacements may result from the combination of these three sources.

The mean fault dip estimated in both Inversion 2 and 3 are within a few degrees, however, the dip tends towards a shallower value. We decide to constrain the minimum dip to 65° based on numerical and analogue modelling, as well as geological observations, of steep, inward-dipping normal caldera-ring faults for calderas with low aspect ratios (ratio of chamber depth to width of caldera surface expression) (Roche et al. (2001) and references within). In extreme cases, caldera sagging can result in material slumping along shallowly-dipping normal detachments formed within the footwall of steeper normal faults (Holohan et al., 2011), but whether or not this case is relevant for Ambrym is not constrained in this study and would need to be investigated further.

The depth of the fault’s bottom edge also reaches the limits of the parameter search space. However, we fix the maximum depth at 4 km b.s.l to ensure that there is no interaction between intersecting elements of the fault plane and the reservoir. We acknowledge that the similarities between the fault dip and depth for Inversions 2 and 3 may be artificially imposed by the parameter limits.

The total volume change in the dike varies between 2.6 and $3.0 \times 10^7 \text{ m}^3$ for the three inversions. All estimates and uncertainties for pressure changes, shear stress changes, total volume changes, and maximum and average slip values can be found in the Table S5 and Table S6.

4 Discussion

4.1 Reservoir decompression– not diking– induces faulting

In Section 3.4, we note that Inversion 3 has the lowest misfit (or AIC), indicating that it is the most likely source configuration. We conclude that contributions from three sources– a dike intrusion, caldera ring-fault, and reservoir– best fit the data. However, the misfit value relies solely on the data fit and data covariance matrix, without incorporating information about stress interactions between the various sources. In order to provide a complementary justification of our choice of the best-fit model, we now discuss whether this configuration of three deformation sources is mechanically consistent.

In Inversion 2, we invert for shear stress change on the caldera ring-fault in order to fit the surface displacements. In reality, an external stress perturbation must generate this shear stress change. Static stress transfer from the dike is the most obvious source of perturbation. In the context of rifting events, for example, stress transfer from an inflating dike has been invoked as the mechanism that explains normal faulting and graben subsidence, with normal faults slipping either above the dike or ahead of the dike’s prop-

agation path, as these are the locations that do not undergo dike-induced compression (Rubin & Pollard, 1988; Grandin et al., 2009). In the context of a caldera, to test if stress perturbations due to dike opening promote normal caldera ring-faulting, we calculate the Coulomb stress change on the fault plane (King et al., 1994; Lin & Stein, 2004). The Coulomb stress change is calculated by $\tau_{CSC} = \tau + \mu'\sigma$, where τ is the shear stress change, σ is the normal stress change (positive is unclamping), and μ' is the effective friction coefficient, where $\mu' = \mu(1 - B)$. B is Skempton's coefficient, which relates pore pressure to confining stress, and we set $\mu' = 0.4$, approximated from laboratory values (Nostro et al., 1998). A positive τ_{CSC} indicates that the stress perturbation promotes fault failure. Because we have no information regarding the initial stress state, Coulomb stress change calculations can only be used to estimate if the fault has been brought closer to failure, not if the yield strength has been reached.

We calculate the Coulomb stress change in 3D, having a direction of shear stress consistent with families of normal dip-slip faults, parallel to those estimated in the inversions. The source geometries are fixed based on the results of Inversions 2 and 3. The normal and shear stress changes due to a pressurized dike are computed using the Mixed BEM. For each fault mesh element i , the strike, dip, normal and shear stress change are used to calculate $\tau_{CSC,i}$. The first row in Figure 5 shows the Coulomb stress change on each element of the fault from Inversion 2. We find that the dike opening prohibits normal dip-slip at the fault's southern end, where surface displacements are dominated by compression perpendicular to the dike plane (Rubin & Pollard, 1988). Normal dip-slip is also prohibited at depth. The Coulomb stress change calculation from Inversion 2 has a slight increase in the northern portion of the fault, where InSAR measures more than 20 cm of surface displacement. We then calculate the Coulomb stress change from Inversion 3, when the stress perturbation results from a combination of a pressurized dike and a decompressing reservoir. There is a positive Coulomb stress change at the fault's north end, both at the surface and at depth, which promotes normal fault failure.

Numerical modelling has shown that the stress field of a caldera is complex, influenced by the combination of regional tectonic stresses, edifice loading, unloading due to caldera formation, and other sources of local stresses (Buck et al., 2006; Pinel & Jaupart, 2000; Corbi et al., 2015). Given the unknown initial stress state of the caldera, we cannot discount the possibility that the fault was brought closer to failure due to stress transfer from only the dike intrusion, given the slight CSC increase. However, the Coulomb stress change calculations indicate that it is more likely that fault activation was caused by the reservoir's decompression as it fed the dike intrusion and fissure eruption, rather than by stress transfer from the dike intrusion itself.

Nevertheless, stress transfer from the decompressing reservoir alone is not sufficient to explain the magnitude of fault slip resulting in the measured surface displacements. The stress transfer reaches a maximum value of 0.5 MPa on the fault (Fig. 5). In Inversion 3, we accordingly invert for an additional shear stress change on the fault. This initial shear stress change may result from the accumulation of previous reservoir decompression events, and the stress transfer from the dike and reservoir during the 2015 eruption brought the fault to its failure threshold. The fault's inverted mean shear stress change

decreases from -0.26 MPa in Inversion 2 to -0.13 MPa in Inversion 3, a change of 50% (see Figure 5). In other words, in Inversion 3, less initial stress is required to produce the observed slip on the caldera fault, due to the stress transfer from the decompressing reservoir.

In Inversion 3, the initial shear stress is -0.13 MPa, which is equivalent to the shear stress transferred by the reservoir. We hypothesize that each fissure eruption and reservoir decompression event of this size may induce ~ -0.13 MPa of shear stress on the fault. If this were the case, a second fissure eruption of similar size, such as the eruption that occurred in 1988-1989 (Fig. 1c), may have sufficed to generate the stress accumulation necessary to prime fault slip during the 2015 eruption.

4.2 Critical threshold for ring-fault activation

4.2.1 *The influence of caldera roof aspect ratio*

Caldera ring-faults are formed during caldera collapse. In basaltic systems, calderas develop due to lateral magma propagation which drains a central plumbing system, activating caldera ring-faults and resulting in gradual collapse of the caldera (Sigmundsson, 2019). The plumbing system's geometry influences the critical fraction of magma needed to trigger collapse (defined as $f_{crit} = \frac{-\Delta q_f}{V}$, where Δq_f is the magma extraction volume and V is the reservoir volume). Analytical, analogue, and numerical models conclude that thresholds are lower for shallower, broader calderas (low roof aspect ratios, $R_a = \frac{h}{2r}$, where h is reservoir depth and r is the reservoir radius) (Roche et al., 2000; Geshi et al., 2014; Holohan et al., 2011). Studies of caldera collapse events at Kilauea, Piton de la Fournaise, Fernandina, Miyakejima, and Bárðarbunga conclude that f_{crit} calculated from observations is smaller than estimated from analogue modelling. Recent studies concerning the best-documented basaltic caldera collapse, the Kilauea caldera collapse in 2018, emphasize the importance of moving beyond f_{crit} . Because the initial stress state is unknown, it is important to estimate reservoir pressure change before collapse in order to physically explain the caldera roof failure due to stresses imparted upon it (K. R. Anderson et al., 2019).

The caldera ring-faulting event at Ambrym, although not a full-scale caldera collapse event, allows us to draw bounds on the minimum reservoir depressurization needed to trigger caldera ring-faulting at a broad, shallow basaltic caldera. Ambrym has an especially low roof aspect ratio, estimated by comparing the depth of the main decompressing deformation source in 2018 and the width of the caldera surface expression. Based on estimates from Shreve et al. (2019); Hamling et al. (2019), R_a at Ambrym may be lower than 0.4.

4.2.2 *Pressure change bounds and minimum reservoir volume*

Using the Mixed BEM, we adjust the reservoir dimensions to establish bounds on V and ΔP , after fixing the shear modulus μ (here we have $\mu = 2$ GPa). These bounds

will allow us to estimate magma compressibility and constrain f , which we here define as the critical fraction of magma needed to trigger fault slip.

Given the tradeoff between ΔP and V , we set the semi-minor axis of the reservoir geometry found in Inversion 3 to values that range between 2.5 m and 750 m. We then adjust ΔP to ensure the forward Mixed BEM calculation results in a surface displacement that is within 2% error of the displacement field from Inversion 3 (Fig. S12). As the reservoir becomes more spherical ($c \rightarrow a$), the ratio of vertical to horizontal displacements decreases (Lisowski, 2006), inconsistent with the best-fit model’s displacement field. A sill-like reservoir ($a \gg c$) is consistent with caldera floor subsidence measured after Ambrym’s 2018 rift zone intrusion (Shreve et al., 2019). This 2018 post-intrusion signal was modelled by a rectangular tensile dislocation (Okada, 1985), as opposed to a spherical point source (Mogi, 1958).

To obtain pressures within the tensile strength of the rock (conservative estimates being $\sim 1 - 50$ MPa based on Sparks (1997); K. Anderson and Segall (2013); Delgado et al. (2019)), c has to range from 50 to 750 m, resulting in ΔP ranging between -11.1 and -16.8 MPa, and the corresponding V ranging from 0.2 to 3 km³. Given this ΔP range, ΔV varies by less than 7%, from -1.18 to -1.25×10^7 m³. Although the estimated V ranges over one order of magnitude, from 0.2 to 3 km³, we note that Allard et al. (2015) estimates Ambrym’s *minimum* reservoir volume to be 0.5 km³. Allard et al. (2015) estimates this volume by first calculating a magma residence time τ of 240 days, using a model similar to Gauthier et al. (2000) based on measurements of radionuclide ²¹⁰Po, ²¹⁰Bi, and ²¹⁰Pb fluxes and activity ratios. This model assumes that radionuclides are in radioactive equilibrium when they are dissolved in melt stored in the deeper magma reservoir, and remain in radioactive equilibrium until the melt is degassed. This degassed melt is then either recycled, intruded or erupted. Then, Allard et al. (2015) multiplies the magma residence time by the estimated magma influx Φ_0 of 2.2×10^6 m³ day⁻¹ into the shallow magma reservoir, which sustains the measured SO₂ flux. The minimum shallow magma reservoir size is thus $V = \tau \cdot \Phi_0 = 0.5$ km³.

This value is a minimum estimate of the total magma stored in Ambrym’s plumbing system. If magma is not intruded or erupted during its residence in the shallow magma chamber, according to Allard et al. (2015); Gauthier et al. (2000), it must be recycled into a deeper magmatic system. To find a maximum estimate of V based on passive degassing estimates from Carn et al. (2017), we neglect magma recycling into a deeper magmatic system, and assume the entire magmatic system contributes to degassing over a period of ~ 10 years, the time period of the Carn et al. (2017) study. Given 7 kt day⁻¹ of SO₂ degassing, if we perform the same calculation as in Section 1.2, we obtain a volume of degassed magma of $V \approx 6$ km³, without taking into account the effects of magma compressibility. Therefore, the independent bounds obtained from SO₂ flux, radioactive equilibria, and geodetic modelling have significant overlap. In addition, estimates for the reservoir volume change during the 2018 rift zone intrusion lie between 0.3 and 0.7 km³ (Shreve et al., 2019; Hamling et al., 2019). If we assume that the reservoir volume change was 0.7 km³ in 2018 and that the entire reservoir did not drained, we conclude that the

shallowest compartment of Ambrym’s reservoir (i.e. the portion that contributes to feeding lava lake activity and degassing) has a minimum size of 1 – 3 km³.

More than 0.4 km³ of magma migrated into the rift zone in 2018, emphasizing the large size of the entire magmatic system, but this intrusion was most likely fed from multiple storage zones beneath the caldera. We hypothesize that the reservoir tapped during the 2015 dike intrusion is a liquid lens within a trans-crustal magmatic system, which hosts both magma lenses and regions of uneruptible crustal-rich mush (Edmonds et al., 2019). The bounds on V should therefore be taken as a minimum of the total amount of magma stored within Ambrym’s plumbing system.

4.2.3 Magma compressibility estimate

By comparing the ratio of reservoir volume change to the volume of intruded material, r_v , we can estimate to the first-order the magma compressibility (Rivalta & Segall, 2008; Rivalta, 2010). Magma compressibility is one factor that contributes to the discrepancy between estimates of reservoir volume change and the amount of magma extracted from the reservoir (Johnson et al., 2000). Rivalta and Segall (2008); Rivalta (2010) derived the generic formula for r_v based on chamber compressibility β_c and magma compressibility β_m , such that

$$r_v = \frac{\Delta V_s}{\Delta V_c} = 1 + \frac{\beta_m}{\beta_c}, \quad (1)$$

where ΔV_s and ΔV_c are the volume change in the sink (dike) and reservoir, respectively. β_c expresses how the host rock responds elastically to pressure change, $\beta_c = \frac{1}{V} \frac{dV}{dP}$, while β_m defines the relationship between magmatic pressure change and density change, $\beta_m = \frac{1}{\rho} \frac{\partial \rho}{\partial p}$. The relationship in Equation 1 can be expressed analytically for end-member reservoir shapes (penny-shaped sills ($a = b \gg c$), spheres ($a = b = c$), and vertical pipes ($a \gg b = c$))(Amoruso & Crescentini, 2009), and K. Anderson and Segall (2011) interpolated these estimations using finite element calculations for intermediate aspect ratios.

The reservoir that drained during the 2015 Ambrym eruption has an aspect ratio $\frac{c}{a}$ that ranges from 0.05–0.75 when imposing reasonable bounds on ΔP . We calculate chamber compressibility using analytical expressions (Amoruso & Crescentini, 2009), extrapolations of these expressions using finite element calculations (K. Anderson & Segall, 2011), and the Boundary Element Method. We confirm that the chamber compressibility ranges derived from these methods are comparable. Using the analytical expressions derived in Amoruso and Crescentini (2009), when $a = b \gg c$, the following equation can be used to calculate chamber compressibility

$$\beta_c = \frac{3}{\mu} \left(\frac{a}{c} \frac{1}{2\pi} - \frac{1}{5} \right). \quad (2)$$

Although Equation 2 fails for shallow penny-shaped sills (K. Anderson & Segall, 2011), the “medium” depth (4-5 km b.s.l) of Ambrym’s reservoir allows us to reasonably approximate β_c using this expression for the aspect ratio lower-bounds. For the upper-bounds, chamber compressibility can, when aspect ratios range between ~ 0.6 - 10, be approximated as for a sphere ($\beta_c = \frac{3}{4\mu}$) within 25% error, as shown in K. Anderson and Segall

(2011). Using Equation 2, it follows that β_c ranges from $3.8 \times 10^{-10} - 4.5 \times 10^{-9} \text{ Pa}^{-1}$. The lower-bounds are based on a spheroidal geometry, and the upper-bounds are based on an assumption of a penny shaped sill with an aspect ratio of 0.05. We confirm these analytical approximations by calculating β_c using the Boundary Element Method. β_c in this case ranges from $3.9 \times 10^{-10} - 3.1 \times 10^{-9}$. The differences between the analytical and the computational values are consistent with K. Anderson and Segall (2011), and we will proceed with the discussion using the latter range of values.

As mentioned in Section 2.5, the reservoir deflation and caldera ring-fault activation occurred before the end of the eruption, so the propagating dike had a larger volume than the modelled intrusion volume ΔV_s arrested at depth. Wauthier et al. (2015) derived an equation to include both erupted and intruded volumes in estimates of r_v , and concluded that, in the case when the erupted volume V_e accounts for 90% of the total volume, the erupted volume only contributes to 5% of the total r_v value. However, during the Ambrym 2015 eruption, V_e accounts for <40% of the total magma volume. Therefore, we choose to neglect the emitted lava.

Our estimate of r_v will be an underestimate, as it does not include the erupted volume. From Equation 1, given the modelled value of $r_v \approx 2.2$ (implying $\beta_m \approx \beta_c$) from Inversion 3, we obtain a magma compressibility that ranges from $4.7 \times 10^{-10} - 3.7 \times 10^{-9} \text{ Pa}^{-1}$. Although spanning one order of magnitude, we can conclude that this value is higher than that for degassed basalts (Rivalta & Segall, 2008). This magma compressibility estimate is consistent with recent studies of the Ambrym 2015 eruption, which hypothesize that Ambrym’s shallow reservoir was pressurized due to bubble nucleation and growth (Hamling & Kilgour, 2020). The existence of gas bubbles within the chamber may explain the relatively high magma compressibility.

Estimates of magma compressibility at Kilauea during the 2018 lava lake drainage and rift zone eruption ranged from $2 \times 10^{-10} - 9 \times 10^{-10} \text{ Pa}^{-1}$, also higher than values estimated assuming gas-poor basalt (K. R. Anderson et al., 2019). K. R. Anderson et al. (2019) concludes that this may indicate the presence of bubbles in the reservoir, even though the value of β_m relies strongly on prior estimates of the shear modulus μ and $R = \frac{\beta_m}{\beta_c}$. Similarly, at Erta Ale, another volcano which hosts a lava lake, no significant cumulative post-intrusion subsidence was measured after the 2017 intrusion, indicating either highly compressible magma or magma fed from a deep source (Moore et al., 2019). The observations listed above regarding high compressibility magma at Ambrym, Kilauea, and Erta Ale need to be investigated in more detail before further conclusions can be drawn regarding magma compressibility at volcanoes hosting active lava lakes.

An alternative explanation for the discrepancy between the ΔV_s and ΔV_c is magma recharge of the plumbing system. However, even after the 2018 eruption, no post-eruptive uplift related to magmatic recharge was measured, despite SAR acquisitions every 6 days (Shreve et al., 2019). In addition, the caldera floor subsided in the months following the 2015 eruption, as measured with both ALOS-2 and Sentinel-1 (Fig. S13).

4.2.4 *Minimum depressurization and critical fractions for caldera ring-fault activation*

Given the estimated β_c , V , ΔP , and ΔV , we determine the critical volume fraction needed to trigger caldera ring faulting. Only the western portion of the caldera ring-fault is activated, because the drained reservoir during the February 2015 event is located beneath the active vents and lava lakes, and this is thus where the largest stress transfer occurred onto the ring-fault. In the 2018 rift zone intrusion and reservoir drainage event, the northern portion of the caldera ring-fault was activated, possibly due to withdrawal of a larger quantity of magma from a more central storage area within Ambrym’s magmatic system (Shreve et al., 2019; Hamling et al., 2019). We hypothesize, given the conclusion drawn in Section 4, that a reservoir drainage events (1988-1989) occurred before the caldera ring fault was activated in 2015. We will therefore assume that the estimated ΔV and ΔP values need to be doubled in order to account for this event, and the event in 2015. We further assume that magma compressibility does not vary with time, which may not be the case due to possible changes in magma volatile content over the past few decades.

We assume a volume of reservoir change $-\Delta V = 2.6 \times 10^7 \text{ m}^3$, a volume of extracted material $-\Delta q = 5.8 \times 10^7 \text{ m}^3$, a ΔP from -22.2 to -33.6 MPa, and a reasonable range of reservoir volumes from 1–3 km³. The critical fraction $V_{crit} = \frac{-\Delta V}{V}$ thus ranges from 0.9–2.6%, and after taking into account the compressibility of the system, the critical fraction $f = \frac{-\Delta q}{V}$ ranges from 1.9 – 5.8%. This range of values is consistent with the fraction of extracted material found in analogue models f_{exp} for the onset of fracture formation at the surface. Geyer et al. (2006) estimates that f_{exp} may be as low as 2% for calderas with the same roof aspect ratio as Ambrym ($r \sim 0.4$). This estimate for f , however, is an upper-bound, considering the total volume of stored magma at Ambrym may be significantly larger than the assumed reservoir volume range (see Section 4.2.2).

4.3 Co-eruptive gas emission

The magma compressibility estimate at Ambrym from Section 4.2.3 implies that the reservoir feeding the eruption was not fully degassed. Magma may instead be degassed at shallow levels through persistent lava lake activity. This is consistent with Allard et al. (2015), who concludes that Ambrym’s degassing occurs in a “closed system” (Edmonds, 2008). Bubbles and melt coexist in equilibrium in the reservoir and conduit until magma vesiculation has reached a threshold of 50%. Bubbles can then percolate and rise through the magma column independent of the speed of the rising melt. In the case of Ambrym, this threshold is reached when dissolved water has exsolved, causing degassing to occur at very shallow levels (~ 10 MPa, or < 0.5 km depth). This was concluded by Allard et al. (2015) from the H₂O-CO₂ evolution pattern at decreasing pressure steps. In addition, the CO₂ and H₂O mass degassed by the lava lakes is remarkably consistent with the difference between the H₂O and CO₂ wt % in the primitive magma and that of the degassed basalt. Any exsolved gas was in chemical equilibrium with the melt as it rose

from deeper levels to the surface. This degassing scheme—closed-system degassing at depth within the conduit, followed by open-system degassing at shallow levels—is also supported by observations at another lava lake-hosting volcano, Nyiragongo (Sawyer et al., 2008). Their conclusion is based on stable proportions of gases that exsolve at depth (CO_2 , SO_2 , and CO) on timescales ranging from seconds to months. On the other hand, SO_2 -HCl-HF compositions (HCl and HF are more soluble gases and exsolve at shallower depths) fluctuate on time scales of seconds to minutes (Sawyer et al., 2008).

“Closed system” degassing at Ambrym is consistent with the mass balance between the degassing during the eruption and the volume of erupted material. If the melt degasses at very shallow levels, we could assume that there would be no significant degassing through the dike. When comparing the degassed SO_2 mass, conservatively 40 kt, which is equivalent to a degassing of $9.5 \times 10^6 \text{ m}^3$ of lava, we indeed notice this is the same order of magnitude as the volume of erupted lava (see Section 1.2). Therefore, we conclude that none of the degassing during this eruption was related to degassing from deeper within the magmatic system, whether from the dike intrusion or the reservoir. This balance between the degassed sulfur mass and erupted lava volume has already been documented at other effusive volcanic eruptions (Barnie et al., 2016), yet this is not necessarily the case in explosive eruptions, as emphasized by the “excess” sulfur problem (Wallace, 2001; Kilbride et al., 2016).

4.4 Implications for basaltic caldera formation

The 2015 eruption at Ambrym is an example of caldera ring-fault activation during a moderate-sized eruption. It is possible that localized caldera subsidence may occur during moderate-sized eruptions, which occur on decadal time scales at Ambrym. Caldera-wide subsidence events, on the other hand, occur during rift zone intrusions, because they typically involve a greater volume of magma withdrawal (Shreve et al., 2019). According to Eissen et al. (1991), more than 10 rift zone eruptions have occurred at Ambrym in the past 120 years. Assuming fault slip values similar to the the amount measured during the 2018 rift zone intrusion, ~ 0.4 meters, this results in ~ 4 meters of fault slip in a little over 100 years. Assuming the time frame estimated by Robin et al. (1993) since caldera formation (~ 2000 years ago) and stability of Ambrym’s activity, we calculate almost 80 meters of fault slip related to reservoir drainage due to rift zone intrusions and eruptions. The largest subsidence events at Ambrym, which occur during rift zone intrusions, contribute the most to caldera development. As observed in 2018, a more laterally extensive and slightly deeper magma lens may be tapped during these events than the moderate-sized eruption in 2015. Better constraining the scaling relations between (1) intrusion size and frequency, and between (2) intrusion size and fault slip magnitude, would allow for determining whether incremental caldera subsidence is dominated by larger, rarer events, or by numerous, repeated, moderate events.

The cumulative subsidence due to these discrete subsidence events is non-negligible for a caldera of this diameter. This subsidence is comparable with the magnitude of the Bárðarbunga caldera collapse in 2014-2015, where the caldera floor deepened by ~ 65 me-

ters over the course of 6 months (Gudmundsson et al., 2016). However, the dynamics of these two collapse styles contrast, caused by differences in the stress change on the ring-faults during reservoir drainage events.

Ambrym and Bárðarbunga host two of the largest basaltic calderas on the planet, with 12 and 8 km diameters, respectively. The difference in their caldera collapse dynamics may be derived from the difference in the depth of the magmatic reservoir feeding lateral dike intrusions, ~ 4 km depth at Ambrym (Shreve et al., 2019) and >6 km depth at Bárðarbunga (Ágústsdóttir et al., 2019). This results in respective roof aspect ratios of <0.4 for Ambrym and ranging from 0.75–1.38 for Bárðarbunga. The threshold on pressure change or critical volume fraction activating caldera ring faults is smaller at Ambrym than at calderas with larger roof-aspect ratios. The lower the roof aspect ratio, the smaller the fault surface area, and the lower the reservoir depressurization needed for caldera ring-fault activation.

This may be further supported by deformation at Galápagos volcanoes that have broad and shallow systems, such as at Sierra Negra (Munro & Rowland, 1996). Previous studies have concluded that Sierra Negra’s reservoir may be a thin ellipsoid 0.4 km tall and 7 km wide at ~ 3 km depth, resulting in a roof aspect ratio of ~ 0.4 , similar to Ambrym (Amelung et al., 2000; S. Yun et al., 2006). Much attention has been given to the uplift episodes that cumulate in trap-door faulting along the intra-caldera sinuous ridge-fault system in the southwestern portion of the caldera. Little is known, however, about the caldera formation itself, which has been classified as a coherent “piston-type” collapse (Jónsson, 2009). Sierra Negra has hosted meter-scale co-eruptive subsidence events in both 2005 and 2018 (Geist et al., 2008; Abe et al., 2019). The magnitude of recent co-eruptive subsidence events— 5 and 8 meters, respectively— makes them difficult to study with InSAR (S. H. Yun et al., 2007; Casu et al., 2011), and there has been no modelling attempts to determine whether or not caldera ring-faults were activated during subsidence, separately from trap-door faulting along the sinuous ridge.

Future studies concerning subsidence during moderate-sized eruptions at broad mafic calderas, for example, in the Galápagos, Hawaii, or Iceland are needed to understand the role played by the depth, geometry, and size of the underlying magmatic plumbing system. An outstanding question is whether or not cumulative deformation over geologically significant time scales is net negative or positive. At Ambrym, over the short period of study (20 years), subsidence dominates caldera floor motion (cumulative maximum subsidence of >4 meters, including subsidence in 2018-2019 and post-eruptive subsidence in 2015, Fig. S13). In addition, geodetic measurements have observed only normal caldera ring-faulting associated with subsidence. However, many other volcanoes, such as those in the Galápagos, have cycles of pre-eruptive inflation and co-eruptive deflation, which may result in net uplift or no net displacement over longer periods of time (La Femina et al., 2019). It is possible that Ambrym may be an exceptional case where cumulative subsidence results in caldera deepening over hundreds of events, however, more extensive monitoring will be needed to confirm this hypothesis. Furthermore, little is known regarding the history of the construction of Ambrym’s shield volcano prior to the on-

set of caldera formation. Such knowledge is essential in order to compare Ambrym’s volcanic activity on geological (millennial) and geodetic (decadal) timescales.

5 Conclusion

The February 2015 dike intrusion, which resulted in more than 1 meter of surface uplift, was concomitant with the partial activation of Ambrym’s caldera ring-faults, inducing localized subsidence along the caldera rim. Using the Boundary Element Method, we conclude that the stress transfer from a decompressing reservoir most likely promoted ring-faulting. This hypothesis would have been challenging to address using inversions that do not take into consideration mechanical source interactions. By comparing the volume change in the dike and the reservoir, we estimate a magma compressibility at Ambrym that ranges from $4.7 \times 10^{-10} - 3.7 \times 10^{-9} \text{ Pa}^{-1}$. The critical fraction of extracted material to activate ring faults at Ambrym has an upper-bound ranging from $f = 1.9 - 5.8\%$, and a pressure change upper-bound ranging from $\Delta P = -22.2$ to -33.6 MPa , for a reservoir with a minimum volume ranging from $V = 1 - 3 \text{ km}^3$. It is possible that the value of f may be much lower, if we consider that the reservoir volume estimates do not take into consideration the complexity of an extensive, trans-crustal magmatic system. Continued geodetic monitoring of Ambrym, in conjunction with widespread observations at basaltic calderas around the world, will allow us to further constrain how moderate-sized eruptions contribute to basaltic caldera development.

Acknowledgments

We thank the Italian Space Agency (ASI Science project No 702) and the Japan Aerospace Exploration Agency (JAXA 6th Research Agreement No 3245) for providing access to the radar imagery used in this study. A part of ALOS-2 data was provided under a cooperative research contract between Geospatial Information Authority of Japan and JAXA. We thank Francisco Delgado, Marie Boichu, and Yves Moussallam for discussions which contributed to developing the ideas within this manuscript. Several calculations used the S-CAPAD cluster of IPGP. The ownership of ALOS-2 data belongs to JAXA. D. Smittarello, V. Cayol, and V. Pinel acknowledge the support of projet ANR-18-CE92-0037. M. Boichu kindly thanks Lieven Clarisse for providing the IASI SO₂ height data. This project has also received funding from the European Union’s Horizon 2020 research and innovation programme under the Marie Skłodowska-Curie grant agreement No 665850. The authors declare no conflict of interests. Data will be made available on an appropriate repository. This is IPGP contribution number XXXX.

References

- Abe, T., Ohki, M., & Tadono, T. (2019). Surface Changes Due to the 2018 Eruption of Sierra Negra Volcano in Galápagos Island Revealed by ALOS-2/PALSAR-2. *IGARSS 2019 - 2019 IEEE International Geoscience and Remote Sensing Symposium*, 9334–9337. doi: 10.1109/igarss.2019.8900424
- Acocella, V. (2007). Understanding caldera structure and development: An overview

- of analogue models compared to natural calderas. *Earth-Science Reviews*, 85(3-4), 125–160. doi: 10.1016/j.earscirev.2007.08.004
- Ágústsdóttir, T., Winder, T., Woods, J., White, R. S., Greenfield, T., & Brandsdóttir, B. (2019). Intense seismicity during the 2014-2015 Bárðarbunga-Holuhraun rifting event, Iceland, reveals the nature of dike-induced earthquakes and caldera collapse mechanisms. *Journal of Geophysical Research: Solid Earth*, 124(8), 8331–8357. doi: 10.1029/2018JB016010
- Akaike, H. (1974, December). A new look at the statistical model identification. *IEEE Transactions on Automatic Control*, 19(6), 716-723. doi: 10.1109/TAC.1974.1100705
- Allard, P., Aiuppa, A., Bani, P., Métrich, N., Bertagnini, A., Gauthier, P., ... Garaebiti, E. (2015). Prodigious emission rates and magma degassing budget of major, trace and radioactive volatile species from Ambrym basaltic volcano, Vanuatu island Arc. *Journal of Volcanology and Geothermal Research*, 304, 378 – 402. doi: 10.1016/j.jvolgeores.2015.08.022
- Amelung, F., Zebker, H., & Segall, P. (2000). Widespread uplift and ‘trapdoor’ faulting on Galapagos volcanoes observed with radar interferometry. *October*, 407(October), 993–996. doi: 10.1038/nature01526.1.
- Amoruso, A., & Crescentini, L. (2009). Shape and volume change of pressurized ellipsoidal cavities from deformation and seismic data. *Journal of Geophysical Research: Solid Earth*, 114(2), 1–8. doi: 10.1029/2008JB005946
- Anderson, K., & Segall, P. (2011). Physics-based models of ground deformation and extrusion rate at effusively erupting volcanoes. *Journal of Geophysical Research: Solid Earth*, 116(7), 1–20. doi: 10.1029/2010JB007939
- Anderson, K., & Segall, P. (2013). Bayesian inversion of data from effusive volcanic eruptions using physics-based models: Application to Mount St. Helens 2004-2008. *Journal of Geophysical Research: Solid Earth*, 118(5), 2017–2037. doi: 10.1002/jgrb.50169
- Anderson, K. R., Johanson, I. A., Patrick, M. R., Gu, M., Segall, P., Poland, M. P., ... Miklius, A. (2019). Magma reservoir failure and the onset of caldera collapse at Kāñlauea Volcano in 2018. *Science*, 366(6470). doi: 10.1126/science.aaz1822
- Bagnardi, M., González, P. J., & Hooper, A. (2016). High-resolution digital elevation model from tri-stereo Pleiades-1 satellite imagery for lava flow volume estimates at Fogo Volcano. *Geophysical Research Letters*, 43(12), 6267–6275. doi: 10.1002/2016GL069457
- Barnie, T. D., Keir, D., Hamling, I., Hofmann, B., Belachew, M., Carn, S., ... Wright, T. (2016). A multidisciplinary study of the final episode of the Manda Hararo dyke sequence, Ethiopia, and implications for trends in volcanism during the rifting cycle. *Geological Society, London, Special Publications*, 420(1), 149–163. doi: 10.1144/SP420.6
- Beauducel, F., De Natale, G., Obrizzo, F., & Pingue, F. (2004). 3-D modelling of Campi Flegrei ground deformations: Role of Caldera boundary discontinuities. *Pure and Applied Geophysics*, 161(7), 1329–1344. doi:

10.1007/s00024-004-2507-4

- Bechor, N. B., & Zebker, H. A. (2006). Measuring two-dimensional movements using a single InSAR pair. *Geophysical Research Letters*, *33*(16), 1–5. doi: 10.1029/2006GL026883
- Buck, W. R., Einarsson, P., & Brandsdóttir, B. (2006). Tectonic stress and magma chamber size as controls on dike propagation: Constraints from the 1975-1984 Krafla rifting episode. *Journal of Geophysical Research: Solid Earth*, *111*(12), 1–15. doi: 10.1029/2005JB003879
- Carn, S. A., Fioletov, V. E., Mclinden, C. A., Li, C., & Krotkov, N. A. (2017). A decade of global volcanic SO₂ emissions measured from space. *Scientific Reports*, *7*, 1–12. doi: 10.1038/srep44095
- Casu, F., Manconi, A., Pepe, A., & Lanari, R. (2011). Deformation time-series generation in areas characterized by large displacement dynamics: The SAR amplitude pixel-offset SBAS technique. *IEEE Transactions on Geoscience and Remote Sensing*, *49*(7), 2752–2763. doi: 10.1109/TGRS.2010.2104325
- Cayol, V., Catry, T., Michon, L., Chaput, M., Famin, V., Bodart, O., ... Romagnoli, C. (2014). Sheared sheet intrusions as mechanism for lateral flank displacement on basaltic volcanoes: Applications to Réunion Island volcanoes. *Journal of Geophysical Research: Solid Earth*, *119*.
- Cayol, V., & Cornet, F. H. (1997). 3D mixed boundary elements for elastostatic deformation field analysis. *International journal of rock mechanics and mining*, *34*(2), 275–287. doi: 10.1016/S0148-9062(96)00035-6
- Cayol, V., & Cornet, F. H. (1998). Three-dimensional modeling of the 1983-1984 eruption at Piton de la Fournaise Volcano, Réunion Island. *Journal of Geophysical Research*, *103*, 18,025–18,037.
- Clarisse, L., Coheur, P. F., Theys, N., Hurtmans, D., & Clerbaux, C. (2014). The 2011 Nabro eruption, a SO₂ plume height analysis using IASI measurements. *Atmospheric Chemistry and Physics*, *14*(6), 3095–3111. doi: 10.5194/acp-14-3095-2014
- Coppola, D., Laiolo, M., & Cigolini, C. (2016). Fifteen years of thermal activity at Vanuatu's volcanoes (2000 - 2015) revealed by MIROVA. *Journal of Volcanology and Geothermal Research*, *322*, 6–19. doi: 10.1016/j.jvolgeores.2015.11.005
- Coppola, D., Laiolo, M., Cigolini, C., Delle Donne, D., & Ripepe, M. (2016). Enhanced volcanic hot-spot detection using MODIS IR data: Results from the MIROVA system. *Geological Society Special Publication*, *426*(1), 181–205. doi: 10.1144/SP426.5
- Corbi, F., Rivalta, E., Pinel, V., Maccaferri, F., Bagnardi, M., & Acocella, V. (2015). How caldera collapse shapes the shallow emplacement and transfer of magma in active volcanoes. *Earth and Planetary Science Letters*, *431*, 287–293. doi: 10.1016/j.epsl.2015.09.028
- Crawford, A. M., Stunder, B. J., Ngan, F., & Pavolonis, M. J. (2016). Initializing HYSPLIT with satellite observations of volcanic ash: A case study of the 2008 Kasatochi eruption. *Journal of Geophysical Research*, *121*(18), 10,786–10,803.

doi: 10.1002/2016JD024779

- Cronin, S. J., & Németh, K. (2005). Where are the giant tuff cone and ignimbrites of Ambrym? A more conventional story of mafic volcanism at Ambrym Volcano, Vanuatu. In *Geological society of new zealand 50th annual conference* (pp. 21–22). Kaikoura, New Zealand: Geological Society of New Zealand.
- Crouch, S. L. (1976). Solution of plane elasticity problems by the displacement discontinuity method. *International Journal for Numerical Methods in Engineering*, *10*(2), 301–343.
- Delgado, F., Kubanek, J., Anderson, K., Lundgren, P., & Pritchard, M. (2019). Physicochemical models of effusive rhyolitic eruptions constrained with InSAR and DEM data: A case study of the 2011–2012 Cordón Caulle eruption. *Earth and Planetary Science Letters*, *524*, 115736. doi: 10.1016/j.epsl.2019.115736
- Doin, M.-P., Lodge, F., Guillaso, S., Jolivet, R., Lasserre, C., Ducret, G., . . . Pinel, V. (2011). Presentation of the small baseline NSBAS processing chain on a case example: the Etna deformation monitoring from 2003 to 2010 using Envisat data. In *Proceedings of the esa 'fringe 2011 workshop', frascati, italy, (19-23 september 2011)* (pp. 19–23).
- Du, Y., Aydin, A., & Segall, P. (1992). Comparison of various inversion techniques as applied to the determination of a geophysical deformation model for the 1983 Borah Peak earthquake. *Society*, *82*(4), 1840–1866.
- Edmonds, M. (2008). New geochemical insights into volcanic degassing. *Philosophical Transactions of the Royal Society A: Mathematical, Physical and Engineering Sciences*, *366*(1885), 4559–4579. doi: 10.1098/rsta.2008.0185
- Edmonds, M., Cashman, K. V., Holness, M., & Jackson, M. (2019). Architecture and dynamics of magma reservoirs. *Philosophical Transactions of the Royal Society A: Mathematical, Physical and Engineering Sciences*, *377*(2139). doi: 10.1098/rsta.2018.0298
- Eissen, J. P., Blot, C., & Louat, R. (1991). *Chronology of the historic volcanic activity of the New Hebrides island arc from 1595 to 1991* (Tech. Rep.). Nouméa: ORSTOM.
- Favalli, M., Fornaciai, A., Mazzarini, F., Harris, A., Neri, M., Behncke, B., . . . Boschi, E. (2010). Evolution of an active lava flow field using a multitemporal LIDAR acquisition. *Journal of Geophysical Research: Solid Earth*, *115*(11), 1–17. doi: 10.1029/2010JB007463
- Fukushima, Y., Cayol, V., & Durand, P. (2005). Finding realistic dike models from interferometric synthetic aperture radar data: The February 2000 eruption at Piton de la Fournaise. *Journal of Geophysical Research: Solid Earth*, *110*(3), 1–15. doi: 10.1029/2004JB003268
- Fukushima, Y., Cayol, V., Durand, P., & Massonnet, D. (2010). Evolution of magma conduits during the 1998–2000 eruptions of Piton de la Fournaise volcano, Réunion Island. *Journal of Geophysical Research: Solid Earth*, *115*(10), 1–21. doi: 10.1029/2009JB007023
- Gauthier, P., Cloarec, M. L., & Condomines, M. (2000). Degassing processes at Stromboli volcano inferred from short-lived disequilibria in volcanic gases.

- Journal of Volcanology and Geothermal Research*, 102, 1–19.
- Geist, D. J., Harpp, K. S., Naumann, T. R., Poland, M., Chadwick, W. W., Hall, M., & Rader, E. (2008). The 2005 eruption of Sierra Negra volcano, Galápagos, Ecuador. *Bulletin of Volcanology*, 70(6), 655–673. doi: 10.1007/s00445-007-0160-3
- Geshi, N., Ruch, J., & Acocella, V. (2014). Evaluating volumes for magma chambers and magma withdrawn for caldera collapse. *Earth and Planetary Science Letters*, 396, 107–115. doi: 10.1016/j.epsl.2014.03.059
- Geshi, N., Shimano, T., Chiba, T., & Nakada, S. (2002). Caldera collapse during the 2000 eruption of Miyakejima Volcano, Japan. *Bulletin of Volcanology*, 64(1), 55–68. doi: 10.1007/s00445-001-0184-z
- Geyer, A., Folch, A., & Martí, J. (2006). Relationship between caldera collapse and magma chamber withdrawal : An experimental approach. *Journal of Volcanology and Geothermal Research*, 157, 375–386. doi: 10.1016/j.jvolgeores.2006.05.001
- Goldstein, R. M., & Werner, C. L. (1998). Radar Interferogram Filtering for Geophysical Applications. *Geophysical Research Letters*, 25(21), 4035–4038. doi: <https://doi.org/10.1029/1998GL900033>
- Grandin, R., Doin, M.-P., Bollinger, L., Pinel-Puysségur, B., Ducret, G., Jolivet, R., & Sapkota, S. N. (2012). Long-term growth of the Himalaya inferred from interseismic InSAR measurement. *Geology*, 40(12), 1059. doi: 10.1130/G33154.1
- Grandin, R., Lauer, B., Klinger, Y., & Jolivet, R. (2018). *Significance of near-field geodetic data and diversified geometries of acquisition to model coseismic slip and refine shallow slip deficit: the case of the Balochistan earthquake (2013, M_w 7.7, Pakistan)*. Retrieved from <https://agu.confex.com/agu/fm18/meetingapp.cgi/Paper/452841> (American Geophysical Union Fall Meeting)
- Grandin, R., Socquet, A., Binet, R., Klinger, Y., Jacques, E., De Chabalier, J. B., ... Pinzuti, P. (2009). September 2005 Manda hararo-dabbahu rifting event, Afar (Ethiopia): Constraints provided by geodetic data. *Journal of Geophysical Research: Solid Earth*, 114(8). doi: 10.1029/2008JB005843
- Gudmundsson, M. T., Jónsdóttir, K., Hooper, A., Holohan, E. P., Halldórsson, S. A., Ófeigsson, B. G., ... Aiuppa, A. (2016). Gradual caldera collapse at Bárðarbunga volcano, Iceland, regulated by lateral magma outflow. *Science*, 353(6296), aaf8988. doi: 10.1126/science.aaf8988.sciencemag.org
- Hamling, I. J., Cevuard, S., & Garaebiti, E. (2019). Large-Scale Drainage of a Complex Magmatic System: Observations From the 2018 Eruption of Ambrym Volcano, Vanuatu. *Geophysical Research Letters*, 46(9), 4609–4617. doi: 10.1029/2019GL082606
- Hamling, I. J., & Kilgour, G. (2020). Goldilocks conditions required for earthquakes to trigger basaltic eruptions : Evidence from the 2015 Ambrym eruption. *Science Advances*, 6(14). doi: 10.1126/sciadv.aaz5261
- Heap, M. J., Villeneuve, M., Albino, F., Farquharson, J. I., Brothelande, E., Amelung, F., ... Baud, P. (2019). Towards more realistic values of elastic

- moduli for volcano modelling. *Journal of Volcanology and Geothermal Research*, 106684. doi: 10.1016/j.jvolgeores.2019.106684
- Holohan, E. P., Schöpfer, M. P., & Walsh, J. J. (2011). Mechanical and geometric controls on the structural evolution of pit crater and caldera subsidence. *Journal of Geophysical Research: Solid Earth*, 116(7). doi: 10.1029/2010JB008032
- Johnson, D. J., Sigmundsson, F., & Delaney, P. T. (2000). Comment on ‘volume of magma accumulation or withdrawal estimated from surface uplift or subsidence, with application to the 1960 collapse of Kilauea volcano’ by P.T. Delaney and D.F. McTigue. *Bulletin of Volcanology*, 61(7), 491–493. doi: 10.1007/s004450050006
- Jónsson, S. (2009). Stress interaction between magma accumulation and trapdoor faulting on Sierra Negra volcano, Galápagos. *Tectonophysics*, 471(1-2), 36–44. doi: 10.1016/j.tecto.2008.08.005
- Jónsson, S., Zebker, H., Segall, P., & Amelung, F. (2002). Fault slip distribution of the 1999 M_w 7.1 Hector Mine, California, earthquake, estimated from satellite radar and GPS measurements. *Bulletin of the Seismological Society of America*, 92(4), 1377–1389. doi: 10.1785/0120000922
- Kilbride, B. M. C., Edmonds, M., & Biggs, J. (2016). Observing eruptions of gas-rich compressible magmas from space. *Nature Communications*, 7, 1–8. doi: 10.1038/ncomms13744
- King, G. C. P., Stein, R. S., & Lin, J. (1994). Static Stress Change and the Triggering of Earthquakes. *Bulletin of the Geological Society of America*(March), 46.
- Kobayashi, T., Morishita, Y., & Yurai, H. (2015). Detailed crustal deformation and fault rupture of the 2015 Gorkha earthquake, Nepal, revealed from ScanSAR-based interferograms of ALOS-2. *Earth, Planets and Space*, 67(1). doi: 10.1186/s40623-015-0359-z
- La Femina, P. C., Bell, A. F., Higgins, M., Meier, N. J., Hernandez, S., Bean, C. J., ... Grannell, J. (2019, Dec). Deformation of a basaltic shield volcano: Uplift, trapdoor Faulting, eruption Triggering and subsidence associated with the 2018 eruption of Sierra Negra Volcano, Galapagos. In *Agu fall meeting abstracts* (p. V11B-01).
- Lachat, J. C., & Watson, J. O. (1976). Effective numerical treatment of boundary integral equations: A formulation for three-dimensional elastostatics. *International Journal for Numerical Methods in Engineering*, 10(5), 991–1005. doi: 10.1002/nme.1620100503
- Li, C., Krotkov, N. A., Carn, S., Zhang, Y., Spurr, R. J., & Joiner, J. (2017). New-generation NASA Aura Ozone Monitoring Instrument (OMI) volcanic SO_2 dataset: Algorithm description, initial results, and continuation with the Suomi-NPP Ozone Mapping and Profiler Suite (OMPS). *Atmospheric Measurement Techniques*, 10(2), 445–458. doi: 10.5194/amt-10-445-2017
- Liang, C., & Fielding, E. J. (2017). Measuring Azimuth Deformation with L-Band ALOS-2 ScanSAR Interferometry. *IEEE Transactions on Geoscience and Remote Sensing*, 55(5), 2725–2738. doi: 10.1109/TGRS.2017.2653186
- Lin, J., & Stein, R. S. (2004). Stress triggering in thrust and subduction earth-

- quakes and stress interaction between the southern San Andreas and nearby thrust and strike-slip faults. *Journal of Geophysical Research: Solid Earth*, *109*(B2), 1–19. doi: 10.1029/2003jb002607
- Lindsey, E. O., Natsuaki, R., Xu, X., Shimada, M., Hashimoto, M., Melgar, D., & Sandwell, D. T. (2015). Line-of-sight displacement from ALOS-2 interferometry: M_w 7.8 Gorkha Earthquake and M_w 7.3 aftershock. *Geophysical Research Letters*, *42*(16), 6655–6661. doi: 10.1002/2015GL065385
- Lisowski, M. (2006). Analytical volcano deformation source models. In D. Dzurisin (Ed.), *Volcano deformation* (pp. 279 – 304). doi: 10.1007/978-3-540-49302-0
- Liu, Y.-K., Ruch, J., Vasyura-Bathke, H., & Jónsson, S. (2019). Influence of ring faulting in localizing surface deformation at subsiding calderas. *Earth and Planetary Science Letters*, *526*, 115784. doi: 10.1016/j.epsl.2019.115784
- McCall, G.J.H. and Lemaitre, R.W. and Malahoff, A. and Robinson, G.P. and Stephenson, P.J. (1969). The Geology and Geophysics of the Ambrym Caldera, New Hebrides. In *Symposium volcanoes and their roots* (pp. 681–696). Oxford, England.
- Michel, R., Avouac, J.-p., & Taboury, J. (1999). Measuring ground displacements from SAR amplitude images : application to the Landers earthquake. *Geophysical Research Letters*, *26*(7), 875 – 878.
- Mogi, K. (1958). Relations between the eruptions of various volcanoes and the deformations of the ground surfaces around them. *Bulletin of the Earthquake Research Institute*, *36*, 99–134.
- Moore, C., Wright, T., Hooper, A., & Biggs, J. (2019). The 2017 Eruption of Erta 'Ale Volcano, Ethiopia: Insights into the Shallow Axial Plumbing System of an Incipient Mid-Ocean Ridge. *Geochemistry, Geophysics, Geosystems*, *20*, 5727–5743. doi: 10.1029/2019GC008692
- Munro, D. C., & Rowland, S. K. (1996). Caldera morphology in the western Galápagos and implications for volcano eruptive behavior and mechanisms of caldera formation. *Journal of Volcanology and Geothermal Research*, *72*, 85–100.
- Natsuaki, R., Nagai, H., Motohka, T., Ohki, M., Watanabe, M., B. Thapa, R., . . . Suzuki, S. (2016). SAR interferometry using ALOS-2 PALSAR-2 data for the M_w 7.8 Gorkha, Nepal earthquake. *Earth, Planets and Space*, *68*(1). doi: 10.1186/s40623-016-0394-4
- Neal, C. A., Brantley, S., Antolik, L., Babb, J., Burgess, M., Calles, K., . . . Fisher, G. (2018). The 2018 rift eruption and summit collapse of Kilauea Volcano. *Science*, *7046*(December), 1–14. doi: 10.1126/science.aav7046
- Németh, K., & Cronin, S. J. (2008). Volcanic craters, pit craters and high-level magma-feeding systems of a mafic island-arc volcano: Ambrym, Vanuatu, South Pacific. *Geological Society, London, Special Publications*, *302*(1), 87–102. doi: 10.1144/SP302.6
- Newhall, C., Self, S., & Robock, A. (2018). Anticipating future Volcanic Explosivity Index (VEI) 7 eruptions and their chilling impacts. *Geosphere*, *14*(2), 572–603. doi: 10.1130/GES01513.1
- Nostro, C., Stein, S., Cocco, M., Belardinelli, M. E., & Marzocchi, W. (1998). Two-

- way coupling between Vesuvius eruptions and southern Apennine earthquakes, Italy, by elastic stress transfer. *Journal of Geophysical Research*, *103*(B10), 24,487–24,504.
- Okada, Y. (1985). Surface Deformation Due to Shear and Tensile Faults in a Half-Space. *Bulletin of the Seismological Society of America*, *75*(4), 1135–1154. doi: 10.1016/0148-9062(86)90674-1
- Ortiz, A. B., Member, S., & Zebker, H. (2007). ScanSAR-to-Stripmap Mode Interferometry Processing Using ENVISAT / ASAR Data. *IEEE Transactions on Geoscience and Remote Sensing*, *45*(11), 3468–3480. doi: 10.1109/TGRS.2007.895970
- Peltier, A., Staudacher, T., Bachèlery, P., & Cayol, V. (2009). Formation of the April 2007 caldera collapse at Piton de La Fournaise volcano: Insights from GPS data. *Journal of Volcanology and Geothermal Research*, *184*(1-2), 152–163. doi: 10.1016/j.jvolgeores.2008.09.009
- Pinel, V., & Jaupart, C. (2000). The effect of edifice load on magma ascent beneath a volcano. *Philosophical Transactions of the Royal Society A: Mathematical, Physical and Engineering Sciences*, *358*(1770), 1515–1532. doi: 10.1098/rsta.2000.0601
- Pinel, V., Poland, M. P., & Hooper, A. (2014). Volcanology: Lessons learned from Synthetic Aperture Radar imagery. *Journal of Volcanology and Geothermal Research*, *289*, 81–113. doi: 10.1016/j.jvolgeores.2014.10.010
- Reynolds, R. W., Geist, D., & Kurz, M. D. (1995). Physical volcanology and structural development of Sierra Negra volcano, Isabela Island, Galapagos archipelago. *Geological Society of America Bulletin*, *107*(12), 1398–1410. doi: 10.1130/0016-7606(1995)107<1398:PVASDO>2.3.CO;2
- Rivalta, E. (2010). Evidence that coupling to magma chambers controls the volume history and velocity of laterally propagating intrusions. *Journal of Geophysical Research: Solid Earth*, *115*(7), 1–13. doi: 10.1029/2009JB006922
- Rivalta, E., & Segall, P. (2008). Magma compressibility and the missing source for some dike intrusions. *Geophysical Research Letters*, *35*(4), 1–5. doi: 10.1029/2007GL032521
- Robin, C., Eissen, J. P., & Monzier, M. (1993). Giant tuff cone and 12-km-wide associated caldera at Ambrym Volcano (Vanuatu, New Hebrides Arc). *Journal of Volcanology and Geothermal Research*, *55*(3-4), 225–238. doi: 10.1016/0377-0273(93)90039-T
- Roche, O., Druitt, T. H., & Merle, O. (2000). Experimental study of caldera formation. *Journal of Geophysical Research*, *105*(B1), 395–416.
- Roche, O., Van Wyk De Vries, B., & Druitt, T. H. (2001). Sub-surface structures and collapse mechanisms of summit pit craters. *Journal of Volcanology and Geothermal Research*, *105*(1-2), 1–18. doi: 10.1016/S0377-0273(00)00248-1
- Rosen, P. A., Gurrola, E., Sacco, G. F., & Zebker, H. (2012, April). The InSAR scientific computing environment. In *Eusar 2012; 9th european conference on synthetic aperture radar* (p. 730-733).
- Rosen, P. A., Hensley, S., Peltzer, G., & Simons, M. (2004). Updated Repeat Orbit

- Interferometry Package Released. *Eos*, 85(5), 47.
- Rubin, A. M., & Pollard, D. D. (1988). Dike-induced faulting in rift zones of Iceland and Afar. *Geology*, 16, 413–417.
- Rupnik, E., Pierrot-Deseilligny, M., & Delorme, A. (2018). 3D reconstruction from multi-view VHR-satellite images in MicMac. *ISPRS Journal of Photogrammetry and Remote Sensing*, 139, 201–211. doi: 10.1016/j.isprsjprs.2018.03.016
- Sambridge, M. (1998). Exploring multidimensional landscapes without a map. *Inverse Problems*(14), 427–440.
- Sambridge, M. (1999a). Geophysical inversion with a neighbourhood algorithm– II. Appraising the ensemble. *Geophysical Journal International*, 138(2), 727–746. doi: 10.1046/j.1365-246X.1999.00876.x
- Sambridge, M. (1999b). Geophysical inversion with a neighbourhood algorithm– I. Searching a parameter space. *Geophysical Journal International*, 138, 479–494. doi: 10.1046/j.1365-246x.1999.00900.x
- Sawyer, G. M., Carn, S. A., Tsanev, V. I., Oppenheimer, C., & Burton, M. (2008). Investigation into magma degassing at Nyiragongo volcano, democratic Republic of the Congo. *Geochemistry, Geophysics, Geosystems*, 9(2), 1–17. doi: 10.1029/2007GC001829
- Shreve, T., Grandin, R., Boichu, M., Garaebiti, E., Moussallam, Y., Ballu, V., ... Pelletier, B. (2019). From prodigious volcanic degassing to caldera subsidence and quiescence at Ambrym (Vanuatu): the influence of regional tectonics. *Scientific Reports*, 9(18868). doi: <https://doi.org/10.1038/s41598-019-55141-7>
- Sigmundsson, F. (2019). Calderas collapse as magma flows into rifts. *Science*, 366(6470), 1200–1201. doi: 10.1126/science.aaz7126
- Smittarello, D., Cayol, V., Pinel, V., Peltier, A., Froger, J. L., & Ferrazzini, V. (2019). Magma Propagation at Piton de la Fournaise From Joint Inversion of InSAR and GNSS. *Journal of Geophysical Research: Solid Earth*, 124(2), 1361–1387. doi: 10.1029/2018JB016856
- Sokolnikoff, I. (1956). *Mathematical theory of elasticity*. New York: McGraw-Hill.
- Sparks, R. S. (1997). Causes and consequences of pressurisation in lava dome eruptions. *Earth and Planetary Science Letters*, 150(3-4), 177–189. doi: 10.1016/S0012-821X(97)00109-x
- Stein, A. F., Draxler, R. R., Rolph, G. D., Stunder, B. J., Cohen, M. D., & Ngan, F. (2015). NOAA’s hysplit atmospheric transport and dispersion modeling system. *Bulletin of the American Meteorological Society*, 96(12), 2059–2077. doi: 10.1175/BAMS-D-14-00110.1
- Sudhaus, H., & Jónsson, S. (2009). Improved source modelling through combined use of InSAR and GPS under consideration of correlated data errors: Application to the June 2000 Kleifarvatn earthquake, Iceland. *Geophysical Journal International*, 176(2), 389–404. doi: 10.1111/j.1365-246X.2008.03989.x
- Tachikawa, T., Hat, M., Kaku, M., & Iwasaki, A. (2011). Characteristics of ASTER GDEM Version 2. *Geoscience and Remote Sensing Symposium (IGARSS), 2011 IEEE International*, 3657–3660. doi: 10.1109/IGARSS.2011.6050017
- Tarantola, A. (1987). *Inverse problem theory: Method for data fitting and model pa-*

- parameter estimation. Elsevier.
- Tobita, M. (2003). Development of SAR interferometry analysis and its application to crustal deformation study. *Journal of the Geodetic Society of Japan*, *49*(1), 1–23. doi: 10.11366/sokuchi1954.49.1
- Tridon, M., Cayol, V., Froger, J. L., Augier, A., & Bachèlery, P. (2016). Inversion of coeval shear and normal stress of Piton de la Fournaise flank displacement. *Journal of Geophysical Research: Solid Earth*, *121*(11), 7846–7866. doi: 10.1002/2016JB013330
- Walker, G. P. (1984). Downsag calderas, ring faults, caldera sizes, and incremental caldera growth. *Journal of Geophysical Research*, *89*(B10), 8407–8416. doi: 10.1029/JB089iB10p08407
- Wallace, P. J. (2001). Volcanic SO₂ emissions and the abundance and distribution of exsolved gas in magma bodies. *Journal of Volcanology and Geothermal Research*, *108*(1-4), 85–106. doi: 10.1016/S0377-0273(00)00279-1
- Walstead, S. T. (1999). *Fractal and wavelet image compression techniques*. Bellingham, Washington: SPIE Optical Engineering Press.
- Wauthier, C., Cayol, V., Smets, B., D’Oreye, N., & Kervyn, F. (2015). Magma pathways and their interactions inferred from InSAR and stress modeling at Nyamulagira Volcano, D.R. Congo. *Remote Sensing*, *7*(11), 15179–15202. doi: 10.3390/rs71115179
- Wessel, B. (2016). *TanDEM-X Ground Segment - DEM Products Specification Document* (Tech. Rep. No. 3.1). Oberpfaffenhofen, Germany: EOC, DLR. Retrieved from <https://tandemx-science.dlr.de/> doi: DOI:10.1002/hyp.3360050103
- Wright, R. (2016). MODVOLC: 14 years of autonomous observations of effusive volcanism from space. *Geological Society, London, Special Publications*, *426*, 23–53. doi: 10.1144/SP426.12
- Wright, R., Flynn, L. P., Garbeil, H., Harris, A. J. L., & Pilger, E. (2004). MODVOLC: Near-real-time thermal monitoring of global volcanism. *Journal of Volcanology and Geothermal Research*, *135*(1-2), 29–49. doi: 10.1016/j.jvolgeores.2003.12.008
- Wright, T. J., Parsons, B. E., & Lu, Z. (2004). Toward mapping surface deformation in three dimensions using InSAR. *Geophysical Research Letters*, *31*(1), 1–5. doi: 10.1029/2003GL018827
- Yun, S., Segall, P., & Zebker, H. (2006). Constraints on magma chamber geometry at Sierra Negra Volcano, Galápagos Islands, based on InSAR observations. *Journal of Volcanology and Geothermal Research*, *150*(1-3), 232–243. doi: 10.1016/j.jvolgeores.2005.07.009
- Yun, S. H., Zebker, H., Segall, P., Hooper, A., & Poland, M. (2007). Interferogram formation in the presence of complex and large deformation. *Geophysical Research Letters*, *34*(12), 1–6. doi: 10.1029/2007GL029745
- Zebker, H. A., Rosen, P., Goldstein, R. M., Gabriel, A., & Werner, C. (1994). On the derivation of coseismic displacement fields using differential radar interferometry: the Landers earthquake. *Journal of Geophysical Research: Solid Earth*

Earth, 99(B10), 19617–19634.

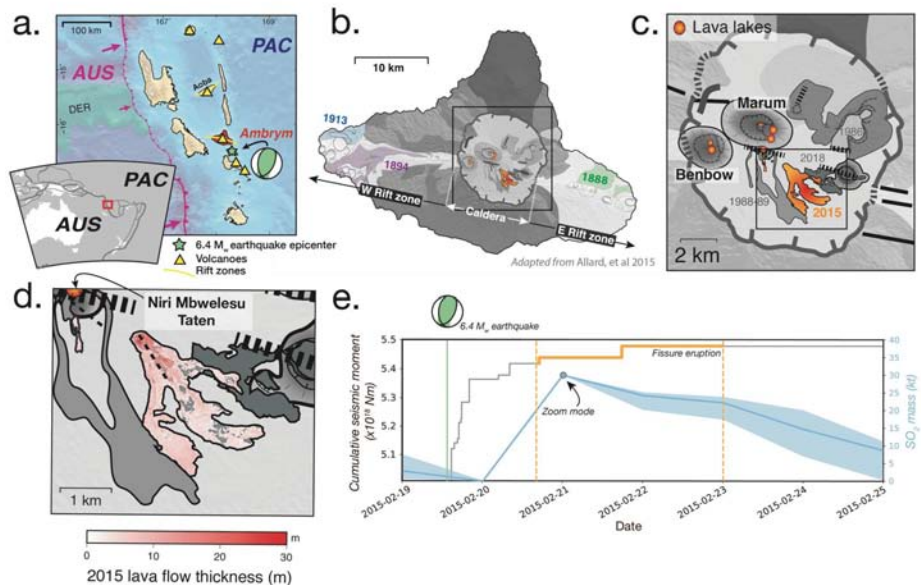


Figure 1. **a.** Tectonic setting of Ambrym volcano, located in the central portion of the New Hebrides subduction zone (pink). AUS is the Australian plate, PAC is the Pacific plate, and DER is the colliding D’Entrecasteaux Ridge. Yellow triangles are active volcanoes, and yellow lines indicate rift zones. The green star indicates the location of the 6.4 M_w earthquake that preceded the 2015 Ambrym eruption. Adapted from Shreve et al. (2019). **b.** Ambrym island, showing both the caldera and the rift zones. Dates of extra-caldera lava flows associated with rift-zone intrusions and eruptions are labelled. Adapted from Allard et al. (2015). **c.** Zoom of Ambrym’s caldera, including the volcanic cones of Marum and Benbow, caldera rim, historical volcanic vents, and dates corresponding to historical lava flows. Lighter shades of gray indicate older volcanic deposits, and the lava flow from the February 2015 is shown in orange. **d.** Difference between a pre-eruptive TanDEM-X DEM and a post-eruptive Pléiades DEM (Fig. S1). Newly opened fissures are denoted by dotted lines. **e.** The cumulative seismic moment and daily SO_2 mass (as measured by the Ozone Mapping and Profiler Suite, OMPS) emitted throughout the duration of the eruption. The 6.4 M_w earthquake on 19 February is plotted, alongside the earthquake’s focal mechanism. The cumulative seismic moment, as recorded by the ORSNET catalogue, is calculated from earthquakes with depths of less than 50 km. It is important to consider that SO_2 measurements on two consecutive days may measure the same parcel of SO_2 , and we should not simply sum each day’s SO_2 mass measurements during the entire eruption. The bounds on the SO_2 mass estimate (shown in light blue) are determined by changing the Dobson Unit (DU) threshold from 2 DU for the lower-bounds, 1 DU for the solid blue line, and 0.8 DU for the upper-bounds. Only pixels above each of these thresholds are included in the daily mass calculation (see Fig. S2, which also includes a MODVOLC thermal anomaly time series (R. Wright et al., 2004; R. Wright, 2016)). On 21 February, the OMPS satellite was in Zoom Mode, and the Level 2 middle tropospheric (TRM) data products were not accessible. The SO_2 mass for this day was estimated using NASA’s website (https://so2.gsfc.nasa.gov/pix/daily/ixxxza/loopall_omps.php?yr=15&mo=02&dy=21&bn=vanuatu).

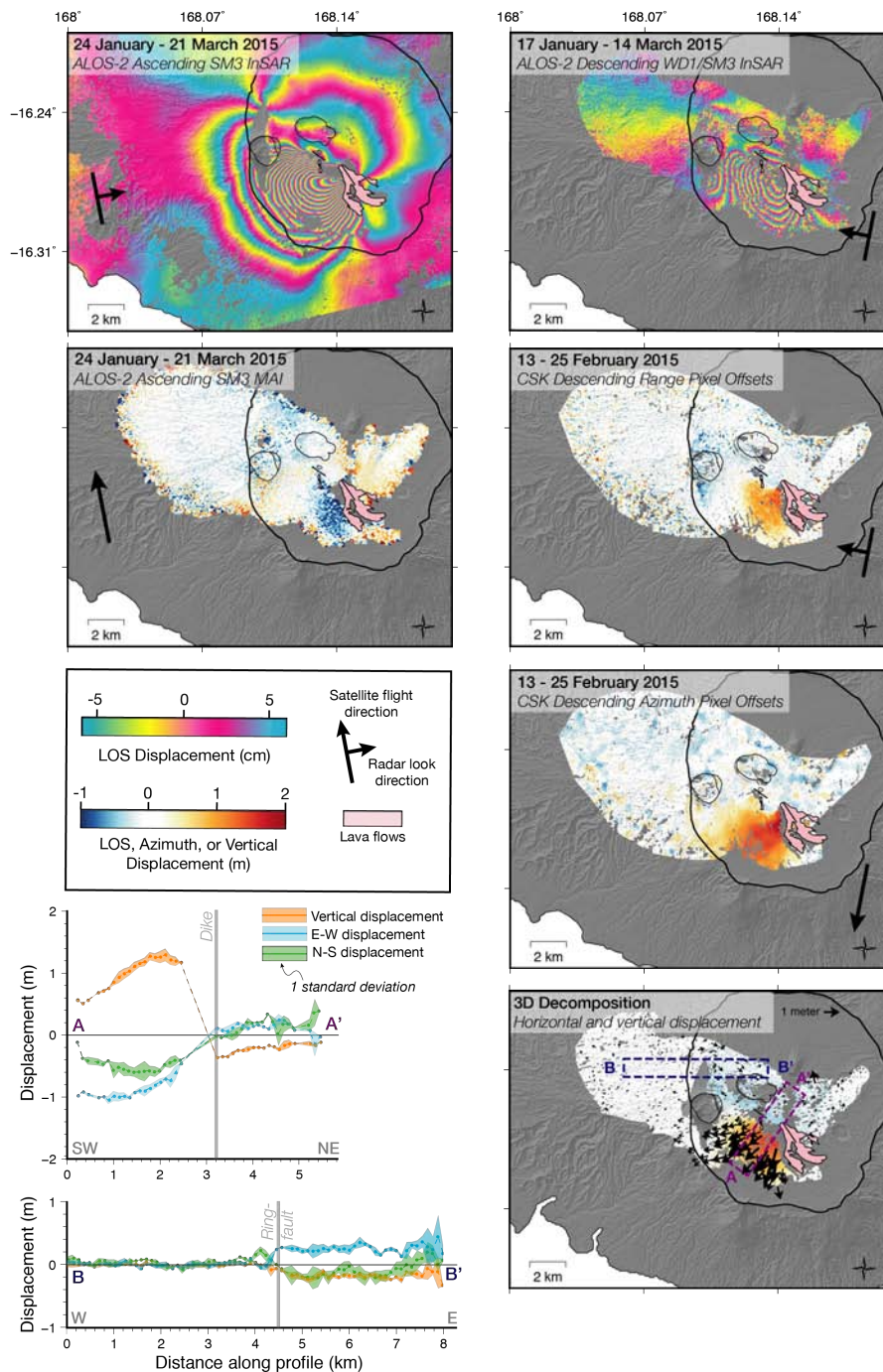


Figure 2. Measurements spanning the February 2015 eruption, including InSAR, MAI, and pixel offsets. The bottom right panel shows the 3D decomposition, with the arrows representing horizontal displacement and the blue-red colormap representing vertical displacement. The arrow in the upper right hand corner of the figure represents 1 meters of eastward displacement. The average and standard deviation of vertical, east-west and north-south displacement within two 1-km wide swath profiles, Profiles A-A' and B-B', are shown in the lower left hand corner of the figure. Positive displacement values indicate uplift, eastward, and northward ground movement. The caldera is outlined with a thick black line, and Marum and Benbow craters are outlined with thin black lines.

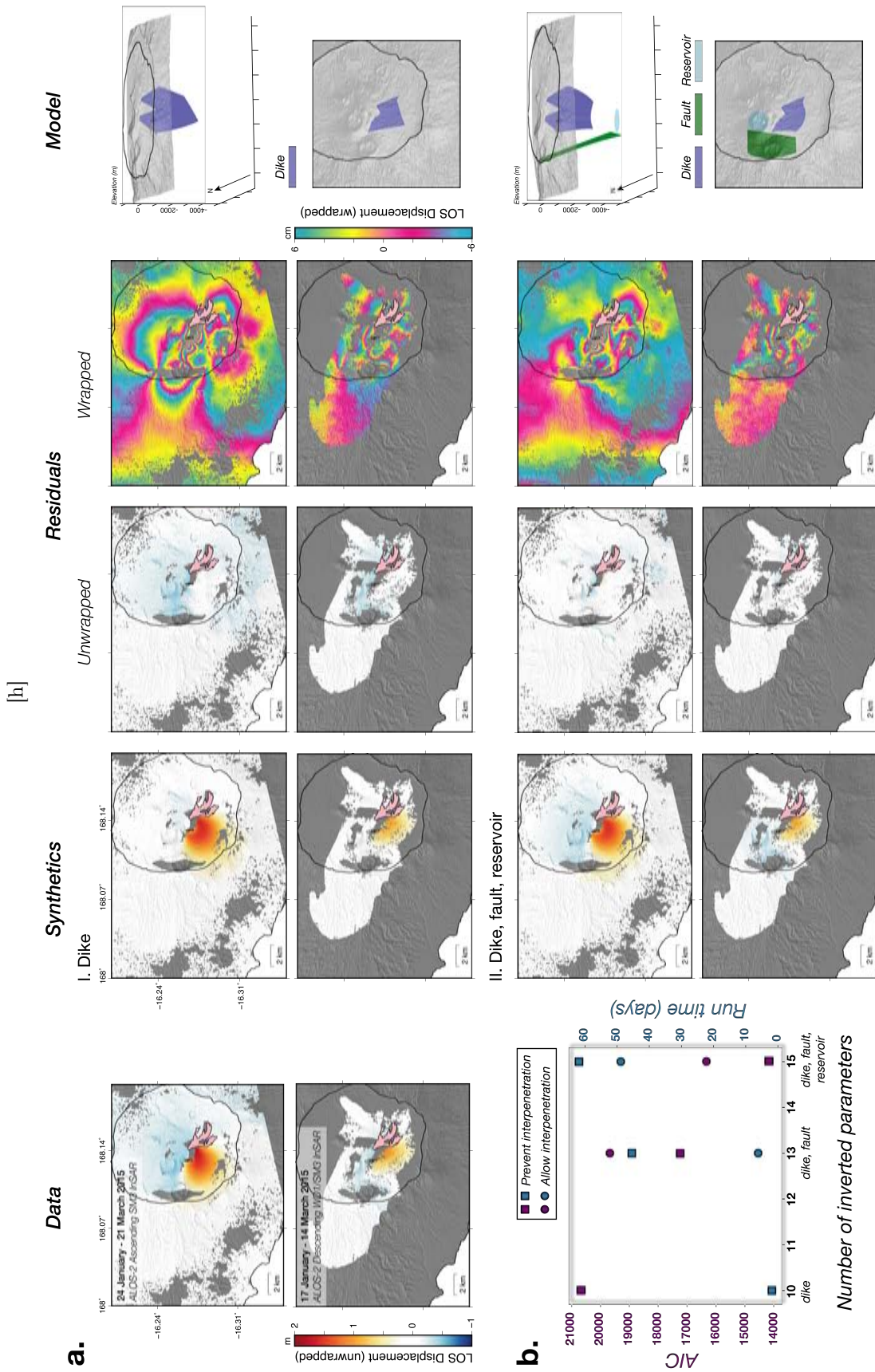


Figure 3. **a.** The left hand column shows the ascending and descending InSAR measurements, while the second column shows the modelled synthetic displacement field. The third and fourth columns show the residuals of the modelled and measured displacements, visualized as both unwrapped and wrapped. The final column shows the model geometry in both cross-section and map view. The first two rows are for Inversion 1, which includes a dike, and the last two rows are for Inversion 3, which includes a dike, fault and reservoir. Refer to Figure S11 for the displacement field and residuals from Inversion 2, which includes the dike and fault. **b.** The misfit and run time plotted against the number of non-linearly inverted parameters. The squares correspond to the inversions that prevent interpenetration, while the circles correspond to the inversions that allow interpenetration. Purple shapes plot the total run time, and the blue shapes plot the total run time, in days.

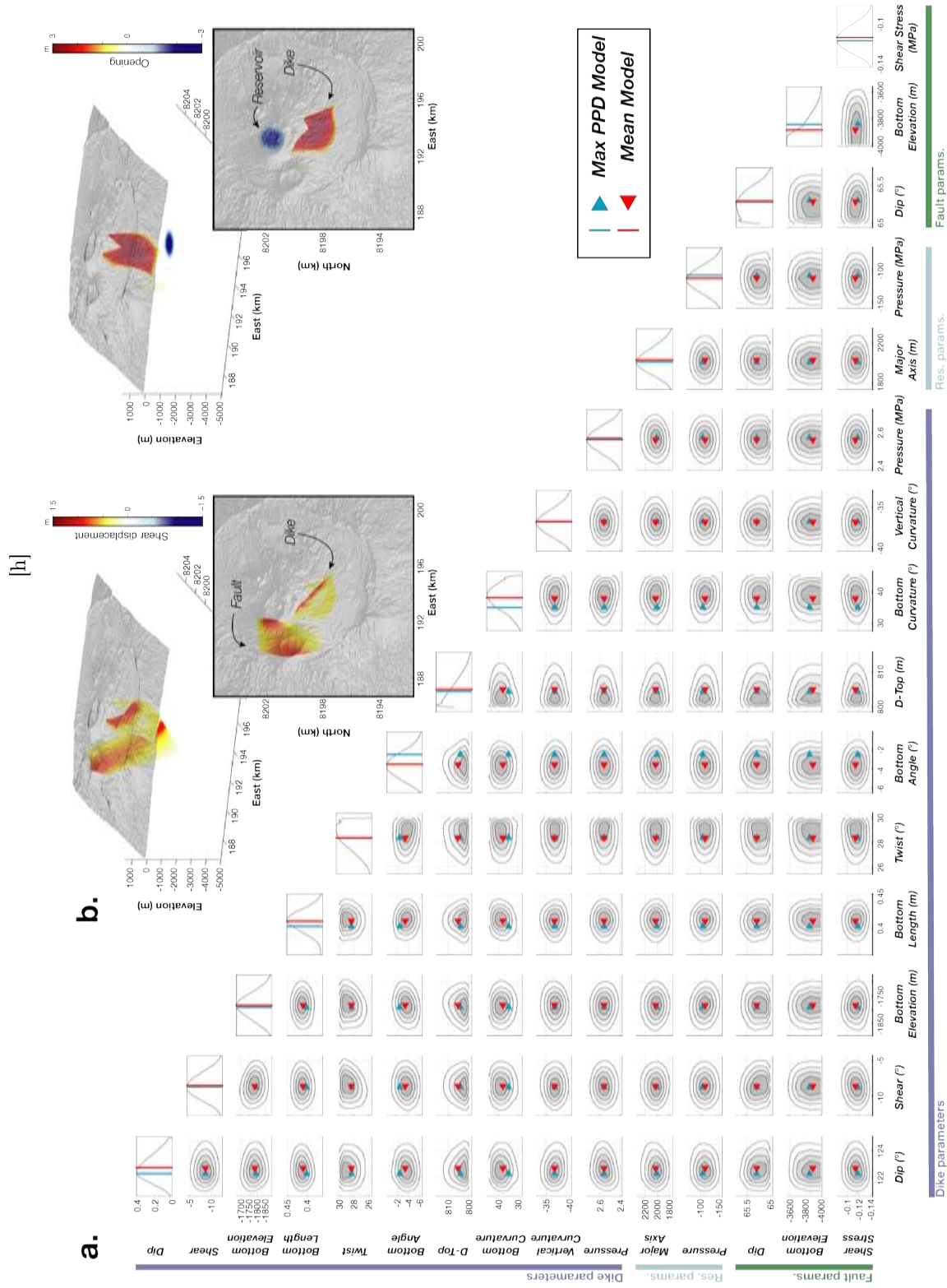


Figure 4. a. Marginal posterior probability density (PPD) functions showing tradeoffs between the 15 non-linearly inverted parameters. The first 9 parameters concern the dike geometry and pressure change, the next 2 parameters concern the reservoir size and pressure change, and the last three parameters concern the fault geometry and shear stress change. Parameter units are displayed in the bottom row next to each column label. b. Shear displacements and opening of the max PPD models of the dike, fault, and reservoir from Inversion 3, shown in both perspective and map view.

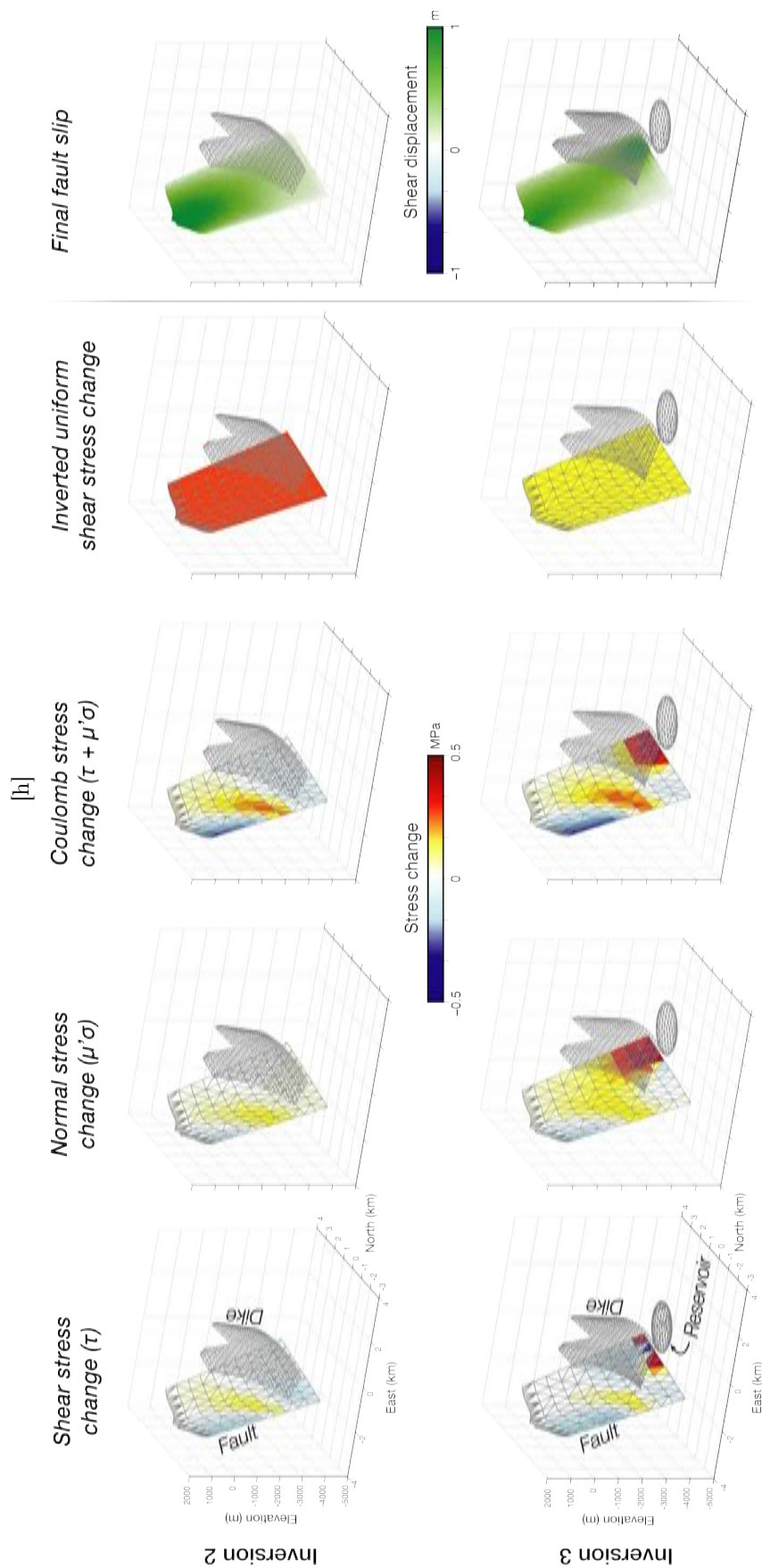


Figure 5. Normal (positive for unclamping), shear (positive for shear in the direction of normal slip, rake= -90°) and Coulomb stress change on the caldera ring-fault. Also shown is the uniform shear stress change estimated in the inversion, as well as the final slip distribution on the fault, resulting from both the inverted uniform shear stress change and stress transfer from the dike and/or reservoir. The first row is the stress change and slip due to only dike opening (Inversion 2), and the second row is the stress change and slip due to both dike opening and reservoir decompression (Inversion 3). In the northern portion of the fault, where the fault-induced surface deformation is measured, the Coulomb stress change is higher at depth in Inversion 3.

Supporting Information for “What triggers caldera ring-fault subsidence at Ambrym volcano? Insights from the 2015 dike intrusion and eruption”

T. Shreve¹, R. Grandin¹, D. Smittarello^{2*}, V. Cayol³, V. Pinel², M. Boichu⁴,
Y. Morishita⁵

¹Université de Paris, Institut de physique du globe de Paris, CNRS, F-75005, Paris, France

²University Grenoble Alpes, University Savoie Mont Blanc, CNRS, IRD, IFSTTAR, ISTerre, Grenoble,
France

³Université Clermont Auvergne, CNRS, IRD, OPGC, Laboratoire Magmas et Volcans, F-63000
Clermont-Ferrand, France

⁴Université Lille, UMR 8518 – LOA – Laboratoire d’Optique Atmosphérique, F-59000, Lille, France

⁵Geospatial Information Authority of Japan, Ibaraki, Japan

Contents of this file

1. Text S1 to S7
2. Figures S1 to S13
3. Tables S1 to S6

Introduction

This Supporting Information document includes seven additional text sections. They discuss in detail the eruption onset and timing constrained by satellite remote sensing, the processing and uncertainty of the Pléiades digital elevation model (DEM), the mass of co-eruptive gas emission as measured by satellite remote sensing, InSAR data processing, data preparation for the inversion, the mixed boundary element method, and the appraisal step of the non-linear inversion. It also includes thirteen supporting figures, which supplement the manuscript’s main text and figures. Finally, six tables record the DEM uncertainties, SAR datasets, post-processing parameters, and final parameter estimates from the inversions.

Text S1 - Eruption Onset and Timing

To further constrain the eruption onset, we use National Oceanic and Atmospheric Administration (NOAA) Air Resources Laboratory’s (ARL) Hybrid Single-Particle Lagrangian Integrated Trajectory model (HYSPLIT) (https://www.ready.noaa.gov/HYSPLIT_traj.php) to find the back-trajectory of SO₂ parcels in the leading edge of the eruption’s volcanic plume (Stein et al., 2015; Crawford et al., 2016). The initialization parameters were set to a plume altitude of 8 km, as measured using height retrieval algorithms developed for observations from the Infrared Atmospheric Sounding Interferometer (IASI) (Clarisse et al., 2014). The forefront of the plume is located near 159.1°E, 17.53°S at 10:30 AM UTC 21 February (see Figure 2b). Using the Global Data Assim-

*Currently at the European Center for Geodynamics and Seismology, 19 rue Josy Welter, L-7256 Walferdange, Gd Duchy of Luxembourg

ilation System (GDAS) 1° global meteorological model, HYSPLIT estimates that the SO₂ parcels were emitted from Ambrym between 15:00 and 16:00 UTC 20 February at an altitude of ~8800 m above ground level, consistent with the time-frame established by MIROVA for the onset of the eruption.

At the end of the eruption, MODVOLC, a volcanic thermal alert detection system (see Figure 2d), did not detect any thermal anomalies between 22 and 28 February. According to Coppola, Laiolo, and Cigolini (2016), using MIROVA, two thermal anomalies were still present in Marum, with no thermal anomalies present in Benbow. Although both MODVOLC and MIROVA detection algorithms use observations from the moderate resolution imaging spectro-radiometer (MODIS) sensors mounted on NASA’s satellite Terra and Aqua (Figure 2c), MODVOLC detects and classifies thermal anomalies based on a normalized difference between radiance in the long-wave infrared (LWIR, 12.02 μm) and middle infrared (MIR, 3.959 μm) spectrums, and a pixel is considered a thermal anomaly if this normalized difference is greater than an empirically-established threshold (Wright et al., 2004; Wright, 2016). MIROVA, on the other hand, uses a normalized and enhanced thermal index, as well as including a spatial analysis, resulting in more sensibility to local hotspot detection, explaining the discrepancy between these two systems (Coppola, Laiolo, Cigolini, Delle Donne, & Ripepe, 2016).

Text S2 - Lava Flow Digital Elevation Model

In addition to ground displacement measurements, we also used MicMac software and Pléiades satellite imagery to construct a Digital Elevation Model (DEM) of the lava flow, to calculate the total emplaced lava flow volume (Rupnik et al., 2018)(<http://logiciels.ign.fr/?Micmac>). We calculated the DEM from two 50 cm spatial resolution Pléiades panchromatic images acquired after the eruption (one on 20 March 2015 at 23:15 UTC and another on 30 September 2017 at 23:00 UTC).

The DEM was downsampled to 12 m, the resolution of the TanDEM-X (TDX) DEM. Due to the spatial extent of the lava flow ($>2.5 \text{ km}^2$), a coarser resolution should not bias the lava flow volume calculation. We then subtracted this downsampled DEM from the TDX DEM. There was an elevation ramp visible across this DEM difference, which could possibly be due to the lack of absolute calibration of the Pléiades DEM with Ground Control Points, or due to topography-related height errors. We masked the lava flow, fit a Gaussian to the binned elevation values, after removing unreasonable values between -15.5 m and 15.5 m. We calculated and removed the mean, $\mu = 1.4268 \text{ m}$, the best-fitting plane, and the unreasonable values from the original Pléiades DEM. The difference between this final Pléiades DEM, and the TDX DEM is shown in Figure 1a. The total volume of the lava flows was estimated to be $\sim 12.4 \times 10^6 \text{ m}^3$, with an average height of $\sim 5 \text{ m}$.

Uncertainty Estimates

To estimate the uncertainty of the lava flow volume, we follow the method of Bagnardi et al. (2016) and Favalli et al. (2010). These estimations include calculating the standard deviation of the variance propagation associated with both spatially correlated and

uncorrelated errors. We fit σ and λ of an exponential, $C_r = \sigma^2 \exp(\frac{-r}{\lambda})$, where r is the distance between two pixels, to the covariograms of three control areas (see Figure 1 and Table 1). The equation for uncertainties given variance propagation when all errors are spatially correlated is the following

$$\sigma_V^2 = A^2 \sum_i \sum_j C_{ij}, \quad (1)$$

where A is a pixel's surface area and C_{ij} is the covariance between the height error of pixels i and j .

Given the covariances shown in Figure 1b, we note that pixels separated by less than ~ 60 m are spatially correlated for all control areas (pixel size of 12.1×12.1 m). We can therefore simplify Equation 1 to

$$\sigma_V^2 = A^2 N (\sigma_Z^2 + \sum_{r=1}^n C_r), \quad (2)$$

where σ_Z is the uncorrelated elevation standard deviation in each control area (see Table 1), N is the number of pixels, and $n = 5$ when pixels are correlated within ~ 60 m. Given the estimates of σ and λ for the three control areas, σ_V for $N = 18721$, the size of the lava flow, are 0.048, 0.041, and $0.035 \times 10^6 \text{ m}^3$. The average σ_V is $0.041 \times 10^6 \text{ m}^3$. We conclude that the lava flow volume estimate, including an error of two standard deviations from the mean, is $12.4 (\pm 0.08) \times 10^6 \text{ m}^3$. If we assume an average vesiculation of basaltic a' lava flows to be 25%, similar to Bagnardi et al. (2016), we obtain an adjusted volume of $9.3 (\pm 0.08) \times 10^6 \text{ m}^3$ DRE.

Even within the caldera, which is relatively flat, we still observe elevation errors that correlate with topographic relief and errors due to the presence of vegetation. A tri-stereo Pléiades acquisition would decrease the uncertainty due to topography. Nonetheless, the error on the total volume is less than 2%.

Text S3 - SO₂ Mass Calculation

Near the eruptive vent, IASI measures that the volcanic plume has an altitude of ~ 5 km on 21 February $\sim 10:30$ UTC. HYSPLIT trajectories show that, if parcels initiate at 5 km altitude at 3h00 21 February (approximate time of UV spectrometer Ozone Mapping and Profiler Suite (OMPS) Zoom acquisition (Li et al., 2017)), they travel first to the west, then circulate counter-clockwise back eastwards towards Ambrym, finally travelling to the southeast on 24 February (see Fig. 2a). The parcels' altitudes range between 5 - 7 km. We assume that any SO₂ measured after the end of the eruption is due to the recirculation of SO₂ parcels in the region. The SO₂ measured is overestimated, as the same SO₂ parcels are likely measured on two consecutive dates. We resample the OMPS products using Delaunay triangulation to a regular grid, and apply a threshold of between 0.8 - 2 Dobson Units (DU, where $1 \text{ DU} = 2.69 \times 10^{16} \text{ molecules/cm}^2$) before calculating the total SO₂ mass.

As mentioned in the main text, we conservatively estimate ~ 40 kt of SO₂ emitted during the eruption. Given the small crystal fraction (< 5 wt%) and 0.075 wt% of sul-

phur in the melt (Allard et al., 2015; Shreve et al., 2019), this corresponds to 9.5×10^6 m³ of degassed lava, consistent with the erupted volume.

Text S4 - Geodetic Data Processing

Ascending stripmap-to-stripmap interferograms

The coregistration, topographic and orbital fringe removal, interferogram formation, multilooking, and geocoding steps are performed using the Interferometric SAR scientific computing environment (ISCE)(Rosen et al., 2012), while filtering and unwrapping are performed with NSBAS modules (Doin et al., 2011). Topographic fringes are removed with DLR’s TanDEM-X 12 meter global DEM (an average of DEM’s acquired before November 2014) (Wessel, 2016).

The phase is most coherent in regions with little vegetation, such as in the western portion of Ambrym’s caldera. The interferogram near-field (areas which show more than 1 m of surface displacement, SW of the eruptive fissure) is multilooked 2 times in range and 4 times in azimuth, while the far-field is multilooked 8 times in range and 16 times in azimuth. Higher multilooking in the densely vegetated far-field increases coherence, while preserving the broad, long-wavelength signature of the signal.

Filtering and unwrapping

The filtering and unwrapping procedure followed for both the ascending and descending interferograms is outlined as follows. The interferometric phase is smoothed using a weighted power spectrum filter (Rosen et al., 2004), followed by a cascading high-pass filter (Grandin et al., 2012). Due to the high gradient of interferometric fringes near the fissure, we unwrap the interferograms using an iterative, coherence-based method called MPD, which is a module in NSBAS (Grandin et al., 2012). This method uses the interferogram’s coherence to optimize the unwrapping path. Unwrapping begins at a chosen seed pixel that is above a certain coherence threshold. At each iteration, MPD slightly decreases the coherence threshold, and unwraps the nearby pixels above the new threshold. Pixels below the minimum coherence threshold, γ_{min} , will not be unwrapped. For the ascending interferogram, the seed pixel is located southwest of the main fissure in the near-field interferogram and northwest of Benbow in the far-field interferogram. For both the near- and far-fields of the ascending interferogram, $\gamma_{min,asc} = 0.05$, given a maximum coherence of 1.0. For the descending interferogram, $\gamma_{min,desc} = 0.1$.

MPD is advantageous because the iteration number depends on the pixel coherence, and can be used to mask the final, unwrapped interferogram, acting as a proxy for confidence in the unwrapped phase value. For the ascending interferogram, we mask the near-field and the far-field with a threshold of 25000 and 15000 iterations, respectively. The descending interferogram is masked at 14000 unwrapping iterations. These filtered, unwrapped interferograms are then geocoded with ISCE. The far-field of the ascending interferogram is then oversampled to the near-field resolution, resulting in a pixel posting of ~ 14 m x 14 m after geocoding. The descending interferogram has a pixel posting of ~ 30 m x 20 m after geocoding. Finally, we mask the 2015 lava flow, as well as in-

coherent regions near the fissure and caldera rim. We also apply a water mask to the island.

Bridges connect fringes that are determined, by eye, to be continuous, but which pass through incoherent regions. Without bridges, MPD would not unwrap correctly across the incoherent regions, resulting in unwrapping errors. Remaining unwrapping errors are masked by hand. Interferograms are then referenced to the median of a box to the north-west of the caldera, near 168.07°E, 16.23°S. Due to more than 1 m of line of sight (LOS) motion, the phase contribution from atmospheric effects (which can be more than 10 cm in tropical regions) was negligible, and no atmospheric corrections were applied.

Text S5 - Data subsampling

The data is subsampled using an adaptive quadtree decomposition algorithm, which finely samples areas characterised by mean displacements or displacement gradients above empirically-derived thresholds (Table S4 and Fig. S5) (Walstead, 1999; Jónsson et al., 2002). The algorithm first divides the image into four equal-sized blocks, and within each block, the average deformation value, \bar{d} , and the deformation gradient, $\Delta d = d_{max} - d_{min}$, are calculated. Each block is further divided into four equal-sized blocks if either Δd or \bar{d} are above a given threshold, until the block size reaches a minimum size. The displacement value at the center of each block is then used as an input for the non-linear inversion. Respectively, 1329 and 1229 data points are included in the inversion for the ascending and descending interferograms (see Fig. S5).

Text S6 - Displacement discontinuity and direct boundary element methods

The displacement discontinuity method approximates a boundary as N elements, and solves the system of equations $\mathbf{AB} = \mathbf{P}$, where \mathbf{P} is the vector of $3N$ imposed traction conditions, \mathbf{A} is the matrix of influence coefficients which relates a unit displacement across element j to the stress on the centroid of element i according to linear elasticity. Finally, \mathbf{B} is the vector of $3N$ amplitudes of displacements D_j across an element ($D_j = u_j^+ - u_j^-$, $j = (x, y, z)$, where u_j^+ and u_j^- are the displacement on the positive and negative sides of j). \mathbf{B} is the only unknown, and can be found by solving the system of $3N$ linear equations with $3N$ unknowns. After inverting for D_j , stresses and displacements anywhere within the finite elastic body can be calculated using the sum of known analytical solutions of displacement across a planar element (Crouch, 1976).

The direct method, on the other hand, solves for unknown displacements and stresses on the boundary, as opposed to first solving for the amplitude of displacements (Lachat & Watson, 1976). This is done by leveraging the reciprocal theorem (Sokolnikoff, 1956), considering reciprocity of work between the unknown boundary conditions of the current problem and the boundary conditions of a problem with a known analytical solution. In this case, the latter is a point load in an infinite body. We can then set up and solve a system of equations $\mathbf{HU} = \mathbf{F}$. \mathbf{H} is the matrix of influence coefficients computed by evaluating the boundary integral of stresses produced on element j by a unit load on element i in an infinite medium, and the integrals of displacements produced on element j by a unit load on element i . \mathbf{F} is a known vector of size $3N$, including the pre-

scribed boundary tractions, and \mathbf{U} is the vector of $3N$ unknowns corresponding to the displacement on the boundary Γ of a finite elastic body Ω (Cayol & Cornet, 1997). Between these two methods, the former is numerically stable for fractures, while the latter is more exact and computationally efficient for massive boundaries (such as topographies and pressurized magmatic reservoirs).

Text S7 - Neighborhood Algorithm Appraisal

The appraisal problem is essentially an interpolation of the multidimensional parameter space, constructing an approximate PPD using 10000 resampled points through a random walk (Gibb's sampling) of the Voronoi cells of the forward models calculated in Section 3.3 of the main text. No further forward models need to be calculated, as the PPD of each Voronoi cell is considered uniform. The only calculations, for each step, include that of the intersection between Voronoi cells along each axis i in the parameter space, as well as the direction in which the next step will occur. This will always be in the direction of higher probability density (lower misfit).

References

- Allard, P., Aiuppa, A., Bani, P., Métrich, N., Bertagnini, A., Gauthier, P., ... Garaebiti, E. (2015). Prodigious emission rates and magma degassing budget of major, trace and radioactive volatile species from Ambrym basaltic volcano, Vanuatu island Arc. *Journal of Volcanology and Geothermal Research*, *304*, 378–402. doi: 10.1016/j.jvolgeores.2015.08.022
- Bagnardi, M., González, P. J., & Hooper, A. (2016). High-resolution digital elevation model from tri-stereo Pleiades-1 satellite imagery for lava flow volume estimates at Fogo Volcano. *Geophysical Research Letters*, *43*(12), 6267–6275. doi: 10.1002/2016GL069457
- Cayol, V., & Cornet, F. H. (1997). 3D mixed boundary elements for elastostatic deformation field analysis. *International journal of rock mechanics and mining*, *34*(2), 275–287. doi: 10.1016/S0148-9062(96)00035-6
- Clarisse, L., Coheur, P. F., Theys, N., Hurtmans, D., & Clerbaux, C. (2014). The 2011 Nabro eruption, a SO₂ plume height analysis using IASI measurements. *Atmospheric Chemistry and Physics*, *14*(6), 3095–3111. doi: 10.5194/acp-14-3095-2014
- Coppola, D., Laiolo, M., & Cigolini, C. (2016). Fifteen years of thermal activity at Vanuatu's volcanoes (2000 - 2015) revealed by MIROVA. *Journal of Volcanology and Geothermal Research*, *322*, 6–19. doi: 10.1016/j.jvolgeores.2015.11.005
- Coppola, D., Laiolo, M., Cigolini, C., Delle Donne, D., & Ripepe, M. (2016). Enhanced volcanic hot-spot detection using MODIS IR data: Results from the MIROVA system. *Geological Society Special Publication*, *426*(1), 181–205. doi: 10.1144/SP426.5
- Crawford, A. M., Stunder, B. J., Ngan, F., & Pavolonis, M. J. (2016). Initializing HYSPLIT with satellite observations of volcanic ash: A case study of the 2008

- Kasatochi eruption. *Journal of Geophysical Research*, 121(18), 10,786–10,803. doi: 10.1002/2016JD024779
- Crouch, S. L. (1976). Solution of plane elasticity problems by the displacement discontinuity method. *International Journal for Numerical Methods in Engineering*, 10(2), 301–343.
- Doin, M.-P., Lodge, F., Guillaso, S., Jolivet, R., Lasserre, C., Ducret, G., . . . Pinel, V. (2011). Presentation of the small baseline NSBAS processing chain on a case example: the Etna deformation monitoring from 2003 to 2010 using Envisat data. In *Proceedings of the esa 'fringe 2011 workshop', frascati, italy, (19-23 september 2011)* (pp. 19–23).
- Favalli, M., Fornaciai, A., Mazzarini, F., Harris, A., Neri, M., Behncke, B., . . . Boschi, E. (2010). Evolution of an active lava flow field using a multitemporal LIDAR acquisition. *Journal of Geophysical Research: Solid Earth*, 115(11), 1–17. doi: 10.1029/2010JB007463
- Grandin, R., Doin, M.-P., Bollinger, L., Pinel-Puysségur, B., Ducret, G., Jolivet, R., & Sapkota, S. N. (2012). Long-term growth of the Himalaya inferred from interseismic InSAR measurement. *Geology*, 40(12), 1059. doi: 10.1130/G33154.1
- Jónsson, S., Zebker, H., Segall, P., & Amelung, F. (2002). Fault slip distribution of the 1999 M_w 7.1 Hector Mine, California, earthquake, estimated from satellite radar and GPS measurements. *Bulletin of the Seismological Society of America*, 92(4), 1377–1389. doi: 10.1785/0120000922
- Lachat, J. C., & Watson, J. O. (1976). Effective numerical treatment of boundary integral equations: A formulation for three-dimensional elastostatics. *International Journal for Numerical Methods in Engineering*, 10(5), 991–1005. doi: 10.1002/nme.1620100503
- Li, C., Krotkov, N. A., Carn, S., Zhang, Y., Spurr, R. J., & Joiner, J. (2017). New-generation NASA Aura Ozone Monitoring Instrument (OMI) volcanic SO_2 dataset: Algorithm description, initial results, and continuation with the Suomi-NPP Ozone Mapping and Profiler Suite (OMPS). *Atmospheric Measurement Techniques*, 10(2), 445–458. doi: 10.5194/amt-10-445-2017
- Rosen, P. A., Gurrola, E., Sacco, G. F., & Zebker, H. (2012, April). The InSAR scientific computing environment. In *Eusar 2012; 9th european conference on synthetic aperture radar* (p. 730-733).
- Rosen, P. A., Hensley, S., Peltzer, G., & Simons, M. (2004). Updated Repeat Orbit Interferometry Package Released. *Eos*, 85(5), 47.
- Rupnik, E., Pierrot-Deseilligny, M., & Delorme, A. (2018). 3D reconstruction from multi-view VHR-satellite images in MicMac. *ISPRS Journal of Photogrammetry and Remote Sensing*, 139, 201–211. doi: 10.1016/j.isprsjprs.2018.03.016
- Shreve, T., Grandin, R., Boichu, M., Garaebiti, E., Moussallam, Y., Ballu, V., . . . Pelletier, B. (2019). From prodigious volcanic degassing to caldera subsidence and quiescence at Ambrym (Vanuatu): the influence of regional tectonics. *Scientific Reports*, 9(18868). doi: <https://doi.org/10.1038/s41598-019-55141-7>
- Smittarello, D., Cayol, V., Pinel, V., Peltier, A., Froger, J. L., & Ferrazzini, V.

- (2019). Magma Propagation at Piton de la Fournaise From Joint Inversion of InSAR and GNSS. *Journal of Geophysical Research: Solid Earth*, *124*(2), 1361–1387. doi: 10.1029/2018JB016856
- Sokolnikoff, I. (1956). *Mathematical theory of elasticity*. New York: McGraw-Hill.
- Stein, A. F., Draxler, R. R., Rolph, G. D., Stunder, B. J., Cohen, M. D., & Ngan, F. (2015). NOAA’s hysplit atmospheric transport and dispersion modeling system. *Bulletin of the American Meteorological Society*, *96*(12), 2059–2077. doi: 10.1175/BAMS-D-14-00110.1
- Walstead, S. T. (1999). *Fractal and wavelet image compression techniques*. Bellingham, Washington: SPIE Optical Engineering Press.
- Wessel, B. (2016). *TanDEM-X Ground Segment - DEM Products Specification Document* (Tech. Rep. No. 3.1). Oberpfaffenhofen, Germany: EOC, DLR. Retrieved from <https://tandemx-science.dlr.de/> doi: DOI:10.1002/hyp.3360050103
- Wright, R. (2016). MODVOLC: 14 years of autonomous observations of effusive volcanism from space. *Geological Society, London, Special Publications*, *426*, 23–53. doi: 10.1144/SP426.12
- Wright, R., Flynn, L. P., Garbeil, H., Harris, A. J. L., & Pilger, E. (2004). MODVOLC: Near-real-time thermal monitoring of global volcanism. *Journal of Volcanology and Geothermal Research*, *135*(1-2), 29–49. doi: 10.1016/j.jvolgeores.2003.12.008

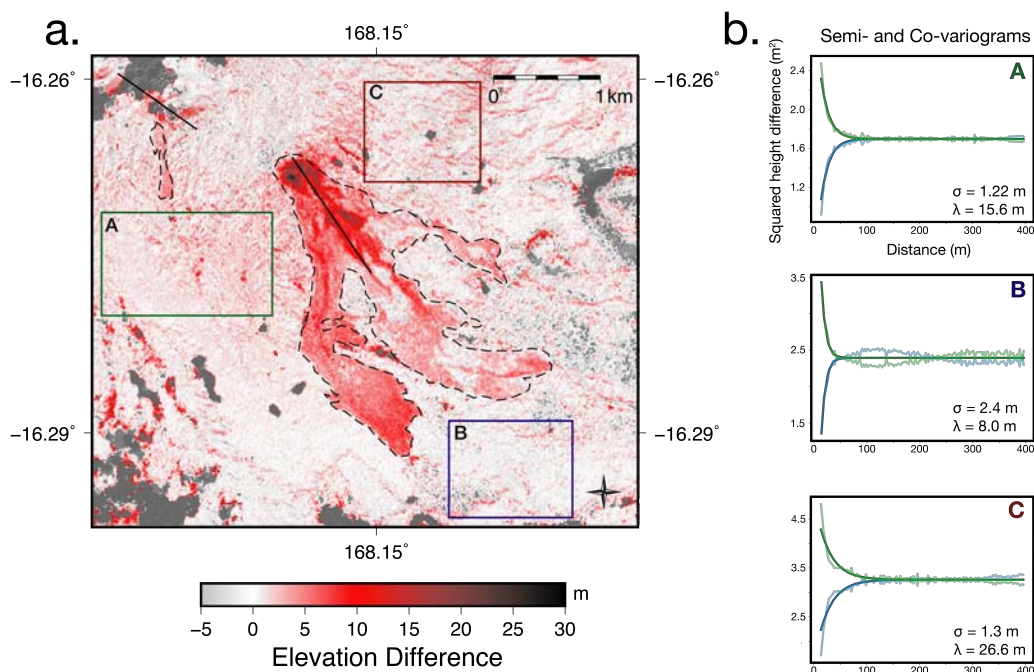


Figure 1. **a.** The elevation difference between DEMs pre- and post- February 2015, as explained in Text S2. The main and secondary flows are outlined with dotted lines, new fissures are mapped with solid lines, and the control areas are outlined with solid, colored lines. Adapted from Shreve et al. (2019). **b.** The semi- and co-variograms for each of the control areas (light colored lines), and the best-fitting exponentials (solid colored lines). The estimates for σ and λ are shown.

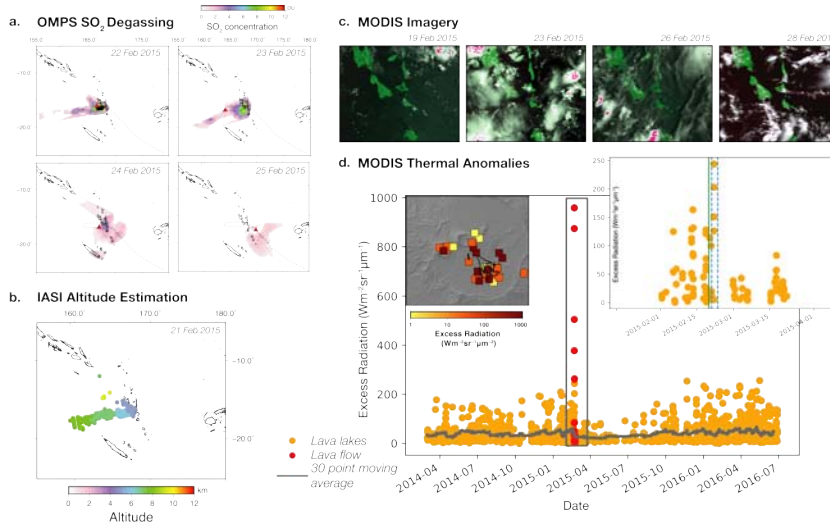


Figure 2. **a.** SO_2 concentration during the eruption measured by OMPS, using the TRM data product, as described in the main text. The largest plotted circles indicate the pixels above the 2 DU threshold, while the smaller plotted circles indicate those above the 0.8 - 1 DU threshold. Datapoints with SO_2 concentrations higher than 12 DU are saturated with black. The dotted line is the trajectory calculated by HYSPLIT of SO_2 parcels emitted at 5 km altitude at 3h00 21 February. The red triangle indicates the location of these SO_2 parcels at the time of the OMPS acquisition. **b.** The altitude estimated by IASI at $\sim 10:30$ UTC 21 February. **c.** MODIS images with the least cloud cover before, during, and after the eruption. The cloud cover extent may effect the detection of lava lake thermal anomalies during and after the eruption. **d.** A time series of excess radiation of thermal anomalies at Ambrym, as detected by MODIS. The orange dots correspond to lava lakes, while the red dots are due to lava effusion. The gray line is a moving average calculated using the lava lake thermal anomalies. The inset shows the lava lake thermal anomalies before, during, and after the eruption. The green line indicates the timing of the 6.4 M_w earthquake, and the dotted blue lines indicate the maximum eruption duration. The second inset shows the thermal anomalies from 19-27 February in map view.

Table 1. DEM statistical analysis of three control areas, including the surface area, mean elevation, and uncorrelated elevation standard deviation.

Control area	Surface area ($\times 10^6 \text{ m}^2$)	Mean elevation, μ_Z (m)	Uncorrelated elevation standard deviation, σ_Z (m)
A	1.62	1.11	1.40
B	1.10	-0.299	1.64
C	1.06	0.233	1.87

Table 2. SAR datasets used in this study.

Master date (UTC)	Slave date (UTC)	Sensor	Mode	Geometry/Track	Heading/Look Angle	Data type
2015/01/24 13:14	2015/03/21 13:14	ALOS-2	Stripmap (SM3)	Ascending T101	-13.6°/39.7°	InSAR/azimuth pixel offsets
2015/01/24 13:14	2015/04/04 13:14	ALOS-2	Stripmap (SM3)	Ascending T101	-13.6°/39.7°	MAI
2015/1/17 00:24	2015/03/14 00:24	ALOS-2	Wideswath (WD1)/Stripmap (SM3)	Descending T203	192.7°/33°	InSAR
2015/02/13 06:13	2015/02/25 06:13	CSK	Stripmap (H4-04)	Descending	192.8°/32.2°	Range/azimuth pixel offsets

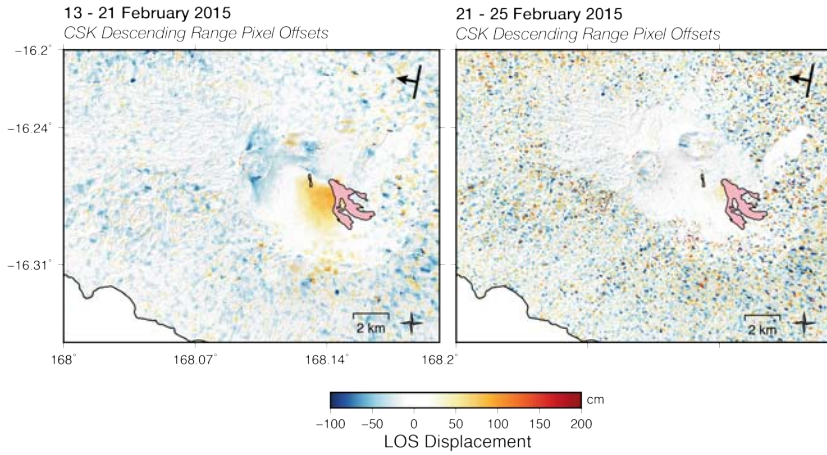


Figure 3. Displacement field during the first and final 24 hours of the eruption, as measured by CSK range pixel offsets. Caldera-ring fault activation, and the majority of dike-induced deformation, occurred during the first 24 hours. All images were acquired at 6:00 UTC.

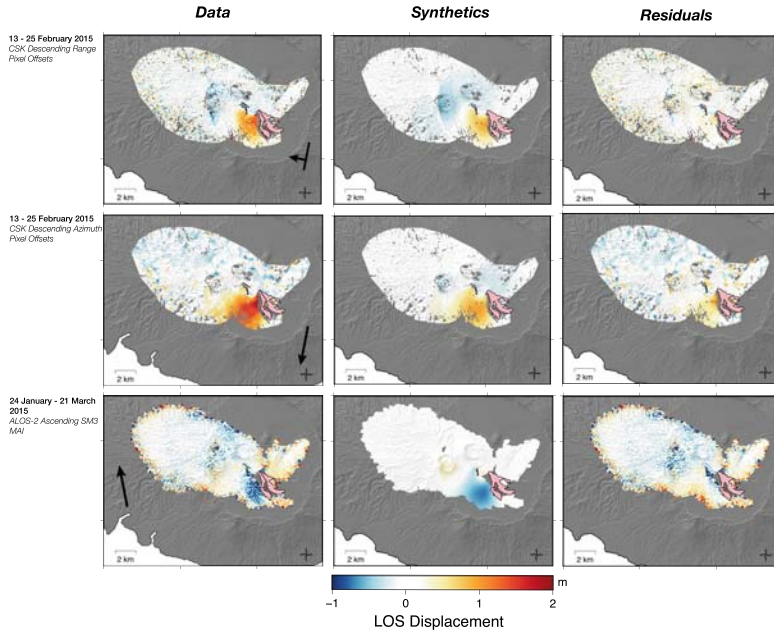


Figure 4. Data, synthetics, and residuals for datasets not included in the inversion. The left hand column shows the data, the middle column shows the ground displacements produced by the best-fit model from Inversion 3, projected into the LOS of each dataset. The right hand column shows the difference between the data and synthetic ground displacements. The colorbar is the same for all figures.

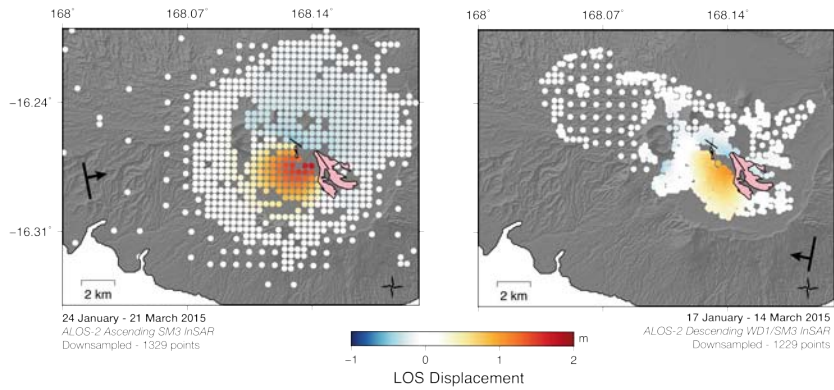


Figure 5. The ascending and descending interferograms, downsampled using the adaptive quadtree decomposition algorithm.

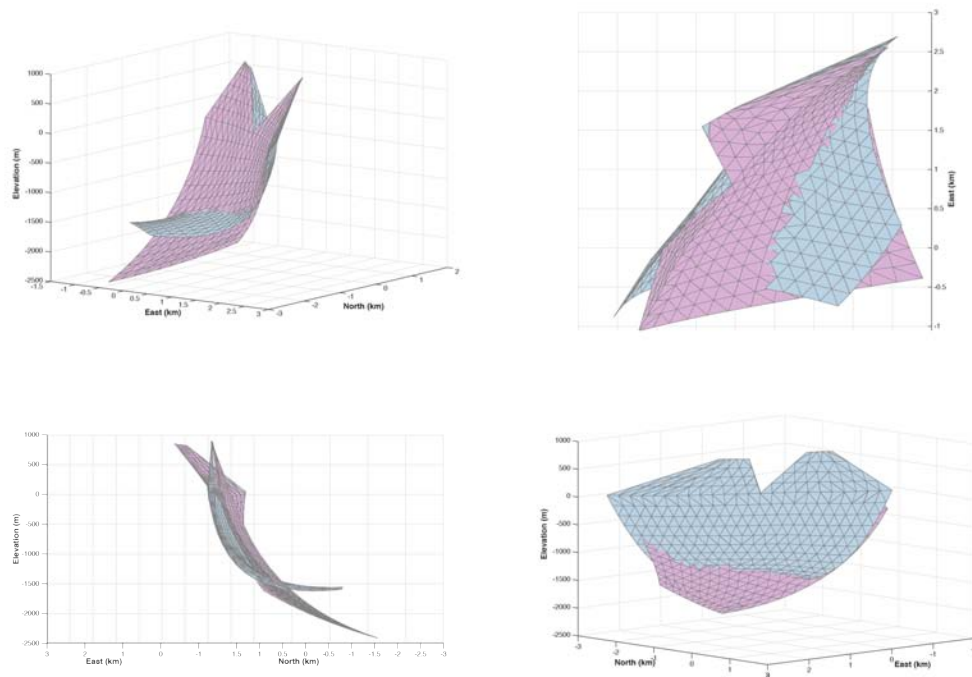


Figure 6. The dike geometry after varying the data covariance matrix. The correlation distance and variance of the residuals are calculated at the end of the neighborhood inversion. We used these values to reset the correlation length to $a = 51$ km and $\sigma^2 = 0.0187$ m² for the ascending interferogram and $a = 11$ km and $\sigma^2 = 0.0160$ m² for the descending interferogram. Here we compare the inverted dike geometry using these values (light blue mesh) to the geometry found in Inversion 1 (light purple mesh), as described in the main text. The total volume change was 2.9×10^7 m³ in the updated inversion, compared to 3.0×10^7 m³ in Inversion 1.

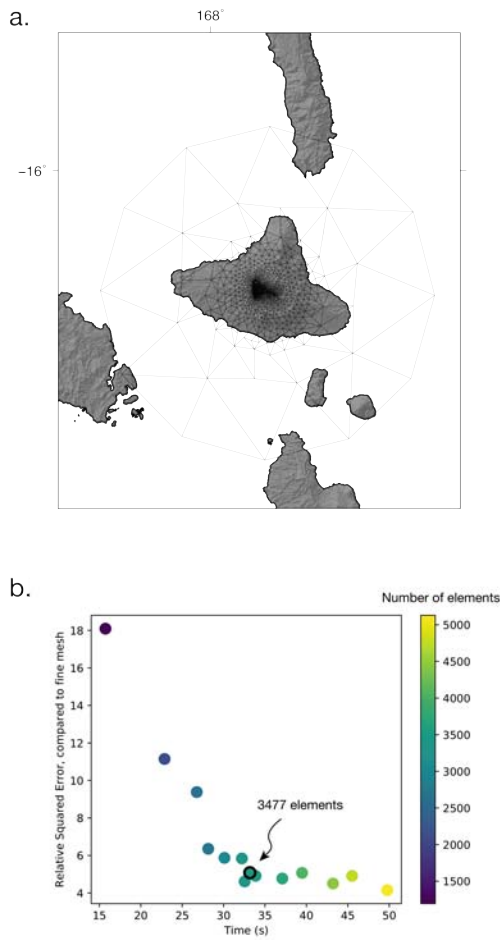


Figure 7. **a.** The topography mesh in map view. Elements are finer where the dike and fault intersect the surface. **b.** A plot showing the relative squared error of the calculated ground displacement using a particular topography mesh, compared to a very fine topography mesh (>25000 elements), versus run time of the forward boundary element calculation. Color represents the number of elements in a particular mesh. The mesh used in the final inversions has 3477 elements, and is indicated by the dot outlined in black.

Table 3. Specifications used for pixel offset post-processing, including masking and filtering.

Measurements	Displacement bounds	Filter	SNR Mask
ALOS-2 azimuth pixel offsets	$-2.7 \text{ m} < \Delta x < 1.6 \text{ m}$	None	$\Delta x_{SNR} < 8$
CSK range pixel offsets	$-1.5 \text{ m} < \Delta x < 3 \text{ m}$	None	$\Delta x_{SNR} < 5$
CSK azimuth pixel offsets	$-2.7 \text{ m} < \Delta x < 1.6 \text{ m}$	Median filter, block size $500 \text{ m} \times 500 \text{ m}$	$\Delta x_{SNR} < 5$

Table 4. Quadtree specifications used for downsampling.

Dataset	Min/Max block size (m)	Deformation gradient threshold (m)	Maximum deformation threshold (m)
ALOS-2 ascending (2015/01/24 - 2015/03/21)	387/6190	0.05	0.13
ALOS-2 descending (2015/01/17 - 2015/03/14)	96/770	0.11	0.3

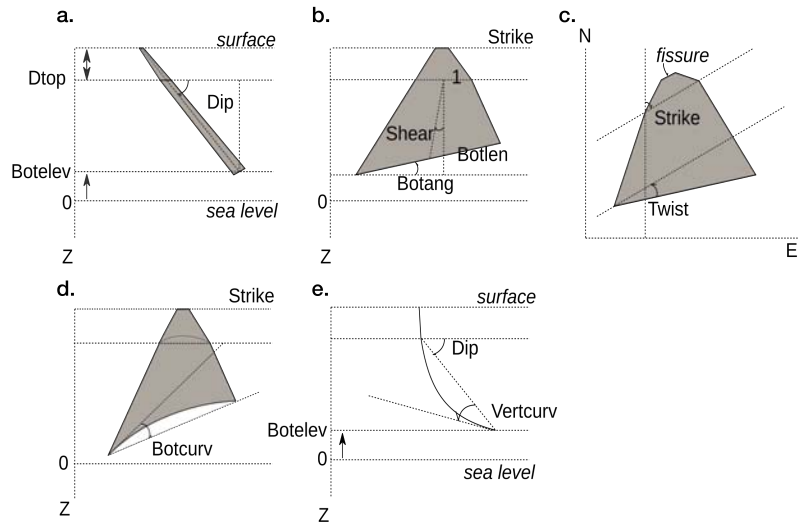


Figure 8. Non-linearly inverted dike geometry parameters. Figure from Smittarello et al. (2019). **a.** The *dip* is the angle measured from the surface, *dtop* is the distance measured from the surface echelons to the top of the quadrangle, and *botelev* is the distance measured from sea level to the quadrangle's bottom edge. **b.** The *shear* is the angle between the line perpendicular to the upper edge of the quadrangle's strike (clockwise angle from North), and the line formed by the center of the quadrangle's upper edge to the center of its bottom edge. The *botlen* is the ratio between the length of the quadrangle's upper and bottom edges. The *botang* is the angle of the bottom edge measured vertically from a line at the *botelev* elevation, parallel to the strike of the quadrangle's upper edge. **c.** The *twist* is the horizontal angle between the upper edge of the quadrangle's strike and the quadrangle's bottom edge. **d.** The *botcurv* is the angle between a line that connects both corners of the bottom edge and a line that is tangent to the bottom edge at one of the corners. **e.** The *vertcurv* is the vertical angle between a line connecting the center of the upper edge to the center of the bottom edge, and a line that is tangent to the center of the bottom edge.

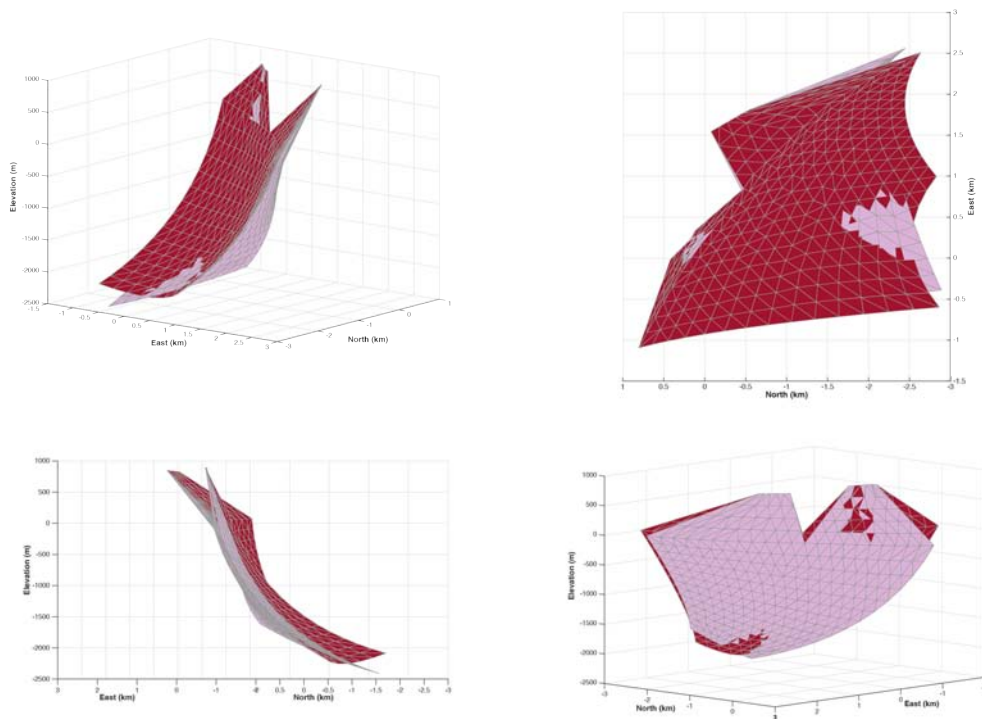


Figure 9. Dike geometry after removing a ramp from the ascending interferogram. A ramp is fit to and removed from the far-field of the ascending interferogram, after the deformation is masked, and the deramped dataset is used in the neighborhood inversion. Here we compare the inverted dike geometry using these values (red mesh) to the geometry found in Inversion 1 (light purple mesh). The total volume change was $2.7 \times 10^7 \text{ m}^3$ in the updated inversion, compared to $3.0 \times 10^7 \text{ m}^3$ in Inversion 1.

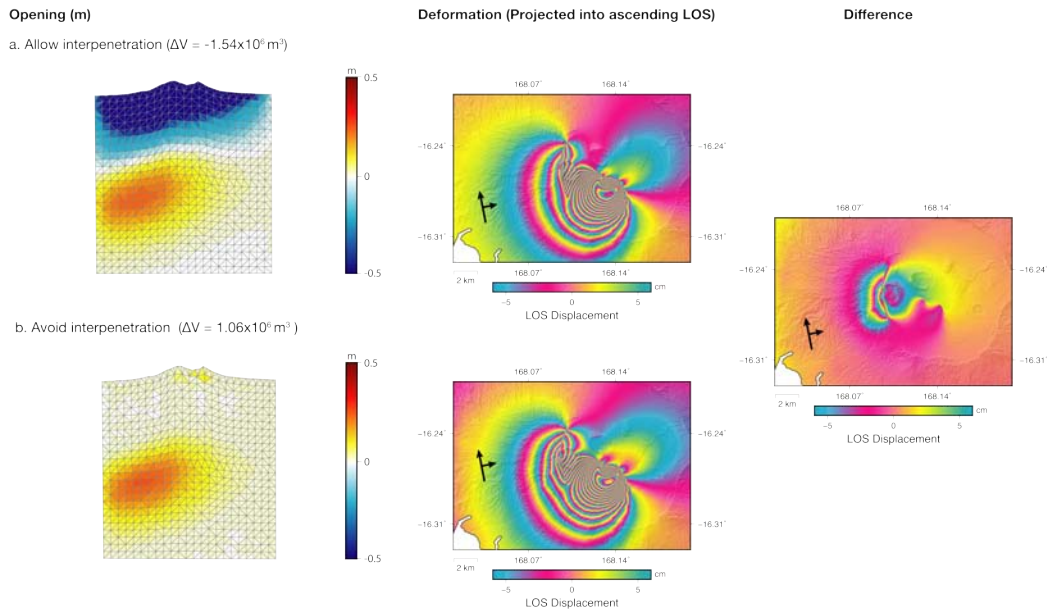


Figure 10. **a.** Using the best-fit model parameters found in Inversion 2 (see Table 5), we calculate a forward model allowing fracture wall interpenetration. The figure in the left hand column shows the opening (and closing) on the fault elements, while the figure in the middle column shows the ground displacement resulting from both the fault slip and the dike opening, projected into the ascending line of sight. **b.** The left hand column is the opening on the fault when the nonnegativity constraint (preventing interpenetration) is applied. The middle column shows the ground displacement produced by both the fault and dike, projected into the ascending line of sight. The right hand column shows the difference between the two displacement fields, with more than 20 cm of difference in the displacement field of the two models, particularly to the west of the fault.

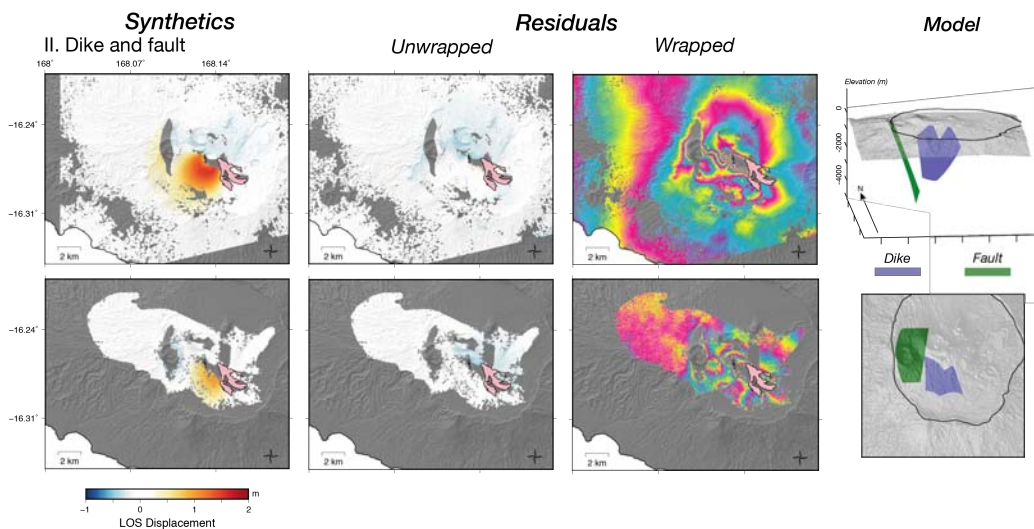


Figure 11. Synthetics, wrapped residuals, and source geometries for the ascending and descending interferograms, using the results from Inversion 2. This inversion included both an opening dike and normal fault, but no decompressing reservoir.

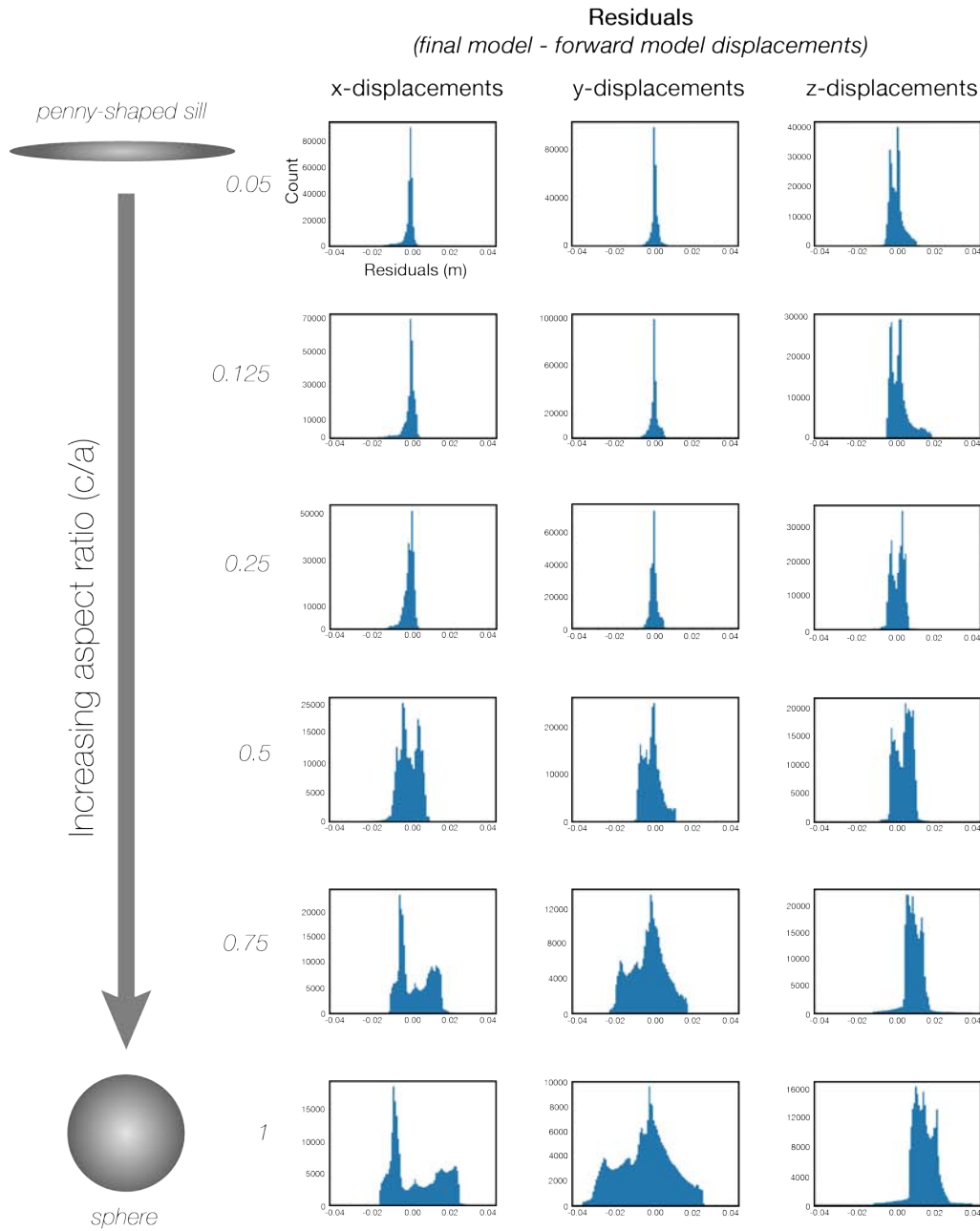


Figure 12. Histograms of the residuals after subtracting the modelled displacement field from Inversion 3 from the displacement field with a reservoir with an increasing aspect ratio (semi-minor axis ranges from 50 m to 1000 m). A larger aspect ratio indicates a more spherical source. We note that the error in the residuals is less than 2% for semi-minor axes ranging from 50 - 500 m (aspect ratios 0.05 - 0.5).

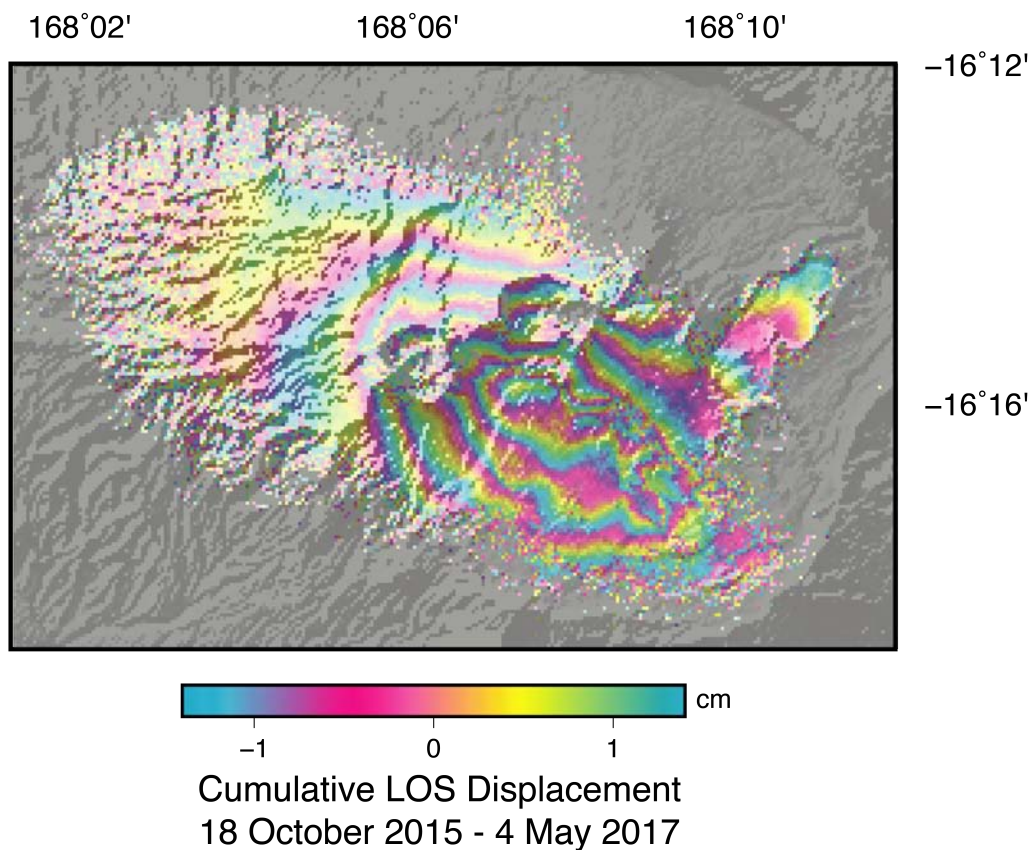


Figure 13. Cumulative LOS lengthening (subsidence) measured by ESA's C-band SAR Satellite Sentinel-1 (ascending Track 81). A small-baseline time series was processed using interferograms spanning about two years after the 2015 eruption, from 18 October 2015 to 4 May 2017 (Doin et al., 2011). Subsidence within the caldera dominated during this time period, at a rate of approximately 1 cm/month, elongated in the direction of the rift zone. Figure from Shreve et al. (2019).

Table 5. Mean and best-fit models from the non-linear inversion, including 95% confidence intervals and the full explored parameter bounds.

Inversion	Parameter	Mean \pm Standard Deviation	Best Fit Model	95% Confidence Interval	Explored Interval
<i>Inversion 1</i>	Dike				
	Dip ($^{\circ}$)	118.73 \pm 0.52	118.56	[117.63, 119.76]	[0, 180]
	Shear ($^{\circ}$)	-21.27 \pm 0.80	-20.21	[-22.60,-19.25]	[-80,80]
	Bottom Elevation (m)	-2014.97 \pm 49.43	-2034.90	[-2102.90,-1910.45]	[-8000,-500]
	Bottom Length	0.419 \pm 0.0142	0.415	[0.391,0.453]	[0.2,10]
	Twist ($^{\circ}$)	69.69 \pm 0.287	69.59	[68.93,69.97]	[-70,70]
	Botang ($^{\circ}$)	-17.05 \pm 1.34	-19.47	[-19.93,-14.60]	[-45,45]
	D-Top ($^{\circ}$)	897.66 \pm 8.25	904.31	[882.44,916.48]	[0,3000]
	Bottom Curvature ($^{\circ}$)	-6.56 \pm 1.43	-8.46	[-9.68,-4.02]	[-60,60]
	Vertical Curvature ($^{\circ}$)	-34.14 \pm 1.02	-33.77	[-36.11,-32.12]	[-60,60]
	Pressure (MPa)	2.79 \pm 0.056	2.85	[2.70,2.92]	[1,10]
<i>Inversion 2</i>	Dike				
	Dip ($^{\circ}$)	124.95 \pm 0.044	124.95	[124.84, 125.00]	[110,125]
	Shear ($^{\circ}$)	-7.16 \pm 0.90	-6.70	[-8.76,-5.44]	[-30,10]
	Bottom Elevation (m)	-2237.72 \pm 39.27	-2240.63	[-2315.66,-2164.60]	[-3000,-1000]
	Bottom Length	0.23 \pm 0.00287	0.23	[0.226,0.237]	[0,0.5]
	Twist ($^{\circ}$)	29.26 \pm 0.92	29.61	[27.09,29.96]	[-30,30]
	Botang ($^{\circ}$)	7.70 \pm 0.62	7.11	[6.24,8.72]	[-20,20]
	D-Top ($^{\circ}$)	801.05 \pm 0.87	801.72	[800.07,803.06]	[800,1500]
	Bottom Curvature ($^{\circ}$)	-26.41 \pm 1.30	-26.74	[-28.65,-23.71]	[-45,45]
	Vertical Curvature ($^{\circ}$)	-30.072 \pm 0.43	-30.50	[-30.784,-29.137]	[-60,60]
	Pressure (MPa)	2.37 \pm 0.0125	2.39	[2.34,2.39]	[1,6]
Fault	Dip ($^{\circ}$)	65.024 \pm 0.0161	65.012	[65.002,65.061]	[65,90]
	Shear ($^{\circ}$)	0	-	-	[0,0]
	Bottom Elevation ($^{\circ}$)	-3980.16 \pm 10.48	-3995.32	[-3964.65,-3823.23]	[-4000,-500]
	Bottom Length	1	-	-	[1,1]
	Twist ($^{\circ}$)	0	-	-	[0,0]
	Botang ($^{\circ}$)	0	-	-	[0,0]
	D-Top ($^{\circ}$)	0	-	-	[0,0]
	Bottom Curvature ($^{\circ}$)	0	-	-	[0,0]
	Vertical Curvature ($^{\circ}$)	0	-	-	[0,0]
	Shear Stress (MPa)	-0.258 \pm 0.0036	-0.257	[-0.265,-0.250]	[-1.5,0]
	<i>Inversion 3</i>	Dike			
Dip ($^{\circ}$)		122.73 \pm 0.92	122.29	[121.080,124.58]	[110,125]
Shear ($^{\circ}$)		-8.53 \pm 1.62	-8.68	[-11.72,-5.30]	[-30,10]
Bottom Elevation (m)		-1783.58 \pm 43.07	-1790.13	[-1868.68,-1696.998]	[-3000,-1000]
Bottom Length		0.41 \pm 0.0167	0.403	[0.37,0.44]	[0,0.5]
Twist ($^{\circ}$)		28.41 \pm 1.05	28.38	[26.085,29.85]	[-30,30]
Botang ($^{\circ}$)		-3.53 \pm 1.26	-2.51	[-5.80,-0.85]	[-20,20]
D-Top ($^{\circ}$)		805.095 \pm 3.72	804.45	[800.53,13.76]	[800,1500]
Bottom Curvature ($^{\circ}$)		37.99 \pm 3.83	34.98	[29.75,44.168]	[-45,45]
Vertical Curvature ($^{\circ}$)		-36.81 \pm 1.48	-36.77	[-39.63,-33.76]	[-60,60]
Pressure (MPa)		2.83 \pm 0.0758	2.85	[2.69,2.99]	[1,6]
Fault	Dip ($^{\circ}$)	65.29 \pm 0.171	65.30	[65.034,65.64]	[65,90]
	Shear ($^{\circ}$)	0	-	-	[0,0]
	Bottom Elevation ($^{\circ}$)	-3889.48 \pm 86.59	-3846.76	[-3964.65,-3611.11]	[-4000,-500]
	Bottom Length	1	-	-	[1,1]
	Twist ($^{\circ}$)	0	-	-	[0,0]
	Botang ($^{\circ}$)	0	-	-	[0,0]
	D-Top ($^{\circ}$)	0	-	-	[0,0]
	Bottom Curvature ($^{\circ}$)	0	-	-	[0,0]
	Vertical Curvature ($^{\circ}$)	0	-	-	[0,0]
	Shear Stress (MPa)	-0.127 \pm 0.0132	-0.13	[-0.151,-0.0993]	[-1.5,0]
	Reservoir	X0 (UTM)	193142	-	-
Y0 (UTM)		8201632	-	-	[8201632,8201632]
Semi-major Axis (m)		2033.80 \pm 119.73	2012.23	[1806.45,2281.16]	[1000,6000]
Semi-minor Axis (m)		5	-	-	[5,5]
Depth (m)		-4100	-	-	[-4100,-4100]
Strike ($^{\circ}$)		0	-	-	[0,0]
Dip ($^{\circ}$)		0	-	-	[0,0]
Plunge ($^{\circ}$)		0	-	-	[0,0]
Pressure (MPa)		-124.29 \pm 17.66	-118.9	[-164.82,-82.41]	[-350,0]

Chapter 5

Discussion

Chapters 3 and 4 summarize and discuss the eruptions at Ambrym which occurred in the past 5 years. In this chapter, we will discuss additional deformation episodes that have been measured with InSAR from 2004 – 2020. We will start by synthesizing the results from Chapters 3 and 4 with these additional 10 years of measurements, as well as with results from petrological studies. This allows us to develop an updated conceptual model of Ambrym’s magmatic plumbing system and discuss the system’s dynamics. We also explore possible physical mechanisms driving inter-eruptive subsidence, in particular the potential role of passive degassing in driving reservoir depressurization. Then, we will discuss whether the organization of Ambrym’s current day magma plumbing system could, at least in part, be explained by the Plinian eruption and subsequent caldera collapse proposed by [Robin et al. \[1993\]](#). We also extend the caldera formation model of [Robin et al. \[1993\]](#) to include an additional caldera development stage– episodic, meter scale deepening of the caldera by subsidence along caldera ring-faults. Finally, we end by qualitatively combining InSAR measurements with thermal anomalies and gas emissions measurements from 2004 – 2020. We jointly interpret these datasets to hypothesize the occurrence of a magma intrusion in 2005, and briefly discuss the influence of magma replenishment on Ambrym’s lava lake activity.

5.1 Organization of Ambrym’s magmatic plumbing system

5.1.1 Magma storage inferred from geodesy: evidence for a vertically extensive plumbing system

5.1.1.1 Synthesis of observations and geodetic modelling

Over the past twenty years, Ambrym has experienced episodes of subsidence and uplift during both co-eruptive and inter-eruptive periods. We invert InSAR surface displacements spanning 2004 to the current day to estimate volume and location changes of pressure sources. We assume that each inverted source represents a magma reservoir. Accordingly, this is a simplification of reality, and the implications of this assumption will be discussed in Sections

5.1.1.2 and 5.1.1.3. Our inversions suggest that the depths and geometries of the pressure sources comprising Ambrym's magmatic system change over time (See Figures 5-1 and 5-2).

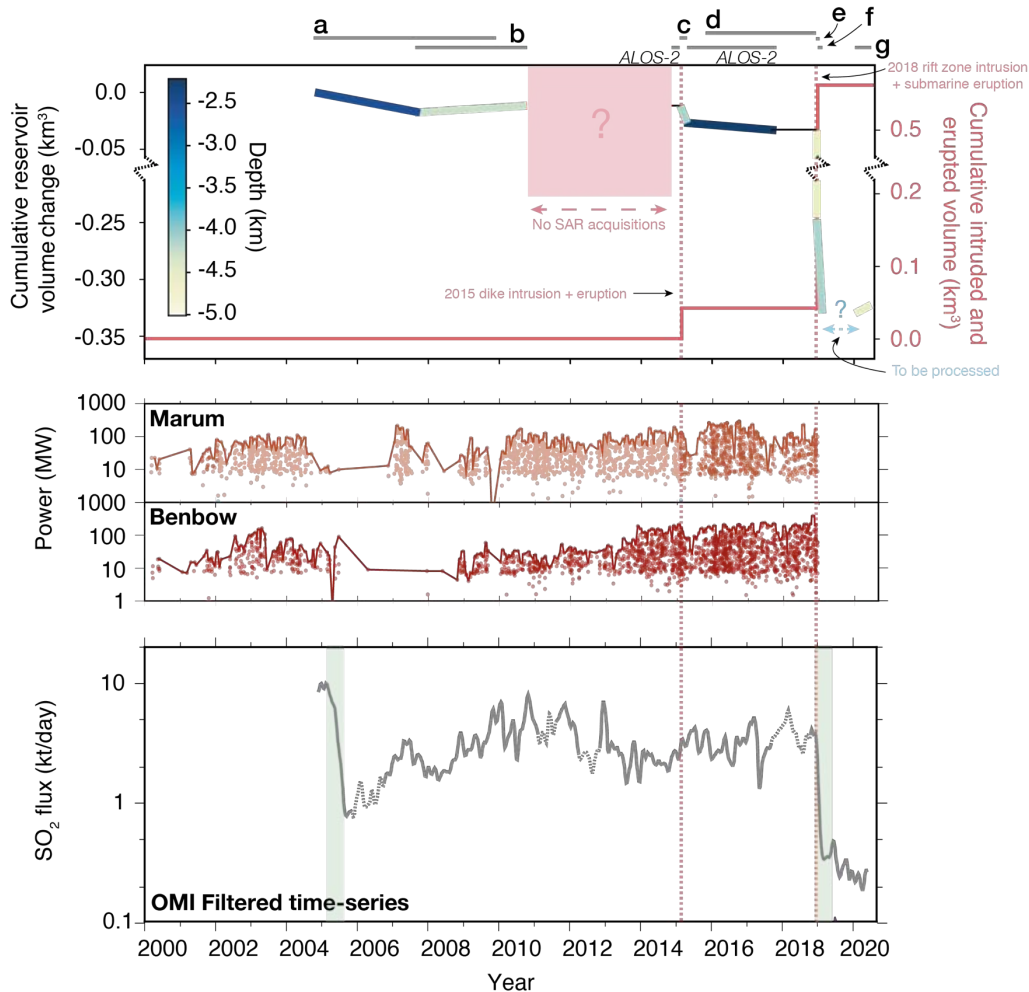


Figure 5-1: **Summary of geodetic modelling, thermal anomalies, and gas emissions.** The top plot shows the cumulative reservoir volume change on the left y-axis, and the color of the line indicates the depth of the source beneath the summit. Note that a different source may be activated during different time spans, given the variation in the depths. The right y-axis shows cumulative intruded and erupted volume. Eruptions are marked with red dotted lines. The middle plot shows the radiated thermal power at Marum and Benbow, associated to MODVOLC thermal alerts from MODIS observations. The bottom plot is the daily SO_2 mass flux at Ambrym derived from OMI satellite SO_2 observations (TRL product assuming a center of mass altitude at 3 km). A procedure was created to calculate the flux, adjusting for daily wind velocities at a pressure level of 900 hPa (~ 1000 m a.s.l), as well as identify and remove measurements with contributions from nearby volcanic sources [Boichu et al., 2021]. The dotted portions of the curve correspond to periods of high degassing at nearby volcanoes (e.g., Ambae and Lopevi). A 90-day Gaussian filter was applied to the corrected time series. The light green bars indicate drastic degassing drops that coincide with at least partial lava lake drainage.

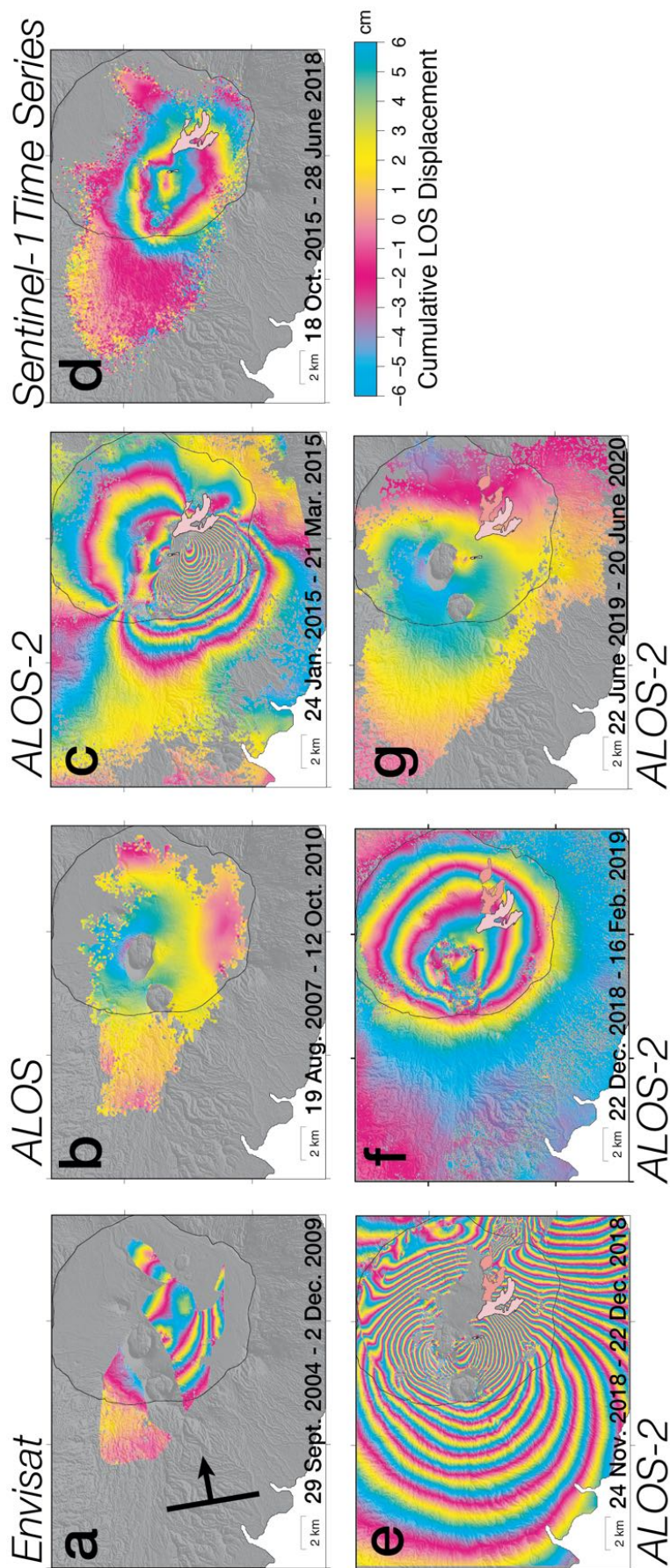


Figure 5-2: Episodes of ground displacement from 2004 – 2020. Ascending interferograms inverted to obtain the reservoir volume changes and depths shown in Figure 5-1. The interferograms have been rewrapped to have the same fringe rate.

In Chapters 3 and 4, geodetic inversions estimate co-eruptive reservoir volume changes. We model the drainage of magmatic sources during three events. The first is associated with the 2015 dike intrusion and eruption. A ~ 4.1 km deep, sill-like reservoir beneath Marum crater deflated by $\sim 13 \times 10^6$ m³ due to magma withdrawal (See Chapter 4, Figure 5-2c). During the 2018 rift zone intrusion and submarine eruption, a spherical point-source was estimated at ~ 4.5 km depth, with a volume change of $195 - 231 \times 10^6$ m³. It was also located beneath Marum crater, and deflated due to magma withdrawal and migration into the rift zone (See Chapter 3, Figure 5-2e). Magma continued to flow from the reservoir to an eruption site offshore until at least February 2019, causing the deflation of another sill-like reservoir (See Figure 5-2f). This source’s volume decreased by $\sim 85 \times 10^6$ m³, and it was located at a depth of ~ 4.1 km. This source extended laterally beneath the caldera, while the deflating source in 2015 was restricted to beneath Marum crater. Despite different lateral extents, the consistent depth may indicate a semi-permanent reservoir located ~ 4 km beneath Ambrym. It is difficult to conclude whether the source that drained during the rift-zone intrusion is deeper (> 4.5 km) than the aforementioned sill. The depth difference may be due to modelling uncertainties (e.g., tradeoff between volume change and source depth, not taking into account topographic effects, etc.). Nonetheless, the different source geometries (spherical point-source vs. sill) may indicate that magma was extracted from two distinct storage regions during the eruptions in 2015 and 2018. This is corroborated by petrological analysis of the 2018 eruptive products (See Section 5.1.3.2).

In addition to these co-eruptive magmatic sources, we observe two inter-eruptive subsidence episodes (See Figure 5-2a,d). The first episode spans 2004 – 2009. More than 30 cm of subsidence is measured with Envisat. The second episode begins almost immediately after the 2015 eruption, resulting in ~ 20 cm of subsidence over 2.5 years. In August 2017, this subsidence stops abruptly (See Figure 5-5). In Sections 5.1.2.1 and 5.3.1 we will demonstrate that these sources are shallower (< 3 km deep) than the co-eruptive magmatic sources active in 2015, 2018, and 2019. A period of uplift is also observed sometime between 2007 – 2010, as shown in Figure 5-2b. At the time of writing (August 2020), a second uplift episode has been ongoing since the beginning of 2020 (See Figure 5-2g). We model source location and volume change during these uplift episodes with both uniform opening on a sill and pressurization of a spherical point-source using a nonlinear geodetic inversion [Briole et al., 1987].

5.1.1.2 Variability in InSAR-derived reservoir depths: Is it real?

At Ambrym, deformation source models vary in geometry, lateral extent, and depth. On one hand, these variations may be due to low data quality or modelling biases. For example, if a dataset has low coherence or low temporal resolution, the estimated model parameters will be less reliable. There are also inherent trade-offs in the geodetic inversions, which can affect the estimated source depth. Tradeoffs exist between reservoir depth and geometry, or reservoir depth and pressure change (See Section 2.2.2). On the other hand, if we have redundant data with a high SNR, we can conclude that the estimated depth variations are reliable. These variations may then be explained by multiple storage levels within the magmatic system, or a combination of physical processes occurring at different levels within the system.

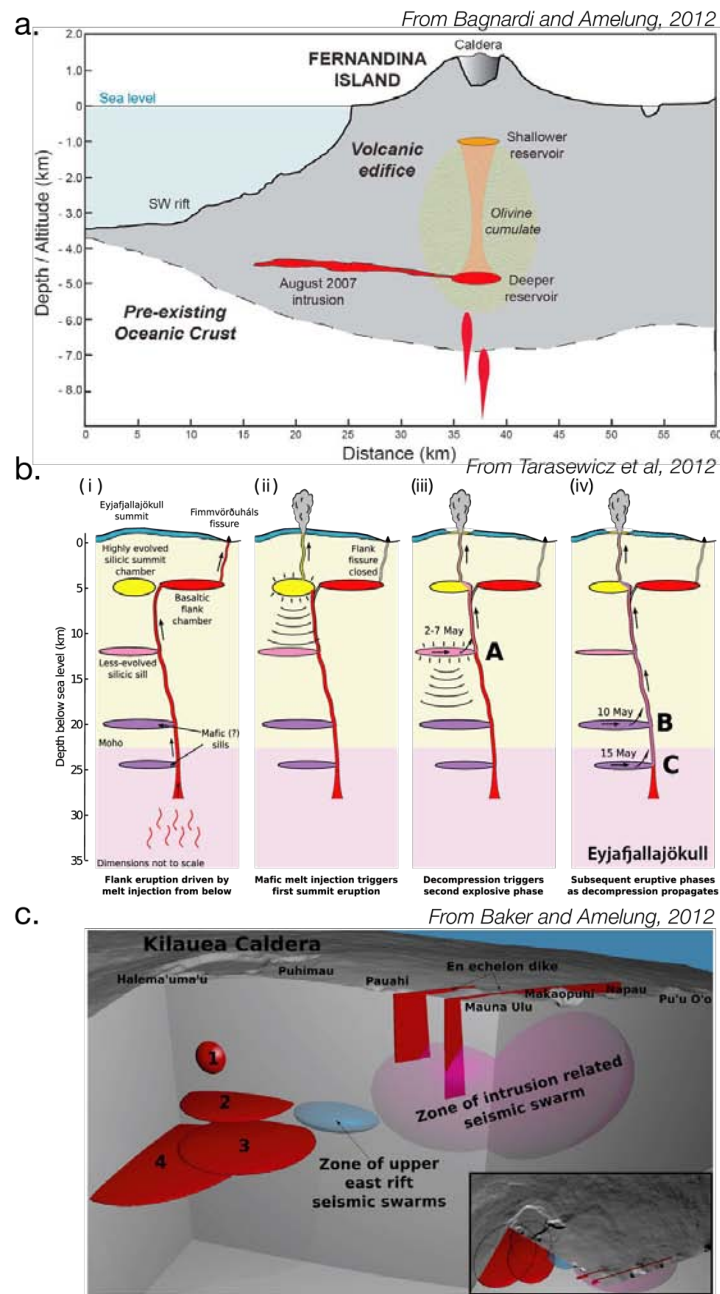


Figure 5-3: **Examples of vertically extensive basaltic systems.** Each system is composed of either stacked sills within rigid host rock or magma lenses in a crystalline mush network. **a.** The magmatic system of the basaltic shield volcano Fernandina, as imaged by modelling of interferograms spanning various time periods. The magmatic system is inferred to be made of at least two semi-permanent sills that are hydraulically connected. Illustration from [Bagnardi and Amelung \[2012\]](#). **b.** Temporal evolution of progressive decompression at Eyjafjallajökull. Eruptions were first fed from the shallow sills. The sources deepened throughout the course of the eruption. Schematic illustration from [Tarasewicz et al. \[2012\]](#). **c.** The schematic illustration from [Baker and Amelung \[2012\]](#) showing the numerous pressure sources beneath Kilauea volcano that were active between 2004 and 2008.

In the case of the 2015 and 2018 eruptions, we jointly invert multiple InSAR and pixel offset tracking datasets. Robust model parameter estimates are ensured by combining ascending and descending interferograms, as well as pixel offset azimuth displacements. Therefore, neither sparse data, nor trade-offs, can explain the different source geometries and locations during the 2015 and 2018 eruptions. We proceed by assuming differences in source geometry or location reflect differences in the active magma reservoirs.

Inter-eruptive time periods (2004 – 2009, 2015 – 2017), however, have not been analyzed in as much detail as co-eruptive periods, and the model estimates are therefore less reliable. The geodetic models for these time periods, presented in Sections 5.1.2.1 and 5.3.1, are performed with limited datasets, resulting in uncertain source geometries and depths. Nonetheless, the deformation wavelength of the InSAR measurements from 2004 – 2009 and 2015 – 2017 seem to indicate that these sources are shallower than the magma lenses drained during the 2015 and 2018 eruptions. Bearing in mind these limitations, as well as the constraints obtained from detailed modelling of co-eruptive periods, we make preliminary interpretations of the physical mechanisms driving inter-eruptive deformation episodes (Sections 5.1.2.3 and 5.3.1). We acknowledge that further studies should be undertaken to test the hypotheses proposed in these sections (See Section 6.3).

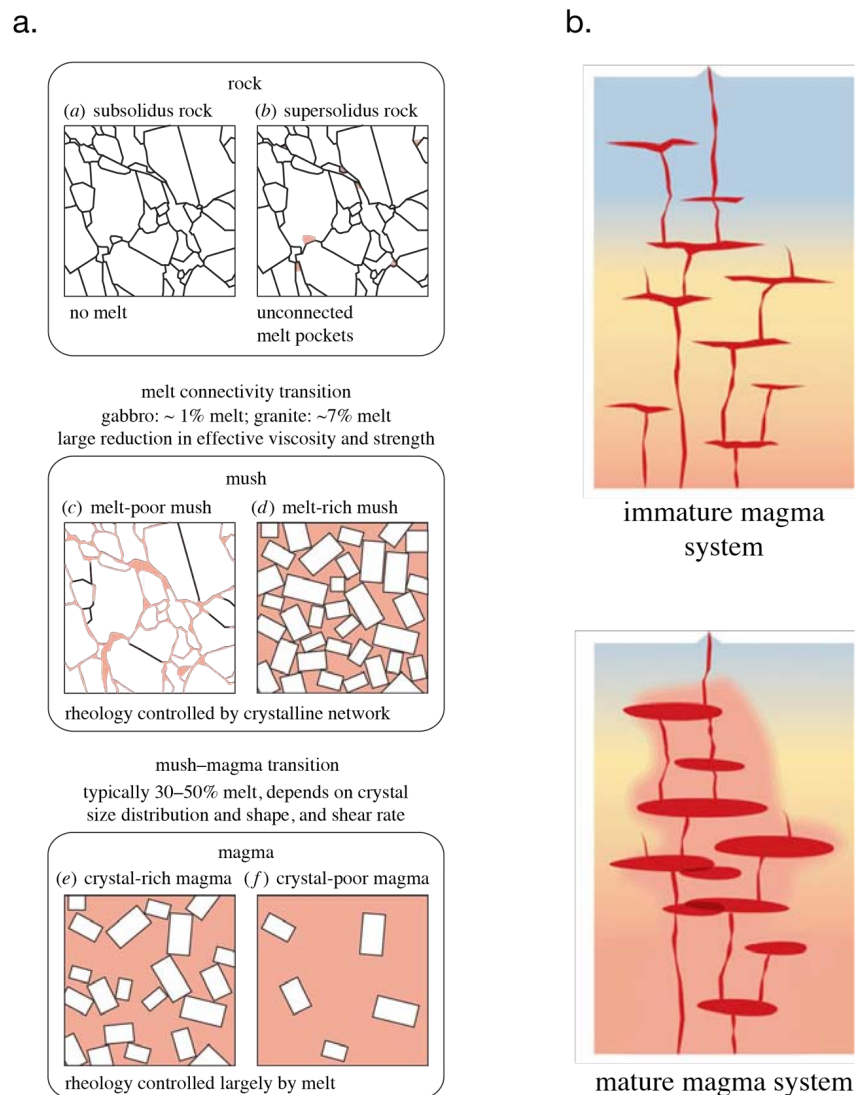
5.1.1.3 Interpretation of geodetic models: Ambrym’s mature, vertically extensive magmatic system

A first-order interpretation of the geodetic inversions suggests that at least two different sources of deformation at Ambrym are active between 2004 and 2020. The first is a source located < 3 km b.s.l, and is active during the inter-eruptive subsidence episodes. This source has not yet been linked to magma injection or drainage. The second source, located < 5 km b.s.l, is active during eruptions. Activation of different sills may explain the variations in estimated source location. The presence of multiple sills has been proposed at basaltic volcanoes such as Fernandina, Kīlauea, and Eyjafjallajökull (See Figure 5-3) [Bagnardi and Amelung, 2012, Baker and Amelung, 2012, Sigmundsson et al., 2010, Tarasewicz et al., 2012]. If the sills are hydraulically connected, magma can migrate between them. Stacked sills may exist within rigid, sub-solidus host rock when there is a relatively low heat flux into the system, or significantly long pauses between magma injections (See Figure 5-4b).

An alternative explanation is that these sources represent lenses of eruptible melt within a crystalline mush (See Figure 5-4a) [Cashman and Giordano, 2014]. This is envisaged to exist in a mature transcristal magmatic system with a sustained and high magma flux (See Figure 5-4b). A high input of magma would heat the surrounding crust and alter its physical properties (such as viscosity, density, and strength) [Sparks et al., 2019]. The existence of semi-permanent lava lakes, the high levels of passive degassing, and the quick construction of the main cones after caldera formation ~ 2 ka all suggest a high magma flux at Ambrym, and hence a mature magmatic system.

According to Sparks et al. [2019], a “transcristal magmatic system” is composed of magma (melt, crystals, exsolved fluids), mush (melt and fluids in a crystalline network), supersolidus rocks, and subsolidus host rocks (See Figure 5-4a). A “magma reservoir” is a domain which contains melt, including both melt-dominated domains (“magma chambers” or “magma lenses”) and crystal-dominated domains (“mush”) [Sparks et al., 2019] (See Figure

5-4b).



Adapted from Sparks et al, 2019

Figure 5-4: **Domains of a magmatic system.** **a.** A description of the physical and rheological properties of the rock, mush, and magma domains in a magmatic system. **b.** A schematic depicting crustal properties at the onset of magmatism or at a system with low magma flux (“immature” system) and at a system with a developed, transcrustal magmatic system (“mature” system). Blue indicates a cold, brittle crust while red indicates a hot, ductile crust. The crust has an arbitrary depth. From Sparks et al. [2019].

These domains are divided by two main transitions– the melt connectivity transition and the mush–magma transition– determined in part by the strain rate, crystal size and shape, and melt fraction. The rheology of magma is controlled primarily by the melt viscosity and may become more complex (i.e., develop non-Newtonian rheologies) with increasing proportions of crystals and bubbles. The rheology of mush is a topic of ongoing research,

and can be thought to be generally controlled by the deformation of the crystalline network, whose behavior depends on the melt fraction. In subsequent sections, we refer to regions with high fractions of eruptible melt as magma lenses, and use magma reservoir to describe regions of melt more generally.

This framework of a transcrustal magmatic system with domains of magma and mush forces us to rethink the physical mechanisms driving volcanic deformation. In this new paradigm, classic explanations for surface deformation— such as the injection or extraction of incompressible magma— are challenged. Sparks et al. [2019] proposes that reorganization in the magmatic system, such as upwards movement of magma, is compensated by downward movement of the mush. There is thus no net pressure change. Decompression and exsolution of volatiles (for uplift) or degassing (for subsidence) may therefore be the primary drivers of surface deformation [Sparks and Cashman, 2017, Sparks et al., 2019, Kazahaya et al., 2015]. At Ambrym, geodetic modelling provides evidence for a vertically extensive magmatic system, where pressure changes in the shallow magma reservoirs cannot be explained solely by magma injection or drainage. We therefore wish to test the hypothesis that the 2015 – 2017 inter-eruptive subsidence episodes is instead due to the passive degassing of volatiles.

5.1.2 A candidate physical mechanism driving inter-eruptive subsidence: passive degassing

From now on, we assume that Ambrym’s magmatic system consists of vertically stacked magma lenses. Ambrym’s inter-eruptive surface deformation, spanning 2004 – 2009 and 2015 – 2017, is dominated by subsidence. This is unusual, as inter- or pre-eruptive volcanic deformation often consists of uplift [Biggs and Pritchard, 2017]. In the absence of a recorded eruption or intrusion, ground subsidence by drainage of a magma lens is difficult to justify [Caricchi et al., 2014, Hamlyn et al., 2018]. If subsidence is not caused by magma lens drainage, we must explore alternative physical mechanisms that cause depressurization within the magmatic system. From 2005 to 2015, Ambrym’s SO₂ gas flux was ~ 7 kt day⁻¹, the strongest passively degassing volcano on earth [Carn et al., 2017]. Ambrym continued to passively degas at similar levels from 2015 – 2017 (See Figure 5-1). The observation of an enigmatic episode of subsidence, coupled with persistent degassing, provides a unique opportunity to explore the potential relationship between mass loss by open-system degassing and subsequent magma reservoir depressurization.

5.1.2.1 Constraining depressurization from geodetic models

To estimate magma reservoir depressurization, we invert measurements obtained between March 2015 and October 2017, as measured by ALOS-2. A Sentinel-1 InSAR time series analysis [Doin et al., 2011] (un-corrected for atmospheric effects) measures a rate of subsidence of ~ 9 cm year⁻¹ during the time period 18 October 2015 to the end of August 2017 (See Figure 5-5). The Sentinel-1 time series has been shifted so that the best-fitting slope of displacement spanning September 2017 – December 2018 intersects with the ALOS-2 cumulative displacement in October 2017. The best fitting slope for the time period March 2015 – October 2017 was found using both the Sentinel-1 and ALOS-2 displacement measurements, assuming the majority of displacement is vertical.

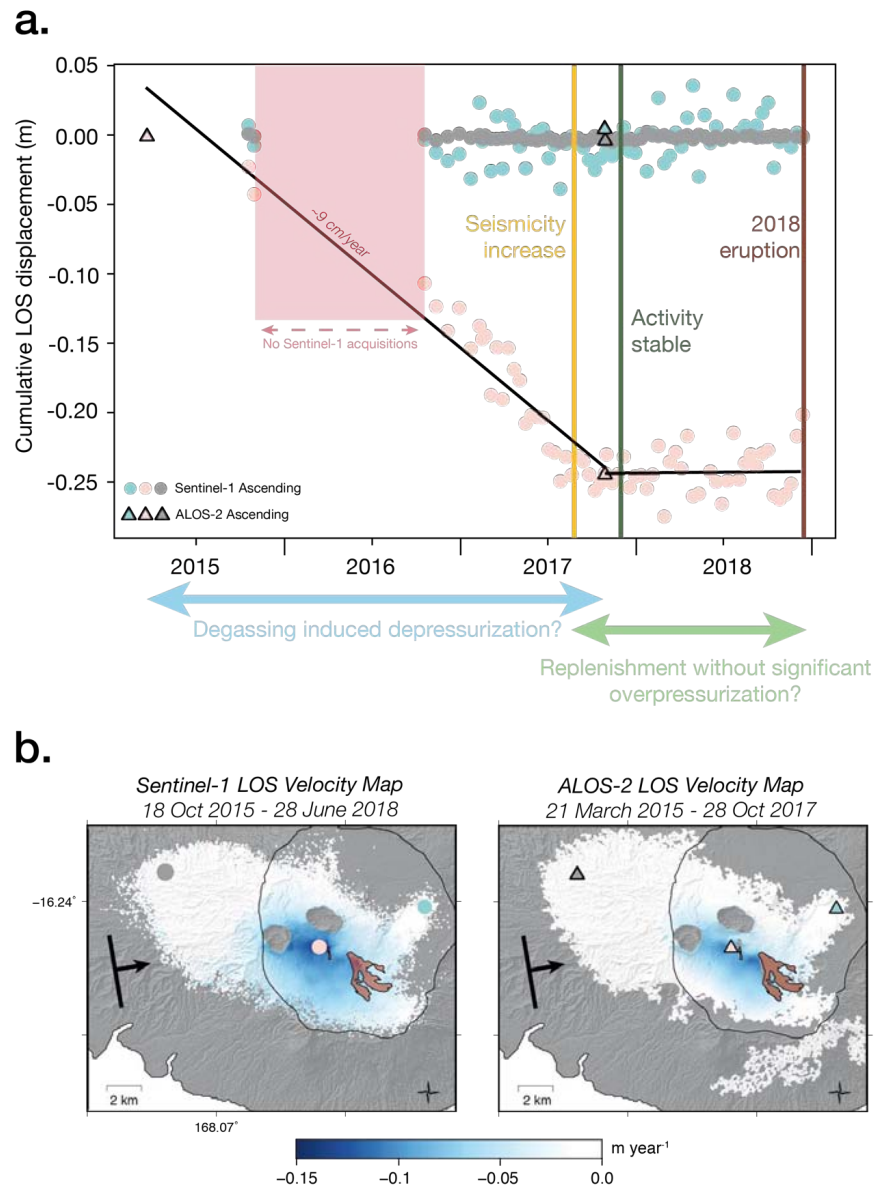


Figure 5-5: **Sentinel-1 Time Series.** **a.** The colored dots correspond to the cumulative LOS displacement calculated from a Sentinel-1 ascending time series in three different locations. At each location, the mean of a 3×3 pixel box is calculated. The triangles indicate the cumulative LOS displacement of a single ALOS-2 interferogram. **b.** On the left is a velocity map of the Sentinel-1 time series, assuming deformation spans 18 October 2015 – 30 August 2017. The map on the right is the ALOS-2 interferogram, scaled by the assumed timespan of active deformation, 21 March 2015 – 30 August 2017. The points plotted in the time series are identified with the colored dots and triangles, the caldera is outlined in black, and the extent of the 2015 lava flow is shown in red.

We note that the subsidence ends around the same time as seismicity increases, according to a report by the Vanuatu Meteorology and Geo-Hazards Department [[Global Volcanism](#)

Program, 2017a] (yellow vertical line, Figure 5-5). Activity stabilizes a few months later (green vertical line, Figure 5-5) [Global Volcanism Program, 2017b]. Using the DEFVOLC Mixed Boundary Element method code (See Section 2.2.2.5.2), we perform an inversion of an ALOS-2 ascending interferogram which spans the longest consecutive period of inter-eruptive subsidence, 21 March 2015 – 28 October 2017. We invert for the location, depth, and axes lengths of a sub-horizontal sill or ellipsoid, as well as for its total pressure change (See Table 5.1 and Figures 5-6, 5-7 and 5-8 for the inverted parameters and final geometries). The final geometry of the source is a sill or an ellipsoid elongated N^o125 at a depth of ~ 2.2 km beneath the craters (1.3 km b.s.l., See Figures 5-6, 5-7 and 5-8). The northwest tip of the source is located between Benbow and Marum, and the source extends beneath the caldera for more than 7 km to the SE. The direction is slightly oblique to the N^o110 rift zone.

The cumulative pressure change ranges from -1 to -3.7 MPa (See Table 5.1), given a Young’s modulus of 5 GPa and Poisson’s ratio of 0.25. Because the time series subsidence rate is approximately constant, we will assume that the depressurization rate and the source geometry remain constant throughout the deformation episode. The depressurization ends in the beginning of September 2017, as constrained by the Sentinel-1 InSAR time series. The subsidence persists for a total of ~ 2.5 years, and the pressure change rate ranges between -0.4 to -1.5 MPa year⁻¹. By combining this mean depressurization rate with the mean degassing flux estimated by Carn et al. [2017], we can investigate whether these estimates are reasonably explained by a model coupling mass loss by passive degassing and magma reservoir depressurization.

5.1.2.2 Examples of physical models coupling deformation and degassing

Within the framework of a transcrustal magmatic system, Sparks and Cashman [2017], Sparks et al. [2019] hypothesize that ground subsidence may result from degassing, as opposed to migration of incompressible magma. Here we default to the terminology “reservoir” to refer to a general region of melt, as we have no constraints on this region’s level of melt connectivity. In order to test the hypothesis that reservoir depressurization and ground subsidence can be explained by degassing of volatiles, we would need a theoretical model that couples the system’s pressure change with volatile exsolution within and escape from a magmatic system (i.e., degassing processes). Existing theoretical models which couple degassing processes and reservoir pressure change explore a wide range of spatial and temporal scales. They may investigate inter- or co-eruptive time periods, and time scales that span many orders of magnitudes. They may also concern either closed or open volcanic systems, as well as either mafic or silicic systems. Some consider the entire magmatic system, while others consider only one part (reservoir, conduit, etc.). Below we summarize a few examples of such models, without attempting to perform an exhaustive literature review.

Model	Depth (m b.s.l.)	Axis 1 (m)	Axis 2 (m)	Axis 3 (m)	Rotation (°)	V_r (km ³)	ΔV ($\times 10^6$ m ³)	ΔP (MPa)
Sill	-1349 \pm 173	7887 \pm 81	1687 \pm 139	N/A	147 \pm 3.4	N/A	-6.6	-0.97
Ellipsoid	-1314 \pm 218	7849 \pm 132	1055 \pm 303	217 \pm 128	148 \pm 4	0.94	-6.1	-3.7

Table 5.1: **Inverted parameters.** The parameters inverted with DEFVOLC and their estimated uncertainties. Estimated model geometrical parameters are similar between the two inversions.

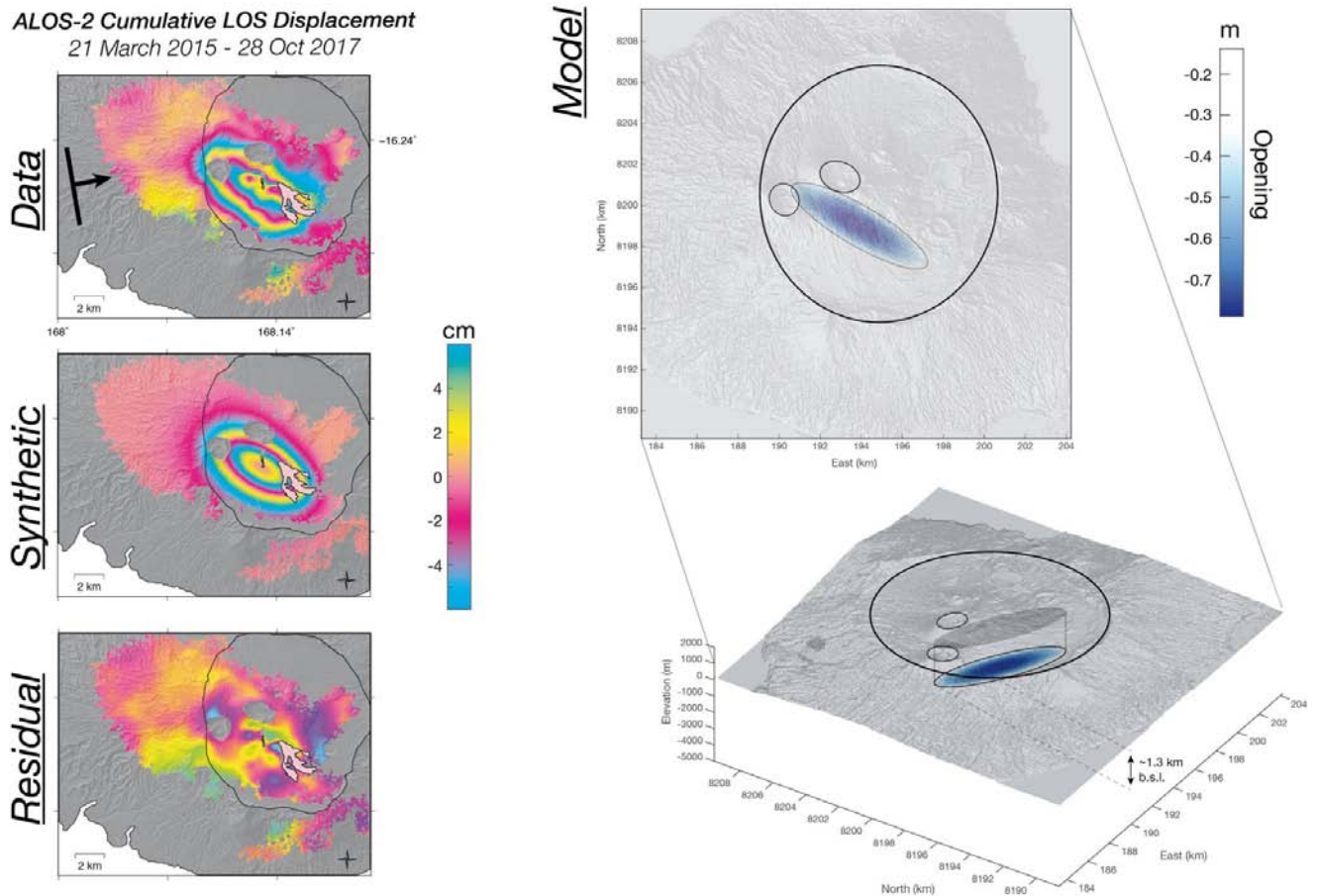


Figure 5-6: **Geodetic inversion of sill.** The left-hand column shows the data (March 2015 – October 2017), synthetics and residuals of the DEFVOLC inversion of a sill at ~ 1.3 km b.s.l (2.2 km beneath the vents). The right-hand column shows a map and aerial view of closing on the depressurized sill. The caldera and the crater rims are outlined in black.

For example, [Tait et al. \[1989\]](#) investigates inter-eruptive reservoir pressurization and ground inflation over timescales of 10^0 – 10^1 years. They do so by accounting for magma cooling-induced crystallisation, followed by volatile exsolution and reservoir pressure increase [[Tait et al., 1989](#)]. During fractional crystallization, melt becomes volatile saturated and volatiles eventually exsolve as bubbles. The presence of this gas phase pressurizes the reservoir, assuming the gas within the reservoir cannot escape through a conduit or through edifice fractures surrounding the reservoir (i.e., it is a closed system). This pressurization would be expected to result in uplift above the reservoir (but is not modelled by [Tait et al. \[1989\]](#)). Uplift would provide an alternative mechanism to the classical interpretation of volcano inflation resulting mainly from magma replenishment. More generally, pressurization may occur if gas exsolution exceeds the system’s capability to release gas into the atmosphere. Although this model does not have an explicit time dependence, it estimates reservoir overpressure at a given crystal mass fraction. It predicts when the overpressure will reach a threshold necessary to fracture the host rock, emplacing a dike or resulting in an

eruption. As a result of this magma withdrawal, the reservoir will depressurize, which may cause the ground above the reservoir to subside (i.e., co-eruptive subsidence). This model is applied conceptually to explain periodic dike intrusions at mafic systems such as Kilauea or Krafla (See Chapter 3) [Tait et al., 1989]. It has also been extended to describe the episodic degassing of magma intrusions, later applied to the case of episodic degassing and seismic activity observed at La Soufrière de Guadeloupe in the 15 years following the 1975 – 1977 crisis [Boichu et al., 2008, 2011]. In summary, the model of Tait et al. [1989] would predict an anticorrelation between gas flux and uplift [Biggs and Pritchard, 2017, and references within]. However, this anticorrelation does not seem to apply to Ambrym’s open system, where concurrent passive degassing and subsidence (not uplift) are observed.

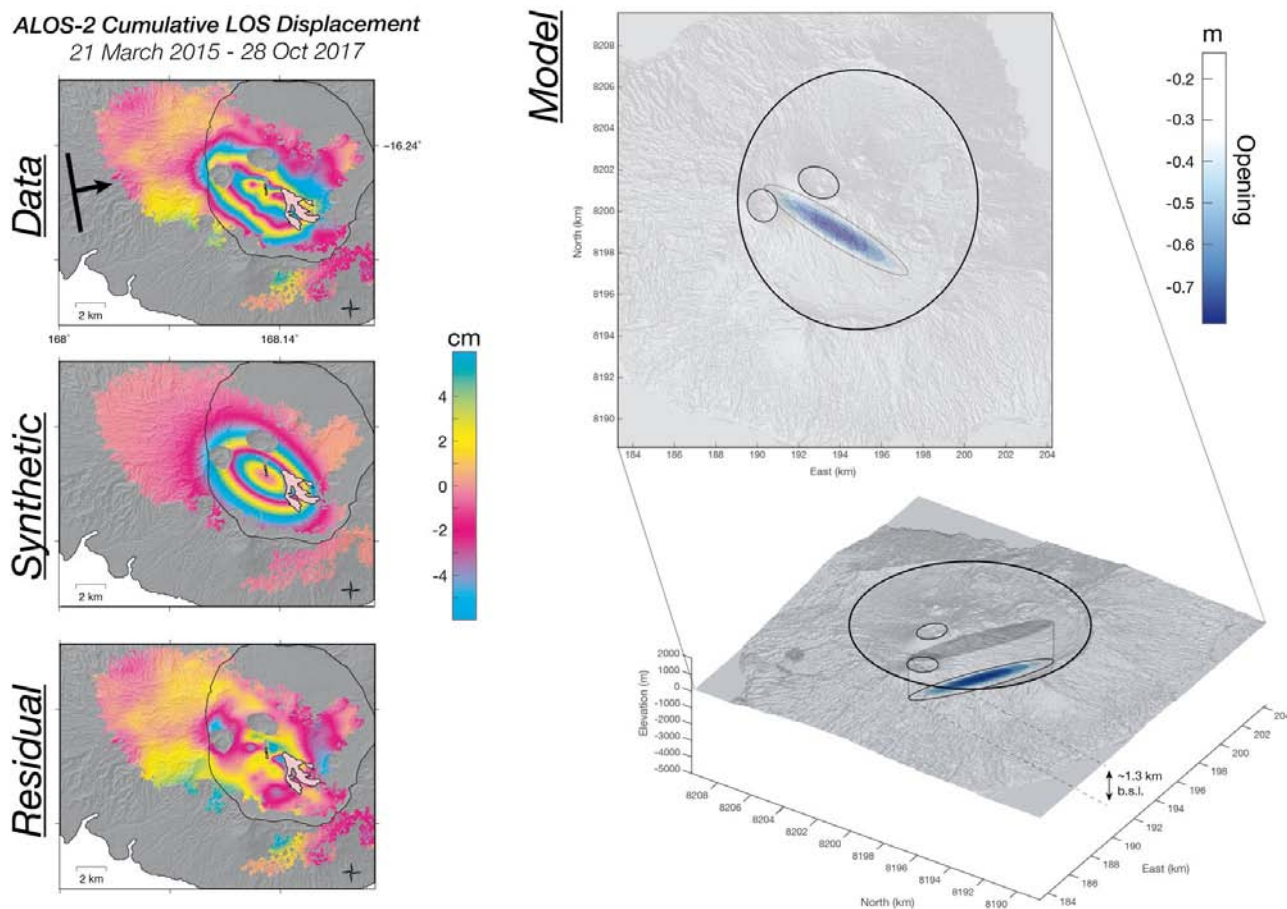


Figure 5-7: **Geodetic inversion of ellipsoid.** The left-hand column shows the data (March 2015 – October 2017), synthetics and residuals of the DEFVOLC inversion of an ellipsoid at ~ 1.3 km b.s.l (2.2 km beneath the vents). The right-hand column shows a map and aerial view of closing on the depressurized ellipsoid. The caldera and the crater rims are outlined in black.

Anderson and Segall [2011] exploit ground subsidence measurements spanning months to years to investigate the evolution and duration of Mount St. Helens’ silicic, effusive eruptive

activity. They are able to model reservoir depressurization and resulting deformation by taking into account magma extraction from the reservoir, exsolution of H_2O and CO_2 in the reservoir and conduit, the presence of phenocrysts in the conduit, a solidifying plug in the conduit which can slip with rate-dependent friction (resulting in a stick-slip behavior), the weight of the accumulating lava dome, and post-eruptive magma recharge. Wong et al. [2017] further develops their model to include pressure-dependent crystallization and gas escape from the conduit, which were neglected in the original model. However, like the model of Tait et al. [1989] mentioned above, the system remains mostly closed.

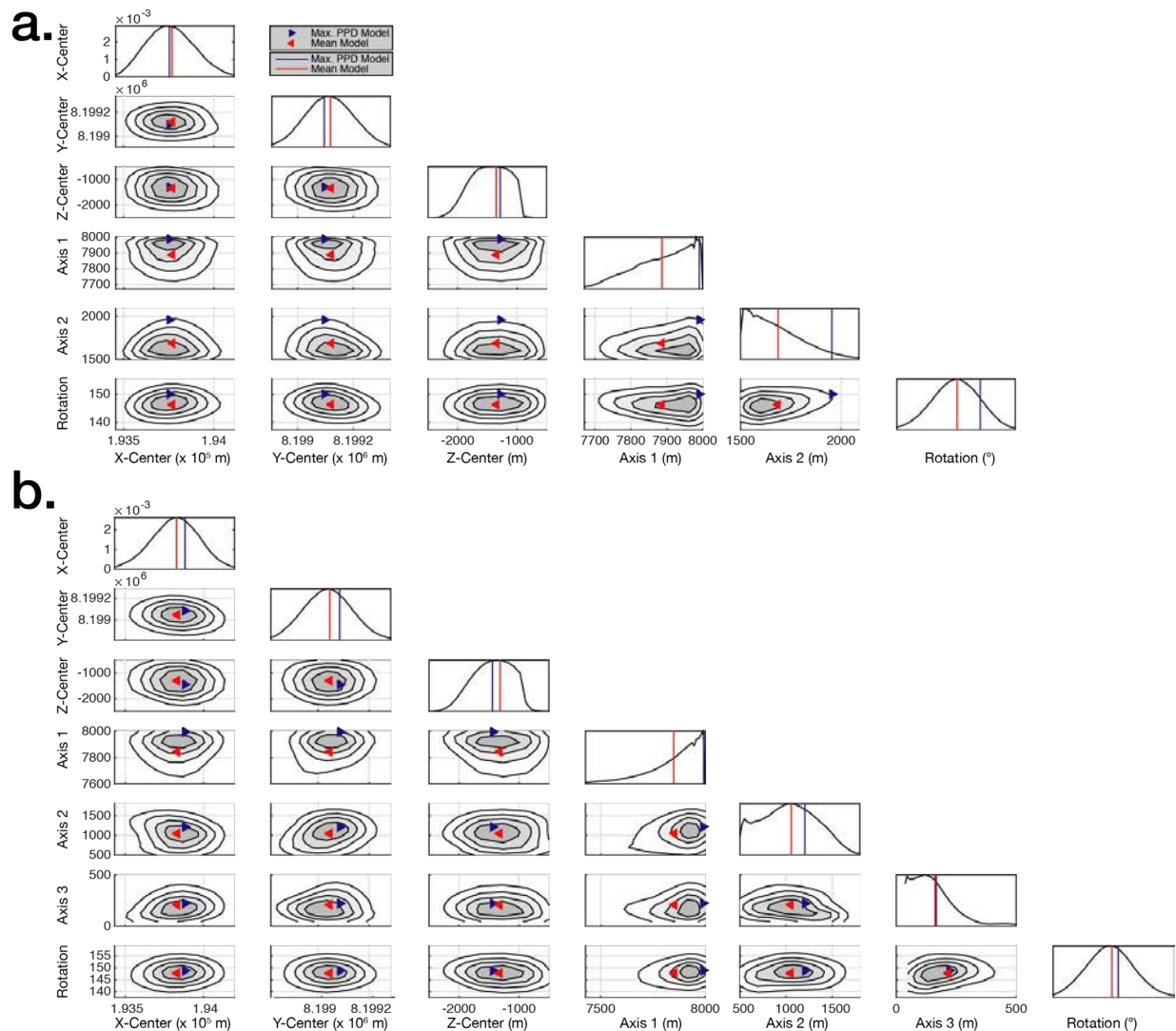


Figure 5-8: **Marginal PPDs.** The marginal posterior probability density functions, showing the uncertainties of the inverted parameters for the **a.** sill and **b.** ellipsoid.

At much shorter time scales and shallower levels, Strombolian or Vulcanian eruptions cause conduit and reservoir depressurization on timescales of minutes. In response to a pressure drop, magma migrates upwards through a conduit, repressurizing the system and

causing surface deformation. The model of Nishimura [2009] investigates three different ascent processes—magma injection into the conduit from a deeper reservoir, bubble expansion causing magma to rise in the column, and upwards migration and expansion of bubbles in the viscous melt by buoyancy. They assume an open system, that deformation is due to the shear and normal stress on the conduit wall, and that there is no crystallization or degassing. The temporal evolution of surface deformation can ideally be used to distinguish between the three aforementioned physical mechanisms of magma ascent.

On similar short timescales (minutes to hours), a model developed by Poland and Carbone [2018] couples transient reservoir depressurization with the onset of lava lake gas pistoning events. Gas pistoning occurs when the permeability and/or porosity near the lava lake surface decreases and bubbles accumulate, resulting in changes to the lava lake level and spattering [Poland and Carbone, 2018]. This model was applied at Kīlauea, where both the lava lake level and gravity changes increased before gas pistoning. However, simultaneously, tiltmeters located less than 3 km from the shallow reservoir measured reservoir depressurization. This anticorrelation is counterintuitive, given that Kīlauea’s lava lakes are commonly believed to act as piezometers of the shallow reservoir (i.e., a reservoir depressurization would result in a decrease in lava lake level). Assuming that the density of the gas in the conduit is negligible, Poland and Carbone [2018] explain the reservoir depressurization by an increase in the gas volume in the conduit during gas ascent and expansion, and hence a decrease in the overall density in the conduit. The lava lake level change resulting from this volume increase is negligible. Therefore, if the reservoir responds passively to the pressure change in the conduit, a density decrease in the conduit results in reservoir depressurization. However, both the Nishimura [2009] and Poland and Carbone [2018] models are relevant for shallow, short duration gas emissions, not long-term passive degassing, as observed at Ambrym.

Finally, a theoretical model developed by Girona et al. [2014] addresses the relationship between passive degassing and inter-eruptive reservoir depressurization on timescales of years. They assume the reservoir is connected to the surface by an open conduit, and that the pressure in the reservoir sustains the weight of the magma in the conduit. Consequently, mass changes within the system (either in the conduit or reservoir) due to degassing result in reservoir depressurization, causing ground subsidence. This model can take into account whether volatiles are degassed from the conduit or reservoir, as well as the viscoelastic behavior of the host rock, possible magma replenishment, and any magma density changes in the conduit.

5.1.2.3 Theoretical modelling of reservoir depressurization by passive degassing

Persistent passive degassing is observed at volcanoes worldwide [Carn et al., 2017], and we posit that gas mass removed from the magmatic system should affect the system’s pressurization, especially in cases of large gas flux. Among the ten strongest passively degassing volcanoes on earth are Ambrym, Kīlauea, Nyiragongo, and Etna (See Carn et al. [2017] for an exhaustive ranking). However, only at Ambrym do we observe substantial inter-eruptive ground subsidence accompanying the significant gas flux (the highest of any volcano when considering SO₂ passively degassed from 2005-2015 [Carn et al., 2017]). For comparison, at Etna, which emits 3 kt day⁻¹ of SO₂ during inter-eruptive phases, periods of volcano inflation (associated with magma intrusions and measured by continuous GPS stations), not subsi-

Adapted from Girona et al, 2014

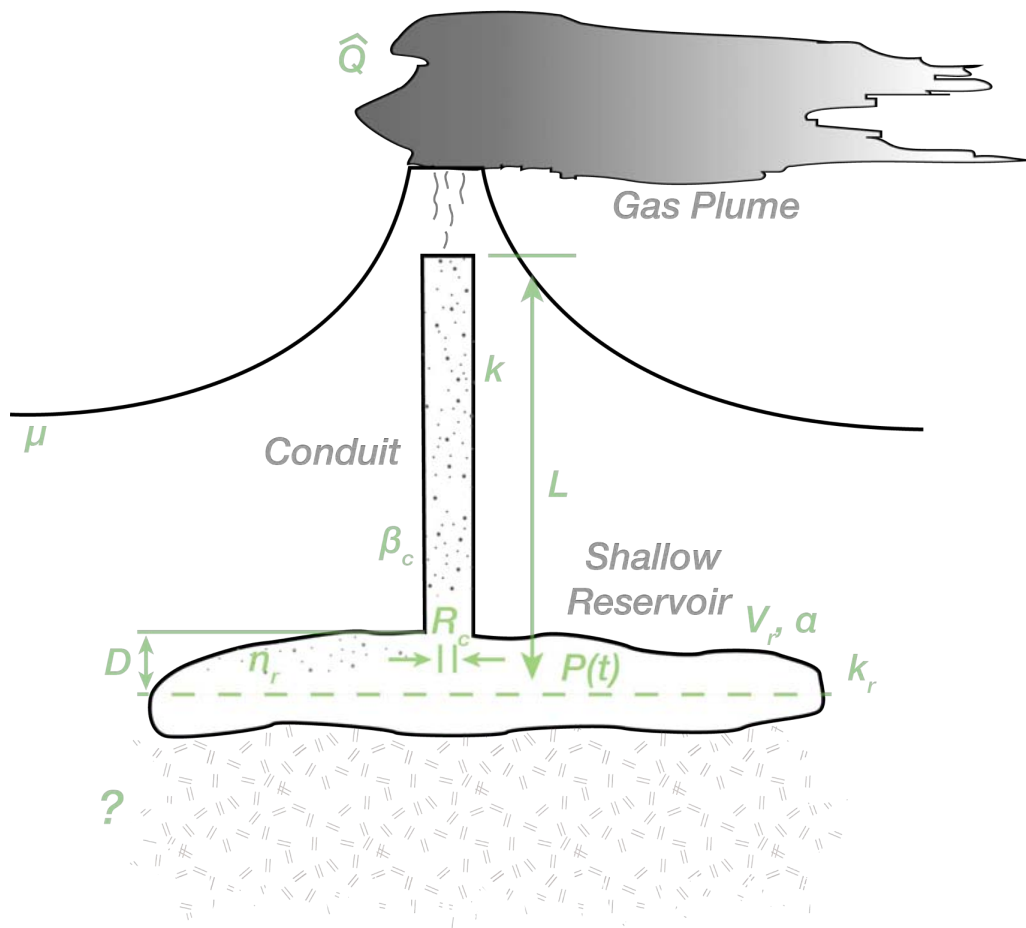


Figure 5-9: **Illustration of an open magmatic system and the model parameters.** The mean H₂O gas flux is \hat{Q} . The reservoir (which has a sill-like geometry) is located at a mean depth of L , has a volume of V_r , an initial bulk mass fraction of dissolved volatiles of α , and a weight percent of exsolved volatiles of n_r . The magma conduit extends D into the reservoir, has a radius of R_c , and an initial volume fraction of exsolved gas of β_c . The pressure of the system is $P(t)$. The compressibility of the sill is accounted for by a bulk modulus k_r , while the bulk modulus of the host rock surrounding the conduit is k . The effective viscosity of the host rock is μ . Currently, we have no constraints on the characteristics of the crust beneath the sill, although we can postulate that it is comprised of an immobile, crystal-rich mush that does not contribute to degassing. Adapted from Girona et al. [2014].

dence, coincide with periods of high SO₂ emissions measured by satellite [Coppola et al., 2019].

5.1.2.3.1 Starting assumptions

We therefore proceed with the theoretical model developed by Girona et al. [2014] to investigate the coupling of ground subsidence and passive degassing. The Girona et al. [2014] model simplifies the relationship between mass loss by degassing and reservoir depressurization by assuming the following:

1. A magma reservoir is connected to an open, magma-filled cylindrical conduit. The reservoir's magma pressure is magmastatic (See Figure 5-9).
2. Gas mass in the conduit is much smaller than the (incompressible) melt (liquid and solid phase) mass in the conduit (i.e., $m_{m,c}(t) \gg m_{g,c}(t)$).
3. The melt in the conduit is a mixture of a degassed melt and an undegassed parent melt. The former is denser than the latter.
4. Gas separation may occur in the conduit, or in the reservoir. If there is no magma recharge, degassing can continue until the total degassed volatile mass equals that of the initial mass of bulk dissolved volatiles in the undegassed magma.
5. We assume a mean degassing rate of \hat{Q} that is constant over months to years.
6. Crystal content is neglected, temperature (T) of the system is constant, gas solubility depends only on pressure, and the gas mass within the reservoir is calculated at a mean depth.
7. Melt volume decreases during degassing of H₂O. No other volatiles are considered in this model.
8. The host rock of the system is a half-space with a Maxwell viscoelastic rheology (it has a bulk modulus k and an effective viscosity μ).

5.1.2.3.2 Governing equation

Using these assumptions, this model can be used to gain a first-order understanding of the relationship between a system's degassing and depressurization. This is especially useful when the neglected parameters cannot be constrained. We will investigate whether this model is consistent with the reservoir depressurization estimated from geodetic models at Ambrym. If so, we will then discuss if the model allows us to infer properties of Ambrym's magmatic system, such as conduit radius and reservoir volume.

Based on the first assumption mentioned above, the pressure change at the base of the conduit at time t can be written as

$$\Delta P(t) = P(t) - P(t_0) = \frac{g(m_{m,c}(t) + m_{g,c}(t))}{\pi R_c(t)^2} - P(t_0), \quad (5.1)$$

where $P(t)$ and $P(t_0)$ are the pressure within the reservoir at time t and t_0 , $m_{m,c}(t)$ is the mass of melt within the conduit of constant length L (See Figure 5-9), $m_{g,c}(t)$ is the mass of gas within the conduit, $R_c(t)$ is the radius of the conduit, and g is gravity. Equation 5.1 describes a pressurized reservoir which is sustaining the weight of the magma-filled conduit, which is acting on a surface area of $\pi R_c(t)^2$ [Girona et al., 2014].

Taking the derivative of this equation, we can obtain the rate of pressure change:

$$\frac{d\Delta P(t)}{dt} = \frac{g\hat{\rho}_{m,c}(t)V_{m,c}(t)}{\pi R_c(t)^2} \left\{ \frac{1}{\hat{\rho}_{m,c}(t)V_{m,c}(t)} \left[\hat{\rho}_{g,c}(t) \frac{dV_{g,c}(t)}{dt} + V_{g,c}(t) \frac{d\hat{\rho}_{g,c}(t)}{dt} \right. \right. \\ \left. \left. + \hat{\rho}_{m,c}(t) \frac{dV_{m,c}(t)}{dt} + V_{m,c}(t) \frac{d\hat{\rho}_{m,c}(t)}{dt} \right] - \frac{2}{R_c(t)} \frac{dR_c(t)}{dt} \right\}. \quad (5.2)$$

We have substituted $m_{m,c}(t) = \hat{\rho}_{m,c}(t)V_{m,c}(t)$ and $m_{g,c}(t) = \hat{\rho}_{g,c}(t)V_{g,c}(t)$, where $\hat{\rho}_{m,c}(t)$, $V_{m,c}(t)$, $\hat{\rho}_{g,c}(t)$, $V_{g,c}(t)$ are the mean density and volume of the melt and gas in the conduit, respectively. Starting from Equation 5.2, we will discuss how ΔP evolves as a function of time according to four model scenarios of increasing fidelity.

5.1.2.3.3 Scenario 0: Elastic rheology

To derive a first-order relationship between ΔP and the gas flux, conduit radius, reservoir volume, and properties of the magma and host rock, we will derive Equation 45 in Girona et al. [2014] from Equation 5.2. To do so, a number of simplifications are made.

We will first assume that the host rock is an elastic half-space. Next, we will address the conduit radius change $\frac{dR_c(t)}{dt}$. Girona et al. [2014] provides a simplified formulation for the conduit radius responding to an internal pressure change in a medium with a Maxwell viscoelastic rheology. In Scenario 0, we assume an elastic rheology, and we therefore simplify this formulation as follows

$$\frac{dR_c(t)}{dt} \approx \frac{R_c(t)}{2k} \frac{d\Delta P(t)}{dt}. \quad (5.3)$$

We will assume a depressurization rate of ~ 10 MPa (larger than that estimated from geodetic models) over our time span of interest— 2.5 years— and a host rock bulk modulus of $k = 10^{10}$ Pa. The conduit radius change will be only 0.05% of the original conduit radius, indicating that R_c will not vary significantly with time. We will therefore hold the conduit radius R_c constant (also assuming no changes to the conduit radius due to thermal erosion or magma solidification), allowing us to eliminate the right-most term of Equation 5.2. Holding R_c constant also entails that the conduit volume, $V_{m,c} + V_{g,c} = \pi R_c^2 L$, remains constant, which leads to $\frac{dV_{m,c}(t)}{dt} = -\frac{dV_{g,c}(t)}{dt}$. As a result, the first term in the square brackets can be eliminated because $\hat{\rho}_{g,c}(t) \ll \hat{\rho}_{m,c}(t)$.

In the second term, the density variation of gases $\frac{d\hat{\rho}_{g,c}(t)}{dt}$ can be related to pressure change in the system according to the ideal gas law: $\frac{d\hat{\rho}_{g,c}(t)}{dt} = \frac{M_{H_2O}}{R_g T} \frac{d\Delta P(t)}{dt}$, where

M_{H_2O} is the molar mass of water¹, R_g is the ideal gas constant and T is the temperature. Factorizing by $\frac{d\Delta P(t)}{dt}$ leads to a modified pressure change $\left(1 - \frac{gV_{g,c}(t)}{\pi R_c^2} \frac{M_{H_2O}}{R_g T}\right) \frac{d\Delta P(t)}{dt}$ on the left-hand side of Equation 5.2. An upper bound for the dimensionless number $\frac{gV_{g,c}(t)}{\pi R_c^2} \frac{M_{H_2O}}{R_g T}$ can be estimated, bearing in mind that $V_{g,c}(t)$ is always smaller than the conduit volume, i.e. $V_{g,c}(t) < \pi \frac{R_c^2 L}{4}$, so that $\frac{gV_{g,c}(t)}{\pi R_c^2} \frac{M_{H_2O}}{R_g T} < gL \frac{M_{H_2O}}{R_g T}$. Taking $L=2.2$ km and a magma temperature of 1300 K, this upper bound is smaller than 0.04. Hence, the second term in the square brackets of Equation 5.2 can be safely dropped.

Finally, we assume steady-state magma convection within the conduit, which ensures a constant volume fraction of degassed and undegassed magma in the conduit and thus a constant $\hat{\rho}_{m,c}(t)$, resulting in $\frac{d\hat{\rho}_{m,c}(t)}{dt} = 0$.

We are left with a simplified version of Equation 5.2:

$$\frac{d\Delta P}{dt} = \frac{g\hat{\rho}_{m,c}(t)}{\pi R_c^2} \frac{dV_{m,c}(t)}{dt}. \quad (5.4)$$

Since the total volume of melt in the system $V_{m,r+c}$ is the sum of the volume of melt in the conduit $V_{m,c}$ and the volume of melt in the reservoir $V_{m,r}$, the derivative of $V_{m,c}$ can be written:

$$\frac{dV_{m,c}(t)}{dt} = \frac{dV_{m,r+c}(t)}{dt} - \frac{dV_{m,r}(t)}{dt}. \quad (5.5)$$

According to Girona et al. [2014], the total volume change of the melt in the system results entirely from the loss of dissolved volatiles as they are transferred to the gas phase by volatile exsolution, hence $\frac{dV_{m,r+c}(t)}{dt} = \frac{dV_d(t)}{dt}$ (here neglecting replenishment from a deeper reservoir). Assuming that water is the dominant volatile species, this rate of volume loss is directly related to the mass flux of water \hat{Q} released at the vent (in the form of water vapour). Considering that this mass was initially present in the condensed (dissolved) phase prior to its escape, $\frac{dV_d(t)}{dt} = -\frac{\hat{Q}}{\rho_w}$ (neglecting in particular gas scrubbing in the hydrothermal system, among other processes that may divert gas away from the summit vents). The parameter ρ_w is the partial density of dissolved water in an anhydrous melt when all dissolved volatiles are exsolved and there is no degassing-induced crystallization. It can be calculated by $\rho_w = \frac{\alpha\rho_c\rho_{nd}}{\rho_c - (1-\alpha)\rho_{nd}}$, where ρ_c is the density of degassed melt and ρ_{nd} is the density of the parent melt (undegassed) [Girona et al., 2014].

Moreover, magma volume in the reservoir $V_{m,r}(t)$ is assumed equal to the reservoir volume itself $V_r(t)$ if there is no exsolved gas at the reservoir depth, so that $\frac{dV_{m,r}(t)}{dt} = \frac{dV_r(t)}{dt}$. The reservoir responds elastically to internal pressure change, which allows for relating its volume change and its pressure change according to $\frac{dV_{m,r}(t)}{dt} = \frac{dV_r(t)}{dt} = \frac{V_r(t)}{k_r} \frac{d\Delta P}{dt}$ (neglecting magma compressibility in the reservoir in absence of exsolved gas). When the reservoir volume decreases, magma migrates into the conduit. The reservoir's elastic response to

¹Girona et al. [2014] relates this term to the *molecular weight* of water.

the pressure change is determined by an effective bulk modulus k_r , which depends on the reservoir's shape.

Girona et al. [2014] assumes that the reservoir feeding the magma conduit is spherical. Models of Ambrym's magmatic reservoir (Chapters 3 and 4) argue for the existence of a sill. Sill-like reservoirs are more compressible than spherical reservoirs [Amoruso and Crescentini, 2009, Rivalta, 2010]. We adjust the reservoir bulk modulus to a value k_r , which accounts for this compressibility difference. The uncertainties imposed by this parameter are discussed in Section 5.1.2.7.1.

Substituting $\frac{dV_{m,c}(t)}{dt}$ into Equation 5.4 and grouping like terms, we obtain

$$\frac{d\Delta P}{dt} \left(\frac{\pi R_c^2}{g\hat{\rho}_{m,c}} + \frac{V_r(t)}{k_r} \right) = -\frac{\hat{Q}}{\rho_w}. \quad (5.6)$$

We will assume that the time-dependent term $V_r(t)$ does not vary significantly from its initial value $V_r(t_0)$ [Girona et al., 2014]. After time integration, we obtain Equation 45 of Girona et al. [2014]

$$\Delta P(t) = -\frac{g\hat{\rho}_{m,c}k_r\hat{Q}t}{\pi R_c^2\rho_w k + g\rho_w\hat{\rho}_{m,c}V_r(t_0)}. \quad (5.7)$$

Equation 5.7 is the simplest scenario (which we call ‘‘Scenario 0’’) that couples reservoir depressurization with degassing.

5.1.2.3.4 Scenario 1: Viscoelastic rheology, gas exsolves in conduit

If we assume that the host rock has a Maxwell viscoelastic rheology, we obtain Scenario 1 of Girona et al. [2014]. As a result, we can only eliminate the terms in Equation 5.2 that include $\frac{d\hat{\rho}_{m,c}(t)}{dt}$, which we continue to assume is zero due to a constant $\hat{\rho}_{m,c}(t)$. For this case, the pressure change can be calculated analytically with an equation of the form

$$\Delta P(t) = -\Delta P_\infty(1 - e^{-\Gamma t}), \quad (5.8)$$

where $\Delta P_\infty = \frac{C_1(t_0)}{C_2(t_0)}$ and $\Gamma = -\frac{C_2(t_0)}{C_3(t_0)}$. The constants $C_1(t_0)$, $C_2(t_0)$, and $C_3(t_0)$ are functions of the parameters summarized in Figure 5-9. The full expansion of these constants and a table of parameters used in this study can be found in Appendix D.

5.1.2.3.5 Scenario 2: Viscoelastic rheology, gas can exsolve in reservoir

In the next scenario, Scenario 2, we will assume that gas can exsolve in the reservoir. The depressurization during this scenario can also be described by Equation 5.8. The depth at which gas (here, water) will exsolve can be calculated using Henry's Law for water solubility in silicate melts and assuming thermodynamic equilibrium [Burnham and Jahns, 1962, Burnham, 1975, Huppert and Woods, 2002, Girona et al., 2014]. The density of the gas in the reservoir can be calculated using the ideal gas law. The weight % of exsolved water in

the reservoir is

$$n_r(t) = \begin{cases} \alpha - S(P(t_0) + \Delta P(t))^{\frac{1}{2}}, & \text{if } \alpha > S(P(t_0) + \Delta P(t))^{\frac{1}{2}} \\ 0, & \text{if } \alpha \leq S(P(t_0) + \Delta P(t))^{\frac{1}{2}}. \end{cases} \quad (5.9)$$

where S is the solubility coefficient for water ($S = 4 \times 10^{-6} \text{ Pa}^{-1/2}$).

5.1.2.4 Scenario 3: Viscoelastic rheology, magma replenishment

The final fidelity step includes the replenishment of magma in the reservoir from a deeper source. We will discuss the possible relevance of this case in Section 5.3.2. Testing this scenario is outside the scope of this dissertation and will instead be the focus of future studies (See Section 6.3).

5.1.2.5 Depressurization rate comparison: Results

Equations 5.7 and 5.8 can be used to compare the depressurization measured with geodetic modelling (average $\Delta P \propto$ surface deformation) at Ambrym to the theoretical depressurization of the magmatic system by passive degassing (using \hat{Q} as input, measured by satellite-based spectrometers such as NASA's Ozone Monitoring Instrument (OMI) for SO_2 , and then converted to H_2O). The remaining parameters necessary to calculate $\Delta P(t)$ are fixed based on estimates from previous studies. The summary of parameters values used can be found in Table D.1, and the uncertainties on these parameters can be found in Section 5.1.2.7. The theoretically and geodetically estimated values for $\Delta P(t)$ will now be compared for three scenarios of increasing complexity.

5.1.2.5.1 Scenario 0: Elastic rheology

We first calculate the theoretical depressurization rate at Ambrym using Scenario 0 for a range of $V_r(t_0)$ and $R_c(t_0)$. We fix \hat{Q} by converting estimates of passive SO_2 flux ($\sim 7 \text{ kt day}^{-1}$) [Carn et al., 2017] to water vapor flux using a mass ratio of ~ 13 for $\frac{\text{H}_2\text{O}}{\text{SO}_2}$ measured from Ambrym's bulk gas emissions [Allard et al., 2015]. The water vapor flux is estimated to be $\hat{Q} \approx 90 \text{ kt day}^{-1}$. We take this value to be a maximum (See Section 5.1.2.7.2). The higher this value, the higher the depressurization rate. The bulk modulus of the reservoir k_r varies between $5 \times 10^8 - 1 \times 10^{10} \text{ MPa}$, as explained in Section 5.1.2.7.1. As k_r increases, the host rock becomes more rigid, and the depressurization rate increases. Finally, we fix the initial bulk volatile content, α (used to calculate ρ_w), to 1.3 wt% (See Section 5.1.2.7.3) [Allard et al., 2015]. The lower the value of α , the higher the depressurization rate (for a given \hat{Q}). The density of the parent melt is $\rho_{nd} = 2430 \text{ kg m}^{-3}$ and the density of the degassed melt is $\rho_c = 2670 \text{ kg m}^{-3}$ (values implemented in Girona et al. [2014], uncertainties discussed in Section 5.1.2.7.4). Following Girona et al. [2014], we assume that the conduit consists of 50% parent melt (undegassed) and 50% degassed melt, the constant mean melt density is $\hat{\rho}_{m,c}(t) = \hat{\rho}_{m,c}(t_0) = 2550 \text{ kg m}^{-3}$.

Figure 5-10a shows the theoretical depressurization rate for Scenario 0 when $k_r = 5 \times 10^8 \text{ Pa}$, $\hat{Q} = 90 \text{ kt day}^{-1}$, and $\alpha = 1.3 \text{ wt}\%$. In Chapter 4, we discuss the possible volume range for Ambrym's shallow reservoir, inferring values from 1 – 3 km^3 based on geodetic models.

These values are a minimum, and for completeness we will run the theoretical model for reservoir values ranging from 0.5 – 30 km³.

When $k_r = 5 \times 10^8$ MPa, the depressurization rates inferred from geodesy can be reached for large conduit radii ($R_c > 700$ m) when reservoir volumes are small ($V_r = 0.5$ km³). For larger reservoirs ($V_r = 30$ km³), the radius of the conduit feeding the lava lakes must be at least 300 m to obtain reasonable depressurization rates. The sensitivity of depressurization rates on the conduit radius, and realistic values for this parameter, will be discussed further in Section 5.1.2.6. For ranges of conduit radii $R_c = 50 - 1000$ m and reservoir volumes 0.5 – 30 km³, the theoretical model cannot account for the lower depressurization values (-0.4 MPa year⁻¹). We may be able to account for this difference because the lower bounds were obtained using a sill, as opposed to an ellipsoid, and that this reservoir geometry is much more compressible than the ellipsoid. If we lower $k_r \approx 1.2 \times 10^8$ Pa, we obtain depressurization rates of -0.4 MPa year⁻¹ for $V_r = 30$ km³ and $R_c \approx 300$ m. We obtain similarly low depressurization rates if we assume a higher density difference between ρ_{nd} and ρ_c .

It is possible that lower depressurization rates are not obtained in Scenario 0 due to oversimplifications of the model assumptions, including the fact that we eliminate terms that reflect changes to the gas density in the conduit, as well as neglecting viscoelastic effects. Therefore, we proceed with the next model fidelity step to compare with Scenario 0.

5.1.2.5.2 Scenario 1: Viscoelastic rheology, gas exsolves in conduit

For this next fidelity step, we will still assume that there is no exsolved gas in the reservoir, but we assume that the host rock has a Maxwell viscoelastic rheology. Gas is exsolved in and degassed from the conduit of length L , which has an initial gas volume fraction $\beta_c = 0.1$. As in Scenario 0, we impose steady-state magma convection in the conduit.

Despite these adjustments, for the range of parameters of interest ($V_r = 0.5 - 30$ km³ and $R_c = 50 - 1000$ m), no significant difference is noted between Scenario 0 and Scenario 1 (See Figure 5-10b). The solutions begin to diverge for larger values of V_r when the host rock becomes less viscous ($\mu \approx 10^{17}$ Pa s). However, we have no constraints on this parameter for the host rock at Ambrym. Therefore, we will proceed with Scenario 2, which increases the fidelity of the model by allowing for gas exsolution in the reservoir.

5.1.2.5.3 Scenario 2: Viscoelastic rheology, gas can exsolve in reservoir

In the next scenario, we assume that gases may exsolve within the reservoir. Given that $\alpha = 1.3$ wt%, $S = 4 \times 10^{-6}$ Pa^{-1/2} for water, assuming the conduit is completely degassed ($\hat{\rho}_{m,c} = 2670$ kg m⁻³) and that $\Delta P(t) \ll P(t_0) = \rho g L \approx 52$ MPa, the depth of the reservoir when gas exsolution occurs is $L < \frac{1}{g\rho} \left(\frac{\alpha}{S}\right)^2 \approx 400$ m. Geodetic inversions in Section 5.1.2.1 estimate a reservoir depth of ~ 2.2 km beneath Ambrym's lava lakes. We can therefore conclude, according to Henry's Law, that there is no exsolved H₂O in the reservoir. In this case, Scenario 2 will have the same result as Scenario 1, where gas exsolution occurs at shallower depths, within the conduit.

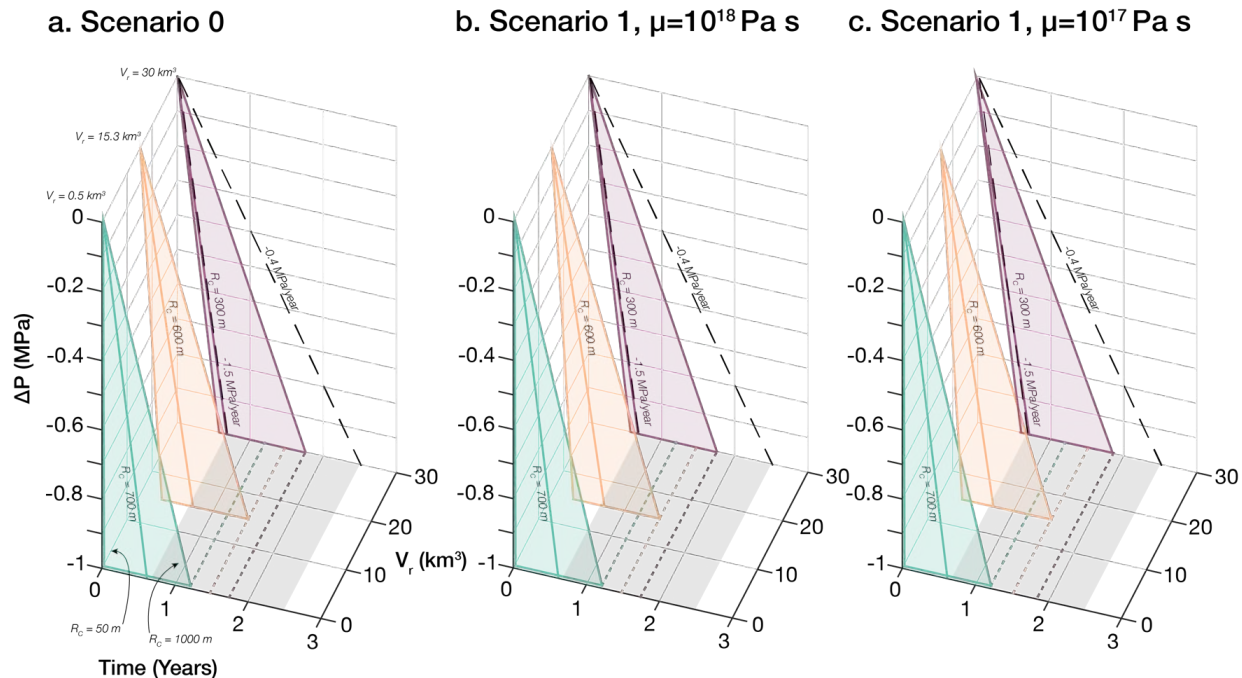


Figure 5-10: **Depressurization rate comparisons.** A comparison of theoretical degassing-induced depressurization rates with the rates obtained from geodetic modelling. **a.** The results for Scenario 0 (elastic rheology), with V_r ranging from 0.5 – 30 km^3 and R_c ranging from 50 – 1000 m. The black dotted lines show the depressurization rates estimated from geodetic modelling. **b.** The results for Scenario 1 (viscoelastic rheology, gas exsolves in conduit), when $\mu = 10^{18}$ Pa s. There is no significant difference between these results and those from Scenario 0. **c.** The results for Scenario 1, after decreasing the effective viscosity. The depressurization rate is slightly lower for larger reservoir volumes. For all of the above scenarios, $\hat{Q} = 90$ kt day $^{-1}$, $k_r = 5 \times 10^8$ Pa, $k = 10^{10}$ Pa, $\alpha = 1.3$ wt%, $\rho_{nd} = 2430$ kg m $^{-3}$, $\rho_c = 2670$ kg m $^{-3}$, $\beta_c = 0.1$, $L = 2.2$ km (derived in Section 5.1.2.1), $T = 1300$ K. A full list of the parameters can be found in Table D.1

However, if we assume a slightly larger α (e.g., 2.1 wt% as estimated by Moussallam *et al.* [2020]), gas exsolution may occur at deeper levels, ~ 1 km. This is still too shallow to exsolve bubbles in a reservoir residing at 2 – 4 km depth, as estimated for the shallowest levels of Ambrym’s magmatic system.

5.1.2.6 Discussion: Constraining magma reservoir and conduit size

We have little to no constraints on the input parameters $R_c(t_0)$, $V_r(t_0)$, μ and k_r . For small values of $R_c(t)$ (< 200 m), varying $V_r(t_0)$ can change the depressurization rates by an order of magnitude (Figure 5-10 and 5-11). The depressurization rate is sensitive to $R_c(t_0)$ due to the fact that Equation 5.7 depends on the reciprocal of $R_c(t_0)^2$. The estimated depressurization rates on the lower-end of our range (-0.4 MPa) may therefore be obtained by increasing $R_c(t_0)$ accordingly. According to Girona *et al.* [2014], realistic bounds on conduit radius range from 5 – 100 m, as obtained from theoretical models linking gas flux to magma convection in

the conduit [Stevenson and Blake, 1998], from models of magma supply rate, which can be related to eruptive column height [Pallister et al., 1992, Carey and Sigurdsson, 1985] or from muon tomography [Tanaka et al., 2009]. These estimates (and, we acknowledge, the model of Girona et al. [2014]) are for single-conduit volcanic systems. Ambrym hosts multiple vents within Marum and Benbow craters, which are separated by ~ 3 km. The vents are fed by the same degassing source, yet gas-melt separation occurs deeper at Marum than Benbow [Allard et al., 2015]. The model discussed above may therefore be further oversimplified, as it does not take into account the complexity of the geometry of Ambrym’s multiple conduits.

We will assume that the conduits feeding the lava lakes at Marum and Benbow connect at depth, although we have no constraints on this depth. The model’s parameter space explores the radius of this single conduit at depth. Conduit radii at lava lake volcanoes range from 1 – 2 m at Kīlauea (based on the magma ascent rate [Edmonds et al., 2013]), 15 m at Nyiragongo (based on the volumetric flow rate during a lava lake drainage event [Burgi et al., 2014]), and 160 m at Masaya (based on geodetic modelling [Stephens et al., 2017]). At Ambrym, the study of Allard et al. [2016] estimated the conduit radius of Benbow’s main lava lake-hosting vent to be 3 m. This value is consistent with the magma supply rate which explains the SO_2 flux measured with differential optical absorption spectroscopy (DOAS) [Allard et al., 2016]. Given the fact that Ambrym’s conduit at depth feeds at least two separate lava lakes at the surface, we may consider that the conduit is wider than the values estimated above. We will consider conduit radii less than 300 m to be reasonable values. The estimated conduit radii obtained for smaller reservoir volumes ($V_r = 0.5 - 15 \text{ km}^3$, $R_c > 600 \text{ m}$) are therefore considered unrealistic.

Due to the high uncertainties of our input model parameters, particularly $R_c(t_0)$ and $V_r(t_0)$, the theoretical model explored does not allow us to constrain with certainty Ambrym’s conduit size. It is also challenging to constrain the volume of the degassed reservoir. Conservatively, the reservoir volume may be $> 10 \text{ km}^3$. Given reasonable ranges of conduit radii of less than 300 m, the volume is estimated to be much higher (Figure 5-12). Such a large volume may be reasonable, as magma at Ambrym may degas from a hydraulically connected stack of magma lenses, whose cumulative volume is much greater than individual volumes estimates made in Chapter 4, for example. We also note that to obtain the depressurization values constrained by geodetic modelling, a low value of k_r is necessary. This may emphasize the importance of taking into consideration the reservoir geometry.

In order to adequately assess the applicability of this theoretical model, it should be implemented in a variety of cases. In the specific case of Ambrym, our input parameters differ significantly from those of Girona et al. [2014]. The degassing flux is one order of magnitude higher (90 kt day^{-1} compared to at most 10 kt day^{-1}), the quantity of dissolved volatiles is much lower (1.3 wt% compared to 3 – 6 wt%), and the reservoir bulk modulus is more than an order of magnitude smaller ($5 \times 10^8 \text{ Pa}$ versus $10^{10} - 10^{11} \text{ Pa}$). These initial assumptions each have their own uncertainties, which are discussed below.

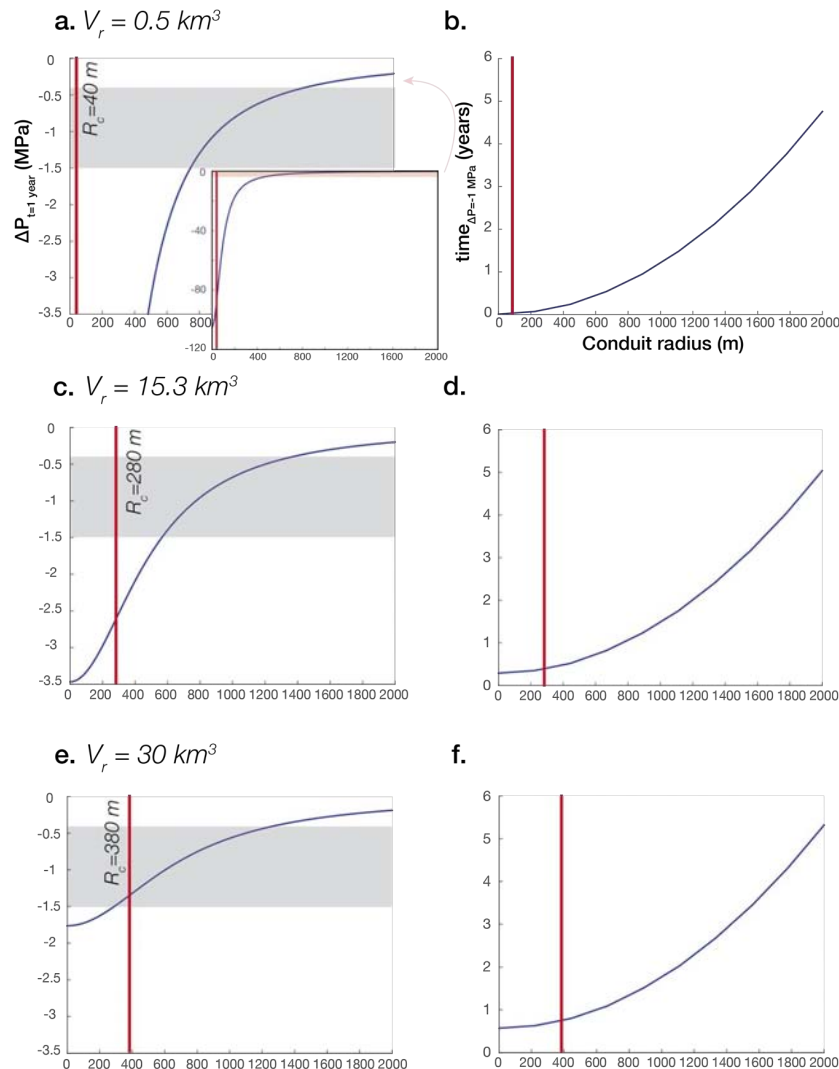


Figure 5-11: **Influence of conduit radius for various reservoir volumes.** The left-hand column shows the pressure change after 1 year for conduit radii ranging from 1 – 2000 m. The volume of the reservoir is fixed to either 0.5, 15.3 or 30 km³. The vertical red line indicates the inflection point of each curve, or where the depressurization rate begins to be less sensitive to changes in the conduit radius. The light gray box indicates the pressure change estimated from geodetic models. The right-hand column shows the time it takes to obtain a pressure change of -1 MPa (a ΔP within the range inferred from geodetic models) as a function of conduit radius. The location of the vertical red line is the radius found in the corresponding plot in the left-hand column.

5.1.2.7 Uncertainties

We fix numerous input parameters based on previous studies. These include the bulk modulus, the mean gas flux, the mass fraction of dissolved volatiles, and the density of undegassed and degassed melt. This allows us to explore the effect of varying the parameters on which we have little to no prior information. The uncertainties on the fixed parameters are as

follows.

5.1.2.7.1 Elastic moduli

As discussed previously, the same reservoir pressure change will result in different reservoir volume changes depending on the reservoir's shape (penny-shaped sill, sphere, vertical pipe, etc.). Ellipsoidal reservoir geometries are more compressible than spheres (See Figure 5-13 from Anderson and Segall [2011] for analytical expressions and numerical estimates of chamber compressibility, β_{ch} , for a range of reservoir geometries).

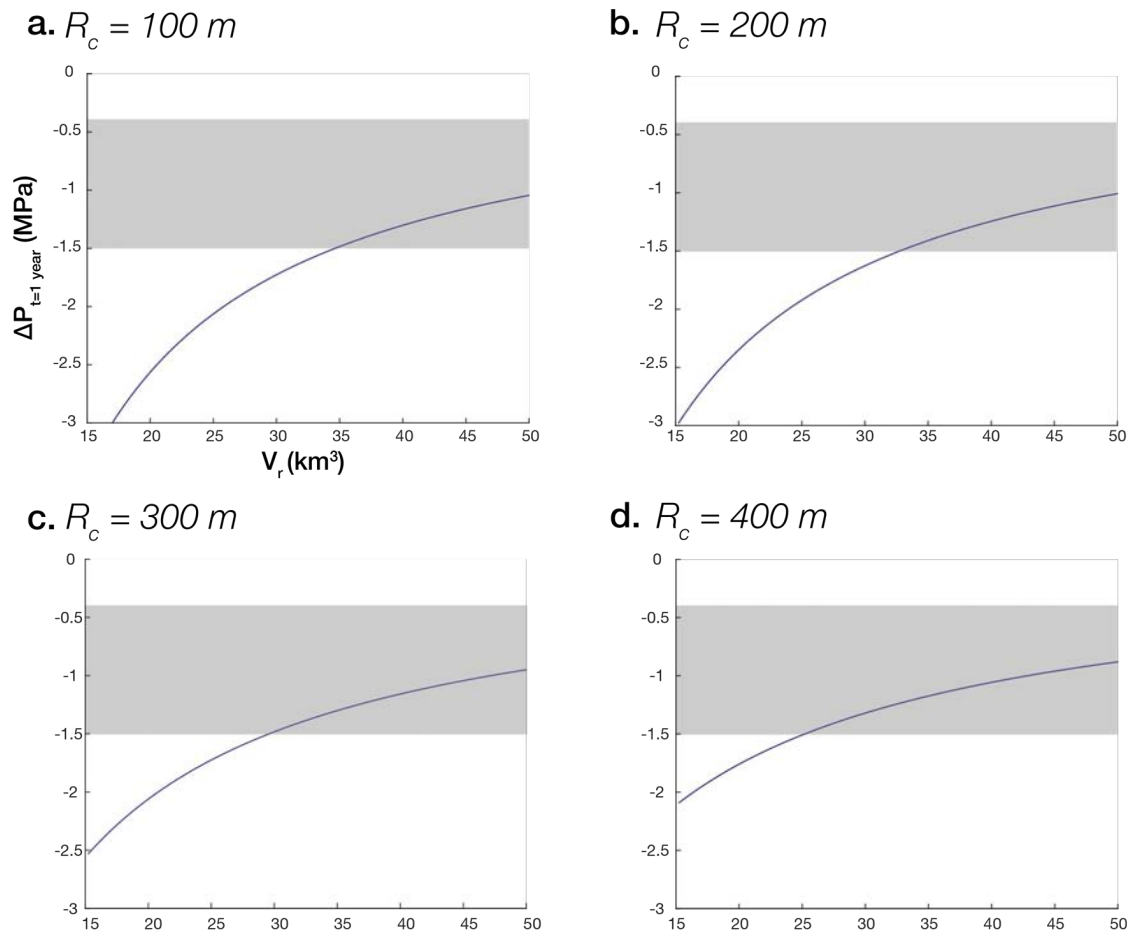


Figure 5-12: **Influence of reservoir volume for various conduit radii.** The pressure change after 1 year as a function of reservoir volume for conduit radii ranging from 100 – 400 m. The light gray box indicates the pressure change estimated from geodetic models.

We would like to scale the bulk modulus in Equation 5.7 to account for the fact that the sill-like geometry of Ambrym's reservoir is more compressible than the spherical reservoir assumed in the model of Girona et al. [2014]. According to Anderson and Segall [2011], the compressibility ratio of a penny-shaped sill (with an aspect ratio of $\frac{c}{a} = 0.05$) to a spherical reservoir is ~ 10 (See Figure 5-13). Given the ratio of the inverted parameters found with DEFVOLC (Ratio of Axis 3 to Axis 1 < 0.03), this is a reasonable approximation. However,

the geodetic inversion may only be sensitive to deformation from the top portion of the active magmatic system. The total volume and thickness of the degassed reservoir may be larger than the inverted source geometry.

Nonetheless, to account for a compressible penny-shaped sill, we will choose the chamber bulk modulus to be

$$k_r = \frac{1}{10}k \approx 0.1k. \quad (5.10)$$

The value of k in pristine host rock ranges from $10^{10} - 10^{11}$ Pa [Girona et al., 2014, Blake, 1981, Touloukian et al., 1981], therefore a reasonable range for k_r in our models is $10^9 - 10^{10}$ Pa. However, a volcanic edifice is most likely not composed of pristine rock, but instead rock that is fractured and porous. These factors, among others, influence the rock's elastic moduli. Recent experimental studies [Heap et al., 2019] concluded that the bulk modulus of volcanic edifices is closer to 4.5×10^9 Pa, or, after taking into account Equation 5.10, $k_r \approx 4.5 \times 10^8$ Pa. Therefore, we have varied the value of k_r between $5 \times 10^8 - 1 \times 10^{10}$ Pa to investigate how this value's uncertainty affects the system's depressurization rate.

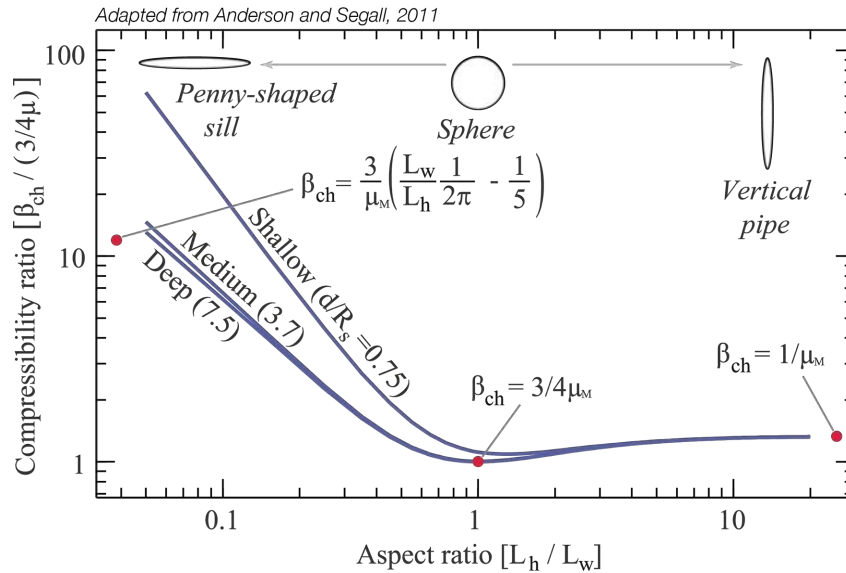


Figure 5-13: **Chamber compressibility.** Chamber compressibility ratio ($\frac{\beta_{ch}}{4\mu}$) as a function of aspect ratio ($\frac{L_h}{L_w}$, such that $L_w = a$ and $L_h = c$ in the text). μ_M is the shear modulus. This figure is adapted from Anderson and Segall [2011] to include a correction in the analytical expression for sill chamber compressibility. This expression should include the inverse of the aspect ratio, $\frac{L_w}{L_h}$, according to Amoruso and Crescentini [2009]. Otherwise the estimate of β_{ch} will be negative.

In addition, the elastic modulus used in the geodetic inversion is not well constrained. Although the chosen Young's modulus is consistent with in-situ measurements, the depth of the inverted reservoirs, and laboratory measurements [Cayol and Cornet, 1998, Heap et al., 2019], it still remains one of the largest uncertainties in the modelling framework. Varying the Young's modulus would change the inferred reservoir depressurization rate, which is compared to the output of the theoretical model. Fully exploring the uncertainties of the

Young’s modulus at the geodetic modelling step, and how these uncertainties are propagated into the theoretical model (i.e., influencing the chamber compressibility), should be addressed more thoroughly in future studies.

5.1.2.7.2 Mean gas flux, \hat{Q}

We obtain estimates of the mean H₂O gas flux by combining mean daily SO₂ gas fluxes measured by the satellite-based UV spectrometer OMI [Carn et al., 2017] with the bulk mass ratio of $\frac{\text{H}_2\text{O}}{\text{SO}_2}$ at Ambrym [Allard et al., 2015]. The bulk mass ratio is estimated given relative gas fluxes measured at Benbow and Marum (Mbwelsu) [Allard et al., 2015]. Carn et al. [2017] obtains a daily average assuming the emissions have a center of mass altitude (CMA) of 0.9 km (planetary boundary layer product, PBL). While they apply a correction factor which accounts for the volcano altitude [Fioletov et al., 2016], this does not necessarily account for variable injection heights of the volcanic plume throughout time. This is especially pertinent because gas flux is proportional to injection height ($Q_0 \propto H^4$) [Carazzo et al., 2008, Mastin et al., 2009, and references therein]. Since SO₂ mass burden can be significantly overestimated if the altitude is underestimated during the analysis [Krueger et al., 1995, Lee et al., 2009], systematic errors are expected to be larger for episodes of strong degassing. The joint analysis of 20 years of wind properties from ECMWF ERA-5 reanalysis data and directions of Ambrym SO₂ plumes from satellite observations shows that Ambrym SO₂ passive gas emissions are generally emitted at altitudes ranging up to 3 km a.s.l. [Boichu et al., 2021]. An unrealistically low CMA will overestimate the total SO₂ mass. Carn et al. [2017] states that SO₂ flux uncertainties for Ambrym are 55%, and we confirm that the average measurements used may bias the mean daily H₂O gas flux.

On the other hand, remote sensing measurements of SO₂ flux do not account for sulfur dioxide that may have been dissolved in the hydrothermal system [Symonds et al., 2001] (i.e., via scrubbing). The removal of SO₂ from the magmatic system by scrubbing, as opposed to degassing, would still contribute to the system’s depressurization. Given an SO₂ flux of more than a few kilotons per day, we suspect that the effect of scrubbing would not significantly alter our results.

5.1.2.7.3 Mass fraction of dissolved volatiles, α

The depressurization rate of the system is controlled by the quantity of dissolved volatiles in the magma. This value also affects the volume of exsolved volatiles in the reservoir in Scenario 2. The value of $\alpha = 1.3$ wt% that we use as an input parameter is derived from olivine-pyroxene-hosted melt inclusions from samples collected within Ambrym’s caldera (the flanks of Benbow), as well as on the SW coast (1913 tuff rung) [Allard et al., 2015]. Post-entrapment processes such as H⁺ or molecular H₂O diffusion may result in an underestimate of the H₂O content [Danyushevsky et al., 2002]. Nonetheless, similarly low (< 2.1 wt%) H₂O contents have been found in other petrological studies [Sheehan, 2016, Moussallam et al., 2020]. Sheehan [2016] also emphasizes that low H₂O contents are found for melt inclusions in various mineral phases. Because these mineral phases have differing H⁺ diffusivities, consistently low H₂O contents would not be expected if post-entrapment H⁺ diffusion had altered the H₂O content.

5.1.2.7.4 Density of undegassed and degassed melt, ρ_c and ρ_{nd}

The chosen densities for the degassed ($\rho_x = \rho_c$) and undegassed parent melt (ρ_{nd}) control both the partial density of water ρ_w and the average melt density in the conduit $\hat{\rho}_{m,c}$. We performed our model calculations using the densities given by [Girona et al. \[2014\]](#), which were calculated for an andesitic magma composition at $T = 1300$ K and 250 MPa ($\rho_c = 2670$ kg m⁻³ and $\rho_{nd} = 2430$ kg m⁻³). Lowering these densities results in a lowering of the depressurization rate. [Allard et al. \[2015\]](#) indicates that the density of the degassed magma is ~ 2650 kg m⁻³. The density of the parent magma could be calculated using the MELTS algorithm, for example, considering the pressure and temperature conditions, as well as the magmatic composition [[Ghiorso and Sack, 1995](#)]. More realistic estimates of magma density will be addressed in a future study using magma density estimates from [Allard et al. \[2016\]](#) (See Section 6.3).

5.1.2.8 How to further constrain the initial parameters

To confirm the fidelity of this theoretical model, it is important to either obtain additional constraints on the input parameters at Ambrym, or to apply this model to other volcanic systems. The latter may be difficult, given the lack of long-term volcanic subsidence during quiescence in the literature. An alternative may be to investigate other time periods of subsidence at Ambrym (e.g., 2004 – 2009). Unfortunately, only one pair of SAR images span this subsidence event, precluding a detailed investigation of the duration of the depressurization.

Measuring Ambrym’s conduit radius and geometry, even to the first-order, would decrease significantly the size of the model’s unknown parameter space. The conduit radius, for example, could be estimated with density measurements from muon tomography or gravimetry [[Tanaka et al., 2009](#)]. An analysis of infrasound tremors [[Yokoo et al., 2019](#)] could provide constraints on the size and shape of the uppermost part of the conduit. Continuous gravity measurements would be useful to identify the physical mechanisms that control lava lake level changes [[Patrick et al., 2019a](#)]. This could help improve our understanding of the dynamics of magma convection and recycling from the surface to deeper parts of the system. In addition, tiltmeters or GPS stations near the vents would provide constraints on the dynamics of magma and bubble ascent within the conduits. Finally, installing a thermal camera at the summit would allow for directly monitoring the lava lake level, which, assuming an open system, responds to reservoir pressure changes.

We have not yet addressed the fact that in the [Girona et al. \[2014\]](#) model, the volcano is considered an open system. The reservoir is connected to the surface and gas can escape through the conduit. This is the case, for example, at Kīlauea’s lava lake in the Halema‘ūma‘ū crater [[Patrick et al., 2015](#)]. When taking into consideration H₂O-CO₂ evolution patterns, Ambrym is best modelled with a closed system at depth and open system degassing at shallow levels (< 0.5 km) [[Allard et al., 2015](#)] (See Section 4.2). If the entirety of Ambrym’s conduit system (which we assume has a depth of 2.2 km) does not allow for gas escape, then the model may be oversimplified by assuming magma convection and degassing from a conduit that is much larger than in reality. However, given that Scenario 0 is not dependent on the length of the conduit L , this simplification will not alter the modelled depressurization rates. In Scenario 2, L determines the volume fraction of exsolved of gas in the reservoir.

For applications of Scenario 2 at other volcanoes, it would be necessary to constrain whether the reservoir can degas directly to the atmosphere through a vesicular conduit filled with degassed magma.

5.1.2.9 Conclusion

We have attempted to explain to the first-order the depressurization rates at Ambrym volcano over a period of ~ 2.5 years. While the geometry of Ambrym's magmatic system remains difficult to resolve, we conclude that the theoretical model of [Girona et al. \[2014\]](#) is compatible with the depressurization rates estimated from geodetic modelling. Degassing-induced depressurization is therefore a plausible physical mechanism that could drive subsidence at Ambrym volcano.

For realistic conduit radii (< 300 m), this model estimates that the degassing magma body has a volume > 10 km³. This model may need to be revisited in order to incorporate multiple conduits, as well as multiple magma lenses that are hydraulically connected. Incorporating the latter element would be more consistent with a vertically extensive magmatic system. It would also be worthwhile to investigate Scenario 3, which includes magma replenishment, to account for changes in the subsidence rate over time.

Nonetheless, this is a model representing a “textbook” magmatic system, and there are large uncertainties in the model parameters. Testing other physical mechanisms would help determine if there are other reasonable, and better-constrained, explanations for the subsidence. For example, [Caricchi et al. \[2014\]](#) evokes a combination of crystallization, cooling, degassing, and partial melting of residual andesitic magma to explain year-long subsidence at Okmok volcano. At a volcano with a high magma influx rate, like Ambrym, it is difficult to envision cooling and crystallization of the system, although we cannot discount this as a possible mechanism given the potential existence of a reservoir hosting more evolved magma in the eastern part of the caldera [[Moussallam et al., 2020](#), [Picard et al., 1994](#)]. Partial melting could result in reabsorption of volatiles that were exsolved from a cooling basaltic magma which was previously injected into the system [[Caricchi et al., 2014](#)]. Reabsorption of volatiles is not consistent with the high passive degassing flux at Ambrym, and is therefore not a plausible mechanism. Alternatively, a temperature increase in the system before or during the 2015 eruption could cause changes to the hydrothermal system (evaporation of water or drainage of the system resulting from changes in the crust's permeability), which may result in subsidence [[Lundgren et al., 2001](#), [Caricchi et al., 2014](#), [Lundgren et al., 2020](#)].

5.1.3 A broader view of the magmatic system provided by petrology

We propose that both magma withdrawal during eruptions, as well as volatile degassing during inter-eruptive periods, can drive reservoir depressurization. At least two magma lenses are imaged with geodetic modelling, one that is tapped during the eruptions at a depth of < 5 km b.s.l. and one that is active during inter-eruptions periods and has a depth of < 3 km b.s.l. However, geodetic modelling has limitations. For example, deformation may only be sensitive to the shape of the top of the magma storage region [Yun et al., 2006], and it may not be sensitive to pressure changes from deep sources [Du et al., 1992]. To complement geodetic source models, we integrate our results with petrological studies. We then synthesize these findings in an updated conceptual model of Ambrym’s mature magmatic system.

5.1.3.1 Multiple storage depths and mixing conditions

Petrological studies impose additional constraints on magma storage depths and magma properties (composition, volatile content, etc.). Sheehan and Barclay [2016] collected samples from scoria and reticulite erupted from the lava lakes in 2005 and 2007, respectively. The whole rock composition of the former is 50.79 SiO₂ wt% and the latter is 51.45 SiO₂ wt%. Mineral-melt (plagioclase and clinopyroxene) thermobarometry indicates that this magma stalls at depths of 24 – 29 km (crust/mantle interface), then again at 11 – 18 km (base of volcanogenic crust) (assuming $\rho = 2700$ kg m⁻³) (See Figure 5-15b).

Although Sheehan and Barclay [2016] propose that the magma doesn’t evolve any further after stalling at the base of the volcanogenic crust, a petrological study by Firth et al. [2016] concludes that crystallization of magma feeding the lava lakes also occurs at shallow levels. Firth et al. [2016] analyzed eruptive products from eight different eruptions (See Figure 5-14). These included samples from the lava lakes– lapilli from 2005, three scoria samples and reticulate from 2009, and a bomb from 2014. They also collected lavas from the 1942 and 1988 intra-caldera eruptions, as well as lavas from the 1913, 1929, and 1937 NW rift zone eruptions. The lava lake samples have the most evolved whole-rock compositions– 50.8 – 52.75 SiO₂ wt%. We note that no samples were taken from the 1986 trachy-andesitic lava flow in the eastern portion of the caldera, which is the most evolved of all post-caldera collapse products.

Using clinopyroxene-melt thermobarometry, Firth et al. [2016] estimates that initial fractional crystallization occurs at pressure ranges of 100 – 600 MPa (or 4 – 20 km depth, if $\rho = 2700$ kg m⁻³). They conclude that primitive magmas erupting from the rift zones are sourced from this deep reservoir, and show no signs of mixing. This indicates they may bypass the shallow storage region(s) beneath the caldera (alternatively, the magma ascent rate may be too high for interactions between magmas to occur) (See Figure 5-15a) [Firth et al., 2016]. The magma feeding the lava lakes is stored in these shallower regions, with the magma undergoing subsequent differentiation, possibly as a result of H₂O exsolution. This would thus occur at low pressures, $\ll 100$ MPa [Firth et al., 2016].

Intra-caldera eruption samples show evidence of magma mixing. For example, plagioclase and clinopyroxene crystals have chemical similarities to minerals in the erupted flank and

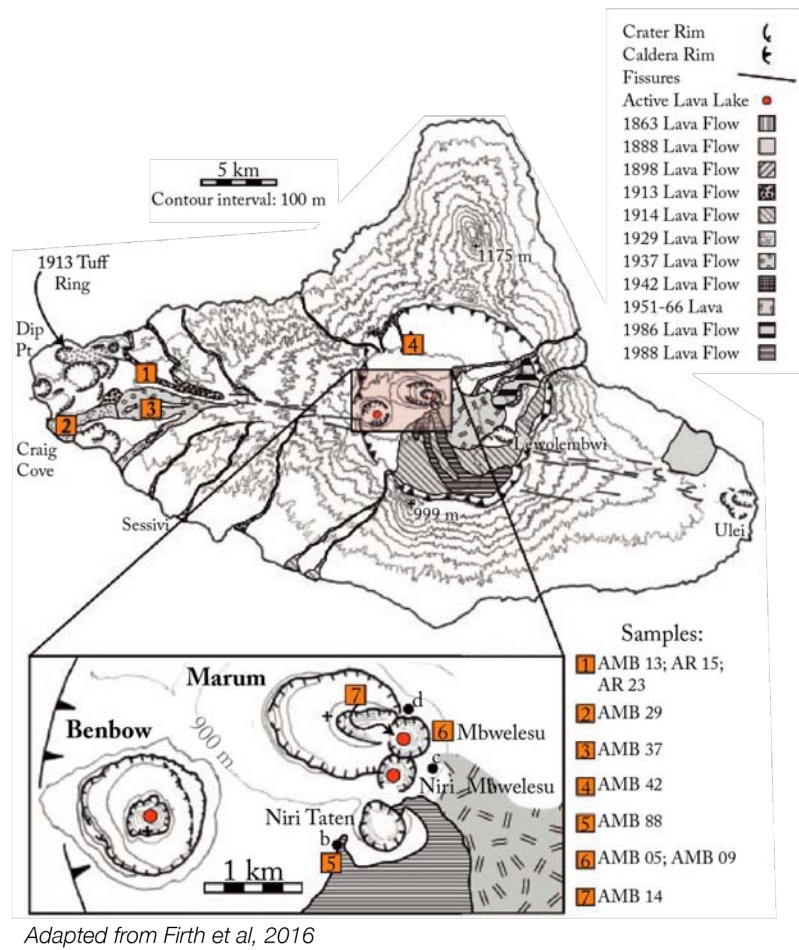


Figure 5-14: **Historical lava flows.** A map of Ambrym island showing the historical lava flows, as well as the locations of samples collected by Firth et al. [2016]. Adapted from Firth et al. [2016].

lava lakes products, as well as display resorption textures (re-fusion of a mineral back into the original melt) and, in the case of the 1988 lava, reverse zoning. [Firth et al. \[2016\]](#) concludes that the mafic magma that is involved in the rift zone intrusions is one of the mixing components, which provides the reabsorbed, high-anorthite plagioclase antecrysts. Pheno/antechrysts found in both the intra-caldera and flank lavas are geochemically similar [[Firth et al., 2016](#)]. A second mixed magma may have been more evolved, pointing to possible mixing with the magma feeding the lava lakes [[Firth et al., 2016](#)]. Disequilibrium textures in the lava lake samples may be due to recycling of plagioclase crystals during magma convection in the conduit, instead of mixing [[Firth et al., 2016](#)].

By analyzing entrapment depths of melt inclusions (MIs), [Allard et al. \[2015\]](#) found depths slightly shallower than the aforementioned studies. MI entrapment pressures range from 70 – 220 MPa (corresponding to depths of 2.6 – 8.3 km beneath the vents if $\rho = 2700 \text{ kg m}^{-3}$). Due to rapid entrapment and quenching during fast magma ascent, there was likely little volatile diffusion after MI entrapment [[Allard et al., 2015](#)].

These studies conclude that magma stalls at multiple levels within the crust before being erupted. Crystallization depths range from 4 – 20 km, with evidence for deeper (up to 29 km) and shallower (up to 2.6 km) storage regions. These findings are consistent with our hypothesis of a vertically extensive transcrustal magmatic system, comprised of stacked magma lenses. Petrological studies also complement geodetic inversions by resolving storage levels that are too deep to be detected by geodesy.

5.1.3.2 Lateral separation of melt lenses

Preliminary results from the petrological analysis of the 2018 eruptive products provide new constraints on magma storage, ascent and mingling during rift zone intrusions. They also constrain the composition and volatile content of the erupted lavas. [Moussallam et al. \[2020\]](#) collected lapilli-size tephra from the intra-caldera eruption in Lewolembwi crater, an ash sample south of the main craters, and two samples of highly vesicular pumice washed onshore during the submarine eruption (one collected on 18 December 2018 and another on 4 February 2019).

Clinopyroxene and olivine melt inclusions and the matrix glass show compositions ranging from 50 – 63 wt% SiO₂ [[Moussallam et al., 2020](#)]. The intra-caldera melt inclusion compositions span this entire range. The pumice sample that was collected in December 2018 has a basaltic trachy-andesite composition (similar to the composition found by [Firth et al. \[2016\]](#), [Allard et al. \[2015\]](#), [Sheehan \[2016\]](#) for products erupted from the main craters). In contrast, the February 2019 sample shows a mingling (physical mixing) of a basaltic trachy-andesite composition as well as trachy-andesite to trachy-dacite components (similar to products erupted in the eastern portion of the caldera and during the caldera forming sequence, i.e. Ambrym Pyroclastic Series [[Robin et al., 1993](#), [Picard et al., 1995](#)]). However, limited chemical mixing occurred between the two end members due to their brief interaction time [[Moussallam et al., 2020](#)]. Analysis of volatiles entrapped in melt inclusions estimate up to 2.1 wt% of H₂O, slightly higher than previous studies [[Allard et al., 2015](#)]. However, H₂O content may be underestimated due to H⁺ diffusion, and there may be a difference between the initial H₂O content in the basaltic and dacitic melt.

[Moussallam et al. \[2020\]](#) also calculates inclusion entrapment pressures. The highest

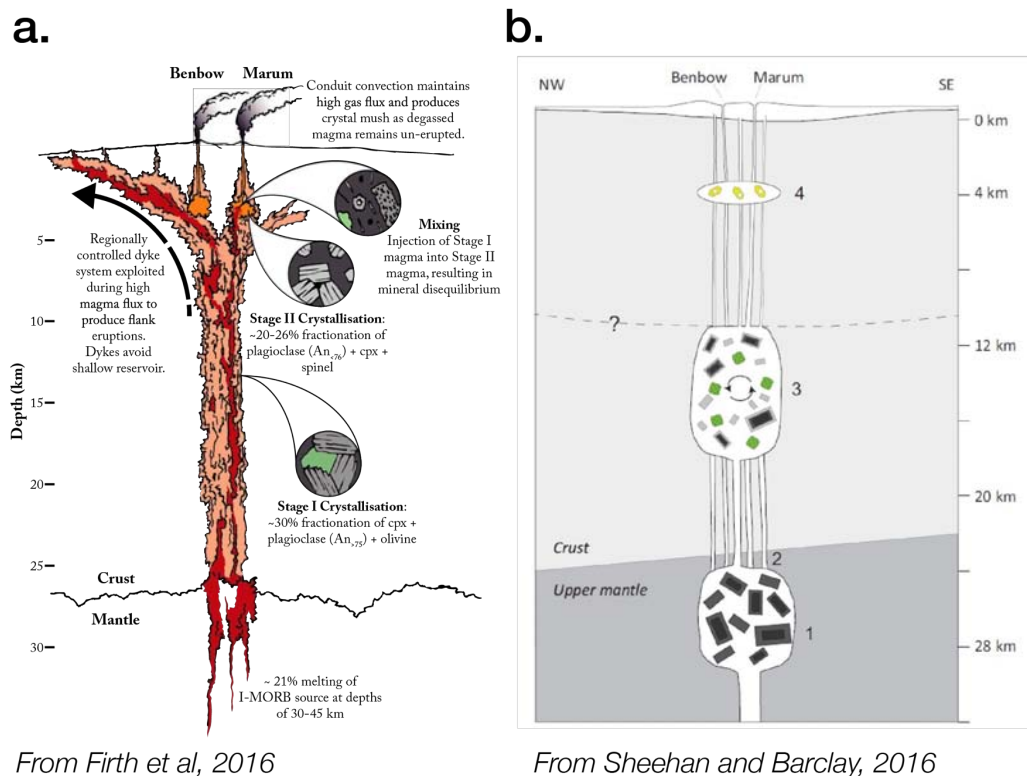


Figure 5-15: **Magmatic system from petrological studies.** Schematic illustration summarizing the findings of **a.** Firth et al. [2016] and **b.** Sheehan and Barclay [2016]. The numbers 1 – 4 in **b.** indicate 1. stalling of primitive magma near the crust-mantle interface, 2. crystallization or recharge causing magma to ascend, 3. magma stalling, clinopyroxene and lower-anorthite plagioclase crystallization occurring at this level, thought to be the base of the volcanogenic crust, and 4. thermal/volatile recharge causing further ascent, and magma stalling at shallower levels (3 – 5 km depth), as concluded by Allard et al. [2015] and Legrand et al. [2005].

entrapment pressures (180 – 280 MPa) were found for melt inclusions in the pumice, and the lowest entrapment pressures (< 24 MPa, < 1 km depth, assuming $\rho = 2700$ kg m⁻³) were found for the melt inclusions in the intra-caldera eruptive products. Although [Firth et al. \[2016\]](#) hypothesizes that magma intruded into the rift zone bypasses the shallow storage zone, there is evidence of magma mixing and mingling during both the 2018 intra-caldera and submarine eruptions. This indicates that the primitive magma intruding into the rift zone did not bypass the shallow storage for the entire span of the eruption. [Moussallam et al. \[2020\]](#) concludes that the primitive and evolved melts are derived from two separate, vertically extensive storage regions that span similar depths, but are laterally separated and isolated from one another (See Section 5.2.1.1). Lateral separation of magma lenses was overlooked in past petrological studies [[Allard et al., 2015](#), [Firth et al., 2016](#), [Sheehan and Barclay, 2016](#)].

In summary, Ambrym’s magmatic storage system is both vertically and laterally extensive. Magma moves between (and sometimes through) vertically separated lenses as it ascends through the crust. Magma mingling occurs between laterally separated lenses during lateral magma migration (See Figure 5-16).

5.1.4 Synthesis of results from geodesy and petrology

Over the past 20 years, geodetic measurements have imaged 2 separate magma lenses, at least one of which has been tapped during multiple eruptions. Other physical mechanisms, related to the persistent degassing at Ambrym, may explain inter-eruptive subsidence. Figure 5-16 incorporates findings from geodetic modelling during the 2015 – 2017 and 2018 – 2019 time periods, as well as storage depths estimated from petrological analyses [[Moussallam et al., 2020](#), [Firth et al., 2016](#), [Sheehan, 2016](#), [Allard et al., 2015](#)].

The deepest source imaged with geodetic models (< 5 km depth) was tapped during the 2018 rift zone intrusion and the ongoing 2020 uplift episode. This source is fed by an even deeper storage zone, which has been estimated from crystallization and melt inclusion entrapment depths [[Allard et al., 2015](#), [Firth et al., 2016](#), [Sheehan, 2016](#), [Moussallam et al., 2020](#)]. This deep source (> 8 km depth) may be connected to the original magma generation source within the mantle [[Firth et al., 2016](#), [Sheehan, 2016](#)].

The lava lakes, on the other hand, are alimented by a shallow source (< 3 km depth), consistent with both geodetic inversions and melt inclusion entrapment depths [[Allard et al., 2015](#)]. Degassing from the lava lakes causes the denser, degassed magma to sink and drives vigorous magma convection within the conduit. If continuous, this same process may also depressurize the shallow magma lens, resulting in subsidence. The possible tapping of this shallow magma lens during intra-caldera dike intrusions will be discussed in Section 5.3. Magma sources (both shallow and deep) in the eastern portion of the caldera may be isolated melt lenses that store crystallizing magma, which is occasionally withdrawn during both intra-caldera and rift-zone intrusion events [[Picard et al., 1994](#), [Moussallam et al., 2020](#)].

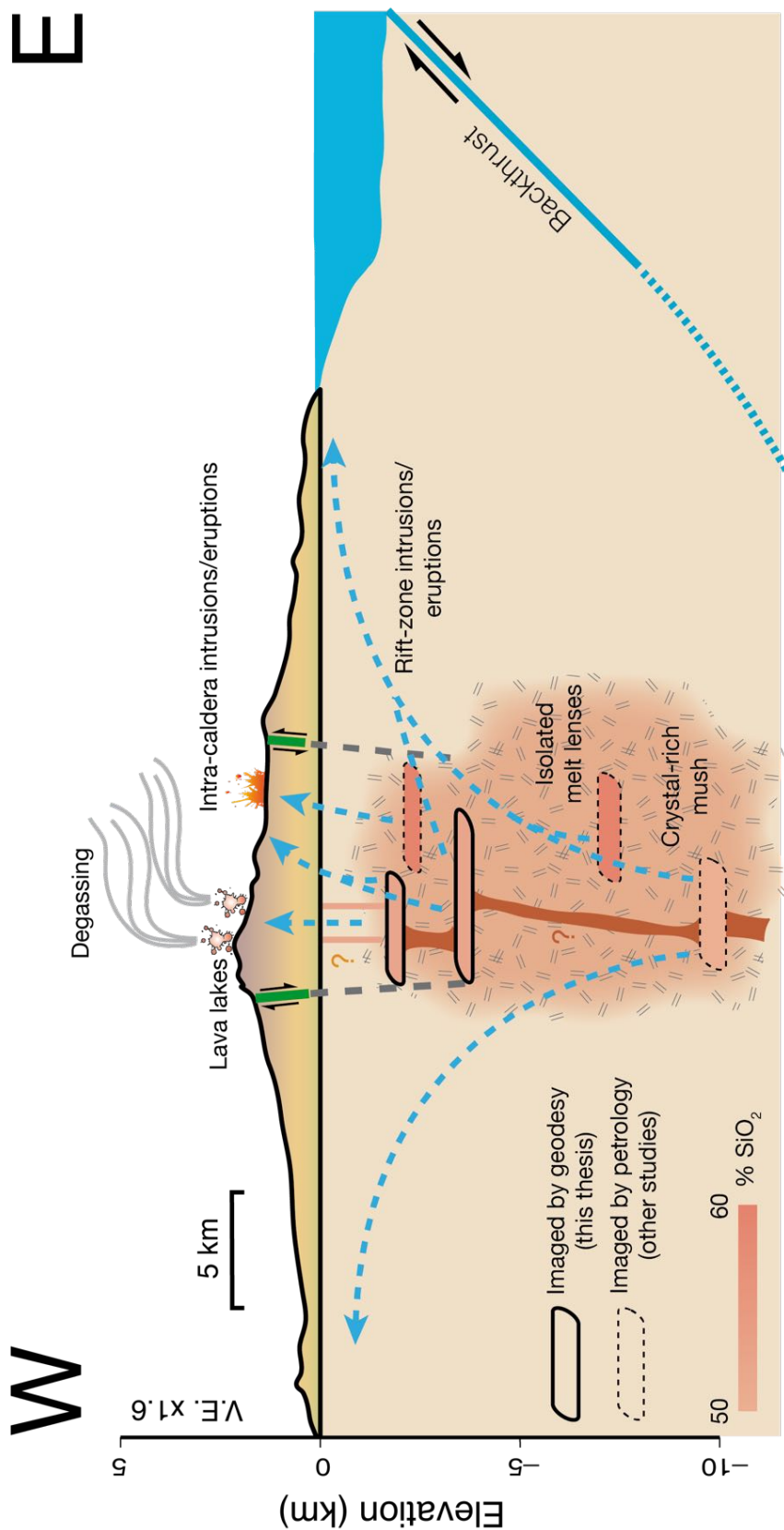


Figure 5-16: **Ambrym's magmatic system.** An updated conceptual model of Ambrym's magmatic system, combining results from geodesy (solid black lines) and petrology (dotted black lines). The depths of the magma lenses imaged with geodesy have also been confirmed by petrological studies. Lighter colors indicate more primitive magma compositions. The depths of the magma lenses in the eastern portion of the caldera, most likely feeds the lava lakes. Intra-caldera entrapment pressures. The shallowest source, in the western source of the caldera, most likely feeds the lava lakes. Intra-caldera eruptions drain the shallowest sources. Erupted intra-caldera products may include more primitive compositions if rift-zone intrusions pass through these storage regions during magma ascent and migration towards the rift zones.

5.2 Ambrym's caldera: formation and long-term development

Now that we have a better understanding of Ambrym's current magmatic system, we can begin to investigate the conditions under which it formed. To investigate the formation of Ambrym's magmatic system, which is both vertically and laterally extensive, and includes isolated melt lenses, we will return to a relatively recent event that may have caused substantial changes to the system—the contentious caldera collapse event that took place ~ 2 ka [Robin et al., 1993]. In addition to caldera formation, we will also discuss new insights regarding the caldera's long-term development, drawn from the caldera ring-faulting observed in Chapters 3 and 4.

Before proceeding with the discussion, we distinguish caldera *formation* from caldera *development* at Ambrym. The former relates to the initial event which formed the caldera ring-faults. The latter occurs incrementally as the caldera continues to deepen along these ring-faults.

Caldera formation at Ambrym occurred ~ 2 ka after either:

1. an initial Plinian eruption and subsequent phreatomagmatic eruptions, or
2. numerous subsidence events due to lateral drainage of magma into the rift zones.

Geodetic modelling provides evidence for caldera deepening mechanisms reminiscent of 2. However, we cannot discount the possibility of a Plinian eruption initiating caldera collapse and the formation of ring-faults.

5.2.1 Ambrym's disputed 2 ka Plinian eruption

Robin et al. [1993] estimates the total erupted volume during the Plinian eruption ~ 2 ka was 70 ± 10 km³ (≥ 20 km³ DRE). This is an order of magnitude larger than the reservoir volume estimated from geodetic ($1 - 3$ km³, Chapter 4) and theoretical (> 10 km³, See Section 5.1.2.6) models. The modelled volumes are underestimates, because they are only considering the shallow magma lenses at < 5 km depth. The shallowest lens sustains magma convection in the conduit, degassing, and lava lake activity, and the deeper lens drains during eruptions (magma may perturb the shallow reservoir as it ascends). It may be reasonable to envision either a larger reservoir, or an ensemble of magma lenses, underlying this shallow part of the system. The total volume of eruptible magma between the shallower and deeper systems may be > 50 km³. We explore how an explosive Plinian eruption ~ 2 ka may have influenced the formation of Ambrym's present-day magmatic plumbing system.

5.2.1.1 Magmatic system reorganization after caldera formation

Ambrym's present-day magmatic system may not represent the interconnected network of magma lenses (or single, large reservoir) which emptied during the Plinian eruption. By combining results from geodesy and petrology, we conclude that Ambrym's magmatic system is comprised of isolated magma lenses, with different SiO₂ compositions (Figure 5-16). For

example, more evolved lavas ($\sim 60\%$ SiO_2) have been emitted from vents in the eastern portion of Ambrym’s caldera in both 1986 and 2018 [Picard et al., 1995, Moussallam et al., 2020].

An explosive, caldera-forming eruption may explain the existence of isolated magma lenses. Such eruptions can change a volcano’s local stress field, leading to a reorganization, or partial destruction, of the pre-collapse magmatic system [Kennedy et al., 2018, Bachmann et al., 2012, Marti and Gudmundsson, 2000]. Ambrym’s Plinian eruption is classified with a Volcanic Explosivity Index (VEI) 6, one of only 17 large VEI 6 or VEI 7 eruptions recorded in the past 10,000 years [Newhall et al., 2018]. Analogously, after the Rotoiti eruption and caldera collapse 45 ka at the silicic Okataina Volcanic Center in New Zealand, a decrease in reservoir interconnectivity explained changes to zircon isotope and trace element composition variability [Rubin et al., 2016]. In the post-Rotoiti collapse magmatic system, different amounts of magma flux into different magma pockets result in varying levels of crystallization throughout the system [Rubin et al., 2016]. This may be similar to the case of Ambrym, where reorganization of the magmatic system may have resulted in decreased interconnectivity of the magma lenses. Magma and thermal flux is currently concentrated beneath the western portion of the caldera, where open conduits feed the lava lakes of Marum and Benbow.

In addition to decreasing the interconnectivity of the magmatic reservoir, gravitational unloading from the initial caldera collapse may have locally rotated the principal stresses. This would have favored the formation of a shallow network of sill-like magma lenses beneath the caldera, consistent with geodetic modelling of the present-day system. Similarly, after the 2007 Dolomieu caldera collapse at Piton de la Fournaise, a rotation of the principal stresses, resulting in a horizontal σ_2 or σ_1 , coupled with the low volumes of migrating magma, favored the stalling of dikes at depth [Peltier et al., 2010]. Stalled dike intrusions had only been recorded 7 times at Piton de la Fournaise from 1981 to 2007 (compared to at least 14 eruptions), yet occurred at least 7 times in the two years following the caldera collapse [Peltier et al., 2010]. Exemplifying a similar concept using Finite Element modelling, Corbi et al. [2015] argues that the circumferential and radial dike intrusions (which initiate as sills) at Fernandina (Galápagos) can be explained by stress changes in the volcano edifice due to unloading from caldera collapse (See Figure 5-17a).

We would like to investigate the potential influence of a σ_3 rotation due to gravitational unloading post-caldera collapse on sill emplacement beneath Ambrym’s caldera. According to Watanabe et al. [2002], Secor and Pollard [1975], in order for changes in σ_3 to control dike trajectory, the excess pressure change associated with unloading ($P_l = \rho g H$, where ρ is the density of the host rock and H is the height of the collapse, or depth of the caldera), should be ~ 5 times greater than the liquid excess pressure change of the ascending crack ($P_e = \frac{\Delta \rho g L}{4}$, where $\Delta \rho$ is the density difference between the liquid and the host rock and L is the length of the liquid-filled crack). To obtain a reasonable value for H during the disputed initial Plinian eruption at Ambrym, we assume the volume of subsidence is equal to the volume of erupted material. Assuming a caldera surface area of 113 km^2 and an erupted volume of 50 km^3 , the collapse height is $H \approx 440 \text{ m}$. This is a minimum estimate, considering the initial caldera diameter may have been smaller than the present-day structure, if it was widened during subsequent phreatomagmatic eruptions [Robin et al., 1993]. We will assume magma propagates from deeper parts of Ambrym’s magmatic system ($\sim 5 \text{ km}$ depth) towards

the surface ($L_z \leq 4$ km). Assuming an initial, unperturbed stress field before the caldera collapse, that $\rho = 2700$ kg m⁻³, $H \approx 400$ m, and $\Delta\rho$ ranges from 100 – 300 kg m⁻³, we find ratios of $\frac{P_i}{P_e}$ ranging from 3.6 to 10.8. The higher end of this ratio reflects the fact that perturbations to σ_3 due to post-caldera collapse may have played a role in controlling magma propagation orientation and sill emplacement at Ambrym. After Ambrym’s caldera formed, gravitational unloading may have encouraged sill formation beneath the caldera (Figure 5-17b).

In addition to sill formation, the local post-collapse stress field modelled by Corbi et al. [2015] encourages circumferential dikes. Volcanic activity following initial caldera formation—such as the creation of Woosantapaliplip cone, the Bogorfan basaltic-andesite lava flow in the NW of the caldera, and the creation of Benbow and Marum cones (See Figure 5-17c)—are consistent with a focusing of magma injection near the caldera rim. However, we cannot confirm if the dikes feeding these eruptions began as sills and rotated into circumferential fissures as they reached the surface, which would be most consistent with the stress field modelled in Figure 5-17a. The competition between buoyancy, magmatic overpressure, and tectonic stresses explains eruptive vents in other locations [Corbi et al., 2015].

Given the high influx of magma at Ambrym [Allard et al., 2015] (which may have been even higher in historic times [McCall et al., 1969]), local post-collapse stresses may have encouraged a well-developed, shallow and broad magmatic plumbing system with isolated melt lenses. The emplacement of shallow sills may also be preferred at Ambrym due to regional compressive tectonic stresses. Analogue modelling shows that dikes propagating in regions subject to a horizontal compressive stress are likely to rotate into sills over length scales of 1 to 10 kilometers, depending on the magnitude of compressive stresses, dike overpressure, and buoyancy ($\Delta\rho$), as well as the rock’s tensile strength and fracture toughness [Menand et al., 2010]. Theoretical models also predict that in environments of high compression, magma is likely to flow horizontally in sills [Ida, 1999]. However, the experiments of Menand et al. [2010] were performed assuming a homogeneous elastic medium, and they conclude their study by emphasizing the importance of crustal heterogeneities in dike orientation and arrest.

5.2.1.2 Next steps

Further discussion of the evolution of Ambrym’s magmatic system post-Plinian eruption should include studies complementing geodetic measurements over the past 20 years. For example, further geochemical, petrological, and geochronological studies would be needed to explore homogeneity of magmas pre-, syn-, and post-caldera formation. These studies would be essential to adequately assess the hazard potential of a future Plinian eruption emplacing tens of cubic kilometers of eruptive products at Ambrym. Only with further field work and petrological studies can we resolve the controversy regarding the existence of dacitic ignimbrites on Ambrym island.

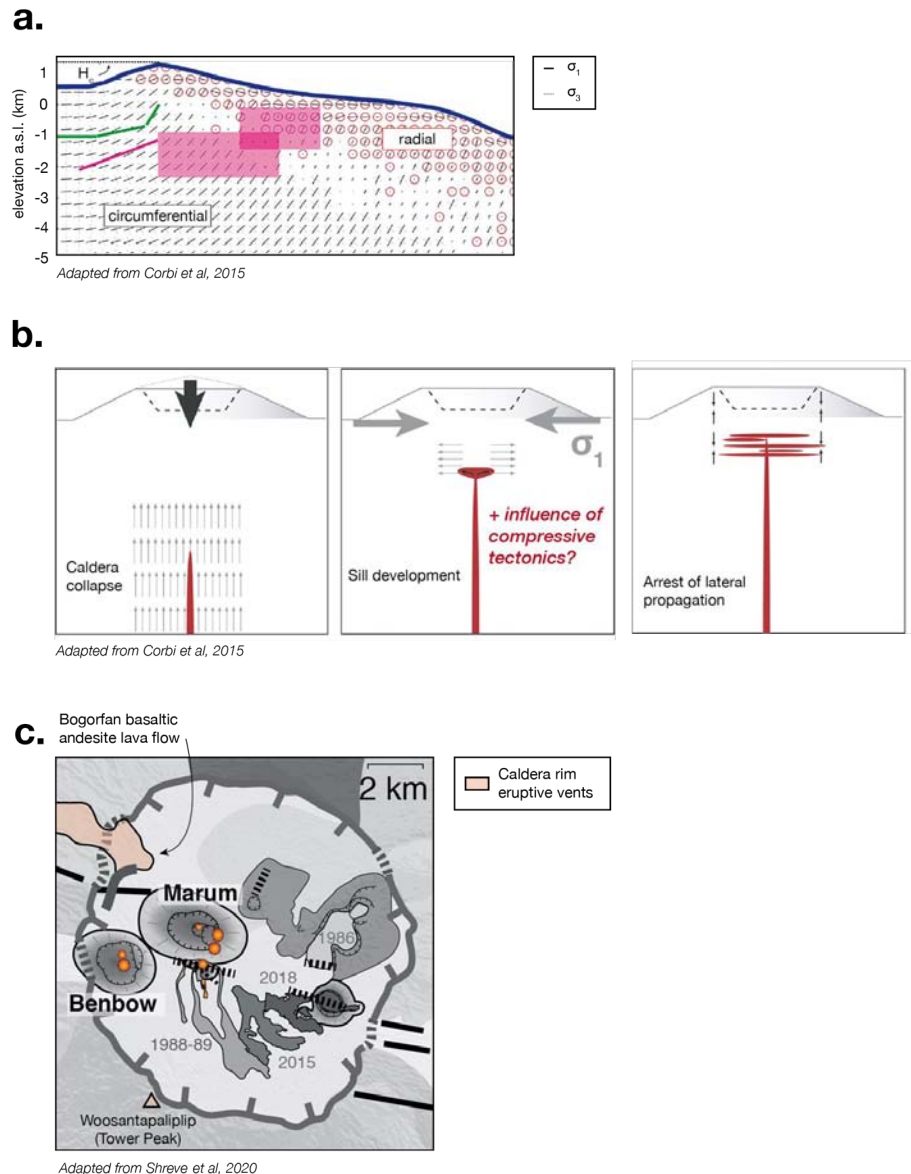


Figure 5-17: **Gravitational unloading post-caldera collapse.** **a.** Results from a Finite Element model showing the minimum and maximum principal stresses due to an isotropic reference stress and gravitational unloading from caldera collapse at Fernandina in the Galapagos. The green line represents the dike feeding the 2005 eruption, while the pink lines and rectangles show the dike feeding the 2009 eruption. H_c is the height of the caldera rim. Adapted from Corbi et al. [2015]. **b.** A schematic illustration showing the first three stages of a magmatic system's evolution post-caldera collapse. Gray and black lines are magma propagation and arrest locations, respectively. The final stage proposed by Corbi et al. [2015], which involves dike bending and twisting during radial fissure eruptions, is not shown here. We do not consider this case relevant to Ambrym, where rift zone eruptions on its flank are most likely controlled by tectonic stresses. Adapted from Corbi et al. [2015]. **c.** Zoom of Ambrym's caldera, adapted from Shreve et al. [2021]. In light pink are the post-collapse Bogorfan basaltic-andesite flow and Woosantapalip cone, both located near the caldera rim. Both features were cut by subsequent caldera subsidence [Robin et al., 1993].

5.2.2 Successive stages of caldera development at Ambrym

Although we cannot resolve the discrepancy concerning Ambrym's possible Plinian eruption, our geodetic observations allow us to add a fourth and final step to the caldera formation model from [Robin et al. \[1993\]](#) (See Figure 5-18),

1. "Earlier caldera collapse" due to a Plinian phase, with the possibility of a pre-existing caldera at the top of the original shield volcano edifice,
2. "Construction of the tuff cone as collapse enlarges,"
3. "Eruptive vents on the ring fracture," and
4. Episodic, meter-scale deepening and caldera ring-fault reactivation due to lateral magma migration into the rift zones.

We therefore relabel this as a model of caldera development, as opposed to caldera formation. Smaller subsidence events, such as those driven by drainage from a magma lens during intra-caldera eruptions (Chapter 4) and degassing-induced decompression (Section 5.1.2.3), may also have contributed to caldera deepening during Stage 4. We cannot currently constrain the effect of magma replenishment on caldera deepening and ring-fault slip before large intrusive and eruptive events. Through continued monitoring of the current uplift episode (See Figure 5-2g), future studies may be able to estimate the cumulative caldera floor displacement and ring-fault slip spanning a magma lens drainage and replenishment cycle.

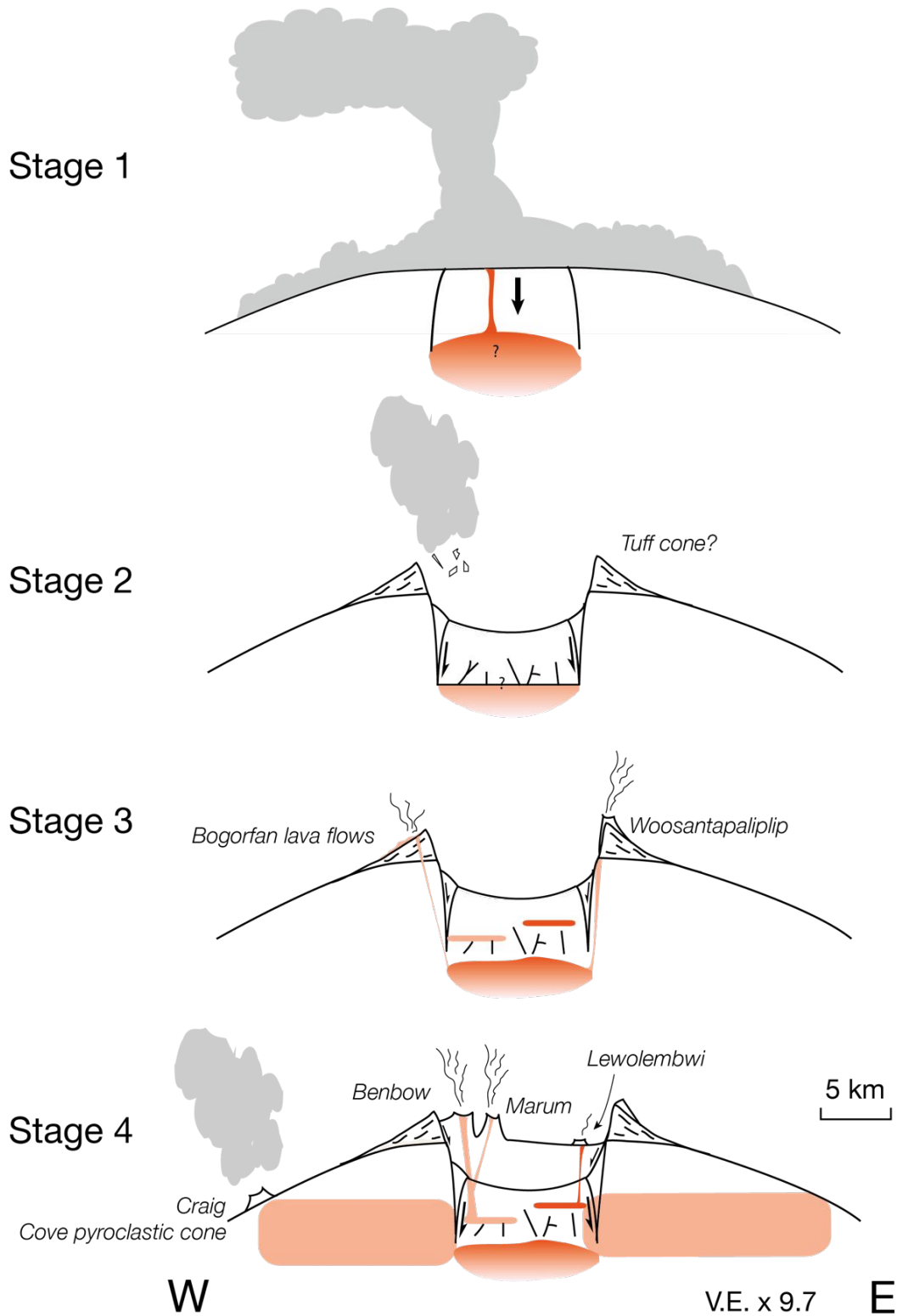
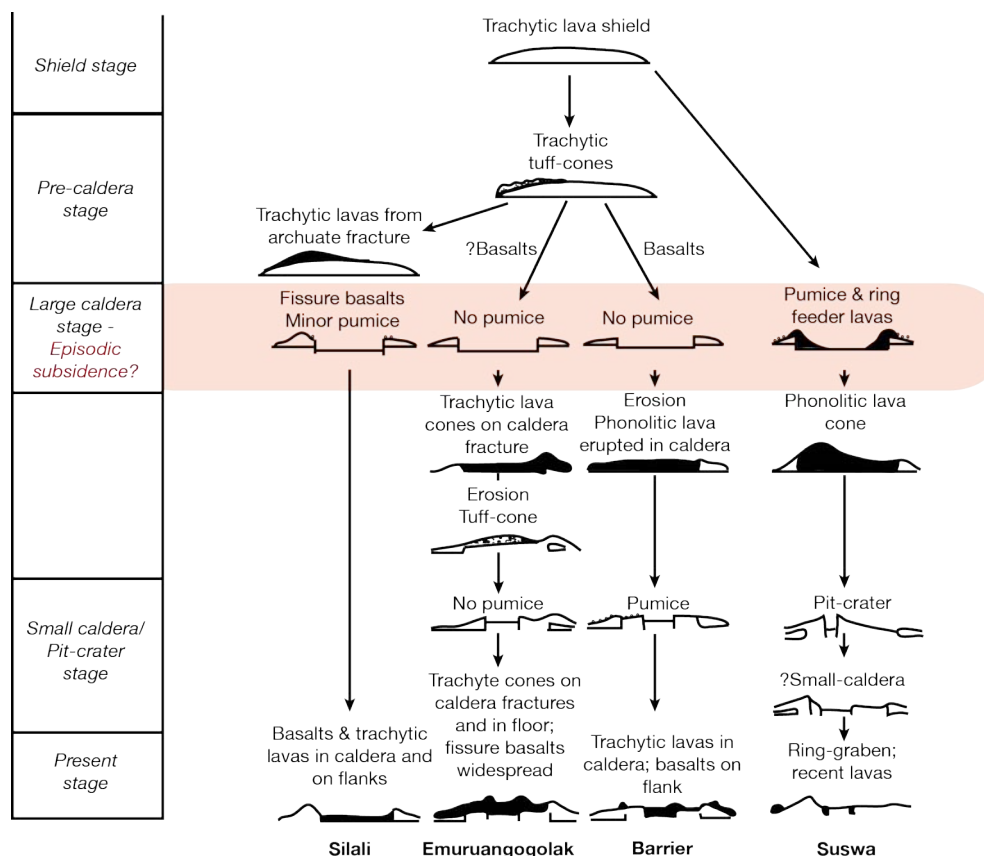


Figure 5-18: **Caldera development.** The four stages of caldera development at Ambrym volcano. The sketch is not to scale.

5.2.3 Episodic subsidence at other volcanic systems

Basaltic calderas are known to develop as a result of multiple collapses, occurring every few hundred to few thousand of years [Geshi et al., 2002, Tsukui and Suzuki, 1998, Simkin and Howard, 1970, Swanson et al., 2012, Anderson et al., 2019]. Collapses can be distinguished in geological sections when they are associated with substantial volumes of erupted lava flows or pyroclastic deposits. However, episodic modes of subsidence along caldera ring-faults, which contribute to caldera deepening, may be overlooked when there are little to no associated deposits. Taking Ambrym as an example, we would expect this mode of caldera development to be prevalent at volcanoes with voluminous rift-zone dike events which drain a shallow (< 5 km depth) magma reservoir that underlies a broad (> 6 km diameter) caldera. The low roof aspect ratio of such systems encourages ring-fault activation during both moderate and large magma withdrawals from the reservoir. In Chapter 4, Sierra Negra in the Galápagos was mentioned as another caldera which may deepen during meter-scale events that reactivate the bordering caldera ring-faults (although this reactivation has yet to be recorded), in addition to activating the fault along the sinuous ridge. Below we discuss three other calderas that may undergo “quiet” subsidence and caldera deepening, in a fashion similar to Ambrym. They are specifically associated with rift zone volcanism, emphasizing the importance of the regional tectonic stresses in directing lateral basaltic magma migration.

The first example concerns the broad, trachytic shield volcanoes hosting prominent calderas in the Kenyan (or Gregory) Rift, a segment of the East African Rift System. Among others, the formation of the Silali (7.5×5 km) and Suswa (12 km diameter) calderas are associated with no significant ash flow deposits [Williams et al., 1984, Skilling, 1993] (See Figure 5-19). For example, Suswa’s largest caldera, with a 12 km diameter, is thought to have formed incrementally by magma drainage at depth, explaining the discrepancy between erupted (6 km^3 DRE) and subsidence (22 km^3) volumes [Skilling, 1993]. Ring-fault formation at Suswa’s caldera was not correlated with a specific sequence of deposits, possibly indicating that reservoir underpressurization may have occurred after a dike intrusion arrested at depth, or propagated and erupted a significant distance from the central reservoir [Skilling, 1993]. The second, smaller (5.5 km) caldera at Suswa is thought to have formed entirely by magma withdrawal at depth, because no deposits associated with this collapse are recorded. The caldera of Silali, located further to the north, is also thought to have subsided incrementally either during or after the eruption of fluid basalt lavas (“Katenmening Basalts”, $\sim 100 - 65$ ka) from a volcanic rift zone that had recently developed. This subsidence may have been localized by ring-faults that had formed during two previous periods of explosive activity [Smith et al., 1995].



Adapted from Williams et al., 1984

Figure 5-19: **Episodic caldera subsidence in the Kenyan Rift.** The evolution of four of the large calderas in the Kenyan Rift. Although we only discuss Suswa and Silali in the text, caldera formation at Emuruangogolak and Barrier are also associated with little co-collapse pumice deposits. Adapted from Williams et al. [1984].

The above conjectures do not address the magnitude of subsidence during these incremental events. Given their large diameters, we hypothesize the deepening mechanism would depend on the depth of the magma chamber. A shallower magma chamber results in a lower roof aspect ratio, and subsequently a lower threshold for reactivation of the caldera ring-faults. At Suswa, for example, source models of ground deformation measured with InSAR are best fit by a shallow (< 3.7 km) penny-shaped crack [Biggs et al., 2009]. Silali has also been observed to undergo periods of subsidence, with the signal centered above the caldera [Robertson et al., 2016]. These deformation signals may be associated with changes in exsolved volatile content at the top level of a shallow magma chamber, in response to magma injection [Biggs et al., 2009]. In the case of shallow magma reservoirs, incremental caldera subsidence (on the scale of meters) along activated ring-faults would be the preferred mechanism of caldera deepening, as opposed to catastrophic caldera collapse (10's to 100's of meters). The total caldera deepening, however, depends on the magnitude and frequency of replenishment-driven uplift (and possibly reverse ring-fault motion) between reservoir drainage events. The formation of the ring-faults themselves also remains to be investigated in further detail, but seems to be associated with explosive events that incorporated

magma-water interaction.

An extreme case of incremental caldera deepening may occur at Axial Seamount, where the Juan de Fuca Ridge intersects the Cobb Hotspot (NE Pacific). Before and during the April 2015 dike intrusion and eruption, earthquake hypocenters were located along outward-dipping ring-faults on the east and west walls of the 8.5 km \times 3 km caldera [Wilcock et al., 2016]. Approximately 2.5 meters of subsidence coincided with the draining of the shallow magma reservoir, with most of the displacement occurring within the first day [Levy et al., 2018, Nooner and Chadwick, 2016]. The Axial Seamount may be considered the “end-member” of this mode of caldera deepening due to its frequent eruption recurrence time (\sim 13 years [Clague et al., 2013]). The high magma supply rate, the low roof aspect ratio of the caldera, and the rift extension (all relevant to the case of Ambrym as well), lead to single diking events, and short-duration (at most a few days) subsidence events which reactivate caldera ring-faults [Nooner and Chadwick, 2009, Clague et al., 2013, Levy et al., 2018]. The shallower caldera of the Axial Seamount may be a result of the regular inflation-deflation cycles, both of which have been shown to reactivate caldera ring-faults. Fault slip was greater during co-eruptive deflation in 2015 than pre-eruptive inflation, as discussed by Levy et al. [2018] based on locations of microearthquakes (magnitude $<$ 2) and the events’ cumulative seismic moments. Using the scalar seismic moment equation, Levy et al. [2018] estimated 44 – 175 cm of dip-slip during deflation vs. 8 – 30 cm of dip-slip during inflation. Cumulative fault displacement and caldera deepening would thus be related to the ratio of ring-fault reactivation during inflation and deflation events over geological time scales.

We conclude that in order for incremental caldera deepening to occur at a given volcanic system, three conditions should be met— 1. the magmatic storage system should be shallow and broad, 2. the regional or local stress regime should drive repeated rift-zone intrusions, and 3. magma replenishment must not produce enough uplift to compensate the long-term subsidence. The Kenyan Rift and Juan de Fuca Ridge are both located on divergent plate boundaries, and the regional stresses control the rift zone orientations. If we assume Ambrym is a large tension fracture resulting from compression in the central portion of the New Hebrides subduction zone (See Chapter 3), extension perpendicular to σ_1 is accommodated by magma injection. Similar to the tectonic rifts mentioned above, magma injections at Ambrym have preferential orientations dictated by the regional tectonic stress, leading to the formation of the rift-zone. Assuming that there is a high thermal flux directly beneath the caldera, tectonic stresses in this region may undergo viscoelastic relaxation. In this case, local stresses (gravitational, magmatic overpressure, etc.) dominate near the caldera, while regional stresses dominate in the brittle crust of the volcano’s flanks.

5.2.4 Caldera fault reactivation: silicic vs. basaltic systems

To explore similarities and differences between full-scale and meter-scale caldera deepening at both silicic and basaltic systems, we will compare these styles using the analytical model of Geshi et al. [2014]. This study derives reservoir volume and critical volume fraction for caldera collapse onset (See Chapter 4) from the caldera dimensions, reservoir depth, and volume of erupted material at the onset of collapse. We note that Geshi et al. [2014] does not include data from basaltic caldera collapse events because it is difficult to estimate intruded magma volumes. However, in-depth monitoring and analysis has been performed during

and after the 2018 Kīlauea and 2014 – 2015 Bárðarbunga caldera collapses. We therefore compare the findings of Geshi et al. [2014] with the values obtained from the literature for the lateral rift zone intrusions and caldera collapses during these two events, as well as the event at Ambrym in 2018. We wish to investigate whether these styles of caldera collapse follow relationships similar to collapses at silicic systems.

In order to proceed with this comparison, we must account for the piston collapse repressurizing the magma reservoir, which affects the eruption dynamics by increasing the magma outflow rate and possibly prolonging the eruption [Gudmundsson et al., 2016]. We therefore only consider the volume of magma that has been withdrawn from the reservoir at the onset of collapse, which has been determined by various studies [Anderson et al., 2019, Segall et al., 2020, Gudmundsson et al., 2016, Sigmundsson et al., 2020]. In the case of Ambrym, this value cannot be directly constrained. We conclude that the volume of magma extracted from the reservoir at the onset of collapse would be at most the volume of the dike intrusion measured in an ALOS-2 interferogram spanning 24 November to 22 December 2018, although this may be an overestimate.

We first compare the caldera diameters to the analytically calculated reservoir volumes, the volumes of magma intruded and erupted at the onset of collapse, and the total volumes intruded and erupted (See Figure 5-20). For Bárðarbunga, the total volume intruded in the dike (0.5 km^3), and the intruded volume at the onset of collapse ($0.25 - 0.35 \text{ km}^3$), were obtained through geodetic modelling of InSAR and GPS measurements [Sigmundsson et al., 2014]. The total erupted volume ($1.6 \pm 0.3 \text{ km}^3$) was estimated from the lava flow's surface area (obtained using aircraft-based SAR) and its thickness (obtained through DEM differencing) [Gfslason et al., 2015]. For Kīlauea, the volume of magma extracted from the reservoir at the onset of collapse ($0.027 - 0.086 \text{ km}^3$) was obtained from the pressure change at roof failure and the estimated reservoir volume [Anderson et al., 2019]. The total intruded volume (0.08 km^3) was estimated through geodetic modelling of InSAR measurements [Neal et al., 2018], and the total volume of erupted lava flows ($0.593 \pm 0.011 \text{ km}^3$) was estimated by DEMs generated with the airborne SAR GLISTIN-A instrument [Lundgren et al., 2019]. The caldera radii are 1, 4.3, 6 km and the chamber depths are 1.9, 10, and 4.5 km for Kīlauea, Bárðarbunga, and Ambrym, respectively [Segall et al., 2020, Sigmundsson et al., 2020, Shreve et al., 2019]. Values for the magma bulk modulus are estimated in Anderson et al. [2019] for Kīlauea ($0.67 - 5.0 \times 10^9 \text{ Pa}$). For Bárðarbunga, Sigmundsson et al. [2020] estimates a bulk modulus of $\sim 1 \times 10^9 \text{ Pa}$, but we allow for a broader range of values, $0.5 - 5 \times 10^9 \text{ Pa}$. In Chapter 4, we estimate the bulk modulus at Ambrym during the 2015 eruption to range from $0.27 - 2.13 \times 10^9 \text{ Pa}$.

Geshi et al. [2014] accounts for magma compressibility, but does not take into account chamber compressibility. This can be done by replacing the erupted volume V_e in Equation 1 of Geshi et al. [2014] by the sum of the volume change from magma compressibility and the volume change of the reservoir, which is a function of its geometry [Sigmundsson et al., 2020]. To calculate the total volume extracted from the chamber, V_{total} , we add the intruded and erupted volumes, and thus neglect changes to magma compressibility, as well as chamber compressibility. While reasonable for our first-order interpretation, magma and chamber compressibility should be rigorously accounted for in future comparisons, possibly in a fashion similar to Wauthier et al. [2015].

Given the above assumptions, as well as vertical ring-faults, we can use the analytical

solution of [Geshi et al. \[2014\]](#) to estimate the reservoir volume,

$$V_r = V_{prec} \frac{rk}{\rho gh^2 \tan(\phi)}, \quad (5.11)$$

where V_{prec} is the sum of the magma volume erupted and intruded at collapse onset, ρ is the host rock density (2700 kg m^{-3}), k is the magma bulk modulus, g is gravity, h is the depth of the chamber, and ϕ is the angle of internal friction of the host rock. Figure 5-20 plots analytically-obtained estimates of V_r for Bárðarbunga, Kīlauea, Ambrym, and the silicic caldera collapse events compiled by [Geshi et al. \[2014\]](#).

The reservoir volume estimated at Kīlauea ($\sim 4 \text{ km}^3$) is within the range estimated by [Anderson et al. \[2019\]](#) ($2.5 - 7.2 \text{ km}^3$), although they acknowledge that their data does not preclude a reservoir with a volume $> 10 \text{ km}^3$. It is also consistent with the relationship $V_r \sim 10r^{2.9}$, as estimated by [Geshi et al. \[2014\]](#) (Figure 5-20). Nonetheless, we note that the volume of erupted and intruded magma at collapse onset is much lower than that at silicic systems, which would result in a smaller critical volume fraction. The average V_r estimated at Bárðarbunga (2.6 km^3) is lower than expected for silicic volcanoes with a similar caldera diameter. It is also an order of magnitude smaller than the reservoir volume estimate of [Sigmundsson et al. \[2020\]](#), who assumed a reservoir with a semi-major axis of 4.3 km and a semi-minor axis of 0.4 km, or $V_r \approx 31 \text{ km}^3$. Finally, the V_r estimated for Ambrym (12 km^3) is also lower than that estimated using the relationship between V_r and r stated above, but it is consistent with theoretical modelling from Section 5.1.2.6.

We cannot draw firm conclusions with only three examples of basaltic caldera ring-fault reactivation driven by lateral intrusions. However, a first-order interpretation is that basaltic, intrusion-driven collapses may not follow the relationship between caldera diameter and reservoir volume derived for silicic systems, especially for broad calderas. The model parameter that is the most uncertain and may influence our estimates of V_r is the magma bulk modulus, which is rarely well-constrained and may vary over an order of magnitude. If the model parameters are reasonable, we may hypothesize that there are upper limits to the size of V_r at large basaltic-caldera rift systems that are not analogous to the limits of silicic reservoir size.

Ambrym’s reservoir volume estimate may also be lower than expected due to the fact that the reservoir roof did not completely collapse. While the magnitude of ring-fault slip at the surface may not seem significant at Ambrym, other characteristics of the event—specifically the very long period vertical-CLVD earthquakes—are similar to earthquakes recorded at full-scale caldera collapse events (See Chapter 3) [[Duputel and Rivera, 2019](#), [Shuler et al., 2013](#)]. This indicates a partial collapse of the reservoir roof at depth. The low critical volume fraction estimated at Kīlauea supports the idea that calderas may collapse earlier than previously thought [[Anderson et al., 2019](#)]. Nonetheless, we reiterate the caveat of [Anderson et al. \[2019\]](#), stating that pressure, not volume, change initiates roof failure. In future studies, attempts should be made to focus on the ΔP at the onset of caldera collapse, as opposed to the critical volume fraction. Translating ΔV to ΔP requires knowledge of the reservoir size and shape (See Section 2.2.2.1).

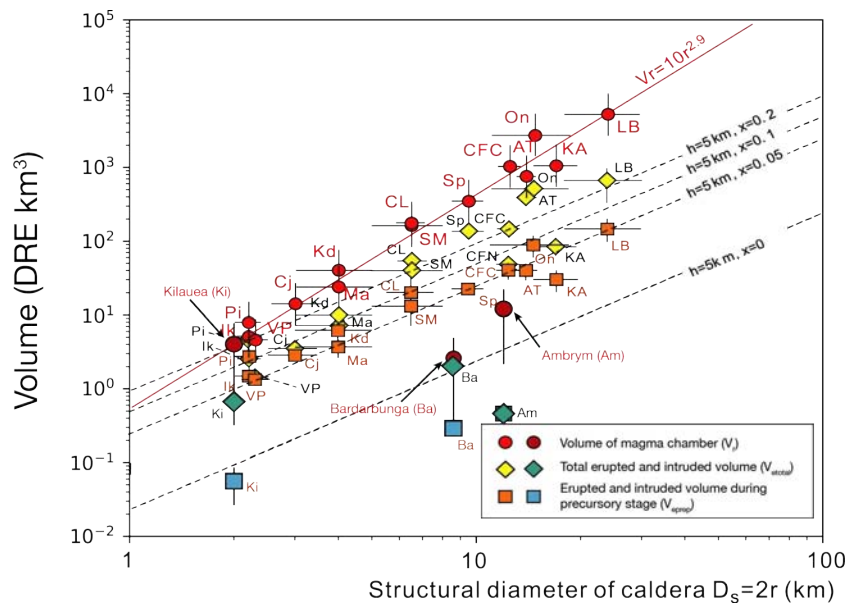


Figure 5-20: **Chamber relationship with caldera diameter.** Magma chamber volume, total erupted and intruded volume, and erupted and intruded volume during precursory stage for a compilation of silicic caldera collapse events, as well as for the Kīlauea, Bárðarbunga, and Ambrym events. The red line plots the relationship between caldera diameter and reservoir volume for the silicic systems. The dashed lines show the threshold of magma withdrawal before collapse for various reservoir depths h and bubble fractions x . Adapted from Geshi et al. [2014].

To explore the differences between the dynamics of caldera deepening induced by either Plinian eruptions or lateral injection [Druitt and Sparks, 1984, Sigmundsson, 2019], Ambrym may serve as a unique example. If the existence of dacitic ignimbrites is confirmed, then caldera ring-fault formation, reactivation, and subsidence may have occurred during both explosive eruptions, as well as “quiet” intrusion-driven subsidence. This would imply that these caldera development styles are not mutually exclusive at a particular volcano. A remaining open question is whether Ambrym’s present day magmatic system would be capable of producing a Plinian eruption in the future.

5.3 Revisiting 20 years of volcanic activity using multisensor observations: Evidence for an unreported dike intrusion in 2005

Over the past two decades, we observe correlations and anticorrelations between ground displacement, gas emissions, and radiated thermal power (See Figure 5-1). These observations may reflect changes in system pressurization over time, manifesting at the surface as changes to lava lake activity. We will jointly interpret these datasets to propose a hypothesis for the physical mechanism driving the currently unexplained 2004 – 2009 inter-eruptive subsidence episode.

Among the observations over the past 20 years is the drastic SO₂ degassing drop in December 2018. This drop is associated with the 2018 rift zone intrusion, which drained the lava lakes and collapsed the summit craters. A similar degassing drop is also measured by OMI and SCIAMACHY satellite SO₂ sensors in the middle of 2005 (See Figure 5-1) [Boichu et al., 2021]. SO₂ flux remained at low levels until around November 2006.

More subtle multi-year trends can also be identified. However, variations in degassing should be taken with caution, due to the dataset’s uncertainties. To obtain the SO₂ flux time series, measurements that include gas emissions from the nearby volcanoes Ambae and Lopevi are removed [Boichu et al., 2021]. The daily wind velocity is also taken into consideration to obtain the daily SO₂ flux [Boichu et al., 2021]. Even after applying these corrections and a Gaussian filter, the SO₂ flux estimates remain uncertain, making it difficult to constrain subtle changes to gas emissions. However, there is a clear increase in degassing from 2007 – 2012, followed by a pause, and another slight increase in gas emissions starting in the months before the 2015 eruption and continuing until the 2018 eruption. Higher frequency SO₂ flux variations may be of magmatic origin, but are difficult to deconvolve from meteorological processes.

The progressive disappearance of thermal anomalies over the course of 12 hours at Ambrym in December 2018 was interpreted as lava lake drainage, which was further confirmed by field observations [Shreve et al., 2019]. This lava lake drainage coincided with an abrupt decrease in SO₂ degassing. In 2005, thermal anomalies also disappeared around the same time as the SO₂ degassing decrease. No thermal anomalies were reported from 19 June 2005 until April 2006, when a single anomaly was detected at Benbow crater. Thermal anomalies were detected in Marum crater from November 2006 onwards (accompanied by an increase in SO₂ degassing, See Figure 5-23). A second hiatus in Marum crater’s thermal anomalies occurred from July to November 2007, and again from December 2007 to October 2008. Radiated thermal power progressively increased in both craters starting from November 2008.

According to the [Global Volcanism Program \[2005\]](#), ash stopped falling on 1 June 2005. A lava lake was reported in Marum (Mbwelesu) crater in May 2007 until at least 12 June 2007 [[Global Volcanism Program, 2007](#)]. These ground observations are consistent with the absence and reappearance of thermal anomalies. SO₂ flux increased when the thermal anomalies returned to Benbow crater (See Figure 5-23).

A decrease in radiated thermal power, or complete absence of thermal anomalies, can be interpreted as either draining of the lava lakes or cooling and formation of a solidified top layer [[Wright and Pilger, 2008b](#), [Oppenheimer et al., 2004](#)]. Heavy cloud cover (or volcanic

particulates) may also decrease the radiated power. No field observations confirmed the draining of the lava lakes, but the multi-year absence of thermal anomalies and decreased degassing suggest that all lava lakes at least partially drained from mid-2005 to November 2006. There are additional time periods when no thermal anomalies are detected (e.g., 2000 and 2009). However, they are brief and do not correlate strongly with degassing changes.

The 2018 drop in degassing and thermal anomalies has been explained by the drainage of Ambrym’s central magma lens and lava lakes, associated with the lateral migration of a major dike intrusion into the rift zone. Keeping this event in mind, we will propose a possible explanation for the degassing and thermal anomaly decrease that occurred in 2005.

5.3.1 2004 – 2009 deformation episode

One Envisat interferogram (images acquired on 29 September 2004 and 2 December 2009) spans the 2005 – 2006 hiatus in lava lake activity and degassing (See Figure 5-2a). Ground displacement in this interferogram is dominated by > 30 cm of subsidence within the caldera. In addition to subsidence, this interferogram has two unusual characteristics. First, two troughs of maximum subsidence are measured SE of Marum. Second, there is an increase in the displacement gradient and change in fringe orientation in the SE corner of the interferogram (corresponding to uplift– See Insets 1 and 2, Figure 5-21). Unfortunately, only a portion of this uplift signal is coherent.

An ALOS interferogram (images acquired on 19 August 2007 and 12 October 2010) also spans the reappearance of thermal anomalies at Benbow (See Figure 5-2b). This interferogram measures ~ 5 cm of uplift centered to the NE of Marum crater. However, it measures no subsidence, indicating that the subsidence episode measured by Envisat occurred between 29 September 2004 and 19 August 2007.

We hypothesize that the anomalous uplift in the SE corner of the Envisat interferogram is associated with a dike intrusion. If this dike intrusion drained the shallow magma lens feeding the lava lakes, this would explain the disappearance of the thermal anomalies and the decrease in degassing. To test this hypothesis, we use a non-linear inversion to estimate the parameters of an opening dike and a horizontal deflating sill (See Figures 5-21a and 5-22a). This inversion estimates a dike volume change of 14.8×10^6 m³ and a sill volume change of -12.6×10^6 m³. The orientation of the dike is nearly E-W, aligned with the southern edge of the horizontal sill (See Figures 5-21a and 5-22a). The depth of the sill is ~ 2 km beneath the craters.

Both the dike and sill volume changes are underestimated. For the dike, we have no far field measurements to constrain its length or depth. For the sill, post-eruptive magma replenishment may have the same spatial footprint as the deflating source, cancelling out a portion of the co-eruptive subsidence. However, deformation sources at Ambrym have been shown to have a variety of geometries (See Figure 5-2). We therefore test the possibility that the Envisat interferogram captures a post-eruptive inflating source with a geometry different than the deflating sill. The hypothesis of magma replenishment is further supported by the fact that the Envisat interferogram spans the lava lake reappearance.

This second non-linear inversion includes three sources– an opening dike, a deflating sill, and an inflating spherical point-source (See Figures 5-21b and 5-22b). The volume of magma intruded into the near-vertical dike is $\sim 16 \times 10^6$ m³, the volume change in the horizontal

sill is $\sim -15.1 \times 10^6 \text{ m}^3$ (depth $\sim 2.6 \text{ km}$), and the volume change in the spherical source is $\sim 2.7 \times 10^6 \text{ m}^3$ (depth $\sim 2 \text{ km}$). We then explore if this inflating spherical point-source could explain the uplift measured with the ALOS interferogram.

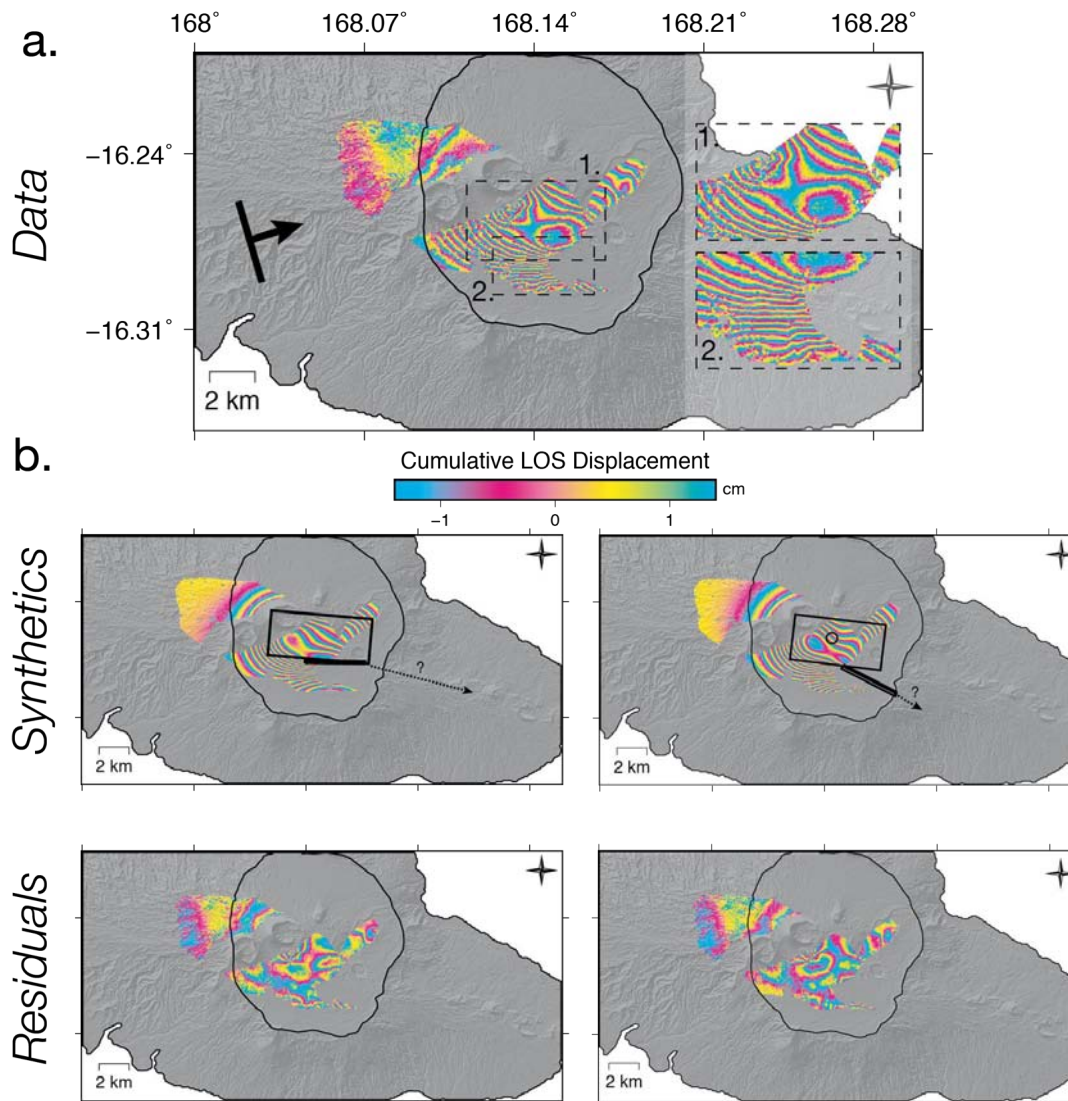


Figure 5-21: **Geodetic modelling of Envisat interferogram spanning 2004 – 2009.**

a. The Envisat interferogram with two unusual fringe patterns, shown in Insets 1 and 2. **b.** The synthetics and residuals for the inversion with an opening dike and deflating sill (lefthand column) and an opening dike, a deflating sill, and an inflating spherical point-source (righthand column). The source projections at the surface are shown by the heavy black lines.

We invert displacements measured by the aforementioned ALOS interferogram to estimate the depth and volume change of a spherical point-source. The estimated depth (~ 4.1

km) is deeper than that found in the Envisat interferogram inversion. The location of this source is shifted to the north compared to the Envisat inversion, and the volume is doubled ($\sim 5.4 \times 10^6 \text{ m}^3$). Further modelling of the entire dataset of ALOS interferograms spanning 2007 – 2010 would provide insights as to whether the Envisat and ALOS interferograms are imaging the same uplift episode. This would also provide further justification for including an inflating spherical source in the inversion of the Envisat interferogram.

Because these models underestimate source volume changes, we can conclude that this event involved a slightly larger volume of magma than in 2015 (which had a dike volume change of $30 \times 10^6 \text{ m}^3$ and a magma lens volume change of $-13 \times 10^6 \text{ m}^3$). Nonetheless, the event was still an order of magnitude smaller than the 2018 rift zone intrusion and caldera subsidence episode. Although similar volume source changes are estimated during the 2015 eruption, we consider the 2005 event noteworthy because it drastically changed Ambrym's surface activity. The 2005 dike intrusion may have tapped only the shallow magma lens feeding the lava lakes, as opposed to the deeper sources tapped in 2015 and 2018. A relatively small depressurization event in 2005 may have led to the complete draining of the lava lakes. In 2015, the lava lakes may not have completely drained due to continuous replenishment of the magma lens from a deeper source (See Section 5.3.2). In other words, Ambrym's shallow magma lens may not have had enough magma available in 2005 to sustain lava lake activity. No anomalously high thermal anomalies are associated with the 2005 event, implying that magma did not erupt at the surface. This emphasizes the importance of using remote sensing observations to monitor volcanic unrest at Ambrym, as dikes stalling at depth can play a significant role in modulating lava lake activity and degassing.

In summary, we conclude that a moderate-sized dike intrusion occurred at Ambrym in 2005, leading to a >1 year-long hiatus in lava lake activity and degassing. This event was not associated with an eruption, likely explaining why it went unnoticed. Similar diking events with no surface eruption have occurred in Afar, Iceland, and Saudi Arabia [Grandin et al., 2010, Einarsson and Brandsdottir, 1980, Pallister et al., 2010].

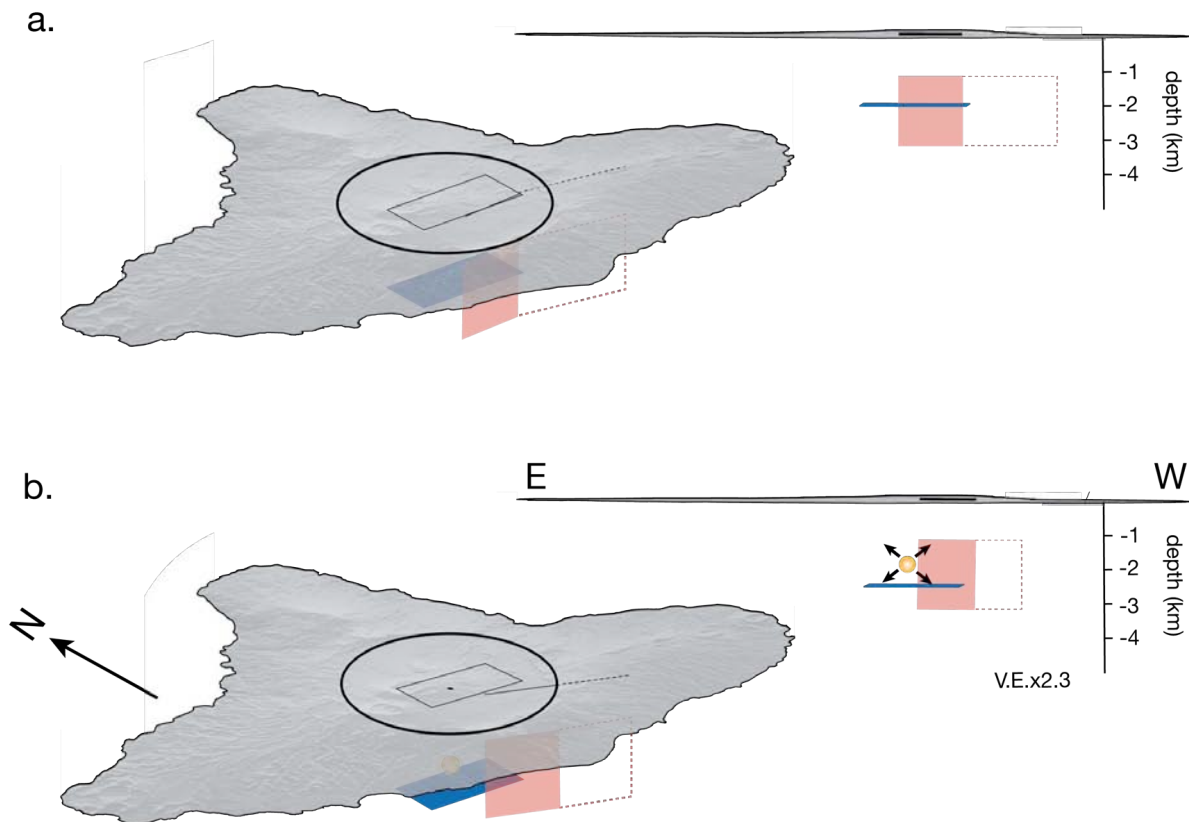


Figure 5-22: **Geodetic modelling results for the 2004 – 2009 Envisat interferogram.** Aerial and profile view of the two inversions mentioned in the text. The pink and blue rectangles are the opening dike and deflating sill, respectively. The orange circle is the inflating spherical point-source.

5.3.2 Evidence for system repressurization

Since the 2018 rift zone intrusion, no degassing or lava lake activity has been observed from space at Ambrym for almost 2 years. In the beginning of 2020, uplift within the caldera was measured for the first time since the event (See Figure 5-2g). Due to the large volume of magma that was withdrawn from the magma lens in 2018, we can assume that pressure differences drive replenishment from deeper levels into Ambrym’s 3 – 5 km deep storage system. Assuming this uplift is due to magma replenishment, the modelled volume gives a magma influx rate of $\sim 0.65 \text{ m}^3 \text{ s}^{-1}$.

There is also evidence for magma replenishment spanning previous time periods. For example, a trend of increasing radiated thermal power from the vents in Benbow crater is observed starting 6 years prior to the 2015 eruption (See Figure 5-23 and also Coppola et al. [2016a]). This increase begins with the return of thermal anomalies at Benbow in November 2008, after more than 3 years of inactivity. Aside from a brief decrease in radiated power after the 2015 eruption, overall radiated power continues to increase until 2016. Unfortunately, in the years prior to the 2015 eruption, the only available InSAR measurements span 2007

– 2010, merely a portion of the time period when radiated power increases. The ALOS interferogram spanning this epoch measures uplift, modelled by a volume change of 5.4×10^6 m³ of a ~ 4 km deep source (See Section 5.3.1). This is also consistent with the hypothesis of magma replenishment.

An increase in radiated thermal power either indicates an increase in lava lake surface area, an increase in the thermal renewal of the lake’s surface (i.e., by increased convection), the formation of an additional lava lake, or some combination of these factors [Wright and Pilger, 2008a]. On timescales longer than weeks, changes to the lava temperature does not contribute significantly to the radiated power [Oppenheimer et al., 2004]. If the conduit is funnel-shaped, a pressure increase within the system due to replenishment would cause the lava lake level to rise and the surface area to increase. Alternatively, more vigorous magma convection could be favored by the replenishment of volatile-rich magma, which increases the density contrast between the degassed and undegassed magma [Palma et al., 2011]. Increased magma convection may also be favored by an increase in conduit radius.

Immediately after the brief drop in radiated power associated with the 2015 eruption, the radiated power from Benbow’s vents appears to stay constant, while the radiated power from Marum’s vents increases briefly. Post-eruptive replenishment of the shallow magma lens with volatile-rich magma from a deeper source may result in a more vigorous magma convection in the conduit. This could increase the mean gas flux, which, according to the model of Girona et al. [2014], would increase the depressurization rate in the shallow magma lens. This would be consistent with degassing-induced depressurization of a shallow source during the time periods 2015 – 2017, as measured with InSAR. However, the complexity of the multiple-conduit system is not taken into account in this interpretation, and differences in radiated power between the two craters’ vents needs to be studied in more detail.

If we assume that the 2015 – 2017 subsidence episode is due to increased degassing, the abrupt end in this subsidence could be explained by continued magma replenishment into the shallow magma lens. Degassing-induced magma lens depressurization can cause magma replenishment due to pressure differences between the deeper and shallower magma lens. This passive magma replenishment can continue without an overpressured deep magma source [Girona et al., 2014]. The depressurization rate of the system will reach zero after a few years of magma replenishment, due to a balance between the depressurization induced by degassing and the pressurization induced by replenishment (See Figure 6 in [Girona et al., 2014]). This may explain in part the abruptly ending subsidence in September 2017 (i.e., the system reaches a pressure balance at this time, See Figure 5-5). This is also consistent with the conclusion from Chapter 3 that Ambrym’s magmatic system was not significantly overpressurized before the 2018 rift zone intrusion.

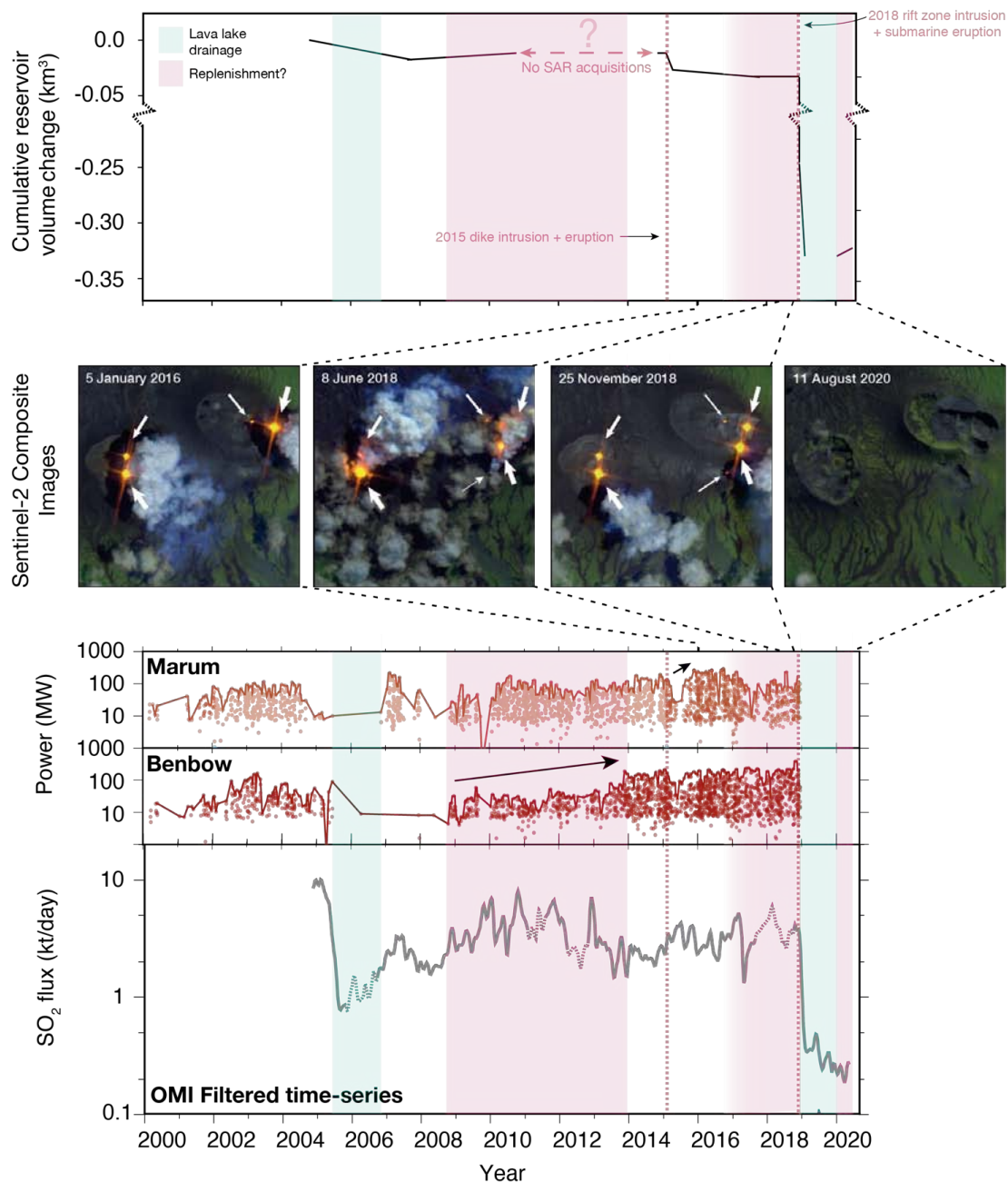


Figure 5-23: **Annotated summary of geodetic modelling, thermal anomalies, and gas emissions.** An annotated version of Figure 5-1, showing periods of lava lake drainage (light green) and possible magma replenishment (light red). Although magma replenishment may have been ongoing since the reappearance of the lava lakes in 2007 up until December 2018, we highlight only the periods that show evidence of replenishment from multiple datasets. For example, from 2009 – 2014 we observe uplift measured with InSAR, an increase in radiated thermal power, and an increase in gas emissions (until ~ 2012). Also, from 2017 to 2018, we observe an abrupt end to ground subsidence, and an increase in the number of thermal anomalies (from Sentinel-2, See middle pannel). Finally, we measure uplift starting in the beginning of 2020, following the major reservoir drainage in 2018. The middle panel shows Sentinel-2 RGB composite images using Band 12 (red), Band 11 (green), and Band 4 (blue). The white arrows indicate hot spots detected by Sentinel-2, with the arrow thickness corresponding to the (approximate) relative brightness of the hot spot.

Finally, in the year leading up to the 2018 eruption, lava lake activity increased substantially. According to field reports from [Volcano Discovery \[2018\]](#), lava lake activity in Niri-Mbwelesu resumed in January 2018, consistent with Sentinel-2 imagery (See [Figure 5-23](#)). During a visit in October 2018, a second vent in Niri crater was incandescent. Between August and September 2018, the lava lake level in Benbow lowered 20 m [[Volcano Discovery, 2018](#)]. Local guides, however, remarked that the intensity of the convection was the strongest they had witnessed in more than 10 years [[Volcano Discovery, 2018](#)]. In the weeks prior to the eruption, the lava lake level in Marum crater increased noticeably [[Moussallam et al., 2020](#)].

During the increase in lava lake activity, the Sentinel-1 time series does not detect displacement above the noise level (> 5 cm) (See [Figure 5-5](#)). Further analysis of the time series will include atmospheric corrections to verify whether pre-eruptive uplift occurred. It may be possible that uplift occurs only when the system is closed (i.e., no lava lakes), as has been observed at other open-system volcanoes [[Chaussard et al., 2013](#), [Newhall, 2015](#)]. During periods of lava lake persistence, no significant pressurization occurs within the system because gas can freely escape and magmatic equilibrium is maintained within the system by fluctuations of lava lake level. Counterintuitively, perhaps, the same open system that prohibits uplift can subside as mass is lost from the system through persistent degassing. It is also possible that increased radiated thermal power may not be due to lava lake level rise, but due to more a vigorous convection when volatile-rich magma is injected at depth.

The first period of replenishment may have spanned November 2008 to December 2018, ultimately leading to the 2018 rift zone intrusion and caldera subsidence episode. A second period of repressurization began a little over a year after the rift zone intrusion, beginning in early 2020. This may be caused by magma replenishment, but could also be due to the collapse of the summit vents, preventing gas from escaping the system. During the possible replenishment episode from 2008 to 2018, a combination of physical mechanisms contributed to pressure changes within Ambrym's magma lenses (See [Figure 5-24](#)). The summary and interpretations presented in this section and [Figure 5-24](#) are preliminary and require more detailed analysis of correlations between ground displacements, radiated thermal power and SO_2 mass flux. The number of deformation sources imaged at Ambrym over the past two decades reflects the complexities of caldera magmatic plumbing systems. In open systems, a pressure balance between replenishment and degassing may make it challenging to anticipate large eruptions by analysing only ground displacements.

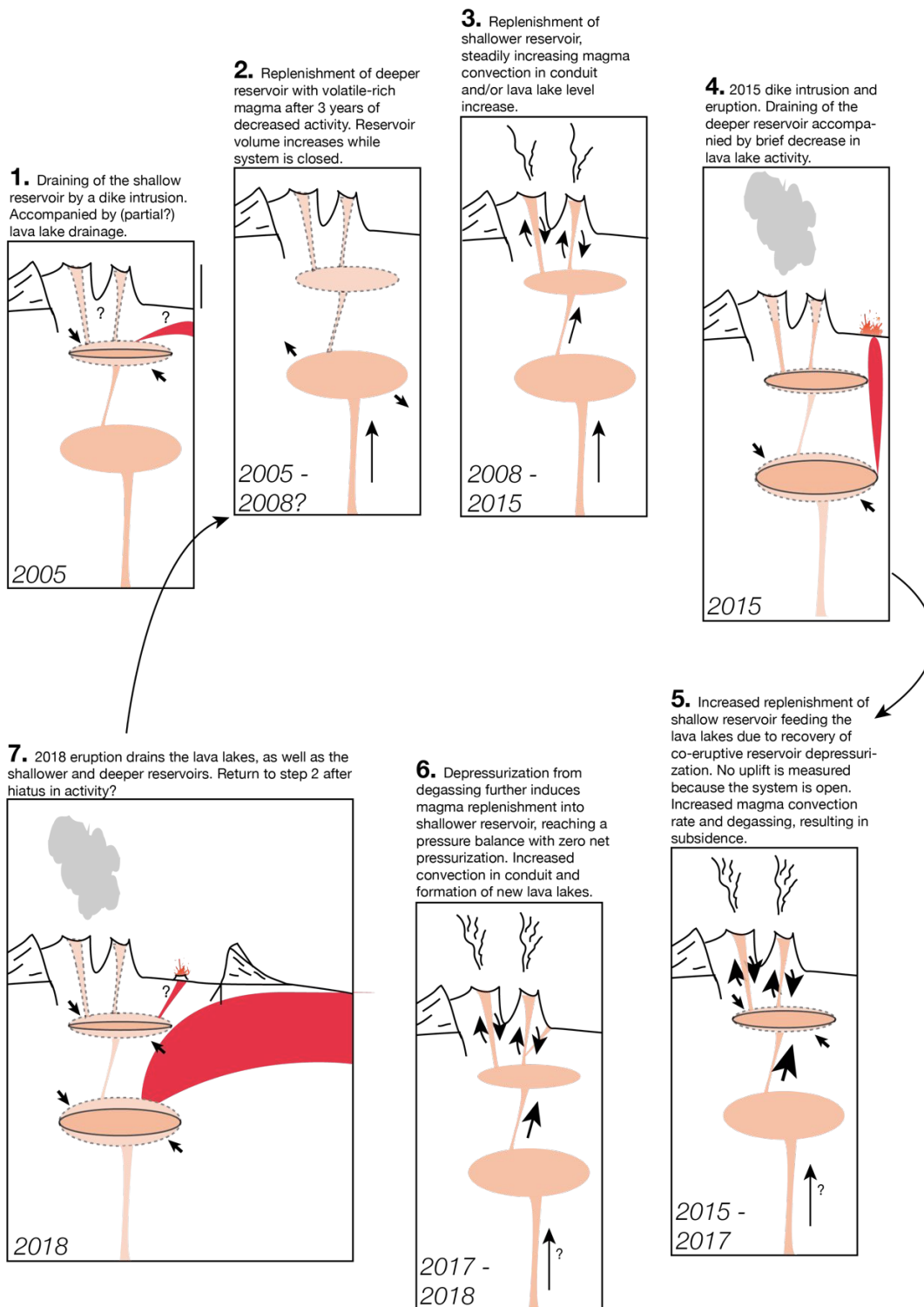


Figure 5-24: **15 years of magmatic activity at Ambrym.** The cycle of magma replenishment, lava lake activity, eruption, and inter-eruptive subsidence at Ambrym over the past 15 years. Results are synthesized from geodetic modelling, thermal anomalies, and SO_2 gas emissions. Not to scale. The shallower magma lens resides at a depth < 3 km and the deeper magma lens resides at a depth of $3 - 5$ km. Magma lenses are indicated by light pink colors, while dike intrusions are indicated by red colors.

Chapter 6

Conclusion and perspectives

This dissertation has summarized Ambrym volcano’s unrest over the past two decades using satellite geodesy, complemented by other remote sensing and in-situ geophysical techniques, when available. By jointly interpreting these results, we provide a conceptual model of magma storage at Ambrym, insights on magma migration within this system, and the effects of magma outgassing on system depressurization. In this final chapter, we will revisit the focus questions presented in Section 1.4, and address these questions using the results presented in the previous chapters. While investigating these questions, new ideas emerged which could not be fully addressed within the scope of this PhD project. We briefly discuss remaining open questions that can be the subject of future research, as well as ongoing collaborations developed over the course of this PhD. We finish with final thoughts on the direction of multidisciplinary remote sensing in the field of volcanology.

6.1 Focus questions

6.1.1 Question 1: Ambrym’s vertically and laterally extensive magma plumbing system

The first focus question— *How is Ambrym’s magmatic plumbing system organized?*— was addressed by combining the results of geodetic modelling of deformation episodes from 2004 – 2020 (Chapters 3, 4, and 5.1.1). We imaged at least two magma lenses beneath Ambrym’s caldera. The shallower lens (< 3 km depth), located beneath Marum and Benbow craters, most likely feeds the lava lakes, whose level lowered during the 2015 eruption, and completely drained during the 2018 event. The deeper source (< 5 km depth) may be tapped during rift zone intrusions, as well as intra-caldera eruptions. However, we posit that rift-zone intrusions have the potential to withdraw a substantially larger volume from the magma lenses than intra-caldera dike intrusions.

Petrological studies undertaken by collaborators concluded that there is an additional magma reservoir located in the eastern portion of Ambrym’s caldera [Moussallam et al., 2020], consistent with seismological studies [Legrand et al., 2005]. This reservoir is physically isolated from other magma lenses in the system. As a result, lava erupted from this reservoir has a more evolved, trachy-andesite to trachy-dacite composition. This evolved magma may

erupt out of vents in the eastern portion of the caldera, as observed in 1986. This magma may also interact with dikes that intersect this reservoir before migrating into the rift zone, as recorded in 2018.

These findings draw us to the conclusion that the plumbing system located beneath Ambrym's caldera is both vertically and laterally extensive. We hypothesize that this system can be depressurized by magma withdrawal from the magma lenses, and/or during long-term passive degassing. Gas emissions at Ambrym are anomalously high, and Ambrym's degassing therefore deserves special attention for its possible influence on surface deformation during inter-eruptive periods. Magmatic recharge may also result in refilling of the deeper magma lens, causing uplift when the system is closed (i.e., no lava lakes at the surface). When lava lakes are present, connecting the magmatic plumbing system to the surface, magmatic injection may not necessarily result in uplift. This emphasizes the importance of incorporating complementary observations to identify periods of magma replenishment preceding eruptions.

6.1.2 Question 2: Episodic caldera subsidence and ring-fault re-activation at Ambrym

To answer the second focus question—*How did Ambrym's caldera form and develop?*—we draw on the observations of caldera ring-faulting during both the 2015 and 2018 events. In 2018, we observe widespread caldera ring-faulting along the northern caldera rim caused by magma withdrawal from the central magma lenses. Three years earlier, we also observed more modest caldera ring-faulting subsidence along the western ring-fault. These observations led us to conclude that the ring-faults can be reactivated during both moderate and large dike intrusions/eruptions, resulting in episodic, meter-scale deepening of the caldera. The majority of this deepening occurs during lateral rift zone intrusions, which are capable of extracting large volumes from the magma lenses without necessarily producing subaerial eruptions. However, we must continue to monitor the ongoing uplift episode at Ambrym to conclude whether co-eruptive and/or co-intrusive subsidence is compensated by uplift due to post-eruptive magmatic recharge when the lava lakes are inactive. This mechanism of caldera development may be present at other caldera-rift systems with low roof aspect ratios (i.e., broad and shallow magmatic systems).

6.1.3 Question 3: Decadal fluctuations in Ambrym's volcanic activity

What are the dynamics of Ambrym's magmatic system? is the third and final focus question. Changes to Ambrym's magmatic system over time were investigated using a qualitative joint analysis of ground deformation, gas emissions, and thermal anomalies. This analysis led us to a conceptual understanding of the dynamics of Ambrym's magmatic system over the past two decades. We conclude that Ambrym's shallow magma lens was drained following a dike intrusion in 2005, causing a drastic decrease in both gas emissions and thermal anomaly detections associated with the lava lakes. After this event, we infer that replenishment continued at depth until \sim 2008, when the shallowest magma lens began to refill, resulting in

renewed activity of the lava lakes. This replenishment eventually led to a moderate-sized dike intrusion in 2015, followed by renewed magma replenishment in the shallow magma lens. Replenishment of volatile-rich magma may have triggered vigorous convection of the lava lakes and continued degassing. Counterintuitively, increased convection and degassing removed mass from the system, and the shallow magma lens may have depressurized, producing ground subsidence. Eventually the depressurization may have been cancelled by pressurization due to further magma replenishment, leading to no net ground displacement. Fifteen years after the previous lava lake drainage, a rift zone intrusion and submarine eruption in 2018 drained the central magma lenses and caused the disappearance of the lava lakes once again. While dike intrusions at Ambrym were recorded and studied in detail throughout this dissertation, the magmatic activity during inter-eruptive periods requires a more thorough investigation. Nonetheless, the possibility of magma replenishment without measurable uplift means that other observations that may precede eruptive activity (e.g., increased gas emissions, thermal anomalies, or seismicity) should be closely monitored at Ambrym.

6.2 Open questions

In order to improve forecasting of unrest episodes, and to better assess the associated hazards, at Ambrym, and other caldera-rift systems, four main questions should be addressed:

1. What signs precede the onset of lateral dike propagation and rift zone intrusions?
2. What is the recurrence time of rift zone intrusions?
3. How far will magma travel laterally from the volcanic center?
4. How much lava will erupt at the surface?

The results of this dissertation provide the following insights into these questions:

1. Precursors of lateral dike propagation include surface manifestations of replenishment at depth. If the magmatic system is open, replenishment may not necessarily manifest itself as uplift, but instead as an increase in either the lava lake convection (and hence increased degassing), the number of lava lakes, or the lava lake level. The timing of onset of lateral dike propagation, however, needs to be investigated further.
2. The recurrence time of rift zone intrusions at Ambrym may be higher than originally thought, especially in light of the possible 2005 dike intrusion and lava lake drainage. Although the geodetic inversion estimates a modest amount of magma migrating towards the rift zone, we have no further constraints on the distance this dike travelled away from the main craters. It is also possible that a rift zone intrusion occurred co-eval with the 1988 intra-caldera eruption, due to evidence of magma mixing with a deeply-source magma component, as cited by [Firth et al. \[2016\]](#). Therefore, it is possible that rift zone intrusions occur every ~ 20 years. This points to the possibility of caldera ring-fault activation on similar timescales, and continued deepening of the caldera by subsidence along these faults.

3. The distance magma will travel laterally from the central reservoir depends on the dike's driving stress. A strong horizontal gradient in driving stress allows dikes to travel long distances and erupt offshore at Ambrym. Further studies should try to quantify the influence of the regional tectonic stress, as well as magma availability, on the driving pressure, and hence distance travelled, by rift zone intrusions.
4. The volume of lava that erupts at the surface depends on the magmatic overpressure and the tectonic stress. Dikes tend to erupt more frequently when their overpressure is higher (See Chapter 3). Continued monitoring of the current uplift episodes at Ambrym will be necessary to understand magma lens overpressurization while Ambrym's system is closed (i.e., no lava lake activity).

Nonetheless, these questions remain to be fully answered, and consequently may direct future research projects at Ambrym and other caldera-rift systems.

6.3 Next steps

The original research contributed in this dissertation includes the analysis and modelling of geodetic data. However, interpretations of Ambrym's magmatic activity could not have been possible without insights from collaborators whose expertise include atmospheric sciences, active tectonics, petrology, and seismology, among others. These multidisciplinary collaborations have inspired the following projects:

- A more thorough study of Ambrym's 2015 – 2017 subsidence episode, which we hypothesize may be due to magma lens depressurization due to passive degassing. This study will include a more careful analysis of the uncertainties mentioned in Section 5.1.2.7, will take into consideration the effect of magma replenishment, and attempt to extend the theoretical model of [Girona et al. \[2014\]](#) so that changes to the lava lake level can be calculated from depressurization rates.
- Further studies jointly interpreting ground deformation, gas emissions, and thermal anomalies. This will include a more detailed study of the theorized dike intrusion and lava lake drainage event at Ambrym in 2005. In addition, another study may focus on the short-term coupling of passive degassing and ground deformation (Collaboration with R. Grandin, IPGP and M. Boichu, Université de Lille).
- A comparison of geodetic models to the petrological study of magma ascent and migration during the Ambrym 2018 eruption led by Y. Moussallam, Columbia University, and collaborators [[Moussallam et al., 2020](#)].
- Coupling of geodetic and thermodynamic models to infer pre-eruptive magma reservoir conditions at Ambae volcano, located 100 km to the north of Ambrym. These models will follow the framework of [Kilbride et al. \[2016\]](#). They will attempt to exploit ground deformation and gas emissions to estimate the exsolved gas content in the reservoir before episodes of volcanic unrest at Ambae in 2017 – 2018. This event culminated in a paroxysmal Plinian eruption in July 2018 (Project will be undertaken at Carnegie Institution for Science, under the supervision of H. Le Mével).

- A geodetic study estimating magma compressibility during the 2018 eruption at Sierra Negra, Galápagos, which included both co- and post-eruptive ring-fault subsidence (Collaboration with F. Delgado, Universidad de Chile).

6.4 Take home message

SAR data is more available and abundant than ever before. In addition to unprecedented availability of these datasets, processors such as LIC SAR have been developed to automatically generate interferograms in volcanically active areas [Lazecký et al., 2020]. To address the need to analyse large datasets, convolutional neural networks have been developed to automatically detect both rapid and slow volcanic deformation [Anantrasirichai et al., 2019a,b]. Such initiatives will allow the volcano geodesy community to identify candidate volcanoes which, like Ambrym, are actively deforming (but whose deformation has been overlooked).

Although a powerful tool, volcano geodesy by no means tells the whole story of a volcano's unrest. Volcanology is an inherently multidisciplinary field, given the complex nature of volcanic systems. A prime example of multidisciplinary volcano monitoring occurs at volcano observatories around the globe, where joint interpretations of seismicity, ground deformation, and gas emissions are often the basis for alert systems [e.g., Beauducel et al., 2020]. However, not every active volcano has a dedicated observatory [Sparks et al., 2012]. Remote sensing can, at least partially, fill the observational gap. Analysis of remote sensing data— whether detecting ground deformation, gas emissions, or thermal anomalies— is routine in the field of volcanology. Nonetheless, the field has yet to fully realize the potential of systematically combining these complementary datasets [Poland et al., 2020]. There is room to improve monitoring, modelling, and forecasting of volcanic systems by fully integrating satellite data from multiple disciplines.

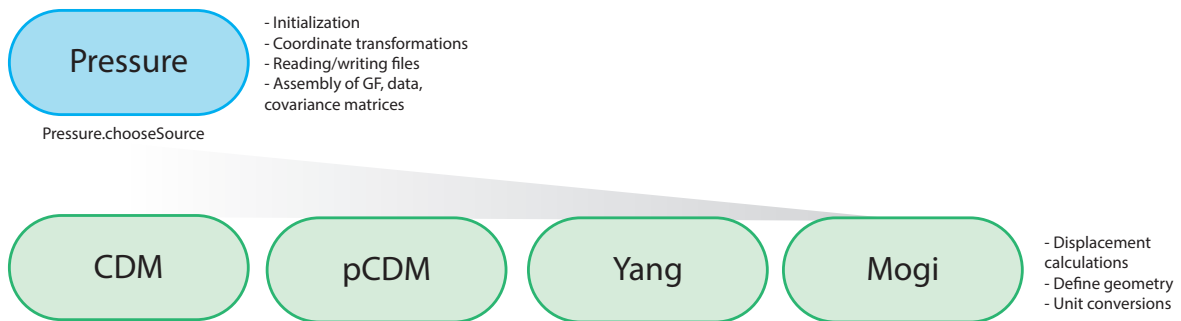
Appendix A

Classic Slip Inversion software: Analytical volcano source models

The Classic Slip Inversion (CSI) software is written in Python, and a description can be found at <http://www.geologie.ens.fr/~jolivet/csi/> [Jolivet et al., 2015]. The software was originally designed for distributed modelling of fault slip (See Section 2.2.2.5.1). During my PhD, I implemented the analytical solutions for the point compound dislocation model (pCDM), compound dislocation model (CDM), Mogi and Yang in CSI. The implementation was motivated by the 2018 Ambrym unrest episode, which necessitated an inversion of both distributed opening along a dike, as well as a cavity volume change. This appendix includes a manual of the updated CSI software, which describes the new Python classes for volcanic sources, the workflow, and the benchmarking of the models against the DMODELS software package of Battaglia et al. [2013] and the CDM models of Nikkhoo et al. [2017].

CSI Pressure Sources - User Guide

1 Class hierarchy



2 Workflow

1. Set source location and geometrical shape.

- (a) Run `Pressure.chooseSource` to choose the appropriate pressure source (CDM, Mogi, or Yang) based on the input parameters. Either a CDM, Mogi, or Yang object will be created.

```
pressure = Pressure.chooseSource('Name', xc, yc, -z0, ax, ay, az, θ, φ, β, utmzone=utm,
                                lon0=lon, lat0=lat)
```

where

x_c, y_c : source center (lat/lon or UTM)

$-z_0$: depth in m

a_x, a_y, a_z : length of principle semi-axes in m along x-, y- and z- axes (respectively E-W, N-S, and up-down) before rotations are applied

θ, ϕ, β : dip, strike and plunge (respectively $90^\circ - \omega_Y, \omega_Z$, and ω_X from Nikkhoo et al. (2017) (Fig. 1))

- i. Attributes include: `pressure.source` (pressure source category), `pressure.ellipshape` (source geometrical shape), and `pressure.type` ("Pressure" as opposed to "Fault").
- ii. When appropriate, a simpler, degenerate case will be assigned, as shown below:

Mogi if $a_x = a_y = a_z$ (Mogi, 1958),

Yang if the shortest axes are equal, i.e. $a_x = a_y < a_z$ (Battaglia et al., 2013). Semi-major axis set to a_z so that source oriented vertically when $\theta = 90$.

CDM will be used if the above conditions are not met (Nikkhoo et al., 2017).

- (b) If you would like to use pCDM, set $a_x, a_y,$ and a_z to **None**. The linear inversion will solve for the change in potency (same dimensions as volume, m^3 (Nikkhoo et al., 2017)) along each of the orthogonal semi-axes directions (DV_x, DV_y, DV_z):

```
pressure = Pressure.chooseSource('Name', x_c, y_c, -z_0, None, None, None,  $\theta, \phi, \beta,$ 
                                utmzone=utm, lon0=lon, lat0=lat)
```

- (c) Alternatively, create either a Mogi, Yang, pCDM, or CDM source directly.

```
pressureMogi = Mogi('Name', x_c, y_c, -z_0, a_x, utmzone=utm, lon0=lon, lat0=lat)
pressureYang = Yang('Name', x_c, y_c, -z_0, a_x, a_y, a_z,  $\theta, \phi,$  utmzone=utm, lon0=lon, lat0=lat)
pressurepCDM = pCDM('Name', x_c, y_c, -z_0, None, None, None,  $\theta, \phi, \beta,$  utmzone=utm,
                    lon0=lon, lat0=lat)
pressureCDM = CDM('Name', x_c, y_c, -z_0, a_x, a_y, a_z,  $\theta, \phi, \beta,$  utmzone=utm, lon0=lon, lat0=lat)
```

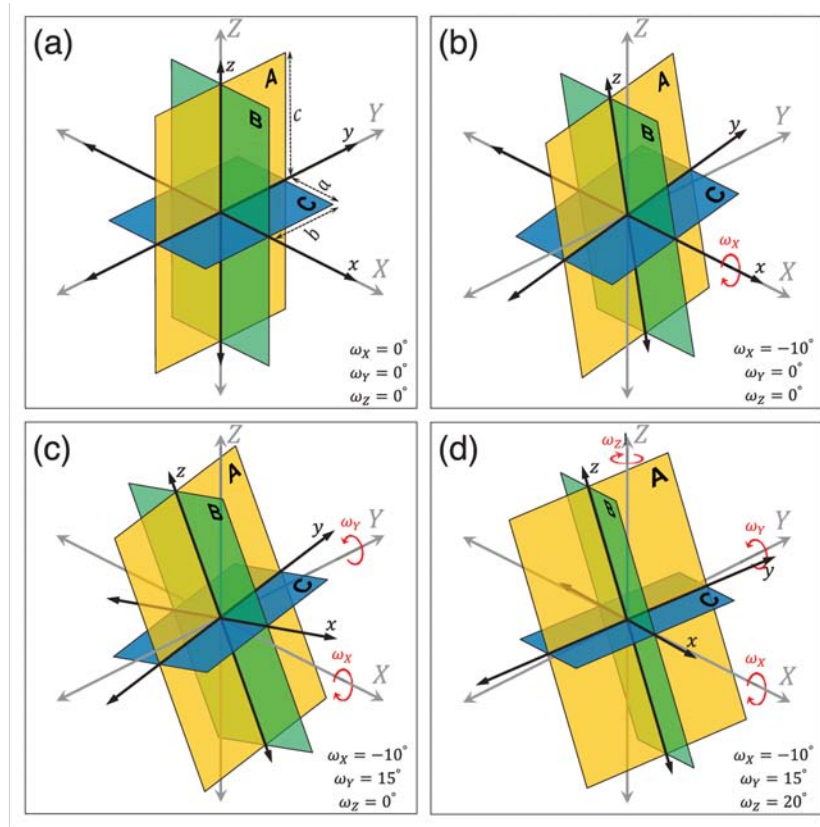


Figure 1: **From Nikkhoo et al. (2017)**. The geometrical structure and rotation angles of a compound dislocation model (CDM) composed of three rectangular dislocations (RDs), labelled as ‘A’, ‘B’ and ‘C’ (the yellow, green and blue planes). The origin of the XYZ coordinate system is at the Earth’s surface and the positive X, Y and Z axes point to the east, north and up, respectively. The origin of the xyz coordinate system is located on the CDM centroid and the x, y and z axes are normal to ‘A’, ‘B’ and ‘C’, respectively. The xyz coordinate system is fixed to the CDM. The a, b and c are the semi-axes of the CDM along the x, y and z axes, respectively. The ω_X, ω_Y and ω_Z are angles of rotation about the X, Y and Z axes, respectively. Positive values of these angles correspond to clockwise rotations. (a) The initial orientation of the CDM. (b) The orientation of the CDM after applying ω_X . (c) The orientation of the CDM after applying ω_X and ω_Y . (d) The final orientation of the CDM. The numerical values of the rotation angles for this given example are denoted on the bottom right of each panel.

2. Save source parameters to text file.

```
pressure.writePressure2File('fileName', add_volume='volume')
```

(a) Text file has the following format:

```
> -Z0.0 # pressure.deltavolume or pressure.deltapressure
Source of type pressure.source [ $\Delta$ pressure or  $\Delta$ volume]
# x0 y0 -z0
pressure.lon pressure.lat pressure.depth
# ax ay az (if pCDM, then DVx, DVy, DVz)
pressure.ellipshape['ax'] pressure.ellipshape['ay'] pressure.ellipshape['az']
# strike dip plunge
pressure.ellipshape['strike'] pressure.ellipshape['dip'] pressure.ellipshape['plunge']
```

(ex. `pressure.createShape(168.099913, -16.386700, 3000, 2000, 400, 500, 40, 30, 20)`):

```
> -Z0.0 # 0.0
Source of type CDM
# x0 y0 -z0
168.099913 -16.3867 3000.0
# ax ay az (if pCDM, then DVx, DVy, DVz)
2000.0 400.0 500.0
# strike dip plunge
30.0 40.0 20.0
```

3. Once you have a parameter file saved, you can reread it at any point to define an object's location and geometrical shape. First define a geometry-less pressure object of the appropriate type. i.e., a Mogi:

```
pressureMogi = Mogi('Name', utmzone=utm, lon0=lon, lat0=lat)
```

Then read the location and geometrical shape from a given file.

```
pressureMogi.readPressureFromFile('fileName', donotreadvolume=True)
```

A `ValueError` will be thrown if the pressure object you defined is inconsistent with the pressure source type in the file.

4. Define data. The example below will use one dataset, but we can define as many as we wish and append them to a list.

```
sar = insar('dataName')
sar.read_from_varres('dataFileName', factor=1.0, step=0.0, header=2, cov=True)
```

5. For every data point, calculate the displacement (Green's functions) for unit opening (CDM), dimensionless unit pressure (Mogi or Yang), or potency change of 1000000 m^3 along each axis (pCDM). The latter value is arbitrarily chosen and defined in the `_init_` of `pCDM.py`.

```
pressure.buildGFs(sar, vertical=True, verbose=True)
```

6. Save these Green's functions.

```
pressure.saveGFs('GFDirectory')
```

7. Set GF's in the pressure object, as follows for CDM, Mogi, and Yang:

```
pressure.setGFsFromFile(sar, pressure='GFFilename', vertical=True))
```

and as follows for pCDM:

```
pressure.setGFsFromFile(sar,
DVx='GFFilenameDVx', DVy='GFFilenameDVy', DVz='GFFilenameDVz', vertical=True))
```

8. Assemble GF's, data vector, and data covariance matrix.

```
pressure.assembleGFs(sar, polys=[3])
pressure.assembled(sar)
pressure.assembleCd(sar)
```

9. Define model covariance matrix. User can choose the weight for both the pressure source and the polynomial estimator.

```
pressure.builddummyCm(user.Cm=500., extra_params=
np.ones((pressure.TransformationParameters,))*1000.)
```

10. Create the solver object and assemble the GF and model covariance matrices. Can include as many sources as you want.

```
slv = multifaultsolve('Solver Name', pressure)
slv.assembleGFs()
slv.assembleCm()
```

11. Solve using the Generalized Least Square's Method (Tarantola and Valette, 1982).

```
slv.GeneralizedLeastSquareSoln()
slv.writeMpostBinaryFile('name.GLSmodel', dtype='f')
slv.distributem(verbose=True)
```

12. Save solution to file. Set `add_pressure` as either `'volume'` (CDM, pCDM, Mogi, or Yang) or `'pressure'` (Mogi or Yang). This will determine whether `pressure.deltavolume` or `pressure.deltapressure` is written to the output file.

```
pressure.writePressure2File('outputFileName', add_pressure='volume', scale=1.0)
```

13. Remove ramps and estimate model fit to data.

```
sar.buildsynth(pressure, direction=None)
initVar, reducVar = sar.getVariance()
print('Data set {} to type {}:' .format(data.name, data.dtype))
print('Variance: From {} to {} ({}%)' .format(initVar, reducVar,
100.*(1-reducVar/initVar)))
```

3 Benchmarking source code

1. Corrected Yang (prolate spheroid) analytical equations were taken from the Matlab software DMODEL-ELS of Battaglia et al. (2013). To ensure consistency between the displacements produced by the Python and Matlab scripts, the following tests have been run.

- (a) Parameters:

Parameters	Yang
$-z_0$	2000 m
a_x, a_y, a_z	300 m, 300 m, 600 m
θ, ϕ, β	40°, 70°, 0°
ΔP	0.5 GPa
Poisson's ratio	0.25
Shear modulus	30 GPa

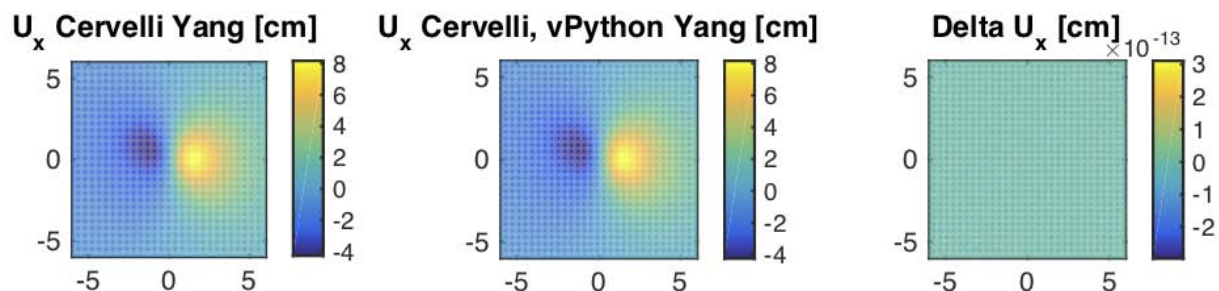


Figure 2: Map view comparison between E-W ground displacements from Matlab and Python.

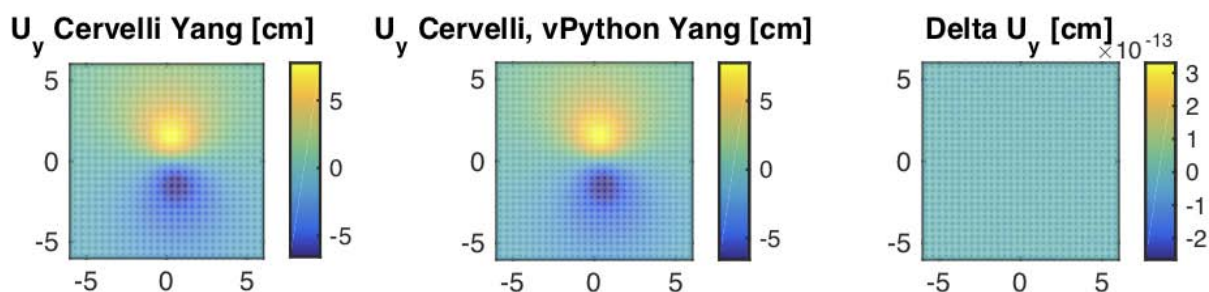


Figure 3: Map view comparison between N-S ground displacements.

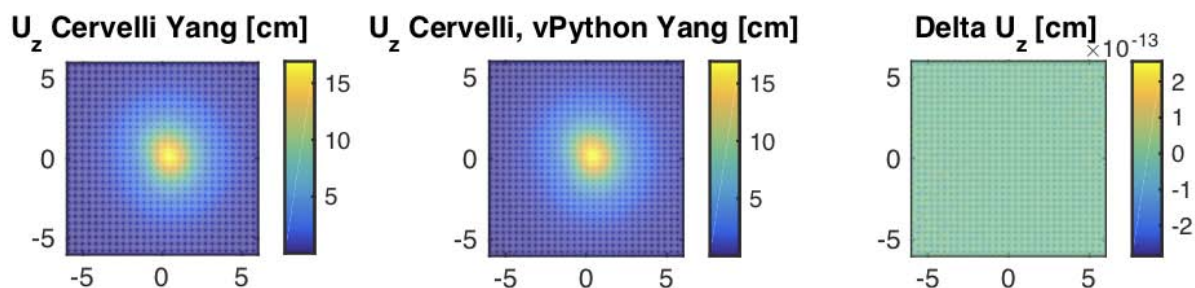


Figure 4: Map view comparison between vertical ground displacements.

(b) Run time is notably faster in Python: Matlab: 0.3698 seconds, Python: 0.06454 seconds.

2. The pCDM code (Nikkhoo et al., 2017) was vectorized by François Beauducel, and the vectorized version was translated into Python. Ground displacements are compared below.

(a) Parameters:

Parameters	CDM
$-z_0$	2000 m
θ, ϕ, β	$0^\circ, 15^\circ, 60^\circ$
DV_x	70000000 m ³
DV_y	30000000 m ³
DV_z	400000000 m ³
Poisson's ratio	0.25

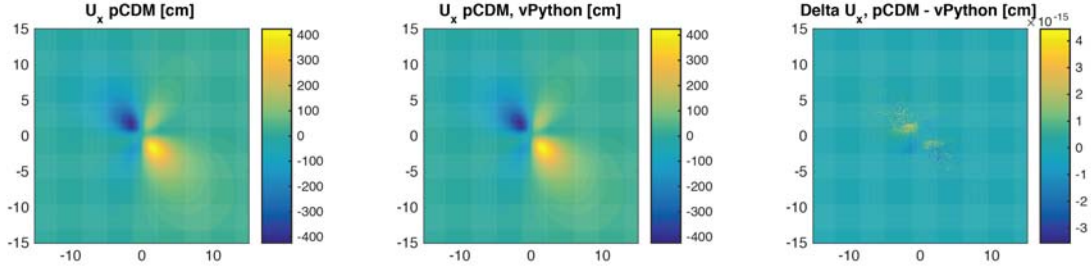


Figure 5: Map view comparison between E-W ground displacements from Matlab and Python.

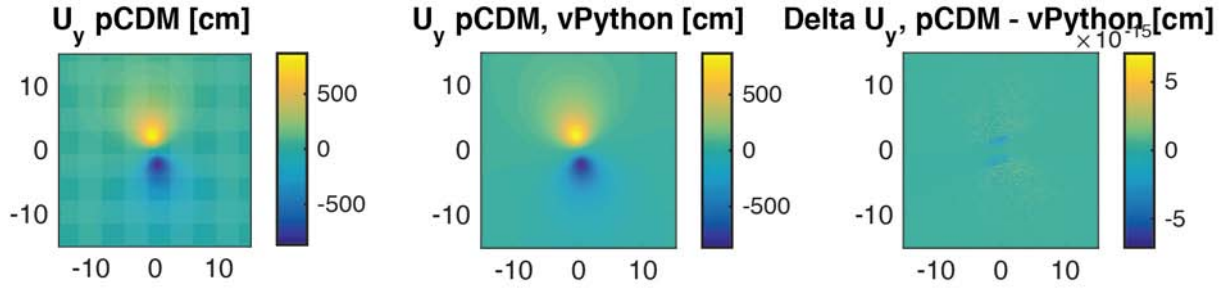


Figure 6: Map view comparison between N-S ground displacements.

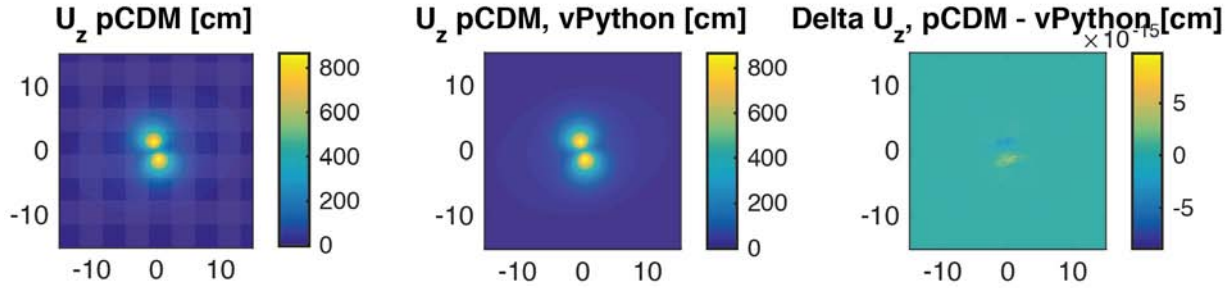


Figure 7: Map view comparison between vertical ground displacements.

(b) Run time is slightly faster in Matlab: Matlab: 0.0544 seconds, Python: 0.0731 seconds.

3. The CDM code (Nikkhoo et al., 2017) was also vectorized by François Beauducel, then translated into Python. Ground displacements are compared below.

(a) Parameters:

Parameters	CDM
$-z_0$	1000 m
a_x, a_y, a_z	1000 m, 600 m, 500 m
θ, ϕ, β	$105^\circ, 110^\circ, 40^\circ$
Opening	2 m
Poisson's ratio	0.25

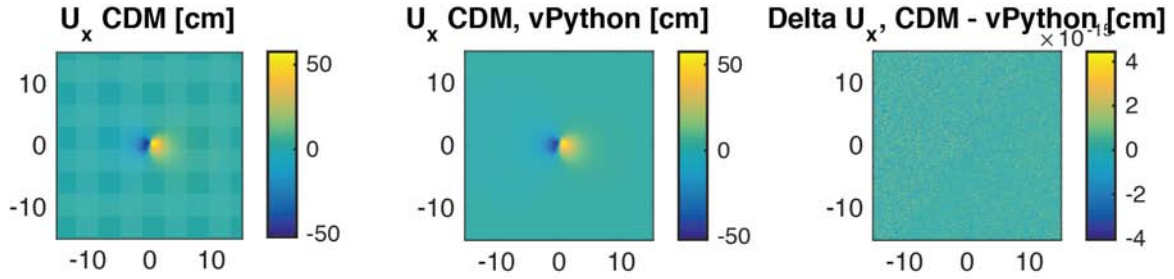


Figure 8: Map view comparison between E-W ground displacements from Matlab and Python.

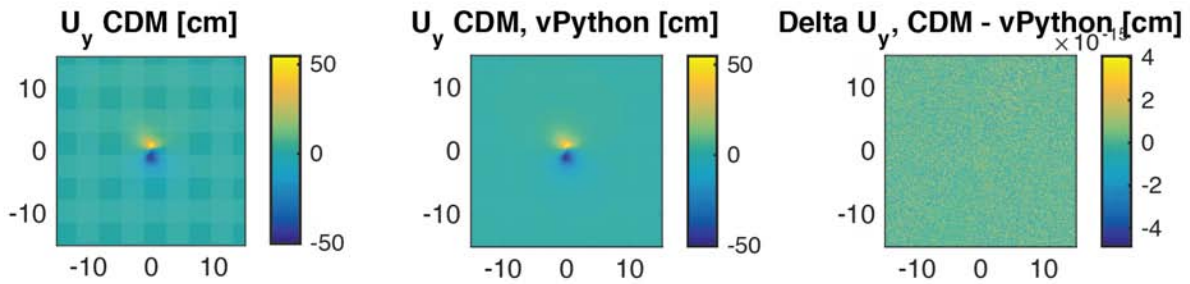


Figure 9: Map view comparison between N-S ground displacements.

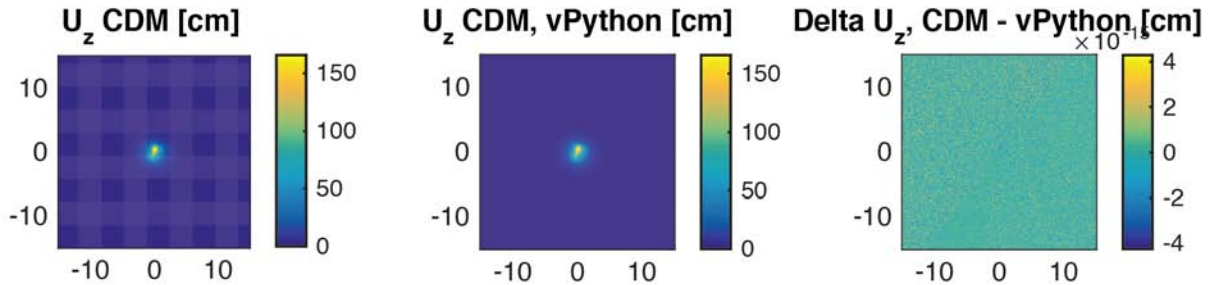


Figure 10: Map view comparison between vertical ground displacements.

(b) Run time is faster in Matlab by a factor of 2. Matlab: 0.7144 seconds, Python: 1.465 seconds.

4 Examples

1. Synthetic data: 3 pressure sources.

We use a Generalized Linear Squares Inversion to solve for volume change and opening for a synthetic dataset using Mogi, Yang, and CDM pressure sources. The dataset is projected into the line of sight (LOS vector: $-0.634, -0.146, 0.759$). A synthetic ramp was added, and the datasets were downsampled using a distance-based algorithm.

(a) Geometrical parameters:

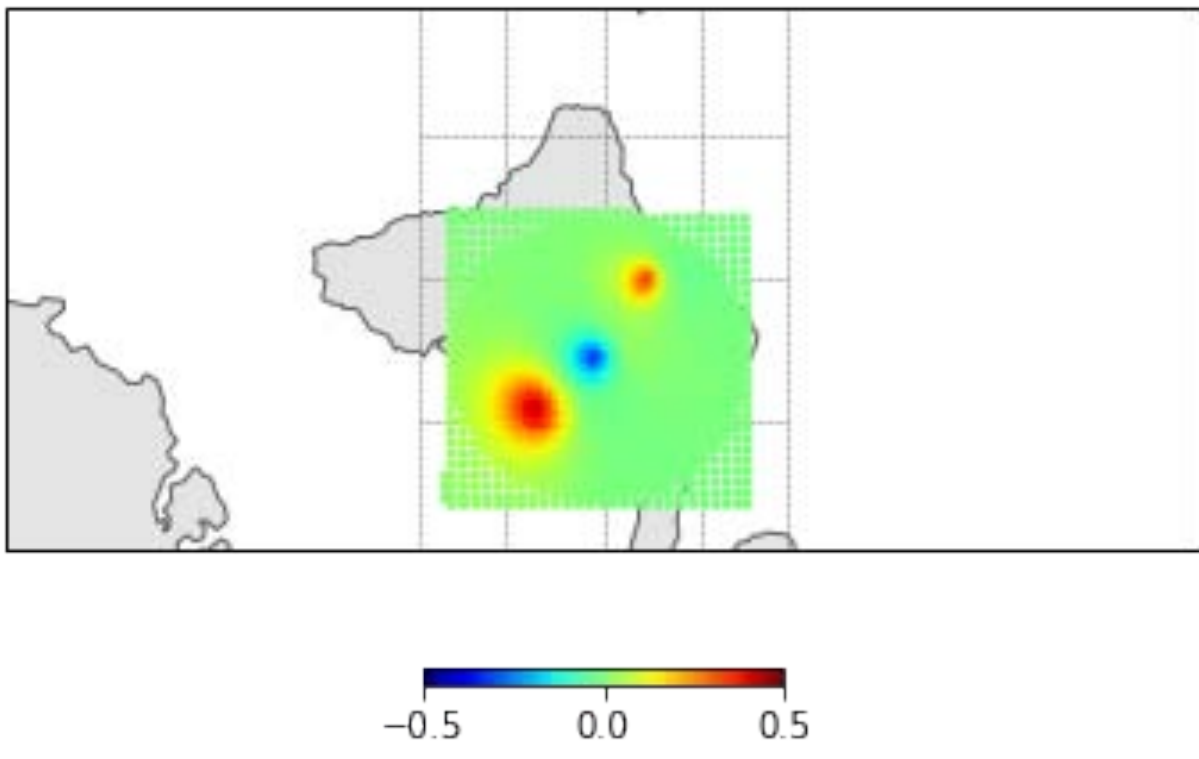
Parameters	Mogi	Yang	CDM
$x_0, y_0, -z_0$	168.167357, -16.32353, 2000 m	168.119, -16.3689, 4000 m	168.21418, -16.2528, 2000 m
a_x, a_y, a_z	500 m, 500 m, 500 m	900 m, 300 m, 300 m	1000 m, 600 m, 500 m
θ, ϕ, β	$0^\circ, 0^\circ, 0^\circ$	$-20^\circ, -20^\circ, 0^\circ$	$105^\circ, 110^\circ, 40^\circ$

(b) Ramp Parameters :

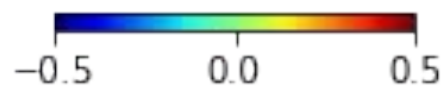
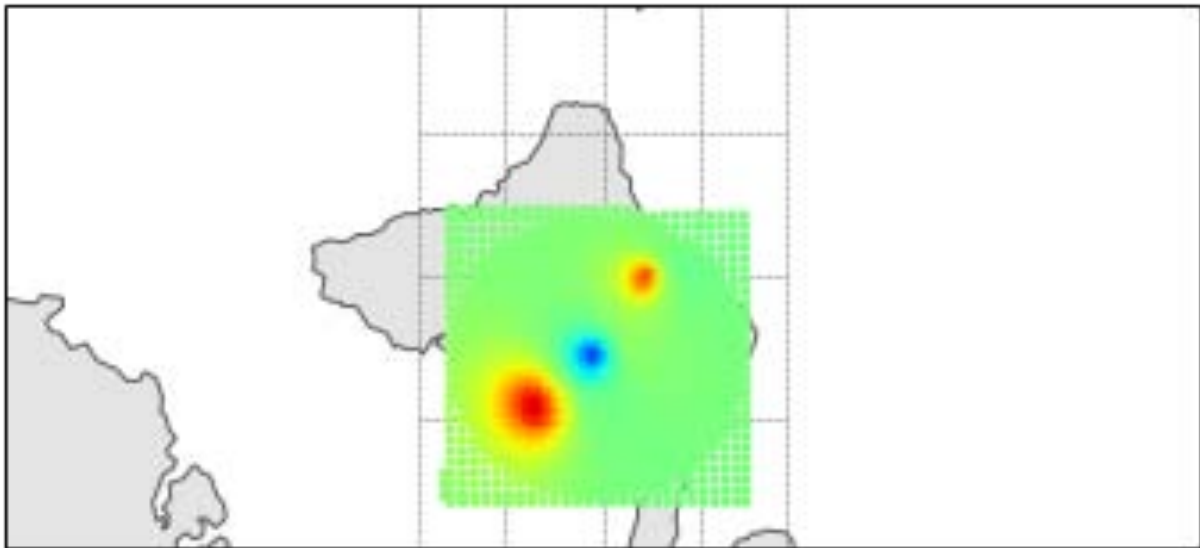
Parameters	Ramp ($z = a + bx + cy$)
a	0.3
b	0.03
c	0.02

(c) Results:

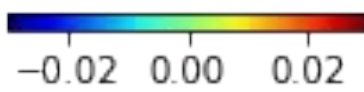
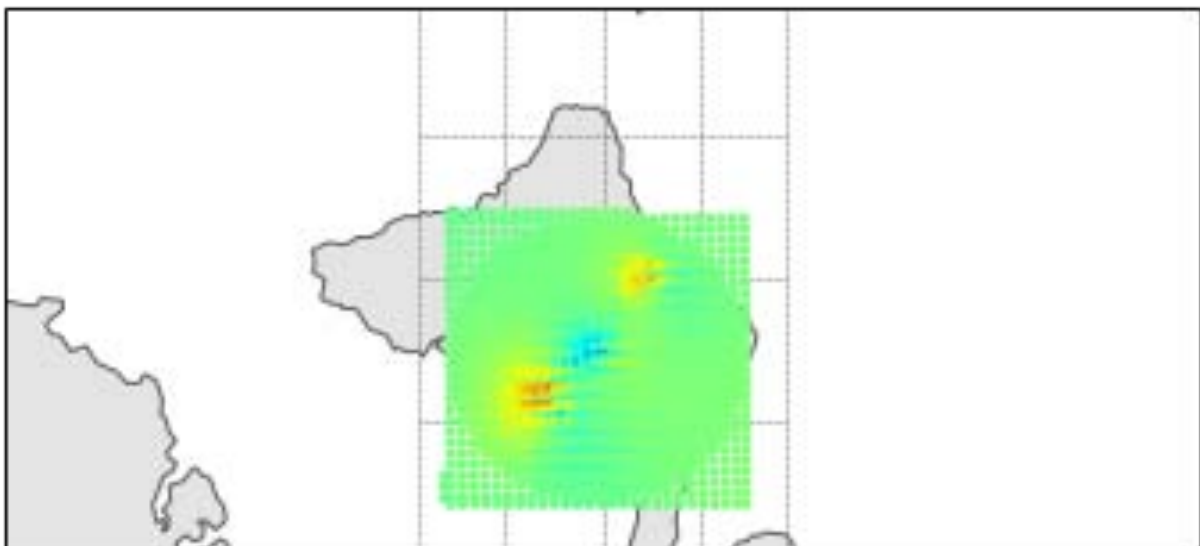
Pressure Test Data



Pressure Test Synth



Pressure Test Res



Source	Inverted parameter	Model-derived	Actual	Percent error
Mogi	Δ Volume	-6288149 m ³	-6544984 m ³	3.9%
Yang	Δ Volume	38599405 m ³	39822828 m ³	3.1%
CDM	Δ Opening	2 m	1.91 m	4.7%
Ramp	a, b, c	0.27, 0.014181, 0.01	0.3, 0.03, 0.02	10%, 52.73%, 50%

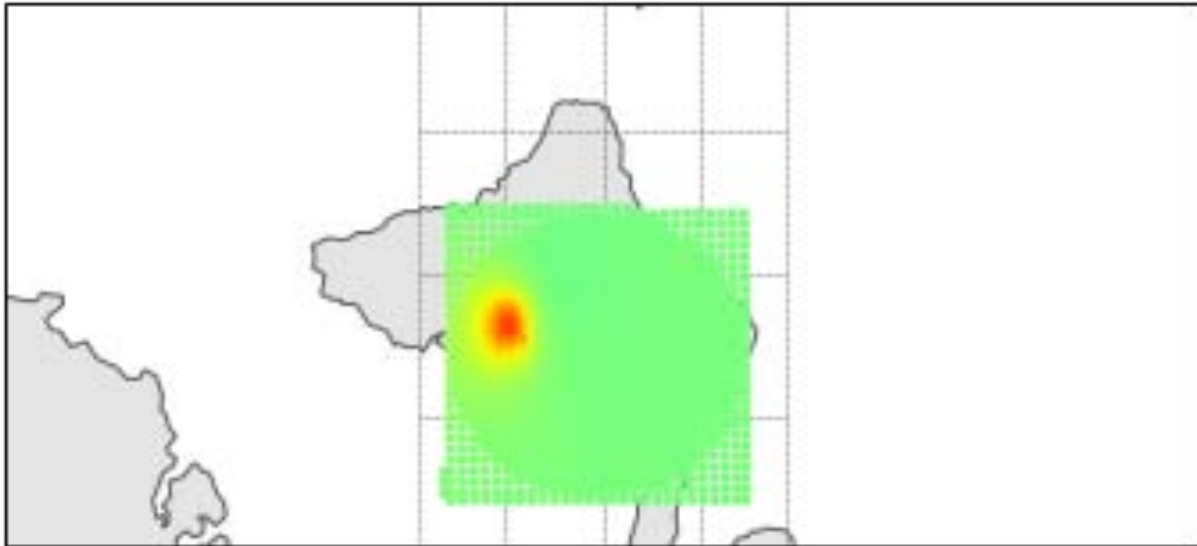
2. Synthetic data - pCDM

(a) Geometrical parameters

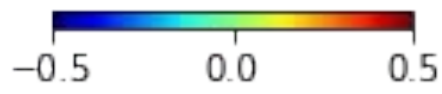
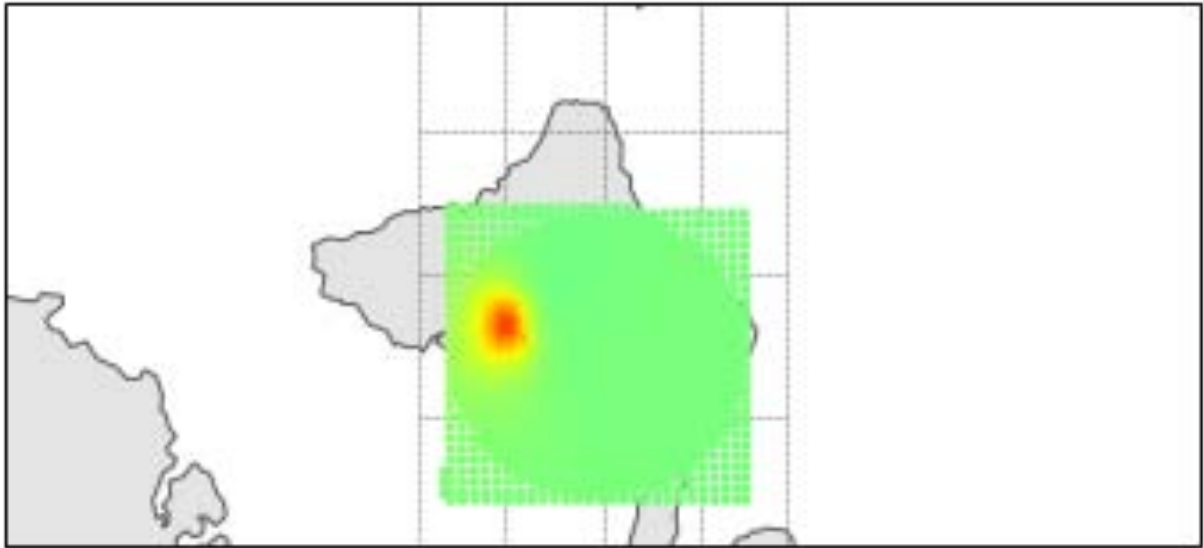
Parameters	pCDM
$x_0, y_0, -z_0$	168.09, -16.296, 3000 m
θ, ϕ, β	170°, 0°, 0°
DV_x, DV_y, DV_z	9600000 m ³ , 14400000 m ³ , 6000000 m ³

(b) Results

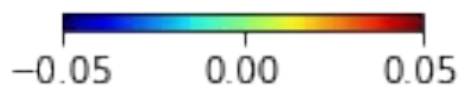
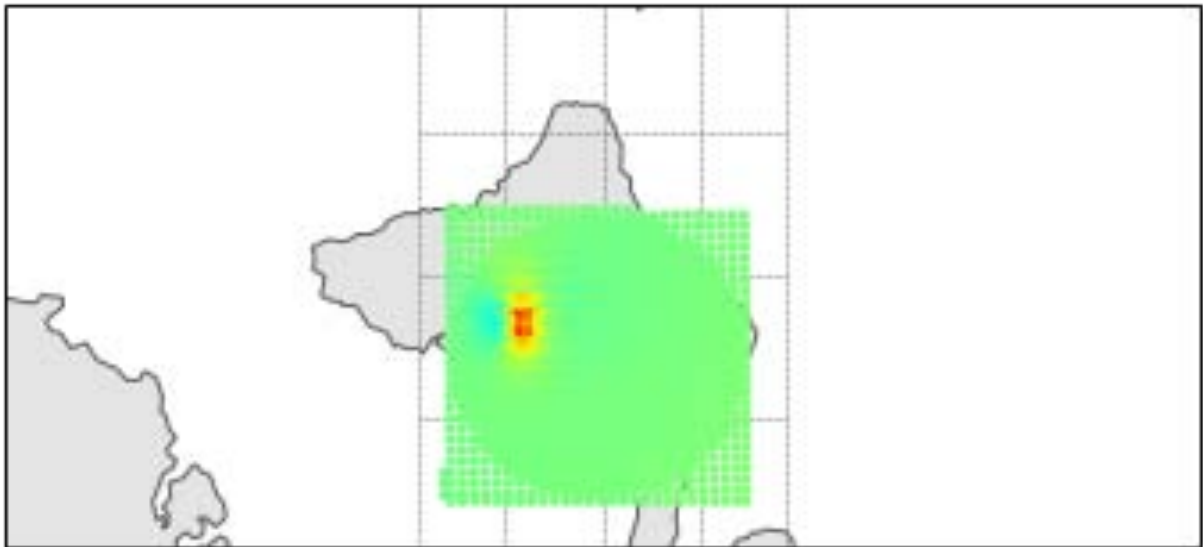
pCDM1 Data



pCDM1 Synth



pCDM1 Res



Source	Inverted parameter	Model-derived	Actual	Percent error
pCDM	DV_x	9296995 m ³	9600000 m ³	3.2%
pCDM	DV_y	14188095 m ³	14400000 m ³	1.47%
pCDM	DV_z	5548614 m ³	6000000 m ³	7.5%

3. Ambrym 2018 dike intrusion: Combining fault and pressure sources using a Constrained Least Squares Solution.

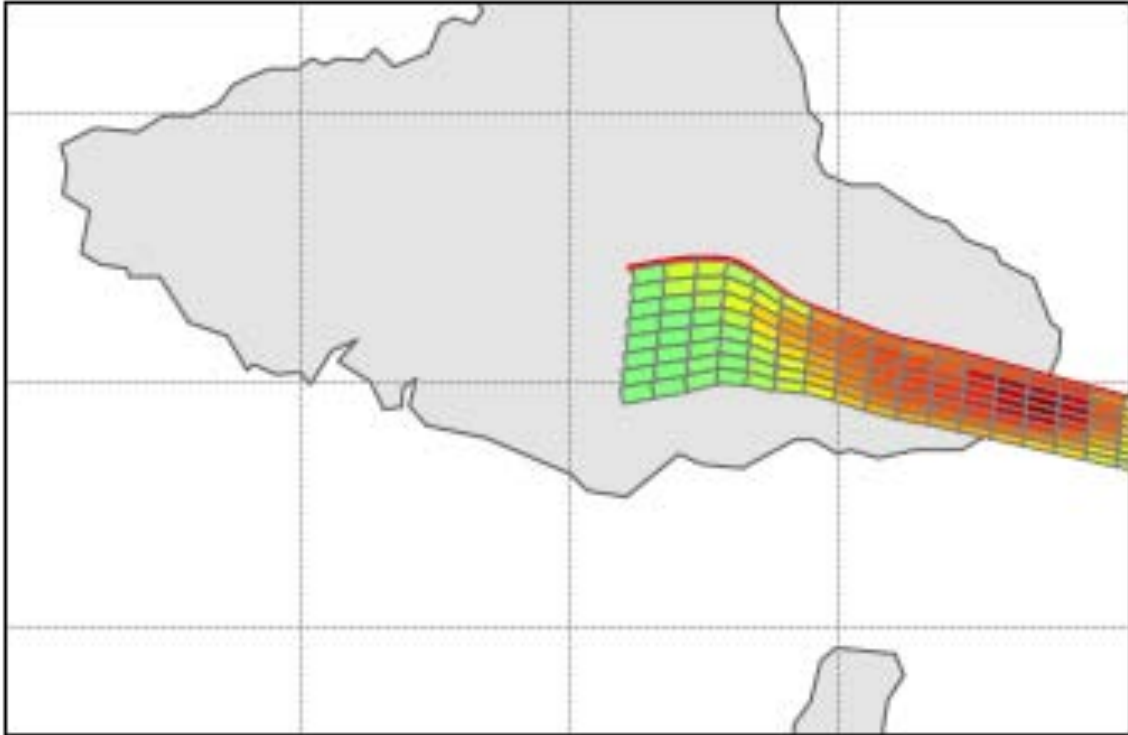
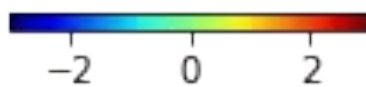
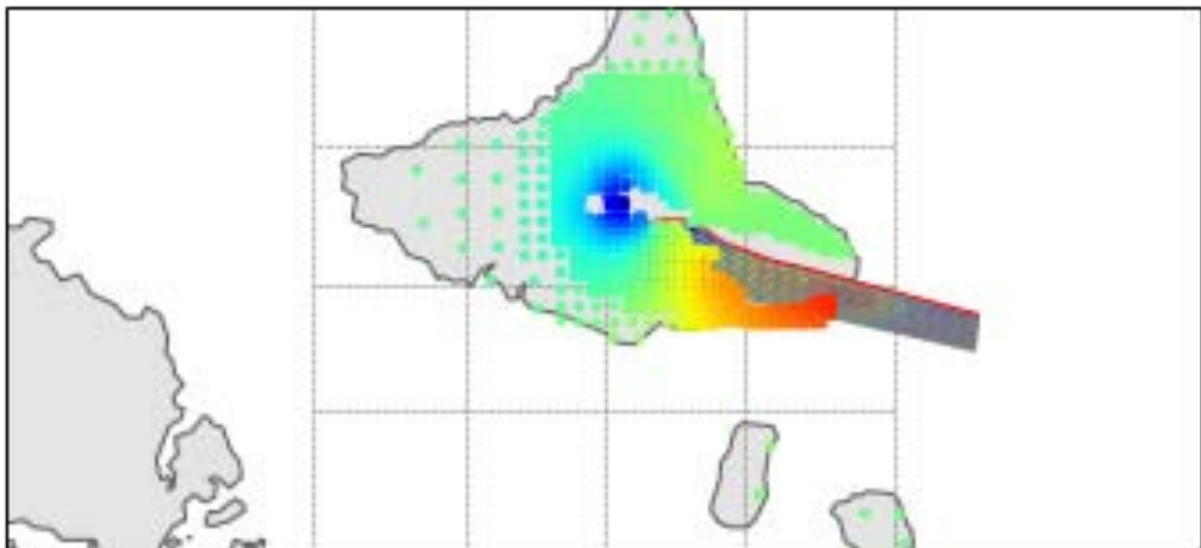
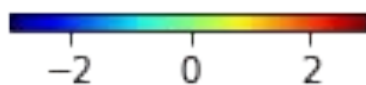
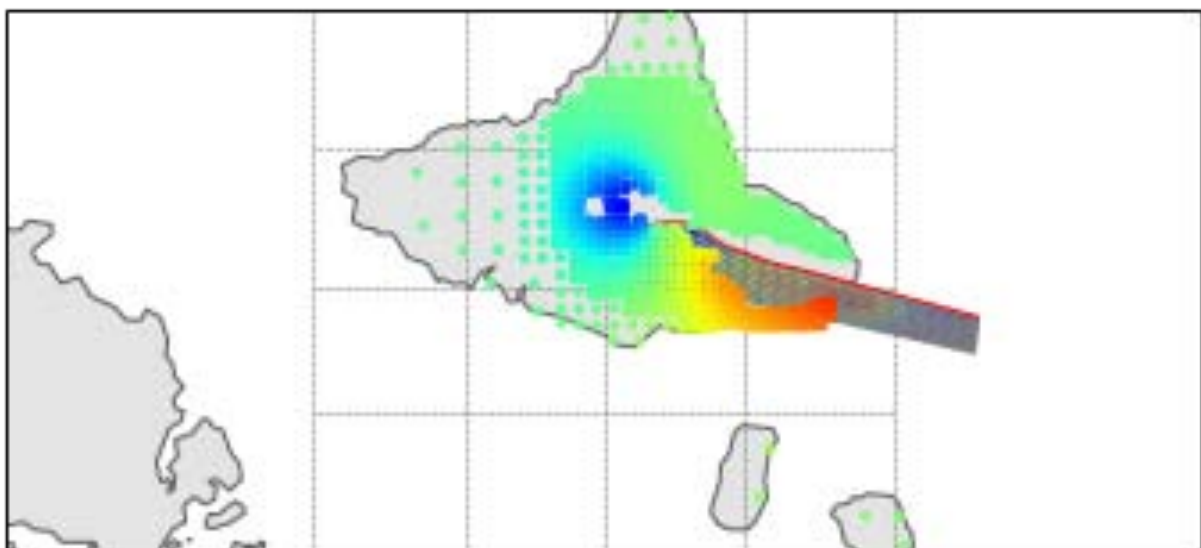


Figure 11: Opening distribution on dike.

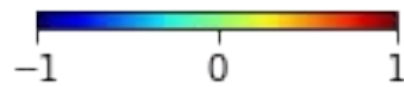
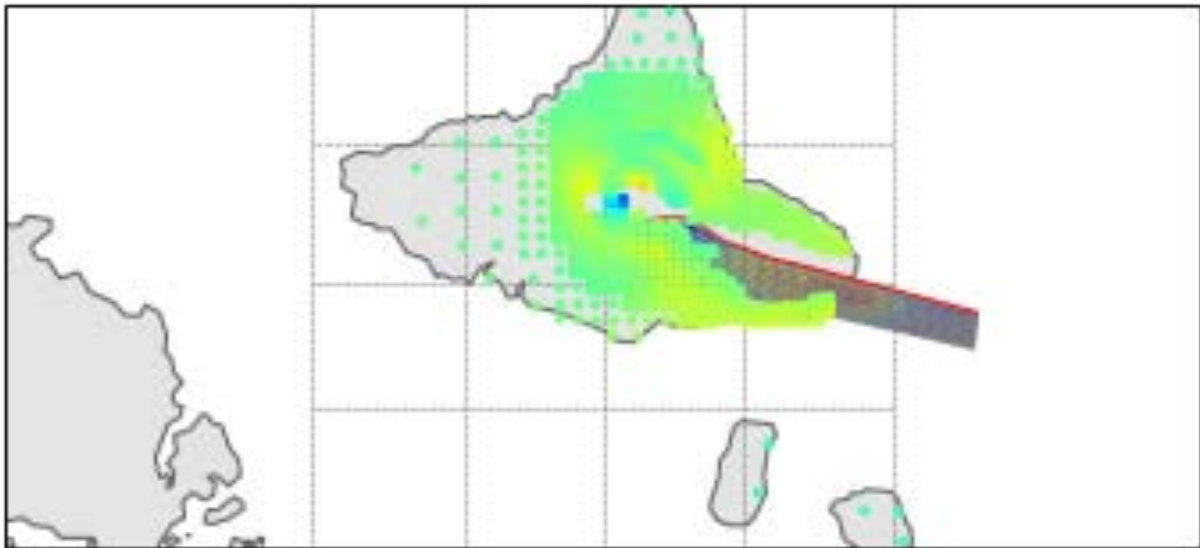
ALOS2 INSAR Asc 20181124-20181222 try 4 Data



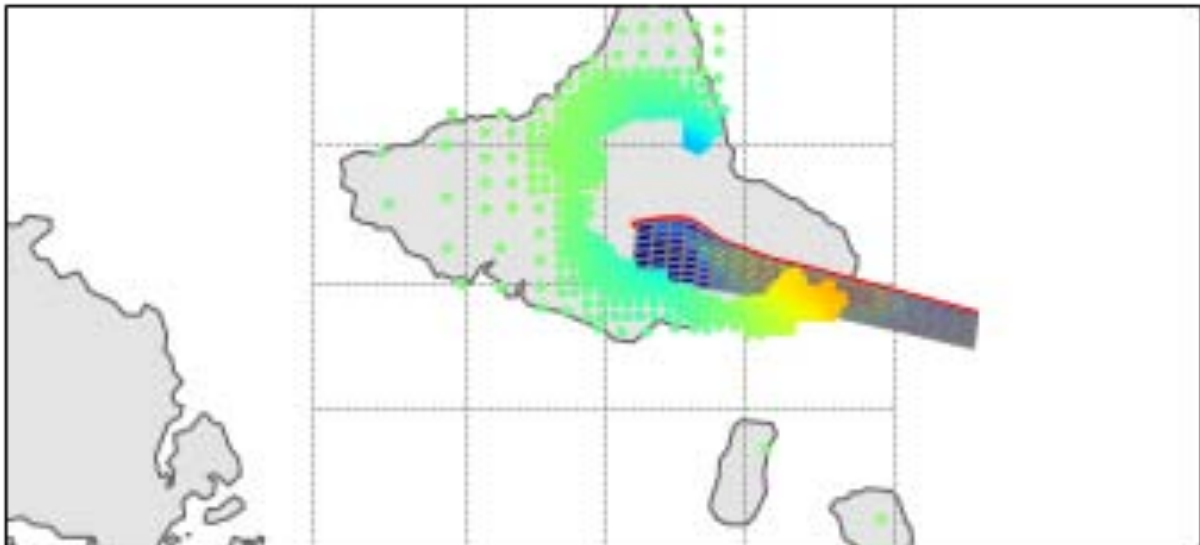
ALOS2 INSAR Asc 20181124-20181222 try 4 Synth



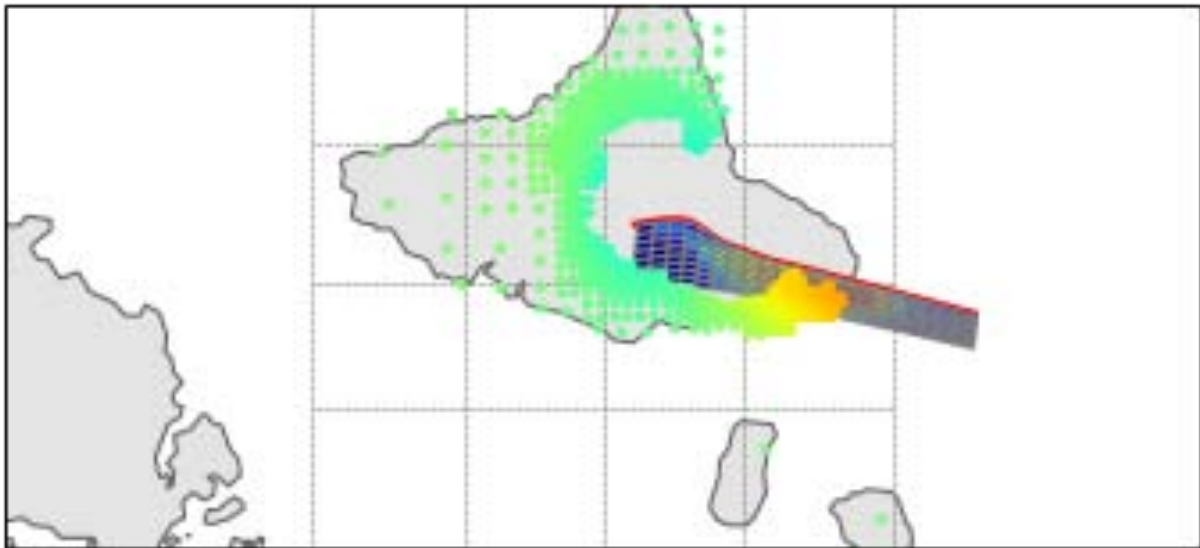
ALOS2 INSAR Asc 20181124-20181222 try 4 Res



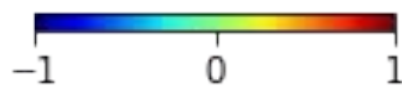
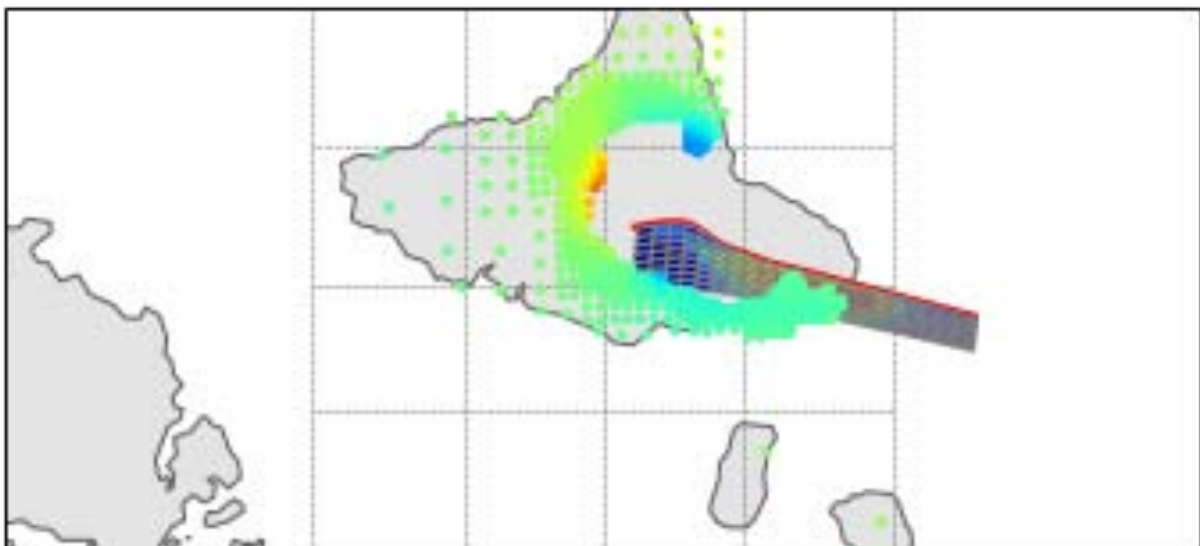
ALOS2 INSAR Desc 20181215-20190126 try 4 Data



ALOS2 INSAR Desc 20181215-20190126 try 4 Synth



ALOS2 INSAR Desc 20181215-20190126 try 4 Res



Source	(x0,y0,-z0)	Inverted parameter	Model-derived
Dike	N/A	Δ Volume	479000000 m ³
Mogi	168.136, -16.253, 4500 m	Δ Volume	-228789711 m ³

References

- Battaglia, M., Cervelli, P. F., and Murray, J. R. (2013). DMODELS: A MATLAB software package for modeling crustal deformation near active faults and volcanic centers. *Journal of Volcanology and Geothermal Research*, 254:1–4.
- Mogi, K. (1958). Relations between the eruptions of various volcanoes and the deformations of the ground surfaces around them. *Bulletin of the Earthquake Research Institute*, 36:99–134.
- Nikkhoo, M., Walter, T. R., Lundgren, P. R., and Prats-Iraola, P. (2017). Compound dislocation models (CDMs) for volcano deformation analyses. *Geophysical Journal International*, 208(2):877–894.
- Tarantola, A. and Valette, B. (1982). Generalized nonlinear inverse problems solved using the least squares criterion. *Reviews of Geophysics*, 20(2):219–232.

Appendix B

Lava dome growth at Ibu volcano from 2000 – 2018 (Molucca Islands, Indonesia)

B.1 Ibu volcano

Ibu volcano is located on Halmahera Island (Molucca Islands, Indonesia), as shown in Figure B-1a. An eruption began in 1998, building up a dacitic lava dome ($\sim 67\%$ SiO₂ content) in the volcano's central 1 km wide nested crater [Boyson and Bani, 2014]. Three vents contribute to the growth of Ibu's lava dome, which had a height of 20 m and a radius of 200 m by February 2000. At the time of writing, the vents were still intermittently extruding lava (See the lava dome extent as of May 2020 in Figure B-1b). These lava flows either accumulated in the northern valley or within the nested crater.

B.2 Digital Elevation Models of dome growth

To assess lava dome volume change during the first 15 years of dome growth, we calculate the difference between two global Digital Elevation Models (DEMs)– the Shuttle Radar Topography Mission (SRTM, 2000) and TanDEM-X global DEM (2014) (See Figure B-2). We measure a total volume difference of $127 \times 10^6 \text{ m}^3$, or an extrusion rate of $0.29 \text{ m}^3 \text{ s}^{-1}$.

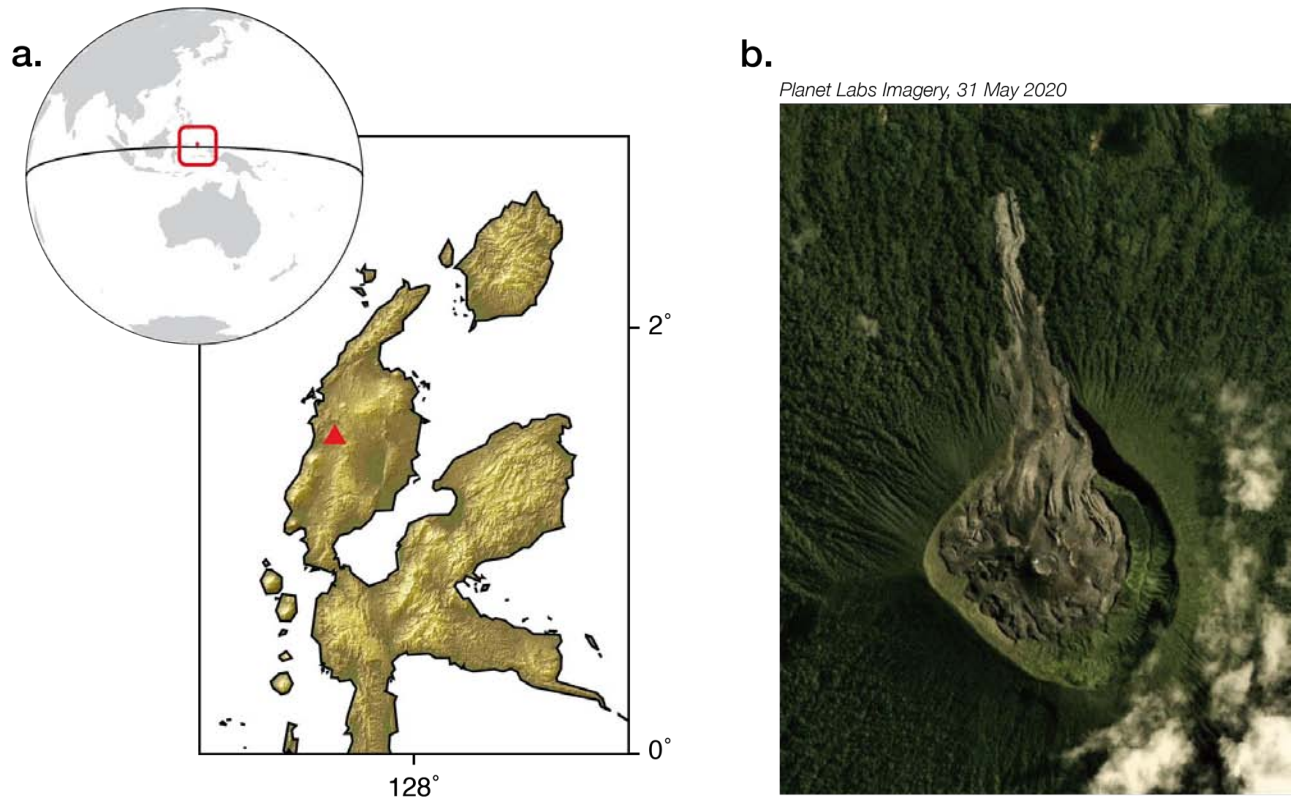


Figure B-1: **Ibu volcano.** **a.** Ibu is located in the western portion of Halmahera Island in Indonesia. **b.** Optical image of Ibu on 31 May 2020, from Planet Labs.

We then processed DEMs of Ibu’s lava dome using TanDEM-X bistatic acquisitions spanning throughout 2018 (using a modified version of ROI-PAC and NSBAS modules), as well as a DEM using tri-stereo high-resolution Pléiades optical images acquired in 2013. By differencing the Pléiades and TanDEM-X DEMs acquired at different dates, we can measure the volume change of the lava dome over time. By blending multiple TanDEM-X DEMs acquired at similar time periods but with different acquisition geometries, we obtain a coherent DEM of Ibu’s lava dome in 2018 that is not subject to geometrical effects such as shadow resulting from the sidelooking radar (See Figures B-3 and B-4). The total volume change between 2013 and 2018 was $49.5 \times 10^6 \text{ m}^3$, which is equivalent to an extrusion rate of $0.34 \text{ m}^3 \text{ s}^{-1}$.

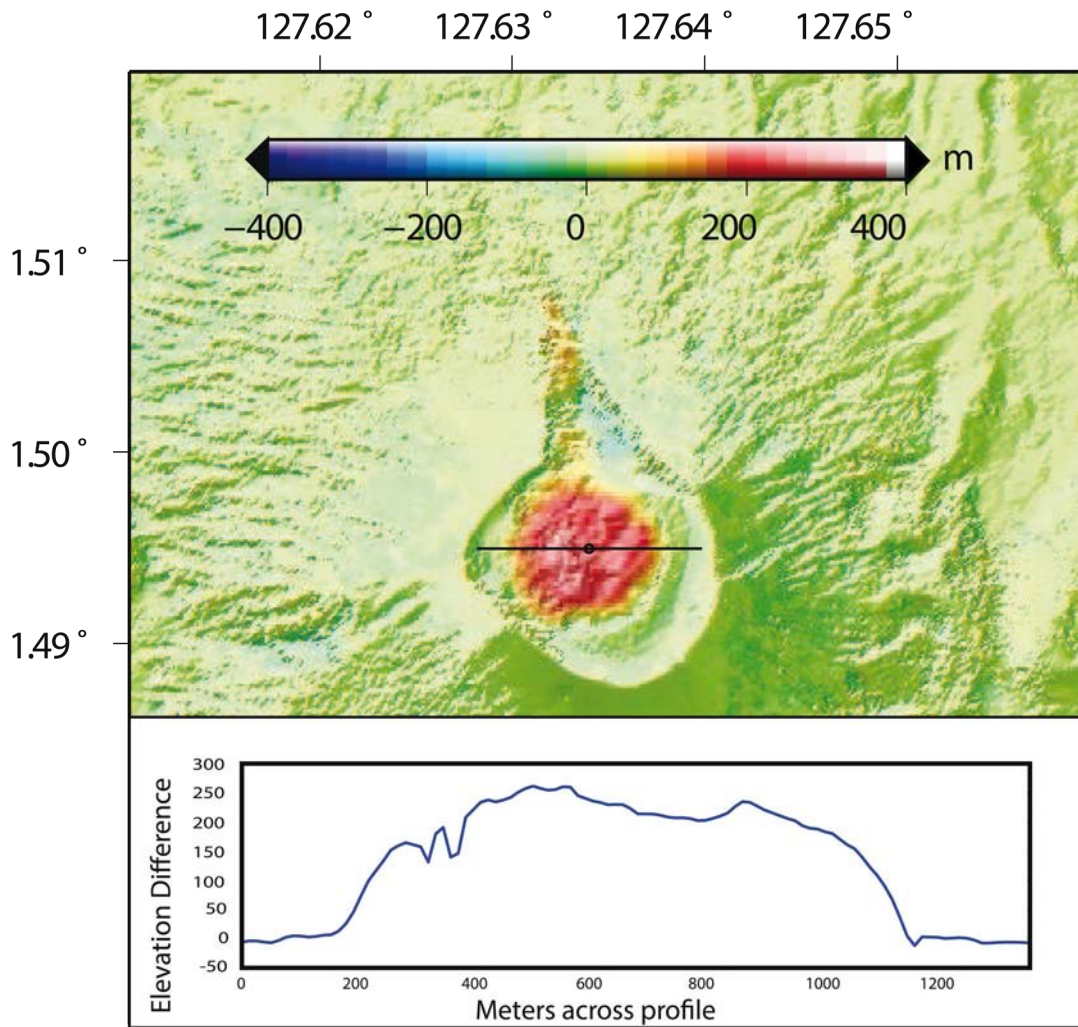


Figure B-2: **Volume change from 2000 – 2014.** The elevation difference measured using a DEM difference between SRTM and the TanDEM-X global DEM.

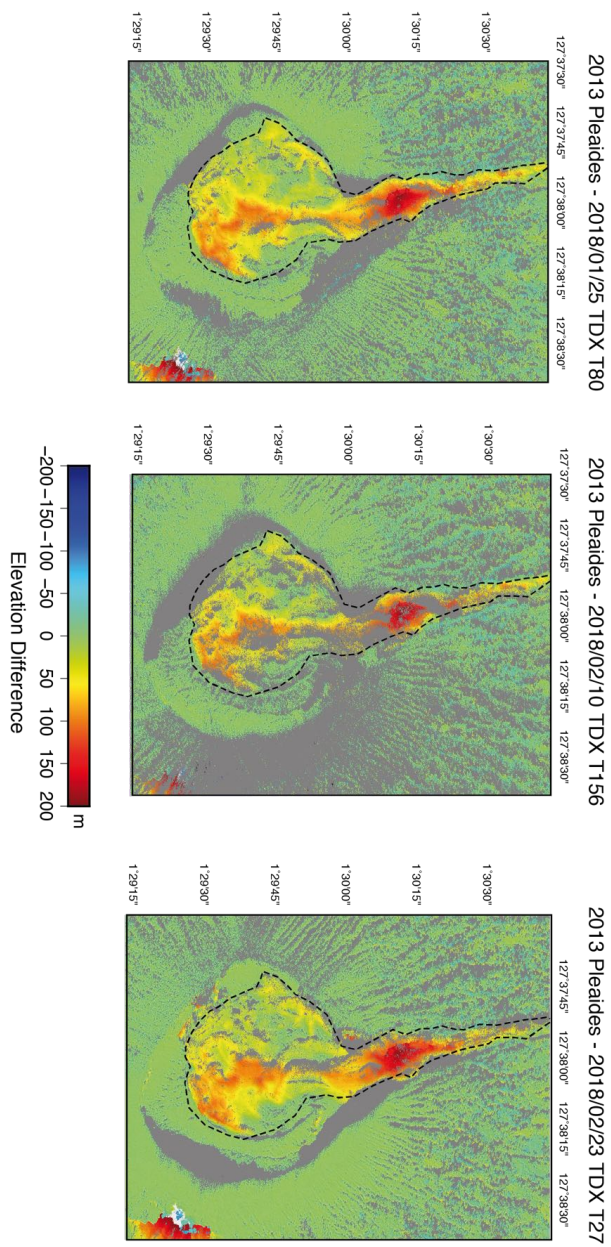


Figure B-3: **Elevation difference from 2013 – 2018.** The elevation difference between Pleiades DEM from 2013 and various Tandem-X DEMs from the beginning of 2018.

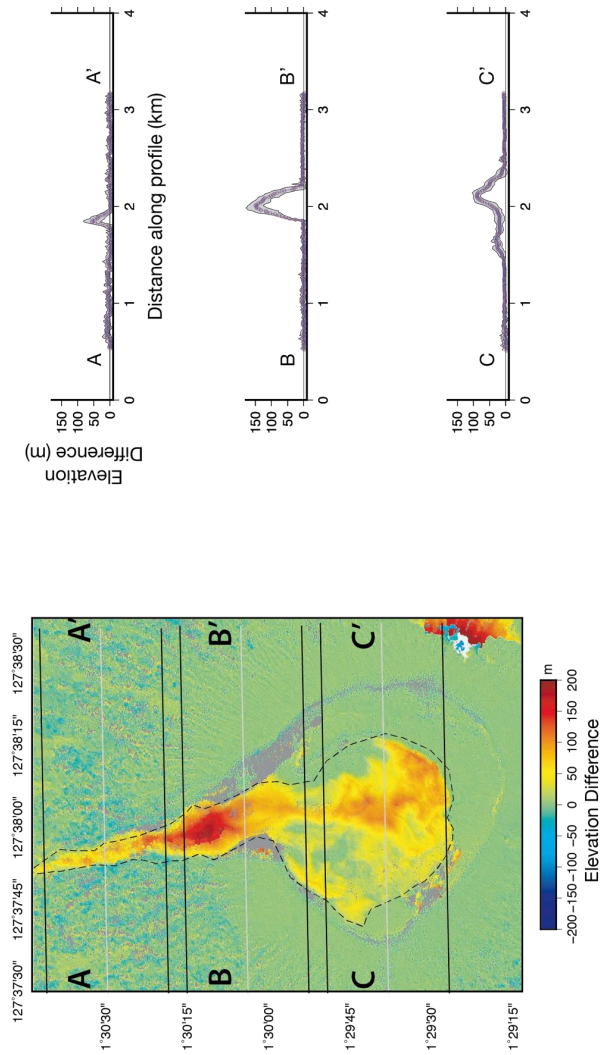
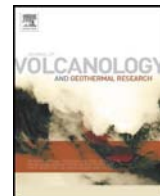


Figure B-4: **Total elevation difference, 2013 – 2018.** The lefthand column shows elevation difference between Pleiades DEM from 2013 and blended TanDEM-X DEMs from the beginning of 2018. The three profiles are plotted in the righthand column.

Appendix C

Paper 3: The 2018 unrest phase at La Soufrière of Guadeloupe (French West Indies) andesitic volcano: Scrutiny of a failed but prodromal phreatic eruption



The 2018 unrest phase at La Soufrière of Guadeloupe (French West Indies) andesitic volcano: Scrutiny of a failed but prodromal phreatic eruption

Roberto Moretti^{a,b,*}, Jean-Christophe Komorowski^a, Guillaume Ucciani^{a,b}, Séverine Moune^{a,b,c}, David Jessop^{a,b,c}, Jean-Bernard de Chabalière^a, François Beauducel^{a,d}, Magali Bonifacie^{a,b}, Arnaud Burtin^{a,b}, Martin Vallée^a, Sébastien Deroussi^{a,b}, Vincent Robert^{a,b}, Dominique Gibert^e, Tristan Didier^{a,b}, Thierry Kitou^{a,b}, Nathalie Feuillet^a, Patrick Allard^a, Giancarlo Tamburello^f, Tara Shreve^a, Jean-Marie Saurel^a, Arnaud Lemarchand^a, Marina Rosas-Carbajal^a, Pierre Agrinier^a, Anne Le Friant^a, Marc Chaussidon^a

^a Université de Paris, Institut de physique du globe de Paris, CNRS, F-75005 Paris, France

^b Observatoire volcanologique et sismologique de Guadeloupe, Institut de physique du globe de Paris, F-97113 Gourbeyre, France

^c Université Clermont Auvergne, CNRS, IRD, OPGC, Laboratoire Magmas et Volcans, F-63000 Clermont-Ferrand, France

^d Institut des Sciences de la Terre - Institut de Recherche pour le Développement - BPPTKG - PVMBG Badan Geologi, Yogyakarta, Indonesia

^e Geosciences Rennes UMR 6118 - Univ. Rennes I, Rennes, France

^f Istituto Nazionale di Geofisica e Vulcanologia sezione di Bologna, via Donato Creti, Bologna, Italy

ARTICLE INFO

Article history:

Received 17 June 2019

Received in revised form 3 January 2020

Accepted 4 January 2020

Available online 11 January 2020

Keywords:

Volcanic unrest

Hydrothermal systems

Phreatic eruptions

Degassing

Hydrofracturing and hydroshearing

ABSTRACT

After 25 years of gradual increase, volcanic unrest at La Soufrière of Guadeloupe reached its highest seismic energy level on 27 April 2018, with the largest felt volcano-tectonic (VT) earthquake (M_L 4.1 or M_W 3.7) recorded since the 1976–1977 phreatic eruptive crisis. This event marked the onset of a seismic swarm (180 events, 2 felt) occurring after three previous swarms on 3–6 January (70 events), 1 st February (30 events, 1 felt) and 16–17 April (140 events, 1 felt). Many events were hybrid VTs with long-period codas, located 2–4 km below the volcano summit and clustered within 2 km along a regional NW-SE fault cross-cutting La Soufrière. Elastic energy release increased with each swarm whereas inter-event time shortened. At the same time, summit fractures continued to open and thermal anomalies to extend. Summit fumarolic activity increased significantly until 20 April, with a maximum temperature of 111.4 °C and gas exit velocity of 80 m/s, before declining to ~95 °C and ~33 m/s on 25 April. Gas compositions revealed increasing C/S and CO₂/CH₄ ratios and indicate hydrothermal P-T conditions that reached the critical point of pure water. Repeated MultiGAS analysis of fumarolic plumes showed increased CO₂/H₂S ratios and SO₂ contents associated with the reactivation of degassing fractures ($T = 93$ °C, H₂S/SO₂ ≈ 1). While no direct evidence of upward magma migration was detected, we attribute the above phenomena to an increased supply of deep magmatic fluids that heated and pressurized the La Soufrière hydrothermal system, triggering seismogenic hydro-fracturing, and probable changes in deep hydraulic properties (permeability) and drainage pathways, which ultimately allowed the fumarolic fluxes to lower. Although this magmatic fluid injection was modulated by the hydrothermal system, the unprecedented seismic energy release and the critical point conditions of hydrothermal fluids suggest that the 2018 sequence of events can be regarded as a failed phreatic eruption. Should a similar sequence repeat, we warn that phreatic explosive activity could result from disruption of the shallow hydrothermal system that is currently responsible for 3–9 mm/y of nearly radial horizontal displacements within 1 km from the dome. Another potential hazard is partial collapse of the dome's SW flank, already affected by basal spreading above a detachment surface inherited from past collapses. Finally, the increased magmatic fluid supply evidenced by geochemical indicators in 2018 is compatible with magma replenishment of the 6–7 km deep crustal reservoir feeding La Soufrière and, therefore, with a potential evolution of the volcano's activity towards magmatic conditions.

© 2020 Elsevier B.V. All rights reserved.

* Corresponding author at: Université de Paris, Institut de physique du globe de Paris, CNRS, F-75005 Paris, France.

E-mail address: moretti@ipgp.fr (R. Moretti).

1. Introduction

Andesitic volcanoes develop hydrothermal systems that hamper a direct interpretation of the subterranean magma state and evolution from the physical and chemical signals measured at the surface. This limitation contributes enormously to the dilemma of whether observed volcanic unrest has a magmatic origin (“magma on the move”) or a non-magmatic origin from a change in the hydrothermal system (“fluids that are not magma on the move”) (Pritchard et al., 2019) and produces major uncertainties in the short-term forecasting of an imminent eruption. Such uncertainties are severe also for the short-term eruption hazard from non-magmatic unrest, as andesitic volcanoes may develop explosive phreatic eruptions (e.g., Barberi et al., 1992). Characterized by the absence of juvenile magmatic material, phreatic eruptions are triggered by the injection of fluids and heat of magmatic origin into the hydrothermal system, which becomes strongly overpressured (Barberi et al., 1992; Mastin, 1995; Rouwet et al., 2014 and references therein). In many cases phreatic eruptions are precursors to magmatic eruptions of both explosive or effusive nature, or could serve as the decompression mechanism prior to phreatomagmatic eruptions (Rouwet et al., 2014). However, the input of mass and heat into the hydrothermal system challenges monitoring systems, being often a short-term and too low amplitude event that does not result in clear precursory signals within the time frame of monitoring (Barberi et al., 1992; Rouwet et al., 2014). If on one hand the hydrothermal system tends to buffer and mask the inputs of deep hot fluids, on the other side secondary mineral precipitation and the presence of low-permeable elemental sulphur can seal hydrothermal systems in localized, shallow and overpressured portions that can rapidly reach the threshold to phreatic eruptive activity (Salaün et al., 2011; Rouwet et al., 2014). Therefore, it is of the utmost importance to track and understand the anomalies in observation data that are related to the input of deep hot magmatic fluids into the hydrothermal system. The ongoing unrest at La Soufrière explosive andesitic volcano, on the island of Guadeloupe (French West Indies), well represents the aforementioned issues and offers us this possibility.

2. Introduction and volcanological background

La Soufrière de Guadeloupe is located in the Lesser Antilles arc under which the Northern Atlantic ocean plate is subducting beneath the Caribbean plate at a rate of ~2 cm/year (Feuillet et al., 2002, 2011). La Soufrière belongs to the Grande Découverte volcanic complex, built during the past 445,000 years and comprising three stratovolcanoes: Grande Découverte, Carmichael and Soufrière (Komorowski et al., 2005). La Soufrière is the most recent volcanic edifice and its eruptive history began about 9150 years ago. It is an active explosive volcano that has experienced magmatic and non-magmatic “phreatic” eruptions, in the past (Komorowski et al., 2005; Feuillard et al., 1983; Legendre, 2012). The most recent major magmatic eruption dates from 1530 CE and began with a collapse of the volcanic edifice causing a landslide that reached the coast 10 km away. The explosive eruption that followed resulted in ash and pumice fallout on southern Basse-Terre, the outpouring of pyroclastic flows (incandescent avalanches of gas, ashes and rocks) that reached distances of 5–7 km from the volcano, and mudflows (Boudon et al., 2008; Komorowski et al., 2008). It ended with the formation of the present Soufrière dome. This magmatic eruption is representative of the hazards caused by an explosive eruption of medium magnitude, although more intense eruptions have been identified in the last 10,000 years (Komorowski et al., 2005; Legendre, 2012). Recent studies suggest that a smaller magmatic eruption took place in 1657 (Legendre, 2012; Hincks et al., 2014).

Since that time the historical activity of La Soufrière has been characterized by persistent hydrothermal manifestations (fumaroles, solfataras, hot springs) culminating into intermittent non-magmatic steam-driven (phreatic) eruptions. Major phreatic eruptions occurred in 1797–1798, 1797–1798, 1812, 1836–1837, 1976–1977, and

minor ones in 1690 and 1956 (Lherminier, 1837a, 1837b, 1837c; Komorowski et al., 2005; Legendre, 2012; Hincks et al., 2014).

After the 1976–77 phreatic eruption (Feuillard et al., 1983; Komorowski et al., 2015 and references therein), the volcano remained in a state of repose notwithstanding low levels of fumarolic activity at the SW base of the dome, along the Ty fault (Zlotnicki et al., 1994; Allard et al., 1998; Komorowski et al., 2005; Villemant et al., 2005; Fig. 1) until 1992. Concomitant with the revival of shallow seismicity, degassing renewed on top of the lava dome in 1992, in parallel with reactivation of thermal springs that have remained dry since 1977 and the appearance of new ones at the southern base of the dome (Villemant et al., 2005, 2014). Fumarolic degassing was initially concentrated at the Cratère Sud (hereafter CS, Figs. 1,2), but gradually extended along the Napoleon fracture (1997) and to the Tarissan crater lake (1998). In 1998, the sudden onset of chlorine-enriched degassing from the CS fumaroles marked a significant change in the behaviour of the magmatic-hydrothermal system (Komorowski et al., 2001; Komorowski et al., 2005; Villemant et al., 2005, 2014). In parallel, boiling ponds of extremely acid water formed in 1997 at CS (mean pH of -0.1 and $T^{\circ}\text{C} = 88.8 \pm 8.6$ between 1998 and 2001; OVSG-IPGP data and Rosas-Carbajal et al., 2016), and since 2001 at the bottom of the Cratère Tarissan (mean pH of -0.2 in 2014) (Komorowski et al., 2005; Villemant et al., 2005; Komorowski et al., 2001; OVSG-IPGP, 1999–2019) (Figs. 1,2). Whereas the acid pond at the CS persisted for seven years, leaving place to an intense fumarolic degassing in 2003 (Komorowski et al., 2005), the acid thermal lake in the Cratère Tarissan continued to be active until now (OVSG-IPGP, 1999–2019).

After 2007, fumarolic activity also propagated to Gouffre 56 (the explosion pit formed during the 1956 phreatic eruption, hereafter G56; Jolivet, 1958 and Figs. 1,2) then to the nearby Lacroix fracture (late 2011) and more eastward to the Breislack crater (2013, Figs. 1,2). The so-called Breislack fracture cutting the lava dome was involved in 4 of the 6 historical non-magmatic phreatic explosive eruptions of La Soufrière in 1797–1798, 1836–1837, 1956 (October), and 1976–1977 (eruption onset on 8 July 1976) (Komorowski et al., 2005, 2015; Rosas-Carbajal et al., 2016). The degassing area continued to expand on top of the lava dome, with the appearance of a new fumarole (Napoleon Nord, hereafter NAPN; Figs. 1,2) in July 2014, and of new vents (Napoleon Est 1 and Napoleon Est 2, hereafter NAPE1 and NAPE2) that opened further east (Figs. 1,2) between 8 and 10 February 2016 with a very small steam blast (in the sense of Mastin, 1995) with hot mud projections over a distance of 5–10 m radius.

The high concentration of hydrochloric and sulphuric acid plumes accompanied by high gas flows and a steady trade wind regime has destroyed the vegetation on the southwest flank of La Soufrière, contributing to small landslides of the degraded slopes, and to gas smell nuisances potentially harmful to people’s health and felt since December 1997 by the population living downwind the volcanic plume (OVSG-IPGP, 1999–2019).

This reactivation ongoing since 1992 has required the implementation of an alert level scale set as of 1999 at the yellow level (i.e., vigilance), on a four-level scale (green, yellow, orange and red; OVSG-IPGP, 1999–2019). However, concern further increased recently owing to an accelerating unrest phase that developed in February–April 2018 and culminated with a magnitude 4.1 seismic activity peak, of same magnitude as the strongest earthquake recorded during the 1976–77 phreatic crisis (Feuillard et al., 1983).

In this study, we report and discuss the geophysical and geochemical features we observed to be associated with this recent peaking activity. Based on various data types, we attempt to interpret the triggering mechanism (magmatic versus hydrothermal) of this event and its significance within the unrest sequence initiated since 1992 at La Soufrière. Specifically, we try to decipher whether the observed phenomena may involve or not changes in a deep magmatic source and how unrest observables relate to the vigorous circulation and interaction of water, steam and hot gases in the porous and fractured host rocks.

3. Monitoring data: observations and preliminary assessments

In this section we present the data and observations resulting from our networks and measurements campaigns. A preliminary assessment is also given for each class of observation (seismic, geodetic, thermal, geochemical; see also Supplementary Table 1) with reference to the existing literature, in order to highlight the information to be extracted and then discussed quantitatively in Section 4.

3.1. Seismic activity

As mentioned above, after a brief repose period that followed the 1976–77 eruptive crisis, volcanic seismicity at La Soufrière renewed in 1992 (Fig. 3), concomitantly with the degassing unrest. Since then >14,000 earthquakes of volcanic origin were recorded (Fig. 3). Most of them were of low local magnitude M_L (<1) and clustered in swarms lasting from a few days to a few weeks. Seventeen of all these volcanic earthquakes were strong enough to be felt locally, including five in 2013, one in 2014, and the most recent ones on 1 February, 16 April and 27 April 2018 (OVSG-IPGP, 1999–2019). After a relative minimum in both energy and number of events in 2016, the volcanic seismicity increased drastically since 2017 (Fig. 3). Compared to previous years, this increase can only partly be explained by improvements in the resolution of the seismic network. Thereafter, we describe the temporal and energy pattern of recent seismicity (from 1 st January 2017 to 30 July 2018). First of all, we list here the main features of observed waveforms (Fig. 4):

- volcano-tectonic (VT) signals, showing a high-frequency content (5–20 Hz) (Fig. 4a);
- long period (LP) signals, characterized by a low frequency (1–5 Hz), often appearing as nearly monochromatic signals (Fig. 4b) and associated with resonance phenomenon of the hydrothermal fluids in cracks (Ucciani, 2015);
- hybrid (HY) signals, showing the high-frequency content typical of VT events, most often at the beginning of the waveforms and accompanied by a low frequency content which often appears at the signal onset and is observed to the end of the event, in the signal coda (Ucciani, 2015; Fig. 4c);
- nested volcanic (VE) signals, appearing as small seismic packets in which events occur on the coda of the previous one (Fig. 4d), and which are not concomitant or precursor to a particular phenomenon. VE events differ from spasmodic burst defined in Hill et al. (1990) and consist in a sequence of several seismic events with very short inter-times, with very often >6 seismic events in a short sequence (~10s; Ucciani, 2015).

During 2017, the OVSG identified a total of 1432 volcanic earthquakes (Fig. 5a), all with local magnitude M_L < 0.9, except for three events M_L 1–to 1.3 on 13 December. Seventy-two of the recorded events were of the LP type, whereas the majority (1360) were HY-type, with few VTs, and were similar to the seismic activity of dominantly volcanic origin observed in the previous years, implying a temporal continuity of seismic sources and processes (Ucciani, 2015; Ucciani et al., 2015). HY events are produced by fracturing and reservoir resonance phenomena related to the propagation of fluids. Some of these events (250 in 2017) are nested (VE-type), thus representing multiple closely-spaced ruptures within a patchy fractured medium. Given the superficial distribution of the hypocenters (mainly at depths between –0.8 km and 0.8 km below sea level – b.s.l.) (Figs. 5b,6a) such a low-energy micro-seismicity

attests to the vivacity of hydrothermal circulations within the shallow part of La Soufrière edifice (Ucciani, 2015; Ucciani et al., 2015; OVSG-IPGP, 2017). The 2017 activity released a total of 48.5 MJ of seismic energy (Fig. 5c).

The overall seismicity measured at La Soufrière in the first half of the year 2018 (Figs. 5a–c,6b) will be here discussed for four different relevant periods (January, February–March, April, May to July) that were chosen to provide a clear explanation of the sequence of observed key events, which are illustrated in Supplementary Figs. S1–S5. In January 2018, 78 earthquakes of volcanic origin were detected and located essentially under the dome of La Soufrière, at <0.5 km depth b.s.l., with the exception of an event (Fig. 5b, Supplementary Fig. S1). Most of them occurred concentrated in a swarm between January 2 and 5 (key event 1). The total energy released was about 3 MJ (Fig. 5c). A stronger seismic swarm of >30 earthquakes (key event 2) then succeeded on 1 st February 2018 between 12:55 local (16,55 UT) and 15:31 local. All hypocenters were located between 0.5 and 1 km b.s.l. (2 and 2.5 km deep under the dome summit) (Fig. 5b, Supplementary Fig. S2). The swarm started with events of very small magnitude but showed an increasing energy that ended with three earthquakes of magnitude ≥ 1.4 , among which a felt one (M_L 2.1, depth 1 km b.s.l., intensity III in the Saint-Claude commune (OVSG-IPGP, 2018a)). The seismic energy released reached about 130 MJ (Fig. 5c). Between 2 February and 31 March the seismicity continued with 170 VT and hybrid-type earthquakes. An intensification of the activity can be observed since mid-March (Fig. 5a); Earthquakes were located under the dome of La Soufrière, at <0.5 km depth b.s.l. (Fig. 5b), and of very low magnitude, releasing a total seismic energy of 14.7 MJ from 2 February to 31st March (Fig. 5c).

During April 2018, 545 volcanic earthquakes occurred beneath but also around the dome of La Soufrière, within a depth interval extending from –1 to 5.7 km b.s.l. The most prominent seismic activity concentrated in two swarms: on 16–17 April (key event 3; >140 VT and hybrid earthquakes in 48 h; Fig. 5a,b, Supplementary Fig. S3) and 27–28 April (key event 4: >180 earthquakes in 24 h; Supplementary Fig. S4). The first swarm was located under the SW base of the volcano (between –0.5 and 2.6 km b.s.l.). Twelve events had a magnitude ≥ 1.0 and hypocenters between 1 km and 1.6 km b.s.l. (or 2.5 to 3.1 km of depth below the summit). The main earthquake, at 18 h59 local on 17 April 2018 (M_L 2.1 and depth 1.2 b.s.l.) was very slightly felt by the inhabitants of St Claude (weak macroseismic intensity, II; OVSG-IPGP, 2018b).

The second seismic swarm was instead located about 2 km north-west of La Soufrière summit dome. Two-thirds of the earthquakes occurred in the first two hours of activity and were of very small magnitude, with foci distributed between 1.0 and 3.1 km b.s.l. (or 2.5 to 4.6 km below the summit, Fig. 5b). However, at 20:15 (local) on 27 April a strong shock with M_L 4.1 occurred, becoming the strongest volcanic earthquake recorded at La Soufrière for 42 years. Located 1.9 km below sea level, this earthquake was largely felt throughout Guadeloupe. In the nearest affected areas, a macroseismic intensity of V was estimated (OVSG-IPGP, 2018c). These two swarms in April 2018 released about 200 MJ and 90,000 MJ, respectively (Fig. 5c), the majority of which during the M_L 4.1 earthquake on 27 April. Interestingly, the 27–28 April swarm is characterized by purely VT events, not showing any long-period coda (Fig. 4b). However, between 18 and 25 April, it was preceded by ~30 hybrid events that occurred in a zone surrounding the hypocentral region of the 16–17 April swarm.

During May, June and July 2018, 195 VT and particularly HY earthquakes of weak magnitude (≤ 1) occurred, beneath (between –1 and 2 km depth b.s.l.) and around the dome of La Soufrière (Fig. 5a,b, Supplementary Fig. S5). Seismic activity in May–July released 10 MJ of

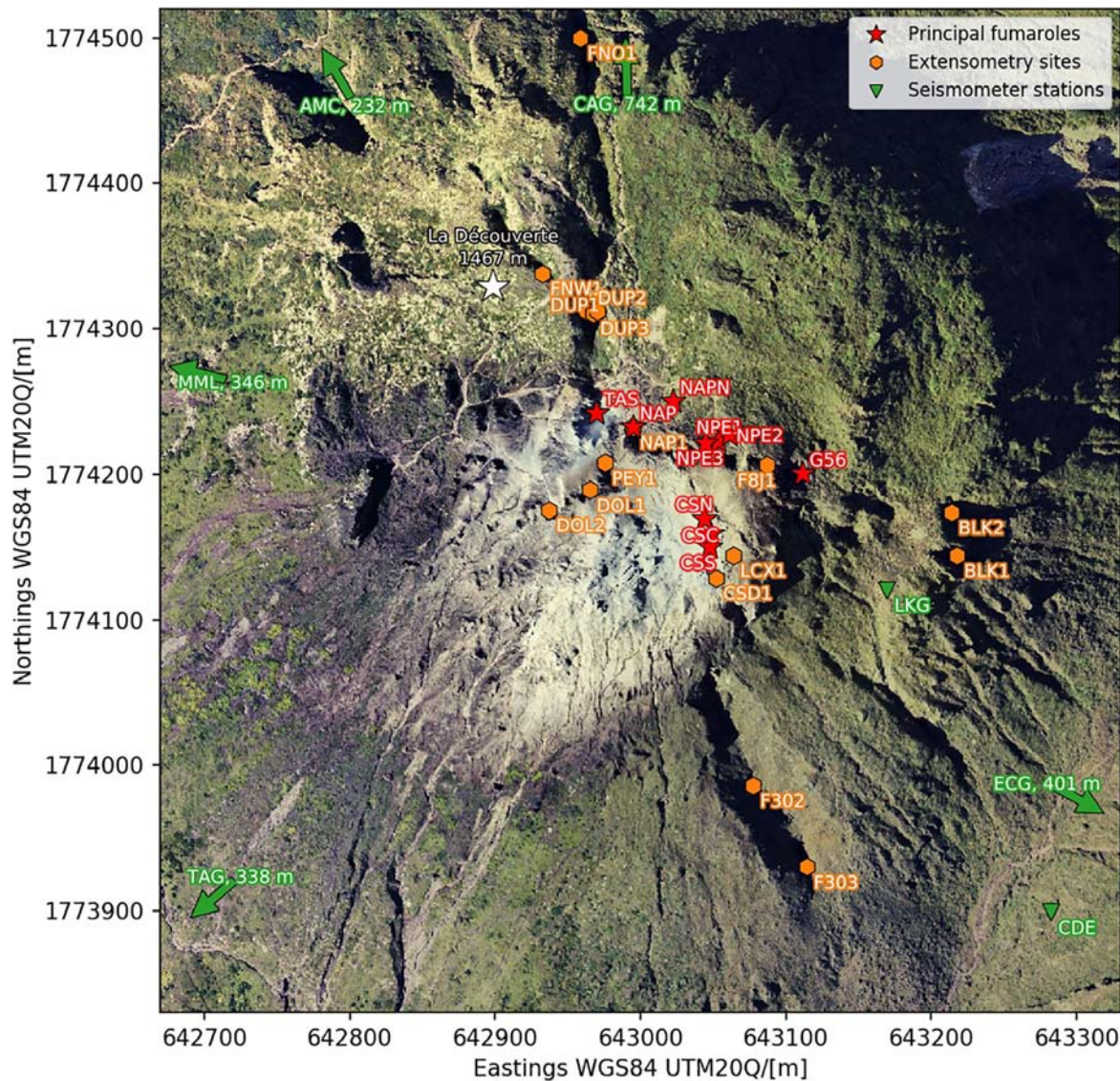


Fig. 2. Location of the principal fumaroles, extensometry sites and seismometer stations on the summit of La Soufrière. Site codes are as indicated in the text. The white star indicates the location of the highest point. Green arrows indicate directions to several volcanic seismometer stations which are off the current map view. The base image is a georectified orthophoto derived from aerial photographs acquired by Institut National de l'Information Géographique et Forestière (IGN) in 2010. (For interpretation of the references to colour in this figure legend, the reader is referred to the web version of this article.)

seismic energy and marks a period of relative seismic calm after the highly energetic 27–28 April swarm.

3.2. Ground deformation

3.2.1. GNSS data and patterns of deformation

Fig. 7 presents the velocity field determined by Global Navigation Satellite System (GNSS) continuous and campaign measurements of La Soufrière network, with respect to the Guadeloupe archipelago. The network has evolved significantly since the first measurements in 1995 and the two first permanent stations in 2000 (HOUE and SOUF). The most important step occurred around 2015, with deployment of new permanent stations (CBE0, MAD0, PAR1, FNG0, AMCO, PSA1, TAR1) and more frequent reiteration campaigns. Therefore, velocity uncertainties depend mainly on the observation timespan and vary from 0.5 mm/yr for the oldest stations with about 20 years of data recording, to several mm/yr for stations installed recently. Stations located on the flanks of La Soufrière massif (HOUE, MAD0, CRB0, CBE0, FNG0, MAT0, and PAR1 in Fig. 7a) show velocities that vary from 0 to 1.5 mm/yr. The time series of these stations display remarkably steady state rate suggesting no significant variations of processes at depth during the

last twenty years. In particular, the general pattern of the deformation is not consistent with any inflation/deflation at depth.

To estimate the sensitivity of the network, we computed the Green's functions of a simple isotropic point source model using the varying-depth method to take the topography into account (Williams and Wadge, 1998) to determine the volume variations, ΔV , in a 3-D grid (not shown) that can induce a maximum of 1 mm of displacement on the GNSS stations at the surface, considered here as an arbitrary threshold (de Chabalière et al., in preparation). For a source located at 10 km of depth below the dome, the detectability threshold of ΔV decreases from 800,000 m³ in 1995 to about 500,000 m³ after 2015. We also conclude that since 2015 the maximum depth of detection for a $\Delta V \approx 100,000\text{ m}^3$ reaches 4–5 km. The deformation field of the flanks of the volcano does not reveal significant intrusion during the period of observation but we cannot exclude small intrusions, especially at depth larger than 6–7 km and in any case below the brittle-ductile transition. Nevertheless, the Basse-Terre deformation field can then be chosen as a reliable reference to determine the volcanic deformation of La Soufrière dome.

At the scale of the La Soufrière volcano, there is little deformation (<math><2\text{ mm/yr}</math> on horizontal components) on the peripheral (>0.5 km)

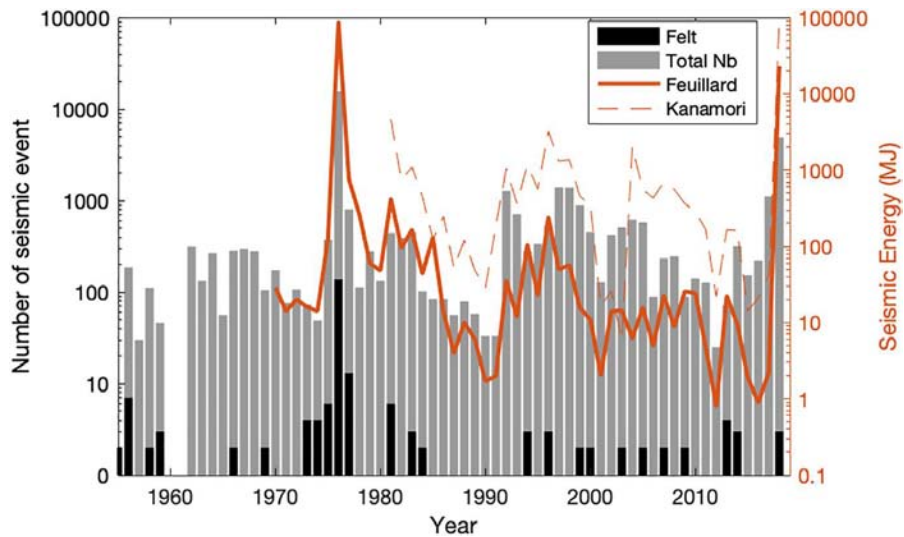


Fig. 3. Seismic activity of volcanic origin from 1955 to July 2018 (yearly histogram, with exception of 2018). Grey bars are the number of events per year. Black bars represent earthquakes felt by population. The two red lines indicate the released seismic energy, following Feuillard et al. (1983) (solid line) and Hanks and Kanamori (1979) (dashed line). The Feuillard et al. (1983) seismic energy is shown only for the purposes of continuity with the historical record. (For interpretation of the references to colour in this figure legend, the reader is referred to the web version of this article.)

sectors (NEZ2, AMC0, AMC1, RCB1, RCL2 in Fig. 7b), except in the southwestern one. On the summit lava dome, the deformation signal is globally radial and reaches 3 to 7 mm/yr. Large displacement vectors (up to 9 mm/yr) towards the southwest point to a sliding zone downslope to the Bains Jaunes site, 1.3 km away from the top of the dome (Fig. 7).

In first approximation the horizontal components of GNSS velocities show that the pattern of the dome deformation is radial and centered on the Cratère Tarissan and Cratère Napoleon. Such a pattern, however, is disturbed by major faults and fractures crossing through the dome (North, Napoleon-Gouffre 56-Breislack system and the Dolomieu

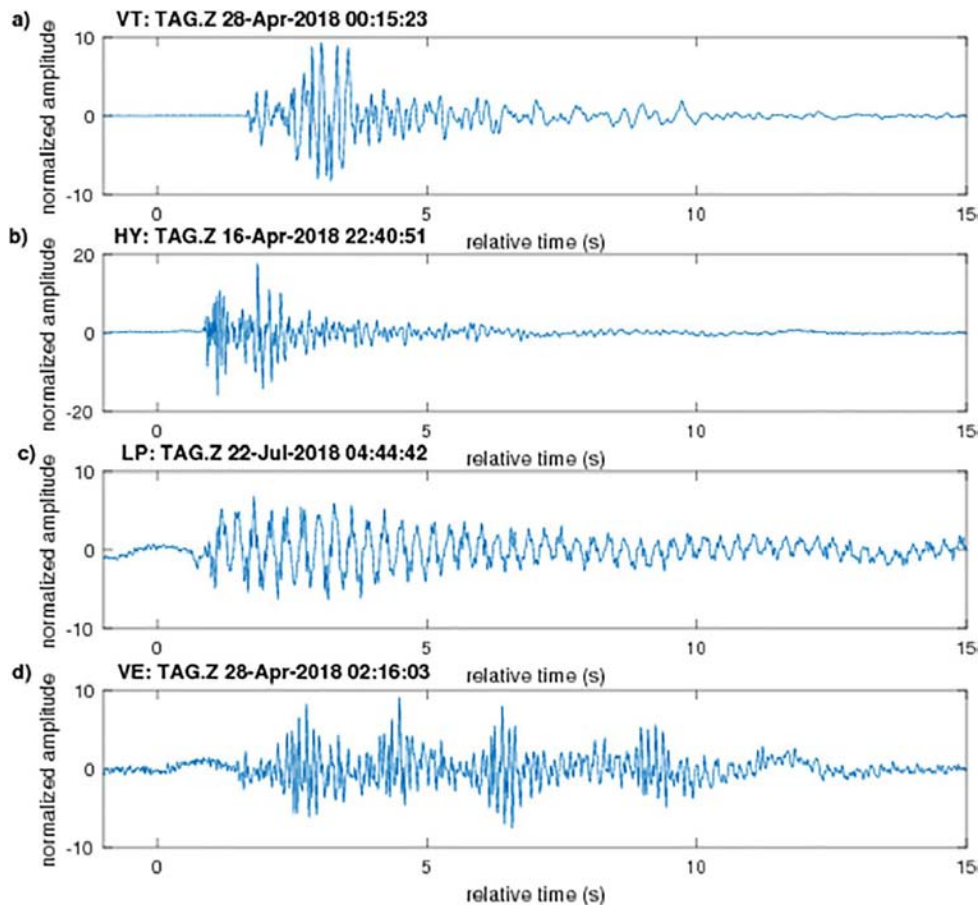


Fig. 4. Typical waveforms observed on the vertical component of TAG station, La Soufrière volcano. Panel a) “Pure” volcano-tectonic (VT) event. Panel b) Hybrid (HY) event (examples from shallow hydrothermal microseismicity and from ~2 km deep events recorded between the two subsequent swarms of April 2018). Panel c) example of “monochromatic” long-period (LP) event. Panel d) Nested (VE) event, typically of hybrid nature (examples from shallow hydrothermal microseismicity and from the 1st February swarm). Note that VE events are observed by the OVSG since the 80’s; because of the absence of a specific class in the literature, the observatory decided since the 90’s to name these events as nested (*Volcaniques Emboîtés* in French).

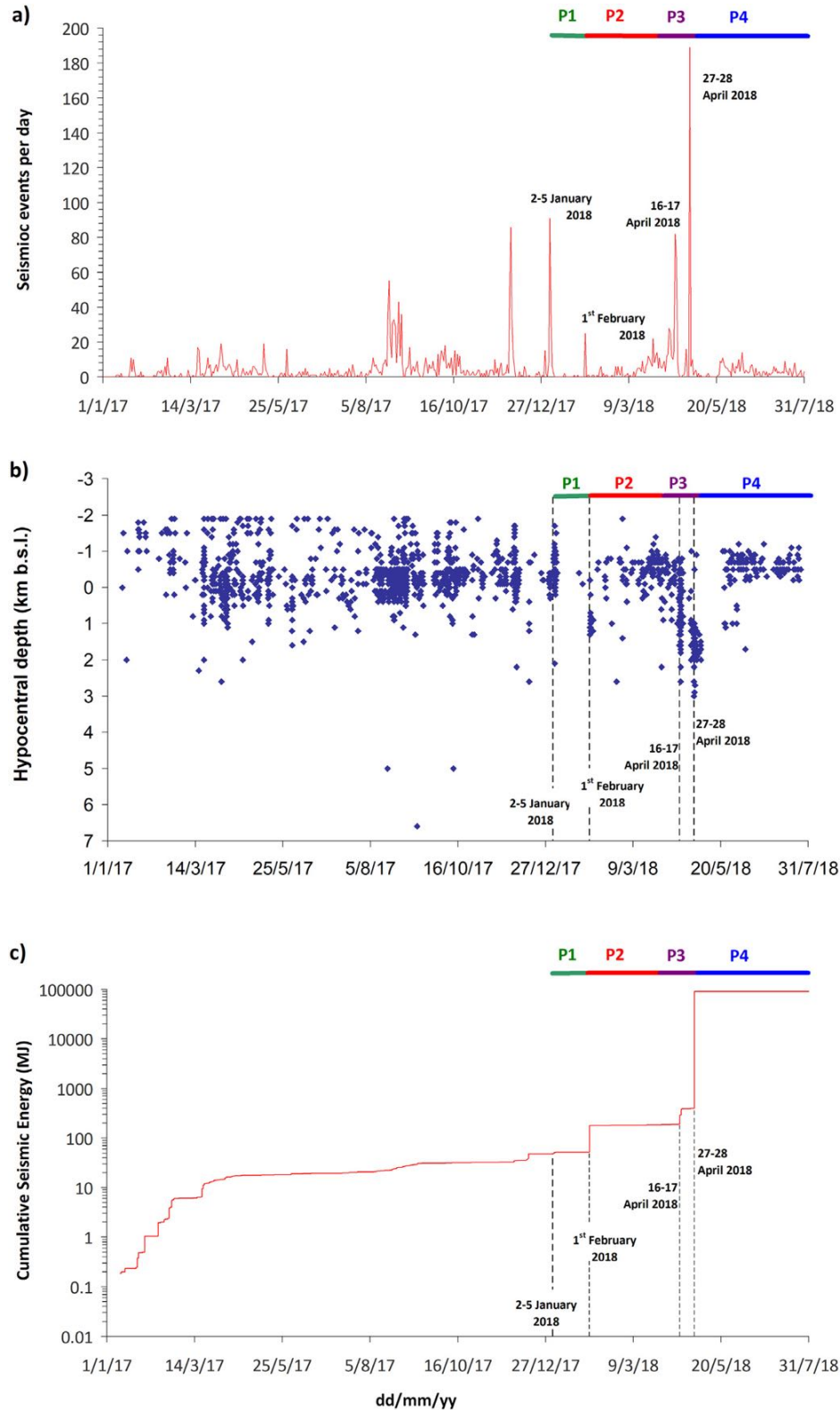


Fig. 5. Panel a) Seismic events observed on a daily basis from 1 st January 2017 to 31st July 2018. Panel b) Depths of hypocenters of seismic events observed from 1 st January 2017 to 31st July 2018, based on the adoption of the 1D velocity model of Dorel et al. (1979) and the use of the NonLinLoc algorithm (Lomax et al., 2000) for hypocentral location. Panel c) Semi-logarithmic diagram of cumulative (daily basis) seismic energy (Hanks and Kanamori, 1979) released by volcanic activity from 1 st January 2017 to 31st July 2017. Dashed lines mark the seismic swarms of 1 st February 2018, 16–17 April 2018 and 28–29 April 2018. The seismic energy release is dominated by the M_L 4.1 event of 27 April 2018.

system, Fig. 1), resulting in three well identified blocks: a western block, an eastern block and a southern block (Fig. 7b). The aforementioned spreading to the south and southwest further superimposes on this pattern. The single exception in above pattern is the point ECH1, on top of a

scoria cone (Fig. 7b), which slides downslope at a rate of 3.4 mm/yr to the north-northwest.

The thin orange zone in Fig. 7b highlights the dome sector where the strongest azimuthal direction gradients occur, together with important

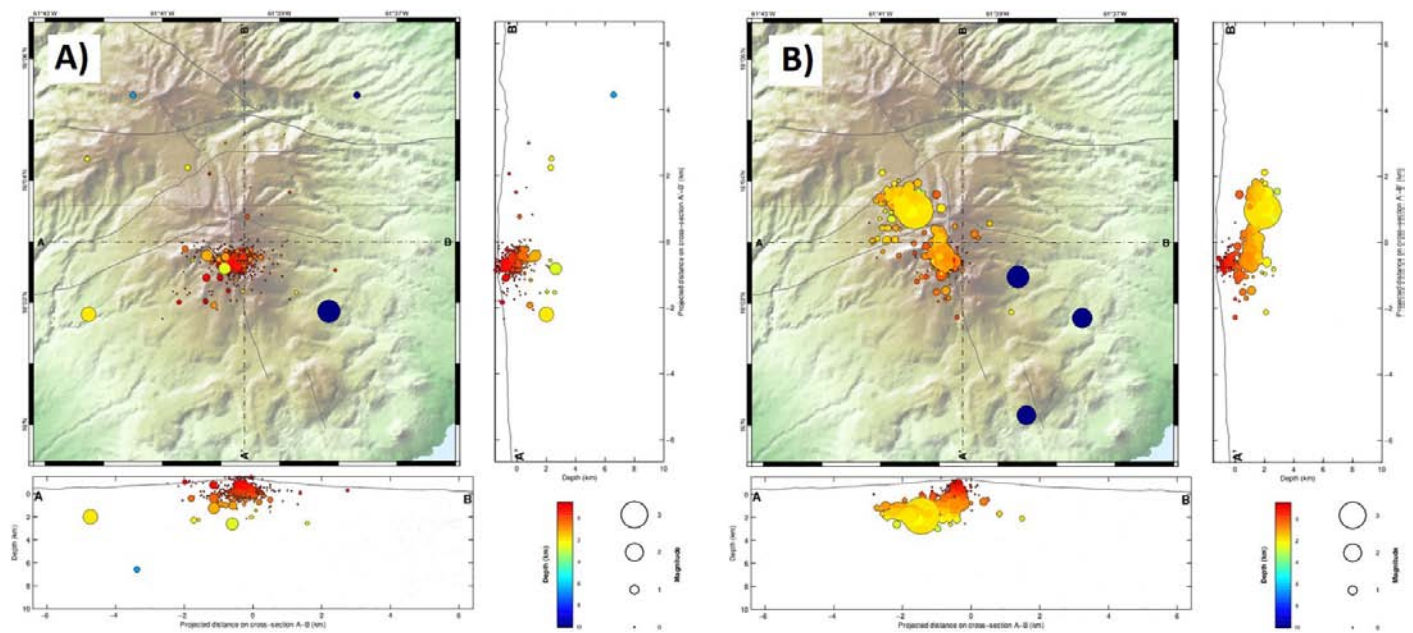


Fig. 6. Maps of the seismic activity recorded within, below and around the La Soufrière dome. Panel a) Seismic records in year 2017. Panel b) Seismic records from 1st January 2018 to 31st July 2018. See Supplementary Figs. S1–S5 for relevant periods described in text. Blue circles refer to mid-crustal seismic (depth > 6 km b.s.l.) events which occurred off-volcanic axis and with maximum magnitude of 2.5. Results are based on the adoption of the 1D velocity model of Dorel et al., 1979 and the use of the NonLinLoc algorithm (Lomax et al., 2000) for hypocentral location. (For interpretation of the references to colour in this figure legend, the reader is referred to the web version of this article.)

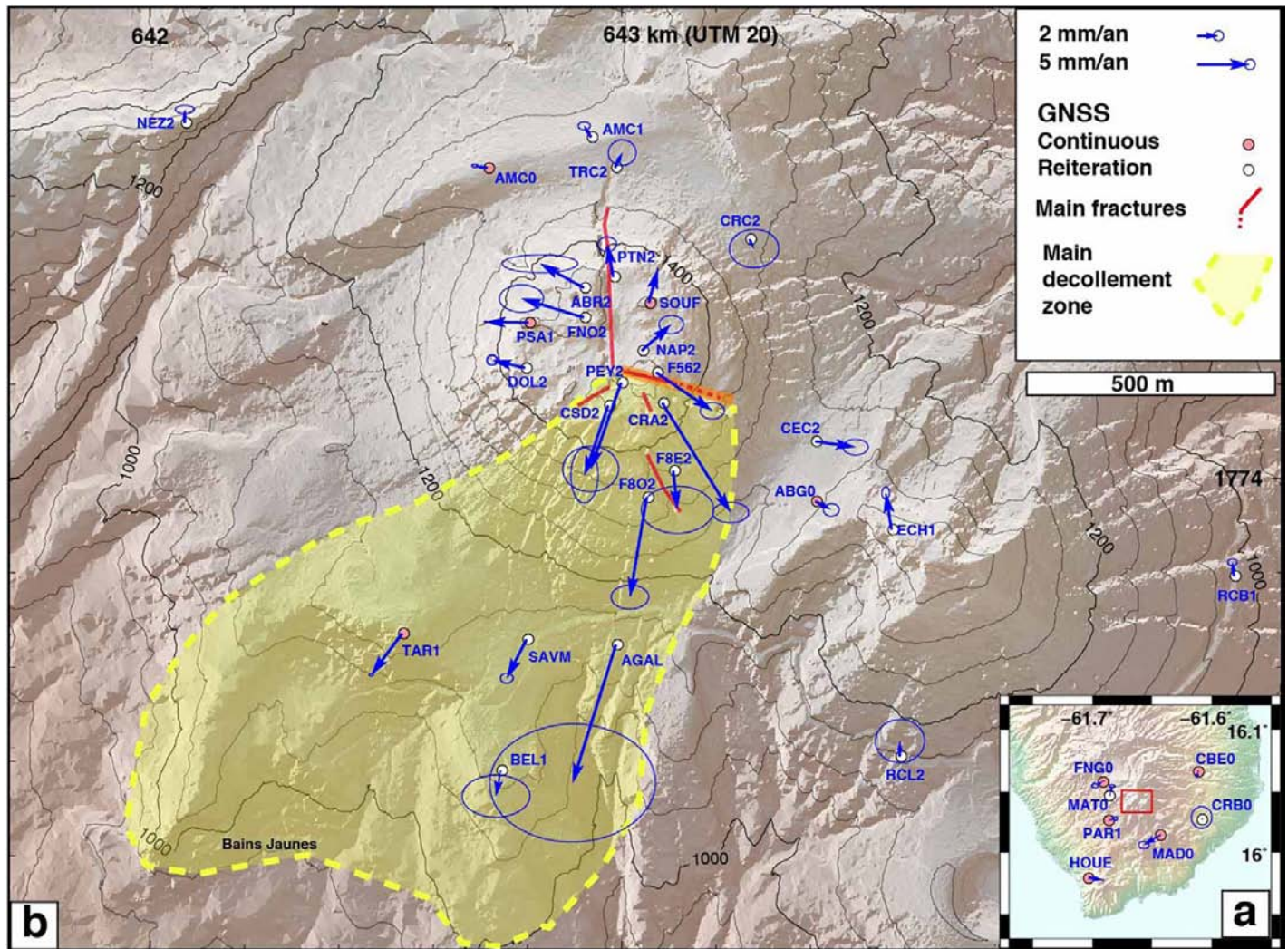


Fig. 7. GNSS horizontal velocities from 1995 to 2018 with respect to Guadeloupe archipelago (de Chabaliere et al., in preparation). Error ellipses are 95% of confidence. The same scale have been used for south Basse-Terre Island (panel a) and La Soufrière volcano (panel b). Red box on panel a give location of panel b. (For interpretation of the references to colour in this figure legend, the reader is referred to the web version of this article.)

deformation. It corresponds to the Napoleon-Breislack fracture where fumaroles reactivated most recently between 2006 and 2014. This is the main extension zone whose opening reflects the combined effect of both hydrothermal flow (Rosas-Carbajal et al., 2016) and the southwest flank sliding of the dome. The other gradient zones (yellow-dashed in Fig. 7b) are scarcely or not at all marked by fumarolic activity and fracturing, but in some sectors are characterized by diffuse soil degassing (Allard et al., 1998; Komorowski et al., 2013; Fig. 1).

3.2.2. Extensometry

One-dimensional extensometry measurements are taken on fractures 0.4 to 20 m wide. Since the installation of the extensometry network in 1995, measurements showed a general tendency of opening of the faults and fractures in the active fumarolic zones, as well as along the dome fracture that formed during the phreatic eruption of 30 August 1976. Gouffre Napoleon (NAP1 in Fig. 8) is the site affected by the largest extension and shows that extensional movements occurred with different rates in different periods (Fig. 8b). Specifically, we recognize four consecutive periods (1995–1999, 1999–2003, 2003–2016, 2016–to date), the second marked by quiescence and the others by extension, with the most recent period characterized by the largest extension rate.

In general, fracture opening at some sites appears to be partially compensated by local closing of other, adjacent, fractures located

outside or on the margins of the active fumarolic zone. This behaviour strongly suggests that the shallow stress field is determined at the depth of the hydrothermal system by a mechanism similar to simple shear (Buck et al., 1988). The opening trend at almost all fractures observed since mid-2016 is thus compatible with a pressure increase in the hydrothermal source, determining the displacement field and the switch to conditions close to pure shear (Buck et al., 1988).

Interestingly, a closer inspection of data between 9 March and 25 April 2018 shows a reversal in this opening trend (Fig. 8a), implying a slight closure of the active fumarolic zones on the top of the dome except for one point along Gouffre Dupuy (DUP1, Fig. 8a). Such a reversal thus indicates a hydrothermal pressure drop. Instead, subsequent measurements in June and August 2018 reveal a renewal of the generalized extensional trend (Fig. 8a), suggesting a new overpressure phase of the hydrothermal source of deformation.

3.3. Fumarole thermal data

CS fumaroles (CSS, CSC, CSN; Fig. 2) show generally high flow rates and large deposits of solid sulphur. A decrease in the discharges was observed after the passage of hurricane Maria (mid-September 2017), probably in response to the huge amount of water infiltrated into the subsoil and thus into the shallow hydrothermal system (the measured rain water level on top of the dome was 440 mm in 24 h due to the

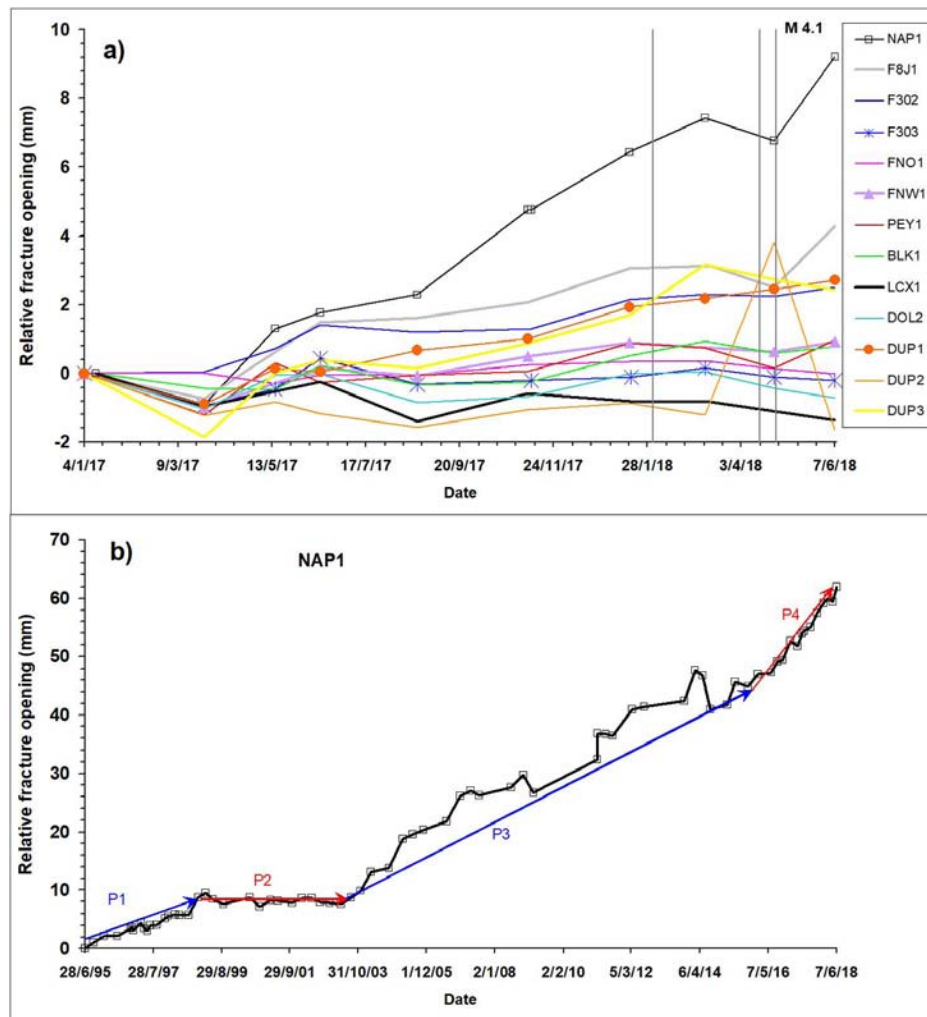


Fig. 8. Panel a) Extensometric measurements during the last year (August 2017–July 2018) at all sites. Note the enhanced dynamics shown by the NAP1 site. Panel b) Extensometric measurements at the NAP1 site since network installation (1995) with indication of the four periods, corresponding to different extensional velocities (see text). See Fig. 2 for location of measurement sites.

hurricane's passage, 2017; OVSG-IPGP, 2017). Starting in November 2017 fumarole fluxes have begun to increase to pre-hurricane values.

Driven by the interaction between hot magmatic fluids and the hydrothermal system, La Soufrière manifestations develop a number of sites where heat is preferentially transported to the surface, as commonly observed at many volcanoes in hydrothermal stage (e.g. Chiodini et al., 2001; Harris, 2013; Sigurdsson et al., 2015). Convection of water vapour transports heat from depth to the surface. Vapour travelling through the most porous conduits leads to fumaroles (e.g. CS). Near-surface steam condensation leads to large temperature gradients, conduction of heat to the surface forming thermal anomalies (e.g. Faille de la Ty, FTY; Fig. 1). Condensed water escapes laterally, mixing with meteoric water and forming hot springs. At La Soufrière the latter contribute marginally to the overall heat budget (Allard et al., 2014; Gaudin et al., 2016) and we will not discuss them further. Moreover their chemistry and temperature have remained stable over the last 10 years (Villemant et al., 2005, 2014; Ruzié et al., 2012, 2013; OVSG-IPGP, 1999–2019). Accordingly, thermal monitoring in the form of (discrete) manual temperature measurements have been carried out over the last 20 years, roughly one per month. More recently, continuous measurement stations utilising PT100/PT1000 resistance temperature detectors have been installed at several key fumarolic sites with acquisition rates of 1 s. At the time of the 2018 crisis, the CS fumaroles (central, north and south, labelled CSC, CSN, CSS, respectively; see Fig. 2 for

location) had been instrumented with continuous measurements commencing on 14 April, and were routinely measured manually (for CSC, CSN and NAPN). Additionally, vent speed measurements were made using a Pitot tube instrument at CSC, CSN, CSS and NAPN though, especially in the case of CSS which requires specialised roped-access techniques, these were done less frequently.

The historical temperature record shows that fumarolic vents typically have temperatures corresponding to saturated steam vapour at the pressure of the summit ($\sim 95^\circ\text{C}$) (Fig. 9a). Fumaroles CSC and CSN have shown short-lived fluctuations up to 140°C (cf. June–1999 to Feb–2000 at CSN) and longer-duration increases up to 110 or 120°C (cf. Sept–2011 to Mar–2013 at CSC). Early during the April–2018 unrest phase, the fumarole temperatures rose again, attaining maxima of 111.4°C at CSC on 3rd April, and 109.7°C at CSN on 23rd March (according to the manual measurements). We also note the remarkably constant temperature at NAPN at around 95°C since its appearance in 2014 (Fig. 9b). After the aforementioned maxima, temperatures dropped rapidly to 104°C (19 April 2018) and then to the background saturated vapour value (96°C , 28 April 2018). The rapid temperature drop in the CS area is well detailed by the continuous measurements at CSC and CSN (Fig. 9b) which demonstrates that the saturated steam temperature was reached on 26 April, one day prior the M_L 4.1 earthquake. Indeed, the continuous measurements indicate that the temperature decreased in several stages, the temperature decreasing by 2 – 4°C

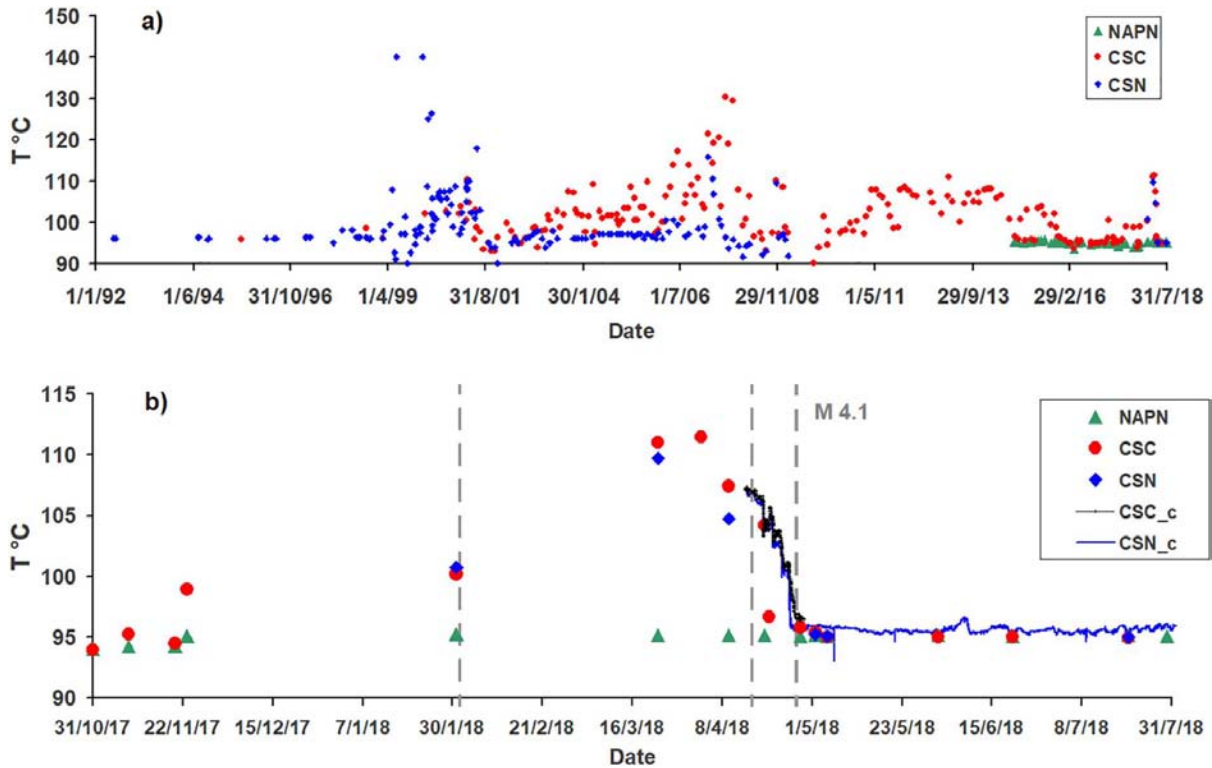


Fig. 9. Panel a) Temperatures (discrete measurements) at CSC, CSN and NAPN fumarolic sites over the last 26 years. Panel b) Temperatures since October 2017; symbols refer to discrete measurements at fumarolic sites, the solid lines refer to continuous measurements at the CSN and CSC (CSN_c and CSC_c, respectively) since installation in April 2018. Vertical lines correspond to the onset of the three major seismic swarms of 2018 (1st February, 16 April and 27 April).

at each stage. From these data, we conclude that during the early 2018 unrest phase, fumarolic fluid at CS was superheated with respect to the temperature of boiling water at the elevation (Fig. 9).

In parallel, venting gas speeds measured at CSC and CSN dropped from 80 and 53 m/s, respectively on 6th April to 20 and 33 m/s, respectively, on 25th April. Following the M_L 4.1 earthquake fumarolic flow rates decreased, becoming so low that, on 29th April, it was not possible to reliably measure gas speeds from vents located at any of the CS vents. Fumarole heat flux, which is globally proportional to vent speed, thus also decreased by a factor of four from around 20.0 ± 4.5 MW to around 5.0 ± 1.1 MW (see Fig. 10; for details of these calculations, please refer to Supplementary Material). These vent speeds and the temperature measurements noted above suggest that the total steam flux at CS dropped from a maximum of around 8.0 ± 1.0 kg/s at the beginning of April to about 3.5 ± 0.5 kg/s soon after the 27 April. This latter

value is of same order as CS steam fluxes previously estimated from MultiGAS traverses in 2006 (0.87 kg/s), 2012 (1.72 kg/s) and May 2016 (0.52 kg/s) (Allard et al., 2014; Tamburello et al., 2019), indicating a slow but significant over the past decade or so. Instead, our values of steam and enthalpy flux are substantially lower than those of Gaudin et al. (2016), who estimated the CS steam and enthalpy fluxes (thermal camera data collected in 2010) to be 19.5 ± 4.0 kg/s and 48.0 ± 9.8 MW, respectively. We note that Gaudin et al. (2016) estimated the fluxes at some distance from the vent and did not correct for the effect of entrainment of ambient air into the plume and the resulting increase in plume volume. As such, it is peculiar, even given the fluctuating though increasing activity at La Soufrière, that the 2010 survey found such large values for both steam and enthalpy flux, particularly with respect to the 2006 and 2012 MultiGas-based estimation. It may be the case that the approximations made during their study affected their results

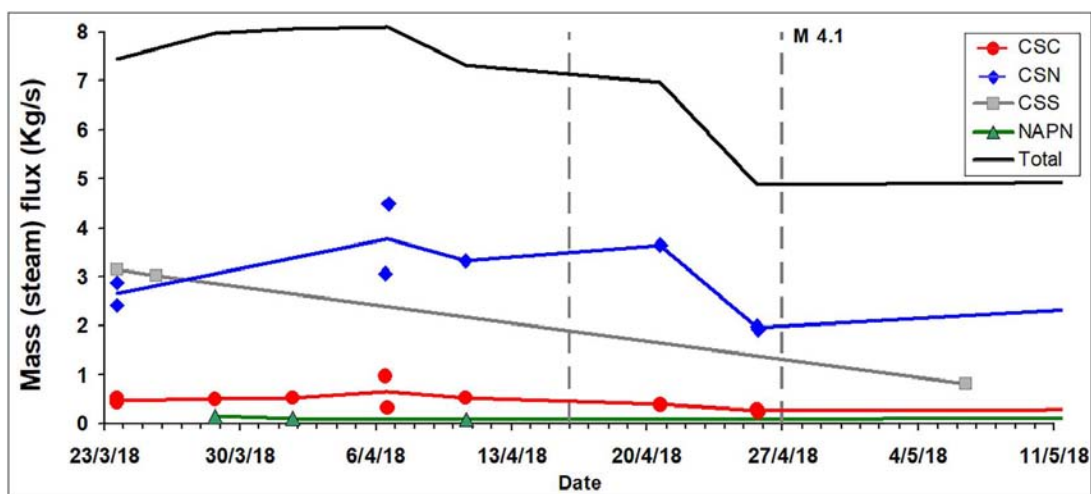


Fig. 10. Steam fluxes determined from gas exit velocities (measured by Pitot tube) from 23 March 2018 to mid-May 2018.

more than was anticipated, potentially doubling the measurement uncertainty, in which case their values fall more in line with those found here. A complete inventory of the heat flux discharged by the dome (particularly its partitioning between fumarolic, soil diffuse and hot spring fluxes) is currently missing. Its temporal evolution since the 2010 estimate (Gaudin et al., 2016) is thus uncertain. However, we must suspect a thermal flux increase since 2010, because of the reactivation of many emission sites (e.g., G56, Lacroix Superieur, NAP; see below), the emergence of new sites (NAPN, NAPE1, NAPE2) and the concurrent increases in soil temperatures and extent of vegetation decay in soils with degassing at the summit (OVSG bulletins).

3.4. Fluid Geochemistry

3.4.1. Fumarole chemistry

For fumarolic sampling and gas analysis at La Soufrière the OVSG-IPGP Observatory uses the “Giggenbach”-type soda bottle methodology (e.g., Giggenbach and Goguel, 1989; see Supplementary Material). This method permits to obtain the complete, internally consistent, chemical composition of the fumarolic fluid, with an accuracy and precision that could not be attained by previous chemical routines, essentially based on P₂O₅-filled sampling bottles (Fabre and Chaigneau, 1960). The reader may refer to Allard et al. (2014) and particularly to Villemant et al. (2014) for the database of gas samples obtained with this latter sampling technique. Since November 2017, the procedures for gas sampling and analysis were improved at OVSG-IPGP. For consistency, we here report and discuss only the data obtained from that date. Fig. 11 shows the temporal evolution of major chemical indicators (molar ratios for gas/steam, C/S, CO₂/CH₄, He/CH₄, H₂/H₂O and CO/CO₂) in the CSC fumarole, the most accessible and surveyed fumarole on top of La Soufrière (see Table 1 for chemical analyses). For comparative thermodynamic calculations (see Section 4.2), we also include the other available and fully consistent soda-based data from summit emissions, sampled in 1997 by Brombach et al. (2000) and in July 1976 by Chevrier et al. (1976).

Since water vapour in La Soufrière fumaroles is essentially of meteoric (rainwater) origin whereas the major gas components have a magmatic derivation (Brombach et al., 2000; Villemant et al., 2014; Allard et al., 2014), variations of gas/steam ratio essentially reflect changes in the proportion of the deep, magma-derived, gas with respect to the meteoric component in the hydrothermal system. This ratio can increase due to either the arrival of magmatic gases or/and the condensation of water vapour. Instead, increased boiling will make it decreasing because of steam addition. As regards the C/S ratio, it can increase either due to either the uprise of deep magmatic gas (often associated with a temperature increase), because CO₂ in magmas is much less soluble than sulphur-bearing gas species and then degasses much earlier (e.g., Moretti et al., 2003 and reference therein) or a loss of sulphur in the hydrothermal system (scrubbing of SO₂ and H₂S, as well as precipitation of sulfides and/or native sulphur; Allard et al., 2014; Villemant et al., 2005; Tamburello et al., 2019), this latter process being often associated with a decrease in temperature.

Methane is absent in hot magmatic gases and is a typical component of low-temperature or/and reduced hydrothermal fluids (Giggenbach, 1987). The CO₂/CH₄ ratio is thus a powerful indicator of magma degassing episodes because it is orders of magnitude higher in magmatic gases than in hydrothermal fluids. Accordingly, an increase of CO₂/CH₄ in fumaroles clearly indicates an enhanced supply of CO₂-rich oxidized and hot magmatic gas whose effect will be to oxidize and potentially warm the base of the hydrothermal system, thereby limiting the conversion of CO₂ in CH₄ at low temperature (Chiodini, 2009). Depending on the extension of the hydrothermal system and the intensity of the magmatic gas injection, there may be a time delay between the gas arrival and the observation of a CO₂/CH₄ peak anomaly at the surface (Chiodini, 2009).

Similarly, peak increases of the He/CH₄ ratio point to the arrival of deeply derived gases of either magmatic (e.g., Chiodini et al., 2015) or crustal origin, which can be discriminated on basis of the ³He/⁴He isotopic ratio. At La Soufrière, helium present in both fumaroles and hot springs has been shown to be of pure MORB-type magmatic origin (e.g. Allard, 1983; Ruzié et al., 2012, 2013; Jean-Baptiste et al., 2014). Owing to their much lower mass than CO₂, both ³He and ⁴He can diffuse much faster than CO₂ over the ascent path of fluids, so that deep gas inputs into a hydrothermal system should be first detected by increasing He/CH₄ and later on by increasing CO₂/CH₄.

CO and H₂ are fast reactive species obeying the following equilibria.



Owing to the fast kinetics of these two reactions, both the CO/CO₂ and H₂/H₂O ratios are insensitive indicators of late-stage gas re-equilibration upon ascent and changing oxidation environment (fO₂). Increasing fO₂, at a given T, favors the oxidized molecule (either H₂O or CO₂). The geothermal literature has shown that along typical unspecified hydrothermal mineral buffers of the type $\log f\text{O}_2 = a - b / T$ (K) (with *a* and *b* being positive constants) both H₂/H₂O and CO/CO₂ ratios increase with increasing T, hence fO₂ (e.g., D'Amore and Panichi, 1980; Giggenbach, 1980; Chiodini and Marini, 1998). In addition, H₂/H₂O values can also reflect the occurrence of secondary phenomena, such as boiling and steam condensation from separated and equilibrated single vapours (Chiodini and Marini, 1998; Brombach et al., 2000; see also Section 4.2). On the other hand, the CO/CO₂ ratio is not affected by secondary effects, so that its increase is more directly associated to the heating of the hydrothermal system (Chiodini and Marini, 1998; Chiodini et al., 2015). It is worth recalling that coexistence of water vapour and the liquid (boiling pure water or brines) implies that heating and pressurization are associated, determining the joint increase of both temperature and pressure fixed along the liquid-gas univariant equilibrium.

We note that the gas/steam ratio did not change appreciably in concomitance with seismic swarms, though it did increase by a factor of four (Fig. 11a) on 2 June, before rapidly returning to previous value on 21 June. The present-day gas/steam ratios, except the peak values, are in line with those measured in 1997 (Brombach et al., 2000) and also 1976 (Chevrier et al., 1976). The C/S ratio fluctuates around a mean value of 4 (Fig. 11b), within the range of 1976 values (Chevrier et al., 1976). This is however well below the 1997 data, that were recorded after the dome summit re-activation, when the “dry” gas was essentially made of CO₂ (Brombach et al., 2000), prior to the sulphur enrichment and the appearance of HCl in 1998 (Komorowski et al., 2005; Villemant et al., 2014). No change of the C/S ratio is recorded before, during or after the seismic swarms. The rise in the CO₂/CH₄ ratio (Fig. 11c) appears to occur gradually throughout the period of observation (from 100,000 in November 2017 to 150,000 on 30 July 2018) and is characterized by an increase on late April, followed by a peak at 260000 on 2 June. We note also that Brombach et al. (2000) did not report CH₄ emanating from the summit fumaroles in 1997, which suggests that the activity of the summit hydrothermal system was at its early stage, developing under the forcing of deep magmatic gases.

The behaviour of gas/steam and CO₂/CH₄ indicators is likely related to the increasing influx of a deep gas component, heavily discharged at the surface on 2 June, and bearing a magmatic signature particularly evidenced by the CO₂/CH₄ ratio. Nevertheless, we cannot exclude that secondary effects such as steam condensation upon cooling, and the consequent scrubbing of soluble components, play a role in determining the observed values, especially for sulphur species and so the C/S ratio. This effect is well known to have been important at La Soufrière de Guadeloupe (Brombach et al., 2000), and has certainly contributed to the development of the shallow hydrothermal system. However, its role is

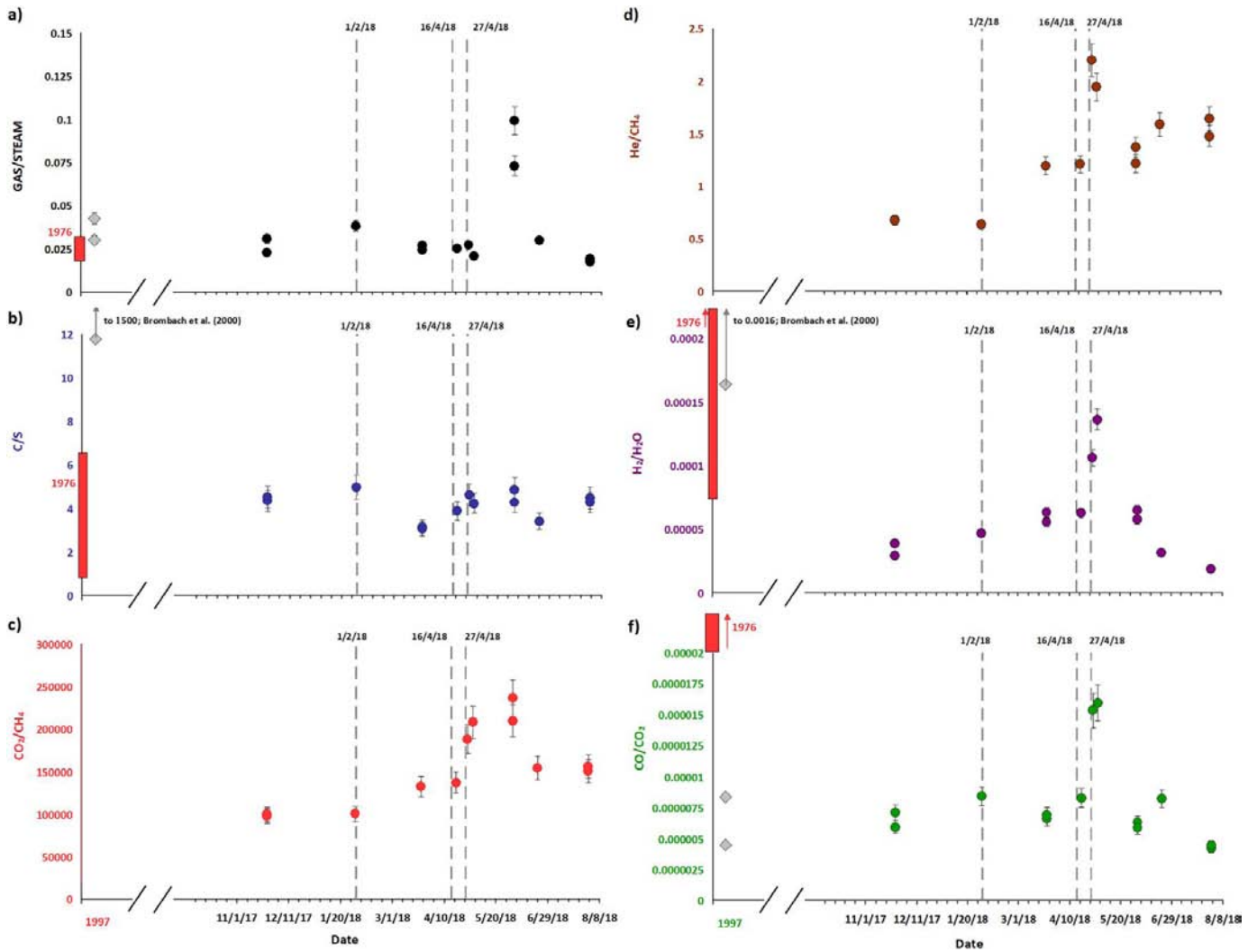


Fig. 11. Molar ratios of relevant chemical species at CSC fumarole since November 2017. Also shown are data from the 1997 sampling in Brombach et al. (2000). Left-side diagrams (panels a–c) show maxima on 2 June 2018, associated with the arrival of the most magmatic gas composition. Right-side diagrams (panels d–f) show maxima on 28 April 2018, revealing a peak in hydrothermal pressure and temperature related with the onset of the M 4.1 earthquake on 27 April 2018. Due to the very low flux at CSC, on 2nd May sampling was carried out at the nearby “twin” CSN fumarole. Vertical lines refer to the 2018 seismic swarms. Error bars are $\pm 11\%$, or within symbol size if not shown. See Table 1 for errors on concentration measurements and the Supplementary Material for additional details.

Table 1

Chemical analyses of fumarolic gases from Cratère Sud Central (CSC) fumarole. Note that the 2 May sample was taken at the Cratère Sud Nord (CSN) fumarole, which is conjugated to the CSC one. Errors on concentrations are given beneath the name of each gas species in the table heading. See Supplementary Material for details.

Date	Fumarole	H ₂ O	CO ₂	H ₂ S	H ₂	CH ₄	CO	N ₂	He	Ar	O ₂
		±2%	±8%	±7%	±5.4%	±4.5%	±4%	±2%	±5.5%	±12.5%	±58%
30/07/2018	CSC	981,210	15,283	3412	18	0.10	0.06	75	0.14	0.34	0.06
30/07/2018	CSC	982,650	13,983	3274	18	0.09	0.06	74	0.15	0.35	0.05
21/06/2018	CSC	970,960	22,321	6574	30	0.14	0.18	112	0.23	0.59	0.43
02/06/2018	CSC	931,921	54,947	12,830	54	0.26	0.35	245	0.36	2.07	0.29
02/06/2018	CSC	909,747	74,557	15,305	59	0.32	0.44	313	0.38	3.07	14.11
02/05/2018	CSN	979,901	15,990	3777	134	0.08	0.26	195	0.15	2.38	1.05
28/04/2018	CSC	973,404	21,630	4695	103	0.12	0.33	165	0.25	1.50	0.60
19/04/2018	CSC	975,536	19,334	4982	61	0.14	0.16	85	0.17	0.49	0.76
23/03/2018	CSC	973,775	19,639	6427	62	0.15	0.13	94	0.18	0.73	2.04
23/03/2018	CSC	976,232	17,878	5706	54	0.13	0.12	127	0.16	1.25	0.69
31/01/2018	CSC	963,147	30,514	6139	45	0.30	0.26	153	0.19	1.39	0.39
24/11/2017	CSC	977,581	18,134	4171	28	0.18	0.11	85	0.12	0.35	0.09
24/11/2017	CSC	969,947	24,491	5402	37	0.25	0.17	120	0.17	0.79	0.75

presently subordinate and the chemical variations shown by the hydrothermal fluids are dominated by primary compositional variations due to degassing of the source. This is in fact well testified by 2 June samples, for which steam condensation cannot explain why they also have the largest CO₂/CH₄ value, given the much larger solubility of CO₂ with respect to CH₄ in condensed steam (Giggenbach, 1980).

These elements, along with the temperature increase, confirm that the hydrothermal system was infiltrated by a major pulse of deep gas. This pulse determined also the rise in He/CH₄, H₂/H₂O, and CO/CO₂ ratios, all peaking around 28 April and 2 May (Fig. 11d–f). The He/CH₄ ratio (Fig. 11d) increases between November 2017 and late July 2018 by a factor of three, showing the increasing contribution of a deep gas, likely of magmatic origin (e.g., Chiodini et al., 2015). A sharp peak in He/CH₄ is observed on 28 April 2018, right after the M_L 4.1 earthquake, which anticipates any other peak, including the CO₂/CH₄ peak (Fig. 11c). Both H₂/H₂O and CO/CO₂ show sharp peaks on 2 May (0.00013 and 0.000015, respectively; Fig. 11e) consistent with the onset of more oxidized conditions and the heating up of the hydrothermal system upon the arrival of hot and oxidized deep gases (e.g., Chiodini and Marini, 1998). Contrary to the He/CH₄ ratio, both ratios do not show an increasing baseline, as shown by the fact that after the peak phase the both attained their lowest values on 30 July 2018. H₂/H₂O peak values overlap with 1976 (Chevrier et al., 1976) values but plot below 1997 data, which were much higher than those observed nowadays because of important steam condensation (Brombach et al., 2000). On the contrary, CO/CO₂ values compare very well with 1997 data but are much lower than those of 1976, suggesting that 2018 heat inputs are below those involved in the 1976 phreatic eruption.

3.4.2. MultiGAS measurements

The OVSG-IPGP uses routinely a portable MultiGAS station (Aiuppa et al., 2005; Shinohara, 2005) to measure the concentration of gas emitted by major craters and structures, and also perform gas flux measurements along traverses through main fumarole plumes (e.g., Allard et al., 2014; Tamburello et al., 2019).

From 2012 to 2016, gas fluxes increased by a factor ~3 and ~2 at CS and Tarissan, respectively, while gas fluxes from G56 have varied from below detection limit to values that are comparable to those from Tarissan (e.g., Allard et al., 2014; Tamburello et al., 2019). Since 2016, measurements show constant gas fluxes at Tarissan and South Crater, with mean values of 5.7 (± 1.6) and 7.5 (± 1) t/d, respectively. Taking into account the high error (~40%) on the flux determination (Tamburello et al., 2019), the gas fluxes at Gouffre 56 can be also considered constant, despite a noticeable variability (4.7 ± 2.6 t/d). Gas concentrations measured on the dome (Fig. 12a) show that a strong chemical perturbation started in March 2018, characterized by increasing CO₂/H₂S and SO₂/H₂S ratios. In details, the C/S ratio is constant at Cratère Sud, as observed with the Giggenbach bottle. The average C/S

value returned by MultiGAS is however ~2 (Fig. 12a), instead of 4 for the data from Giggenbach bottles (Fig. 11). From March 2018, the C/S MultiGAS ratio increased at Tarissan and Napoléon Nord, but not at Cratère Sud and G56. At the same time, the SO₂/H₂S ratio increased slightly at Napoléon Nord and significantly at Cratère Sud reaching a maximum value of 0.18 (Fig. 12b). This is the highest SO₂/H₂S ratio, by at least a factor 2, measured at La Soufrière since the start of MultiGAS measurements in 2012. After 2 May 2018, this ratio returned to previous values, even below detection limit. Furthermore, a MultiGAS survey was also carried out between 16 and 23 March 2018 in the surroundings of the NAPN vent, at a site around twenty meters away from the NAPN vent (Fig. 2b) that does not show a proper fumarolic activity (i.e. a visible flux of steam) but was reactivated with a dry gas emission. Measurements yielded values up to T = 94 °C, SO₂/H₂S = 1.4 and CO₂/H₂S > 50. In addition, OVSG-IPGP also operates a network of three permanent MultiGAS stations at the summit (Cratère Tarissan, G56 and Cratère Sud). Nevertheless, this network, that was partly re-installed after September 2017 hurricanes, suffered further damages by hostile conditions. Therefore, the only reliable measurement in the period of interest is the concentration of SO₂ detected in the plume at Cratère Sud. Data available until 20 April 2018 show a net anomaly starting in early March 2018 and culminating at 1.9 ppm of SO₂ on 7 April 2018 (Fig. 12b). This early start of chemical perturbation is also observed in data from in-situ Giggenbach gas sampling on 23 March 2018, especially for He/CH₄ and to a lesser extent for CO₂/CH₄ (Fig. 11). It is important to note that the MultiGAS measurements show that the chemical perturbation is not only present at Cratère Sud but on the entire dome. These relatively high SO₂ levels at the Cratère Sud occur at the time when the aforementioned SO₂-rich signals were found in the periphery of the NAPN site (on 18–23 March 2018) and are correlated with portable MultiGAS data.

4. Data elaboration and discussion

4.1. Magmatic vs hydrothermal sources and the origin of overpressures: seismic and geodetic assessment

Fig. 5a shows the occurrence of clusters of seismicity increasing in frequency and rate until the 27–29 April swarm. Nevertheless, the seismicity until February 2018 is superficial, being in average observed down to a depth of 1 km b.s.l. (Fig. 5b), thus very distant from the supposed depth of the magma chamber (about 4.5 to 5.5 km b.s.l., or 6 to 7 km of depth below the summit; Pichavant et al., 2018; Villemant et al., 2014). This seismicity comes from the interactions between the flow of heat and gas from the magma at great depths and the presence of superficial phreatic groundwater layers in the volcano. Multiple factors (changes in fracturing, changes in pressure, flow, and temperature of gases, variation in the proportion of liquid water and gas, variation in

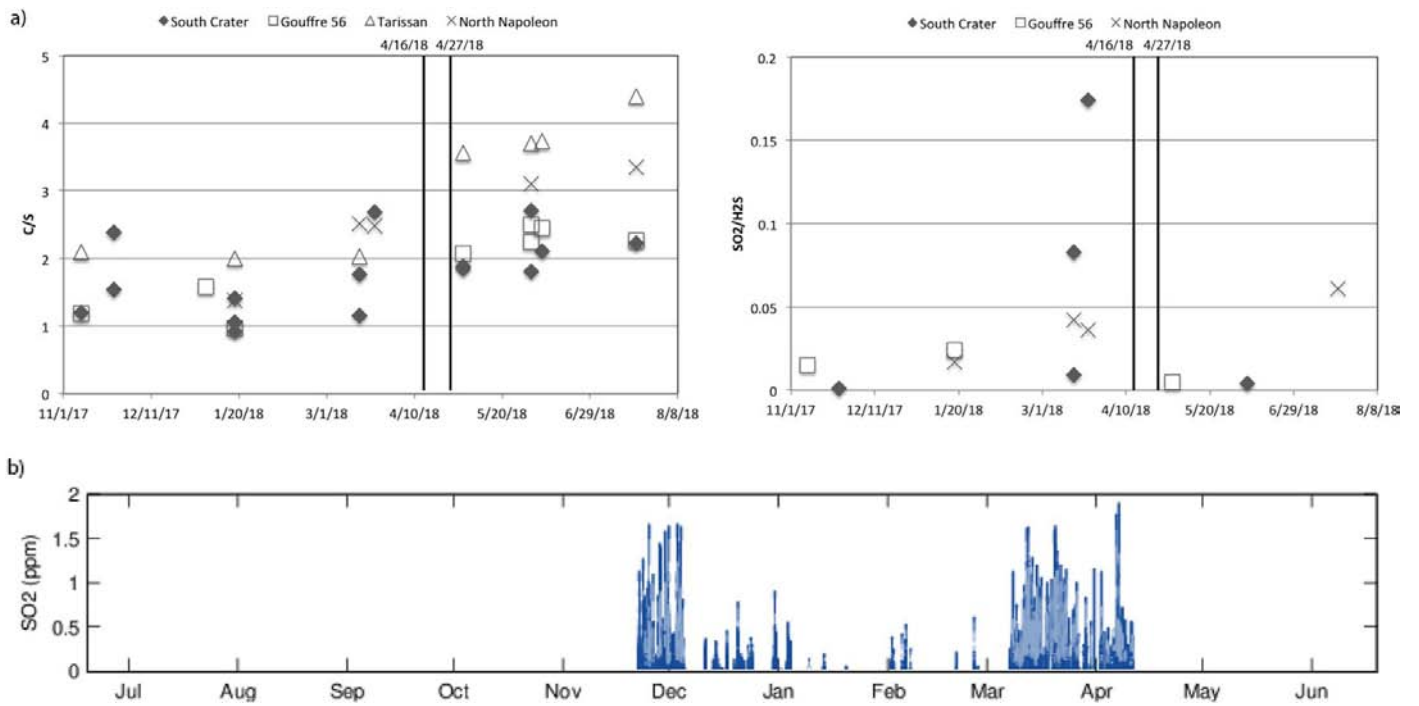


Fig. 12. SO₂ concentration and concentration ratios at major fumarolic vents (Figs. 1,2). Panel a) Chronogram of the C/S ratio (portable MultiGas station) at South crater (CSC and CSS vents), NAPN, G56, Tarissan crater lake (TAS). Panel b) Chronogram of SO₂ concentration (ppm) at South Crater (permanent MultiGas station).

the interaction depth between gases and liquid water) locally generate overpressures that favor an accumulation of deformation until the rock breaks. The corresponding waveforms are of hybrid-type, generally with a long period coda (Fig. 4). It is therefore the activity of the (shallow) hydrothermal system in the broad sense that seems to be at the origin of the typical La Soufrière seismicity, which translates into a weak total dissipated energy (Fig. 5) and does not testify to a deep reactivation of the volcano or to major modifications of its geomechanical response.

Values of the compressional to shear wave velocity, V_p/V_s , were estimated by the slope of P and S arrival time differences as a function of P arrival time (Wadati, 1933) and plotted versus the time to evaluate variations of the medium properties (Fig. 13). The red line in figure represents a moving average of 50 consecutive seismic events. Although an average V_p/V_s value of 1.74 (Fig. 13b) can be estimated, in agreement with the regional value of 1.73 reported by Bazin et al. (2010), Fig. 13 displays major V_p/V_s fluctuations differentiating the 2017 activity from that of January to July 2018. The 2017 activity is in fact characterized by V_p/V_s ratios up to 1.8, whereas two major negative V_p/V_s anomalies (Valley 1 and Valley 2 in Fig. 13) can be observed from December 2017 to the end of February 2018 and from the end of March 2018 to the beginning of June 2018. Highest values in 2017 occur when activity is lowest, i.e. prior to September 2017 (see also Fig. 5a). A significant decrease of the V_p/V_s ratio is observed since the early January 2018 seismic activity peak (V1 in Fig. 13; see also Fig. 5a and Supplementary Fig. S1) giving rise to a negative anomaly in concomitance to the February 2018 seismic swarm (Valley 1, with lowest V_p/V_s at 1.64; Fig. 13), which occurred within the hydrothermal system below the dome. High V_p/V_s ratios are recovered in March 2018, but a strong decrease is then observed since the last week of March 2018, which gives rise to a second negative anomaly (Valley 2, with lowest average V_p/V_s at 1.61; Fig. 13) that lasts until the end of June 2018 and that includes the off-axis seismic swarms that started on 16 April and 27 April 2018. The beginning of this second anomaly is related to the intensification in seismicity observed before the 16 April 2018 swarm (V2 in Figs. 13, 5a) and occurs when fumarole steam fluxes were highest (Fig. 10) and temperature peaks were measured at Cratère Sud fumaroles (23 March, Fig. 9) and in the dry vent surrounding the NAPN fumarole, along with increased SO_2 contents (Fig. 12).

The observed V_p/V_s ratios are representative of the volcanic highly fractured, fluid-filled, rocky medium. V_p/V_s variations are then related to the mechanical reaction of the volcanic medium to pore fluid flow, hence to the joint effects of hydrothermal dynamics and hydrological forcing. The two negative V_p/V_s valleys reflect the fact that rock saturated with water at a temperature near water-steam transition would result in a large change in V_p , a small change in V_s , and a large change in V_p/V_s , as reported in Sanders et al. (1995) and shown by experiments conducted by Spencer Jr. and Nur (1976) and Ito et al. (1979). This is consistent with the evidence that high hydrothermal activity, is the main cause of the velocity anomalies (low V_p , low V_s , and low V_p/V_s)

beneath active volcanoes (Chatterjee et al., 1985; Walck, 1988; Nugraha et al., 2019), also favoured by the large aspect ratio (-0.1) of water-filled cracks (Nakajima et al., 2001).

Therefore, it seems that the observed seismicity reflects the weakening of the rocky medium due to fluid infiltration and hydrofracturing, determined by the increase of pore pressure (e.g., Nakamura, 1977; Miller et al., 1996; Miller and Nur, 2000; Sibson, 2000; Terakawa et al., 2010). Pore pressure increase on infiltration is not necessarily homogeneous, and when it is localized into a narrow source, seepage forces originate that modify locally the stress-state (Mourgues and Cobbold, 2003; Rozhko et al., 2007). However, recovery of the V_p/V_s ratio, hence of nominal rock properties, was rapid after the 1 st February swarm, while it was much slower after the 27–28 April 2018 swarm and still incomplete in July 2018. This is related to the high energy of the 27 April M_L 4.1 earthquake (Fig. 5c), with the involvement of a much larger seismogenic volume.

Geodetic data in the Basse Terre sector show that, down to a depth of 8 km b.s.l., the measured inflation is not associated with large intrusions. In addition, the nearly radial shape of the (shallow) dome deformation (Fig. 7a) suggests that deformation is associated to fluid overpressures within the hydrothermal system (e.g., Battaglia et al., 2006). The pattern of dome radial spreading is however perturbed by the detachment of the southwestern sector over 1.3 km of distance at a speed of 5–7 mm/year. This is consistent with imaging by electrical-resistivity tomography (Rosas-Carbajal et al., 2016), and with the superposition of three major fracture systems (Northern Fault, the Napoléon-56-Breislack system, and the Dolomieu system; Fig. 1) which divide the whole dome in three major blocks. In agreement with extensometric data (Fig. 8), rapid pressure fluctuations of the hydrothermal system may determine a differential response of each block, particularly the emergence of a mechanism of simple shear, more superficial and important during low-pressure phases when the perturbation to the radial, symmetric, deformation is largest and produces the closure of some fractures (Fig. 8).

One might expect that observed deformations and seismicity are related to the switch from drained to undrained conditions of the boiling hydrothermal system and of shallow phreatic fluids circulating through the porous medium. Under undrained conditions, rapid pore pressure build-up takes place until the occurrence of hydraulic fracturing breaks the host rock; as testified by the low V_p/V_s values observed in April 2018 (Fig. 13). Nakamura (1977) first suggested that hydraulic fracturing is an important process in generating volcano-hydrothermal seismicity and in the case of La Soufrière de Guadeloupe this argument was invoked by West et al. (1978). Hydraulic fracturing of a rock occurs when the effective fluid pressure overcomes the tensile strength of the rock and any confining pressures. This is expressed as $P_b = 3\sigma_3 - \sigma_1 + T - P_0$ where P_b is the formation breakdown pressure of rock of tensile strength T at a pore pressure P_0 in a compressive stress field with σ_3 and σ_1 the minimum and maximum principal stresses, respectively, on the plane orthogonal to the infiltrating fluid stream

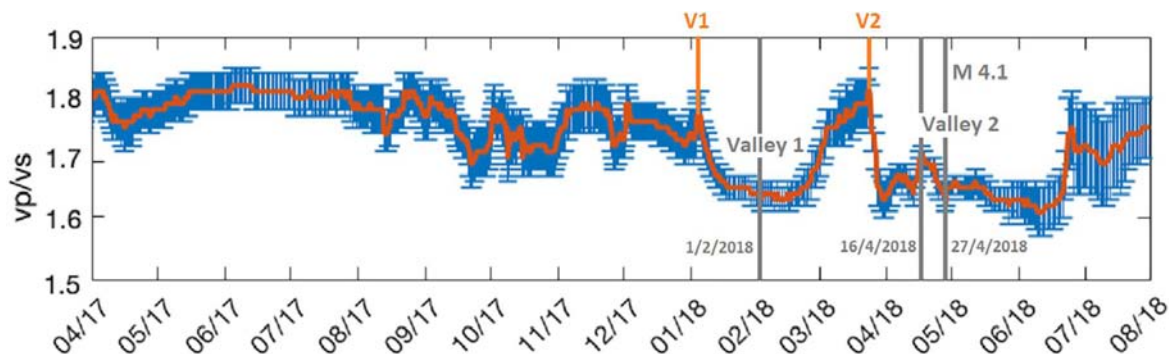


Fig. 13. Chronogram of V_p/V_s ratio, calculated from the Wadati method (1933) (panel c). Solid lines in each panel represent moving averages of 50 events, according to the expression for seismic rate (see text).

(Kehle, 1964). Only fluids with a low viscosity, such as steam, have a great ability to influence the pore pressure P_0 and reducing the pressures necessary for fracturing. In addition, low viscosity fluids can open existing fractures even if their orientation is other than parallel to the maximum principal stress (Zoback et al., 1977). This is the reason why some fractures and faults of the summit (including the 8 Juillet and Napoléon faults) behave very dynamically, as observed via extensometric measurements.

It must be noted that the rate of pressurization also affects the breakdown pressure, a high rate of pressurization resulting in an anomalously high breakdown pressure (Haimson and Zhao, 1991; Schmitt and Zoback, 1992). As the rate of pressurization increases, in a volcano, the mode of deformation may change from viscous to plastic and then to elastic, at high rates of pressurization (West et al., 1978). We then definitely hypothesize that the rapid pressurization determined by the onset of undrained conditions led to the M_L 4.1 (or M_w 3.7) earthquake of 27 April. Indeed, its focal mechanism and features (see Supplementary Material and Supplementary Fig. 6) identify a NW-SE normal fault dipping $\sim 40^\circ$ to the NE (Fig. 14), coherent with active regional faults (Feuillet et al., 2011). Shallowly dipping faults in extensional tectonic regimes are known to be reactivated by elevated fluid pressure (e.g., Collettini and Barchi, 2002; Sibson, 1990, 2000; Mickelthwaite and Cox, 2006; Cox, 1995; Terakawa et al., 2010) and variations of fluid pore pressure related to hydrothermal fluid circulation are known to explain seismic activity in volcanic environments (e.g., Ventura and Vilardo, 1999 and references therein). A good analogy is offered by the seismic activity of Mount Vesuvius (Italy), particularly its 9 October 1999 earthquake ($M_L = 3.6$), for which no significant departure of the fault mechanism from a double-couple source can be inferred (Del Pezzo et al., 2004; Zollo et al., 2002).

The epicentres of 16–17 and 27–29 April 2018 swarms, although separated by an aseismic segment (Fig. 6b, Supplementary Figs. 3,4), define a structure whose direction is that of all the active regional faults that cut the volcanic arc and cross the Basse-Terre through the La Grande Decouverte-Soufrière complex (Fig. 1). A fault of the same orientation has so far not been mapped in this area, perhaps because hidden by recent volcanic deposits. We suggest that the hybrid waveforms of the 16–17 swarm and especially of the subsequent ~ 30

hybrid events, point to invading high-pressure fluids along the shallowly dipping NW-SE structure, which may have locally weakened the fault through the rapid reduction (on the scale of days) of the effective normal stress acting on the fault plane (e.g., Collettini and Barchi, 2002; Sibson, 1990; Terakawa et al., 2010; Rozhko et al., 2007). We also suggest that the lack of spatially continuous seismicity between 16 and 17 and 27–29 April swarms can be explained by a change in dilatation and pore pressure polarity (contraction at the 27–29 April site, expansion in the 16–17 April one, near the La Soufrière de Guadeloupe dome), in line with the explanation provided by Miller et al. (2010) for the lack of seismicity observed in 1995 at Montserrat along the structure connecting the Soufrière Hills volcano and the St. George Hills.

Feuillet et al. (2011) have studied the collocation of active and recent volcanic vents (e.g., La Soufrière of Guadeloupe and Soufrière Hills, Montserrat) and faults in the Lesser Antilles arc, and have shown that faulting and volcanism are organically connected and likely interact, through coupling mechanisms determined by static or dynamic stress changes (e.g., Brodsky et al., 1998; Nostro et al., 1998; Linde and Sacks, 1998; Hill et al., 2002; Marzocchi, 2002; Troise, 2001; Walter and Amelung, 2007 and references therein). It appears in fact that such coupling mechanisms can lead to unrest or eruptions within few days, months, and perhaps years at neighbouring volcanoes (Nostro et al., 1998; Watt et al., 2009).

4.2. Magmatic vs hydrothermal sources and the origin of fluid pressures: geochemical assessment

4.2.1. Gas end-members and secondary processes

The elements shown and listed so far clearly point out an indirect forcing of deep hydrothermal and/or magmatic origin. A first increase in SO_2 content and in SO_2/H_2S via MultiGAS (Fig. 12), and in fumarolic CO_2/CH_4 and He/CH_4 (Fig. 11c,d), was in fact seen on 23 March. The further sharp evolution leading to the peaks in the He/CH_4 , H_2/H_2O and CO/CO_2 ratios (Fig. 11d–f) that occurred in concomitance with the 27 April 2018 highly energetic earthquake (M_L 4.1), suggests that a direct link exists between the heating and overpressurization of the hydrothermal system and the rock failure process. This is very likely in relation with the thermal and pressure perturbation of hydraulic boundaries at

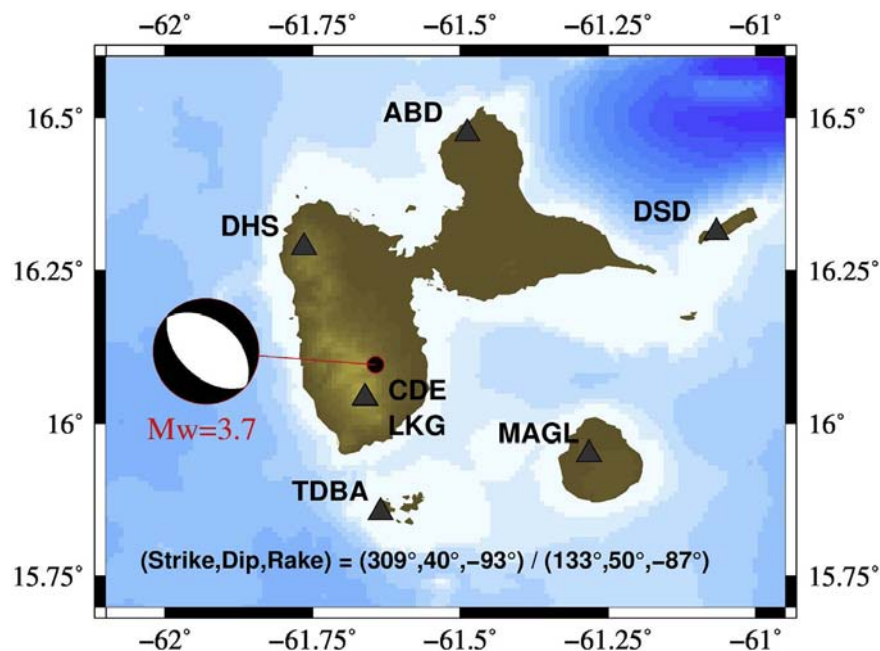


Fig. 14. Focal mechanism and moment magnitude of the 27 April M_L 4.1 earthquake. The 3-component displacement waveforms provided by the 7 seismic stations (indicated by triangles) were used for source parameter determination. The MECAVEL waveform-based method (see Supplementary Material) retrieves an $M_w = 3.7$ moment magnitude and a pure normal-faulting mechanism, whose strike, dip and rake (for the two possible planes) are shown on the map. The optimal epicentral location (lat = 16.08, lon = -61.66) is consistent with the location determined by arrival times (lat = 16.06, lon = -61.67), given the frequency range used in the inversion (0.04–0.7 Hz).

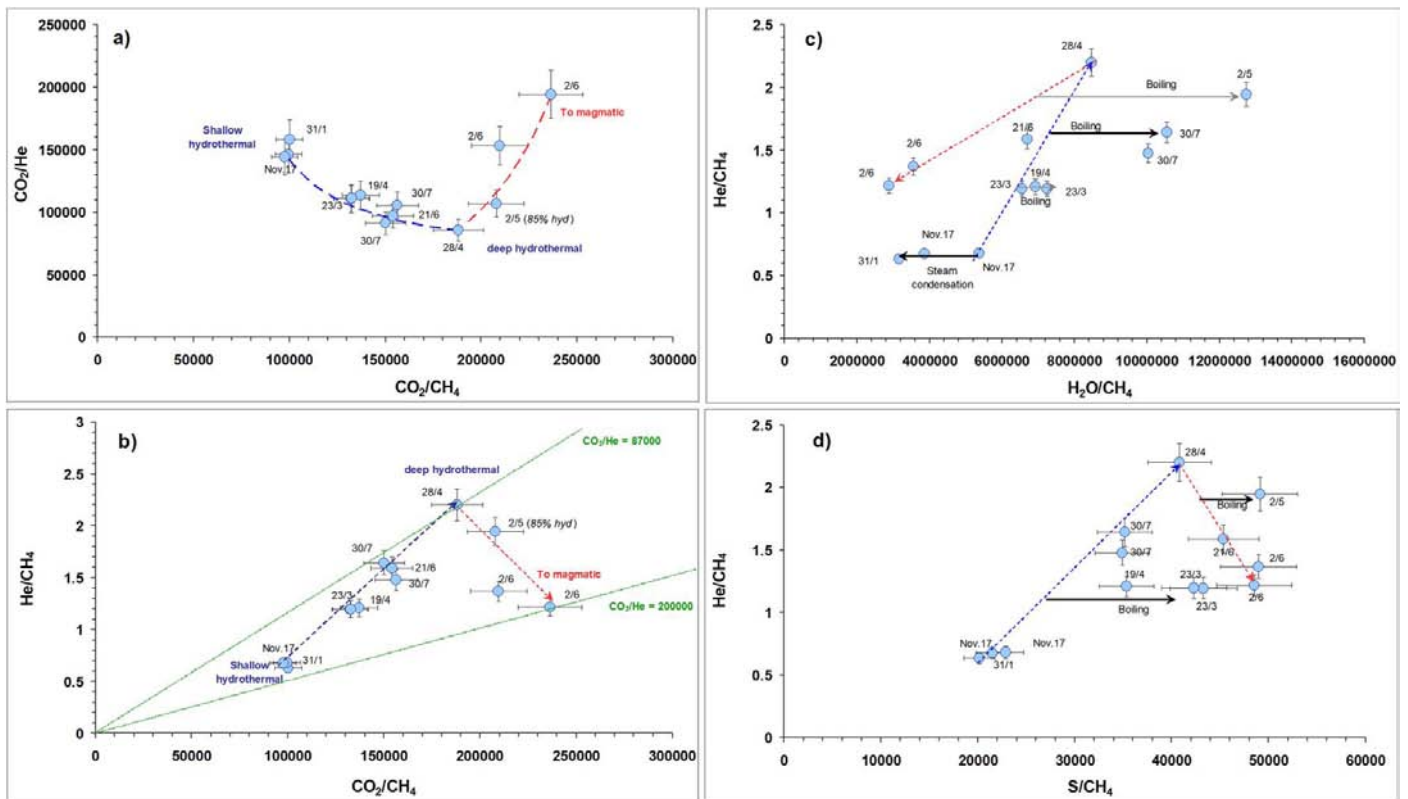


Fig. 15. Covariation of CO_2/He with CO_2/CH_4 (panel a), He/CH_4 vs CO_2/CH_4 (panel b), He/CH_4 vs $\text{He}/\text{H}_2\text{O}$ (panel c) and He/CH_4 vs $\text{He}/\text{H}_2\text{S}$ (panel d), showing a He-rich hydrothermal component (meteoric-local hydrothermal line) mixing with a deep, magma-derived gas component. Secondary effects due to either steam condensation or boiling can be observed in panel c. These effects due to either scrubbing or hydrothermal sulphur remobilization can be observed in panel d. See Supplementary Material for discussion on error bars, which are within symbol size if not shown.

depth due to the arrival of deep gas pulse(s). This produced an enhancement of boiling, which however contrasts with the very low fluxes observed at CS fumaroles, CSC particularly, since late April, and the concomitant temperature drop to values consistent with water boiling at the local atmospheric pressure (~95 °C). This(these) gas pulse (s) was(were) released until 2 June 2018 at least, when maxima in the gas/steam and CO₂/CH₄ ratios were observed (Fig. 11a,c).

In order to discriminate between the different gas end-members (e.g., meteoric, hydrothermal, magmatic) and understand more how they do interact, we first look at the covariation of compositional indicators (e.g. CO₂/He, He/CH₄, CO₂/CH₄) which are not appreciably affected by secondary hydrothermal phenomena (steam condensation, boiling, component scrubbing, remobilization, precipitation). The relative effect of these secondary phenomena can then be assessed by enlarging the approach to indicators such as S/CH₄ and H₂O/CH₄. On this basis, Fig. 15a,b shows that fumarolic fluids prior to the M_L 4.1 event of 27 April 2018, follow a mixing line (dashed lines in all panels), characterized by a CO₂/He ratio evolving from 150,000 (November 2017 and 31st January 2018 samples) to 87,000 (28 April 2018 sample). Along this mixing line, increasing CO₂/CH₄ reflects an approach towards the hot and oxidized conditions typical of the deeper hydrothermal component, which then boils off in the roots of the volcanic dome upon interaction with the oxidized, nearly CH₄-free, magmatic gases. This is accompanied by the CO₂/He decrease (panel a) and He/CH₄ increase (panel b), which point to a He-rich deep hydrothermal component. The helium enrichment of the local deep hydrothermal system can be ascribed to the long-term interaction of the deep hydrothermal fluid with magmatic rocks and the accumulation of radiogenic He, as well as to the contribution of a basal flux mostly determined by a contribution of background andesitic magma degassing. On the other hand, the shallow hydrothermal component is enriched in the very He-poor meteoric component.

We do not know hitherto the chemical composition of the hydrothermal liquid phase that contributes to the groundwaters circulating in the volcanic complex (Ruzié et al., 2012, 2013; Villemant et al., 2005, 2014) and, that underneath La Soufrière dome, boils off the fumarolic fluids discharged at the volcano summit. However, it is highly probable that the deep hydrothermal fluid is a NaCl aqueous solution (Brombach et al., 2000; Villemant et al., 2014). These fluids readily form in active volcanic environments through (1) the absorption of SO₂ and HCl-rich magmatic gases in deeply circulating groundwaters and (2) neutralization of these initially acidic groundwaters by reaction with wall rock containing minerals capable of neutralizing acids, such as feldspars, micas, and other silicates (Giggenbach, 1988, 1997; Reed, 1997; Chiodini et al., 2001). The (deep) NaCl-rich hydrothermal aquifer in its portion surrounding the dome is boiled off upon receiving a considerable input of fluids from a degassing magma body (4.5 to 5.5 km b.s.l., or 6–7 km deep below the dome summit; Pichavant et al., 2018). It then mixes with fast circulating meteoric waters having an average residence time of three months (Bigot et al., 1994). This results in the shallow-to-deep local hydrothermal trend of Fig. 15.

Fig. 15a,b show the presence of another mixing line (red dashed lines in all panels), which we identify as that trending to the more magmatic end-member characterized by the high CO₂/CH₄ ratios (2 June samples, see also Fig. 11c), but also CO₂/He and He/CH₄ ratios higher and lower, respectively, than those of the gas discharged on 28 April (assumed representative of the deep hydrothermal component). This new gas of magmatic origin is different from the one typically interacting with the hydrothermal system because it is characterized by a much larger CO₂/He ratio, consistent with degassing from a deeper or more compressed magma as CO₂ solubility is lower than He solubility in basaltic and andesitic magmas (Nuccio and Paonita, 2000; Caliro et al., 2014). The release of this new gas component becomes evident in the 2 May sample and reaches its maximum in the 2 June samples, which were particularly steam-poor and CO₂-rich (Table 1; Fig. 11a,c). Using the steam-poorest composition from 2 June sampling as the new gas

end-member and the 28 April one for the hydrothermal end-member, we estimate 85% of the 02 May sample consists of the hydrothermal component (Fig. 15a,b).

Hence, the behaviour of CO₂/CH₄, CO₂/He and He/CH₄ ratios suggests that a magmatic gas deeper than that usually soliciting the hydrothermal system has intervened and led to the unrest episode recorded between February and late April 2018. Therefore, this gas, discharged after the seismic peak of 28 April, heated up and then pressurized the hydrothermal system prior to becoming detectable at the fumaroles. This mechanism explains the He/CH₄, H₂/H₂O and CO/CO₂ peaks (Fig. 11d–f) roughly concomitant with the M_L 4.1 earthquake and should imply increasing boiling of the hydrothermal system feeding summit fumaroles. Fig. 15a,b also highlights that after having discharged the “anomalous” deep magmatic gas, fluid compositions returned along the hydrothermal mixing line (21 June and 30 July samples). However, pre-crisis conditions (e.g. November 2017) are not fully regained and sample position along the trend (close to the 28 April values) suggests an important residual deep hydrothermal component.

The He/CH₄ vs H₂O/CH₄ covariation in Fig. 15c shows both negative and positive departures from mixing trends identified in Fig. 15a,b. Negative departures represent steam condensation, and affect early samples (November 2017, 31 January 2018) as well as the 21 June one, which marks the return of the fluid system along the hydrothermal trend. On the other hand, positive departures of the H₂O/CH₄ ratio mean increased boiling with respect to the hydrothermal trend. These are observed for 23 March 2018 (when fumarole temperature reached 111 °C, Fig. 9a), 19 April 2018, but also for 30 July samples. However, the most important boiling effects are seen for the 2 May composition, especially considering that these results by mixing with the “anomalous” magmatic gas that started to be discharged after the seismic peak. It must be noted that the evolution of any hydrothermal system from depth to surface is most likely characterized by a multi-step sequence of secondary processes such as boiling and steam condensation. These are nearly invariantly present at La Soufrière’s summital fumaroles, in light of the vent temperature normally buffered by coexisting liquid and vapour at the local atmospheric pressure (Fig. 9a,b). Nevertheless, the information provided by Fig. 15c summarizes the dominant secondary effect with respect to the current standard conditions occurring along the trends identified in Fig. 15a,b.

Similarly, Fig. 15d allows us to evaluate that secondary effects influencing sulphur concentration (scrubbing versus remobilization of the stored hydrothermal sulphur). It shows that hydrothermal sulphur was remobilized on 19 April, and particularly on 23 March, when anomalous temperatures and degassing were measured in the surrounding of the NAPN site (Fig. 1), with the dry emission of H₂S and SO₂ in nearly equal amounts measured by MultiGAS (Fig. 12). This likely resulted from the start of the heating cycle due to the arrival of relatively high-temperature fluids, which led to the local remobilization of the earlier deposited elemental sulphur (S_e) according to the following reaction (Mizutani and Sugiura, 1982; Giggenbach, 1987):

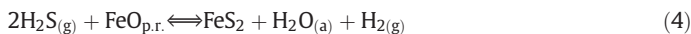


In addition, the difference in C/S ratios measured by MultiGAS between CS and G56 on one side, and Tarissan and NAPN on the other one (Fig. 12a), is likely the result of the larger sulphur scrubbing operated by the acid lake (Tarissan) and the shallow circulating groundwaters (NAPN) with respect to CS and G56 sites.

In Fig. 15d, the 2 May fluid composition appears to be enriched in sulphur with respect to the mixing trend of deep local hydrothermal and magmatic components, in agreement with the boiling effect described in Fig. 15c. Instead, the position of datapoints from 21 June and 30 July, close to each other and along the mixing trend of deep local hydrothermal and magmatic components, contrasts with the findings of Fig. 15c (steam condensation and boiling dominant on 21 June and 30 July, respectively). It also appears that their S/CH₄ ratios are

akin to the one due to the mixing of the deep local hydrothermal gas and the “anomalous” one of deep magmatic origin. Following Giggenbach (1980), it is in fact possible that the many secondary reactions involving sulphur modify the simple picture associating boiling to sulphur remobilization and steam condensation to sulphur scrubbing.

Following the approach described in Moretti et al. (2013a, 2017), the occurrence of perturbations on the hydrothermal equilibrium involving total sulphur as H_2S can be identified by considering the following equilibrium:



in which $FeO_{p.r.}$ refers to a generic oxide component of divalent iron in the pyroclastic rocks, FeS_2 is the pyrite component of sulfide solid phases of the hydrothermal system and the superscripts (a) and (g) refer to aqueous solution and gas, respectively. By considering that activities of $FeO_{p.r.}$ and FeS_2 can be considered constant because fixed by average rock compositions of the hydrothermal systems and that H_2O activity is constant and also close to unity for the system of interest, the equilibrium constant reduces to:

$$\log K_4 = \log \frac{[H_2]}{[H_2S]^2} + const. \quad (5)$$

A hydrothermal system not perturbed by anomalous heating and oxidation phenomena, for example related to the arrival of magmatic gases, should display constant $\log K_4$ with time. Fig. 16 then suggests that the usual hydrothermal equilibrium conditions recorded at the CSC fumarole ($\log K_4 \approx 0$ in Fig. 16) appear being definitely perturbed in concomitance with the 16–17 April 2018 swarm. An increase of $\log K_4$ is in fact observed until 2 May, implying that the hydrothermal system experiences a relative increase of H_2 due to the temperature raise and boiling. The perturbation becomes negative on 2 June, reflecting the arrival of the deep “anomalous” gas (corresponding to the gas/steam and CO_2/CH_4 peaks, Fig. 11a,c), which injects additional sulphur and oxidizes the system. On late June 2018 the perturbation on $\log K_4$ has disappeared.

4.2.2. Thermal and baric evolution of the hydrothermal system

To understand more about the thermal (T) and baric (P) anomalies associated with the progressive arrival of the deep gas, the thermochemistry of discharged fluids must be considered, in order to calculate the P-T conditions of the boiling hydrothermal reservoir. From the chemistry of fumarolic gases, we then compute the P-T conditions of the boiling hydrothermal system feeding summit fumaroles following Chiodini and Marini (1998) (Fig. 17). This method is based on the sum of log ratios between pairs of species making up redox exchanges in

the gas phase and accounts for the fact that multiple oxidation states may be active within the hydrothermal system and that all species ($H_2O-CO_2-CH_4-CO-H_2$) attain the condition of chemical equilibrium (Chiodini and Marini, 1998; Moretti et al., 2017).

From the 1997 data (Brombach et al., 2000) appearing in the diagram of Fig. 17, but for which methane was undetected, we estimated a detection limit concentration of $0.1 \mu\text{mol/mol}$, based on the data from the Authors. The vertical error bars cover two orders of magnitude in CH_4 concentration (0.01 to $1 \mu\text{mol/mol}$) and show the low-weight that this species has on $3\log(CO/CO_2) + \log(CO/CH_4)$ (Chiodini and Marini, 1998). Similarly, 1976 data (Chevrier et al., 1976) were plotted by considering, conservatively, a CH_4 detection limit of $1 \mu\text{mol/mol}$ and a vertical error bar covering two orders of magnitude (0.1 to $10 \mu\text{mol/mol}$). Note that vertical error bars for CSC samples include data dispersion on concentration measurements from replicate samples. Therefore, they are highly conservative and greatly exaggerate the purely instrumental error, which is contained within symbol size.

Fig. 17 shows that CS samples plot within the two-phase field, and that fluids sampled on 28 April 2018 (few hours after the earthquake) and 2 May 2018 fall very close to the critical point of pure water (CP; $374 \text{ }^\circ\text{C}$, 220 bar). Within the two-phase field, boiling occurs and the gas separates from the liquid, theoretically by an isenthalpic process of single-step vapour separation (svss, Chiodini and Marini, 1998). Under this approximation, each sample represent a vapour which falls on a svss line related to the original temperature and pressure of the corresponding boiling liquid on the saturated liquid line (Fig. 17).

This does not mean that the rising hydrothermal fluid does not experience multiple sequential secondary processes, such as vapour gain or loss and multi-step vapour condensation and separation. However, when falling within the two-phase field, measured data are in agreement with an isenthalpic single step vapour separation, which includes all intervening secondary effects and implies that boiling is the dominant one. We notice that the fluid system points to an original boiling liquid normally at $340 \text{ }^\circ\text{C}$ and that since November 2017 the conditions of gas separation have shifted towards the saturated vapour line, i.e. very close to the P-T condition of the original boiling liquid. Assuming the simple scenario of single-step isenthalpic vapour separation, we find that the P-T peak is recorded by the 2 May sample, which represents a vapour separated at $350 \text{ }^\circ\text{C}$ from a liquid phase originally at $370 \text{ }^\circ\text{C}$ and 210 bar . The fraction of separated steam from the boiling liquid is $21 \text{ mol}\%$. Afterwards, the hydrothermal system relaxes, experiencing a P-T decrease, until 30 July samples, when pre-crisis P-T conditions seem to be restored. Fig. 17 thus confirms the hypothesis that the boiling hydrothermal system was thermally solicited up to the critical point of water. Because of the low sampling frequency, we do not know if the critical point of water was finally exceeded, as was seen for July 1976 samples (Chevrier et al., 1976), but this is likely to have occurred. However, the supercritical excursion recorded by 1976

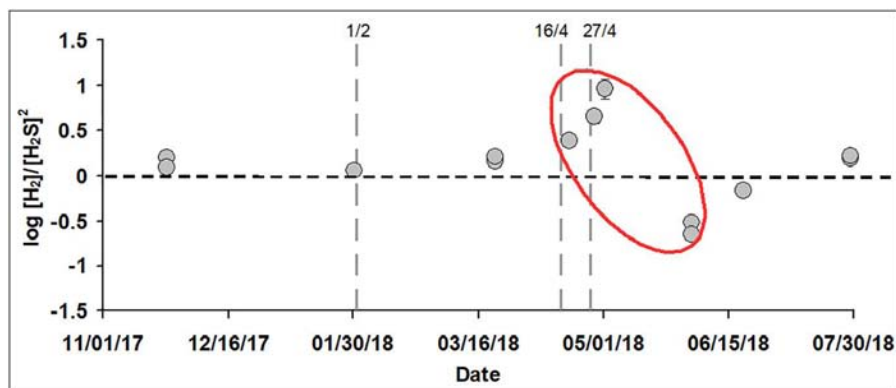


Fig. 16. Chronogram of the hydrothermal sulphur equilibrium (Moretti et al., 2013a, 2017), showing the April perturbation (red ellipse). H_2S is used for total sulphur. (For interpretation of the references to colour in this figure legend, the reader is referred to the web version of this article.)

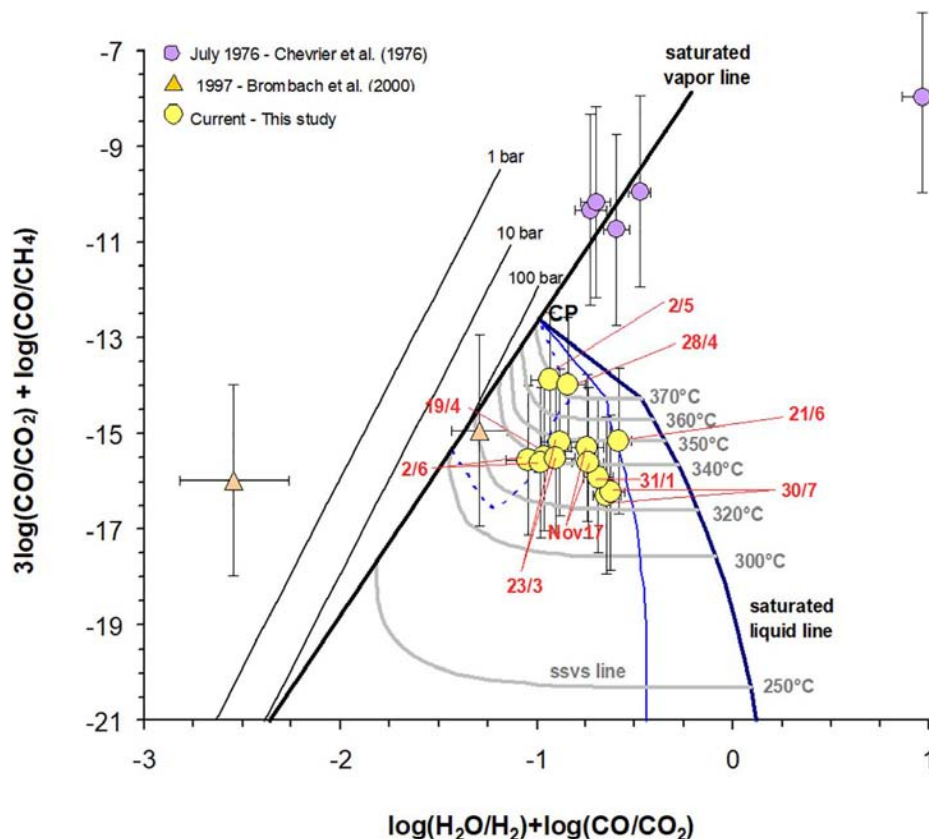


Fig. 17. Plot of the sum of chemical log-ratios within the $\text{H}_2\text{O}-\text{CO}_2-\text{H}_2-\text{CO}-\text{CH}_4$ system. See Chiodini and Marini (1998) for details on the construction of the diagram. Present-day data plot within the field of boiling liquids and represent separated vapour phases. Note that data tend to define a baseline at 340°C , corresponding to the base temperature of the current hydrothermal liquid. Different single-step vapour separation (svss) lines are plotted for different temperatures, connecting the saturated liquid and the saturated vapour. Blue lines are common loci for vapour separation occurring at 100°C (solid line) and 300°C (dashed line). Horizontal error bars are $\pm 11\%$, or within symbol size if not shown. For CSC sample, vertical error bars are $\pm 10\%$, or within symbol size if not shown. In both cases, errors account for the average long-term external reproducibility on gas concentration measurements in our laboratory, by averaging measurements on replicate successive samplings. Therefore, they greatly exaggerate the purely instrumental error, which is contained within symbol size. See also Table 1 for errors on concentration measurements and the Supplementary Material for additional details. For data from Brombach et al. (2000) and Chevrier et al. (1976) error bars are given by the strong uncertainty in CH_4 content (see text). (For interpretation of the references to colour in this figure legend, the reader is referred to the web version of this article.)

data might also reflect separation from a NaCl-brine, whose critical point would be located along the saturated vapour line at temperatures higher than that of pure water (Chiodini et al., 2001). Under both hypotheses (supercritical excursion of pure water vs boiling of a brine), it is supposed that the hydrothermal reservoir feeding the 1976 eruption was much more sealed than the present one (Boichu et al., 2011; Komorowski et al., 2005; Villemant et al., 2014), such that it could either rise in temperature and pressure more easily than currently, or let much less meteoric component to be introduced and to dilute the locally boiling liquid (water or brine). In all cases, the hydrothermal system has clearly evolved since 1997, when steam condensation upon cooling (i.e.; high $\text{H}_2/\text{H}_2\text{O}$ ratios in 1997, Fig. 11e) was the dominant secondary process, as demonstrated by datapoints falling on the left of the saturated vapour line (Fig. 17). Steam condensation thus favoured the growth of the very shallow hydrothermal system, accompanying the formation of acid ponds (Komorowski et al., 2005). Nevertheless, the continuous forcing of magmatic gases, has in time favoured boiling, progressively embracing circulating shallow groundwaters of meteoric origin.

Figs. 11, 15, 16 and 17 show that at the end of June 2018, the hydrothermal system seems to return to the pre-crisis situation observed in late 2017. Given the infiltration of magmatic gases into the hydrothermal system, as well as the high temperatures and pressures inside the hydrothermal system, we believe that the volcanic system was at that time being recharging and was accumulating energy. Additionally, Fig. 17 suggests that the present-day hydrothermal system is in a pre-

1976 condition, such that additional overpressure peaks associated with deep pulses of magmatic gas may destabilize the hydrothermal system and lead to phreatic explosive activity, such as in 1976.

At present, we cannot establish exactly the origin of the deep “anomalous” gas and the mechanism determining its release and ascent into the hydrothermal system. Nevertheless, two reasonable hypotheses can be formulated given our analysis of conjugated chemical indicators based on conservative gas species in the discharged fumarolic fluids:

- 1) the deep “anomalous” magmatic fluid is stored at mid-to low-crustal depths and when a relevant amount is reached, it is transported upward via buoyancy-driven or pressure-driven flow mechanisms (Norton and Knight, 1977; Connolly, 1997). This takes place through a surrounding ductile medium, the brittle-ductile transition being likely located at around 1.5 km b.s.l. (3 km below the Soufrière summit) based on the geochemical conceptual model of Villemant et al. (2014). This deep upstreaming gas fluxes the shallow cooling and crystallizing magma body remnant of the 1530 eruption through cyclic mechanisms rejuvenating its exsolution behaviour (Boichu et al., 2008, 2011; Moretti et al., 2013a, 2013b, Moretti et al., 2019).
- 2) The deep “anomalous” magmatic fluid is released in pulses each related to episodes of fresh injections of basaltic magma in the long-lived (up to thousand years) andesitic chamber located at 4.5 km b.s.l. (6 km depth below the summit, Semet et al., 1982; Touboul et al., 2007. Poussineau, 2005; Pichavant et al., 2018). However, such inputs are likely, too small to be detected by the current

geophysical instruments. Notably, $^3\text{He}/^4\text{He}$ determinations in fumarolic and hot spring gases and considerations on the thermal evolution of springs, together with the observation of contrasting halogen behaviour in spring waters and fumarolic condensates, point to recurrent injection of fresh basaltic magma (Ruzi  et al., 2012; Villemant et al., 2014). Archetype examples of these fresh magma injections would be the one triggering the 1976–77 phreatic crisis, and another one, of smaller size that marked the onset of the long-lasting current unrest around year 1992 (Villemant et al., 2014).

It is of course possible that observed deep magmatic pulses are related to a combination of these two scenarios. Nevertheless, as far as the unrest sequence observed in 2018 were to reoccur, this might escalate to a magmatic phase following the initial phreatic activity, due to the availability of either *a*) rejuvenated magma in the shallow, 1.5 km b.s.l. deep, magma chamber (Villemant et al., 2014), or *b*) deep-sourced (≥ 4.5 km b.s.l.) fresh magma which in the future could directly supply the shallow reservoir.

4.3. Why the 2018 unrest episode must be regarded as a failed phreatic eruption

The evidence that hot springs do not record significant thermal and chemical variations, contrary to summit fumaroles, implies that the hydrothermal system is disconnected from shallower aquifers in the area surrounding the dome. In fact, summit vents are located along a dome axial zone of high vertical permeability due to faults and deep fractures. This allows the rapid ascent of the steam separated by one or more boiling aquifers whereas hot springs discharge from an outer zone, where groundwaters are heated through conduction or addition of small amounts of hot saline liquids coming from deeper hydrothermal aquifer(s) (Brombach et al., 2000; Ruzi  et al., 2012, 2013; Villemant et al., 2014; Rosas-Carbajal et al., 2016), which are too small and readily absorbed.

For simplicity, we assume that the deep hydrothermal system below and surrounding the La Soufriere dome represents a continuum. Consequently, we relate the observed phenomena to the flow of water and steam, thus to the resulting competition between drained and undrained hydraulic conditions, which at the different sites is determined by existing hydrological boundaries (mainly permeability). Therefore, we propose that the P-T variations of the hydrothermal continuum yielded rapid pore pressure increase and undrained conditions particularly along the NW-SE fault structure activated during the 16–17 April and 27–29 April swarms, outside the La Soufriere dome. On the other hand, the fractures connecting the actively degassing dome summit area (a free-surface boundary condition) with the deep overpressured source at the base of the dome, allow the ascending fluids to be discharged and to remain at nearly hydrostatic pressure (Miller et al., 1996; Miller and Nur, 2000; Terakawa et al., 2010), thus approximating a drained condition. On this basis, Fig. 18 provides a conceptual model for the La Soufriere system and summarizes the main current features of the La Soufriere magmatic and hydrothermal system, as well as the temporal evolution through the recent unrest episode (see Supplementary Fig. 7 for a comprehensive picture of various changes and their timing).

In the representation of Fig. 18, we locate the pressure source below the dome by considering the P-T conditions of the hydrothermal liquid and right above the sealing cap marking the top of the brittle-ductile transition zone inferred at about 1.5 km bsl (Villemant et al., 2014). This sealing cap separates the lower plastic region where magma-derived fluids accumulate from the upper hydrothermal region, where fluids at hydrostatic pressure circulate through the brittle rock and maintain permeability via persistent seismicity (Fournier, 2007). The depth at which we place the sealing cap agrees with observations indicating that the brittle–plastic transition commonly occurs at about 370–400 °C within presently active continental hydrothermal systems

(Fournier, 2007). Considering that the high-magnitude VT seismicity is associated with breaching of the self-sealed zone (Fournier, 2007), we constrain the geometry of the brittle-ductile transition zone outside the volcanic axis by considering hypocentral depths of 16 and 27 April events just on top of it. A crystal mush extending downward from depths of 5 km bsl is pictured as the source of heat and deep fluids.

Boiling of the hydrothermal liquid separates the vapour responsible of the upward fluid circulation feeding the fumaroles and nurturing the shallow seismicity and deformation. Because the temperature of such a liquid is normally 340 °C (see Fig. 17), fluid pressure is 146 bar and liquid density 611 kg/m³ (NIST, 2018). Hydrostatic conditions are then established with the free-surface at the top of the dome. Considering at first approximation a constant fluid density in response to the convective homogenization, we can calculate ($z = P/[\rho g]$) a source depth of 0.9 km b.s.l. (or 2.4 km below the summit). This corresponds very well to the hypocentral depth of three most energetic earthquakes of 1 st February (1 km b.s.l.; OVSG-IPGP, 2018a). Based on 28 April and 2 May gas samples, which separate from a liquid originally at 370 °C (Fig. 17), we infer that this source was overpressured until reaching the critical point of pure water on 27 April 2018. Because the critical point occurs at $P = 220$ bar (NIST, 2018), an overpressure of 64 bar was attained in the source below the dome. Nevertheless, this overpressure in the dome roots was released aseismically. It is now worth recalling that the seismicity along fracture/fault planes infiltrated by fluids is produced by the instantaneous switch to large permeability values at the onset of cracking (Miller et al., 1996; Miller and Nur, 2000; Miller, 2015). Below the dome this process occurred evidently on February 1 st, but on 27 April the volcanic dome was able to restore aseismically the hydrostatic gradient because the overpressured source was already tapped by a network of structures with high vertical permeability and already critically stressed (i.e. the fractures and faults activated or created during the 1976 phreatic eruption, which modified the dome and reactivated since the 1992 onset of volcanic unrest; Komorowski et al., 2005; Ruzi  et al., 2012; Villemant et al., 2014). These structures then lowered the tensional state of the volcanic edifice by discharging the accumulated overpressure. The latter is testified by the episodic locking of fractures measured in April 2018 (Fig. 8b), as well as by the behaviour of fumarolic temperatures and heat fluxes. These were in fact rapidly increasing since the beginning of the year and then started decreasing right after the 16–17 April swarm (Fig. 9), showing that the heat flux is not stored in different aquifers but is evacuated through the main fractures.

The “usual” La Soufriere hybrid micro-seismicity concentrated within the dome, between –1 and 0.5 km of depth b.s.l. (Figs. 5b, 6b; see also Ucciani, 2015; Ucciani et al., 2015). This depth range is likely determined by the mechanic interplay of volcano loading with the non-homogenous distribution of the permeability within the shallow network of fractures. This network, upon fluid circulation, continuously evolved being characterized by patches of opening cracks, and patches of sealing cracks, with the sudden recovery of permeability (Miller et al., 1996; Miller and Nur, 2000; Fournier, 2007; Miller, 2015). Nevertheless, one major question is why this shallow microseismicity was not observed for a long time following the late April 2018 swarm. Diffuse hybrid seismicity (see for example December 2017 and early January 2018 swarms; Fig. 5a,b and Supplementary Fig. S1) was expected to be triggered, but it did not occur simply because the flux of liquid water phase migrating upward in the shallow hydrothermal system lowered considerably as demonstrated by the subsequent net decrease of fumarolic fluxes and the drop in vent temperatures (Figs. 9,10). After the 16–17 April, the water was drained away, outside the dome, likely penetrating along the NW-SE regional structure further activated in late April 2018. Thus, pore pressure was released to areas away from the paths leading to the dome-hosted and steam-rich shallow hydrothermal system and to the summit fumarolic zone. Therefore, only gases, enriched in the “anomalous” magma-related component, could flow upward after separating from the deep hydrothermal system.

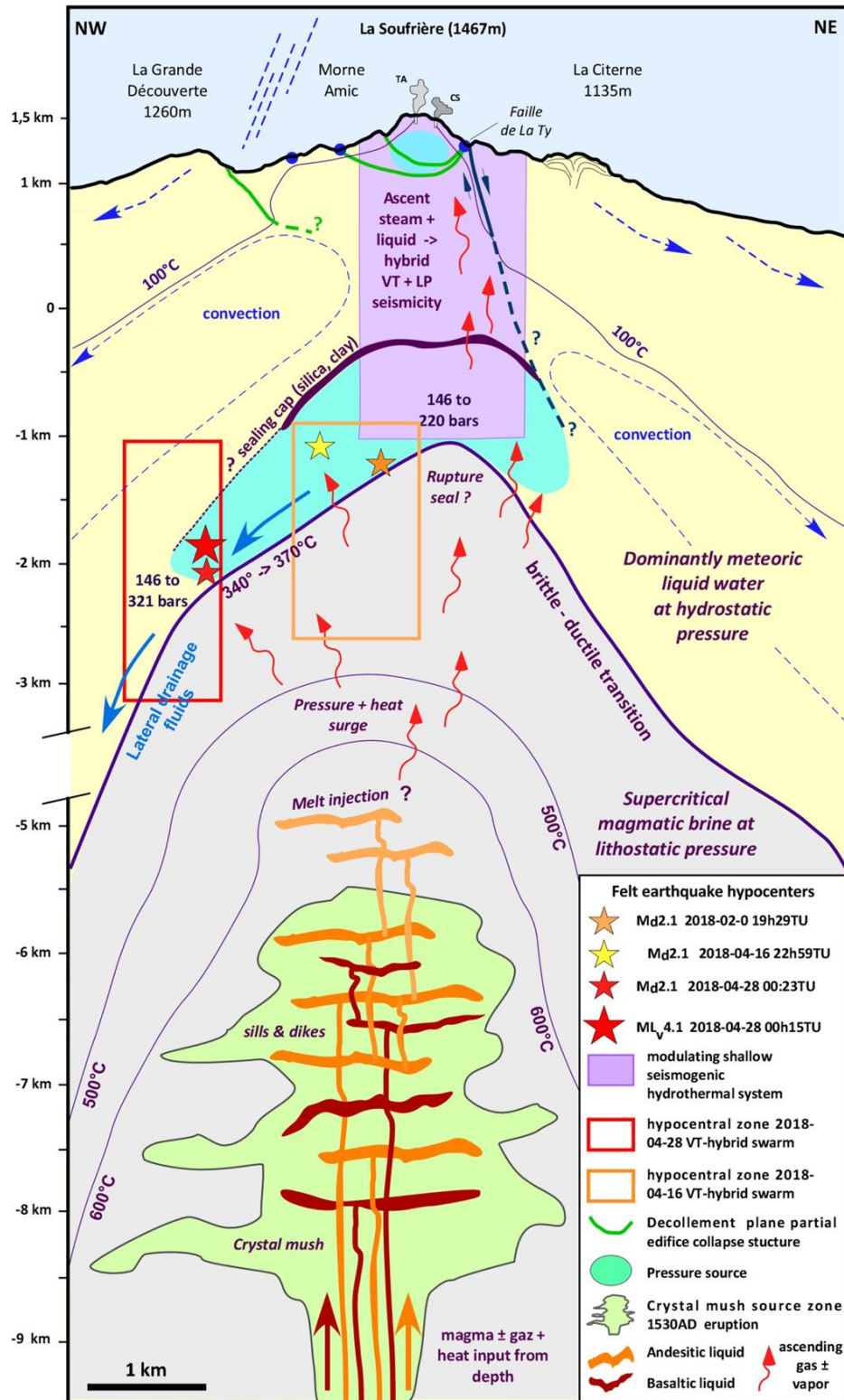


Fig. 18. Conceptual model of the La Soufrière of Guadeloupe and the February–April 2018 unrest episode. The conceptual model summarizes the evolution of observed geophysical and geochemical processes, including the build-up of pore pressures of thermal derivation.

Vapour separation, i.e. the mechanical decoupling of gas and liquid, occurs very likely when boiling water soon abandon undrained conditions, experiencing at depth a significant horizontal displacement (Arnorsson and Gunnlaugsson, 1985) due to deep lateral drainage outside the dome, along the NW-SE fault segment that was seismically activated on 16–17 April 2018 (Fig. 18). This mechanism is testified for by the samples from 23 March 2018 to 2 June 2018 in Fig. 17, which plot following along the vapour separation curve at 300 °C and 80 bar. This

suggests that the vapour separation process was deeper - hence closer to the overpressure boiling source - than before 23 March and after 2 June.

Along the NW-SE fault structure, the same temperature rise (from 340 °C to the critical point, 374 °C, or from 613 K to 647 K) inferred from fumarolic fluid compositions (Fig. 17) determined a dramatic rise of overpressures. This can be estimated by considering the isochoric build-up of thermal pressure, that is, the fluid pressure increase caused

by heating a single finite fluid-filled pore volume (e.g., [Delaney, 1982](#); [Norton, 1984](#); [Turcotte and Schubert, 1982](#); [Ganguly, 2009](#)):

$$\Delta P = \int_{613 \text{ K}}^{647 \text{ K}} \frac{\alpha}{\beta} dT \quad (6)$$

in which α is the isobaric thermal expansivity and β is the isothermal compressibility, their ratio being unity at the water critical point because both parameters tend to converge. Given the T-dependence of the α/β ratio in the T-range of interest by fitting NIST steam tables ([NIST, 2018](#)), Eq. (6) gives an overpressure of 175 bar, that is, a pore pressure of 321 bar at the hypocenter of the 27 April, M 4.1, earthquake (2 km b.s.l or 3.1 below the local ground-level; [Fig. 18](#)). This value is remarkably higher than the 220 bar inferred for an open system in which high-permeable fractures released the overpressure accumulated at 1 km b.s.l. (2.5 km depth below the volcano summit). These numbers are useful to give an idea of how the pore pressure increase along the same isotherm can affect rock behaviour. However, we cannot push further the argument as a precise treatment of thermoelastic effects and rock failure at the different sites would first demand the reconstruction of the local variations of the thermal field, and should include how fluid flow and resulting seepage forces modify the effective stresses ([Barenblatt et al., 1960](#); [Mourgues and Cobbold, 2003](#); [Rozhko et al., 2007](#)).

Nevertheless, given the current state of the dome, a thermally-driven build-up of overpressures comparable to the one reported in this study can lead to important rock failure and a phreatic eruption only when 1) self-sealing phenomena occur to confine fixed-fluid volumes, hence overpressure sources, sufficiently developed in the shallow hydrothermal system (rather than at 1 km b.s.l., i.e. 2.5 km below the summit), particularly in the sector currently responsible of measured deformations, and/or 2) the flow rate of the ascending hot fluids exceeds considerably both vertical and horizontal permeability-driven drainage through the deep dome fractures, thus impeding the pressure drop to nearly hydrostatic conditions. In this study we show evidence that this second scenario was initiated during the February-late April unrest phase, but could not reach its critical stage because water was effectively drained 2 km NW the dome axis through rock sectors of the NW-SE fault structure already solicited by the 16–17 swarm. This however produced 3 km NW away of the dome the M_L 4.1 seismic episode, which is related to the sudden release of fluid overpressure initiating rock brecciation ([Fournier, 2007](#); [Sibson, 1986](#); [Sillitoe, 2010](#)) and can then be seen as a “failed phreatic” eruption.

As reported of the end of [Section 4.2](#), one highly possible origin for the infiltration of deep magmatic gases is replenishment of the deep (≥ 4.5 km b.s.l.) magma chamber. In our view, the sudden 30 °C heating inferred from February to late April 2018 at depth > 0.5 km b.s.l. can only be achieved by the sudden arrival of a magma batch transferring its heat to the surrounding crustal fluids and triggering the thermoelastic effects that lead to undrained conditions ([Delaney, 1982, 1984](#); [McTigue, 1986](#)), rapid overpressure build-up and rock failure. It is outside the scopes of the present study to provide a thorough treatment of this matter, which would also demand to account for the role played by tectonic stresses, but we can refer to the model developed by [White and McCausland \(2016\)](#) who have shown that distal volcano-tectonic (dVT) earthquakes are usually the earliest known precursor to eruptions at long dormant volcanoes. It is worth noting that the database in the work includes also the 1976 subsequent phreatic explosions of La Soufrière de Guadeloupe. The same may be said for the seismic swarms described here as dVT locations are disconnected spatially from the LP/hybrid (micro)seismicity beneath the volcano crater. The dVTs occur typically in swarm-like pulses of seismicity, characterized by large non-double component to the focal mechanism and with peaks in both event rate and average magnitude about the time of the initial (either magmatic or phreatic) activity. Coherent with the

observations reported in our study, swarm-like dVT seismicity ramps up in number and magnitude over weeks. As pulses of magma intrude, they gradually over-pressurize the aquifers and lubricate the local tectonically pre-stressed fault, allowing more and larger patches to slip ([White and McCausland, 2016](#)). We suggest that this activity may thus have peaked up with the 28 April M 4.1 earthquake although this initiated a typical main shock/aftershock swarm, rather than be the major event during a ramping up sequence, as in principles required for distal VT earthquakes swarms described by [White and McCausland \(2016\)](#). By using the Authors' relation cumulative seismic moment with the magma intruding volume ($\text{Log}_{10} V = 0.77 \times \text{Log}_{10} M_0 - 5.32$, with volume V in cubic meters and moment M_0 in Nm; [White and McCausland, 2016](#)), we see that an intrusion of $2.7 \times 10^6 \text{ m}^3$, corresponding to a sphere of only 173 m in diameter, may have emplaced between February and late April 2018. Based on the sensitivity of our GPS network ([Section 3.2.1](#)) and in line with the physico-numerical findings in [Coulon et al. \(2017\)](#) on distal pressure changes triggering dVT seismicity, we conjecture that such a small intrusion might have emplaced well below the brittle-ductile transitions.

4.4. Lessons learnt: implications for volcanic surveillance and the monitoring strategy

Geophysical and geochemical data of this study show that a phreatic eruption at La Soufrière volcano did not occur during the 2018 unrest because of the high degree of fracturing and permeability of the volcanic dome, whose mechanical state has deeply changed after the 1976 eruption ([Komorowski et al., 2005](#); [Rosas-Carbajal et al., 2016](#)). However, episode of deep magmatic degassing point to the likely replenishment of the magma storage zones. This increases the probability for a future eruption to start with a sudden phreato-magmatic phase anticipated by a very short-lived phreatic phase. For the very same reasons, seismic activities and unrest episodes like the one recorded in February–April 2018 must be seen on one side as failed phreatic eruptions, and on the other side as episodes prodromal to even major energy releases implying the destabilization of the hydrothermal system within the dome or the rise of magma batches.

The system has been evolving towards reactivation since 1992, as evidenced by geochemical data pointing to the 1976 (supercritical) cluster of points. The presence of acid species (HCl and SO₂) and the lack of important sealing, active in 1976, should not mask the arrival of deep magmatic gas inputs prior to any future eruption. However, we cannot yet exclude that this may be preceded by a short phase in which fumarole chemistry becomes more hydrothermal. This can be also suggested by the composition of gases discharged around 28 April 2018, in concomitance with the locking episode of summit fractures ([Fig. 8](#)). A similar, but far more important behaviour, was in fact observed at Galeras, because of pre-eruptive sealing phenomena ([Brombach et al., 2000](#); [Fischer et al., 1997](#)). In the case of La Soufrière, sealing could lead to fluid accumulation and rapid pore pressure build up under undrained conditions, and destabilize the shallow hydrothermal pressure source, leading the system to explosive activity. In addition, it can also favor the sliding of the volcano south-west flank, subject to a basal gravitational spread, because of the reduction of the coefficient of friction and the increase of pore pressure along mechanically weak areas in the dome. A rapidly escalating unrest could in fact trigger slope instability and partial collapse of the south-western flank as suggested by [Komorowski et al. \(2005\)](#) and [Rosas-Carbajal et al. \(2016\)](#) and modelled by [Peruzzetto et al. \(2019\)](#).

This scenario and, particularly, the fact that we could not forecast the 227 April 2018 event (intended as a phreatic eruption) call upon the need for the in-situ high-frequency collection and full analysis of the fumarolic fluids, in order to track the short-lived P-T transients of the hydrothermal system ([Barberi et al., 1992](#); [Rouwet et al., 2014](#); [Stix and de Moor, 2018](#)). This strategy, elsewhere successfully implemented via in-situ mass spectrometry (e.g., [Campi Flegrei](#); [Fedele et al., 2017](#)), at La

Soufrière presents many challenges related to intrinsic limits (high required power supply, instrumental fragility, costs and also logistics) and its hostile environment (rainy and windy conditions in a tropical environment, difficult accessibility, exposition to corrosion and unstable working conditions). At La Soufrière, it is however necessary to couple a full analysis including minor species (e.g., H₂, CO, CH₄, He) to the plume continuous measurements already operated via Multigas stations. Moreover, at La Soufrière Multigas sensors cannot provide the same levels of accuracy as at other volcanic sites where the sampled plumes emit superheated steam, much less affected by humidity than at La Soufrière (Aiuppa et al., 2011, 2018; De Moor et al., 2016).

In light of the strong role played by fluid release, hence by advective heat transport, it is then priority to improve our monitoring systems and surveillance protocols to 1) detect rapid hydrothermal transients in heat flux, 2) map and track variations in the distribution of deep isotherms. We want to stress here that joining thermal calculations based on energy conservation (e.g., Di Renzo et al., 2016; Moretti et al., 2018) to the deformation modeling adopted here would be a strict test for magma plumbing models as well as for sources responsible of observed rapid deformations, because they considerably narrow the domain of solutions to a set that are very similar (temporal similarity) and congruent (spatially similar). In this respect, a reasonable development of geothermal activity in the La Soufrière surroundings could represent a major contribution to track the evolution of deep temperatures, as well as anomalous chemical signatures of deep fluids. In addition, a detailed survey of spring water chemistry and isotope chemistry, extended to dissolved gases, will provide the necessary basis to model the chemical and hydraulic interaction between deep volcanic gases, the hydrothermal system and groundwaters, also contributing to the identification of possible high-pressure groundwater pathways.

On the geophysical side, the likely occurrence of rapid deformation pulses warns of the possibility of contamination of the broadband seismic signal due to tilt change, especially for long-period signals (Aoyama and Oshima, 2008; Pino et al., 2011), and suggests that effective tiltmetric measurements should be performed, also considering the role played by aseismic slip along the deep fractures cutting the dome. These should be accompanied by permanent gravity measurements, as well as dilatometric measurements (e.g., Scarpa et al., 2007), in order to track the evolution of the 6 km deep magma chamber and its refilling. These measurements would also help understanding better the mass transfer-stress-strain relationships occurring on La Soufrière and accompanying distal seismicity, which has the potential for estimating intrusive volumes and forecasting eruptions (White and McCausland, 2016; Coulon et al., 2017). Hence, future accurate assessments should also add to scrutiny the seismic swarms periodically occurring in the Les Saintes archipelago, located km SE of La Soufrière between the Guadeloupe and Dominica (see also Bazin et al., 2010; Feuillet et al., 2011 and references therein) and often characterized by important non-double component.

In light of the small volume of magma emplaced (see Section 4.3) and the short timescales between mafic recharge and eruption, which for the 1530 CE eruption span from tens of days to tens of hours (Pichavant et al., 2018), the improvement of the observatory capability to detect and interpret subtle variations related to the refilling of the 6–7 km deep magma chamber is obviously a major task. As shown here, as well as in other critical volcanic-hydrothermal areas (e.g. Campi Flegrei, Italy; Troise et al., 2019), such a task can be accomplished only through accurate joint consideration and analysis of geophysical and geochemical data (Supplementary Fig. S7 and Supplementary Table 1).

5. Conclusions

The La Soufrière of Guadeloupe unrest attained on 27 April 2018 its relative maximum since 42 years, i.e. after the 1976–1977 phreatic eruption. Recorded events include:

- 1 felt earthquake M 2.1 on 1 st February 2018 in a sequence of 30 earthquakes located at 1 km bsl (2.5 km depth below the volcano summit);

- 1 felt earthquake M 2.1 on 16–17 April in a sequence of 140 earthquakes located up to 1 km NW away of the dome, with most energetic events ($M > 1$) at a depth between 1 and 1.6 km bsl (2.5 and 3.1 km below the volcano summit);

- 2 felt earthquakes on April 27, including that of magnitude M_L 4.1 in a sequence of 180 earthquakes located at about 2–3 km NW away from the dome, with most energetic events ($M > 2$) at a depth of 2 km bsl (3 km below the local ground-level).

This level of volcanic seismicity, unprecedented since 1976, has been associated with

- 1) a clearly magmatic signature of “pulses” of gases rich in CO₂, HCl, H₂S, and SO₂ in significant concentration around the vents;

- 2) the emission of hot hydrothermal fluids discharged by a hydrothermal system heated and pressurized (ΔP between 64 and 175 bar) from the deep areas of the volcanic system due to arrival of a major magmatic gas pulse;

- 3) horizontal deformation velocities around the dome (<1 km) up to 9 mm/year between 1995 and 2018 that are related to the shallow pressurization of the system hydrothermal as well as the gravitational spreading of the south-west flank of the dome.

- 4) renewed phases of fracture opening on the dome.

Geochemical analysis, and its thermodynamic interpretation, show that there has been a rise in fluids of deep origin (magmatic). This caused transient phases of overpressure and overheating at the base of the hydrothermal system, particularly in a source volume that we locate 2.5 km deep below the volcano summit. This excess fluid pressure was responsible for the 2018 considerable increase of volcanic seismicity on the Grande Découverte-Soufrière massif. The seismicity recorded along the NW-SE regional fault crossing the volcanic massif presents elements compatible with a process of hydrofracturing and/or hydroshearing. Nevertheless, at the scale of the dome, overpressure was dissipated either upward, through the highly permeable vertical fractures dissecting the dome, and laterally, by triggering slip along the NW-SE fault. This sequence of events preserved the stability of the shallow hydrothermal system, whose currently small pressure source at about 0.5 km depth is responsible for the radial component of the deformation observed at the summit.

Comparison of thermochemical features of current fumarolic discharges with 1997 and July 1976 data indicates that the hydrothermal system, reactivated since 1992, has increased its vigor, evolving from an early development phase dominated by important steam condensation (1997 data) to a mature condition in which boiling accompanies a clear increase of hydrothermal temperature, hence heat flux, and pressure, thus re-approaching the pre-1976 state.

Drainage of the hydrothermal liquid (water) outside the dome after the 16–17 April swarm along a NW-SE regional structure, inhibited the occurrence of a phreatic eruption which points to the conclusion that the 27 April M_L 4.1 earthquake represents a failed phreatic eruption. No clear evidence can indicate so far the rise of magma to depths lower than those of the andesitic magma chamber (i.e. <6–7 km below the La Soufrière summit), although He-based chemical ratios and contrasting halogen behaviour have already suggested the occurrence of refreshment and/or replenishment of such a magma chamber. Based on distal seismicity evaluations, particularly the ramp up of magnitudes, a magmatic volume of $2.7 \cdot 10^6 \text{ m}^3$ may have intruded between February and late April 2018.

The main lesson we have learnt from this record of events is that La Soufrière of Guadeloupe has changed behaviour and is at a significantly higher level of activity than it has been over the last 40 years. Given the increase in seismic and fumarolic activity recorded since February 2018, we cannot exclude an intensification of phenomena in the future, the present-day hydrothermal system being recharging in a P-T condition corresponding to the pre-1976 one, and not

dissimilar to Montserrat before the eruption that started in 1995 (Chiodini et al., 1996). Only a high-frequency joint geophysical, thermal and geochemical monitoring can disclose the rapid transient in pressure and temperature able to destabilize the hydrothermal system. Future eruptive activity may be preceded by a short phase in which fumarole chemistry becomes more hydrothermal due to sealing phenomena. This could bring to fluid accumulation and rapid pore pressure build-up destabilizing the shallow hydrothermal pressure source, leading to the (initial) phreatic explosion and favoring the sliding of the volcano south-west flank.

Supplementary data to this article can be found online at <https://doi.org/10.1016/j.jvolgeores.2020.106769>.

CRedit authorship contribution statement

Roberto Moretti: Conceptualization, Investigation, Project administration, Formal analysis, Writing - original draft, Writing - review & editing, Supervision, Visualization, Data curation, Validation. **Jean-Christophe Komorowski:** Conceptualization, Project administration, Funding acquisition, Writing - review & editing, Supervision. **Guillaume Ucciani:** Formal analysis, Visualization, Investigation. **Séverine Mouné:** Visualization, Data curation, Conceptualization, Investigation, Writing - review & editing. **David Jessop:** Formal analysis, Data curation, Conceptualization, Investigation, Writing - review & editing. **Jean-Bernard de Chaballier:** Formal analysis, Visualization, Data curation, Investigation. **François Beauducel:** Formal analysis, Software, Investigation, Visualization. **Magali Bonifacie:** Formal analysis, Investigation. **Arnaud Burtin:** Data curation, Validation. **Martin Vallée:** Formal analysis, Software, Visualization. **Sebastien Deroussi:** Resources, Data curation, Investigation, Validation. **Vincent Robert:** Resources, Formal analysis, Data curation, Validation. **Dominique Gibert:** Data curation, Validation. **Tristan Didier:** Resources, Data curation, Validation. **Thierry Kitou:** Resources, Data curation, Validation. **Nathalie Feuillet:** Conceptualization. **Patrick Allard:** Conceptualization, Writing - review & editing. **Giancarlo Tamburello:** Writing - review & editing. **Tara Shreve:** Writing - review & editing. **Jean-Marie Saurel:** Data curation, Validation. **Arnaud Lemarchand:** Funding acquisition, Data curation, Validation. **Marina Rosas-Carbajal:** Writing - review & editing. **Pierre Agrinier:** Formal analysis. **Anne Le Friant:** Project administration, Funding acquisition, Supervision. **Marc Chaussidon:** Project administration, Funding acquisition, Writing - review & editing, Supervision.

Declaration of competing interest

The authors declare that they have no known competing financial interests or personal relationships that could have appeared to influence the work reported in this paper.

Acknowledgements

We thank IPGP for general funding to *Observatoires Volcanologiques et Sismologiques (OVS)* as well as for financial support via the AO-IPGP 2018 project “Depth to surface propagation of fluid-related anomalies at La Soufrière de Guadeloupe volcano (FWI): timing and implications for volcanic unrest” (coord.: R. Moretti), INSU-CNRS for funding provided by *Service National d’Observation en Volcanologie (SNOV)*, the ANR “DIAPHANE” project (coord.: D. Gibert) and the Ministère pour la Transition Ecologique et Solidaire (MTES) for financial support. Part of the G. Ucciani’s postdoc was funded by the project Vers la Plateforme Régionale de Surveillance Tellurique du futur (PREST) co-funded by INTERREG Caraïbes for the European Regional Development Fund. We also thank the Parc National de Guadeloupe for logistic support and assistance during field work. Willy Aspinall is acknowledged for his helpful insights into distal seismicity. The manuscript benefited of precious suggestions by P. Bernard (IPGP) and two anonymous reviewers. This study contributes to the IdEx Université de Paris ANR-18-IDEX-0001.

References

- Aiuppa, A., Federico, C., Giudice, G., Gurrieri, S., 2005. Chemical mapping of a fumarolic field: la Fossa crater, Vulcano Island (Aeolian Islands, Italy). *Geophys. Res. Lett.* 32 (13).
- Aiuppa, A., Shinohara, H., Tamburello, G., Giudice, G., Liuzzo, M., Moretti, R., 2011. Hydrogen in the gas plume of an open vent volcano (Mt. Etna, Italy). *JOURNAL OF GEOPHYSICAL RESEARCH: SOLID EARTH* 116, 1–5.
- Aiuppa, A., de Moor, J.M., Arellano, S., Coppola, D., Francofonte, V., Galle, B., Giudice, G., Liuzzo, M., Mendoza, E., Saballos, A., Tamburello, G., Battaglia, A., Bitetto, M., Gurrieri, S., Laiolo, M., Mastrolia, A., Moretti, Roberto, 2018. Tracking formation of a lava lake from ground and space: Masaya volcano (Nicaragua), 2014–2017. *Geochem. Geophys. Geosyst.* 19 (2), 496–515.
- Allard, P., 1983. The origin of hydrogen, carbon, Sulphur, nitrogen and rare gases in volcanic exhalations: Evidence from isotope geochemistry. Chapter 25. *Forecasting Volcanic Events*, pp. 337–386.
- Allard, P., Hammouya, G., Parello, F., 1998. Diffuse magmatic soil degassing at Soufrière de Guadeloupe, Antilles. *Comptes Rendus de l’Académie des Sciences Series IIA Earth and Planetary Science* 5 (327), 315–318.
- Allard, P., Aiuppa, A., Beauducel, F., Gaudin, D., Di Napoli, R., Calabrese, S., Parello, F., Crispi, O., Hammouya, G., Tamburello, G., 2014. Steam and gas emission rate from La Soufrière volcano, Guadeloupe (Lesser Antilles): implications for the magmatic supply during degassing unrest. *Chem. Geol.* 384, 76–93.
- Aoyama, H., Oshima, H., 2008. Tilt change recorded by broadband seismometer prior to small phreatic explosion of Meakan-dake volcano, Hokkaido, Japan. *Geophys. Res. Lett.* 35 (6).
- Arnorsson, S., Gunnlaugsson, E., 1985. New gas geothermometers for geothermal exploration - Calibration and application. *Geochim. Cosmochim. Acta* 49, 1307–1325.
- Barberi, F., Bertagnini, A., Landi, P., Principe, C., 1992. A review on phreatic eruptions and their precursors. *J. Volcanol. Geotherm. Res.* 52 (4), 231–246.
- Barenblatt, G.I., Zheltov, I.P., Kochina, I.N., 1960. Basic concepts in the theory of seepage of homogeneous liquids in fissured rocks. *J. Appl. Math. Mech.* 24, 1286–1303.
- Barrabé, L., Jolivet, J., 1958. Les récentes manifestations d’activité de la Guadeloupe (Petites Antilles). (French) Recent activity manifestations of Guadeloupe (Lesser Antilles). *Bull. Volcanol.* 19, 143–157.
- Battaglia, M., Troise, C., Obrizzo, F., Pingue, F., De Natale, G., 2006. Evidence for fluid migration as the source of deformation at Campi Flegrei caldera (Italy). *Geophys. Res. Lett.* 33 (1).
- Bazin, S., Feuillet, N., Duclos, C., Crawford, W., Nercessian, A., Bengoubou-Valérius, M., Beauducel, F., Singh, S.C., 2010. The 2004–2005 Les Saintes (French West Indies) seismic aftershock sequence observed with ocean bottom seismometers. *Tectonophysics* 489 (1–4), 91–103.
- Bigot, S., Boudon, G., Semet, M.P., Hammouya, G., 1994. Traçage chimique de la circulation des eaux souterraines sur le volcan de la Grande Découverte (la Soufrière), Guadeloupe. *CR Acad. Sci. Paris* 318, 1215–1221.
- Boichu, M., Villemant, B., Boudon, G., 2008. A model for episodic degassing of an andesitic magma intrusion. *Journal of Geophysical Research: Solid Earth* 113 (B7).
- Boichu, M., Villemant, B., Boudon, G., 2011. Degassing at La Soufrière de Guadeloupe volcano (Lesser Antilles) since the last eruptive crisis in 1975(77): result of a shallow magma intrusion? *J. Volcanol. Geotherm. Res.* 203, 102–112.
- Brodsky, E.E., Sturtevant, B., Kanamori, H., 1998. Earthquakes, volcanoes, and rectified diffusion. *Journal of Geophysical Research: Solid Earth* 103 (B10), 23827–23838.
- Brombach, T., Marini, L., Hunziker, J.C., 2000. Geochemistry of the thermal springs and fumaroles of Basse-Terre Island, Guadeloupe, Lesser Antilles. *Bull. Volcanol.* 61 (7), 477–490.
- Brothelande, E., Finizola, A., Peltier, A., Delcher, E., Komorowski, J.C., Di Gangi, F., Borgogno, G., Passarella, M., Trovato, C., Legendre, Y., 2014. Fluid circulation pattern inside La Soufrière volcano (Guadeloupe) inferred from combined electrical resistivity tomography, self-potential, soil temperature and diffuse degassing measurements. *J. Volcanol. Geotherm. Res.* 288, 105–122.
- Boudon, G., Dagain, J., Semet, M.P., Westercamp, D., 1988. Notice explicative de la carte géologique au 1/20.000 ème du massif volcanique de la Soufrière (Département de la Guadeloupe, Petites Antilles). BRGM, CNRS, DRM, IGP, Paris 43 pp.
- Boudon, G., Komorowski, J.C., Villemant, B., Semet, M.P., 2008. A new scenario for the last magmatic eruption of La Soufrière of Guadeloupe (Lesser Antilles) in 1530 AD Evidence from stratigraphy radiocarbon dating and magmatic evolution of erupted products. *J. Volcanol. Geotherm. Res.* 178 (3), 474–490.
- Buck, W.R., Martinez, F., Steckler, M.S., Cochran, J.R., 1988. Thermal consequences of lithospheric extension: pure and simple. *Tectonics* 7 (2), 213–234.
- Caliro, S., Chiodini, G., Paonita, A., 2014. Geochemical evidences of magma dynamics at Campi Flegrei (Italy). *Geochim. Cosmochim. Acta* 132, 1–15.
- Chatterjee, S.N., Pitt, A.M., Iyer, H.M., 1985. Vp/Vs ratios in the Yellowstone national park region, Wyoming. *J. Volcanol. Geotherm. Res.* 26, 213–230.
- Chevrier, R.M., Dajlevic, D., Le Guern, F., Rouyerr, J.L., 1976. Données recueillies sur la phase gazeuse de la Soufrière (Guadeloupe) du 13 juillet au 20 septembre 1976. Rapport CEA, Département de protection, Novembre 1976.
- Chiodini, G., 2009. CO₂/CH₄ ratio in fumaroles a powerful tool to detect magma degassing episodes at quiescent volcanoes. *Geophys. Res. Lett.* 36 (2).
- Chiodini, G., Marini, L., 1998. Hydrothermal gas equilibria: the H₂O-H₂-CO₂-CO-CH₄ system. *Geochim. Cosmochim. Acta* 62 (15), 2673–2687.
- Chiodini, G., Cioni, R., Frullani, A., Guidi, M., Marini, L., Prati, F., Raco, B., 1996. Fluid geochemistry of Montserrat Island, West Indies. *Bull. Volcanol.* 58 (5), 380–392.
- Chiodini, G., Marini, L., Russo, M., 2001. Geochemical evidence for the existence of high-temperature hydrothermal brines at Vesuvio volcano, Italy. *Geochim. Cosmochim. Acta* 65 (13), 2129–2147.

- Chiodini, G., Vandemeulebrouck, J., Caliro, S., D'Auria, L., De Martino, P., Mangiacapra, A., Petrillo, Z., 2015. Evidence of thermal-driven processes triggering the 2005–2014 unrest at Campi Flegrei caldera. *Earth Planet. Sci. Lett.* 414, 58–67.
- Collettini, C., Barchi, M.R., 2002. A low-angle normal fault in the Umbria region (Central Italy): a mechanical model for the related microseismicity. *Tectonophysics* 359 (1–2), 97–115.
- Connolly, J.A.D., 1997. Devolatilization-generated fluid pressure and deformation-propagated fluid flow during prograde regional metamorphism. *J. Geophys. Res.* 102 (B8), 18149–18173.
- Coulon, C.A., Hsieh, P.A., White, R., Lowenstern, J.B., Ingebritsen, S.E., 2017. Causes of distal volcano-tectonic seismicity inferred from hydrothermal modelling. *J. Volcanol. Geotherm. Res.* 345, 98–108.
- Cox, S.F., 1995. Faulting processes at high fluid pressures: an example of fault valve behavior from the Wattle Gully Fault, Victoria, Australia. *Journal of Geophysical Research (Solid Earth)* 100, 12,841–12,859. <https://doi.org/10.1029/95JB00915>.
- D'Amore, F., Panichi, C., 1980. Evaluation of deep temperatures of hydrothermal systems by a new gas geothermometer. *Geochim. Cosmochim. Acta* 44 (3), 549–556.
- de Moor, J.M., Aiuppa, A., Avaró, G., Wehrmann, H., Dunbar, N., Müller, C., Tamburello, G., Giudice, G., Liuzzo, M., Moretti, R., 2016. Turmoil at Turrialba Volcano (Costa Rica): Degassing and eruptive processes inferred from high-frequency gas monitoring. *J. Geophys. Res. Solid Earth* 121 (8), 5761–5775.
- Del Pezzo, E., Bianco, F., Saccorotti, G., 2004. Seismic source dynamics at Vesuvius volcano, Italy. *J. Volcanol. Geotherm. Res.* 133 (1–4), 23–39.
- Delaney, P.T., 1982. Rapid intrusion of magma into wet rock: groundwater flow due to pore pressure increases. *J. Geophys. Res.* 87, 7739–7756.
- Delaney, P., 1984. Heating of a fully saturated Darcian half-space: pressure generation fluid expulsion and phase change. *Int. J. Heat Mass Transf.* 27, 1327–1335.
- Di Renzo, V., Wohletz, K., Civetta, L., Moretti, R., Orsi, G., Gasparini, P., 2016. The thermal regime of the Campi Flegrei magmatic system reconstructed through 3D numerical simulations. *J. Volcanol. Geotherm. Res.* 328, 210–221.
- Dorel, J., Eschenbrenner, S., Feuillard, M., 1979. Coupes sismiques des structures superficielles dans les petites antilles—I: Guadeloupe. *Pure Appl. Geophys.* 117 (9), 1050–1069.
- Fabre, R., Chaigneau, M., 1960. Technique de prélèvement et d'analyse de gaz de fumerolles de volcans. Exemples d'analyses de gaz prélevés à la montagne Pelée (Martinique) et à la Grande Soufrière (Guadeloupe). *Bull. Volcanol.* 23 (1), 21–30.
- Fedele, A., Pedone, M., Moretti, R., Wiersberg, T., Somma, R., Troise, C., De Natale, G., 2017. Real-time quadrupole mass spectrometry of hydrothermal gases from the unstable Pisciarelli fumaroles (Campi Flegrei): trends, challenges and processes. *Int. J. Mass Spectrom.* 415, 44–54.
- Feuillard, M., et al., 1983. The 1975–1977 crisis of La Soufrière de Guadeloupe (FWI): a still-born magmatic eruption. *J. Volcanol. Geotherm. Res.* 16, 317/334.
- Feuillard, M., 2011. In: Jasar, Pointe-à-Pitre (Ed.), *La Soufrière de la Guadeloupe : un volcan et un peuple* pp 246.
- Feuillet, N., Manighetti, I., Tapponnier, P., Jacques, E., 2002. Arc parallel extension and localization of volcanic complexes in Guadeloupe, Lesser Antilles. *Journal of Geophysical Research: Solid Earth* 107 (B12), ETG 3–1-ETG 3-29 107.B12.
- Feuillet, N., Beauducel, F., Tapponnier, P., 2011. Tectonic context of moderate to large historical earthquakes in the lesser antilles and mechanical coupling with volcanoes. *Journal of Geophysical Research: Solid Earth* 116.
- Fischer, T.P., Sturchio, N.C., Stix, J., Arehart, G.B., Counce, D., Williams, S.N., 1997. The chemical and isotopic composition of fumarolic gases and spring discharges from Galeras Volcano, Colombia. *J. Volcanol. Geotherm. Res.* 77 (1–4), 229–253.
- Fournier, R.O., 2007. Hydrothermal systems and volcano geochemistry. *Volcano deformation*. Springer, Berlin, Heidelberg, pp. 323–341.
- Ganguly, J., 2009. *Thermodynamics in Earth and Planetary Sciences*. Springer Science & Business Media.
- Gaudin, D., Beauducel, F., Coutant, O., Delacourt, C., Richon, P., de Chabalière, J.B., Hammouya, G., 2016. Mass and heat flux balance of La Soufrière volcano (Guadeloupe) from aerial infrared thermal imaging. *J. Volcanol. Geotherm. Res.* 320, 107–116.
- Giggenbach, W.F., 1980. Geothermal gas equilibria. *Geochim. Cosmochim. Acta* 44 (12), 2021–2032.
- Giggenbach, W., 1987. Redox processes governing the chemistry of fumarolic gas discharges from White Island, New Zealand. *Appl. Geochem.* 2, 143–161.
- Giggenbach, W.F., 1988. Geothermal solute equilibria. Derivation of Na-K-Mg-Ca geothermometers. *Geochim. Cosmochim. Acta* 52, 2749–2765.
- Giggenbach, W.F., 1997. The origin and evolution of fluids in magmatic-hydrothermal systems. In: Barnes, H.L. (Ed.), *Geochemistry of Hydrothermal Ore Deposits*, 3rd edition John Wiley & Sons, New York, pp. 737–796.
- Giggenbach, W.F., Goguel, R.L., 1989. Collection and Analysis of Geothermal and Volcanic Water and Gas Discharges. Report No. CD 2401. Department of Scientific and Industrial Research. Chemistry Division, Petone, New Zealand.
- Haimson, B.C., Zhao, Z., 1991. Effect of borehole size and pressurization rate on hydraulic fracturing breakdown pressure. The 32nd US Symposium on Rock Mechanics (USRMS). American Rock Mechanics Association.
- Hanks, T.C., Kanamori, H., 1979. A moment magnitude scale. *J. Geophys. Res.* 84 (B5), 2348–2350.
- Hapel-Lachenaie, T., Peyre, A., Fontelliau, C., 1798. Rapport fait aux citoyens Victor Hugues et Lebas, agents particuliers du directoire exécutif aux îles du vent, par la commission établie en vertu de leur arrêté du 12 vendémiaire, an 6 de la république, pour examiner la situation du Volcan de la Guadeloupe, et les effets de l'éruption qui a eu lieu dans la nuit du 7 au 8 du même mois. An VI. Facsimile, Société d'Histoire De la Guadeloupe, Basse-Terre, p. 179.
- Harris, A., 2013. *Thermal Remote Sensing of Active Volcanoes: A user's Manual*. Cambridge University Press (728 pp).
- Hill, D.P., Ellsworth, W.L., Johnston, M.J.S., Langbein, J.O., Oppenheimer, D.H., Pitt, A.M., Reasenber, P.A., Sorey, M.L., McNutt, S.R., 1990. The 1989 earthquake swarm beneath Mammoth Mountain, California: an initial look at the 4 May through 30 September activity. *Bull. Seismol. Soc. Am.* 80 (2), 325–339.
- Hill, D.P., Pollitz, F., Newhall, C., 2002. Earthquake-volcano interactions. *Phys. Today* 55 (11), 41–47.
- Hincks, T.K., Komorowski, J.-C., Sparks, S.R., Aspinall, W.P., 2014. Retrospective analysis of uncertain eruption precursors at La Soufrière volcano, Guadeloupe, 1975(77): volcanic hazard assessment using a Bayesian belief network approach. *J. Appl. Volcanol.* 3 (1), 26.
- Ito, H., DeVilbiss, J., Nur, A., 1979. Compressional and shear waves in saturated rock during water-steam transition. *J. Geophys. Res.* 84, 4731–4735.
- Jean-Baptiste, P., Allard, P., Fourré, E., Parello, F., Aiuppa, A., 2014. Helium isotope systematics of volcanic gases and thermal waters of Guadeloupe Island, Lesser Antilles. *J. Volcanol. Geotherm. Res.* 283, 66–72.
- Jolivet, J., 1958. La crise volcanique de 1956 à la Soufrière de la Guadeloupe. (French). The volcanic crisis of 1956 at La Soufrière de Guadeloupe. *Annales de Géophysique*. vol. 14, p. 305.
- Kehle, R., 1964. The determination of tectonic stresses through analysis of hydraulic well fracturing. *J. Geophys. Res.* Q 259–273.
- Komorowski, J.-C., et al., 2001. L'activité éruptive et non-éruptive de la Soufrière de Guadeloupe: problèmes et implications de la phénoménologie et des signaux actuellement enregistrés. (French). Eruptive and non-eruptive activity from the Soufrière de Guadeloupe: problems and implications posed by the current phenomenology and monitoring signals. Workshop on volcanic hazards - Lesser Antilles volcanoes: from processes to signals. 18. PNRN (CNRS){INSU, BRGM, CEA, CEMAGREF, CNES, IRD, p. 19.
- Komorowski, J., et al., 2005. Guadeloupe. Volcanic Atlas of the Lesser Antilles. 65. Seismic Research Unit. The University of the West Indies Trinidad, p. 102.
- Komorowski, J.-C., Legendre, Y., Caron, B., Boudon, G., 2008. Reconstruction and analysis of subplinian tephra dispersal during the 1530 AD Soufrière (Guadeloupe) eruption: Implications for scenario definition and hazards assessment. *J. Volcanol. Geotherm. Res.* 178, 491/515.
- Komorowski, J.-C., Legendre, Y., Barsotti, S., Esposti Ongaro, T., Jenkins, S., Baxter, P., Boudon, G., Leone, F., Neri, A., Spence, R., Aspinall, W., Grancher, D., Redon, M., Chopineau, C., de Chabalière, J.-B., 2013. Assessing long term hazards for the Soufrière de Guadeloupe volcano: insights from a new eruptive chronology, credible scenario definition, and integrated impact modelling. International Association of Volcanology and Chemistry of the Earth's Interior (IAVCEI), Scientific Assembly, Kagoshima, Japan 19-24 July 2013, abstract, 4W_4D-P1, poster.
- Komorowski, J., Hincks, T., Sparks, R., Aspinall, W., et al., 2015. Improving crisis decision-making at times of uncertain volcanic unrest (Guadeloupe, 1976). *Global Volcanic Hazards and Risk*. Cambridge University Press, p. 255.
- Le Guern, F., Bernard, A., Chevrier, R., 1980. Soufrière de Guadeloupe 1976-1977 eruption. Mass and energy transfer and volcanic health hazards. *Bull. Volcanol.* 43, 577–593.
- Legendre, Y., 2012. Reconstruction de l'histoire éruptive et scénarii éruptifs à La Soufrière de Guadeloupe: vers un modèle intégrale de fonctionnement du volcan. (French) [A high resolution reconstruction of the eruptive past and definition of eruptive scenarii at La Soufrière de Guadeloupe]. Ph.D. thesis, Paris, p. 7.
- Lesparre, N., Gibert, D., Marteau, J., Komorowski, J.-C., Nicollin, F., Coutant, O., 2012. Density Muon Radiography of Soufrière de Guadeloupe Volcano: Comparison with Geological, Electrical Resistivity and Gravity data. *Geophys. J. Int.* <https://doi.org/10.1111/j.1365-246X.2012.05546.x>.
- Lherminier, F., 1837a. Sur les produits du volcan de la Guadeloupe. *Comptes rendus de l'Académie des sciences* 454–455.
- Lherminier, F., 1837b. L'éruption du volcan de la Guadeloupe. *La Soufrière de Guadeloupe. Nouvelles Annales de Voyage* 74, 349–350.
- Lherminier, F., 1837c. Note sur l'éruption du volcan de la Guadeloupe. (French). On the products from the volcano of La Guadeloupe. *Comptes rendus de l'Académie des sciences* 294.
- Lherminier, F., 1815. Réflexions sur les volcans, considérations sur la Guadeloupe. *J. Phys.* 80, 260–271.
- Linde, A.T., Sacks, I.S., 1998. Triggering of volcanic eruptions. *Nature* 395 (6705), 888.
- Lomax, A., Virieux, J., Volant, P., Berge-Thierry, C., 2000. Probabilistic earthquake location in 3D and layered models – introduction of a Metropolis-Gibbs method and comparison with linear locations. *Advances in Seismic Event Location*, pp. 101–134.
- Marzocchi, W., 2002. Remote seismic influence on large explosive eruptions. *Journal of Geophysical Research: Solid Earth* 107 (B1).
- Mastin, L.G., 1995. The thermodynamics of steam-blast eruptions. *Bull. Volcanol.* 57, 85–98.
- McTigue, D.F., 1986. Thermoelastic response of fluid-saturated porous rock. *Journal of Geophysical Research: Solid Earth* 91 (B9), 9533–9542.
- Micklethwaite, S., Cox, S.F., 2006. Progressive fault triggering and fluid flow in aftershock domains: examples from mineralized Archean fault systems. *Earth Planet. Sci. Lett.* 250 (1–2), 318–330.
- Miller, S.A., 2015. Modeling enhanced geothermal systems and the essential nature of large-scale changes in permeability at the onset of slip. *Geofluids* 15, 338–349.
- Miller, S.A., Nur, A., 2000. Permeability as a toggle switch in fluid-controlled crustal processes. *Earth Planet. Sci. Lett.* 183 (2000), 133–146.
- Miller, S.A., Nur, A., Olgaard, D.A., 1996. Earthquakes as a coupled shear stress – high pore pressure dynamical system. *Geophys. Res. Lett.* 23 (2), 197–200 JANUARY 15.
- Miller, V., Voight, B., Ammon, C.J., Shalev, E., Thompson, G., 2010. Seismic expression of magma-induced crustal strains and localized fluid pressures during initial eruptive stages, Soufrière Hills Volcano, Montserrat. *Geophys. Res. Lett.* 37, L00E21. <https://doi.org/10.1029/2010GL043997>.

- Mizutani, Y., Sugiura, T., 1982. Variations in chemical and isotopic compositions of fumarolic gases from Showashinzan volcano, Hokkaido, Japan. *Geochem. J.* 16 (2), 63–71.
- Moretti, R., Papale, P., Ottonello, G., 2003. A model for the saturation of COHS fluids in silicate melts. *Geol. Soc. Lond., Spec. Publ.* 213 (1), 81–101.
- Moretti, R., Arienzo, I., Civetta, L., Orsi, G., Papale, P., 2013a. Multiple magma degassing sources at an explosive volcano. *Earth Planet. Sci. Lett.* 367, 95–104.
- Moretti, R., Arienzo, I., Orsi, G., Civetta, L., D'Antonio, M., 2013b. The deep plumbing system of Ischia: a physico-chemical window on the fluid-saturated and CO₂-saturated Neapolitan Volcanism (Southern Italy). *J. Petrol.* 54 (5), 951–984.
- Moretti, R., De Natale, G., Troise, C., 2017. A geochemical and geophysical reappraisal to the significance of the recent unrest at Campi Flegrei caldera (Southern Italy). *Geochem. Geophys. Geosyst.* 18 (3), 1244–1269.
- Moretti, R., Troise, C., Sarno, F., De Natale, G., 2018. Caldera unrest driven by CO₂-induced drying of the deep hydrothermal system. *Sci. Rep.* 8 (1), 8309.
- Moretti, R., Arienzo, I., Di Renzo, V., Orsi, G., Arzilli, F., Brun, F., ... Delouie, E., 2019. Volatile segregation and generation of highly vesiculated explosive magmas by volatile-melt fining processes: The case of the Campanian Ignimbrite eruption. *Chemical Geology* 503, 1–14.
- Mourgues, R., Cobbold, P.R., 2003. Some tectonic consequences of fluid overpressures and seepage forces as demonstrated by sandbox modelling. *Tectonophysics* 376 (1–2), 75–97.
- Nakajima, J., Matsuzawa, T., Hasegawa, A., Zhao, D., 2001. Three-dimensional structure of Vp, Vs, and Vp/Vs beneath northeastern Japan: Implications for arc magmatism and fluids. *Journal of Geophysical Research: Solid Earth* 106 (B10), 21843–21857.
- Nakamura, K., 1977. Volcanoes as possible indicators of tectonic stress orientation—principle and proposal. *J. Volcanol. and Geotherm. Res.* 1–16.
- Nicollin, F., Gibert, D., Beauducel, F., Boudon, G., Komorowski, J.-C., 2006. Electrical tomography of La Soufrière de Guadeloupe Volcano: field experiments, 1D inversion and qualitative interpretation. *Earth Planet. Sci. Lett.* 244, 709–724.
- NIST, 2018. Thermophysical properties of fluid systems. NIST Chemistry WebBook, SRD 69. National Institute of Standards and Technology. U.S. Department of Commerce <https://webbook.nist.gov/chemistry/fluid/>.
- Norton, D.L., 1984. Theory of hydrothermal systems. *Annu. Rev. Earth Planet. Sci.* 12 (1), 155–177.
- Norton, D., Knight, J., 1977. Transport phenomena in hydrothermal systems: cooling plutons. *Am. J. Sci.* 277.
- Nostro, C., Stein, R.S., Cocco, M., Belardinelli, M.E., Marzocchi, W., 1998. Two-way coupling between Vesuvius eruptions and southern Apennine earthquakes, Italy, by elastic stress transfer. *Journal of Geophysical Research: Solid Earth* 103 (B10), 24487–24504.
- Nuccio, P.M., Paonita, A., 2000. Investigation of the noble gas solubility in H₂O–CO₂ bearing silicate liquids at moderate pressure II: the extended ionic porosity (EIP) model. *Earth Planet. Sci. Lett.* 183 (3–4), 499–512.
- Nugraha, A.D., Indrastuti, N., Kusnandar, R., Gunawan, H., McCausland, W., Aulia, A.N., Harlianti, U., 2019. Joint 3-D tomographic imaging of Vp, Vs and Vp/Vs and hypocenter relocation at Sinabung volcano, Indonesia from November to December 2013. *J. Volcanol. Geotherm. Res.* 382, 210–223.
- OVSG-IPGP, 1999–2019. Monthly reports on the activity of La Soufrière de Guadeloupe and on regional seismicity. <http://www.ipgp.fr/fr/ovsg/bulletins-mensuels-de-lovsg>.
- OVSG-IPGP, 2017. September 2017 monthly report. http://www.ipgp.fr/sites/default/files/ovsg_2017_bilan-annuel.pdf.
- OVSG-IPGP, 2018a. seismic report. http://volcano.ipgp.jussieu.fr/guadeloupe/Communiqués/2018/OVSG_20180202_SequenceSeismesVolcaniques_Soufrie%CC%8ARe.pdf.
- OVSG-IPGP, 2018b. seismic report. http://volcano.ipgp.jussieu.fr/guadeloupe/Communiqués/2018/OVSG_20180416_SequenceSeismesVolcaniques_Soufrie%CC%80re.pdf.
- OVSG-IPGP, 2018c. seismic report seismic report. http://volcano.ipgp.jussieu.fr/guadeloupe/Communiqués/2018/OVSG_20180428_SequenceSeismesSoufrie.pdf.
- Peruzzetto, M., Komorowski, J.C., Le Friant, A., Rosas-Carbajal, M., Mangeny, A., Legendre, Y., 2019. Modeling of partial dome collapse of La Soufrière de Guadeloupe volcano: implications for hazard assessment and monitoring. *Sci. Rep.* 9 (1), 1–15.
- Peyssonnel, J.A., Maty, M., 1756. Observations made upon the Brimstone-Hill (in French La Soufrière) in the Island of Guadeloupe; by John Andrew Peyssonnel, M. D. Member of the Royal Academies of Sciences of Paris and Montpellier, and of Marseilles and Rouen; the King of France's physician and Botanist Heretofore on the Coast of Barbary, and now in the Island of Guadeloupe, F. R. S. Translated from the French by M. Maty, M. D. and F. R. S. *Philos. Trans.* 49, 564–579.
- Pichavant, M., Poussineau, S., Lesne, P., Solaro, C., Bourdier, J.L., 2018. Experimental parametrization of magma mixing: application to the ad 1530 eruption of La Soufrière, Guadeloupe (Lesser Antilles). *J. Petrol.* 59 (2), 257–282.
- Pino, N.A., Moretti, R., Allard, P., Boschi, E., 2011. Seismic precursors of a basaltic paroxysmal explosion track deep gas accumulation and slug upraise. *Journal of Geophysical Research: Solid Earth* 116 (B2).
- Poussineau, S., 2005. Dynamique des magmas andésitiques: approche expérimentale et pétrostructurale; application à la Soufrière de Guadeloupe et à la Montagne Pelée. Doctoral dissertation. Université d'Orléans.
- Pritchard, M.E., Mather, T.A., McNutt, S.R., Delgado, F.J., Reath, K., 2019. Thoughts on the criteria to determine the origin of volcanic unrest as magmatic or non-magmatic. *Phil. Trans. R. Soc. A* 377 (2139), 20180008.
- Reed, M.H., 1997. Hydrothermal alteration and its relationship to ore fluid composition. In: Barnes, H.L. (Ed.), *Geochemistry of Hydrothermal Ore Deposits*, 3rd edition John Wiley & Sons, New York, pp. 517–611.
- Rosas-Carbajal, M., Komorowski, J.C., Nicollin, F., Gibert, D., 2016. Volcano electrical tomography unveils edifice collapse hazard linked to hydrothermal system structure and dynamics. *Sci. Rep.* 6, 29899.
- Rouwet, D., Sandri, L., Marzocchi, W., Gottsmann, J., Selva, J., Tonini, R., Papale, P., 2014. Recognizing and tracking volcanic hazards related to non-magmatic unrest: a review. *J. Appl. Volcanol.* 3 (1), 17.
- Rozhko, A.Y., Podladchikov, Y.Y., Renard, F., 2007. Failure patterns caused by localized rise in pore-fluid overpressure and effective strength of rocks. *Geophys. Res. Lett.* 34 (22).
- Ruzié, L., Moreira, M., Crispi, O., 2012. Noble gas isotopes in hydrothermal volcanic fluids of La Soufrière volcano, Guadeloupe, Lesser Antilles arc. *Chem. Geol.* 304, 158–165.
- Ruzié, L., Aubaud, C., Moreira, M., Agrinier, P., Dessert, C., Gréau, C., Crispi, O., 2013. Carbon and helium isotopes in thermal springs of La Soufrière volcano (Guadeloupe, Lesser Antilles): implications for volcanological monitoring. *Chem. Geol.* 359, 70–80.
- Salaün, A., Villemant, B., Gérard, M., Komorowski, J.-C., Michel, A., 2011. Hydrothermal alteration in andesitic Volcanoes: Trace element redistribution in active and ancient hydrothermal systems of Guadeloupe (Lesser Antilles). *J. Geochem. Expl.* 111, 59–83.
- Sanders, C.O., Ponko, S.C., Nixon, L.D., Schwartz, E.A., 1995. Seismological evidence for magmatic and hydrothermal structure in Long Valley caldera from local earthquake attenuation and velocity tomography. *Journal of Geophysical Research: Solid Earth* 100 (B5), 8311–8326.
- Scarpa, R., Amoruso, A., Crescentini, L., Romano, P., De Cesare, W., Martini, M., Scarpato, G., Linde, A.T., Sacks, S.I., 2007. New borehole strain system detects uplift at Campi Flegrei. *Eos Trans. AGU* 88 (18). <https://doi.org/10.1029/2007EO180002>.
- Schmitt, D.R., Zoback, M.D., 1992. Diminished pore pressure in low-porosity crystalline rock under tensional failure: Apparent strengthening by dilatancy. *Journal of Geophysical Research: Solid Earth* 97 (B1), 273–288.
- Semet, M.P., Vatin-Perignon, N., Vincent, P.M., Joron, J.L., 1982. Magma mixing once more: its involvement in triggering the 16th century volcanic activity at La Soufrière, Guadeloupe (FWI). *Bull. PIRPSEV* 60, 63.
- Sheridan, M.F., 1980. Pyroclastic block flow from the September, 1976, eruption of La Soufrière volcano, Guadeloupe. *Bull. Volcanol.* 43 (2), 397–402.
- Shinohara, H., 2005. A new technique to estimate volcanic gas composition: plume measurements with a portable multi-sensor system. *J. Volcanol. Geotherm. Res.* 143 (4), 319–333.
- Sibson, R.H., 1986. Brecciation processes in fault zones: Inferences from earthquake rupturing. *PAGEOPH* 124, 159–175. <https://doi.org/10.1007/BF00875724>.
- Sibson, R.H., 1990. Rupture nucleation on unfavorably oriented faults. *Bull. Seismol. Soc. Am.* 80, 1580–1604.
- Sibson, R.H., 2000. Fluid involvement in normal faulting. *J. Geodyn.* 29, 469–499. [https://doi.org/10.1016/S0264-3707\(99\)00042-3](https://doi.org/10.1016/S0264-3707(99)00042-3).
- Sigurdsson, H., Houghton, B., McNutt, S., Rymer, H., Stix, J. (Eds.), 2015. *The Encyclopedia of Volcanoes*. Elsevier (1456 pp).
- Sillitoe, R.H., 2010. Porphyry copper systems. *Econ. Geol.* 105 (1), 3–41.
- Spencer Jr., J.W., Nur, A., 1976. The effects of pressure, temperature and pore water on velocities in westerly granite. *J. Geophys. Res.* 81, 899–904.
- Stix, J., de Moor, J.M., 2018. Understanding and forecasting phreatic eruptions driven by magmatic degassing. *Earth, Planets and Space* 70 (1), 83.
- Tamburello, G., Mouné, S., Allard, P., Venugopal, S., Robert, V., Rosas-Carbajal, M., Ucciani, G., Deroussi, S., Kitou, T., Didier, T., Komorowski, J.-C., Beauducel, F., de Chabalière, J.-B., Lemarchand, A., Dessert, C., Moretti, R., 2019. Spatio-temporal relationships between fumarolic activity, hydrothermal fluid circulation and geophysical signals at an arc volcano in degassing unrest: La Soufrière de Guadeloupe (French West Indies). *Geosciences* 9 (11), 480.
- Terakawa, T., Zoporowski, A., Galvan, B., Miller, S.A., 2010. High-pressure fluid at hypocentral depths in the L'Aquila region inferred from earthquake focal mechanisms earthquake focal mechanisms. *Geology* 38 (11), 995–998. <https://doi.org/10.1130/G31457.1> November 2010.
- Touboul, M., Bourdon, B., Villemant, B., Boudon, G., Joron, J.L., 2007. 238U–230Th–226Ra disequilibrium in andesitic lavas of the last magmatic eruption of Guadeloupe Soufrière, French Antilles: processes and timescales of magma differentiation. *Chem. Geol.* 246 (3), 181–206.
- Troise, C., 2001. Stress changes associated with volcanic sources: constraints on Kilauea rift dynamics. *J. Volcanol. Geotherm. Res.* 109, 191–203.
- Troise, C., De Natale, G., Schiavone, R., Somma, R., Moretti, R., 2019. The Campi Flegrei caldera unrest: discriminating magma intrusions from hydrothermal effects and implications for possible evolution. *Earth Sci. Rev.* 188, 108–122.
- Turcotte, D.L., Schubert, G., 1982. *Geodynamics: Applications of Continuum Physics to Geological Problems*. 450 pp. John Wiley, New York.
- Ucciani, G., 2015. Caractérisation spatiale et temporelle de la sismicité volcanique de la Soufrière de Guadeloupe: relation avec le système hydrothermal. Doctoral dissertation. Sorbonne Paris Cité.
- Ucciani, G., Beauducel, F., Bouin, M.P., Nercessian, A., 2015. Dynamic of the volcanic activity of La Soufrière volcano (Guadeloupe, Lesser Antilles): Evidence for shallow fluid seismic sources. *AGU Fall Meeting Abstracts*.
- Ventura, G., Vilardo, G., 1999. Seismic-based estimate of hydraulic parameters at Vesuvius Volcano. *Geophys. Res. Lett.* 26 (7), 887–890.
- Villemant, B., et al., 2005. The memory of volcanic waters: shallow magma degassing revealed by halogen monitoring in thermal springs of La Soufrière volcano (Guadeloupe, Lesser Antilles). *Earth Planet. Sci. Lett.* 237, 710–728.
- Villemant, B., et al., 2014. Evidence for a new shallow magma intrusion at La Soufrière de Guadeloupe (Lesser Antilles): insights from long-term geochemical monitoring of halogen-rich hydrothermal fluids. *J. Volcanol. Geotherm. Res.* 285, 247–277.
- Wadati, K., 1933. On the travel time of earthquake waves, Part II. *Geophys. Mag.* 7, 101–111.
- Walck, M.C., 1988. Three-dimensional Vp/Vs variations for the Coso Region, California. *J. Geophys. Res.* 93 (B3), 2047. <https://doi.org/10.1029/JB093iB03p2047>.
- Walter, T.R., Amelung, F., 2007. Volcanic eruptions following M_z ≥ 9 megathrust earthquakes: implications for the Sumatra-Andaman volcanoes. *Geology* 35 (6), 539–542.

- Watt, S.F.L., Pyle, D.M., Mather, T.A., 2009. The influence of great earthquakes on volcanic eruption rate along the Chilean subduction zone. *Earth Planet. Sci. Lett.* 277, 399–407.
- West, F.G., Heiken, G.H., Homuth, E.F., Peterson, R.W., Crowe, B.M., Wohletz, 1978. Tilts Associated with Volcanic Activity Guadeloupe, French West Indies. Fall 1976. LA-7500-MS Informal Report UC-11. Los Alamos National Laboratories.
- White, R., McCausland, W., 2016. Volcano-tectonic earthquakes: a new tool for estimating intrusive volumes and forecasting eruptions. *J. Volcanol. Geotherm. Res.* 309, 139–155.
- Williams, C.A., Wadge, G., 1998. The effects of topography on magma chamber deformation models: application to Mt. Etna and radar interferometry. *Geophys. Res. Lett.* 25 (10), 1549–1552. <https://doi.org/10.1029/98gl01136>.
- Zlotnicki, J., Feuillard, M., Hammouya, G., 1994. Water circulations on La Soufrière volcano inferred by self-potential surveys (Guadeloupe, Lesser Antilles). Renew of volcanic activity? *J. Geomagn. Geoelectr.* 46 (1994), 797{813.
- Zoback, M., Rummel, F., Jung, R., Raleigh, C., 1977. Laboratory hydraulic fracturing experiments in intact and pre-fractured rock. *Int. J. Rock Mech. Min. Sci. and Geomech.* 14, 49–58.
- Zollo, A., Marzocchi, W., Capuano, P., Lomax, A., Iannaccone, G., 2002. Space and time behavior of seismic activity at Mt. Vesuvius volcano, southern Italy. *Bull. Seismol. Soc. Am.* 92 (2), 625–640.

Appendix D

Degassing-induced depressurization model: Constant expansion and symbols

Equation 5.8 of Section 5.1.2.3.4 calculates the final pressure change at time t as a function of $C_1(t_0)$, $C_2(t_0)$, and $C_3(t_0)$ [Girona et al., 2014]. These constants are defined as followed:

$$C_1(t_0) = \left[\frac{(1 - n_c)\Delta\rho_{1,2}A^*}{n_c\rho_{c1}\hat{\rho}_{m,c}(t_0)} - \frac{1}{\rho_w} \right] \hat{Q} + \lambda(t_0)\Delta P_s(t_0) \quad (\text{D.1})$$

$$C_2(t_0) = - \left\{ \left[1 - \frac{n_r(t_0)\rho_{nd}}{\hat{\rho}_{g,r}(t_0)} \right] \frac{V_r(t_0)}{\mu} + \lambda(t_0) + \frac{V_{m,c}(t_0)}{\mu} \right\} \quad (\text{D.2})$$

$$C_3(t_0) = \frac{\pi R_c(t_0)^2}{g\hat{\rho}_{m,c}(t_0)} + \frac{V_{m,c}(t_0)}{k} + \left[1 - \frac{n_r(t_0)\rho_{nd}}{\hat{\rho}_{g,r}(t_0)} \right] \frac{V_r(t_0)}{k_r} + \frac{\rho_{nd}V_r(t_0)S^2B^*}{2\hat{\rho}_{g,r}(t_0)(\alpha - n_r(t_0))} + \left[\frac{n_r(t_0)\rho_{nd}V_r(t_0)}{\hat{\rho}_{g,r}(t_0)^2} - \frac{\pi R_c(t_0)^2L - V_{m,c}(t_0)}{\hat{\rho}_{m,c}(t_0)} \right] \frac{M_{H_2O}}{R_gT} \quad (\text{D.3})$$

In our study, we have $A^* = 0$ (i.e., $\rho_{m,c}(t_0)$ and $\gamma_c(t_0)$ are constant), $B^* = 0$ and $n_r(t_0) = 0$ (i.e., no gas exsolves in the reservoir), $\lambda(t_0) = 0$ (i.e., no magma replenishment), and $\frac{[\pi R_c(t_0)^2L - V_{m,c}(t_0)]M_{H_2O}}{\hat{\rho}_{m,c}(t_0)R_gT}$ is one order of magnitude lower than $\frac{\pi R_c(t_0)^2}{g\hat{\rho}_{m,c}(t_0)}$ (for typical magma temperatures [Girona et al., 2014]). We can therefore simplify the constants as follows:

$$C_1(t_0) = \frac{-\hat{Q}}{\rho_w} \quad (\text{D.4})$$

$$C_2(t_0) = - \frac{V_r(t_0)}{\mu} - \frac{V_{m,c}(t_0)}{\mu} \quad (\text{D.5})$$

$$C_3(t_0) = \frac{\pi R_c(t_0)^2}{g\hat{\rho}_{m,c}(t_0)} + \frac{V_{m,c}(t_0)}{k} + \frac{V_r(t_0)}{k_r} \quad (\text{D.6})$$

The symbols included in these equations are listed below in Table D.1 [Girona et al., 2014].

Symbol	Description	Range used in this study
ΔP	pressure change during quiescence	≤ 10 MPa (absolute value)
\dot{Q}	total mean gas flux	90 kt d ⁻¹
t	time of passive degassing	≤ 10 years
R_c	volcanic conduit radius	≤ 300 m
V_r	volume of the reservoir	$5 \times 10^8 - 3 \times 10^{10}$ m ³
L	length of the magma column (up to the average reservoir depth)	2.2 km
α	mass fraction of dissolved volatiles in parent melt	1.3 wt%
k	bulk modulus of host rock	10^{10} Pa
k_r	bulk modulus accounting for chamber compressibility	$5 \times 10^8 - 1 \times 10^{10}$ Pa
μ	effective viscosity of the crust	$10^{17} - 10^{18}$ Pa s
g	gravity	9.8 m s ⁻²
$\hat{\rho}_{m,c}$	mean density of melt inside the magma column	2550 kg m ⁻³
$\hat{\rho}_{g,c}$	mean density of gas inside the magma column	≤ 200 kg m ⁻³
ρ_c	density of fully degassed melt in the column	2670 kg m ⁻³
ρ_{nd}	density of the parent undegassed magma	2430 kg m ⁻³
ρ_x	density of the melt at gas-magma separation level	$\rho_x = \rho_c$
n_c	wt % of water exsolved in the upper conduit	$\leq \alpha$
n_r	wt % of water exsolved in the reservoir	0%
n_x	wt % of water exsolved in the reservoir or conduit	$n_x = n_c$
γ_c	volume fraction of degassed melt in the magma column	0.5
μ_{nd}	viscosity of undegassed parent melt	$10^2 - 10^5$ Pa s
μ_1	viscosity of degassed melt in the conduit	$> \mu_{nd}$
M_{H_2O}	molar mass of water	18 g mol ⁻¹
T	temperature of magma	1300 K
S	constant of Henry's law for water	4×10^{-6} Pa ^{-1/2}
R_g	universal gas constant	8.31 J (K mol) ⁻¹
A^*	indicator variable	0
B^*	indicator variable	0
ΔP_∞	maximum pressure change	
Γ	parameter defined in equation (39) of Girona et al. [2014]	
ρ_w	parameter defined in equation (20) of Girona et al. [2014]	
$m_{g,c}$	mass of gas within the column of length L	
$m_{m,c}$	mass of melt within the column of length L	
$m_{g,r}$	mass of gas within the reservoir	
$V_{g,c}$	volume of gas inside the column of length L	
$V_{g,r}$	volume of gas that exsolves in the reservoir	
$V_{m,c}$	volume of melt inside the column of length L	
$\frac{dV_d}{dt}$	volume decrease of melt in the system due to gas exsolution	
$V_{m,r+c}$	volume of melt in the conduit-reservoir	
$V_{m,r}$	volume of melt in the reservoir	
D	portion of the magma column which is within the reservoir	
β_r	gas volume fraction in the reservoir	
β_c	gas volume fraction in the magma column	

Table D.1: **List of symbols.** A description of the symbols used in Chapter 5.1.2.3, as well as the ranges chosen for the parameters in this study. Symbols with no range presented are calculated from the defined parameters.

Bibliography

- V. Acocella. Understanding caldera structure and development: An overview of analogue models compared to natural calderas. *Earth-Science Reviews*, 85(3-4):125–160, 2007. doi: <https://doi.org/10.1016/j.earscirev.2007.08.004>.
- V. Acocella, F. Cifelli, and R. Funicello. Analogue models of collapse calderas and resurgent domes. *Journal of Volcanology and Geothermal Research*, 104(1):81 – 96, 2000. ISSN 0377-0273. doi: [https://doi.org/10.1016/S0377-0273\(00\)00201-8](https://doi.org/10.1016/S0377-0273(00)00201-8).
- V. Acocella, B. Behncke, M. Neri, and S. D’Amico. Link between major flank slip 2002 – 2003 eruption at Mt. Etna (Italy). *Geophysical Research Letters*, 30(24):10–13, 2003. ISSN 00948276. doi: <https://doi.org/10.1029/2003GL018642>.
- T. Ágústsdóttir, T. Winder, J. Woods, R.S. White, T. Greenfield, and B. Brandsdóttir. Intense seismicity during the 2014-2015 Bárðarbunga-Holuhraun rifting event, Iceland, reveals the nature of dike-induced earthquakes and caldera collapse mechanisms. *Journal of Geophysical Research: Solid Earth*, 124(8):8331–8357, 2019. ISSN 21699356. doi: <https://doi.org/10.1029/2018JB016010>.
- K. Aki and P.G. Richards. *Quantitative Seismology*. University Science Books, 2002. ISBN 9780935702965.
- P. Allard, A. Aiuppa, P. Bani, N. Métrich, A. Bertagnini, P.J. Gauthier, H. Shinohara, G. Sawyer, F. Parello, E. Bagnato, B. Pelletier, and E. Garaebiti. Prodigious emission rates and magma degassing budget of major, trace and radioactive volatile species from Ambrym basaltic volcano, Vanuatu Island arc. *Journal of Volcanology and Geothermal Research*, 304:378 – 402, 2015. doi: <https://doi.org/10.1016/j.jvolgeores.2015.10.004>.
- P. Allard, M. Burton, G. Sawyer, and P. Bani. Degassing dynamics of basaltic lava lake at a top-ranking volatile emitter: Ambrym volcano, Vanuatu arc. *Earth and Planetary Science Letters*, 448:69–80, 2016. ISSN 0012821X. doi: 10.1016/j.epsl.2016.05.014. URL <http://dx.doi.org/10.1016/j.epsl.2016.05.014>.
- F. Amelung, S.H. Yun, T.R. Walter, P. Segall, and S.W. Kim. Stress control of deep rift intrusion at Mauna Loa Volcano, Hawaii. *Science*, 316:1026–30, 06 2007. doi: <https://doi.org/10.1126/science.1140035>.
- M. Amma-Miyasaka, M. Nakagawa, and S. Nakada. Magma plumbing system of the 2000 eruption of Miyakejima Volcano, Japan. *Bulletin of Volcanology*, 67(3):254–267, 2005. ISSN 02588900. doi: <http://doi.org/10.1007/s00445-004-0408-0>.
- A. Amoroso and L. Crescentini. Shape and volume change of pressurized ellipsoidal cavities from deformation and seismic data. *Journal of Geophysical Research: Solid Earth*, 114(2): 1–8, 2009. ISSN 21699356. doi: <https://doi.org/10.1029/2008JB005946>.
- N. Anantrasirichai, J. Biggs, F. Albino, and D. Bull. A deep learning approach to detecting volcano deformation from satellite imagery using synthetic datasets. *Remote Sensing of*

- Environment*, 230:111179, 2019a. ISSN 0034-4257. doi: <https://doi.org/10.1016/j.rse.2019.04.032>.
- N. Anantrasirichai, J. Biggs, F. Albino, and D. Bull. The application of convolutional neural networks to detect slow, sustained deformation in InSAR time series. *Geophysical Research Letters*, 46(21):11850–11858, 2019b. ISSN 19448007. doi: <https://doi.org/10.1029/2019GL084993>.
- K. Anderson and P. Segall. Physics-based models of ground deformation and extrusion rate at effusively erupting volcanoes. *Journal of Geophysical Research: Solid Earth*, 116(7): 1–20, 2011. ISSN 21699356. doi: <https://doi.org/10.1029/2010JB007939>.
- K.R. Anderson, I.A. Johanson, M.R. Patrick, M. Gu, P. Segall, M.P. Poland, E.K. Montgomery-Brown, and A. Miklius. Magma reservoir failure and the onset of caldera collapse at Kilauea Volcano in 2018. *Science*, 366(6470), 2019. ISSN 10959203. doi: <https://doi.org/10.1126/science.aaz1822>.
- M.O. Anderson, M.D. Hannington, K. Haase, U. Schwarz-Schampera, N. Augustin, T.F. McConachy, and K. Allen. Tectonic focusing of voluminous basaltic eruptions in magma-deficient backarc rifts. *Earth and Planetary Science Letters*, 440(February):43–55, 2016. ISSN 0012821X. doi: <https://doi.org/10.1016/j.epsl.2016.02.002>.
- M. Armstrong and R. Jabin. Variogram models must be positive-definite. *Mathematical Geology*, (13):455 – 459, 1981. doi: <https://doi.org/10.1007/BF01079648>.
- J.M. Auzende, Y. Lafoy, and B. Marsset. Recent geodynamic evolution of the north Fiji basin (southwest Pacific). *Geology*, 16(10):925, 1988. ISSN 0091-7613. doi: [https://doi.org/10.1130/0091-7613\(1988\)016<0925:RGEOITN>2.3.CO;2](https://doi.org/10.1130/0091-7613(1988)016<0925:RGEOITN>2.3.CO;2).
- J.M. Auzende, B. Pelletier, and J.P. Eissen. The North Fiji Basin: geology, structure and geodynamic evolution. In B. Taylor, editor, *Backarc basins: tectonics and magmatism*, pages 139–175. Plenum Press, 1995.
- A. Ayele, E. Jacques, M. Kassim, T. Kidane, A. Omar, S. Tait, A. Necessian, J.B. de Chaballier, and G. King. The volcano-seismic crisis in Afar, Ethiopia, starting September 2005. *Earth and Planetary Science Letters*, 255(1-2):177–187, 2007. ISSN 0012821X. doi: <https://doi.org/10.1016/j.epsl.2006.12.014>.
- O. Bachmann, C.D. Deering, J.S. Ruprecht, C. Huber, A. Skopelitis, and C. Schnyder. Evolution of silicic magmas in the Kos-Nisyros volcanic center, Greece: A petrological cycle associated with caldera collapse. *Contributions to Mineralogy and Petrology*, 163(1): 151–166, 2012. ISSN 00107999. doi: <https://doi.org/10.1007/s00410-011-0663-y>.
- M. Bagnardi and F. Amelung. Space-geodetic evidence for multiple magma reservoirs and subvolcanic lateral intrusions at Fernandina Volcano, Galápagos Islands. *Journal of Geophysical Research B: Solid Earth*, 117(10):1–19, 2012. doi: <https://doi.org/10.1029/2012JB009465>.

- C. Baillard, W.C. Crawford, V. Ballu, M. Régnier, B. Pelletier, and E. Garaebiti. Seismicity and shallow slab geometry in the central Vanuatu subduction zone. *Journal of Geophysical Research: Solid Earth*, 120(8):5606–5623, 2015. ISSN 21699356. doi: <https://doi.org/10.1002/2014JB011853>.
- S. Baker and F. Amelung. Top-down inflation and deflation at the summit of Kīlauea Volcano, Hawai‘i observed with InSAR. *Journal of Geophysical Research*, 117(December): 1–14, 2012. doi: <https://doi.org/10.1029/2011JB009123>.
- P. Bani, C. Oppenheimer, V.I. Tsanev, S.A. Carn, S.J. Cronin, R. Crimp, J.A. Calkins, D. Charley, M. Lardy, and T.R. Roberts. Surge in sulphur and halogen degassing from Ambrym volcano, Vanuatu. *Bulletin of Volcanology*, 71(10):1159–1168, 2009. ISSN 02588900. doi: <https://doi.org/10.1007/s00445-009-0293-7>.
- M. Battaglia, P.F. Cervelli, and J.R. Murray. DMODELS: A MATLAB software package for modeling crustal deformation near active faults and volcanic centers. *Journal of Volcanology and Geothermal Research*, 254:1–4, 2013. ISSN 03770273. doi: <https://doi.org/10.1016/j.jvolgeores.2012.12.018>.
- J.C. Beaglehole. *The journals of Captain James Cook on his voyages of discovery II. The voyage of the Resolution and Adventure 1772-1775*. Hakluyt Soc. extra Ser. 36. Cambridge University, 1961.
- F. Beauducel, P. Briole, and J.L. Froger. Volcano-wide fringes in ERS Synthetic Aperture Radar interferograms of Etna: Deformation or tropospheric effect? *Journal of Geophysical Research*, 105402(10):391–16, 2000. ISSN 0148-0227. doi: <https://doi.org/10.1029/2000JB900095>.
- F. Beauducel, D. Lafon, X. BĀlguin, J.M. Saurel, A. Bosson, D. Mallarino, P. Boissier, C. Brunet, A. Lemarchand, C. Anténor-Habazac, A. Necessian, and A. Jafargholkhanloo. WebObs: The volcano observatories missing link between research and real-time monitoring. *Frontiers in Earth Science*, 8, 02 2020. doi: <https://doi.org/10.3389/feart.2020.00048>.
- A. Beaumais. *Géochimie de l’arc du Vanuatu : évolution spatio-temporelle des édifices volcaniques et des sources mantelliques*. PhD thesis, University of Bretagne occidentale, Brest, France, 2013.
- N.B.D. Bechor and H.A. Zebker. Measuring two-dimensional movements using a single InSAR pair. *Geophysical Research Letters*, 33(16):1–5, 2006. ISSN 00948276. doi: <https://doi.org/10.1029/2006GL026883>.
- D.P. Belcher. Theoretical limits on SAR imposed by the ionosphere. *IET Radar Sonar and Navigation*, 2(6):435–448, 2008. ISSN 1751-8784. doi: <https://doi.org/10.1049/iet-rsn:20070188>.
- N. Bergeot, M.N. Bouin, M. Diament, B. Pelletier, M. Régnier, S. Calmant, and V. Ballu. Horizontal and vertical interseismic velocity fields in the Vanuatu subduction zone from

- GPS measurements: Evidence for a central Vanuatu locked zone. *Journal of Geophysical Research: Solid Earth*, 114(6), 2009. ISSN 21699356. doi: <https://doi.org/10.1029/2007JB005249>.
- J. Biggs and M.E. Pritchard. Global volcano monitoring: What does it mean when volcanoes deform? *Elements*, 13(1):17–22, 2017. ISSN 18115217. doi: <https://doi.org/10.2113/gselements.13.1.17>.
- J. Biggs, E.Y. Anthony, and C.J. Ebinger. Multiple inflation and deflation events at Kenyan volcanoes, East African Rift. *Geology*, 37(11):979–982, 2009. ISSN 00917613. doi: <https://doi.org/10.1130/G30133A.1>.
- R. Bindshadler. Monitoring ice sheet behavior from space. *Reviews of Geophysics*, 36(1):79–104, 1998. doi: <https://doi.org/10.1029/97RG02669>.
- A. Björnsson, K. Saemundsson, P. Einarsson, E. Tryggvason, and K. Grönvold. Current rifting episode in north Iceland. *Nature*, 266:318–323, 1977.
- S. Blake. Volcanism and the dynamics of open magma chambers. 289(5800):783–785, 1981. ISSN 00280836. doi: <https://doi.org/10.1038/289783a0>.
- M. Boichu, B. Villemant, and G. Boudon. A model for episodic degassing of an andesitic magma intrusion. *Journal of Geophysical Research: Solid Earth*, 113(7):1–18, 2008. ISSN 21699356. doi: <https://doi.org/10.1029/2007JB005130>.
- M. Boichu, B. Villemant, and G. Boudon. Degassing at La Soufrière de Guadeloupe volcano (Lesser Antilles) since the last eruptive crisis in 1975–77: Result of a shallow magma intrusion? *Journal of Volcanology and Geothermal Research*, 203(3–4):102–112, 2011. ISSN 03770273. doi: <https://doi.org/10.1016/j.jvolgeores.2011.04.007>.
- M. Boichu, R. Grandin, and et al. Twenty years of multisatellite SO₂ observations at Ambrym volcano (Vanuatu): Insights into passive degassing, SO₂ lifetime and eruptive activity. *in prep.*, 2021.
- A. Bonaccorso, T. Caltabiano, G. Currenti, C. Del Negro, S. Gambino, G. Ganci, S. Giannanco, F. Greco, A. Pistorio, G. Salerno, S. Spampinato, and E. Boschi. Dynamics of a lava fountain revealed by geophysical, geochemical and thermal satellite measurements: The case of the 10 April 2011 Mt. Etna eruption. *Geophysical Research Letters*, 38(24):1–7, 2011. ISSN 00948276. doi: <http://doi.org/10.1029/2011GL049637>.
- A. Borgia. Dynamic basis of volcanic spreading. *Journal of Geophysical Research*, 99(B9):17,791 – 17,804, 1994. doi: <http://doi.org/10.1029/94JB00578>.
- U. Boyson and P. Bani. Ibu volcano, a center of spectacular dacite dome growth and long-term continuous eruptive discharges. *Journal of Volcanology and Geothermal Research*, 282:36–42, 2014. ISSN 0377-0273. doi: <http://doi.org/10.1016/j.jvolgeores.2014.06.011>.
- M. Branney and V. Acocella. *Calderas*. Elsevier Inc., second edition edition, 2015. ISBN 9780123859389. doi: <http://doi.org/10.1016/b978-0-12-385938-9.00016-x>.

- P. Briole, R. Gaulon, G. De Natale, F. Pingue, and R. Scarpa. Inversion of geodetic data and seismicity associated with the friuli earthquake sequence (1976-1977). *Ann. Geophys. (C.N.R.S.); (France)*, 4:4, Aug 1987.
- L. Briquieu, C. Laporte, A.J. Crawford, T. Hasenaka, P.E. Baker, and M. Coltorti. Temporal magmatic evolution of the aoba basin, central New Hebrides sland Arc: Pb, Sr, and Nd isotopic evidence for the coexistence of two mantle components beneath the arc. In *Proceedings of the Ocean Drilling Program, 134 Scientific Results*, number July 2015. 1994. doi: <http://doi.org/10.2973/odp.proc.sr.134.019.1994>.
- D. Broek and J.R. Rice. *Elementary Engineering Fracture Mechanics*, volume 42. 1975. doi: <http://doi.org/10.1115/1.3423697>.
- W.R. Buck, P. Einarsson, and B. Brandsdóttir. Tectonic stress and magma chamber size as controls on dike propagation: Constraints from the 1975-1984 Krafla rifting episode. *Journal of Geophysical Research: Solid Earth*, 111(12):1–15, 2006. ISSN 21699356. doi: <http://doi.org/10.1029/2005JB003879>.
- P. Burgi, T.H. Darrah, D. Tedesco, and W.K. Eymold. Dynamics of the Mount Nyiragongo lava lake. *Journal of Geophysical Research : Solid Earth*, 119:4106–4122, 2014. doi: <http://doi.org/10.1002/2013JB010895>.
- C.W. Burnham. Water and magmas; a mixing model. *Geochimica et Cosmochimica Acta*, 39(8):1077–1084, 1975. ISSN 00167037. doi: [http://doi.org/10.1016/0016-7037\(75\)90050-2](http://doi.org/10.1016/0016-7037(75)90050-2).
- C.W. Burnham and R.H. Jahns. A method for determining the solubility of water in silicate melts. *American Journ*, 260:721–745, 1962. doi: <http://doi.org/10.2475/ajs.260.10.721>.
- S. Calmant, B. Pelletier, P. Lebellegard, M. Bevis, F.W. Taylor, and D.A. Phillips. New insights on the tectonics along the New Hebrides subduction zone based on GPS results. *Journal of Geophysical Research: Solid Earth*, 108(B6):1–22, 2003. doi: <http://doi.org/10.1029/2001jb000644>.
- G. Carazzo, E. Kaminski, and S. Tait. On the rise of turbulent plumes: Quantitative effects of variable entrainment for submarine hydrothermal vents, terrestrial and extra terrestrial explosive volcanism. *Journal of Geophysical Research: Solid Earth*, 113(9):1–19, 2008. ISSN 21699356. doi: <http://doi.org/10.1029/2007JB005458>.
- S. Carey and H. Sigurdsson. The May 18, 1980 eruption of Mount St. Helens 2. Modeling of dynamics of the Plinian phase. *Journal of Geophysical Research*, 90(B4):2948–2958, 1985. doi: <https://doi.org/10.1029/JB090iB04p02948>.
- L. Caricchi, J. Biggs, C. Annen, and S. Ebmeier. The influence of cooling, crystallisation and re-melting on the interpretation of geodetic signals in volcanic systems. *Earth and Planetary Science Letters*, 388:166–174, 2014. ISSN 0012821X. doi: <http://doi.org/10.1016/j.epsl.2013.12.002>.

- S.F. Carle. Three-Dimensional gravity modeling of the geologic structure of Long Valley Caldera. *Journal of Geophysical Research: Solid Earth*, 93(B11):13237–13250, 1988. doi: <http://doi.org/10.1029/JB093iB11p13237>.
- S.A. Carn, K. Yang, A.J. Prata, and N.A. Krotkov. Extending the long-term record of volcanic SO₂ emissions with the Ozone Mapping and Profiler Suite nadir mapper. *Geophysical Research Letters*, 42(3):925–932, 2015. ISSN 19448007. doi: <http://doi.org/10.1002/2014GL062437>.
- S.A. Carn, V.E. Fioletov, C.A. Mclinden, C. Li, and N.A. Krotkov. A decade of global volcanic SO₂ emissions measured from space. *Scientific Reports*, 7:1–12, 2017. ISSN 20452322. doi: <http://doi.org/10.1038/srep44095>.
- J.N. Carney and A. MacFarlane. Geological evidence bearing on the miocene to recent structural evolution of the new hebrides arc. *Tectonophysics*, 87(1):147 – 175, 1982. ISSN 0040-1951. doi: [https://doi.org/10.1016/0040-1951\(82\)90225-6](https://doi.org/10.1016/0040-1951(82)90225-6).
- K.V. Cashman and G. Giordano. Calderas and magma reservoirs. *Journal of Volcanology and Geothermal Research*, 288:28–45, 2014. ISSN 03770273. doi: <http://doi.org/10.1016/j.jvolgeores.2014.09.007>. URL <http://dx.doi.org/10.1016/j.jvolgeores.2014.09.007>.
- V. Cayol and F.H. Cornet. 3D mixed boundary elements for elastostatic deformation field analysis. *International journal of rock mechanics and mining ...*, 34(2):275–287, 1997. ISSN 01489062. doi: [http://doi.org/10.1016/S0148-9062\(96\)00035-6](http://doi.org/10.1016/S0148-9062(96)00035-6).
- V. Cayol and F.H. Cornet. Three-dimensional modeling of the 1983-1984 eruption at Piton de la Fournaise Volcano, Réunion Island. *Journal of Geophysical Research*, 103:18,025–18,037, 1998.
- V. Cayol, T. Catry, L. Michon, M. Chaput, V. Famin, O. Bodart, J.L. Froger, and C. Romagnoli. Sheared sheet intrusions as mechanism for lateral flank displacement on basaltic volcanoes: Applications to Réunion Island volcanoes. *Journal of Geophysical Research: Solid Earth*, 119, 2014. doi: <https://doi.org/10.1002/2014JB011139>.
- International Seismological Centre. On-line Bulletin, 2020. <http://www.isc.ac.uk>.
- S. Cesca, J. Letort, H.N.T. Razafindrakoto, S. Heimann, E. Rivalta, M.P. Isken, M. Nikkhoo, L. Passarelli, G.M. Petersen, F. Cotton, and T. Dahm. Drainage of a deep magma reservoir near Mayotte inferred from seismicity and deformation. *Nature Geoscience*, 13(1):87–93, 2020. ISSN 17520908. doi: <http://doi.org/10.1038/s41561-019-0505-5>.
- C.G. Chase. Tectonic history of the Fiji plateau. *Geol. Soc. Am. Bull.*, (82):3087–3110, 1971. doi: [https://doi.org/10.1130/0016-7606\(1971\)82\[3087:THOTFP\]2.0.CO;2](https://doi.org/10.1130/0016-7606(1971)82[3087:THOTFP]2.0.CO;2).
- T.E. Chase and B.A. Seekins. Submarine topography of the Vanuatu and southeastern Soloman Islands regions. In H.G. Greene, editor, *Geology and offshore resources of Pacific island arcs– Vanuatu region.*, volume 8, pages 35–36. Circum-Pacific Council for Energy and Mineral Resources Earth Science Series, Houston, Texas, 1988.

- E. Chaussard, F. Amelung, and Y. Aoki. Characterization of open and closed volcanic systems in Indonesia and Mexico using InSAR time series. *Journal of Geophysical Research: Solid Earth*, 118(8):3957–3969, 2013. ISSN 21699356. doi: <http://doi.org/10.1002/jgrb.50288>.
- E. Chaussard, S. Wdowinski, E. Cabral-Cano, and F. Amelung. Land subsidence in central Mexico detected by ALOS InSAR time-series. *Remote Sensing of Environment*, 140:94–106, 2014. ISSN 00344257. doi: <http://doi.org/10.1016/j.rse.2013.08.038>.
- C.W. Chen and H.A. Zebker. Two-dimensional phase unwrapping with use of statistical models for cost functions in nonlinear optimization. *Journal of the Optical Society of America A*, 18(2):338, 2001. ISSN 1084-7529. doi: <http://doi.org/10.1364/JOSAA.18.000338>.
- C.A. Chesner and W.I. Rose. Stratigraphy of the Toba Tuffs and the evolution of the Toba Caldera Complex, Sumatra, Indonesia. *Bulletin of Volcanology*, 53:343–356, 1991.
- J.P. Chilés and P. Delfiner. *Geostatistics—Modelling spatial uncertainties*. Wiley Series in Probability and Statistics. Applied Probability and Statistics Section. New York, 1999.
- B.A. Chouet. Long-period volcano seismicity: Its source and use in eruption forecasting. *380(6572):309–316*, 1996. ISSN 00280836. doi: <http://doi.org/10.1038/380309a0>.
- R.L. Christiansen. Yellowstone magmatic evolution: Its bearing on understanding large-volume explosive volcanism. In National Research Council, editor, *Explosive Volcanism: Inception, Evolution, and Hazards*, pages 84–95. The National Academies Press, Washington, DC, 1984. doi: <http://doi.org/10.17226/18602>.
- D.A. Clague, B.M. Dreyer, J.B. Padua, J.F. Martin, W.W. Chadwick, D.W. Caress, R.A. Portner, T.P. Guilderson, M.L. McGann, H. Thomas, D.A. Butterfield, and R.W. Embley. Geologic history of the summit of Axial Seamount, Juan de Fuca Ridge. *Geochemistry, Geophysics, Geosystems*, 14:4403–4443, 2013. doi: <https://doi.org/10.1002/ggge.20240>.
- L. Clarisse, P.F. Coheur, N. Theys, D. Hurtmans, and C. Clerbaux. The 2011 Nabro eruption, a SO₂ plume height analysis using IASI measurements. *Atmospheric Chemistry and Physics*, 14(6):3095–3111, 2014. ISSN 16807324. doi: <http://doi.org/10.5194/acp-14-3095-2014>.
- C. Clerbaux, A. Boynard, L. Clarisse, M. George, H. Herbin, D. Hurtmans, and M. Pommier. Monitoring of atmospheric composition using the thermal infrared IASI/MetOp sounder. *Atmospheric Chemistry and Physics*, 9:6041–6054, 2009. ISSN 16807375. doi: <http://doi.org/10.5194/acpd-9-8307-2009>.
- J.W. Cole, D.M. Milner, and K.D. Spinks. Calderas and caldera structures: A review. *Earth-Science Reviews*, 69(1-2):1–26, 2005. ISSN 00128252. doi: <http://doi.org/10.1016/j.earscirev.2004.06.004>.

- J.Y. Collot, J. Daniel, and R.V. Burne. Recent tectonics associated with the subduction/collision of the d'entrecasteaux zone in the central new hebrides. *Tectonophysics*, 112(1): 325 – 356, 1985. ISSN 0040-1951. doi: [https://doi.org/10.1016/0040-1951\(85\)90185-4](https://doi.org/10.1016/0040-1951(85)90185-4).
- D. Coppola, M. Laiolo, and C. Cigolini. Fifteen years of thermal activity at Vanuatu's volcanoes (2000 – 2015) revealed by MIROVA. *Journal of Volcanology and Geothermal Research*, 322:6–19, 2016a. ISSN 03770273. doi: <http://doi.org/10.1016/j.jvolgeores.2015.11.005>.
- D. Coppola, M. Laiolo, C. Cigolini, D. Delle Donne, and M. Ripepe. Enhanced volcanic hot-spot detection using MODIS IR data: Results from the MIROVA system. *Geological Society Special Publication*, 426(1):181–205, 2016b. ISSN 03058719. doi: <http://doi.org/10.1144/SP426.5>.
- D. Coppola, M. Laiolo, F. Massimetti, and C. Cigolini. Monitoring endogenous growth of open-vent volcanoes by balancing thermal and SO₂ emissions data derived from space. *Scientific Reports*, 9(1):1–12, 2019. ISSN 20452322. doi: <http://doi.org/10.1038/s41598-019-45753-4>.
- F. Corbi, E. Rivalta, V. Pinel, F. Maccaferri, M. Bagnardi, and V. Acocella. How caldera collapse shapes the shallow emplacement and transfer of magma in active volcanoes. *Earth and Planetary Science Letters*, 431:287–293, 2015. ISSN 0012821X. doi: <http://doi.org/10.1016/j.epsl.2015.09.028>.
- A.J. Crawford, L. Briquieu, C. Laporte, and T. Hasenaka. Coexistence of Indian and Pacific ocean upper mantle reservoirs beneath the central New Hebrides Island arc. In B. Taylor and J. Natlund, editors, *Active margins and marginal basins of the western Pacific*, volume Monograph 88, pages 199–217. Am. Geophys. Union Geophys., 1995.
- J.A. Crisp. Rates of magma emplacement and volcanic output. *Journal of Volcanology and Geothermal Research*, 20(3-4):177–211, 1984. ISSN 03770273. doi: [http://doi.org/10.1016/0377-0273\(84\)90039-8](http://doi.org/10.1016/0377-0273(84)90039-8).
- S.J. Cronin and K. Németh. Where are the giant tuff cone and ignimbrites of Ambrym? A more conventional story of mafic volcanism at Ambrym Volcano, Vanuatu. In *Geological Society of New Zealand 50th Annual Conference*, pages 21–22, Kaikoura, New Zealand, 2005. Geological Society of New Zealand.
- S.L. Crouch. Solution of plane elasticity problems by the displacement discontinuity method. *International Journal for Numerical Methods in Engineering*, 10(2):301–343, 1976. doi: <https://doi.org/10.1002/nme.1620100206>.
- S.L. Crouch and A.M. Starfield. *Boundary Element Methods in Solid Mechanics: With Applications in Rock Mechanics and Geological Engineering*. Allen & Unwin, 1983. ISBN 9780046200107.
- I.G. Cumming and F.H. Wong. *Digital Processing of Synthetic Aperture Radar Data: Algorithms and Implementation*. Number v. 1 in Artech House remote sensing library. Artech House, 2005. ISBN 9781580530583.

- L.V. Danyushevsky, A.W. McNeill, and A.V. Sobolev. Experimental and petrological studies of melt inclusions in phenocrysts from mantle-derived magmas: An overview of techniques, advantages and complications. *Chemical Geology*, 183(1-4):5–24, 2002. ISSN 00092541. doi: [http://doi.org/10.1016/S0009-2541\(01\)00369-2](http://doi.org/10.1016/S0009-2541(01)00369-2).
- J.N. Davies and L. House. Aleutian subduction zone seismicity, volcano-trench separation, and their relation to great thrust-type earthquakes. *Journal of Geophysical Research*, 84(8):4583–4591, 1979. doi: <https://doi.org/10.1029/JB084iB09p04583>.
- P.M. Davis. Surface deformation associated with a dipping hydrofracture. *Journal of Geophysical Research*, 88(B7):5826–5834, 1983. ISSN 01480227. doi: <http://doi.org/10.1029/JB088iB07p05826>.
- P.M. Davis. Surface deformation due to inflation of an arbitrarily oriented triaxial ellipsoidal cavity in an elastic half-space, with reference to Kīlauea volcano, Hawaii. *Journal of Geophysical Research: Solid Earth*, 91(B7):7429–7438, 1986. doi: <http://doi.org/10.1029/JB091iB07p07429>.
- F. De Zan and A.M. Guarnieri. TOPSAR: Terrain observation by progressive scans. *IEEE Transactions on Geoscience and Remote Sensing*, 44(9):2352–2360, 2006. ISSN 01962892. doi: <http://doi.org/10.1109/TGRS.2006.873853>.
- D.P. Dee, S.M. Uppala, A.J. Simmons, P. Berrisford, P. Poli, S. Kobayashi, U. Andrae, M.A. Balmaseda, G. Balsamo, P. Bauer, P. Bechtold, A.C.M. Beljaars, L. van de Berg, J. Bidlot, N. Bormann, C. Delsol, R. Dragani, M. Fuentes, A.J. Geer, L. Haimberger, S.B. Healy, H. Hersbach, E.V. Hólm, L. Isaksen, P. Kållberg, M. Köhler, M. Matricardi, A.P. McNally, B.M. Monge-Sanz, J.J. Morcrette, B.K. Park, C. Peubey, P. de Rosnay, C. Tavolato, J.N. Thépaut, and F. Vitart. The ERA-Interim reanalysis: Configuration and performance of the data assimilation system. *Quarterly Journal of the Royal Meteorological Society*, 137(656):553–597, 2011. ISSN 00359009. doi: <http://doi.org/10.1002/qj.828>.
- P.T. Delaney and D.F. McTigue. Volume of magma accumulation or withdrawal estimated from surface uplift or subsidence, with application to the 1960 collapse of Kīlauea volcano. *Bulletin of Volcanology*, 56(6-7):417–424, 1994. ISSN 02588900. doi: <http://doi.org/10.1007/BF00302823>.
- A. Di Muro, N. Métrich, D. Vergani, M. Rosi, P. Armienti, T. Fougereux, E. Deloule, I. Arienzo, and L. Civetta. The shallow plumbing system of Piton de la Fournaise Volcano (La Réunion Island, Indian Ocean) revealed by the major 2007 caldera-forming eruption. *Journal of Petrology*, 55(7):1287–1315, 2014. ISSN 14602415. doi: <http://doi.org/10.1093/petrology/egu025>.
- J. Dieterich, V. Cayol, and P. Okubo. The use of earthquake rate changes as a stress meter at Kīlauea volcano. *Nature*, 408:457–460, 2000. doi: <http://doi.org/10.1038/35044054>.
- J.H. Dieterich. Growth and persistence of Hawaiian Volcanic rift zones. *Journal of Geophysical Research*, 93(B5):4258–4270, 1988. ISSN 01480227. doi: <http://doi.org/10.1029/JB093iB05p04258>.

- J.H. Dieterich and R.W. Decker. Finite element modeling of surface deformation associated with volcanism. *Journal of Geophysical Research*, 80(29):4094–4102, 1975. ISSN 0148-0227. doi: <http://doi.org/10.1029/jb080i029p04094>.
- M.P. Doin, C. Lasserre, G. Peltzer, O. Cavalié, and C. Doubre. Corrections of stratified tropospheric delays in SAR interferometry: Validation with global atmospheric models. *Journal of Applied Geophysics*, 69(1):35–50, 2009. ISSN 09269851. doi: <http://doi.org/10.1016/j.jappgeo.2009.03.010>. URL <http://doi.org/10.1016/j.jappgeo.2009.03.010>.
- M.P. Doin, F. Lodge, S. Guillaso, R. Jolivet, C. Lasserre, G. Ducret, R. Grandin, E. Pathier, and V. Pinel. Presentation of the small baseline NSBAS processing chain on a case example: the Etna deformation monitoring from 2003 to 2010 using Envisat data. In *Proceedings of the ESA ‘Fringe 2011 Workshop’, Frascati, Italy, (19-23 September 2011)*, pages 19–23, 2011.
- T.H. Druitt and R.S.J Sparks. On the formation of calderas during ignimbrite eruptions. *Nature*, 310(5979):679–681, 1984. ISSN 1476-4687. doi: <http://doi.org/10.1038/310679a0>.
- Y. Du, A. Aydin, and P. Segall. Comparison of various inversion techniques as applied to the determination of a geophysical deformation model for the 1983 Borah Peak earthquake. *Society*, 82(4):1840–1866, 1992.
- Z. Duputel and L. Rivera. The 2007 caldera collapse of Piton de la Fournaise volcano: Source process from very-long-period seismic signals. *Earth and Planetary Science Letters*, 527:115786, 2019. ISSN 0012821X. doi: <http://doi.org/10.1016/j.epsl.2019.115786>.
- J.J. Dvorak and D. Dzurisin. Volcano geodesy: The search for magma reservoirs and the formation of eruptive vents. *Reviews of Geophysics*, 35(3):343–384, 1997. ISSN 87551209. doi: <http://doi.org/10.1029/97RG00070>.
- D. Dzurisin. *Volcano deformation—Geodetic monitoring techniques*. Berlin, 2007.
- S.K. Ebmeier, J. Biggs, T.A. Mather, and F. Amelung. Applicability of InSAR to tropical volcanoes: insights from Central America. *Geological Society, London, Special Publications*, 380(1):15–37, 2013. ISSN 0305-8719. doi: <http://doi.org/10.1144/SP380.2>.
- M. Edmonds, I.R. Sides, D.A. Swanson, C. Werner, R.S. Martin, T.A. Mather, R.A. Herd, R.L. Jones, M.I. Mead, G. Sawyer, T. . Roberts, A.J. Sutton, and T. Elias. Magma storage, transport and degassing during the 2008-10 summit eruption at Kīlauea Volcano, Hawai‘i. *Geochimica et Cosmochimica Acta*, 123:284–301, 2013. ISSN 00167037. doi: <http://doi.org/10.1016/j.gca.2013.05.038>.
- P. Einarsson and B. Brandsdottir. Seismological evidence for lateral magma intrusion during the July 1978 deflation of the Krafla volcano in NE-Iceland. *Journal of Geophysics*, 47:160–165, 1980. ISSN 0340062X. doi: <http://doi.org/10.2172/890964>.
- J.P. Eissen, C. Blot, and R. Louat. Chronology of the historic volcanic activity of the New Hebrides Island arc from 1595 to 1991. Technical report, ORSTOM, Nouméa, 1991.

- D.A. Falvey. Part 2. Younger Pacific arcs and the eastern marginal seas: Arc reversals, and a tectonic model for the North Fiji Basin. *Austr. Soc. of Explor. Geophys. Bull.*, (6): 47–49, 1971. doi: <https://doi.org/10.1071/EG975047>.
- T.G. Farr, P.A. Rosen, E. Caro, R. Crippen, R. Duren, S. Hensley, M. Kobrick, M. Paller, E. Rodriguez, L. Roth, D. Seal, S. Shaffer, J. Shimada, J. Umland, M. Werner, M. Oskin, D. Burbank, and D. Alsdorf. The Shuttle Radar Topography Mission. *Reviews of Geophysics*, 45(2), 2007. doi: <http://doi.org/10.1029/2005RG000183>.
- A. Ferretti, C. Prati, and F. Rocca. Permanent Scatters in SAR Interferometry. *IEEE Transactions on Geoscience and Remote Sensing*, 39(1):8–20, 2001. ISSN 01962892. doi: <http://doi.org/10.1109/36.898661>.
- Y. Fialko and A. Rubin. Thermodynamics of lateral dike propagation: Implications for crustal accretion at slow spreading mid-ocean ridges. *Journal of Geophysical Research*, 103(B2):2501–2514, 1998. doi: <https://doi.org/10.1029/97JB03105>.
- Y. Fialko, Y. Khazan, and M. Simons. Deformation due to a pressurized horizontal circular crack in an elastic half-space, with applications to volcano geodesy. *Geophysical Journal International*, 146(1):181–190, 2001. ISSN 0956540X. doi: <http://doi.org/10.1046/j.1365-246X.2001.00452.x>.
- Y.A. Fialko and A.M. Rubin. What controls the along-strike slopes of volcanic rift zones? *Journal of Geophysical Research*, 104(B9):7–20, 1999. doi: <https://doi.org/10.1029/1999JB900143>.
- J. Filson, T. Simkin, and L. Leu. Seismicity of a caldera collapse: Galapagos Islands 1968. *Journal of Geophysical Research*, 78(35):8591–8622, 1973. ISSN 0148-0227. doi: <http://doi.org/10.1029/jb078i035p08591>.
- V.E. Fioletov, C.A. McLinden, N. Krotkov, C. Li, J. Joiner, C. Theys, S. Carn, and M.D. Moran. A global catalogue of large SO₂ sources and emissions derived from the Ozone Monitoring Instrument. *Atmospheric Chemistry and Physics Discussions*, (May):1–45, 2016. ISSN 1680-7375. doi: <http://doi.org/10.5194/acp-2016-417>.
- C. Firth, H. Handley, S. Turner, S. Cronin, and I. Smith. Variable conditions of magma storage and differentiation with links to eruption style at Ambrym volcano, Vanuatu. *Journal of Petrology*, 57(6):1049–1072, 2016. ISSN 14602415. doi: <http://doi.org/10.1093/petrology/egw029>.
- R.S. Fiske and E.D. Jackson. Orientation and growth of Hawaiian volcanic rifts: the effect of regional structure and gravitational stresses. *Proceedings of the Royal Society of London. A. Mathematical and Physical Sciences*, 329:299–326, 1972. ISSN 2053-9169. doi: <http://doi.org/10.1098/rspa.1972.0115>.
- O. Foix, W.C. Crawford, I. Koulakov, C. Baillard, M. Régnier, B. Pelletier, and E. Garaebiti. The 3-D velocity models and seismicity highlight forearc deformation due to subducting features (Central Vanuatu). *Journal of Geophysical Research: Solid Earth*, 124(6):5754–5769, 2019. ISSN 21699356. doi: <http://doi.org/10.1029/2018JB016861>.

- F.R. Fontaine, G. Roult, L. Michon, G. Barruol, and A. Di Muro. The 2007 eruptions and caldera collapse of the Piton de la Fournaise volcano (La Réunion Island) from tilt analysis at a single very broadband seismic station. *Geophysical Research Letters*, 41:2803–2811, 2014. ISSN 19448007. doi: <http://doi.org/10.1002/2014GL061184>. Received.
- F.R. Fontaine, G. Roult, B. Hejrani, L. Michon, V. Ferrazzini, G. Barruol, H. Tkalčić, A. Di Muro, A. Peltier, D. Reymond, T. Staudacher, and F. Massin. Very- and ultra-long-period seismic signals prior to and during caldera formation on La Réunion Island. *Scientific Reports*, 9(1):1–15, 2019. ISSN 20452322. doi: <http://doi.org/10.1038/s41598-019-44439-1>.
- M. Fortin and R. Glowinski. *Augmented Lagrangian Methods: Applications to the Numerical Solution of Boundary-Value Problems*. North-Holland Publ. Co., Amsterdam-New York, 1983.
- M. Frater. The volcanic eruption of 1913 on Ambrym Island, New Hebrides. *Geological Magazine*, 6:496–503, 1917.
- Y. Fukushima, V. Cayol, and P. Durand. Finding realistic dike models from Interferometric Synthetic Aperture Radar data: The February 2000 eruption at Piton de la Fournaise. *Journal of Geophysical Research: Solid Earth*, 110(3):1–15, 2005. ISSN 21699356. doi: <http://doi.org/10.1029/2004JB003268>.
- N. Geshi, T. Shimano, T. Chiba, and S. Nakada. Caldera collapse during the 2000 eruption of Miyakejima Volcano, Japan. *Bulletin of Volcanology*, 64(1):55–68, 2002. ISSN 02588900. doi: <http://doi.org/10.1007/s00445-001-0184-z>.
- N. Geshi, J. Ruch, and V. Acocella. Evaluating volumes for magma chambers and magma withdrawn for caldera collapse. *Earth and Planetary Science Letters*, 396:107–115, 2014. ISSN 0012821X. doi: <http://doi.org/10.1016/j.epsl.2014.03.059>.
- A. Geyer and J. Martí. The distribution of basaltic volcanism on Tenerife, Canary Islands: Implications on the origin and dynamics of the rift systems. *Tectonophysics*, 483(3-4): 310–326, 2010. ISSN 00401951. doi: <http://doi.org/10.1016/j.tecto.2009.11.002>.
- A. Geyer, A. Folch, and J. Martí. Relationship between caldera collapse and magma chamber withdrawal: An experimental approach. *Journal of Volcanology and Geothermal Research*, 157:375–386, 2006. doi: <http://doi.org/10.1016/j.jvolgeores.2006.05.001>.
- S.R. Gfslason, G. Stefánsdóttir, M.A. Pfeffer, S. Barsotti, Th Jóhannsson, I. Galeczka, E. Bali, O. Sigmarsson, A. Stefánsson, N.S. Keller, Sigurdsson, B. Bergsson, B. Galle, V.C. Jacobo, S. Arellano, A. Aiuppa, E.B. Jónasdóttir, E.S. Eiríksdóttir, S. Jakobsson, G.H. Guðfinnsson, S.A. Halldórsson, H. Gunnarsson, B. Haddadi, I. Jónsdóttir, Th Thor-darson, M. Riishuus, Th Högnadóttir, T. Dürig, G.B.M. Pedersen, Höskuldsson, and M T. Gudmundsson. Environmental pressure from the 2014-15 eruption of Bárðarbunga volcano, Iceland. *Geochemical Perspectives Letters*, 1(1):84–93, 2015. ISSN 24103403. doi: <http://doi.org/10.7185/geochemlet.1509>.

- M. Ghiorso and R. Sack. Chemical mass transfer in magmatic processes iv. a revised and internally consistent thermodynamic model for the interpolation and extrapolation of liquid-solid equilibria in magmatic systems at elevated temperatures and pressures. *Contributions to Mineralogy and Petrology*, 119:197–212, 03 1995. doi: <http://doi.org/10.1007/BF00307281>.
- T. Girona, F. Costa, C. Newhall, and B. Taisne. On depressurization of volcanic magma reservoirs by passive degassing. *Journal of Geophysical Research : Solid Earth*, 119:8667–8687, 2014. doi: <https://doi.org/10.1002/2014JB011368>.
- Global Volcanism Program. Report on Piton de la Fournaise (France). *Natural Science Event Bulletin*, 4(2), 1977. URL <https://doi.org/10.5479/si.GVP.NSEB197704-233020>.
- Global Volcanism Program. Report on Ambrym (Vanuatu). *Bulletin of the Global Volcanism Network*, 25(2), 2000. URL <https://doi.org/10.5479/si.GVP.BGVN200002-257040>.
- Global Volcanism Program. Report on Ambrym (Vanuatu). *Bulletin of the Global Volcanism Network*, 26(2), 2001. URL <https://doi.org/10.5479/si.GVP.BGVN200102-257040>.
- Global Volcanism Program. Report on Ambrym (Vanuatu). *Bulletin of the Global Volcanism Network*, 30(5), 2005. URL <https://doi.org/10.5479/si.GVP.BGVN200505-257040>.
- Global Volcanism Program. Report on Ambrym (Vanuatu). *Bulletin of the Global Volcanism Network*, 32(5), 2007. URL <https://doi.org/10.5479/si.GVP.BGVN200505-257040>.
- Global Volcanism Program. Report on Ambrym (Vanuatu). *Weekly Volcanic Activity Report, 30 August-5 September 2017*, 2017a. URL <https://volcano.si.edu/showreport.cfm?doi=GVP.WVAR20170830-257040>.
- Global Volcanism Program. Report on Ambrym (Vanuatu). *Weekly Volcanic Activity Report, 6 December-12 December 2017*, 2017b. URL <https://volcano.si.edu/showreport.cfm?doi=GVP.WVAR20171206-257040>.
- 2013 Global Volcanism Program. *Volcanoes of the World*, 2020. Downloaded 09 Sep 2020.
- R.M. Goldstein and C.L. Werner. Radar interferogram filtering for geophysical applications. *Geophysical Research Letters*, 25(21):4035–4038, 1998. doi: <http://doi.org/10.1029/1998GL900033>.
- R.M. Goldstein, H.A. Zebker, and C.L. Werner. Satellite radar interferometry: Two-dimensional phase unwrapping. *Radio Science*, 23(4):713–720, 1988. ISSN 0048-6604. doi: <http://doi.org/10.1029/RS023i004p00713>.
- G. Gomba, A. Parizzi, F. De Zan, M. Eineder, and R. Bamler. Toward operational compensation of ionospheric effects in SAR interferograms: The split-spectrum method. *IEEE Transactions on Geoscience and Remote Sensing*, 54(3):1446–1461, 2016. ISSN 01962892. doi: <http://doi.org/10.1109/TGRS.2015.2481079>.

- R. Grandin. *L'apport de la géodésie spatiale dans la compréhension du processus de rifting magmatique: l'exemple de l'épisode en cours en Afar Ethiopien (2005 – 2009)*. PhD thesis, Institut de Physique du Globe de Paris, 2009.
- R. Grandin. *From the earthquake source to seismic hazard: contribution of space geodesy*. Habilitation à diriger des recherches, Institut de Physique du Globe de Paris, Université de Paris, 2019.
- R. Grandin, A. Socquet, R. Binet, Y. Klinger, E. Jacques, J. B. De Chabalier, G. C.P. King, C. Lasserre, S. Tait, P. Tapponnier, A. Delorme, and P. Pinzuti. September 2005 Manda hararo-dabbahu rifting event, Afar (Ethiopia): Constraints provided by geodetic data. *Journal of Geophysical Research: Solid Earth*, 114(8), 2009. ISSN 21699356. doi: <http://doi.org/10.1029/2008JB005843>.
- R. Grandin, A. Socquet, E. Jacques, N. Mazzoni, J.B. De Chabalier, and G.C.P. King. Sequence of rifting in Afar, Manda-Hararo rift, Ethiopia, 2005-2009: Time-space evolution and interactions between dikes from Interferometric Synthetic Aperture Radar and static stress change modeling. *Journal of Geophysical Research: Solid Earth*, 115(10):2005–2009, 2010. ISSN 21699356. doi: <http://doi.org/10.1029/2009JB000815>.
- R. Grandin, M.P. Doin, L. Bollinger, B. Pinel-Puysségur, G. Ducret, R. Jolivet, and S.N. Sapkota. Long-term growth of the Himalaya inferred from interseismic InSAR measurement. *Geology*, 40(12):1059–1062, 2012. doi: <https://doi.org/10.1130/G33154.1>.
- D.M. Gray, A. Burton-Johnson, and P.T. Fretwell. Evidence for a lava lake on Mt. Michael volcano, Saunders Island (South Sandwich Islands) from Landsat, Sentinel-2 and ASTER satellite imagery. *Journal of Volcanology and Geothermal Research*, 379:60 – 71, 2019. ISSN 0377-0273. doi: <https://doi.org/10.1016/j.jvolgeores.2019.05.002>.
- H.G. Greene and J.Y. Collot. Ridge-arc collision; timing and deformation determined by Leg 134 drilling, central New Hebrides Island arc. In *Proceedings of the Ocean Drilling Program, Scientific Results*, volume 134, pages 609–621. 1994.
- H.G. Greene, A. Macfarlane, and F.L. Wong. Geology and offshore resources of Pacific Island arcs, Vanuatu Region: introduction and summary. In *Geology and offshore resources of Pacific Island arcs, Vanuatu Region*, pages 1–26. Circum-Pacific Council for Energy and Mineral Resources, Houston, 1988.
- A. Gudmundsson and I.F. Loetveit. Dyke emplacement in a layered and faulted rift zone. *Journal of Volcanology and Geothermal Research*, 144(1-4 SPEC. ISS.):311–327, 2005. ISSN 03770273. doi: <http://doi.org/10.1016/j.jvolgeores.2004.11.027>.
- M.T. Gudmundsson, K. Jónsdóttir, A. Hooper, E.P. Holohan, S.A. Halldórsson, B.G. Ófeigsson, S. Cesca, K.S. Vogfjörð, F. Sigmundsson, T. Högnadóttir, et al. Gradual caldera collapse at Bárðarbunga volcano, Iceland, regulated by lateral magma outflow. *Science*, 353(6296), 2016. doi: <https://doi.org/10.1126/science.aaf8988>.

- I.J. Hamling and G. Kilgour. Goldilocks conditions required for earthquakes to trigger basaltic eruptions : Evidence from the 2015 Ambrym eruption. *Science Advances*, 6(14), 2020. doi: <https://doi.org/10.1126/sciadv.aaz5261>.
- I.J. Hamling, S. Hreinsdóttir, K. Clark, J Elliott, C. Liang, E. Fielding, N. Litchfield, P. Villamor, L. Wallace, T.J. Wright, E. D’Anastasio, S. Bannister, D. Burbidge, P. Denys, P. Gentle, J. Howarth, C. Mueller, N. Palmer, C. Pearson, W. Power, P. Barnes, D.J.A. Barrell, R. Van Dissen, R. Langridge, T. Little, A. Nicol, J. Pettinga, J. Rowland, and M. Stirling. Complex multifault rupture during the 2016 M_w 7.8 Kaikōura earthquake, New Zealand. *Science*, 7194(March):1–17, 2017. ISSN 0036-8075. doi: <http://doi.org/10.1126/science.aam7194>.
- I.J. Hamling, S. Cevuard, and E. Garaebiti. Large-scale drainage of a complex magmatic system: Observations from the 2018 eruption of Ambrym volcano, Vanuatu. *Geophysical Research Letters*, 46(9):4609–4617, 2019. ISSN 19448007. doi: <http://doi.org/10.1029/2019GL082606>.
- J. Hamlyn, T. Wright, R. Walters, C. Pagli, E. Sansosti, F. Casu, S. Pepe, M. Edmonds, B. McCormick Kilbride, D. Keir, J. Neuberg, and C. Oppenheimer. What causes subsidence following the 2011 eruption at Nabro (Eritrea)? *Progress in Earth and Planetary Science*, 5(1), 2018. ISSN 21974284. doi: <https://doi.org/10.1186/s40645-018-0186-5>.
- R.F. Hanssen. *Radar Interferometry: Data Interpretation and Error Analysis*. Kluwer Academic Publishers, 2001. ISBN 0306476339.
- A.J.L. Harris, L.P. Flynn, L. Keszthelyi, P.J. Mougini-Mark, S.K. Rowland, and J A. Resing. Calculation of lava effusion rates from Landstat TM data. *Bulletin of Volcanology*, 60(1): 52–71, 1998. ISSN 02588900. doi: <http://doi.org/10.1007/s004450050216>.
- R.A. Harris and P. Segall. Detection of a locked zone at depth on the Parkfield, California, segment of the San Andreas fault (USA). *Journal of Geophysical Research*, 92(B8):7945–7962, 1987. ISSN 01480227. doi: <http://doi.org/10.1029/JB092iB08p07945>.
- M.J. Heap, M. Villeneuve, F. Albino, J.I. Farquharson, E. Brothelande, F. Amelung, J.L. Got, and P. Baud. Towards more realistic values of elastic moduli for volcano modelling. *Journal of Volcanology and Geothermal Research*, page 106684, 2019. ISSN 03770273. doi: <http://doi.org/10.1016/j.jvolgeores.2019.106684>.
- E.R. Heimgsson, A. Hooper, and F. Sigmundsson. Forecasting the path of a laterally propagating dike. *Journal of Geophysical Research: Solid Earth*, 120:8774 – 8792, 2015. doi: <http://doi.org/10.1002/2015JB012402>.
- H.E. Huppert and A.W. Woods. The role of volatiles in magma chamber dynamics. *Nature*, 420(6915):493–495, 2002. ISSN 00280836. doi: <http://doi.org/10.1038/nature01211>.
- Y. Ida. Effects of the crustal stress on the growth of dikes: Conditions of intrusion and extrusion of magma. *Journal of Geophysical Research*, 104(B8):17897–17909, 1999. ISSN 15312291 08905339. doi: <http://doi.org/10.1097/BOT.0000000000000229>.

- B.L. Isacks, R.K. Cardwell, J.L. Chatelain, M. Barazangi, J.M. Marthelot, D. Chinn, and R. Louat. Seismicity and tectonics of the central New Hebrides Island arc. In D.W. Simpson and P.G. Richards, editors, *Earthquake Prediction*, pages 93–116. Am. Geophys. Union, 1981. Maurice Ewing Series 4.
- R. Jolivet, R. Grandin, C. Lasserre, M.P. Doin, and G. Peltzer. Systematic InSAR tropospheric phase delay corrections from global meteorological reanalysis data. *Geophysical Research Letters*, 38(17):1–6, 2011. ISSN 00948276. doi: <http://doi.org/10.1029/2011GL048757>.
- R. Jolivet, M. Simons, P. S. Agram, Z. Duputel, and Z.K. Shen. Aseismic slip and seismogenic coupling along the central San Andreas Fault. *Geophysical Research Letters*, 42(2):297–306, 2015. ISSN 19448007. doi: <http://doi.org/10.1002/2014GL062222>.
- Sigurjón Jónsson, Howard Zebker, Paul Segall, and Falk Amelung. Fault slip distribution of the 1999 M_w 7.1 Hector Mine, California, earthquake, estimated from satellite radar and GPS measurements. *Bulletin of the Seismological Society of America*, 92(4):1377–1389, 2002. ISSN 00371106. doi: <http://doi.org/10.1785/0120000922>.
- M.L. Jost and R.B. Herrmann. A Student’s Guide to and Review of Moment Tensors. *Seismological Research Letters*, 60(2):37–57, 1989. ISSN 01406736. doi: [http://doi.org/10.1016/S0140-6736\(52\)90232-8](http://doi.org/10.1016/S0140-6736(52)90232-8).
- I. Joughin, W. Abdalati, and M. Fahnestock. Large fluctuations in speed on Greenland’s Jakobshavn Isbræ glacier. *Nature*, 432(7017):608–610, 2004. ISSN 00280836. doi: <http://doi.org/10.1038/nature03130>.
- B.R. Julian, A.D. Miller, and G.R. Foulger. Non-double-couple earthquakes. 1. Theory. *Reviews of Geophysics*, 36(4):525–549, 1998. ISSN 87551209. doi: <http://doi.org/10.1029/98RG00716>.
- B. Kampes and S. Usai. Doris: the Delft Object-oriented Radar Interferometric Software. In *Proc. ITC 2nd ORS symposium*, The Netherlands, 1999.
- H. Kanamori, J. Mori, E. Hauksson, T.H. Heaton, L.K. Hutton, and L.M. Jones. Determination of earthquake energy release and M_L Using TERRAScope. *Bulletin of the Seismological Society of America*, 83(2):330–346, 1993.
- T. Kaneko, A. Yasuda, T. Shimano, S. Nakada, T. Fujii, T. Kanazawa, A. Nishizawa, and Y. Matsumoto. Submarine flank eruption preceding caldera subsidence during the 2000 eruption of Miyakejima Volcano, Japan. *Bulletin of Volcanology*, 67(3):243–253, 2005. ISSN 02588900. doi: <http://doi.org/10.1007/s00445-004-0407-1>.
- R. Kazahaya, Y. Aoki, and H. Shinohara. Budget of shallow magma plumbing system at Asama Volcano, Japan, revealed by ground deformation and volcanic gas studies. *Journal of Geophysical Research: Solid Earth*, 120:2961–2973, 2015. doi: <https://doi.org/10.1002/2014JB011715>.

- B.M. Kennedy, E.P. Holohan, J. Stix, D.M. Gravley, J.R.J. Davidson, and J.W. Cole. Magma plumbing beneath collapse caldera volcanic systems. *Earth-Science Reviews*, 177 (December):404–424, 2018. ISSN 00128252. doi: <http://doi.org/10.1016/j.earscirev.2017.12.002>.
- G. Kieffer, B. Tricot, and P.M. Vincent. Une éruption inhabituelle (avril 1977) du Piton de la Fournaise (Ile de La Réunion): ses enseignements volcanologiques et structuraux. *Comptes rendus de l'Académie des Sciences*, 1977.
- B. Kilbride, M. Edmonds, and J. Biggs. Observing eruptions of gas-rich compressible magmas from space. *Nature Communications*, 7:1–8, 2016. ISSN 20411723. doi: <http://doi.org/10.1038/ncomms13744>.
- J.C. Komorowski, D. Tedesco, M. Kasereka, P. Allard, P. Papale, O. Vaselli, J. Durieux, P. Baxter, M. Halbwachs, M. Akumbe, B. Baluku, P. Briole, M. Ciraba, J.C. Dupin, O. Ettoy, D. Garcin, H. Hamaguchi, N. Houlié, K.S. Kavotha, A. Lemarchand, J. Lockwood, N. Lukaya, G. Mavonga, M. De Michele, S. Mpore, K. Mukambilwa, F. Munyololo, C. Newhall, J. Ruch, M. Yalire, and M. Wafula. The January 2002 flank eruption of Nyiragongo volcano (DRC): chronology, evidence for a tectonic rift trigger, and impact of lava flows on the city of Goma. *Acta Vulcanologica*, 14/15(1-2):27–62, 2002/2003.
- L.W. Kroenke. *Geology of the Ontong Java Plateau*. PhD thesis, Hawaii Institute of Geophysics, 1971.
- A.J. Krueger, L.S. Walter, P.K. Bhartia, C.C. Schnetzler, N.A. Krotkov, I. Sprod, and G.J.S. Bluth. Volcanic sulfur dioxide measurements from the total ozone mapping spectrometer instruments. *Journal of Geophysical Research: Atmospheres*, 100(D7):14057–14076, 1995. doi: <https://doi.org/10.1029/95JD01222>.
- H. Kumagai, T. Ohminato, M. Nakano, M. Ooi, A. Kubo, H. Inoue, and J. Oikawa. Very-long-period seismic signals and caldera formation at Miyake Island, Japan. *Science*, 293 (5530):687–690, 2001. ISSN 00368075. doi: <http://doi.org/10.1126/science.1062136>.
- J.C. Lachat and J.O. Watson. Effective numerical treatment of boundary integral equations: A formulation for three-dimensional elastostatics. *International Journal for Numerical Methods in Engineering*, 10(5):991–1005, 1976. ISSN 10970207. doi: <http://doi.org/10.1002/nme.1620100503>.
- Y. Lagabriele, B. Pelletier, G. Cabioch, M. Regnier, and S. Calmant. Coseismic and long-term vertical displacement due to back arc shortening, central Vanuatu: Offshore and onshore data following the M_w 7.5, 26 November 1999 Ambrym earthquake. *Journal of Geophysical Research*, 108(B11):2519, 2003. ISSN 0148-0227. doi: <http://doi.org/10.1029/2002JB002083>.
- B. Lauer, R. Grandin, and Y. Klinger. Fault geometry and slip distribution of the 2013 M_w 7.7 Balochistan earthquake from inversions of SAR and optical data. *Journal of Geophysical Research: Solid Earth*, 125(7):e2019JB018380, 2020. doi: <http://doi.org/10.1029/2019JB018380>.

- M. Lazecký, K. Spaans, P.J. González, Y. Maghsoudi, Y. Morishita, F. Albino, J. Elliott, N. Greenall, E. Hatton, A. Hooper, D. Juncu, A. McDougall, R.J. Walters, C.S. Watson, J.R. Weiss, and T.J. Wright. LiCSAR: An Automatic InSAR Tool for Measuring and Monitoring Tectonic and Volcanic Activity. *Remote Sensing*, 12(15), 2020. ISSN 2072-4292. doi: 10.3390/rs12152430. URL <https://www.mdpi.com/2072-4292/12/15/2430>.
- C. Lee, R.V. Martin, A. Van Donkelaar, G. O’Byrne, N. Krotkov, A. Richter, L.G. Huey, and J.S. Holloway. Retrieval of vertical columns of sulfur dioxide from SCIAMACHY and OMI: Air mass factor algorithm development, validation, and error analysis. *Journal of Geophysical Research Atmospheres*, 114(22):1–20, 2009. ISSN 01480227. doi: <https://doi.org/10.1029/2009JD012123>.
- D. Legrand, D. Rouland, M. Frogneux, Roberto Carniel, D. Charley, G. Roullet, and C. Robin. Interpretation of very long period tremors at Ambrym volcano, Vanuatu, as quasi-static displacement field related to two distinct magmatic sources. *Geophysical Research Letters*, 32(6):1–5, 2005. ISSN 00948276. doi: <http://doi.org/10.1029/2004GL021968>.
- S. Levy, D.R. Bohnenstiehl, P. Sprinkle, M.S. Boettcher, W.S.D. Wilcock, M. Tolstoy, and F. Waldhauser. Mechanics of fault reactivation before, during, and after the 2015 eruption of Axial Seamount. *Geology*, 46(5):447–450, 2018. ISSN 19432682. doi: <http://doi.org/10.1130/G39978.1>.
- C. Liang, P. Agram, M. Simons, and E.J. Fielding. Ionospheric correction of InSAR time series analysis of C-band Sentinel-1 TOPS data. *IEEE Transactions on Geoscience and Remote Sensing*, 57(9):6755–6773, 2019. ISSN 15580644. doi: <http://doi.org/10.1109/TGRS.2019.2908494>.
- P.W. Lipman. Subsidence of ash-flow calderas: Relation to caldera size and magma-chamber geometry. *Bulletin of Volcanology*, 59(3):198–218, 1997. ISSN 02588900. doi: <http://doi.org/10.1007/s004450050186>.
- M. Lisowski. Analytical volcano deformation source models. In Daniel Dzurisin, editor, *Volcano Deformation*, chapter 8, pages 279 – 304. 2006. ISBN 9783540493020. doi: <http://doi.org/10.1007/978-3-540-49302-0>.
- J.R. Lister and R.C. Kerr. Fluid-mechanical models of crack propagation and their application to magma transport in dykes. *Journal of Geophysical Research*, 96(B6):10049, 1991. ISSN 0148-0227. doi: <http://doi.org/10.1029/91JB00600>.
- Y.K. Liu, J. Ruch, H. Vasyura-Bathke, and S. Jónsson. Influence of ring faulting in localizing surface deformation at subsiding calderas. *Earth and Planetary Science Letters*, 526: 115784, 2019. ISSN 0012821X. doi: <http://doi.org/10.1016/j.epsl.2019.115784>.
- R.B. Lohman and M. Simons. Some thoughts on the use of InSAR data to constrain models of surface deformation: Noise structure and data downsampling. *Geochemistry, Geophysics, Geosystems*, 6(1), 2005. ISSN 15252027. doi: <http://doi.org/10.1029/2004GC000841>.

- R. Louat and B. Pelletier. Seismotectonics and present-day relative plate motions in the Tonga-Lau and Kermadec-Havre region. *Tectonophysics*, 165(1-4):237–250, 1989. ISSN 00401951. doi: [http://doi.org/10.1016/0040-1951\(89\)90049-8](http://doi.org/10.1016/0040-1951(89)90049-8).
- R. Louat, M. Hamburger, and M. Monzier. Shallow and intermediate-depth seismicity in the New Hebrides arc: constraints on the subduction process. In *Geology and offshore resources of Pacific island arcs, Vanuatu region*, number 8, pages 329–356. Circum-Pacific Council for Energy and Mineral Resources, Houston, 1988.
- P. Lundgren, S. Usai, E. Sansosti, R. Lanari, M. Tesauero, G. Fornaro, and P. Berardino. Modeling surface deformation observed with Synthetic Aperture Radar interferometry at Campi Flegrei caldera. *Journal of Geophysical Research: Solid Earth*, 106(B9):19355–19366, 2001. ISSN 21699356. doi: <http://doi.org/10.1029/2001jb000194>.
- P. Lundgren, P. Berardino, M. Coltelli, G. Fornaro, R. Lanari, G. Puglisi, E. Sansosti, and M. Tesauero. Coupled magma chamber inflation and sector collapse slip observed with Synthetic Aperture Radar interferometry on Mt. Etna volcano. *Journal of Geophysical Research: Solid Earth*, 108(B5), 2003. doi: <http://doi.org/10.1029/2001JB000657>.
- P. Lundgren, M.P. Poland, A. Miklius, S. Yun, E.J. Fielding, Z. Liu, A. Tanaka, W.M. Szeliga, and S. Hensley. Source models for the March 5-9, 2011 Kamoamoā fissure eruption, Kilauea Volcano, Hawai‘i, constrained by InSAR and in-situ observations. In *AGU Fall Meeting Abstracts*, December 2011.
- P. Lundgren, T. Girona, M.G. Bato, V.J. Realmuto, S. Samsonov, C. Cardona, L. Franco, E. Gurrola, and M. Aivazis. The dynamics of large silicic systems from satellite remote sensing observations: the intriguing case of Domuyo volcano, Argentina. *Scientific Reports*, 10(1):1–15, 2020. ISSN 20452322. doi: <http://doi.org/10.1038/s41598-020-67982-8>.
- P.R. Lundgren, M. Bagnardi, and H. Dietterich. Topographic Changes During the 2018 Kīlauea Eruption From Single-Pass Airborne InSAR. *Geophysical Research Letters*, c:0–2, 2019. ISSN 0094-8276. doi: <http://doi.org/10.1029/2019gl083501>.
- P. Maillet, E. Ruellan, M. Gérard, A. Person, H. Bellon, J. Cotten, J.L. Joron, S. Nakada, and R. Price. Tectonics, Magmatism, and Evolution of the New Hebrides Backarc Troughs (Southwest Pacific). In B. Taylor, editor, *Backarc Basins: Tectonics and Magmatism*, pages 177–235. Plenum Press, New York, 1995. ISBN 9781461518433. doi: <http://doi.org/10.1007/978-1-4615-1843-3>.
- D.I.J. Mallick. Some petrological and structural variations in the New Hebrides. In P.J. Coleman, editor, *The Western Pacific*, pages 193 – 211. University of Western Australia Press, Perth, 1973.
- D.I.J. Mallick and G. Neef. *Geology of Pentecost, regional report*. New Hebrides Geol. Surv., Vila, 1974.
- P. Marshall. The recent volcanic eruptions on Ambrym Island. *Trans. New Zealand Inst. XLVII*, pages 387–391, 1915.

- J. Marti and A. Gudmundsson. The Las Cañadas caldera (Tenerife, Canary Islands): An overlapping collapse caldera generated by magma-chamber migration. *Journal of Volcanology and Geothermal Research*, 103(1-4):161–173, 2000. ISSN 03770273. doi: [http://doi.org/10.1016/S0377-0273\(00\)00221-3](http://doi.org/10.1016/S0377-0273(00)00221-3).
- J. Marti, G.J. Ablay, L.T. Redshaw, and R.S.J. Sparks. Experimental studies of collapse calderas. *Journal of the Geological Society*, 151(6):919–929, 1994. ISSN 00167649. doi: <http://doi.org/10.1144/gsjgs.151.6.0919>.
- D. Massonnet and K.L. Feigl. Radar interferometry and its application to changes in the earth’s surface. *Reviews of Geophysics*, 36(4):441–500, 1998. ISSN 87551209. doi: <http://doi.org/10.1029/97RG03139>.
- D. Massonnet and J.C. Souyris. *Imaging with Synthetic Aperture Radar*. 01 2008.
- D. Massonnet, M. Rossi, C. Carmona, F. Adragna, G. Peltzer, K. Feigl, and T. Rabaute. The displacement field of the Landers earthquake mapped by radar interferometry. *Nature*, 364(6433):138–142, 1993. ISSN 00280836. doi: <http://doi.org/10.1038/364138a0>.
- D. Massonnet, P. Briole, and A. Arnaud. Deflation of Mount Etna monitored by spaceborne radar interferometry. 375(6532):567–570, 1995. ISSN 00280836. doi: <http://doi.org/10.1038/375567a0>.
- L.G. Mastin, M. Guffanti, R. Servranckx, P. Webley, S. Barsotti, K. Dean, A. Durant, J.W. Ewert, A. Neri, W.I. Rose, D. Schneider, L. Siebert, B. Stunder, G. Swanson, A. Tupper, A. Volentik, and C.F. Waythomas. A multidisciplinary effort to assign realistic source parameters to models of volcanic ash-cloud transport and dispersion during eruptions. *Journal of Volcanology and Geothermal Research*, 186(1-2):10–21, 2009. ISSN 03770273. doi: <http://doi.org/10.1016/j.jvolgeores.2009.01.008>.
- G.J.H McCall, R.W. Lemaitre, A. Malahoff, G.P. Robinson, and P.J. Stephenson. The Geology and Geophysics of the Ambrym Caldera, New Hebrides. In *Symposium Volcanoes and their Roots*, pages 681–696, Oxford, England, 1969.
- D. F. McTigue. Elastic stress and deformation near a finite spherical magma body: Resolution of the point source paradox. *Journal of Geophysical Research*, 92(B12):12931, 1987. ISSN 0148-0227. doi: <http://doi.org/10.1029/jb092ib12p12931>.
- S. Meffre and A.J. Crawford. Collision tectonics in the New Hebrides arc (Vanuatu). *Island Arc*, 10(1):33–50, 2001. ISSN 10384871. doi: <http://doi.org/10.1046/j.1440-1738.2001.00292.x>.
- T. Menand, K.A. Daniels, and P. Benghiat. Dyke propagation and sill formation in a compressive tectonic environment. *Journal of Geophysical Research: Solid Earth*, 115(8):1–12, 2010. ISSN 21699356. doi: <http://doi.org/10.1029/2009JB006791>.
- A. Menant, S. Angiboust, T. Gerya, R. Lacassin, M. Simoes, and R. Grandin. Transient stripping of subducting slabs controls periodic forearc uplift. *Nature Communications*, 11(1):1–10, 2020. ISSN 20411723. doi: <http://doi.org/10.1038/s41467-020-15580-7>.

- F.J. Meyer. Performance requirements for ionospheric correction of low-frequency SAR data. *IEEE Transactions on Geoscience and Remote Sensing*, 49(10):3694–3702, 2011. ISSN 01962892. doi: <http://doi.org/10.1109/TGRS.2011.2146786>.
- R. Michel and E. Rignot. Flow of Glaciar Moreno, Argentina, from repeat-pass Shuttle Imaging Radar images: comparison of the phase correlation method with radar interferometry. *Journal of Glaciology*, 45(149):93–100, 1999. doi: 10.3189/S0022143000003075.
- R. Michel, J.P. Avouac, and J. Taboury. Measuring ground displacements from SAR amplitude images: application to the Landers earthquake. *Geophysical Research Letters*, 26(7): 875 – 878, 1999. doi: <https://doi.org/10.1029/1999GL900138>.
- L. Michon, T. Staudacher, V. Ferrazzini, P. Bachèlery, and J. Marti. April 2007 collapse of Piton de la Fournaise: A new example of caldera formation. *Geophysical Research Letters*, 34(21):1–6, 2007. ISSN 00948276. doi: <http://doi.org/10.1029/2007GL031248>.
- L. Michon, F. Massin, V. Famin, V. Ferrazzini, and G. Roult. Basaltic calderas: Collapse dynamics, edifice deformation, and variations of magma withdrawal. *Journal of Geophysical Research: Solid Earth*, 116(3):1–18, 2011. ISSN 21699356. doi: <http://doi.org/10.1029/2010JB007636>.
- A.H.G. Mitchell and A.J. Warden. Geological evolution of the new hebrides island arc. *Journal of the Geological Society*, 127(5):501–529, 1971. ISSN 0016-7649. doi: <http://doi.org/10.1144/gsjgs.127.5.0501>.
- J. Mittermayer, A. Moreira, and O. Loffeld. Spotlight SAR Data Processing Using the Frequency Scaling Algorithm. *IEEE Transactions on Geoscience and Remote Sensing*, 37(5):2198–2214, 1999. ISSN 03722112. doi: <http://doi.org/10.1109/36.789617>.
- K. Mogi. Relations between the eruptions of various volcanoes and the deformations of the ground surfaces around them. *Bulletin of the Earthquake Research Institute*, 36:99–134, 1958.
- M. Monzier, C. Robin, J.P. Eissen, and J. Cotten. Geochemistry vs. seismo-tectonics along the volcanic New Hebrides Central Chain (Southwest Pacific). *Journal of Volcanology and Geothermal Research*, 78:1–29, 1997.
- J. Mori, R. White, D. Harlow, P. Okubo, J. Power, R. Hoblitt, E. Laguerta, L. Lanuza, and B. Bautista. Volcanic earthquakes following the 1991 climactic eruption of Mount Pinatubo, Philippines: strong seismicity during a waning eruption. In Newhall C. and Punongbayan R., editors, *Fire and Mud: Eruptions and Lahars of Mount Pinatubo, Philippines*, pages 339–350. PHIVOLCS and Univ. Washington Press, 1996.
- J. Mouginot, B. Scheuch, and E. Rignot. Mapping of ice motion in Antarctica using synthetic-aperture radar data. *Remote Sensing*, 4(9):2753–2767, 2012. ISSN 20724292. doi: <http://doi.org/10.3390/rs4092753>.

- Y. Moussallam, E. Médard, G. Georgeais, E.F. Rose-Koga, K.T. Koga, L. Gurioli, B. Pelletier, P. Bani, R. Grandin, M. Boichu, T. Shreve, D. Tari, and N. Peters. How to turn off a lava lake? A petrological investigation of the 2018 intra-caldera and submarine eruptions of Ambrym volcano. *Submitted to Bulletin of Volcanology*, 2020.
- S. Münn, T.R. Walter, and A. Klügel. Gravitational spreading controls rift zones and flank instability on El Hierro, Canary Islands. *Geological Magazine*, 143(3):257–268, 2006. ISSN 00167568. doi: <http://doi.org/10.1017/S0016756806002019>.
- S.W. Murphy, C.R. de Souza Filho, R. Wright, G. Sabatino, and R. Correa Pabon. HOTMAP: Global hot target detection at moderate spatial resolution. *Remote Sensing of Environment*, 177:78 – 88, 2016. ISSN 0034-4257. doi: <https://doi.org/10.1016/j.rse.2016.02.027>.
- K.D. Murray and R.B. Lohman. Short-lived pause in Central California subsidence after heavy winter precipitation of 2017. *Science Advances*, 4(8), 2018. ISSN 23752548. doi: <http://doi.org/10.1126/sciadv.aar8144>.
- K. Nakamura. Volcanoes as possible indicators of tectonic stress orientation - principle and proposal. *Journal of Volcanology and Geothermal Research*, 2:1–16, 1977. ISSN 0013063X. doi: <http://doi.org/10.1007/BF02199968>.
- C.A. Neal, S.R. Brantley, L. Antolik, J. Babb, M. Burgess, K. Calles, M. Cappos, J.C. Chang, S. Conway, L. Desmither, P. Dotray, T. Elias, P. Fukunaga, S. Fuke, I.A. Johanson, K. Kamibayashi, J. Kauahikaua, R.L. Lee, S. Pekalib, A. Miklius, W. Million, C.J. Moniz, P.A. Nadeau, P. Okubo, C. Parcheta, M.P. Patrick, B. Shiro, D.A. Swanson, W. Tollett, F. Trusdell, E. F. Younger, M.H. Zoeller, E.K. Montgomery-Brown, K.R. Anderson, M.P. Poland, J. Ball, J. Bard, M. Coombs, H.R. Dietterich, C. Kern, W.A. Thelen, P.F. Cervelli, T. Orr, B.F. Houghton, C. Gansecki, R. Hazlett, P. Lundgren, A.K. Diefenbach, A.H. Lerner, G. Waite, P. Kelly, L. Clor, C. Werner, K. Mulliken, and G. Fisher. The 2018 rift eruption and summit collapse of Kīlauea Volcano. *Science*, 7046(December):1–14, 2018. ISSN 0036-8075. doi: <http://doi.org/10.1126/science.aav7046>.
- K. Németh and S.J. Cronin. Phreatomagmatic volcanic hazards where rift-systems meet the sea, a study from Ambae Island, Vanuatu. *Journal of Volcanology and Geothermal Research*, 180(2-4):246–258, 2009. ISSN 03770273. doi: <http://doi.org/10.1016/j.jvolgeores.2008.08.011>.
- K. Németh and S.J. Cronin. Drivers of explosivity and elevated hazard in basaltic fissure eruptions: The 1913 eruption of Ambrym Volcano, Vanuatu (SW-Pacific). *Journal of Volcanology and Geothermal Research*, 201(1-4):194–209, 2011. ISSN 03770273. doi: <http://doi.org/10.1016/j.jvolgeores.2010.12.007>.
- K. Németh, S.J. Cronin, R.B. Stewart, and D. Charley. Intra- and extra-caldera volcanoclastic facies and geomorphic characteristics of a frequently active mafic island-arc volcano, Ambrym Island, Vanuatu. *Sedimentary Geology*, 220(3-4):174–188, 2009. doi: <http://doi.org/10.1016/j.sedgeo.2009.04.019>.

- Károly Németh and Shane J. Cronin. Volcanic craters, pit craters and high-level magma-feeding systems of a mafic island-arc volcano: Ambrym, Vanuatu, South Pacific. *Geological Society, London, Special Publications*, 302(1):87–102, 2008. ISSN 0305-8719. doi: <http://doi.org/10.1144/SP302.6>.
- New Hebrides Geological Survey. Geology of Pentecost and Ambrym, 1:100.000. New Hebrides Geological Survey Sheet 6., 1976.
- C. Newhall, S. Self, and A. Robock. Anticipating future Volcanic Explosivity Index (VEI) 7 eruptions and their chilling impacts. *Geosphere*, 14(2):572–603, 2018. ISSN 1553040X. doi: <http://doi.org/10.1130/GES01513.1>.
- C.G. Newhall. Volcanology 101. In Gerald Schubert, editor, *Treatise on Geophysics (Second Edition)*, pages 355 – 387. Elsevier, Oxford, second edition edition, 2015. ISBN 978-0-444-53803-1. doi: <https://doi.org/10.1016/B978-0-444-53802-4.00080-4>.
- M. Nikkhoo, T.R. Walter, P.R. Lundgren, and P. Prats-Iraola. Compound dislocation models (CDMs) for volcano deformation analyses. *Geophysical Journal International*, 208(2):877–894, 2017. ISSN 1365246X. doi: <http://doi.org/10.1093/gji/ggw427>.
- T. Nishimura. Ground deformation caused by magma ascent in an open conduit. *Journal of Volcanology and Geothermal Research*, 187(3-4):178–192, 2009. ISSN 03770273. doi: <http://doi.org/10.1016/j.jvolgeores.2009.09.001>. URL <http://dx.doi.org/10.1016/j.jvolgeores.2009.09.001>.
- T. Nishimura, S. Ozawa, M. Murakami, T. Sagiya, T. Tada, M. Kaidzu, and M. Ukawa. Crustal deformation caused by magma migration in the Northern Izu Islands, Japan. *Geophysical Research Letters*, 28(19):3745–3748, 2001. ISSN 00948276. doi: <http://doi.org/10.1029/2001GL013051>.
- S.L. Nooner and W.W. Chadwick. Volcanic inflation measured in the caldera of axial seamount: Implications for magma supply and future eruptions. *Geochemistry, Geophysics, Geosystems*, 10(2), 2009. ISSN 15252027. doi: <http://doi.org/10.1029/2008GC002315>.
- S.L. Nooner and W.W. Chadwick. Inflation-predictable behavior and co-eruption deformation at Axial Seamount. *Science*, 354(6318):1399–1404, 2016. doi: <http://doi.org/10.1126/science.1259433>.
- Y. Okada. Surface deformation due to shear and tensile faults in a half-space. *Bulletin of the Seismological Society of America*, 75(4):1135–1154, 1985. ISSN 01489062. doi: [http://doi.org/10.1016/0148-9062\(86\)90674-1](http://doi.org/10.1016/0148-9062(86)90674-1).
- C. Oppenheimer and P. Francis. Remote sensing of heat, lava and fumarole emissions from Erta 'Ale volcano, Ethiopia. *International Journal of Remote Sensing*, 18(8):1661–1692, 1997. ISSN 13665901. doi: <http://doi.org/10.1080/014311697218043>.

- C. Oppenheimer, A.J.S. McGonigle, P. Allard, M.J. Wooster, and V. Tsanev. Sulfur, heat, and magma budget of Erta 'Ale lava lake, Ethiopia. *Geology*, 32(6):509–512, 2004. ISSN 00917613. doi: <http://doi.org/10.1130/G20281.1>.
- J.S. Pallister, R.P. Hoblitt, D.R. Crandell, and D.R. Mullineaux. Mount St. Helens a decade after the 1980 eruptions: magmatic models, chemical cycles, and a revised hazards assessment. *Bulletin of Volcanology*, 54:126–146, 1992. doi: <https://doi.org/10.1007/BF00278003>.
- J.S. Pallister, W.A. McCausland, S. Jónsson, Z. Lu, H.M. Zahran, S. El Hadidy, A. Aburukbah, I.C.F. Stewart, P.R. Lundgren, R.A. White, and M.R.H. Moufti. Broad accommodation of rift-related extension recorded by dyke intrusion in Saudi Arabia. *Nature Geoscience*, 3(10):705–712, 2010. ISSN 17520894. doi: <http://doi.org/10.1038/ngeo966>.
- J.L. Palma, S. Blake, and E.S. Calder. Constraints on the rates of degassing and convection in basaltic open-vent volcanoes. *Geochemistry, Geophysics, Geosystems*, 12(11):1–25, 2011. doi: <https://doi.org/10.1029/2011GC003715>.
- K. Pascal, J. Neuberg, and E. Rivalta. On precisely modelling surface deformation due to interacting magma chambers and dykes. *Geophysical Journal International*, 196(1): 253–278, 2013. ISSN 0956540X. doi: <http://doi.org/10.1093/gji/ggt343>.
- M. Patrick, D. Swanson, and T. Orr. A review of controls on lava lake level: insights from Halema'uma'u Crater, Kilauea Volcano. *Bulletin of Volcanology*, 81(3), 2019a. ISSN 14320819. doi: <http://doi.org/10.1007/s00445-019-1268-y>.
- M. R. Patrick, H. R. Dietterich, J. J. Lyons, A. K. Diefenbach, C. Parcheta, K. R. Anderson, A. Namiki, I. Sumita, B. Shiro, and J. P. Kauahikaua. Cyclic lava effusion during the 2018 eruption of Kilauea Volcano. *Science*, 366(6470), 2019b. ISSN 10959203. doi: <http://doi.org/10.1126/science.aay9070>.
- M.R. Patrick, K.R. Anderson, M.P. Poland, T.R. Orr, and D.A. Swanson. Lava lake level as a gauge of magma reservoir pressure and eruptive hazard. *Geology*, 43(9):831–834, 2015. ISSN 19432682. doi: <http://doi.org/10.1130/G36896.1>.
- J.A. Pearce. Role of the Sub-continental Lithosphere in Magma Genesis at Active Continental Margins. In C.J. Hawkesworth, editor, *Continental basalts and mantle xenoliths*, pages 230–249. Shiva Publications, Nantwich, Cheshire, 1983.
- D.W. Peate, J.A. Pearce, C.J. Hawkesworth, H. Colley, C.M.H. Edwards, and K. Hirose. Geochemical variations in Vanuatu arc lavas: The role of subducted material and a variable mantle wedge composition. *Journal of Petrology*, 38(10):1331–1358, 1997. ISSN 00223530. doi: <http://doi.org/10.1093/petroj/38.10.1331>.
- B. Pelletier, M. Meschede, T. Chabernaud, P. Roperch, and X. Zhao. Tectonics of the Central New Hebrides Arc, North Aoba Basin. In *Proceedings of the Ocean Drilling Program, 134 Scientific Results*, volume 134, pages 431–444, 1994. doi: <http://doi.org/10.2973/odp.proc.sr.134.023.1994>.

- B. Pelletier, S. Calmant, and R. Pillet. Current tectonics of the Tonga-New Hebrides region. *Earth and Planetary Science Letters*, 164:263–276, 1998. ISSN 0012821X. doi: [http://doi.org/10.1016/s0012-821x\(04\)00049-4](http://doi.org/10.1016/s0012-821x(04)00049-4).
- B. Pelletier, Y. Lagabriele, M. Benoit, M. Boda, G. Cabioch, S. Calmant, E. Garel, C. Guivel, and J. Perrier. Campagne Alaufi N.0. L’Atalante, 29 février au 17 mars 2000, 2000a. Centre IRD Nouméa, Rapports de missions, Science de la Terre, Géologie-Géophysique.
- B. Pelletier, M. Regnier, S. Calmant, R. Pillet, G. Cabioch, Y. Lagabriele, J.-M. Bore, J.-P. Caminade, I. Christopher, and Temakon S. Le séisme d’Ambrym-Pentecôte (Vanuatu) du 26 novembre 1999: données préliminaires sur la séismicité, le tsunami et les déplacements associés. *C. R. Acad. Sci. Paris. Science de la terre et des planètes*, 331(2):21–28, 2000b.
- A. Peltier, T. Staudacher, and P. Bachèlery. New behaviour of the Piton de La Fournaise volcano feeding system (La Réunion Island) deduced from GPS data: Influence of the 2007 Dolomieu caldera collapse. *Journal of Volcanology and Geothermal Research*, 192(1-2):48–56, 2010. ISSN 03770273. doi: <http://doi.org/10.1016/j.jvolgeores.2010.02.007>. URL <http://dx.doi.org/10.1016/j.jvolgeores.2010.02.007>.
- C. Picard, M. Monzier, J.P. Eissen, and C. Robin. Concomitant evolution of tectonic environment and magma geochemistry, Ambrym volcano (Vanuatu, New Hebrides arc). *Geological Society, London, Special Publications*, 81(1):135–154, 1994. doi: <https://doi.org/10.1144/GSL.SP.1994.081.01.08>.
- C. Picard, M. Monzier, J.P. Eissen, and C. Robin. Concomitant evolution of tectonic environment and magma geochemistry, Ambrym volcano (Vanuatu, New Hebrides arc). In J.L. Smellie, editor, *Volcanism Associated with Extension at Consuming Plate Margins*, number 81, pages 135–154. Geological edition, 1995.
- R.J. Pike. Volcanoes on the inner planets: Some preliminary comparisons of gross topography. In *Proc. Lunar Planet Sci. Conf.*, number 9, pages 3239–3273, 1978.
- V. Pinel, M.P. Poland, and A. Hooper. Volcanology: Lessons learned from Synthetic Aperture Radar imagery. *Journal of Volcanology and Geothermal Research*, 289:81–113, 2014. ISSN 03770273. doi: <http://doi.org/10.1016/j.jvolgeores.2014.10.010>.
- M.P. Poland and K.R. Anderson. Partly cloudy with a chance of lava flows: Forecasting volcanic eruptions in the twenty-first century. *Journal of Geophysical Research: Solid Earth*, 125:1–32, 2020. doi: <https://doi.org/10.1029/2018JB016974>.
- M.P. Poland and D. Carbone. Continuous gravity and tilt reveal anomalous pressure and density changes associated with gas pistonning within the summit lava lake of Kīlauea volcano, Hawai‘i. *Geophysical Research Letters*, 45:2319–2327, 2018. doi: <https://doi.org/10.1002/2017GL076936>.

- M.P. Poland, A. Peltier, A. Bonforte, and G. Puglisi. The spectrum of persistent volcanic flank instability: A review and proposed framework based on Kīlauea, Piton de la Fournaise, and Etna. *Journal of Volcanology and Geothermal Research*, 339:63–80, 2017. ISSN 03770273. doi: <http://doi.org/10.1016/j.jvolgeores.2017.05.004>.
- M.P. Poland, T. Lopez, R. Wright, and M.J. Pavlonis. Forecasting, Detecting, and Tracking Volcanic Eruptions from Space. *Remote Sensing in Earth Systems Sciences*, 3:55–94, 2020. ISSN 2520-8195. doi: <http://doi.org/10.1007/s41976-020-00034-x>.
- D.D. Pollard. Derivation and evaluation of a mechanical model for sheet intrusions. *Tectonophysics*, 19(3):233–269, 1973. ISSN 00401951. doi: [http://doi.org/10.1016/0040-1951\(73\)90021-8](http://doi.org/10.1016/0040-1951(73)90021-8).
- D.D. Pollard and G. Holzhausen. On the mechanical interaction between a fluid-filled fracture and the earth’s surface. *Tectonophysics*, 53(1-2):27–57, 1979. ISSN 00401951. doi: [http://doi.org/10.1016/0040-1951\(79\)90353-6](http://doi.org/10.1016/0040-1951(79)90353-6).
- A.J. Prata and J. Kerkmann. Simultaneous retrieval of volcanic ash and SO₂ using MSG-SEVIRI measurements. *Geophysical Research Letters*, 34(5):1–6, 2007. ISSN 00948276. doi: <http://doi.org/10.1029/2006GL028691>.
- R. Qin and W.R. Buck. Why meter-wide dikes at oceanic spreading centers? *Earth and Planetary Science Letters*, 265(3-4):466–474, 2008. ISSN 0012821X. doi: <http://doi.org/10.1016/j.epsl.2007.10.044>.
- M. Radiguet, F. Cotton, M. Vergnolle, M. Campillo, B. Valette, V. Kostoglodov, and N. Cotte. Spatial and temporal evolution of a long term slow slip event: The 2006 Guerrero Slow Slip Event. *Geophysical Journal International*, 184(2):816–828, 2011. ISSN 0956540X. doi: <http://doi.org/10.1111/j.1365-246X.2010.04866.x>.
- M. Régnier, S. Calmant, B. Pelletier, Y. Lagabrielle, and G. Cabioch. The M_w 7.5 1999 Ambrym earthquake, Vanuatu: A back arc intraplate thrust event. *Tectonics*, 22(4):1–11, 2003. ISSN 02787407. doi: <http://doi.org/10.1029/2002TC001422>.
- D. Remy, S. Bonvalot, P. Briole, and M. Murakami. Accurate measurements of tropospheric effects in volcanic areas from SAR interferometry data: Application to Sakurajima volcano (Japan). *Earth and Planetary Science Letters*, 213(3-4):299–310, 2003. ISSN 0012821X. doi: [http://doi.org/10.1016/S0012-821X\(03\)00331-5](http://doi.org/10.1016/S0012-821X(03)00331-5).
- E. Rivalta. Evidence that coupling to magma chambers controls the volume history and velocity of laterally propagating intrusions. *Journal of Geophysical Research: Solid Earth*, 115(7):1–13, 2010. ISSN 21699356. doi: <http://doi.org/10.1029/2009JB006922>.
- E. Rivalta and P. Segall. Magma compressibility and the missing source for some dike intrusions. *Geophysical Research Letters*, 35(4):0–4, 2008. ISSN 00948276. doi: <http://doi.org/10.1029/2007GL032521>.

- E.A.M. Robertson, J. Biggs, K.V. Cashman, M.A. Floyd, and C. Vye-Brown. Influence of regional tectonics and pre-existing structures on the formation of elliptical calderas in the Kenyan Rift. *Geological Society Special Publication*, 420(1):43–67, 2016. ISSN 03058719. doi: <http://doi.org/10.1144/SP420.12>.
- C. Robin, J.P. Eissen, and M. Monzier. Giant tuff cone and 12-km-wide associated caldera at Ambrym Volcano (Vanuatu, New Hebrides Arc). *Journal of Volcanology and Geothermal Research*, 55(3-4):225–238, 1993. ISSN 03770273. doi: [http://doi.org/10.1016/0377-0273\(93\)90039-T](http://doi.org/10.1016/0377-0273(93)90039-T).
- O Roche, T H Druitt, and O Merle. Experimental study of caldera formation. *Journal of Geophysical Research*, 105(B1):395–416, 2000.
- P. Rosen, M. Lavalle, X. Pi, S. Buckley, W. Szeliga, H. Zebker, and E. Gurrola. Techniques and tools for estimating ionospheric effects in interferometric and polarimetric SAR data. *International Geoscience and Remote Sensing Symposium (IGARSS)*, pages 1501–1504, 2011. doi: <http://doi.org/10.1109/IGARSS.2011.6049352>.
- P.A. Rosen, S. Hensley, I.R. Joughin, F. Li, S.N. Madsen, R. Ernesto, and R.M.I. Goldstein. Synthetic Aperture Radar Interferometry. *Proceedings of the IEEE*, 88(3):333–382, 2000.
- P.A. Rosen, S. Hensley, G. Peltzer, and M. Simons. Updated Repeat Orbit Interferometry Package Released. *Eos*, 85(5):47, 2004.
- P.A. Rosen, E. Gurrola, G.F. Sacco, and H. Zebker. The InSAR scientific computing environment. In *EUSAR 2012; 9th European Conference on Synthetic Aperture Radar*, pages 730–733, April 2012.
- B. Rousset, R. Jolivet, M. Simons, C. Lasserre, B. Riel, P. Milillo, Z. Çakir, and F. Renard. An aseismic slip transient on the North Anatolian Fault. *Geophysical Research Letters*, 43(7):3254–3262, 2016. ISSN 19448007. doi: <http://doi.org/10.1002/2016GL068250>.
- A. Rubin, K.M. Cooper, M. Leever, J. Wimpenny, C. Deering, T. Rooney, D. Gravley, and Q. zhu Yin. Changes in magma storage conditions following caldera collapse at Okataina Volcanic Center, New Zealand. *Contributions to Mineralogy and Petrology*, 171(1):1–18, 2016. ISSN 00107999. doi: <http://doi.org/10.1007/s00410-015-1216-6>.
- A.M. Rubin. A comparison of rift-zone tectonics in Iceland and Hawaii. *Bulletin of Volcanology*, 52:302–319, 1990. doi: <https://doi.org/10.1007/BF00304101>.
- A.M. Rubin. Propagation of magma-filled cracks. *Annu. Rev. Earth Planet Sci.*, 23:287–336, 1995. doi: <http://doi.org/10.15713/ins.mmj.3>.
- A.M. Rubin and D.D. Pollard. Origin of blade-like dikes in volcanic rift zones. In R.W. Decker, T.L. Wright, and P.H. Stauffer, editors, *Volcanism in Hawaii Professional Paper*, pages 1449–1470. U.S. Geol. Surv., 1350 edition, 1987.

- M. Sambridge. Geophysical inversion with a neighbourhood algorithm – I. Searching a parameter space. *Geophysical Journal International*, 138:479–494, 1999a. ISSN 0956540X. doi: <http://doi.org/10.1046/j.1365-246x.1999.00900.x>.
- M. Sambridge. Geophysical inversion with a neighbourhood algorithm – II. Appraising the ensemble. *Geophysical Journal International*, 138(2):727–746, 1999b. ISSN 0956540X. doi: <http://doi.org/10.1046/j.1365-246x.1999.00876.x>.
- D. Sandwell, R. Mellors, X. Tong, M. Wei, and P. Wessel. Open radar interferometry software for mapping surface deformation. *Eos, Transactions American Geophysical Union*, 92(28): 234–234, 2011. doi: <https://doi.org/10.1029/2011EO280002>.
- E. Sansosti, S. Member, P. Berardino, M. Manunta, F. Serafino, and G. Fornaro. Geometrical SAR Image Registration. *IEEE Transactions on Geoscience and Remote Sensing*, 44(10): 2861–2870, 2006. doi: <http://doi.org/10.1109/TGRS.2006.875787>.
- J.C. Savage. A dislocation model of strain accumulation and release at a subduction zone. *Journal of Geophysical Research*, 88(B6):4984–4996, 1983. doi: <https://doi.org/10.1029/JB088iB06p04984>.
- G.M. Sawyer, S.A. Carn, V.I. Tsanev, C. Oppenheimer, and M. Burton. Investigation into magma degassing at Nyiragongo volcano, democratic Republic of the Congo. *Geochemistry, Geophysics, Geosystems*, 9(2):1–17, 2008. ISSN 15252027. doi: <http://doi.org/10.1029/2007GC001829>.
- R. Scandon and S.D. Malone. Magma supply, magma discharge and readjustment of the feeding system of mount St. Helens during 1980. *Journal of Volcanology and Geothermal Research*, 23(3):239 – 262, 1985. ISSN 0377-0273. doi: [https://doi.org/10.1016/0377-0273\(85\)90036-8](https://doi.org/10.1016/0377-0273(85)90036-8).
- D.A. Schmidt and R. Bürgmann. Time-dependent land uplift and subsidence in the Santa Clara valley, California, from a large Interferometric Synthetic Aperture Radar data set. *Journal of Geophysical Research: Solid Earth*, 108(B9):1–13, 2003. ISSN 2169-9356. doi: <http://doi.org/10.1029/2002jb002267>.
- T.P. Scoffin, D.R. Stoddart, B.R. Rosen, D.R. Stoddart, and M. Yonge. The nature and significance of microatolls. *Philosophical Transactions of the Royal Society of London. B, Biological Sciences*, 284(999):99–122, 1978. doi: <http://doi.org/10.1098/rstb.1978.0055>.
- D.T. Secor and D.D. Pollard. On the stability of open hydraulic fractures in the Earth’s crust. *Geophysical Research Letters*, 2(11):510–513, 1975. ISSN 19448007. doi: <http://doi.org/10.1029/GL003i009p00513>.
- P. Segall. *Earthquake and Volcano Deformation*. Princeton University Press, 2010. ISBN 9781400833856.
- P. Segall and R. Harris. Slip deficit on the San Andreas fault at Parkfield, California, as revealed by inversion of geodetic data. 233(4771):1409–1413, 1986. doi: <https://doi.org/10.1126/science.233.4771.1409>.

- P. Segall and R.A. Harris. Earthquake deformation cycle on the San Andreas fault near Parkfield, California (USA). *Journal of Geophysical Research*, 92(B10), 1987. ISSN 01480227. doi: <http://doi.org/10.1029/JB092iB10p10511>.
- P. Segall, P. Cervelli, S. Owen, M. Lisowski, and A. Miklius. Constraints on dike propagation from continuous GPS measurements. *Journal of Geophysical Research*, 106(B9):19301, 2001. ISSN 0148-0227. doi: <http://doi.org/10.1029/2001JB000229>.
- P. Segall, K.R. Anderson, I. Johanson, and A. Miklius. Mechanics of inflationary deformation during caldera collapse: Evidence from the 2018 Kīlauea eruption. *Geophysical Research Letters*, 46(21):11782–11789, 2019. ISSN 19448007. doi: <http://doi.org/10.1029/2019GL084689>.
- P. Segall, K. Anderson, F. Pulvirenti, T. Wang, and I. Johanson. Caldera collapse geometry revealed by near-field GPS displacements at Kīlauea volcano in 2018. *Geophysical Research Letters*, (May 2018):1–8, 2020. ISSN 1944-8007. doi: <http://doi.org/10.1029/2020GL088867>.
- F. Sheehan. *Petrological insights into pre- and syn-eruptive degassing at Ambrym volcano, Vanuatu*. PhD thesis, University of East Anglia, 2016.
- F. Sheehan and J. Barclay. Staged storage and magma convection at Ambrym volcano, Vanuatu. *Journal of Volcanology and Geothermal Research*, 322:144–157, 2016. ISSN 03770273. doi: <http://doi.org/10.1016/j.jvolgeores.2016.02.024>.
- T. Shreve, R. Grandin, M. Boichu, E. Garaebiti, Y. Moussallam, V. Ballu, F. Delgado, F. Leclerc, M. Vallée, N. Henriot, S. Cevuard, D. Tari, P. Lebellegard, and B. Pelletier. From prodigious volcanic degassing to caldera subsidence and quiescence at Ambrym (Vanuatu): the influence of regional tectonics. *Scientific Reports*, 9(18868), 2019. doi: <https://doi.org/10.1038/s41598-019-55141-7>.
- T. Shreve, R. Grandin, D. Smittarello, V. Cayol, V. Pinel, and Y. Morishita. What triggers caldera ring-fault subsidence at Ambrym volcano? Insights from the 2015 dike intrusion and eruption. *Submitted to Journal of Geophysical Research: Solid Earth*, 2021.
- A. Shuler and G. Ekström. Anomalous earthquakes associated with Nyiragongo Volcano: Observations and potential mechanisms. *Journal of Volcanology and Geothermal Research*, 181(3-4):219–230, 2009. ISSN 03770273. doi: <http://doi.org/10.1016/j.jvolgeores.2009.01.011>.
- A. Shuler, G. Ekström, and M. Nettles. Physical mechanisms for vertical-CLVD earthquakes at active volcanoes. *Journal of Geophysical Research: Solid Earth*, 118(4):1569–1586, 2013. ISSN 21699356. doi: <http://doi.org/10.1002/jgrb.50131>.
- R.H. Sibson. A note on fault reactivation. *Journal of Structural Geology*, 7(6):751–754, 1985. ISSN 01918141. doi: [http://doi.org/10.1016/0191-8141\(85\)90150-6](http://doi.org/10.1016/0191-8141(85)90150-6).
- F. Sigmundsson. Calderas collapse as magma flows into rifts. *Science*, 366(6470):1200–1201, 2019. ISSN 10959203. doi: <http://doi.org/10.1126/science.aaz7126>.

- F. Sigmundsson, S. Hreinsdóttir, A. Hooper, T. Árnadóttir, R. Pedersen, M.J. Roberts, N. Óskarsson, A. Auriac, J. Decriem, P. Einarsson, H. Geirsson, M. Hensch, B.G. Ófeigsson, E. Sturkell, H. Sveinbjörnsson, and K.L. Feigl. Intrusion triggering of the 2010 Eyjafjallajökull explosive eruption. *Nature*, 468(7322):426–432, 2010. ISSN 00280836. doi: <http://doi.org/10.1038/nature09558>.
- F. Sigmundsson, A. Hooper, S. Hreinsdóttir, K.S. Vogfjörd, B.G. Ófeigsson, E.R. Heimisson, S. Dumont, M. Parks, K. Spaans, G.B. Gudmundsson, V. Drouin, T. Árnadóttir, K. Jónsdóttir, M.T. Gudmundsson, T. Högnadóttir, H.M. Fridriksdóttir, M. Hensch, P. Einarsson, E. Magnússon, S. Samsonov, B. Brandsdóttir, R.S. White, T. Ágústsdóttir, T. Greenfield, R.G. Green, A.R. Hjartardóttir, R. Pedersen, R.A. Bennett, H. Geirsson, P.C. La Femina, H. Björnsson, F. Pálsson, E. Sturkell, C.J. Bean, M. Möllhoff, A.K. Braiden, and E.P.S. Eibl. Segmented lateral dyke growth in a rifting event at Bárðarbunga volcanic system, Iceland. *Nature*, 517(7533):15, 2014. ISSN 1476-4687. doi: <http://doi.org/10.1038/nature14111>.
- F. Sigmundsson, V. Pinel, R. Grapenthin, A. Hooper, S.A. Halldórsson, P. Einarsson, B.G. Ófeigsson, E.R. Heimisson, K. Jónsdóttir, M.T. Gudmundsson, K. Vogfjörd, M. Parks, S. Li, V. Drouin, H. Geirsson, S. Dumont, H.M. Fridriksdóttir, G.B. Gudmundsson, T.J. Wright, and T. Yamasaki. Unexpected large eruptions from buoyant magma bodies within viscoelastic crust. *Nature Communications*, 11(1), 2020. ISSN 20411723. doi: <http://doi.org/10.1038/s41467-020-16054-6>.
- T. Simkin and K.A. Howard. Caldera collapse in the Galápagos Islands, 1968. *Science*, 169(3944):429–437, 1970. ISSN 00368075. doi: <http://doi.org/10.1126/science.169.3944.429>.
- M. Simons and P.A. Rosen. Interferometric Synthetic Aperture Radar Geodesy. In Gerald Schubert, editor, *Treatise on Geophysics*, volume 3, pages 391–446. Elsevier, Amsterdam, 2007. ISBN 978-0-444-52748-6. doi: <http://doi.org/10.1016/B978-044452748-6.00059-6>.
- M. Simons and P.A. Rosen. Interferometric Synthetic Aperture Radar Geodesy. In Gerald Schubert, editor, *Treatise on Geophysics (Second Edition)*, volume 3, pages 339–385. Elsevier, Oxford, second edition, 2015. ISBN 978-0-444-53803-1. doi: <http://doi.org/10.1016/B978-0-444-53802-4.00061-0>.
- I.P. Skilling. Incremental caldera collapse of Suswa volcano, Gregory Rift Valley, Kenya. *Journal - Geological Society (London)*, 150(5):885–896, 1993. ISSN 0016-7649. doi: <http://doi.org/10.1144/gsjgs.150.5.0885>.
- M. Smith, P.N. Dunkley, A. Deino, L.A.J. Williams, and G.J.H. McCall. Geochronology, stratigraphy and structural evolution of Silali volcano, Gregory Rift, Kenya. *Journal of the Geological Society, London*, 152(2):297–310, 1995. ISSN 0016-7649. doi: <http://doi.org/10.1144/gsjgs.152.2.0297>.
- D. Smittarello, V. Cayol, V. Pinel, J.L. Froger, A. Peltier, and Q. Dumont. Combining InSAR and GNSS to track magma transport at basaltic volcanoes. *Remote Sensing*, 11(19):1–26, 2019. ISSN 20724292. doi: <http://doi.org/10.3390/rs11192236>.

- I.S. Sokolnikoff. *Mathematical Theory of Elasticity*. McGraw-Hill, New York, 1956.
- R. Stephen J. Sparks and Katharine V. Cashman. Dynamic magma systems: Implications for forecasting volcanic activity. *Elements*, 13(1):35–40, 2017. ISSN 18115217. doi: <http://doi.org/10.2113/gselements.13.1.35>.
- R.S.J. Sparks, J. Biggs, and J. W. Neuberg. Monitoring volcanoes. *Science*, 335(6074):1310–1311, 2012. ISSN 10959203. doi: <http://doi.org/10.1126/science.1219485>.
- R.S.J. Sparks, C. Annen, J.D. Blundy, K.V. Cashman, A.C. Rust, and M.D. Jackson. Formation and dynamics of magma reservoirs. 377(2139), 2019. ISSN 1364503X. doi: <http://doi.org/10.1098/rsta.2018.0019>.
- T. Staudacher, V. Ferrazzini, A. Peltier, P. Kowalski, P. Boissier, P. Catherine, F. Lauret, and F. Massin. The April 2007 eruption and the Dolomieu crater collapse, two major events at Piton de la Fournaise (La Réunion Island, Indian Ocean). *Journal of Volcanology and Geothermal Research*, 184(1-2):126–137, 2009. ISSN 03770273. doi: <http://doi.org/10.1016/j.jvolgeores.2008.11.005>.
- K.J. Stephens, S.K. Ebmeier, N.K. Young, and J. Biggs. Transient deformation associated with explosive eruption measured at Masaya volcano (Nicaragua) using Interferometric Synthetic Aperture Radar. *Journal of Volcanology and Geothermal Research*, 344:212–223, 2017. doi: <https://doi.org/10.1016/j.jvolgeores.2017.05.014>.
- D.S. Stevenson and S. Blake. Modelling the dynamics and thermodynamics of volcanic degassing. *Bulletin of Volcanology*, 60(4):307–317, 1998. ISSN 02588900. doi: <http://doi.org/10.1007/s004450050234>.
- J. Stix and T. Kobayashi. Magma dynamics and collapse mechanisms during four historic caldera-forming events. *Journal of Geophysical Research: Solid Earth*, 113(9):1–14, 2008. ISSN 21699356. doi: <http://doi.org/10.1029/2007JB005073>.
- D.R. Stoddart and T.P. Scoffin. Microatolls: Review of form, origin and terminology. *Atoll Res. Bull.*, 228:17, 1979. doi: <https://doi.org/10.5479/si.00775630.224.1>.
- J. Suckale and G. Grünthal. Probabilistic seismic hazard model for Vanuatu. *Bulletin of the Seismological Society of America*, 99(4):2108–2126, 2009. ISSN 00371106. doi: <http://doi.org/10.1785/0120080188>.
- H. Sudhaus and S. Jónsson. Improved source modelling through combined use of InSAR and GPS under consideration of correlated data errors: Application to the June 2000 Kleifarvatn earthquake, Iceland. *Geophysical Journal International*, 176(2):389–404, 2009. ISSN 1365246X. doi: <http://doi.org/10.1111/j.1365-246X.2008.03989.x>.
- D.A. Swanson, T.R. Rose, R.S. Fiske, and J.P. McGeehin. Keanakāko’i Tephra produced by 300 years of explosive eruptions following collapse of Kīlauea’s caldera in about 1500CE. *Journal of Volcanology and Geothermal Research*, 215-216:8–25, 2012. ISSN 03770273. doi: <http://doi.org/10.1016/j.jvolgeores.2011.11.009>.

- D. Sweeney, P.R. Kyle, and C. Oppenheimer. Sulfur dioxide emissions and degassing behavior of Erebus volcano, Antarctica. *Journal of Volcanology and Geothermal Research*, 177(3): 725 – 733, 2008. ISSN 0377-0273. doi: <https://doi.org/10.1016/j.jvolgeores.2008.01.024>. Volcanology of Erebus volcano, Antarctica.
- R.B. Symonds, T.M. Gerlach, and M.H. Reed. Magmatic gas scrubbing: Implications for volcano monitoring. *Journal of Volcanology and Geothermal Research*, 108(1-4):303–341, 2001. ISSN 03770273. doi: [http://doi.org/10.1016/S0377-0273\(00\)00292-4](http://doi.org/10.1016/S0377-0273(00)00292-4).
- S. Tait, C. Jaupart, and S. Vergnolle. Pressure, gas content and eruption periodicity of a shallow, crystallising magma chamber. *Earth and Planetary Science Letters*, 92(1): 107–123, 1989. ISSN 0012821X. doi: [http://doi.org/10.1016/0012-821X\(89\)90025-3](http://doi.org/10.1016/0012-821X(89)90025-3).
- H.K.M. Tanaka, T. Uchida, M. Tanaka, H. Shinohara, and H. Taira. Cosmic-ray muon imaging of magma in a conduit: Degassing process of Satsuma-Iwojima Volcano, Japan. *Geophysical Research Letters*, 36(1):1–5, 2009. ISSN 00948276. doi: <http://doi.org/10.1029/2008GL036451>.
- A. Tarantola. *Inverse problem theory and methods for data fitting and model parameter estimation*. Society for Industrial and Applied Mathematics, 2005.
- J. Tarasewicz, R.S. White, A.W. Woods, B. Brandsdóttir, and M.T. Gudmundsson. Magma mobilization by downward-propagating decompression of the Eyjafjallajkull volcanic plumbing system. *Geophysical Research Letters*, 39(19):1–5, 2012. ISSN 00948276. doi: <http://doi.org/10.1029/2012GL053518>.
- F. W. Taylor, Michael Bevis, B. Schutz, D. Kuang, J. Recy, S. Calmant, D. Charley, M. Regnier, B. Perin, M. Jackson, and C. Reichenfeld. Geodetic measurements of convergence at the New Hebrides Island arc indicate arc fragmentation caused by an impinging aseismic ridge. *Geology*, 23(11):1011–1014, 1995. ISSN 00917613. doi: [http://doi.org/10.1130/0091-7613\(1995\)023<1011:GMOCAT>2.3.CO;2](http://doi.org/10.1130/0091-7613(1995)023<1011:GMOCAT>2.3.CO;2).
- F.W. Taylor, B.L. Isacks, C. Jouannic, A.L. Bloom, and J. Dubois. Coseismic and Quaternary vertical tectonic movements, Santo and Malekula Islands, New Hebrides Island Arc. *Journal of Geophysical Research*, 85(B10):5367–5381, 1980. ISSN 01480227. doi: <http://doi.org/10.1029/JB085iB10p05367>.
- F.W. Taylor, C. Frohlich, J. Lecolle, and M. Strecker. Analysis of partially emerged corals and reef terraces in the central Vanuatu Arc: Comparison of contemporary coseismic and nonseismic with Quaternary vertical movements. *Journal of Geophysical Research*, 92(B6): 4905–4933, 1987.
- F.W. Taylor, P. Mann, M.G. Bevis, R.L. Edwards, H. Cheng, K.B. Cutler, S.C. Gray, G.S. Burr, J.W. Beck, D.A. Phillips, G. Cabioch, and J. Recy. Rapid forearc uplift and subsidence caused by impinging bathymetric features: Examples from the New Hebrides and Solomon arcs. *Tectonics*, 24(6), 2005. ISSN 02787407. doi: <http://doi.org/10.1029/2004TC001650>.

- D. Tedesco, O. Vaselli, P. Papale, S.A. Carn, Mario Voltaggio, G.M. Sawyer, J. Durieux, M. Kasereka, and F. Tassi. January 2002 volcano-tectonic eruption of Nyiragongo volcano, Democratic Republic of Congo. *Journal of Geophysical Research: Solid Earth*, 112(9):1–12, 2007. ISSN 21699356. doi: <http://doi.org/10.1029/2006JB004762>.
- N. Theys, I. De Smedt, H. Yu, T. Danckaert, J. Van Gent, C. Hörmann, T. Wagner, P. Hedelt, H. Bauer, F. Romahn, M. Pedernana, D. Loyola, and M. Van Roozendael. Sulfur dioxide retrievals from TROPOMI onboard Sentinel-5 Precursor: Algorithm theoretical basis. *Atmospheric Measurement Techniques*, 10(1):119–153, 2017. ISSN 18678548. doi: <http://doi.org/10.5194/amt-10-119-2017>.
- Y.S. Touloukian, W.R. Judd, and R.F. Roy. *Physical Properties of Rocks and Minerals*. McGraw Hill, New York, 1981.
- E. Tryggvason. Widening of the Krafla fissure swarm during the 1975-1981 volcano-tectonic episode. *Bulletin Volcanologique*, 47(1):47–69, 1984. ISSN 02588900. doi: <http://doi.org/10.1007/BF01960540>.
- M. Tsukui and Y. Suzuki. Eruptive history of Miyakejima volcano during the last 7000 years. *Bulletin of the Volcanological Society of Japan*, 43(4):149–166, 1998. doi: 10.18940/kazan.43.4_149.
- D. Turcotte and G. Schubert. *Geodynamics*. Cambridge University Press, 3 edition, 2014. doi: 10.1017/CBO9780511843877.
- S.P. Turner, D.W. Peate, C.J. Hawkesworth, S.M. Eggins, and A.J. Crawford. Two mantle domains and the time scales of fluid transfer beneath the Vanuatu arc. *Geology*, 27(11):963–966, 1999. ISSN 00917613. doi: [http://doi.org/10.1130/0091-7613\(1999\)027<0963:TMDATT>2.3.CO;2](http://doi.org/10.1130/0091-7613(1999)027<0963:TMDATT>2.3.CO;2).
- H. Ueda, E. Fujita, M. Ukawa, E. Yamamoto, M. Irwan, and F. Kimata. Magma intrusion and discharge process at the initial stage of the 2000 activity of Miyakejima, Central Japan, inferred from tilt and GPS data. *Geophysical Journal International*, 161(3):891–906, 2005. ISSN 0956540X. doi: <http://doi.org/10.1111/j.1365-246X.2005.02602.x>.
- S. Urbani, V. Acocella, and E. Rivalta. What drives the lateral versus vertical propagation of dikes? Insights From analogue models. *Journal of Geophysical Research : Solid Earth*, 123:3680 – 2697, 2018. doi: <https://doi.org/10.1029/2017JB015376>.
- Volcano Discovery. Ambrym volcano (Vanuatu) field report 1-10 Oct - strong lava lake activity in 3 craters. <https://www.volcanodiscovery.com/ambrym/news/71275/Ambrym-volcano-Vanuatu-field-report-1-10-Oct-strong-lava-lake-activity-in-3-craters.html>, 2018. Accessed: 2020-08-29.
- G.P.L. Walker. Volcanic rift zones and their intrusion swarms. *Journal of Volcanology and Geothermal Research*, 94(1-4):21–34, 1999. ISSN 03770273. doi: [http://doi.org/10.1016/S0377-0273\(99\)00096-7](http://doi.org/10.1016/S0377-0273(99)00096-7).

- T.R. Walter, V. Acocella, M. Neri, and F. Amelung. Feedback processes between magmatic events and flank movement at Mount Etna (Italy) during the 2002 – 2003 eruption. *Journal of Geophysical Research: Solid Earth*, 110(10):1–12, 2005a. ISSN 21699356. doi: <http://doi.org/10.1029/2005JB003688>.
- T.R. Walter, V.R. Troll, B. Cailleau, A. Belousov, H.U. Schmincke, F. Amelung, and P. Bogaard. Rift zone reorganization through flank instability in ocean island volcanoes: An example from Tenerife, Canary Islands. *Bulletin of Volcanology*, 67(4):281–291, 2005b. ISSN 02588900. doi: <http://doi.org/10.1007/s00445-004-0352-z>.
- T. Watanabe, T. Masuyama, K. Nagaoka, and T. Tahara. Analog experiments on magma-filled cracks: Competition between external stresses and internal pressure. *Earth, Planets and Space*, 54(12):1247–1261, 2002. ISSN 18805981. doi: <http://doi.org/10.1186/bf03352453>.
- C. Wauthier, V. Cayol, F. Kervyn, and N. d’Oreye. Magma sources involved in the 2002 Nyiragongo eruption, as inferred from an InSAR analysis. *Journal of Geophysical Research: Solid Earth*, 117(B5), 2012. doi: <https://doi.org/10.1029/2011JB008257>.
- C. Wauthier, V. Cayol, B. Smets, N. D’Oreye, and F. Kervyn. Magma pathways and their interactions inferred from InSAR and stress modeling at Nyamulagira Volcano, D.R. Congo. *Remote Sensing*, 7(11):15179–15202, 2015. ISSN 20724292. doi: <http://doi.org/10.3390/rs71115179>.
- J. Weertman. Theory of water-filled crevasses in glaciers applied to vertical magma transport beneath oceanic ridges. *Journal of Geophysical Research*, 76(5):1171–1183, 1971. doi: <https://doi.org/10.1029/JB076i005p01171>.
- C. Werner, U. Wegmüller, T. Strozzi, and A. Wiesmann. GAMMA SAR and interferometric processing software. *European Space Agency, (Special Publication) ESA SP*, pages 211–219, 2000. ISSN 03796566.
- B. Wessel. TanDEM-X Ground Segment - DEM Products Specification Document. Technical Report 3.1, EOC, DLR, Oberpfaffenhofen, Germany, 2016. URL <https://tandemx-science.dlr.de/>.
- W.S.D. Wilcock, M. Tolstoy, F. Waldhauser, C. Garcia, Y.J. Tan, D.R. Bohnenstiehl, J. Caplan-Auerbach, R.P. Dziak, A.F. Arnulf, and M.E. Mann. Seismic constraints on caldera dynamics from the 2015 Axial Seamount eruption. *Science*, 354(6318):1395–1399, 2016. doi: <http://doi.org/10.1126/science.aah5563>.
- L.A.J. Williams, R. Macdonald, and G.R. Chaptman. Late Quaternary caldera volcanoes of the Kenya Rift Valley. *Journal of Geophysical Research*, 89(4):8553–8570, 1984. doi: <https://doi.org/10.1029/JB089iB10p08553>.
- J.D.N. Winter. *Principles of Igneous and Metamorphic Petrology*. Prentice Hall, 2010. ISBN 9780321681324.

- Y.Q. Wong, P. Segall, A. Bradley, and K. Anderson. Constraining the magmatic system at Mount St. Helens (2004 – 2008) using Bayesian inversion with physics-based models including gas escape and crystallization. *Journal of Geophysical Research: Solid Earth*, 122(10):7789–7812, 2017. ISSN 21699356. doi: <http://doi.org/10.1002/2017JB014343>.
- C.A. Wood. Calderas: a planetary perspective. *Journal of Geophysical Research*, 89(B10): 8391–8406, 1984. ISSN 01480227. doi: <http://doi.org/10.1029/JB089iB10p08391>.
- R.K. Workman and S.R. Hart. Major and trace element composition of the depleted MORB mantle (DMM). *Earth and Planetary Science Letters*, 231(1-2):53–72, 2005. ISSN 0012821X. doi: <http://doi.org/10.1016/j.epsl.2004.12.005>.
- R. Wright and E. Pilger. Radiant flux from Earth’s subaerially erupting volcanoes. *International Journal of Remote Sensing*, 29(22):6443–6466, 2008a. ISSN 13665901. doi: <http://doi.org/10.1080/01431160802168210>.
- R. Wright and E. Pilger. Satellite observations reveal little inter-annual variability in the radiant flux from the Mount Erebus lava lake. *Journal of Volcanology and Geothermal Research*, 177(3):687–694, 2008b. ISSN 03770273. doi: <http://doi.org/10.1016/j.jvolgeores.2008.03.005>.
- R. Wright, M. Blackett, and C. Hill-Butler. Some observations regarding the thermal flux from Earth’s erupting volcanoes for the period of 2000 to 2014. *Geophysical Research Letters*, 42(2):282–289, 2015. ISSN 19448007. doi: <http://doi.org/10.1002/2014GL061997>.
- T.J. Wright. Terrain Motion 2: Volcano Deformation, Models and Examples, 2013.
- T.J. Wright, B.E. Parsons, and Z. Lu. Toward mapping surface deformation in three dimensions using InSAR. *Geophysical Research Letters*, 31(1):1–5, 2004. ISSN 00948276. doi: <http://doi.org/10.1029/2003GL018827>.
- T.J. Wright, C. Ebinger, J. Biggs, A. Ayele, G. Yirgu, D. Keir, and A. Stork. Magma-maintained rift segmentation at continental rupture in the 2005 Afar dyking episode. *Nature*, 442(7100):291–294, 2006. ISSN 14764687. doi: <http://doi.org/10.1038/nature04978>.
- T.J. Wright, F. Sigmundsson, C. Pagli, M. Belachew, I.J. Hamling, B. Brandsdóttir, D. Keir, R. Pedersen, A. Ayele, C. Ebinger, P. Einarsson, E. Lewi, and E. Calais. Geophysical constraints on the dynamics of spreading centres from rifting episodes on land. *Nature Geoscience*, 5(4):242–250, 2012. ISSN 1752-0894. doi: <http://doi.org/10.1038/ngeo1428>.
- X.M. Yang, P.M. Davis, and J.H. Dieterich. Deformation from inflation of a dipping finite prolate spheroid in an elastic half-space as a model for volcanic stressing. *Journal of Geophysical Research*, 93(B5):4249–4257, 1988. ISSN 01480227. doi: <https://doi.org/10.1029/JB093iB05p04249>.
- A. Yokoo, K. Ishii, T. Ohkura, and K. Kim. Monochromatic infrasound waves observed during the 2014–2015 eruption of Aso volcano, Japan. *Earth, Planets and Space*, 71(1), 2019. ISSN 18805981. doi: <http://doi.org/10.1186/s40623-019-0993-y>. URL <https://doi.org/10.1186/s40623-019-0993-y>.

- C. Yu, Z. Li, N.T. Penna, and P. Crippa. Generic atmospheric correction model for Interferometric Synthetic Aperture Radar observations. *Journal of Geophysical Research: Solid Earth*, 123(10):9202–9222, 2018. ISSN 21699356. doi: <http://doi.org/10.1029/2017JB015305>.
- S. Yun, P. Segall, and H. Zebker. Constraints on magma chamber geometry at Sierra Negra Volcano, Galápagos Islands, based on InSAR observations. *Journal of Volcanology and Geothermal Research*, 150(1-3):232–243, 2006. ISSN 03770273. doi: <http://doi.org/10.1016/j.jvolgeores.2005.07.009>.
- A. Zebker, P.A. Rosen, and S. Hensley. Atmospheric effects in Interferometric Synthetic Aperture Radar surface deformation and topographic maps. *Journal of Geophysical Research*, 102(B4):7547–7563, 1997. doi: <https://doi.org/10.1029/96JB03804>.
- H.A. Zebker and J. Villasenor. Decorrelation in interferometric radar echoes. *IEEE Transactions on Geoscience and Remote Sensing*, 30(5):950–959, 1992. ISSN 15580644. doi: <http://doi.org/10.1109/36.175330>.

